

# Paleoceanographic variability on the Agulhas Plateau during the past 150 kyr BP

Miros Stavros James Charidemou

Thesis submitted for the Degree of Doctor of Philosophy

Cardiff University

April 2018



## DECLARATION

This work has not been submitted in substance for any other degree or award at this or any other university or place of learning, nor is being submitted concurrently in candidature for any degree or other award.

Signed ...*Miros Charidemou*..... (candidate) Date ...*3/4/2018*.....

## STATEMENT 1

This thesis is being submitted in partial fulfillment of the requirements for the degree of .....  
**PhD** ...(insert MCh, MD, MPhil, PhD etc, as appropriate)

Signed ...*Miros Charidemou*..... (candidate) Date ...*3/4/2018*.....

## STATEMENT 2

This thesis is the result of my own independent work/investigation, except where otherwise stated, and the thesis has not been edited by a third party beyond what is permitted by Cardiff University's Policy on the Use of Third Party Editors by Research Degree Students. Other sources are acknowledged by explicit references. The views expressed are my own.

Signed ...*Miros Charidemou*..... (candidate) Date ...*3/4/2018*.....

## STATEMENT 3

I hereby give consent for my thesis, if accepted, to be available online in the University's Open Access repository and for inter-library loan, and for the title and summary to be made available to outside organisations.

Signed ...*Miros Charidemou*..... (candidate) Date ...*3/4/2018*.....

## STATEMENT 4: PREVIOUSLY APPROVED BAR ON ACCESS

I hereby give consent for my thesis, if accepted, to be available online in the University's Open Access repository and for inter-library loans **after expiry of a bar on access previously approved by the Academic Standards & Quality Committee.**

Signed ...*Miros Charidemou*..... (candidate) Date ...*3/4/2018*.....

## Thesis Summary

This thesis presents the results of a multi-proxy analysis of two sediment cores recovered from within the Indian-Atlantic Ocean Gateway (I-AOG). The main focus of this study was on sediment core MD02-2588 which was recovered from the southern Agulhas Plateau. This core was used to produce reconstructions of the paleoceanographic variability of the deep and surface ocean during the past 150 kyr BP. Preliminary paleoceanographic records spanning the past 50 kyr BP are also presented from sediment core CD154-23-16P, recovered off southern Africa.

To reconstruct the history of mid-depth ocean circulation on the southern Agulhas Plateau during the past 150 kyr BP, a range of physical and chemical bottom water parameters were derived from the stable isotope, elemental ratio and grain size data from core MD02-2588. These data suggest that, during glacial stages, the southern Agulhas Plateau and the wider mid-depth South Atlantic Ocean came under increased influence of southern-sourced deep waters and experienced an increase in the storage of respired carbon, as CO<sub>2</sub> was sequestered from the glacial atmosphere. The associated decrease in the relative volume of northern-sourced deep waters bathing the MD02-2588 core site appears to be counterbalanced by the lower nutrient content of northern-sourced water masses during glacial stages resulting in an overall reduction of nutrient concentrations in the mid-depth South Atlantic. The glacial lowering of seawater nutrient concentration in the mid-depth South Atlantic was possibly also affected by an increase in the formation of lower-nutrient mid-depth waters by open ocean convection in polynyas within the expanded circum-Antarctic sea ice zone.

During glacial terminations, mid-depth nutrient concentrations with the I-AOG reach their highest values of the past 150 kyr BP. These increases are interpreted as resulting from the upward mixing of nutrient-rich bottom waters from the deepest and most isolated layers in the Southern Ocean following the deglacial breakdown of stratification in the ocean interior. The increases in mid-depth nutrient concentration recorded during deglaciations occur in tandem with increases in the bottom water carbonate saturation state on the southern Agulhas Plateau and increases of *p*CO<sub>2</sub> in Antarctic ice cores. The covariation of these parameters supports the premise of increased outgassing of carbon from the deep Southern Ocean during deglaciations.

This thesis also examines how the position of the subtropical front (STF) within the I-AOG migrated over the past 150 ky BP and considers how these changes may have impacted the nutrient supply to the surface waters of the southern Agulhas Plateau. The record of bulk sediment nitrogen isotope composition ( $\delta^{15}\text{N}_{\text{Bulk}}$ ) from sediment core MD02-2588 suggests that the northward migration of the STF during glacials is associated with increases in nutrient supply relative to interglacial levels. Enhanced nutrient supply to the surface waters of the southern Agulhas Plateau is thought to be caused by increased northward advection of relatively nutrient-rich Subantarctic surface waters to the MD02-2588 core site, along with weaker upper ocean stratification which facilitated vertical mixing of nutrients from the thermocline. The likeness of the  $\delta^{15}\text{N}_{\text{Bulk}}$  record from MD02-2588 with analogous records from the eastern equatorial Pacific may suggest that the temporal variability of the isotopic composition of ocean nitrate within these two regions is linked on glacial-interglacial timescales, possibly as a consequence of changes in the position of the Southern Ocean fronts.

New data from a set of core-top samples collected around New Zealand were used to assess the utility of the deep-dwelling planktonic foraminifera species, *Globorotalia truncatulinoides*, as a recorder of the isotopic composition of dissolved inorganic carbon in seawater. The downcore record of carbon isotopes ( $\delta^{13}\text{C}$ ) in this planktonic foraminifera from MD02-2588 displays a correlation with the Antarctic ice core records of the isotopic composition of carbon in the atmosphere during the past 150 kyr BP. The correlation of these records demonstrates the importance of carbon transfer between the Southern Ocean and the atmosphere.

Preliminary results of the bulk elemental composition and foraminiferal stable isotope records spanning the past 50 kyr BP are presented from sediment core CD154-23-16P, recovered from the Mallory Seamount off southern Africa. These records are used to reconstruct the terrestrial hydroclimate of southeastern Africa and the hydrography of the Agulhas Current.

*Dedicated to John and Charmaine Conlon*

## Acknowledgements

First and foremost, I would like to thank my two supervisors, Ian Hall and Martin Ziegler, for all their support, encouragement and advice during my PhD. They have both been excellent mentors and important role models for me and have played a crucial role in my academic development over the last four years.

I would also like express my gratitude to the paleoclimate technical staff at Cardiff University; Anabel Morte-Ródenas for her assistance with the elemental analyses, Sandra Nederbragt for stable isotope analyses, Lindsey Owen for her help in the lab and Elaine Mawbey for teaching me the foraminiferal cleaning protocols. I thank Ilona Steffen and Heike Eisenlohr for their assistance during their internships at Cardiff. I also extend my gratitude to the academic members of the paleoclimate research group who have all offered me their help and advice at some point or another during my PhD. Special thanks go to Lucas Jonkers and Paola Moffa Sánchez. I thank Markus Kienast for the nitrogen isotope analyses and for his insightful comments and guidance during the interpretation of this dataset. I thank Yair Rosenthal for useful discussions at the Urbino Summer School of Paleoclimatology and for sharing a selection of his sediment core-top materials with me. I thank Samuel Toucanne for inviting me to join my first research cruise onboard the RV L 'Atalante to the Mozambique Channel and for being a great mentor to me during that time. I also thank the rest of the scientific party and the crew of the vessel for making my time at sea a very pleasant experience.

I would also like to say a very big thank you to all my friends and office mates at Cardiff (and beyond) who have made my time here very enjoyable. Doing this PhD has been a great experience and I could not have hoped for a better bunch of people with whom to have shared this with. Special thanks go Robert Gennaro Sposato for being a great friend, housemate and surfing buddy.

I thank my mum, dad, brother and sister for their limitless love and support and I especially thank my grandparents, to whom this work is dedicated, for always being there for me and for always believing in me.

Finally, to Violetta: Thank you for all the love and happiness with which you have filled my life during this time. Thank you for your kindness, your generosity and your patience. Thank you for everything.

The Natural Environment Research Council, U.K. is acknowledged for providing the financial support for this project (studentship NE/K501141/1).

## Commonly used symbols and Abbreviations

AABW	Antarctic Bottom Water
AAIW	Antarctic Intermediate Water
ABR	Agulhas Bank Record
ABS	Agulhas Bank Splice Record
ACC	Antarctic Circumpolar Current
AIM	Antarctic Isotope Maximum
ALF	Agulhas Leakage Fauna
ALK	Alkalinity
AMOC	Atlantic Meridional Overturning Circulation
APF	Polar Front
AR	Agulhas Retroflexion
ARC	Agulhas Return Current
BWT	Bottom Water Temperature
CBR	Cape Basin Record
CDW	Circumpolar Deep Water
CIME	Carbon Isotope Minimum Event
C <sub>org</sub>	Organic Carbon
Cd <sub>sw</sub>	Cadmium dissolved in seawater
DIC	Dissolved Inorganic Carbon
EEP	Eastern Equatorial Pacific
EPICA	European Project for Ice Coring in Antarctica
ESL	Estimated Sea Level
GNAIW	Glacial North Atlantic Intermediate Water
GS	Glacial Stadial
HNLC	High-nutrient, Low-chlorophyll
H	Heinrich Event
I-AOG	Indian-Atlantic Ocean Gateway
IDW	Indian Deep Water
IODP	Integrated/International Ocean Drilling/Discovery Program
IRD	Ice-rafted debris
ITCZ	Intertropical Convergence Zone
IWT	Intermediate Water Temperature

kyr	Thousand years
kyr BP	Thousand years before present
LCDW	Lower Circumpolar Deep Water
LGM	Last Glacial Maximum
LSCW	Lower Southern Component Water
MARGO	Multiproxy Approach for the Reconstruction of the Glacial Ocean surface
MIS	Marine Isotope Stage
MLD	Mixed Layer Depth
MOC	Meridional Overturning Circulation
Myr	Million years
Myr BP	Million years before present
NADW	North Atlantic Deep Water
NCW	Northern Component Waters
ODP	Ocean Drilling Program
OMZ	Oxygen Minimum Zone
$p\text{CO}_2^{\text{atm}}$	Partial pressure of $\text{CO}_2$ in the atmosphere
$p\text{CO}_2^{\text{seawater}}$	Partial pressure of $\text{CO}_2$ in seawater
ppmv	parts per million by volume
RSL	Relative Sea Level
SAF	Subantarctic Front
SAMW	Subantarctic Mode Water
SAZ	Subantarctic Zone
SCW	Southern Component Waters
$\overline{SS}$	Sortable silt mean grain size
SSS	Sea Surface Salinity
SST	Sea Surface Temperature
STF	Subtropical Front
Sv	Sverdrup ( $1 \text{ Sv} = 1 \times 10^6 \text{ m}^3 \text{ s}^{-1}$ )
THC	Thermohaline Circulation
TI, TII, ...	Termination I, Termination II, etc....
TOC	Total Organic Carbon
UCDW	Upper Circumpolar Deep Water
USCW	Upper Southern Component Water

VSMOW	Vienna Standard Mean Ocean Water
VPDB	Vienna Pee Dee Belemnite
XRF	X-ray Fluorescence
YD	Younger Dryas
$\delta^{13}\text{C}_{\text{as}}$	Air-sea fractionation signature of carbon isotope
$\delta^{13}\text{C}_{\text{foram}}$	Foraminiferal carbon isotope ratio (species indicated in subscript)
$\delta^{13}\text{C}_{\text{DIC}}$	Carbon isotope of dissolved inorganic carbon
$\delta^{15}\text{C}_{\text{bulk}}$	Nitrogen isotopic ratio of bulk sedimentary organic nitrogen
$\delta^{15}\text{C}_{\text{nitrate}}$	Nitrogen isotopic ratio of nitrate
$\delta^{18}\text{O}_{\text{foram}}$	Foraminiferal oxygen isotope ratio (species indicated in subscript)
$\delta^{18}\text{O}_{\text{ivc-sw}}$	Ice-volume corrected $\delta^{18}\text{O}$ of Ambient Seawater
$\delta^{18}\text{O}_{\text{sw}}$	$\delta^{18}\text{O}$ of Ambient Seawater
$\delta\text{D}$	Stable Hydrogen Isotope
$\Delta[\text{CO}_3^{2-}]$	Carbonate Saturation State (= $[\text{CO}_3^{2-}]_{\text{in-situ}} - [\text{CO}_3^{2-}]_{\text{saturation}}$ )
$\Delta\delta^{13}\text{C}_{\text{DIC}}$	Vertical carbon isotope gradient of dissolved inorganic carbon
$\Delta\delta^{13}\text{C}_{\text{sp-sp}}$	Carbon isotope gradient between two foraminiferal species
$\Delta\delta^{18}\text{O}_{\text{sp-sp}}$	Oxygen isotope gradient between two foraminiferal species

---

# Table of Contents

---

<b>1</b>	<b>Introduction.....</b>	<b>1</b>
1.1	Late Pleistocene climate variability.....	1
1.2	Carbon transfer and distribution in the global ocean and its impact on $p\text{CO}_2^{\text{atm}}$ .....	4
1.2.1	Basic concepts of marine carbonate chemistry.....	4
1.2.2	The global ocean carbon pump.....	6
1.2.2.1	<i>The impact of the solubility pump and salinity on <math>p\text{CO}_2^{\text{atm}}</math></i> .....	7
1.2.2.2	<i>The biological pumps and their impact on <math>p\text{CO}_2^{\text{atm}}</math></i> .....	9
1.2.3	Terrestrial carbon storage and its impact on $p\text{CO}_2^{\text{atm}}$ .....	13
1.3	The Southern Ocean's role in the glacial-interglacial variability of $p\text{CO}_2^{\text{atm}}$ .....	13
1.3.1	The effects of Southern Ocean biological processes on $p\text{CO}_2^{\text{atm}}$ .....	14
1.3.2	The effects of Southern Ocean physical processes on $p\text{CO}_2^{\text{atm}}$ .....	17
1.4	The low-latitude ocean's role in the glacial-interglacial variability of $p\text{CO}_2^{\text{atm}}$ .....	19
1.4.1	$\text{CaCO}_3/\text{C}_{\text{org}}$ rain ratio.....	19
1.4.2	Silicic acid leakage.....	20
1.5	Global Overturning Circulation.....	22
1.6	The Greater Agulhas System and the Indian-Atlantic Ocean Gateway.....	25
1.7	Aims of this thesis.....	27
1.8	Thesis outline.....	29
<b>2</b>	<b>Paleoceanographic proxies and techniques.....</b>	<b>30</b>
2.1	Foraminiferal stable isotope and elemental geochemistry.....	30
2.1.1	Oxygen isotopic ratios in foraminifera.....	30
2.1.2	Carbon isotopic ratios in foraminifera.....	32
2.1.3	Cd/Ca in foraminifera.....	34
2.1.4	Mg/Ca in foraminifera.....	36
2.1.5	B/Ca in foraminifera.....	38
2.2	Sortable silt mean grain size.....	38
2.3	Nitrogen isotopic ratio of bulk sedimentary organic nitrogen.....	39
2.4	Elemental analysis.....	41
2.5	Radiocarbon dating.....	42
<b>3</b>	<b>Materials and methods.....</b>	<b>43</b>
3.1	Sediment core site locations.....	43
3.1.1	MD02-2588.....	43
3.1.2	CD154-23-16P.....	43
3.1.3	RR03-05 Multicores.....	43
3.2	Sediment core age models.....	48
3.2.1	Age model of sediment core MD02-2588.....	48
3.2.2	Age model of sediment core CD154 23-16P.....	48
3.3	X-ray fluorescence (XRF) core-scanning.....	49
3.3.1	MD02-2588 XRF core-scanning.....	49
3.3.2	CD154-23-16P XRF core-scanning.....	51

3.4	Sediment sampling and processing.....	54
3.5	Stable isotope analysis of foraminiferal calcite .....	55
3.6	Estimating the stable oxygen isotope composition of seawater ( $\delta^{18}\text{O}_{\text{sw}}$ ) from benthic foraminiferal $\delta^{18}\text{O}$ .....	59
3.7	Elemental ratio sample processing and analysis by Inductively Coupled Plasma Mass Spectrometry .....	61
3.7.1	Foraminifera sample processing and elemental ratio analysis.....	61
3.8	Elemental ratio sample processing and analysis by Laser Ablation ICP-MS .....	63
3.9	Elemental ratio data quality evaluation I - contamination from detrital material and diagenetic coatings .....	64
3.9.1	Procedural quality control .....	64
3.9.2	Contaminant screening .....	64
3.9.3	Contaminant monitoring elemental ratios versus target elemental ratios .....	68
3.9.4	LA-ICP-MS results of <i>G. truncatulinoides</i> (s) elemental ratios .....	76
3.9.5	Planktonic versus benthic elemental ratios.....	79
3.9.6	U/Mn of authigenic coatings on foraminiferal tests .....	84
3.9.7	Cd/Mn and Cd/U of authigenic coatings on foraminiferal tests .....	88
3.9.8	Foraminiferal elemental ratios versus stable oxygen isotopic composition .....	92
3.9.9	XRF core-scanning evidence of diagenetic contamination .....	96
3.9.10	Elemental ratio data evaluation for contamination: summary & conclusion .....	99
3.10	Elemental ratio data quality evaluation II – post-depositional dissolution .....	106
3.10.1	Evaluation of post-depositional dissolution of <i>C. wuellerstorfi</i> samples .....	106
3.10.2	Evaluation of post-depositional dissolution of <i>G. truncatulinoides</i> (s.) samples .....	110
3.11	Reconstructing bottom water carbonate ion saturation state from benthic foraminiferal B/Ca.....	112
3.12	Evaluation of <i>C. wuellerstorfi</i> Mg/Ca as a paleotemperature proxy.....	115
3.13	Evaluation of <i>G. truncatulinoides</i> (s) Mg/Ca as a paleotemperature proxy .....	125
3.14	Reconstruction of seawater Cd concentration from foraminiferal Cd/Ca .....	129
3.15	Estimating the air-sea fractionation signature of $\delta^{13}\text{C}_{\text{DIC}}$ from paired benthic foraminiferal Cd/Ca- $\delta^{13}\text{C}$ .....	130
3.16	Sortable silt mean grain size .....	137
3.17	Nitrogen isotopes in bulk sediment .....	140
4	<b>Deep water variability on the southern Agulhas Plateau: implications for ocean circulation in the mid-depth South Atlantic and Southern Ocean during the past 150 kyr BP .....</b>	<b>141</b>
4.1	Chapter Outline .....	141
4.2	Introduction .....	142
4.3	Regional deep water oceanographic setting.....	145
4.4	Materials and methods .....	147
4.5	Results.....	148
4.5.1	Benthic foraminiferal oxygen and carbon isotope records .....	148
4.5.2	Downcore variations of $\delta^{13}\text{C}_{\text{as}}$ .....	149
4.5.3	Benthic foraminiferal B/Ca and carbonate saturation state of seawater .....	152

4.5.4	Benthic foraminiferal Cd/Ca and dissolved Cd concentration in seawater .....	153
4.5.5	Sortable silt mean grain size and changes in bottom-water flow speed.....	154
4.5.6	U/Mn of benthic foraminiferal coatings and bottom water oxygen concentration .....	155
<b>4.6</b>	<b>Discussion .....</b>	<b>156</b>
4.6.1	$\Delta[\text{CO}_3^{2-}]$ variability at the MD02-2588 core site.....	156
4.6.2	$\text{Cd}_{\text{sw}}$ variability at the MD02-2588 core site .....	157
4.6.3	SS and $\Delta U_{\text{g-HOL}}$ variability at the MD02-2588 core site .....	161
4.6.4	U/Mn and bottom water oxygen variability at the MD02-2588 core site .....	162
4.6.5	Glacial versus interglacial bottom water characteristics on the Agulhas Plateau .....	163
4.6.6	Processes driving the glacial-interglacial variability of bottom waters on the Agulhas Plateau	172
4.6.7	Interpretation of the glacial-interglacial bottom water variability on the Agulhas Plateau	178
<b>4.7</b>	<b>Conclusion .....</b>	<b>184</b>
<b>5</b>	<b>Changes in upper ocean nutrient supply on the Agulhas Plateau linked to meridional migrations of the subtropical front during the past 150 kyr BP ....</b>	<b>186</b>
5.1	Chapter outline .....	186
5.2	Introduction .....	187
5.3	Previous work .....	192
5.4	Materials and methods .....	194
5.5	Results.....	195
5.5.1	Planktonic foraminiferal oxygen isotope record.....	195
5.5.2	Bulk sediment nitrogen isotope record ( $\delta^{15}\text{N}_{\text{Bulk}}$ ).....	197
5.5.3	U/Mn ratios of authigenic coatings on foraminiferal tests .....	198
5.6	Discussion .....	199
5.6.1	Evidence for migration of the subtropical front over the Agulhas Plateau .....	199
5.6.2	Nutrient utilisation in the surface waters of the southern Agulhas Plateau .....	203
5.6.2.1	<i>Factors influencing the <math>\delta^{15}\text{N}_{\text{Bulk}}</math> record in sediment core MD02-2588</i> .....	203
5.6.2.2	<i>Interpretation of the <math>\delta^{15}\text{N}_{\text{Bulk}}</math> record from sediment core MD02-2588</i> .....	206
5.6.3	Links between downcore $\delta^{15}\text{N}_{\text{Bulk}}$ variation on the Agulhas Plateau and the eastern equatorial Pacific .....	211
5.7	Conclusion .....	215
<b>6</b>	<b>Carbon isotopic composition of <i>Globorotalia truncatulinoides</i>: application as a proxy of the soft-tissue biological pump and of air-sea gas exchange in the Southern Ocean .....</b>	<b>217</b>
6.1	Chapter outline .....	217
6.2	Introduction .....	218
6.3	Materials and methods .....	221
6.3.1	<i>Globorotalia truncatulinoides</i> .....	222
6.3.1.1	<i>Species description</i> .....	222
6.3.1.2	<i>Evolution and migration</i> .....	222
6.3.1.3	<i>Depth habitat and life cycle</i> .....	223
6.3.1.4	<i>G. truncatulinoides in paleoceanography</i> .....	225
6.3.2	Core-top materials and methodology .....	228

6.3.2.1	<i>Sampling strategy</i> .....	228
6.3.2.2	<i>Estimating calcification depths</i> .....	228
6.3.3	Downcore materials and methodology.....	236
<b>6.4</b>	<b>Results and discussion</b> .....	<b>236</b>
6.4.1	Core-top $\delta^{13}\text{C}_{\text{G.trunc}}$ results.....	236
6.4.2	Downcore $\delta^{13}\text{C}_{\text{G.trunc}}$ results.....	239
6.4.3	Thermodynamic influences on down-core $\delta^{13}\text{C}_{\text{G.trunc(s)}}$ .....	240
6.4.4	Southern Ocean air-sea gas exchange during the past 150 kyr BP.....	245
6.4.4.1	<i>Links between the downcore records of carbon isotopic composition of foraminifera from MD02-2588 and the ice core records of <math>\delta^{13}\text{C}_{\text{atm}}</math></i> .....	245
6.4.4.2	<i>Southern Ocean carbon dioxide leakage and <math>\delta^{13}\text{C}_{\text{G.trunc(s)}}</math></i> .....	250
<b>6.5</b>	<b>Conclusion</b> .....	<b>254</b>
<b>7</b>	<b>Preliminary study of marine sediment core CD154-23-16P: elemental composition and initial stable isotope stratigraphy</b> .....	<b>256</b>
7.1	Chapter outline.....	256
7.2	Introduction.....	256
7.3	Material and Methods.....	257
7.3.1	Sediment core CD154-23-16P: retrieval and sampling.....	257
7.3.2	XRF core scanning.....	259
7.3.3	Stable oxygen and carbon isotope analysis.....	259
7.3.4	Age model.....	260
7.4	Preliminary results and discussion.....	268
7.4.1	Fe/K results.....	268
7.4.2	Interpretation of the Fe/K record from CD154-23-16P.....	270
7.4.3	Stable oxygen and carbon isotope results.....	273
7.4.4	Assessment of the stable oxygen and carbon isotope records from CD154-23-16P....	276
7.4.4.1	<i>Stable oxygen isotopes</i> .....	276
7.4.4.2	<i>Stable carbon isotopes</i> .....	280
7.5	Conclusion.....	285
<b>8</b>	<b>Conclusions and future work</b> .....	<b>289</b>
8.1	Deep water variability in the Indian-Atlantic Ocean Gateway during the past 150 kyr BP	289
8.2	Changes in surface ocean nutrient utilisation in Indian-Atlantic Ocean Gateway during the past 150 kyr BP.....	290
8.3	Carbon isotopic composition of <i>Globorotalia truncatulinoides</i> and applications as a proxy of the soft-tissue biological pump and of air-sea gas exchange in the Southern Ocean	291
8.4	Preliminary study of marine sediment core CD154-23-16P.....	292
8.5	Future work.....	295
	<b>Appendix</b> .....	<b>298</b>
	<b>References</b> .....	<b>i</b>



---

# 1 Introduction

---

## 1.1 Late Pleistocene climate variability

Since the intensification of Northern Hemisphere glaciation (INHG), about 2.7 million years before present (Myr BP), Earth's climate has been characterised by a repeated pattern of glacials (cold intervals with large Northern Hemisphere ice sheets) and interglacials (warmer intervals with much smaller Northern Hemisphere ice sheets, similar to their modern size) (Fig. 1.1) (e.g. Lisiecki and Raymo, 2005; Jouzel *et al.*, 2007). This cyclical climatic behaviour is ultimately driven by changes in the Earth's orbital parameters, with characteristic frequencies of approximately 100, 41 and 23 thousand years (kyr) (Hays *et al.*, 1976; Berger, 1988; Paillard, 2001). However, this orbital forcing alone is unable to explain neither the large amplitude of glacial-interglacial cycles nor the abruptness of transitions from one state to another. A mechanism of positive feedbacks within the climate system must therefore be operating to amplify the orbital signal.

The recognition that the atmospheric partial pressure of CO<sub>2</sub> ( $p\text{CO}_2^{\text{atm}}$ ), as recorded in Antarctic ice cores, has oscillated between values of 170-190 part per million by volume (ppmv) during peak glacials, to 250-300 ppmv during peak interglacials during the past 800 ka, suggests a close coupling between climate and  $p\text{CO}_2^{\text{atm}}$  (Neftel *et al.*, 1982; Barnola *et al.*, 1987; Jouzel *et al.*, 1993; Petit *et al.*, 1999; Siegenthaler *et al.*, 2005, Lüthi *et al.*, 2008) (Fig. 1.1). The general pattern that arises from these  $p\text{CO}_2^{\text{atm}}$  records is of a gradual decline from high interglacial to low glacial levels over tens of thousands of years, punctuated by rapid (millennial timescale) fluctuations (Neftel *et al.*, 1988; Indermühle *et al.*, 2000) and episodes of rapid decline (Ahn and Brook, 2008);  $p\text{CO}_2^{\text{atm}}$  then rises abruptly during glacial terminations on a timescale of only a few thousand years (Monnin *et al.*, 2001) (Fig. 1.1). The timescales associated with the glacial-interglacial climate cycles and the intervening millennial-scale fluctuations has long been suggested to indicate the dominant role of oceanic processes in  $p\text{CO}_2^{\text{atm}}$  change, as the deep ocean is the only reservoir of CO<sub>2</sub> that is large enough and with a fast enough atmospheric equilibration time to explain orbital and millennial-scale  $p\text{CO}_2^{\text{atm}}$  change (Broecker, 1982).

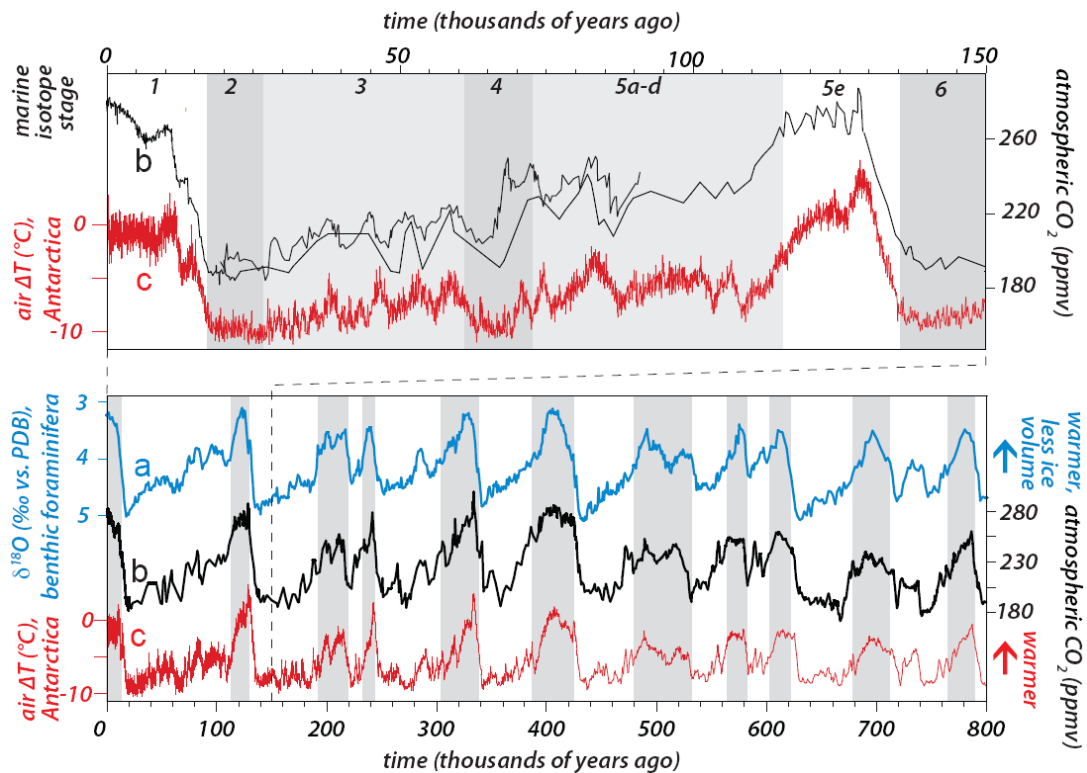


**Figure 1.1.** The history of ice age cycles, atmospheric CO<sub>2</sub> and Antarctic temperature (Hain *et al.*, 2014). A) Stable oxygen isotopes ( $\delta^{18}\text{O}$ ) measured in benthic foraminiferal calcite tests reflecting changes in global ice volume and deep ocean temperature (Lisiecki and Raymo, 2005). B) Atmospheric CO<sub>2</sub> recorded in ice cores from Antarctica (Petit *et al.*, 1999; Indermühle *et al.*, 2000; Monnin *et al.*, 2001; Raynaud *et al.*, 2005; Siegenthaler *et al.*, 2005; Ahn and Brook, 2007, 2008; Lüthi *et al.*, 2008). C) Antarctic ice core temperature reconstructed from the ratio of deuterium to hydrogen of ice (Jouzel *et al.*, 2007). Vertical grey bars in the lower panel represent the full-interglacial stages of the past 800 kyr BP. In the upper panel, which shows the detail in the records during the last 150 kyr BP, full interglacial stages are shown as vertical white bars and full-glacial stages are shown as the darker-grey vertical bars. The lighter-grey bars represent intermediate states. The numbering system in the upper panel refers to the Marine Isotope Stage (MIS) number.

Studies of the phase relationship reveals that, on orbital timescales,  $p\text{CO}_2^{\text{atm}}$  and Antarctic temperature vary synchronously, whereas the stable oxygen isotopic ratio ( $\delta^{18}\text{O}$ ) of benthic foraminifera (a proxy for global ice volume) (Lisiecki and Raymo, 2005) lags behind by several thousand years (Broecker and Henderson, 1998; Shackleton, 2000) (Fig. 1.1). This suggests, first of all, that  $p\text{CO}_2^{\text{atm}}$  is a primary modulator of glacial-interglacial climate change and is directly associated with the waxing and waning of Northern Hemisphere ice sheets. It also indicates that during deglaciations the Southern Hemisphere leads over the North, and hence processes acting in the Southern Hemisphere are driving these changes. On shorter timescales it becomes more difficult to distinguish the leads and lags between the two hemispheres due to the operation of the ‘bipolar seesaw’ whereby records of temperature from each hemisphere are out of phase (e.g. warming in Antarctica/cooling in North Atlantic) (Broecker, 1998). Evidence has been put forward to suggest that rapid changes in temperature during the last deglaciation were in fact instantaneous in both hemispheres and of opposite sign (Barker *et al.*, 2009). Though Northern Hemisphere climate appears to be more tightly coupled with the South on millennial timescales (primarily via reconfigurations of the Atlantic meridional overturning circulation (AMOC), southern oceanic processes seem to dictate the direction of climate change through the slower uptake and release of heat and  $\text{CO}_2$  (Barker *et al.*, 2009).

The importance of the deep ocean  $\text{CO}_2$  reservoir and its communication with the atmosphere via the high-latitude surface oceans, especially the Southern Ocean, was recognised early in the study of glacial-interglacial  $p\text{CO}_2^{\text{atm}}$  change through its effect on the efficiency of the biological pump (Sarmiento and Toggweiler, 1984; Siegenthaler and Wenk, 1984; Knox and McElroy, 1984). In the modern Southern Ocean,  $\text{CO}_2$ - and nutrient-rich deep waters are brought to the surface by wind-driven upwelling, but the incomplete utilisation of the available macronutrients (nitrate and phosphate) results in excess  $\text{CO}_2$  in the surface mixed layer that is not consumed during photosynthesis and which consequently escapes to the atmosphere. Three main processes in the Southern Ocean have been identified that may reduce this leak of  $\text{CO}_2$  during glacials: (1) more efficient consumption of surface macronutrients by marine biota (Francois *et al.*, 1997; Martin, 1990), (2) a reduction in Southern Ocean ventilation such that the exchange between surface waters with the deep ocean was limited

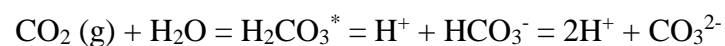
(Francois *et al.*, 1997; Toggweiler, 1999) and (3) an increase in sea ice coverage, reducing the sea-air flux of CO<sub>2</sub> at the ocean surface (Stephens and Keeling, 2000). Additionally, changes in Southern Ocean nutrient consumption may provoke changes in the export of calcium carbonate (CaCO<sub>3</sub>) relative to that of organic matter on a global scale (primarily in the low latitude ocean) which can lead to large changes in  $p\text{CO}_2^{\text{atm}}$  through the process of CaCO<sub>3</sub> compensation (Archer and Maier-Reimer, 1994; Sigman *et al.*, 1998; Archer *et al.*, 2000).

## 1.2 Carbon transfer and distribution in the global ocean and its impact on $p\text{CO}_2^{\text{atm}}$

### 1.2.1 Basic concepts of marine carbonate chemistry

In order to understand the global ocean carbon pump (see Section 1.2.2) and its impact on  $p\text{CO}_2^{\text{atm}}$  it is useful to introduce the following theory of marine carbonate chemistry based on the simplifications and approximations developed by Broecker and Peng (1982), Zeebe and Wolf-Gladrow (2001) and Sarmiento and Gruber (2006).

When CO<sub>2</sub> molecules diffuse into seawater, some react to produce carbonic acid (H<sub>2</sub>CO<sub>3</sub>), but most occur as hydrated CO<sub>2</sub>, where each CO<sub>2</sub> molecule is surrounded by molecules of water. However, due to the analytical difficulties involved with distinguishing between hydrated CO<sub>2</sub> and H<sub>2</sub>CO<sub>3</sub>, it is common to refer to them both as carbonic acid (here symbolised by an asterisk, H<sub>2</sub>CO<sub>3</sub><sup>\*</sup>). H<sub>2</sub>CO<sub>3</sub><sup>\*</sup> subsequently deprotonates (i.e. loses a hydrogen ion (H<sup>+</sup>)) into a bicarbonate-ion (HCO<sub>3</sub><sup>-</sup>) and a carbonate-ion (CO<sub>3</sub><sup>2-</sup>) which together greatly increase the concentration of dissolved inorganic carbon (DIC) in seawater and also partly explains why the ocean carbon reservoir is so much larger than that of the atmosphere. The marine carbonate system is expressed as:



Eq.1.1

where carbon dissolved in seawater ((g) denotes the gaseous form) achieves a state of dynamic chemical equilibrium between  $p\text{CO}_2^{\text{atm}}$  and the three dissolved inorganic compounds. The total amount of DIC is therefore the sum of:

$$\text{DIC} = [\text{H}_2\text{CO}_3^*] + [\text{HCO}_3^-] + [\text{CO}_3^{2-}]$$

Eq.1.2

where square brackets denote concentration. However, as the majority of DIC occurs as  $\text{HCO}_3^-$  and  $\text{CO}_3^{2-}$ , it is possible to simplify equation 1.2 as:

$$\text{DIC} \approx [\text{HCO}_3^-] + [\text{CO}_3^{2-}]$$

Eq.1.3

An equally important parameter in marine carbonate chemistry is alkalinity (ALK). This is the amount of strong acid that needs to be added to fully protonate (i.e. gain  $\text{H}^+$ )  $\text{HCO}_3^-$  and  $\text{CO}_3^{2-}$ . By simplifying this parameter to purely the carbonate alkalinity (i.e., only involving carbonate compounds) it is possible to use the following expression:

$$\text{ALK} \approx [\text{HCO}_3^-] + 2[\text{CO}_3^{2-}]$$

Eq.1.4

Combining equations 1.3 and 1.4 allows the following rearrangements to be made:

$$[\text{HCO}_3^-] \approx 2 \text{ DIC} - \text{ALK}$$

Eq.1.5

$$[\text{CO}_3^{2-}] \approx \text{ALK} - \text{DIC}$$

Eq.1.6

Furthermore, the partial pressure of CO<sub>2</sub> in the seawater ( $PCO_2^{\text{seawater}}$ ) can be related to variations in  $[HCO_3^-]$  and  $[CO_3^{2-}]$ , and the three equilibrium constants  $k_0$ ,  $k_1$  and  $k_2$  (dependent on temperature, salinity and pressure, respectively) as:

$$PCO_2^{\text{seawater}} = \frac{k_0}{k_1 \cdot k_2} \cdot \frac{[HCO_3^-]^2}{[CO_3^{2-}]}$$

Eq.1.7

and using equations 1.5 and 1.6 this approximates as:

$$PCO_2^{\text{seawater}} \approx \frac{k_0}{k_1 \cdot k_2} \cdot \frac{(2 \cdot \text{DIC} - \text{ALK})}{\text{ALK} - \text{DIC}}$$

Eq.1.8

From equation 1.8 it is possible to see how variations in DIC and ALK can drive a change in  $PCO_2^{\text{seawater}}$ . Essentially, an increase in DIC or a decrease in ALK causes an increase in  $PCO_2^{\text{seawater}}$ , while a decrease in DIC or an increase in ALK causes a decrease in  $PCO_2^{\text{seawater}}$  (Fig. 1.2).

### 1.2.2 The global ocean carbon pump

The global ocean is characterised by a pervasive DIC gradient between the surface mixed layer and the deep ocean that is actively maintained by the continuous operation of the so-called global ocean carbon pump (Volk and Hoffert, 1985). The global ocean carbon pump is a system composed of three distinctive pumps all of which operate to vertically redistribute DIC and ALK within the ocean (Fig. 1.3). Two of these pumps are biologically-driven and have been termed the ‘soft-tissue carbon pump’ and the ‘carbonate counter pump’, and are both due to the action of marine organisms that remove DIC from the surface waters during the formation of organic particles and calcium carbonate particles, respectively. These particles are then transported to the ocean interior, carrying with them the DIC from the surface ocean. The third pump termed the ‘solubility pump’ refers to the process of pumping DIC into the ocean interior due to the temperature gradient between the warm surface waters and cold deep

ocean. Carbon dioxide solubility increases as temperature decreases and therefore the surface-to-deep temperature gradient results in greater storage of DIC in the cold, deep ocean reservoir. Below we examine the impact of these pumps on  $p\text{CO}_2^{\text{atm}}$ .

#### 1.2.2.1 *The impact of the solubility pump and salinity on $p\text{CO}_2^{\text{atm}}$*

The solubility pump is perhaps the most straight forward and best constrained in terms of its effect on glacial-interglacial  $p\text{CO}_2^{\text{atm}}$  variability. The simple fact that  $\text{CO}_2$  solubility increases with decreasing temperature means that cold surface waters at high latitudes can take up a larger amount of DIC relative to the warm low-latitude surface ocean. From equation 1.8, it is apparent that the greater DIC capacity of cold surface waters in high latitudes and the subsequent formation of deep water masses that fill the voluminous ocean interior, drives the transfer of DIC from the polar surface waters into the deep ocean. The reduction of DIC in the surface causes a decrease in  $P\text{CO}_2^{\text{sea-water}}$  (Fig. 1.2), and an equivalent decrease in  $p\text{CO}_2^{\text{atm}}$ . The solubility pump is therefore dependent both on the solubility of  $\text{CO}_2$  due to the temperature of the surface ocean, but also on the volume of ocean ventilated by cold, deep water masses. If the volume-averaged temperature of the glacial ocean was lower than the interglacial ocean, then the sequestration of  $p\text{CO}_2^{\text{atm}}$  via the solubility pump may explain some the variability observed in ice cores (Petit *et al.*, 1999; Siegenthaler *et al.*, 2005; Lüthi *et al.*, 2008). Despite uncertainties in the reconstruction of sea surface temperature (SST), especially from low-latitude sites (e.g. CLIMAP Project Members, 1976, 1981 vs Guilderson *et al.*, 1994), estimates of mean ocean glacial-interglacial temperature change (Headly and Severinghaus, 2007) suggest that temperature, via the solubility pump, was responsible for a 30 ppmv reduction of the total glacial-interglacial  $p\text{CO}_2^{\text{atm}}$  change (Sigman and Boyle, 2000).

However, the increase in ice age salinity (Adkins *et al.*, 2002) due to the storage of freshwater on land as vast ice sheets causes an opposing effect on  $p\text{CO}_2^{\text{atm}}$ . Taking account of the salinity dependence of  $p\text{CO}_2^{\text{atm}}$  alone produces a reduction of 6.5 ppmv (Sigman and Boyle, 2000). In addition to this direct salinity effect, the increase in the total concentration of ocean DIC and ALK (a result of removing freshwater with no ALK and minimal DIC), causes a total decrease of 18 ppmv (Sarmiento and Gruber, 2006), substantially reducing the temperature effect on  $p\text{CO}_2^{\text{atm}}$ .

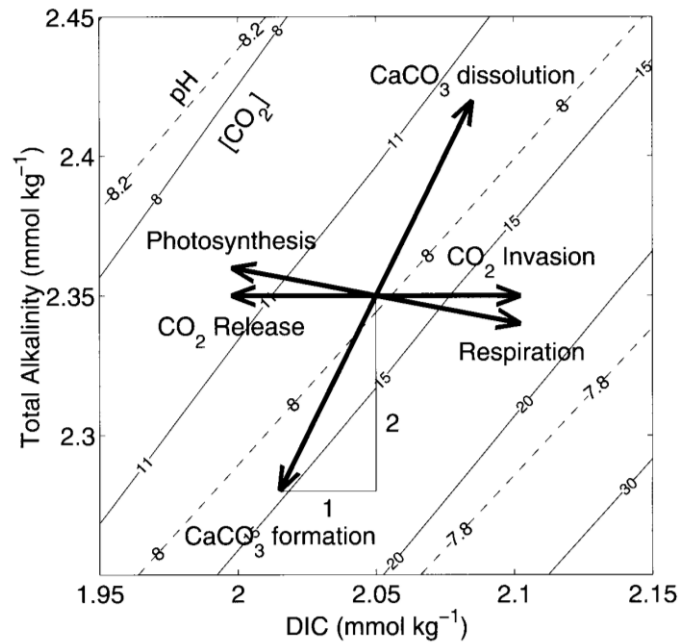


**Figure 1.2.** Effect of various processes on dissolved inorganic carbon (DIC) and total alkalinity (TA) (as indicated by arrows). Solid and dashed lines indicate levels of constant dissolved  $\text{CO}_2$  (in  $\mu\text{mol kg}^{-1}$ ) and  $\text{pH}$ , respectively, as a function of DIC and TA.  $\text{CaCO}_3$  formation, for example reduces DIC by one and TA by two units, therefore driving the system to higher  $\text{CO}_2$  levels and lower  $\text{pH}$ . Invasion of atmospheric  $\text{CO}_2$  into the ocean increases DIC, while release of  $\text{CO}_2$  to the atmosphere has the opposite effect. TA stays constant in these two cases. See section 1.2.1 of main text. Figure taken from Zeebe and Wolf-Gladrow (2001). When considering the process of  $\text{CaCO}_3$  compensation the arrow indicating ‘ $\text{CaCO}_3$  dissolution’ can be substituted for ‘ $\text{CaCO}_3$  supply’ to the ocean from the weathering of exhumed carbonate rocks on land. Similarly, the arrow indicating ‘ $\text{CaCO}_3$  formation’ can be substituted for ‘ $\text{CaCO}_3$  burial’ in seafloor sediments.

So, despite the fact that the solubility pump may account for 35% of the surface to deep DIC gradient (Toggweiler et al., 2003a), the magnitude of the temperature and salinity changes from glacial to interglacials can only account for a small portion of the total change in  $p\text{CO}_2^{\text{atm}}$ . An even smaller effect is predicted on shorter timescales, such as during the rapid temperature oscillations that characterise the last glacial (NGRIP, 2004; EPICA, 2006; Jouzel *et al.*, 2007). While these temperature fluctuations may have been of adequate magnitude (especially in the Northern Hemisphere) to affect the uptake and release of  $\text{CO}_2$  through the solubility pump, this effect would certainly have been subdued by the smaller volume of the ocean interior filled by North Atlantic-derived deep waters (e.g. Lynch-Stieglitz et al., 2007)

#### 1.2.2.2 *The biological pumps and their impact on $p\text{CO}_2^{\text{atm}}$*

The biological pump refers to the formation of organic and inorganic carbon by marine biota in the sunlit surface ocean (euphotic zone) and its subsequent removal as it sinks into the ocean interior where it is remineralised (Volk and Hoffert, 1985) (Fig. 1.3). As mentioned above, it is separated into two components, the organic ‘carbon pump’ also referred to as the ‘soft-tissue biological pump’, and the inorganic ‘carbonate counter pump’; these two components of the biological pump have opposing effects on  $p\text{CO}_2^{\text{atm}}$ .

The formation of  $\text{C}_{\text{org}}$  in the euphotic zone extracts DIC and nutrients (phosphate and nitrate) from the surface ocean causing DIC and hence  $\text{PCO}_2^{\text{seawater}}$  to decline (Fig. 1.2). The downward flux (pumping) of  $\text{C}_{\text{org}}$  is oxidised at intermediate depth (Fig. 1.3), releasing DIC and nutrients to the ocean interior and causing an increase in deep water  $\text{PCO}_2^{\text{seawater}}$  (Fig. 1.2). The small release of nitrate during  $\text{C}_{\text{org}}$  oxidation causes a slight decrease in ALK (nitrate is a negatively charged anion) and a further minor increase in deep water  $\text{PCO}_2^{\text{seawater}}$  (Fig. 1.2).

The carbonate pump involves phytoplankton species that precipitate  $\text{CaCO}_3$  tests. These species extract ALK in addition to DIC from the surface ocean and release it into the ocean interior during dissolution both in the water column and on the seafloor with the removal and addition of ALK and DIC occurring in a 2:1 ratio in terms of the global average (Fig. 1.2). From equation 1.8 it can be seen that the net effect of  $\text{CaCO}_3$  precipitation is an increase of surface water  $\text{PCO}_2^{\text{seawater}}$  (and hence  $p\text{CO}_2^{\text{atm}}$ ), while the net effect during  $\text{CaCO}_3$  dissolution is a decrease of surface water

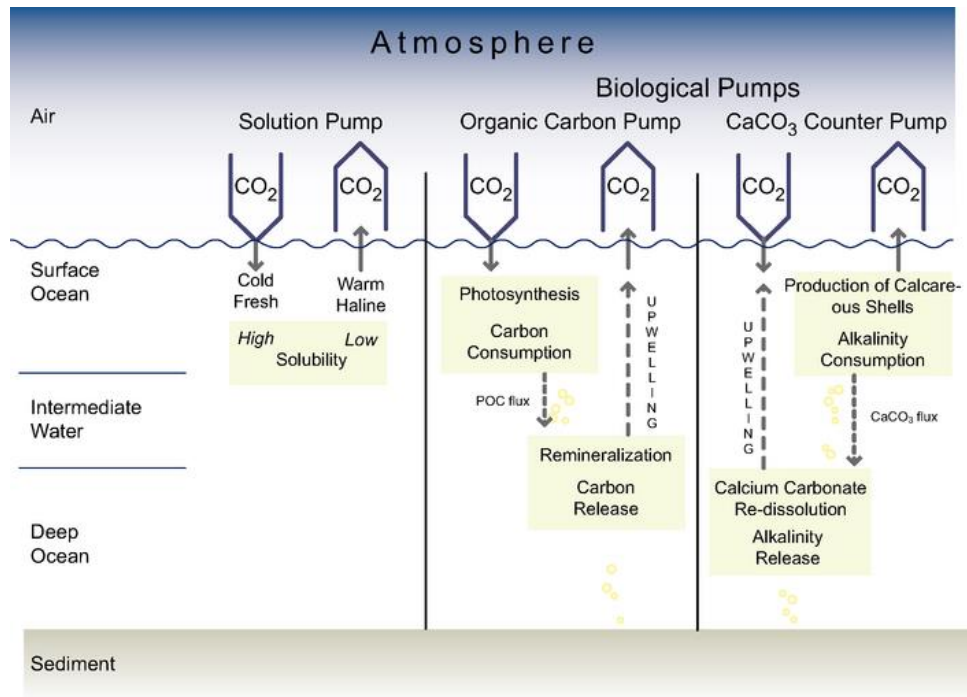


**Figure 1.3.** The three main ocean carbon pumps: the solubility pump, the organic carbon pump, also referred to as the soft-tissue biological pump, and the inorganic carbonate (CaCO<sub>3</sub>) counter pump (original figure of Heinze *et al.*, 1991; modified figure from Intergovernmental Panel on Climate Change (IPCC) Fourth Assessment Report, 2007).

$p\text{CO}_2^{\text{seawater}}$  (Fig. 1.2). Another aspect of the carbonate pump, which is especially important for understanding glacial-interglacial  $p\text{CO}_2^{\text{atm}}$ , is ‘ $\text{CaCO}_3$  compensation’ (Broecker, 1987). This process, which operates on a multi-millennial timescale, involves the balance between the supply of  $\text{CaCO}_3$  to the ocean from the weathering of exhumed carbonate rocks on land, and the burial of  $\text{CaCO}_3$  in seafloor sediments. An increase in the supply of  $\text{CaCO}_3$  to the oceans causes a decrease in  $p\text{CO}_2^{\text{atm}}$ , whereas an increase in burial causes an increase in  $p\text{CO}_2^{\text{atm}}$  (Fig. 1.2; when considering the process of  $\text{CaCO}_3$  compensation the arrows of  $\text{CaCO}_3$  dissolution and formation in fig. 1.2 can be substituted for  $\text{CaCO}_3$  supply and burial, respectively).

The effect of the organic carbon pump on  $p\text{CO}_2^{\text{atm}}$  depends on its efficiency, which is often quantified by the proportion of ‘preformed’ versus ‘regenerated’ nutrients in the ocean interior (e.g. Sigman *et al.*, 2010) (Fig. 1.4). Regenerated nutrients refer to the nutrients that are derived from the oxidation of organic matter that has been removed from the surface ocean during biological export. Hence, the presence of regenerated nutrients in the ocean interior indicates the sequestration of  $\text{CO}_2$  from the surface. On the other hand, preformed nutrients are those nutrients which were not utilised by phytoplankton in the surface and were returned to the ocean interior without contributing to the formation of new biomass. The presence of preformed nutrients in the ocean interior is therefore an indication of the amount of  $\text{CO}_2$  released to the atmosphere and thus, the ratio of regenerated to preformed nutrients can be used to determine the efficiency of the biological pump.

Nutrients brought up to the low-latitude surface ocean are completely utilised by phytoplankton, imposing a strong regenerated nutrient status to the low-latitude surface waters. These waters are eventually incorporated into North Atlantic Deep Water (NADW) and thus sequester  $\text{CO}_2$  into the deep ocean during the downwelling of this major water mass (Toggweiler *et al.*, 2003b) (Fig. 1.4). In the Southern Ocean, phytoplankton are unable to fully utilise the vast quantities of upwelled nutrients and hence the bottom waters that are returned to depth result in a high preformed nutrient concentration in the ocean interior allowing  $\text{CO}_2$  to escape to the atmosphere (Fig. 1.4).

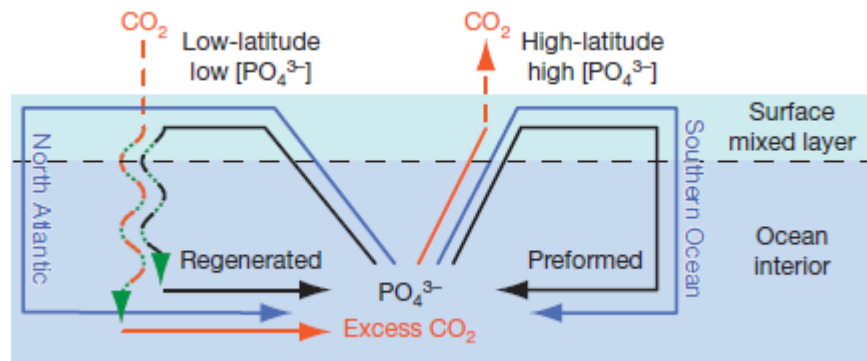


**Figure 1.4.** Schematic diagram of the regenerated and preformed nutrient cycles of the soft-tissue biological pump (from Sigman *et al.*, 2010). The blue, black and orange lines show the transport of water, major nutrients (represented by phosphate,  $\text{PO}_4^{3-}$ ), and  $\text{CO}_2$ , respectively. The solid, wavy and dashed lines indicate transport by water flow, sinking organic matter and air-sea exchange, respectively. The loop on the left shows the high efficiency imparted to the soft-tissue biological pump by the low-latitude, low-nutrient surface ocean. Here, nutrients from the subsurface ocean are completely utilised during the biological assimilation of the major nutrients nitrate and phosphate during the production of organic matter. This then sinks into the ocean interior where is decomposed to ‘regenerated’ nutrients and excess  $\text{CO}_2$  ( $\text{CO}_2$  added by the regeneration of organic matter). The loop on the right shows the low-efficiency imparted to the soft-tissue biological pump by the high-latitude, high-nutrient surface region of the Southern Ocean. Here, nutrient-rich and excess  $\text{CO}_2$ -rich water is upwelled to the surface and is subducted again with most of its dissolved nutrient remaining unutilised (‘preformed’ nutrient). This loop releases  $\text{CO}_2$  to the atmosphere that had been sequestered by the regenerated nutrient loop.

### 1.2.3 Terrestrial carbon storage and its impact on $p\text{CO}_2^{\text{atm}}$

The carbon isotopic ratio ( $\delta^{13}\text{C}$ ) in benthic foraminifera is reported to have been  $\sim 0.4\%$  lower during glacial times compared to its present value (Shackleton, 1977; Curry *et al.*, 1988). This has been interpreted as indicating the addition of an isotopically depleted terrestrial carbon source to the oceans during these times. This transfer of terrestrial carbon to the oceans is likely to have been a consequence of the reduction in the size of the terrestrial biosphere due to the growth of large ice sheets on the northern continents, in conjunction with a reduction of soil organic carbon storage and sedimentary carbon storage on exposed continental shelves. Initially this addition of carbon to the ocean/atmosphere reservoir would have caused an increase in  $p\text{CO}_2^{\text{atm}}$  of 40-45 ppmv followed by a reduction to 15-17 ppmv after  $\text{CaCO}_3$  compensation (see section 1.2.2.2 and fig. 1.2) (Archer *et al.*, 2000; Sigman and Boyle, 2000). Therefore, any model- or data-based study that seeks to explain glacial-interglacial  $p\text{CO}_2^{\text{atm}}$  variability must also be able to account for this source of carbon, in addition to the observed change recorded in ice cores (e.g. Petit *et al.*, 1999).

It is important to note that the dependence of the terrestrial carbon transfer on global ice volume and sea level change suggests that this carbon reservoir should lag behind any  $p\text{CO}_2^{\text{atm}}$  changes during glacial terminations (and inceptions) due to the slower response time of ice sheets to climatic perturbations. This may suggest that on millennial and sub-millennial timescales this process becomes less important. However, records of relative sea-level change from the Red Sea show increases of up to 35 m (Siddall *et al.*, 2003; Grant *et al.*, 2012) associated with catastrophic iceberg discharges from Northern Hemisphere ice sheets during Heinrich Events as recorded in North Atlantic sediments (Heinrich, 1988; Hemming, 2004). Realistically however, any contribution to millennial  $p\text{CO}_2^{\text{atm}}$  variability through changes in sea level (i.e., continental shelf exposure) is likely to be minimal.

### 1.3 The Southern Ocean's role in the glacial-interglacial variability of $p\text{CO}_2^{\text{atm}}$

From the above discussion of the biological pump and the Southern Ocean leak of  $\text{CO}_2$ , it is clear that the physical and biogeochemical processes operating in this region play a vital role in the modulation of  $p\text{CO}_2^{\text{atm}}$ , both on orbital and millennial timescales. The three most likely mechanisms to affect the  $\text{CO}_2$  leak are: (1) changes in the

efficiency of macronutrient consumption by marine biota in the surface ocean (Francois *et al.*, 1997; Martin, 1990), (2) changes in Southern Ocean ventilation rates which effectively determines the transfer of CO<sub>2</sub> from the deep ocean to the surface (Francois *et al.*, 1997; Toggweiler, 1999) and (3) changes in sea ice coverage which can alter the flux of CO<sub>2</sub> from the surface ocean to the atmosphere (Stephens and Keeling, 2000).

### 1.3.1 *The effects of Southern Ocean biological processes on pCO<sub>2</sub><sup>atm</sup>*

The Southern Ocean is the world's largest high-nutrient, low-chlorophyll (HNLC) region, with comparatively low levels of export production relative to the vast availability of macronutrients such as nitrate and phosphate. This implies that phytoplankton in the Southern Ocean are unable to fully exploit the high macronutrient concentration, most likely due to limitation by the micronutrient, iron (Martin, 1990). As discussed above, this results in a large portion of unutilised nutrients (preformed) which are recycled into the ocean interior (Toggweiler *et al.*, 2003b; Sigman *et al.*, 2010). Enhanced aeolian dust deposition during glacials (Rea, 1994; Mahowald *et al.*, 1999; Kohfeld and Harrison, 2001; Wolff *et al.*, 2006; Lambert *et al.*, 2008; Martinez-Garcia *et al.*, 2009) is thought to have relieved the iron-limitation of the Southern Ocean and stimulated enhanced biological productivity and CO<sub>2</sub> drawdown (Martin, 1990). This 'iron hypothesis' has been examined by numerous artificial iron enrichment experiments (de Baar *et al.*, 2005; Boyd *et al.*, 2007) and observations have also been made of large phytoplankton blooms following natural iron fertilisation 'events', by upwelling of iron-rich deep water (Blain *et al.*, 2007) and by additions via aerosols (Cassar *et al.*, 2007). These experiments and natural observations indicate that iron enrichment does indeed promote CO<sub>2</sub> drawdown, but the influence this has on the long term pCO<sub>2</sub><sup>atm</sup> is uncertain (e.g. Watson *et al.*, 1994; Watson and Lef erve, 1999; Lef erve and Watson, 1999). Nonetheless, considering the higher flux and more constant supply of iron-bearing dust during glacials, it is possible that dust fertilisation may have had a role to play in the variations in glacial-interglacial pCO<sub>2</sub><sup>atm</sup> (Watson *et al.*, 2000; Kohfeld *et al.*, 2005; Mart inez-Garc a *et al.*, 2009, 2014). In addition to these orbital variations, Antarctic ice core records indicate that dust deposition also varied in parallel with millennial pCO<sub>2</sub><sup>atm</sup> fluctuations suggesting a link between dust fertilisation of the Southern Ocean and global climate on shorter timescales (R othlisberger *et al.*, 2004; Fischer *et al.*, 2007; Ziegler *et al.*, 2013).

The marine geological record of marine productivity in the Southern Ocean reveals an asymmetrical response to iron fertilisation. Palaeoceanographic records indicate that export productivity in the Polar Antarctic Zone (PAZ), close to the Antarctic continent was lower during the Last Glacial Maximum (LGM) relative to the Holocene (Fig. 1.5) (e.g. Charles *et al.*, 1991 ; Mortlock *et al.*, 1991 ; Kumar *et al.*, 1995 ; Francois *et al.*, 1997; Frank *et al.*, 2000; Chase *et al.*, 2003; Kohfeld *et al.*, 2005 but see Abelmann *et al.*, 2006 for conflicting evidence based on diatom resting spore), whereas north of the Antarctic Polar Front (APF) in the Subantarctic Zone (SAZ) export productivity was higher (Fig. 1.5) (e.g., Kumar *et al.*, 1995; Rosenthal *et al.*, 1997, 2000; Chase *et al.*, 2001; Robinson *et al.*, 2005; Kohfeld *et al.*, 2005; Robinson and Sigman, 2008; Martínez-García *et al.*, 2009, 2014). This difference is in fact not surprising when one considers that the SAZ falls within the same latitude band as the Southern Hemisphere westerly wind belt and is directly downwind of the continental dust sources in South America (Basile *et al.*, 1997; Delmonte *et al.*, 2004; Gaiero, 2007). Additionally, the Subantarctic is much more dependent on the airborne supply of iron, than is the PAZ which receives most of its iron by during the upwelling of iron-rich deep waters. The lower glacial export productivity in the PAZ is reconciled with lower  $p\text{CO}_2^{\text{atm}}$  by invoking a greater fractional utilisation of a reduced nutrient supply to the Antarctic surface ocean, due to increased stratification (Francois *et al.*, 1997), increased sea ice coverage (Stephens and Keeling, 2000) or both. Nutrient utilisation proxies, which record the fraction of nutrient consumption relative to supply, provide conflicting evidence (Francois *et al.*, 1997; De La Rocha *et al.*, 1998; Sigman *et al.*, 1999; Elderfield and Rickaby, 2000; Crosta and Shemesh, 2002; Robinson *et al.*, 2004; Robinson and Sigman, 2008), due in part to complications and uncertainties with the proxies themselves but also due to biological changes that lead to variable usage of nutrients under glacial conditions (e.g. Brzezinski *et al.*, 2002; Matsumoto *et al.*, 2002)

Despite the uncertainties involved with the above records there does appear to be some correlation between glacial episodes of enhanced dust supply,  $p\text{CO}_2^{\text{atm}}$  decline, enhanced Subantarctic productivity and nutrient drawdown (Watson *et al.*, 2000; Robinson *et al.*, 2005; Martínez-García *et al.*, 2009, 2014). Models of the effect of

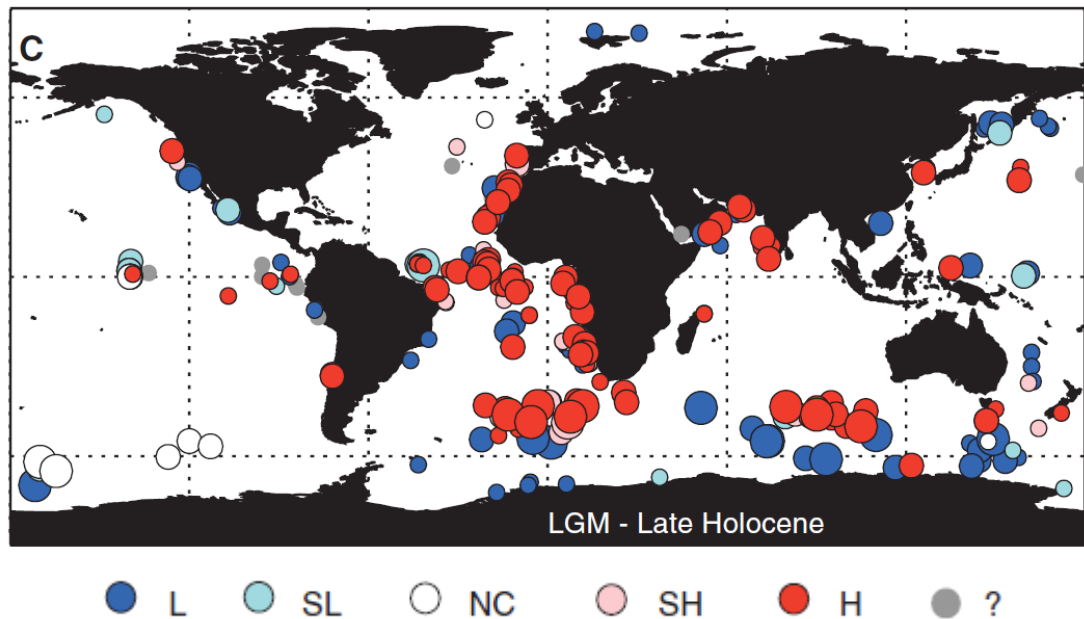


**Figure 1.5.** Relative changes in export production between the Last Glacial Maximum (LGM) and the Late Holocene (from Kohfeld *et al.*, 2005). Dark and pale blue circles indicate lower (L) and slightly lower (SL) export production, respectively; dark and pale red circles indicate (H) and slightly higher (SH) export, respectively; white circles indicate no change (NC) and grey circles represent locations where there is no unambiguous consensus between the different types of data. The size of the circles indicate the level of confidence in the assessment of the change in export production (small circles indicate low confidence and large circles indicate high confidence). The data represents a compilation of marine sediment sedimentary records of marine productivity during the Late Holocene (~the last 5 kyr BP) and LGM (~18 to 22 kyr BP) (Kohfeld *et al.*, 2005).

iron fertilisation predict glacial  $p\text{CO}_2^{\text{atm}}$  10-40 ppmv lower than during interglacials (Watson *et al.*, 2000; Bopp *et al.*, 2003; Ridgwell, 2003a; Brovkin *et al.*, 2007), supporting at least some direct  $\text{CO}_2$  drawdown due to this process alone. As is shown below (section 1.4) when these changes are coupled with processes operating on the seafloor underlying the low-latitude ocean (Archer and Maier-Reimer, 1994; Brzezinski *et al.*, 2002; Matsumoto *et al.*, 2002), iron fertilisation may in fact have been as a more important process for controlling  $p\text{CO}_2^{\text{atm}}$  than is simply suggested by its effect on the high-latitude soft-tissue biological pump.

### 1.3.2 *The effects of Southern Ocean physical processes on $p\text{CO}_2^{\text{atm}}$*

In addition to the biogeochemical mechanism described above, the Southern Ocean's  $\text{CO}_2$  leak may be reduced by a number of physical processes. This includes a reduction in the exchange between the surface and deep ocean (Toggweiler, 1999), or alternatively, by limiting the communication between the ocean and atmosphere due to increased sea-ice cover (Stephens and Keeling, 2000).

A reduction in the exchange between the deep ocean and the surface waters of the Southern Ocean implies an increase in stratification which may be brought about in a number of ways. One proposed mechanism involves an equatorward shift and possible weakening of the Southern Hemisphere westerly winds under glacial conditions (Toggweiler *et al.*, 2006; Kohfeld *et al.*, 2013). Under modern conditions the freshwater cap that develops over the Southern Ocean is effectively dissipated by wind-driven upwelling of relatively salty Circumpolar Deep Water (CDW) (Karsten and Marshall, 2002; Watson and Naveira-Garabato, 2006). The northward shift and/or weakening of the westerlies during glacials may reduce dissipation of the freshwater flux, allowing the fresh surface layer to persist. A similar proposal is centred on changes in the ventilation rate of the deep glacial ocean due to changes in deep water density (Watson and Naveira-Garabato, 2006; Adkins, 2013). The modern deep ocean is relatively rapidly ventilated in the Southern Ocean by a combination of vigorous mixing and upwelling south of the APF (Karsten & Marshall, 2002; Watson and Naveira-Garabato, 2006). During glacial times mixing was slower because of the formation of denser deep waters which resulted in stronger density gradients between water masses in the ocean interior (Adkins *et al.*, 2002; Adkins, 2013). This, in combination with the reduced buoyancy flux at the surface would have worked to suppressed upwelling in

the Southern Ocean effectively isolating the deep waters from the surface and trapping the biologically sequestered CO<sub>2</sub> in the ocean interior, thus lowering  $p\text{CO}_2^{\text{atm}}$ .

An alternative proposal involves the reduced sensitivity of seawater density to temperature during glacials. During winter in the modern polar oceans, the vertical temperature distribution promotes overturning, with colder water overlying warmer water; in contrast, the salinity distribution promotes stratification, with fresher water overlying saltier water. However, the sensitivity of seawater density to temperature is reduced as its temperature reaches the freezing point and salinity-driven stratification becomes the dominant control on the vertical density distribution (Sigman *et al.*, 2004; de Boer *et al.*, 2007). The consequence of this process is that during the colder glacial stages stratification may have been enhanced as the temperature-induced overturning would not be able to overcome the stratifying effect of the vertical salinity distribution.

Though it is difficult to distinguish between the various drivers of surface ocean stratification, the paleoceanographic record does provide some evidence to support a more stratified glacial Southern Ocean; nutrient utilisation proxies ( $\delta^{15}\text{N}$  in particular) provide the best evidence.  $\delta^{15}\text{N}$  (defined as,  $\delta^{15}\text{N} = \left( \frac{^{15}\text{N}/^{14}\text{N}_{\text{sample}}}{^{15}\text{N}/^{14}\text{N}_{\text{standard}}} - 1 \right) * 1000\text{‰}$ , where the standard is atmospheric N<sub>2</sub>) measures the fraction of nitrate consumed relative to the nitrate supply. It is affected both by the preferential uptake of <sup>14</sup>N relative to <sup>15</sup>N during the assimilation organic matter by phytoplankton, as well as the supply of nitrate by lateral advection and vertical convection of water masses with specific <sup>15</sup>N/<sup>14</sup>N signals (Altabet and Francois, 1994). Thus, by constraining the biological effect by other proxies such as <sup>230</sup>Th-normalised opal accumulation rates, it is possible to decipher whether the  $\delta^{15}\text{N}$  of bulk sediments or bound within microfossils are recording a signal of biological uptake or a signal due to changes in nutrient supply. The general picture that arises from such records is of increased stratification primarily within the PAZ, as this zone is most affected by changes in upwelling and increased meltwater flux from sea ice (e.g. Francois *et al.*, 1997; Robinson and Sigman, 2008).

The transfer of CO<sub>2</sub> from the oceans to the atmosphere may have alternatively (or additionally) been limited during glacials by an expansion of sea-ice cover relative to interglacials (Stephens and Keeling, 2000). Attempts to map sea ice extent at the LGM indicate that the winter sea ice may have reached as far as 6–10° latitude further north than at present suggesting an almost entirely sea-ice covered PAZ (Crosta *et al.*, 1998; Gersonde *et al.*, 2005); summer sea ice extent is inferred to be approximately the same

as in the modern. However, there is evidence for sporadic summer sea ice near the northern limits of the PAZ in the Atlantic sector (Allen *et al.*, 2005; Gersonde *et al.*, 2005). In contrast, evidence for sporadic summer sea ice in the Indian sector suggests only a slight northward expansion from the modern limits and largely ice free summers in this sector (Gersonde *et al.*, 2005; Wolff *et al.*, 2006).

#### **1.4 The low-latitude ocean's role in the glacial-interglacial variability of $p\text{CO}_2^{\text{atm}}$**

##### *1.4.1 $\text{CaCO}_3/\text{C}_{\text{org}}$ rain ratio*

The rain ratio hypothesis proposes that the lower  $p\text{CO}_2^{\text{atm}}$  of glacial times may have been brought about by a decrease in the amount of  $\text{CaCO}_3$  burial on the seafloor relative to  $\text{C}_{\text{org}}$  (Archer and Maier-Reimer, 1994). A change in the rain ratio may be caused by a decrease in the production rate of  $\text{CaCO}_3$ , or alternatively an increase in the amount of  $\text{C}_{\text{org}}$  buried on the seafloor. The reasoning behind the increased  $\text{C}_{\text{org}}$  burial is that when it is oxidised in sediments it produces  $\text{CO}_2$  in the sediment pore waters, provoking  $\text{CaCO}_3$  dissolution. During steady state the riverine influx of  $\text{Ca}^{2+}$  and  $\text{CO}_3^{2-}$  to the ocean is balanced by the burial of  $\text{CaCO}_3$  in deep sea sediments (Fig. 1.6; 'I- initial steady state'). A change in the surface ocean ecosystem in such a way so as to decrease the  $\text{CaCO}_3/\text{C}_{\text{org}}$  rain ratio, is communicated to the seafloor sediments, resulting in a decrease in  $\text{CaCO}_3$  preservation and a lower rate of  $\text{CaCO}_3$  burial. The reduced burial of  $\text{CaCO}_3$  means that the input of  $\text{Ca}^{2+}$  and  $\text{CO}_3^{2-}$  via the riverine influx now exceeds the losses (Fig. 1.6; 'II - rain ratio perturbation'). With a reduced loss of  $\text{CO}_3^{2-}$ , its concentration in the ocean increases, driving a subsequent increase in the preservation of  $\text{CaCO}_3$  in the sediments until a new steady state is reached between the riverine input and the loss due to burial at seafloor (Fig. 1.6; 'III- final steady state'). From equation 1.7 (section 1.2) we see that with all else being equal, an increase in  $[\text{CO}_3^{2-}]$  results in a decrease in  $p\text{CO}_2^{\text{atm}}$ .

Coupled ocean-sediment models suggest that a 40% reduction of global  $\text{CaCO}_3/\text{C}_{\text{org}}$  in surface sediments is capable of driving  $p\text{CO}_2^{\text{atm}}$  down by 70-90 ppmv, making this process a very attractive candidate for explain glacial-interglacial  $p\text{CO}_2^{\text{atm}}$  change (Archer and Maier-Reimer, 1994; Ridgwell *et al.*, 2002). However, the 40% reduction of global  $\text{CaCO}_3/\text{C}_{\text{org}}$ , requires a significant shift in the glacial ecosystem composition, with a necessary reduction in the proportion of total productivity composed of calcite-

secreting phytoplankton (i.e., coccolithophores). The most likely way to achieve this is by increasing silicic acid ( $\text{H}_4\text{SiO}_4$ ) availability, so that diatoms - which require  $\text{H}_4\text{SiO}_4$  to build their opal tests - could outcompete coccolithophores (Archer *et al.*, 2000; Ridgwell *et al.*, 2002). A number of studies have suggested that an increase in  $\text{H}_4\text{SiO}_4$  could have arisen during glacial times due to increased silicon (Si) supply rates to the ocean derived from aeolian dust (Harrison, 2000) or continental rock weathering (Tréguer and Pondaven, 2000), or due to decreased rates of Si removal by opal burial on continental shelves (Ridgwell *et al.*, 2002). However, as will be demonstrated below, it may not be necessary to invoke a whole-ocean increase in the  $\text{H}_4\text{SiO}_4$  inventory; an increase the ‘leakage’ of unutilised  $\text{H}_4\text{SiO}_4$  from the Southern Ocean to the low-latitude ocean may in itself be enough to bring about the required  $\text{CaCO}_3/\text{C}_{\text{org}}$  change (Brzezinski *et al.*, 2002; Matsumoto *et al.*, 2002).

#### 1.4.2 Silicic acid leakage

The shift in the  $\text{CaCO}_3/\text{C}_{\text{org}}$  requires an increase in the availability of  $\text{H}_4\text{SiO}_4$  in order to allow diatoms in the low-latitude ocean to outcompete  $\text{CaCO}_3$ -secreting coccolithophores. Instead of invoking a whole-ocean in the  $\text{H}_4\text{SiO}_4$  inventory, the same effect may be achieved if more of the  $\text{H}_4\text{SiO}_4$  from the Southern Ocean ‘leaks’ to the low-latitude ocean (Brzezinski *et al.*, 2002). Under the modern conditions,  $\text{H}_4\text{SiO}_4$  in the Southern Ocean is restricted to the PAZ, close to the Antarctic continent (Sarmiento *et al.*, 2004).  $\text{H}_4\text{SiO}_4$ -rich deep waters are upwelled south of the APF and these surface waters support diatoms that incorporate 4-5 times more silica for each unit of organic matter they produce, compared to most other regions of the world (Brzezinski *et al.*, 2001). Such high uptake rates result in the rapid depletion of  $\text{H}_4\text{SiO}_4$  (relative to nitrate) as the Antarctic surface waters are advected northwards by Ekman transport. These waters are subsequently incorporated into Subantarctic Mode Water (SAMW) and transported to the low latitude upwelling zones carrying with them the  $\text{H}_4\text{SiO}_4$ -depleted signal. As this is the main conduit for  $\text{H}_4\text{SiO}_4$  transfer to the low-latitude ocean, it follows that the concentration of  $\text{H}_4\text{SiO}_4$  in SAMW represents the main limitation to diatom growth in these regions (Sarmiento *et al.*, 2004).

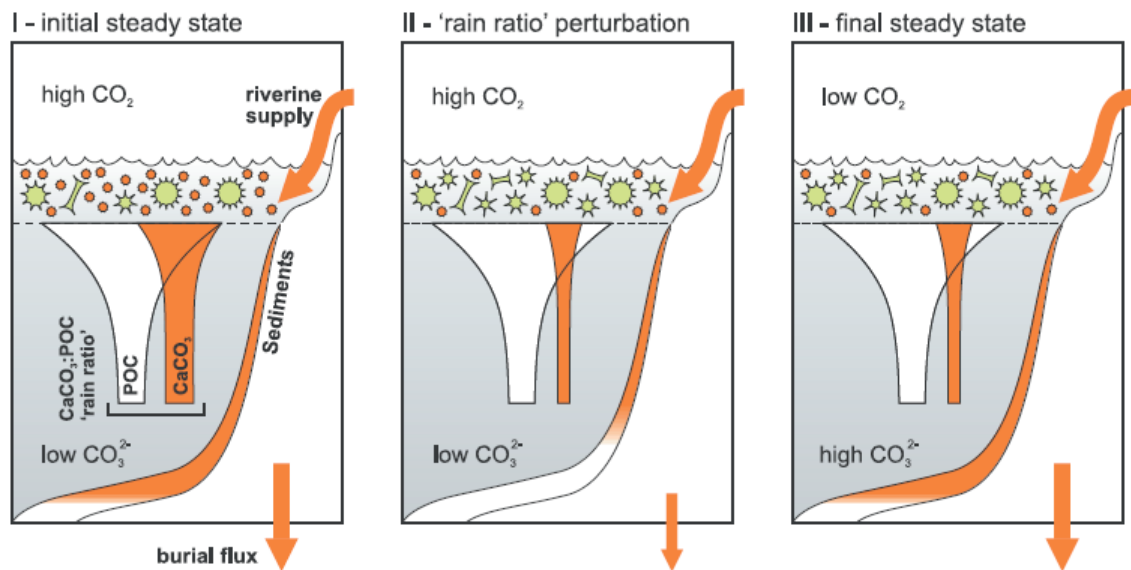


**Figure 1.6.** Sequence of events for the conceptual operation of the “rain ratio” mechanism for lowering atmospheric  $\text{CO}_2$  assuming no change in the efficiency of particulate organic carbon (POC) export to the deep ocean (Archer and Maier-Reimer, 1994). (I) Initial system steady state, with (riverine) influx of  $\text{Ca}^{2+}$  and  $\text{CO}_3^{2-}$  to the ocean balanced by the burial of  $\text{CaCO}_3$  in deep sea sediments. (II) Perturbation of ecosystem composition resulting in a decrease in the surface ocean  $\text{CaCO}_3$ :POC export ratio. The reduction in the  $\text{CaCO}_3$ :POC rain ratio is communicated proportionally to the sediments, resulting in decreased carbonate preservation and a significantly lower global burial rate of  $\text{CaCO}_3$  (manifested in a shoaling of the lysocline). Inputs of  $\text{Ca}^{2+}$  and  $\text{CO}_3^{2-}$  to the ocean now exceed losses. (III) Deep sea  $[\text{CO}_3^{2-}]$  rises, driving an increase in the preservation of  $\text{CaCO}_3$  in the sediments, until the point is reached where the global burial flux once again balances input. Higher oceanic  $[\text{CO}_3^{2-}]$  equates to lower atmospheric  $\text{CO}_2$  (other things being equal). Figure taken from Ridgwell (2003).

Incubation experiments have demonstrated that relieving the iron limitation typical of the modern Southern Ocean, causes a decrease in  $\text{H}_4\text{SiO}_4$  uptake (Takeda, 1998). Therefore, even under a scenario where the enhanced aeolian dust deposition during glacials (Rea, 1994; Mahowald *et al.*, 1999; Kohfeld and Harrison, 2001; Wolff *et al.*, 2006; Lambert *et al.*, 2008; Martínez-García *et al.*, 2009; Martínez-García *et al.*, 2014) does not directly stimulate increased biological productivity in the PAZ (e.g. Charles *et al.*, 1991; Mortlock *et al.*, 1991; Kumar *et al.*, 1995; Francois *et al.*, 1997; Frank *et al.*, 2000; Chase *et al.*, 2003; Kohfeld *et al.*, 2005), it may nonetheless have resulted in excess  $\text{H}_4\text{SiO}_4$  in the glacial Subantarctic and SAMW (Brzezinski *et al.*, 2002; Matsumoto *et al.*, 2002; Romero *et al.*, 2015). It is therefore possible that under such glacial conditions the increased  $[\text{H}_4\text{SiO}_4]$  in SAMW (Sarmiento *et al.*, 2004) may have stimulated the ecosystem shift necessary to trigger the  $\text{CaCO}_3/\text{C}_{\text{org}}$  rain ratio change described in the previous section (Archer and Maier-Reimer, 1994).

The paleoceanographic records that suggest lower export production, or more specifically, lower  $^{230}\text{Th}$ -normalised opal accumulation rates south of the APF during the LGM (Kumar *et al.*, 1995; Francois *et al.*, 1997; Anderson *et al.*, 2002; Kohfeld *et al.*, 2005; Anderson *et al.*, 2009) are consistent with reduced preferential uptake of silicic acid in Antarctic surface waters during glacial times. Additionally,  $\text{H}_4\text{SiO}_4$  utilisation, measured as sedimentary  $\delta^{30}\text{Si}$  from Antarctic sediments, indicates that the depletion of surface silicic acid was lower there during LGM than during the Holocene (De La Rocha *et al.*, 1998). The antiphasing of  $\delta^{30}\text{Si}$  and  $\delta^{15}\text{Ni}$  in the PAZ (e.g. De La Rocha *et al.*, 1998 versus Robinson *et al.*, 2004 and Robinson and Sigman, 2008), which has long been problematic for nutrient utilisation reconstructions could therefore potentially be explained by the ‘silicic acid leakage hypothesis’.

## 1.5 Global Overturning Circulation

The meridional overturning circulation (MOC) represents the large-scale, globally-intertwined system of currents that flows in a continuous loop around all major ocean basins and that reaches all depths (Rahmstorf, 2002; Lumpkin and Speer, 2007; Kuhlbrodt *et al.*, 2007; Talley *et al.*, 2011; Marshall and Speer, 2012; Talley, 2013) (Fig. 1.7). It is driven by a combination of processes including mixing by wind and tidal energy (Munk and Wunsch, 1998) and mixing due to the development of density gradients caused by heat and freshwater fluxes across the sea surface and subsequent

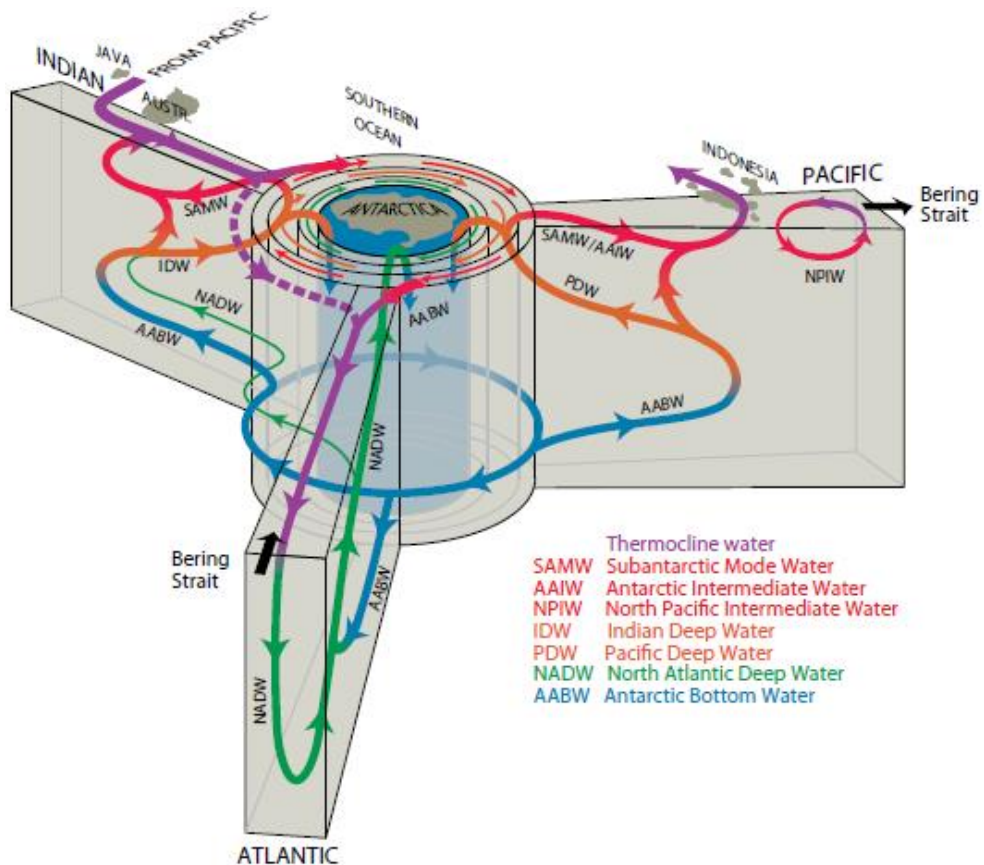
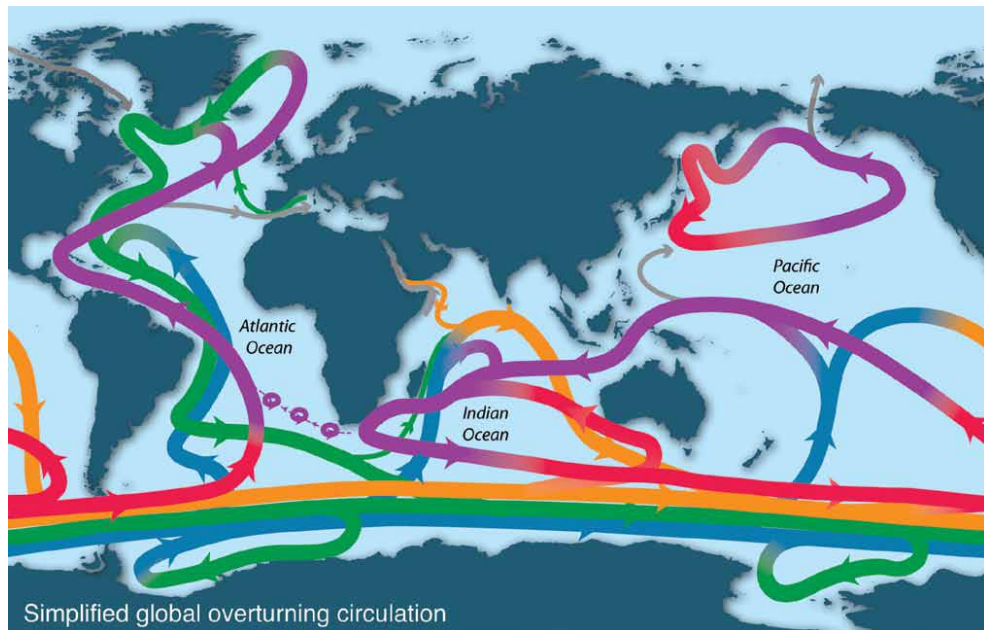


**Figure 1.7.** Schematic of the global overturning circulation in map view (upper panel) and in three-dimensional view from a Southern Ocean perspective (lower panel) (from Talley, 2013). The various water masses are coloured as indicated in the legend of the lower panel. Updated form Talley (2011) after Gordon (1986), Schmitz (1995), Rahmstorf (2002), and Lumpkin and Speer (2007).

mixing of heat and salt within the ocean interior (the so-called Thermohaline Circulation, THC) (Gordon, 1986; Broecker, 1987, 1991).

The surface-ventilated North Atlantic Deep Water (NADW) and the diffusively formed Indian Deep Water (IDW) and Pacific Deep Water (PDW) represent the three main northern-sourced deep water masses. These move southward and upwell in the Southern Ocean where they are incorporated in different proportions into the various southern-sourced water masses. AABW is produced primarily from the denser, and saltier NADW with IDW and PDW making a smaller contribution. The fraction of the upwelled IDW and PDW that is not incorporated into AABW remains near the surface of the Southern Ocean and subsequently merges into the subtropical thermoclines before finally contributing about one third of the volume of NADW. Another third of NADW is derived from AABW upwelling in the Atlantic basin and the remaining third is derived from the upwelling of AABW in the thermocline of the Indian and Pacific Oceans (Fig. 1.7).

The upper ocean and thermocline sources of NADW enter the Atlantic from the Pacific basin via the Drake Passage and from the Indian basin via the Agulhas Corridor (also referred to as the Indian-Atlantic Ocean Gateway in this thesis; see next section). Waters entering the Atlantic via the Drake Passage include Antarctic Intermediate Water (AAIW) and Subantarctic Mode Water (SAMW) which both include a substantial contribution from surface waters that are advected across the Antarctic Circumpolar Current (ACC) by northward Ekman transport. The contribution of waters from the Agulhas region to the Atlantic Ocean represent a mixture of upwelled deep waters from within the Indian and Pacific Ocean and subducted upper ocean waters from the southeastern Indian Ocean and the southeastern Pacific Ocean. The upper ocean waters from the Drake Passage and those from the Agulhas region flow northwards through the Atlantic Ocean, where they cool and eventually sink at several sites of dense-water formation around the North Atlantic (mainly in the Nordic Seas and Labrador Sea). These denser waters then flow southward at depth and exit the North Atlantic region as NADW. Within the Atlantic basin, the southward-flowing NADW lies above the even denser southern-sourced AABW which travels northward along the seafloor and upwells diffusively into the lower-most levels of the NADW. This upwelling and incorporation of AABW into NADW at the boundary between these two water masses ultimately contributes to the southward return of AABW back to the Southern Ocean.

The NADW and the returning upper AABW then exit the Atlantic south of Africa and join the eastward flowing waters of the ACC. Some of the NADW enters the southwest Indian Ocean near the Agulhas region and eventually combines with the upwelling AABW in the Indian Ocean to form IDW. However, the majority of NADW exiting the Atlantic is mixed into the ACC to form Circumpolar Deep Water that eventually upwells in the Antarctic Zone of the Southern Ocean. The upwelling of NADW (as CDW) around Antarctica exposes it to very low temperatures causing it to cool to the near-freezing. Despite the intense brine rejection due to sea ice formation in this region, the net precipitation, combined with the sea ice meltwater, results in a net freshening of the upwelled NADW/CDW mixture. Although the freshening imparts buoyancy to these waters the severe cooling allows this water to sink to depth and combine with the densest waters of the Southern Ocean, formed in the Weddell and Ross Seas. These dense waters then flow northward over the topography of the Southern Ocean and spreading as AABW into the Atlantic, Indian and Pacific Oceans. The exported AABW finally upwells in all three basins, contributing directly to the three northern-source deep water masses (NADW, IDW and PDW) and thus closing the global loop of the MOC (Talley, 2013).

### **1.6 The Greater Agulhas System and the Indian-Atlantic Ocean Gateway**

The greater Agulhas system around southern Africa constitutes a crucial part of the MOC and represents one of the main pathways by which waters from the Indian and Pacific Oceans are transported to the Atlantic (Gordon, 1986; Lutjeharms, 2006). The Agulhas Current itself is part of the South Indian Ocean subtropical gyre and is the largest surface western boundary current in the Southern Hemisphere. It transports ~ 70 Sverdrup (Sv) ( $1 \text{ Sv} = 10^6 \text{ m}^3 \text{ s}^{-1}$ ) of warm and saline tropical and subtropical surface waters southwestwards, along the southeastern African margin toward to the southern tip of the continent (Lutjeharms, 2006) (Fig. 1.8). The current flows as a narrow jet along the steep continental slope between approximately 28 to 34°S before diverging from the coast to continue its course along the Agulhas Bank (Gründlingh, 1983). Near 36°S it detaches from the continental shelf and in the region between 16 and 20°E the Agulhas Current retroflects back toward the Indian Ocean as

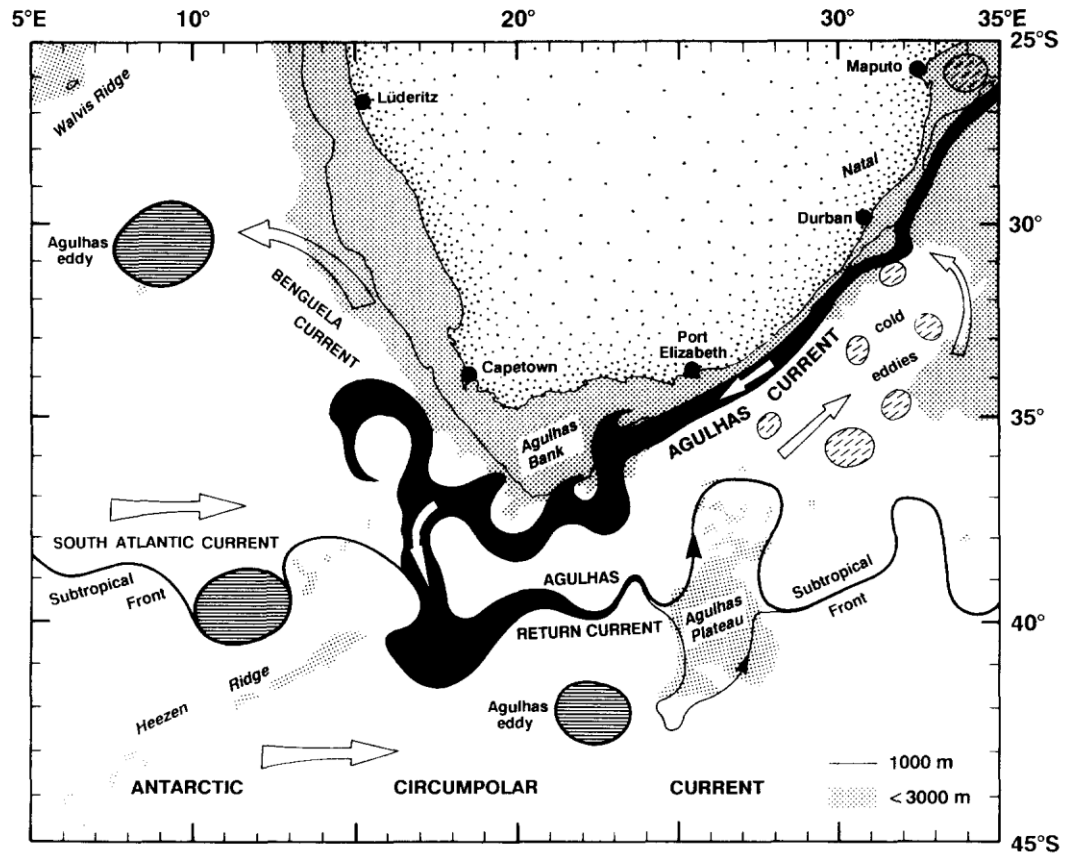


**Figure 1.8.** Schematic representation of the Agulhas Current system (from Peterson and Stramma, 1991; adapted from Lutjeharms and Van Ballegooyen, 1988 and Lutjeharms, 1989). Open arrows indicate the general direction of the surface currents with the black-shaded region highlighting the main path of the waters travelling along the Agulhas Currents, Agulhas Retroflexion and the Agulhas Return Current.

the Agulhas Return Current which then flows eastward along the Southern Ocean Sub-tropical front (STF) (Lutjeharms and Van Ballegooyen, 1988). Instabilities in the retro-reflection cause Agulhas Rings to spin off, which carry warm and saline waters into the South Atlantic through the Indian-Atlantic Ocean Gateway (I-AOG) as Agulhas Leakage (2-15 Sv) (de Ruijter *et al.*, 1999). Modelling studies have shown that this leakage can stimulate regional buoyancy anomalies in the Atlantic basin that can ultimately alter the Atlantic meridional overturning circulation (AMOC) and the climate of the North Atlantic region on various timescales (Weijer *et al.*, 2002; Knorr and Lohmann, 2003; Van Sebille *et al.*, 2009; Biastoch *et al.*, 2008, 2009).

Changes in the position of the STF have been suggested to play an important role in Agulhas Leakage with implications for global climate variability on a range of timescales (Beal *et al.*, 2011). Although previous studies have revealed evidence of meridional migrations of the STF within this region on glacial-interglacial and millennial timescales it still remains unclear what the implications are for the past variability of Agulhas Leakage and even more so for its effect on the AMOC (Flores *et al.*, 1999; Rau *et al.*, 2002; Peeters *et al.*, 2004; Bard and Rickaby, 2009; Martínez-Méndez *et al.*, 2010; Marino *et al.*, 2013; Simon *et al.*, 2013; Dyez *et al.*, 2014; Romero *et al.*, 2015). However, recent observational and modelling studies have suggested that the position of the Southern Hemisphere westerly wind system may not be the main determinant of the position and dynamics of the STF (Graham and De Boer, 2013; De Boer *et al.*, 2013; Durgadoo *et al.*, 2013), bringing into question the theory that the latitude of the STF regulates the volume of Agulhas Leakage into the Atlantic Ocean.

## **1.7 Aims of this thesis**

The overall aim of this study is to enhance our understanding of the evolution of oceanographic conditions within the I-AOG during the past 150 kyr BP. Particular emphasis is placed on reconstructing variations in the deep and surface waters of the I-AOG in relation to ocean and climate change on a regional, hemispheric and global scale. We consider how changes in the chemical composition, physical characteristics and spatial distribution of deep water masses are linked to the glacial to interglacial variability of circulation in the Atlantic and Southern Ocean. We also aim to understand how processes operating in the Southern Ocean impact the physical and chemical properties of surface waters in the I-AOG and eastern equatorial Pacific Ocean. Furthermore, we consider the relationship between processes operating in the Southern Ocean impacts

the exchange of carbon dioxide between the ocean and atmosphere. Finally, we attempt to reconstruct the variability of upper ocean circulation in the I-AOG, and also examine how changes in the terrestrial hydroclimate of south-eastern Africa may be associated with Northern Hemisphere climate change during the last glacial.

In achieving these aims our specific scientific objectives were:

1. To reconstruct the history of mid-depth circulation within the I-AOG by reconstructing the physical and chemical variability of the bottom waters of the southern Agulhas Plateau over the past 150 kyr BP. We applied a multi-proxy approach to reconstruct and derive a range of physical and chemical bottom water parameters along sediment core MD02-2588. We developed downcore records of stable isotopes and elemental ratios measured in benthic foraminifera, and determined the downcore variability of the mean grain size of sortable silt. From these primary data we derived additional paleoceanographic proxy records of the carbonate saturation state of seawater, the concentration of dissolved Cd in seawater, and relative changes in near-bottom flow speeds. Additionally, we isolated the various components that constitute the carbon isotopic composition preserved in benthic foraminifera and generated a qualitative reconstruction of past sediment pore-water oxygen concentration.
2. To investigate how changes in the position of the subtropical front within the I-AOG varied over the past 150 ky BP and to establish how these changes may have impacted the nutrient supply to the surface waters of the southern Agulhas Plateau. We measured the nitrogen isotope composition of bulk sediment samples from sediment core MD02-2588 and examined it in the context of published proxy records from this core, as well as records from the wider I-AOG and Southern Ocean.
3. To assess the utility of the deep-dwelling planktonic foraminifera species, *G. truncatulinoides*, as a recorder of seawater  $\delta^{13}\text{C}_{\text{DIC}}$  by performing a core-top study from a set of samples collected around New Zealand. Additionally, we examine the downcore record of the carbon isotopic composition of *G. truncatulinoides* from sediment core MD02-2588 and attempt to explain the relationship between  $\delta^{13}\text{C}_{\text{DIC}}$  in the Southern Ocean and the exchange of carbon dioxide between the ocean and atmosphere throughout the past 150 kyr BP.

4. To perform a preliminary study of sediment core CD154-23-16P retrieved from the flank of the Mallory Seamount, offshore southern Africa. Our specific objective for this core were twofold. Our first objective was to develop an initial age model based on radiocarbon dating of planktonic foraminifera and graphical tuning to climate records from the Northern Hemisphere. Our second objective was to perform an initial assessment of the utility of this sediment core for reconstructing the variability of the Agulhas Current and the terrestrial hydroclimate of south-eastern Africa.

## **1.8 Thesis outline**

Chapter 2 outlines the paleoceanographic proxies and techniques used in this study and Chapter 3 presents a detailed description of the material and methods applied to tackle the scientific objectives of this thesis. The principal scientific findings are structured into four results and discussion chapters (Chapters 4, 5, 6 and 7) addressing the main objectives outlined above. Chapter 4 focusses on the reconstruction of the deep water variability of the Agulhas Plateau based on the study of marine sediment core MD02-2588 (scientific objective 1). Chapter 5 deals with the reconstruction of the upper ocean hydrographic variability of the Agulhas Plateau based again on the study of marine sediment core MD02-2588 (scientific objective 2). Chapter 6 discusses the results of the core-top assessment of the planktonic foraminiferal signal carriers of  $\delta^{13}\text{C}_{\text{DIC}}$  and the examination of the down-core record of  $\delta^{13}\text{C}_{\text{DIC}}$  as recorded in planktonic foraminiferal  $\delta^{13}\text{C}$  from MD02-2588 (scientific objective 3). Chapter 7 presents the preliminary results from sediment core CD154-23-16P. This includes the construction of the age model for this core and presenting an initial interpretation of elemental ratio profiles and foraminiferal stable isotope results. The conclusions from the key findings presented in this thesis are summarised in Chapter 8.

---

## 2 Paleooceanographic proxies and techniques

---

Paleooceanographic and paleoclimate reconstructions rely on the application of proxies to determine the physical, chemical and biological properties of the ocean and the atmosphere of the geological past. These proxies are sources of information preserved within materials such as sediments, ice and tree rings, that are in some way related to past oceanographic and climatic parameters such as the temperature and chemical composition of the ocean and atmosphere. This chapter briefly introduces the proxies that have been used in this study to reconstruct various oceanographic parameters.

### 2.1 Foraminiferal stable isotope and elemental geochemistry

Foraminiferal tests provide one of the most important materials from which proxy information can be extracted due to their good preservation, their abundance and their ubiquitous distribution in ocean sediments. In this thesis, we make use of the stable isotope and elemental geochemistry of foraminiferal tests from a number marine sediment cores.

#### 2.1.1 Oxygen isotopic ratios in foraminifera

The oxygen isotope ratio of foraminiferal calcite tests ( $\delta^{18}\text{O}_{\text{foram}}$ ) is a well-established and widely-used proxy of paleooceanographic research. The temperature-dependency of oxygen isotope ( $\delta^{18}\text{O}$ ) fractionation between water and calcium carbonate ( $\text{CaCO}_3$ ) has long been recognised (Urey, 1947,1948; Epstein *et al.*, (1953) and was applied as a means to reconstruct past variations of sea surface temperature as early as 1955 (Emiliani, 1955). Later work on benthic foraminifera lead to the recognition that a large component of the  $\delta^{18}\text{O}_{\text{foram}}$  observed in sediment cores was due to past variations of whole-ocean seawater  $\delta^{18}\text{O}$  ( $\delta^{18}\text{O}_{\text{sw}}$ ) as a consequence of the growth and decay of large ice sheets during glacial-interglacial cycles (Shackleton, 1967). Though this complicates the use of  $\delta^{18}\text{O}_{\text{foram}}$  as a proxy of ocean temperatures its use in paleoceanography is invaluable and has proven to be a powerful stratigraphic tool (e.g. Lisiecki and Raymo, 2005). Furthermore, with the advent of independent paleotemperature proxies (Brassell *et al.*, 1986; Nürnberg *et al.*, 1996; Schouten *et al.*, 2002) it has become possible to isolate the temperature dependent component of  $\delta^{18}\text{O}_{\text{foram}}$  and extract the  $\delta^{18}\text{O}_{\text{sw}}$  component. When this  $\delta^{18}\text{O}_{\text{sw}}$  value is corrected for

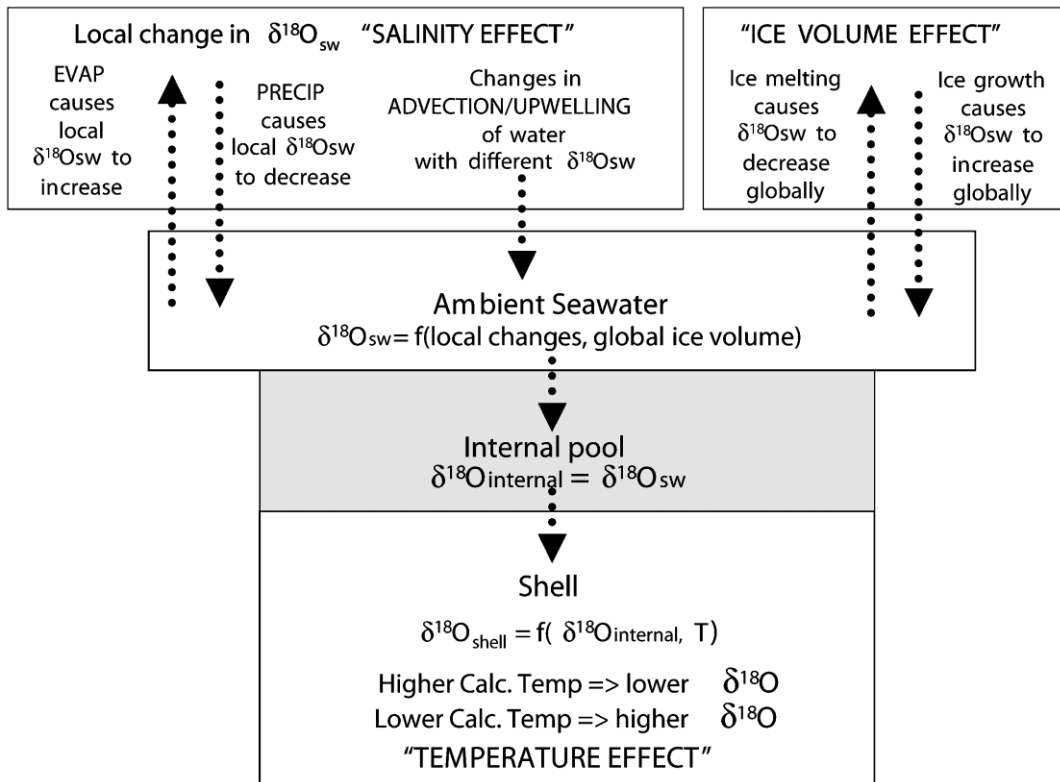


**Figure 2.1.** Schematic summary of the environmental factors that influence the stable oxygen isotopic composition ( $\delta^{18}\text{O}$ ) of foraminiferal tests (reproduced from Ravelo and Hillaire-Marcel, 2007).

the effects of changing ice volume with the use of contemporaneous sea level records (e.g., Waelbroeck et al., 2002; Siddall *et al.*, 2003) it becomes possible to constrain the local  $\delta^{18}\text{O}_{\text{sw}}$  signal of  $\delta^{18}\text{O}_{\text{foram}}$  which provides a qualitative indication of relative changes in salinity (for a review, see Rohling, 2007). The factors influencing the  $\delta^{18}\text{O}_{\text{foram}}$  are schematically summarised in figure 2.1 (from Ravelo and Hillaire-Marcel, 2007).

### 2.1.2 Carbon isotopic ratios in foraminifera

The stable carbon isotopic composition of foraminiferal tests ( $\delta^{13}\text{C}_{\text{forma}}$ ) reflects the carbon isotopic composition of the dissolved inorganic carbon (DIC) of the ambient seawater in which they calcified ( $\delta^{13}\text{C}_{\text{DIC}}$ ).  $\delta^{13}\text{C}_{\text{DIC}}$  and its variability in the geological past is influenced by four principal processes: (i) changes in the distribution of carbon between the various reservoirs, (ii) changes in the biological cycling of carbon (i.e., the soft-tissue biological pump (see detailed discussion in chapter 6 of this thesis), (iii) changes in the thermodynamic equilibration between surface ocean DIC and atmospheric  $\text{CO}_2$  and (iv) changes in water-mass geometry and water-mass mixing.

The mean  $\delta^{13}\text{C}_{\text{DIC}}$  of the whole ocean is determined by the partitioning of carbon between the ocean, atmosphere and terrestrial reservoirs; on longer timescales the crustal and sedimentary reservoirs also become important but these are not discussed in this study. On glacial-interglacial timescales the largest impact on the mean  $\delta^{13}\text{C}_{\text{DIC}}$  of the whole ocean is caused by changes in the size of the terrestrial biosphere. The preferential uptake of  $^{12}\text{C}$  during photosynthesis by terrestrial plants results in the sequestration of carbon with a low  $\delta^{13}\text{C}$  ratio during photosynthesis (-10 to -30‰ depending on photosynthetic pathway, Park and Epstein, 1960; Bender, 1971). An increase in the size of the terrestrial biosphere therefore removes low  $\delta^{13}\text{C}$  carbon from the atmosphere and the ocean and causes  $\delta^{13}\text{C}_{\text{DIC}}$  in the ocean to increase; analogously a decrease in the size of the terrestrial biosphere results in the transfer of low  $\delta^{13}\text{C}$  to the ocean, causing a decrease in  $\delta^{13}\text{C}_{\text{DIC}}$ .

The biological control on  $\delta^{13}\text{C}_{\text{DIC}}$  within the marine environment is caused by the preferential utilisation of  $^{12}\text{C}$  from the surface-layer reservoir of DIC during photosynthesis, which causes an increase in surface-ocean  $\delta^{13}\text{C}_{\text{DIC}}$ . As the exported organic material sinks out of the surface ocean and undergoes oxidation at depth, it returns to its dissolved inorganic form and releases  $^{12}\text{C}$ -enriched carbon to the ocean interior,

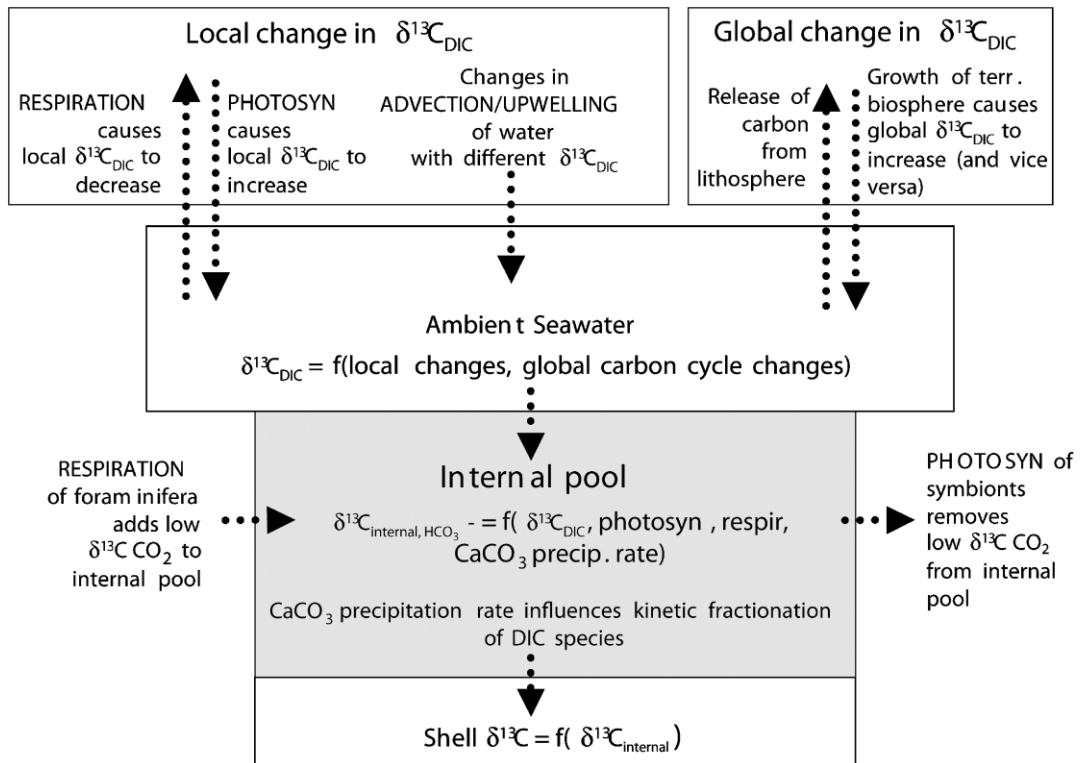


**Figure 2.2.** Schematic summary of the environmental factors that influence the stable carbon isotopic composition ( $\delta^{13}\text{C}$ ) of foraminiferal tests (reproduced from Ravelo and Hillaire-Marcel, 2007).

thereby lowering the deep-ocean  $\delta^{13}\text{C}_{\text{DIC}}$ . The sequestration of  $^{12}\text{C}$ -rich DIC into the ocean interior thus results in the establishment of a  $\delta^{13}\text{C}_{\text{DIC}}$  gradient in the water column that is a function of the strength of the soft-tissue biological pump.

The temperature dependent carbon isotope fractionation during air-sea gas exchange between oceanic DIC and atmospheric  $\text{CO}_2$  is also an important factor determining the  $\delta^{13}\text{C}_{\text{DIC}}$  of seawater;  $\delta^{13}\text{C}_{\text{DIC}}$  increases by 0.1‰ per degree of seawater cooling (Mook *et al.*, 1974). An additional impact on oceanic  $\delta^{13}\text{C}_{\text{DIC}}$  arises due to the invasion and evasion of atmospheric  $\text{CO}_2$  into or out of the surface ocean. The exchange of isotopically light atmospheric  $\text{CO}_2$  with the ocean results in  $\delta^{13}\text{C}_{\text{DIC}}$  depletion in areas of  $\text{CO}_2$  invasion and  $\delta^{13}\text{C}_{\text{DIC}}$  enrichment in areas of  $\text{CO}_2$  evasion (Lynch-Stieglitz *et al.*, 1995).

Finally, the  $\delta^{13}\text{C}_{\text{DIC}}$  at a given location within the ocean may change through time as a function of variations in the regional water-mass geometry (and ocean circulation) and/or changes in the mixing ratios between water masses with different characteristic carbon isotopic compositions (Curry and Oppo, 2005). The factors influencing the  $\delta^{13}\text{O}_{\text{foram}}$  are schematically summarised in figure 2.2 (from Ravelo and Hillaire-Marcel, 2007).

### 2.1.3 Cd/Ca in foraminifera

The distribution of dissolved Cd in seawater is very similar to that of the nutrient phosphate with low concentrations in surface waters, high concentrations in deep waters and an intermediate-depth maximum near 1000 m (Boyle *et al.*, 1976; Boyle, 1988; Elderfield and Rickaby, 2000) (Fig. 2.3). The correlation between Cd and phosphate is described by a slight curve that has been suggested to be the consequence of preferential uptake of Cd relative to phosphate (Elderfield and Rickaby, 2000) (Fig. 2.4). Traditionally however this curve in the global dataset has been defined as a ‘kink’ between two linear equations that represent differences in the relationships for waters with high  $\text{Cd}_{\text{sw}}$  ( $>0.28 \text{ nmol kg}^{-1}$ ) versus those waters with low  $\text{Cd}_{\text{sw}}$  ( $<0.28 \text{ nmol kg}^{-1}$ ) (Boyle, 1988).

Cd is incorporated into the tests of foraminifera and calibration studies have shown that benthic foraminiferal Cd/Ca ratios reflect the Cd concentration of the seawater ( $\text{Cd}_{\text{sw}}$ ) in which they calcify (Boyle, 1992). The incorporation of Cd into benthic foraminifera has been shown to be independent of calcification temperature

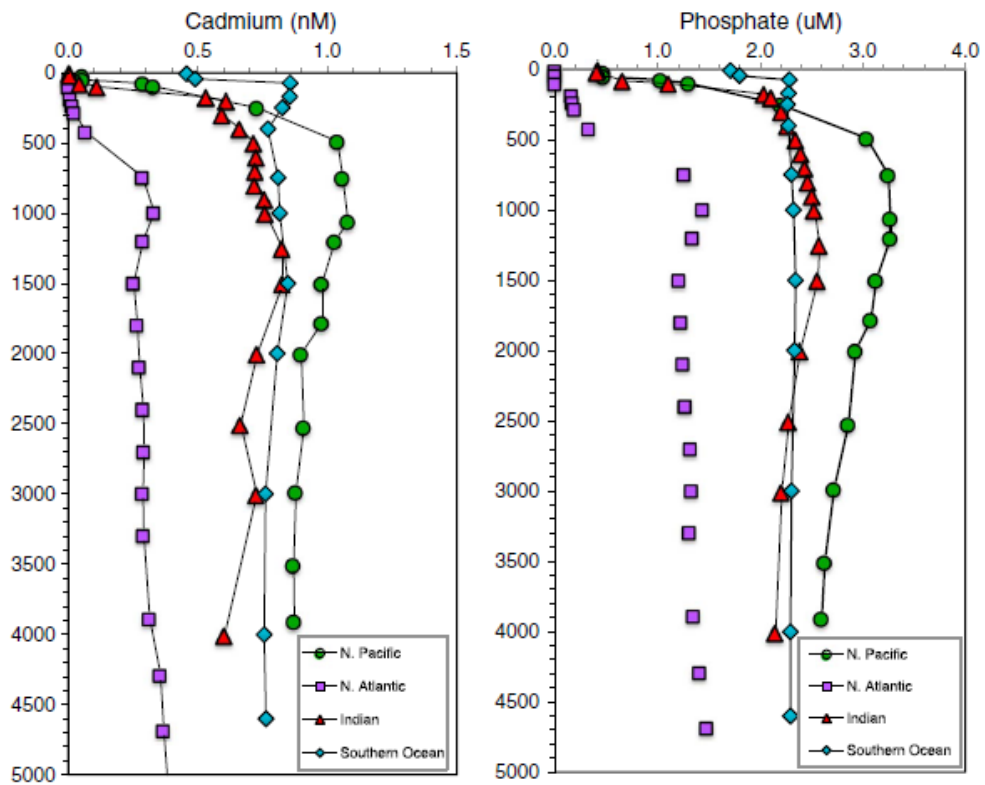


**Figure 2.3.** Depth profiles of dissolved phosphate (right) and Cd (left) measured in the North Pacific at 37°N, 124°W (Bruland, 1980), the North Atlantic at 32°N, 57°W (Quay and Wu, 2014), the Indian Ocean at 14°N, 67°E (Saager *et al.*, 1992) and the Southern Ocean at 67°S, 0°E (Abouchami *et al.*, 2011). Figure reproduced from Quay *et al.*, (2015).

(Marchitto, 2004) whereas in the case of planktonic foraminifera the available evidence suggests that the partition coefficient of Cd between seawater and calcite is exponentially dependent on calcification temperature (Rickaby and Elderfield, 1999; Yu *et al.*, 2013). Details regarding the reconstruction of  $Cd_{sw}$  from benthic foraminiferal Cd/Ca are given in Chapter 3 of this thesis (Material and Methods). Chapter 3 also present the details of calculating the air-sea fractionation signature of  $\delta^{13}C$  ( $\delta^{13}C_{as}$ ) from paired foraminiferal Cd/Ca- $\delta^{13}C$ .  $\delta^{13}C_{as}$  is considered to be a conservative deep water-mass tracer (Lynch-Stieglitz and Fairbanks, 1994).

We note that Cd/Ca measured in benthic foraminifera is prone to effects that cause it to deviate from  $Cd_{sw}$  values. These arise from the susceptibility of foraminiferal tests to contamination by diagenetic coatings such as Fe-Mn-oxides (Boyle, 1983) and CdS (Rosenthal *et al.*, 1995). It is therefore paramount that prior to measuring Cd/Ca in foraminifera their tests are rigorously cleaned following established protocols (see Chapter 3). Additionally, partition coefficients for the incorporation of Cd into the tests of foraminifera may be affected by the carbonate ion saturation state of seawater ( $\Delta[CO_3^{2-}]$ ) (i.e., the difference between the carbonate ion concentration ( $[CO_3^{2-}]$ ) of seawater and the  $[CO_3^{2-}]$  required for saturation). The available evidence suggests that the partition coefficient of Cd may be reduced by more than 50% in the severely undersaturated abyssal waters of the Indian and Pacific Oceans (McCorkle *et al.*, 1995; Marchitto *et al.*, 2000, 2005). These effects are thought to impact Cd incorporation during calcite precipitation rather than being a consequence of post-mortem preferential dissolution (Boyle, 1988; Elderfield *et al.*, 1996; Marchitto *et al.*, 2000).

#### 2.1.4 Mg/Ca in foraminifera

The substitution of  $Mg^{2+}$  into inorganic  $CaCO_3$  involves an endothermic reaction whereby higher temperatures lead to greater inclusion of Mg. The Mg/Ca of inorganic calcite is therefore expected to correlate positively with temperature and has been estimated to increase exponentially by ~3% per each degree Celsius ( $^{\circ}C$ ) of warming between 0 and 30  $^{\circ}C$  (Koziol and Newton, 1995); this estimation is in agreement with calcite precipitation experiments (Katz, 1973, Mucci, 1987, Oomori *et al.*, 1987). An exponential relationship has also been found to occur in the biogenically-precipitated calcite tests of foraminifera (Nurnberg *et al.*, 1996, Lea *et al.*, 1999). However, in the case of biogenic calcite the temperature sensitivity relationship is

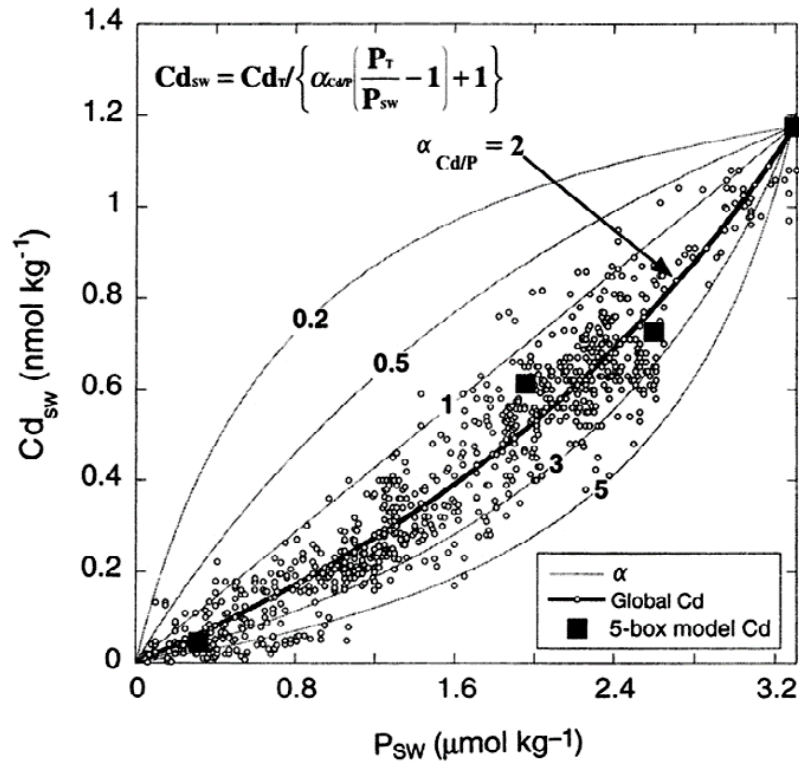


**Figure 2.4.** Dissolved Cd versus dissolved phosphate data for the global ocean, reproduced from Elderfield and Rickaby (2000). The curved lines show different solutions to the inset equation in the upper left-hand corner (where  $Cd_T=1.2$  and  $P_T=3.3$ ) that can explain the regional relationships between the two nutrients. Bold line is the best fit to the global data set with  $\alpha_{Cd/P}=2$ .

stronger than the equivalent relationship for inorganic calcite under the same conditions. Additionally, the relationship between Mg/Ca and temperature in biogenic calcite may be more linear in form rather than exponential and is often species -dependent. These observations highlight the strong influence of biological processes during the biogenic precipitation of calcite and emphasise the need for species-specific calibrations.

The temperature dependence of Mg/Ca in planktonic foraminifera has been calibrated using a number of different approaches ranging from culture-based calibrations (e.g., Nurnberg *et al.*, 1996, Lea *et al.*, 1999), sediment trap calibrations (e.g., Anand *et al.*, 2003) and core-top calibrations (e.g., Elderfield and Ganssen, 2000). The temperature dependence of Mg/Ca in benthic foraminifera has principally been calibrated using the core-top approach (e.g. Lear *et al.*, 2002; Elderfield *et al.*, 2006; Raitzsch *et al.*, 2008). We note that in cold, deep waters where levels of carbonate saturation are low, benthic foraminiferal Mg/Ca has been found to be affected by the carbonate saturation state ( $\Delta[\text{CO}_3^{2-}]$ ) of seawater (Elderfield *et al.*, 2006; Raitzsch *et al.*, 2008). Details of the specific calibrations used for the planktonic and benthic foraminifera used in this study are given in Chapter 3.

### 2.1.5 B/Ca in foraminifera

As was mentioned above, in addition to the temperature-dependence of benthic foraminiferal Mg/Ca, Mg substitution into calcite appear to be susceptible to changes in the  $\Delta[\text{CO}_3^{2-}]$  of seawater. In order to account for the  $\Delta[\text{CO}_3^{2-}]$  effects and isolate the temperature-dependent component of Mg/Ca it is therefore necessary to reconstruct past changes in  $\Delta[\text{CO}_3^{2-}]$  and subtract this signal from the Mg/Ca ratio measured in benthic foraminifera. To that end we use the co-registered and co-measured B/Ca ratio which in benthic foraminifera correlates well with  $\Delta[\text{CO}_3^{2-}]$  (particularly in *Cibicides wuellerstorfi* and *C. mundulus*) and is thus used in our study to reconstruct  $\Delta[\text{CO}_3^{2-}]$  (Yu and Elderfield, 2007; Rae *et al.*, 2011). This allows us to correct the Mg/Ca of *C. wuellerstorfi* (the benthic foraminifera species used in our study) for the effects of changing  $\Delta[\text{CO}_3^{2-}]$ . See Chapter 3 (Materials and Methods) for details of the calculation of  $\Delta[\text{CO}_3^{2-}]$  from benthic foraminiferal B/Ca and for the correction of Mg/Ca for the effects of changing  $\Delta[\text{CO}_3^{2-}]$ .

## 2.2 Sortable silt mean grain size

The sortable silt mean grain size ( $\overline{SS}$ ) paleocurrent proxy is a measure of the mean grain size of the 10-63  $\mu\text{m}$  size fraction of the terrigenous sediment component (McCave *et al.*, 1995). The non-cohesive nature of this particle size range and the dependence of its size sorting on hydrodynamic processes allow the  $\overline{SS}$  to be used to infer relative changes in the near-bottom speeds of the currents which deposit the material (McCave *et al.*, 1995; McCave and Hall, 2006). The fine end of the silt fraction ( $<10 \mu\text{m}$ ) is excluded from the measurement of  $\overline{SS}$  as the presence of clay minerals results in aggregation and flocculation; the deposition of these flocs and their size sorting is unrelated to the hydrodynamic processes that determine the size sorting of the 10-63  $\mu\text{m}$  fraction (McCave *et al.*, 1995; McCave and Hall, 2006).

Sediment sorting of the 10-63  $\mu\text{m}$  fraction occurs during resuspension and deposition, by aggregate break-up and particle selection according to settling velocity and fluid shear stress. The controlling variables are the critical erosion stress ( $\tau_e$ ), the critical suspension stress ( $\tau_s$ ) and the critical deposition stress ( $\tau_d$ ) which is the stress below which particles with a certain settling velocity will be deposited whereas those with lower settling velocity will remain suspended or will be ejected from the boundary layer (McCave and Hall, 2006). Typically for the 10-63  $\mu\text{m}$  fraction the relationship between these critical variables is  $\tau_d < \tau_e < \tau_s$  and sorting of grains and aggregates within this size fraction is controlled by selective deposition. The hydrodynamic processes of sorting therefore result in larger particle mean grain sizes (i.e., higher  $\overline{SS}$ ) in stronger near-bottom currents and smaller particle mean grain sizes (i.e., smaller  $\overline{SS}$ ) in slower near-bottom flows.

### **2.3 Nitrogen isotopic ratio of bulk sedimentary organic nitrogen**

The nitrogen isotopic ratio of bulk sedimentary organic nitrogen ( $\delta^{15}\text{N}_{\text{bulk}}$ ) is a proxy used for studying the history of the ocean nitrogen cycle (e.g., Galbraith *et al.*, 2008). The  $\delta^{15}\text{N}$  signature of organic matter is acquired as a result of the assimilation of N during the production of biomass by marine organisms. This signature is controlled by the preformed  $\delta^{15}\text{N}$  ratio of nitrate ( $\delta^{15}\text{N}_{\text{nitrate}}$ ) as well as by processes that add and remove N along the water mass flow path in the subsurface, such as remineralisation and water column denitrification. Once the surface isotopic signature has been assimilated into organic matter it is transferred to the seafloor as the material settles out of the surface ocean. The  $\delta^{15}\text{N}_{\text{bulk}}$  therefore reflects the isotopic composition of the sink-

ing flux of organic matter to the seafloor in addition to any secondary isotopic alteration that occurs during the sinking and burial of organic matter due either to the removal or addition of N.

Generally, in the deep ocean below 1000 m,  $\delta^{15}\text{N}_{\text{nitrate}}$  has a value of about 5‰ relative to atmospheric  $\text{N}_2$  (that is, relative to the standard used in  $\delta^{15}\text{N}$  measurements) (Sigman *et al.*, 2000). However, in certain regions of the global ocean and at certain depth intervals, the  $\delta^{15}\text{N}_{\text{nitrate}}$  deviates from the mean deep ocean value due to fractionation processes acting on local and regional scales. The dominant nitrogen isotopic fractionation processes that occur during the addition of N to and removal of N from an initial nitrate pool are nitrogen fixation and denitrification; the latter occurs both in the water column and in marine sediments (Gruber, 2004; Galbraith *et al.*, 2008). Fractionation processes associated with the internal cycling of nitrate are controlled by nitrogen uptake by marine organisms during nitrate assimilation to form organic matter (Gruber, 2004; Galbraith *et al.*, 2008).

Fixed nitrogen is supplied to the ocean by specialist microbes named diazotrophs that inhabit the ocean's surface layer. The supply of new  $\text{N}_2$  through nitrogen fixation has a relatively small isotopic effect that causes  $\delta^{15}\text{N}_{\text{nitrate}}$  to be lowered by only 0-2‰ relative to atmospheric  $\text{N}_2$  (0‰) (Carpenter *et al.*, 1997). On the contrary, the removal of nitrate from the ocean by denitrifying bacteria has a very strong isotopic effect due to the preferential removal of  $^{14}\text{N}$  which results in a residual nitrate pool that becomes progressively enriched in  $^{15}\text{N}$  with increasing nitrate consumption; estimates of the isotopic effect of water column denitrification on  $\delta^{15}\text{N}_{\text{nitrate}}$  range between 22 and 30‰ (e.g., Cline and Kaplan, 1975; Liu and Kaplan, 1989; Altabet *et al.*, 1999; Voss *et al.*, 2001). Water column denitrification occurs in the most oxygen-depleted waters of the ocean where concentrations of dissolved oxygen are below 2-5  $\mu\text{M O}_2$  (Codispoti *et al.*, 2005). In the modern ocean, water column denitrification occurs almost entirely in the oxygen minimum zones of the Eastern Tropical Pacific and the Arabian Sea (Galbraith *et al.*, 2008). Though sedimentary denitrification is an equally important process for the removal of nitrogen from the ocean its effect on  $\delta^{15}\text{N}_{\text{nitrate}}$  is considered to be negligible (Brandes and Devol, 2002; Deutsch *et al.*, 2004).

Finally, the most important fractionating process due to the internal cycling of nitrogen within the marine environment occurs during nitrate assimilation into organic matter in the surface ocean. In this case, the preference for the lighter  $^{14}\text{N}$  causes the isotopic signature of the first organic matter produced from a pool of nitrate to be lower

than the original  $\delta^{15}\text{N}_{\text{nitrate}}$  value. Subsequently, both the residual nitrate pool and the organically produced N become progressively enriched in terms of  $\delta^{15}\text{N}$  as nitrate consumption continues. The isotopic effect of nitrate assimilation based on measurements of the  $\delta^{15}\text{N}_{\text{nitrate}}$  in the upper ocean has been estimated to be between 4 to 10‰, although most studies report values closer to 5-8‰ (Altabet, 1988; Altabet *et al.*, 1999b; Sigman *et al.*, 1999; Altabet and Francois, 2001; DiFiore *et al.*, 2006).

Although  $\delta^{15}\text{N}_{\text{bulk}}$  has been an important proxy for reconstructing past biogeochemical cycling processes there is a growing awareness of its susceptibility to alteration during burial and early sedimentary diagenesis, particularly in open ocean settings with low sediment accumulation rates (Robinson *et al.*, 2012). Consequently, the signal recorded in ocean sediments may deviate from the signal expected from biogeochemical processes operating in the overlying water column. These concerns about the impact of seafloor processes on  $\delta^{15}\text{N}_{\text{bulk}}$  in open ocean settings have increasingly led to the study of the isotopic composition of N bound within the silica frustules of diatoms (e.g., Sigman *et al.*, 1999; Crosta and Shemesh, 2002; Robinson *et al.*, 2004) and the calcite tests of planktonic foraminifera (e.g., Altabet and Curry, 1989; Ren *et al.*, 2009; 2012; Straub *et al.*, 2013; Martínez-García *et al.*, 2014). Despite these concerns about alteration of the  $\delta^{15}\text{N}_{\text{bulk}}$  preserved in slowly accumulating open ocean regions, the available empirical data suggest that  $\delta^{15}\text{N}_{\text{bulk}}$  records do in fact primarily reflect changes in the  $\delta^{15}\text{N}$  signature of nitrate exported from the surface ocean, rather than differential alteration on the seafloor and within sediments (Robinson *et al.*, 2012).

## 2.4 Elemental analysis

In this study we evaluated the elemental composition of sediments along a marine sediment core using the X-ray fluorescence (XRF) core scanning technique (Rothwell, 2006). This technique adapts the principles of XRF analysis typically used to measure the composition of rocks and sediments (Ramsey *et al.*, 1995; Jenkins, 1999) to the non-destructive core scanning method that allows element intensities to be measured in near-continuous resolution along sediment cores with minimum analytical effort. The results obtained are typically presented as count rates (i.e., counts per unit time per unit area) or as ratios of counts which only allow the estimation of relative abundances of elements (Rothwell, 2006).

The underlying principle of XRF analysis relies on the excitation of electrons by incident X-radiation which leads to the ejection of electrons from inner atomic shells to

create vacancies that are then filled by electrons falling back from the outer shells. The surplus energy associated with these electron re-adjustments is emitted as a pulse of X-radiation and since emitted fluorescence energy and wavelength spectra are characteristic of atoms of specific elements, the relative abundances of these elements can be estimated (Weltje and Tjallingii, 2008). Details regarding the use of the XRF core scanning results in this study to estimate relative changes in the supply of terrestrial material to marine sediments is given in Chapter 7 of this thesis.

## **2.5 Radiocarbon dating**

Radiocarbon dating has been used in this study to produce the chronostratigraphic frameworks for the upper sections of the two cores presented in this thesis. Radiocarbon ( $^{14}\text{C}$ ) is a cosmogenic isotope that is formed in the atmosphere by the interaction of cosmic rays with nitrogen ( $^{15}\text{N}$ ) in the upper atmosphere. The radiocarbon formed in the upper atmosphere is mostly in the form of  $\text{CO}_2$  molecules that enter the global carbon cycle. Radiocarbon has a half-life of 5730 years and its incorporation into DIC in the ocean makes it one of the most important techniques for dating marine sediments for the last 40 to 50 kyr BP (Stuiver, 1998).

Application of radiocarbon dating to the marine environment requires special considerations as measured dates have to be calibrated for the potential variability of  $^{14}\text{C}$  production as a result of magnetic field intensity and solar variability (Stuiver and Braziunas, 1993b) as well as changes in the distribution of  $^{14}\text{C}$  between the various reservoirs, particularly the ocean (e.g., Siegenthaler and Sarmiento, 1993). Marine carbonates must additionally be corrected for a reservoir effect caused by the delay in exchange rates between atmospheric  $\text{CO}_2$  and bicarbonate in the ocean (see Chapter 1, section 1.2.1 for carbonate chemistry equations) and the dilution effect caused by mixing between surface waters and deep waters with older radiocarbon ages due to the longer duration of their isolation from the atmosphere (i.e., the marine reservoir effect) (Stuiver and Braziunas, 1993a).

---

## 3 Materials and methods

---

### 3.1 Sediment core site locations

#### 3.1.1 MD02-2588

The CASQ (Calypso square-corer) sediment core MD02-2588 was recovered from the southwestern flank of the Agulhas Plateau in 2002 during the RV *Marion Dufresne* cruise MD128 - SWAF (South West African) (Giraudeau, 2002) (Fig. 3.1). The core site is located at 41°19.90'S, 25°49.40'E at a water depth of 2907 m and was recovered from a sediment drift that is closely aligned with the flank of the Agulhas Plateau and which follows the plateau topography (Uenzelmann-Neben, 2001) (Fig. 3.2). The coring operation recovered 1070 cm of sediment that is primarily composed of slightly bioturbated, light grey to olive silty clay.

#### 3.1.2 CD154-23-16P

Marine sediment core CD154-23-16P (piston core) was retrieved from the flank of the Mallory Seamount in 2004 during the RRS *Charles Darwin* cruise number 154 (Hall and Zahn, 2004) (Fig. 3.2). The core site is located at 36°49.08'S, 022°00.02'E at a water depth of 3189 m and was recovered from a sediment pile that had accumulated on the down-current, lee-side of the main seamount peak. Sediment recovery from the coring operation was 1103 cm. The material is composed of soft, watery, green and brown-green mud in the upper part, with abundant foraminifera, radiolaria and sponge spicules. In the lower part of the core the sediments are not as soft and are more green-grey in colour; they are also reported as lacking the siliceous elements (radiolaria, sponge spicules) that are found in the upper sections of the core.

#### 3.1.3 RR03-05 Multicores

We also make use of six multicores recovered from the south west Pacific in 2005 during the R/V *Roger Revelle* cruise RR05-03. The core sites are located to the east and north of New Zealand and were retrieved from water depths ranging from 1335 m to 3575 m. For the core location details see Fig. 3.3 and Table 3.1.

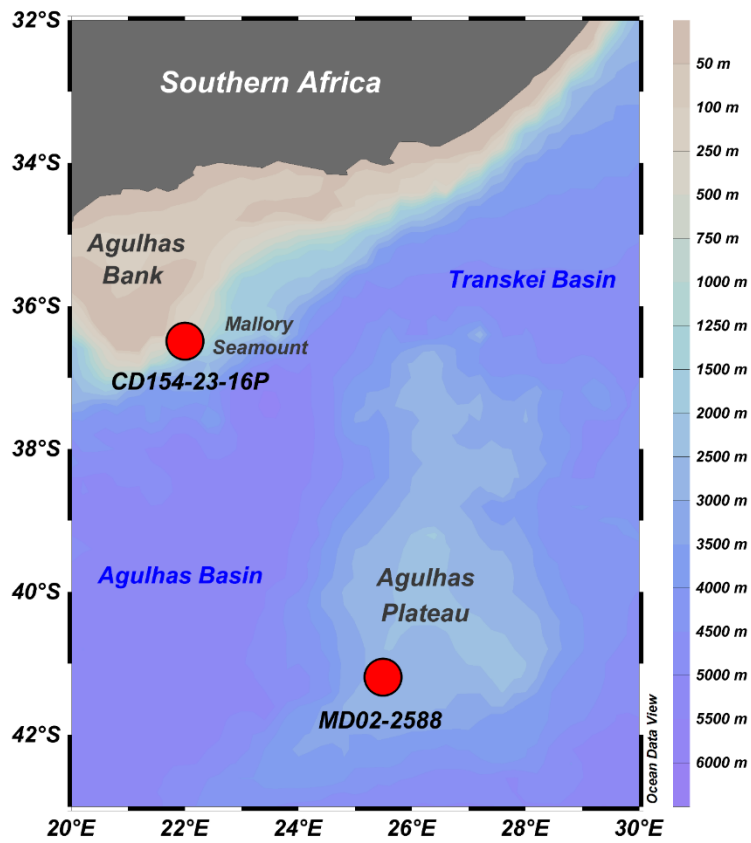


**Figure 3.1.** Bathymetric map showing the location of sediment cores MD02-2588 on the Agulhas Plateau and CD154-23-16P on the Mallory Seamount. Map produced and edited in Ocean Data View (Schlitzer, 2016).

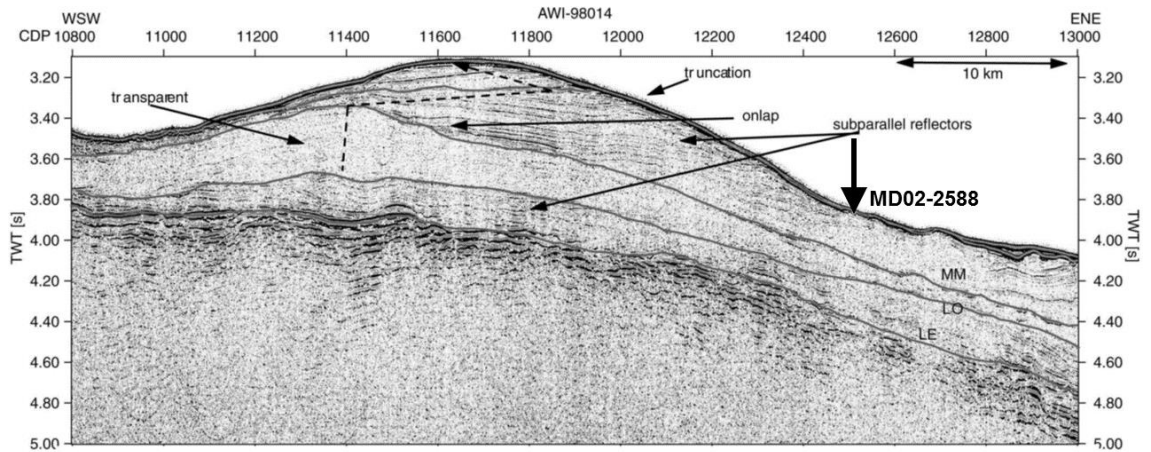


**Figure 3.2.** Multichannel seismic reflection data of the sediment drift deposit on the southern Agulhas Plateau from which sediment core MD02-2588 was recovered (figure adapted from Uenzelmann-Neben, 2001; Seismic Line AWI-98014, gathered in 1997/98). The approximate location of the core site was identified by using the two-way time (TWT) and assuming a velocity through water of  $1500 \text{ m s}^{-1}$  (where  $\text{TWT} = 2 * [\text{Core site water depth} / \text{sound velocity through water}]$ ). For the core site water depth of 2907 m, TWT is 3.88 s. LE = Lower Eocene, LO = Lower Oligocene, MM = Middle Miocene.

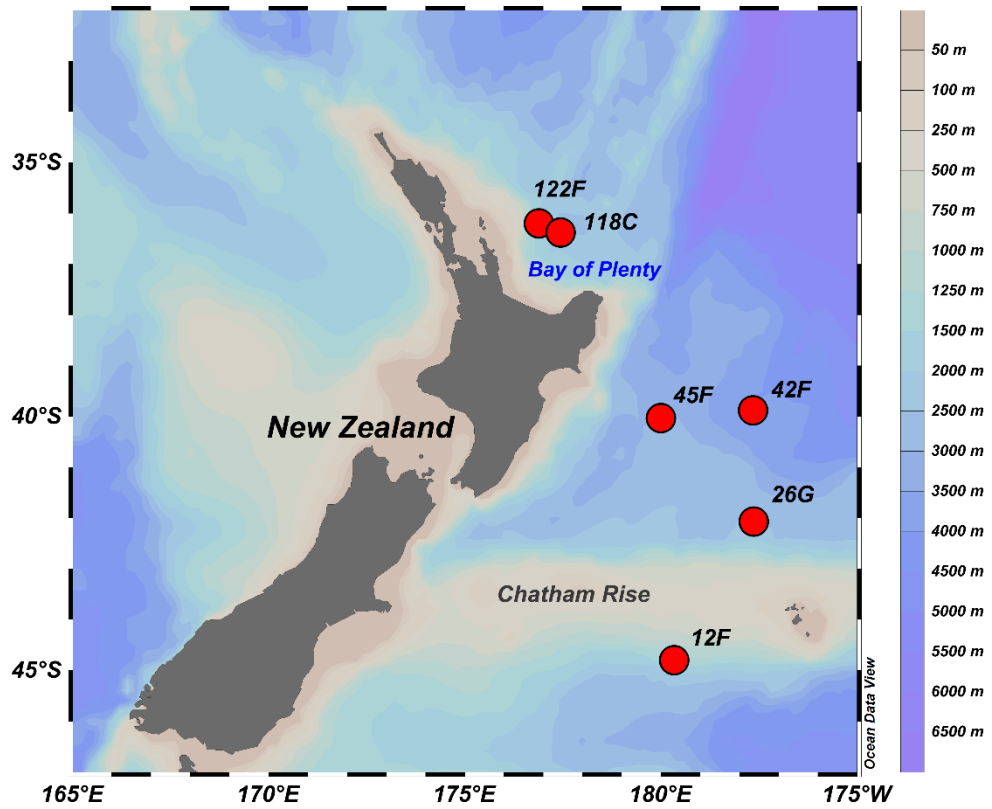


**Figure 3.3.** Bathymetric map showing the location of the multicores from around New Zealand collected during cruise *RR03-05*. Map produced and edited in Ocean Data View (Schlitzer, 2016).

**Table 3.1.** *RR03-05* multicore locations and water depths

<b>Core-top name</b>	<b>Latitude</b>	<b>Longitude</b>	<b>Water Depth (m)</b>
MC-12F	44°47.83 S	179°39.76 W	1335
MC-26G	42°04.47 S	177°37.56 W	2418
MC-42F	39°52.64 S	177°39.46 W	3575
MC-45F	40°01.97 S	179°59.75 W	2991
MC-118C	36°22.63 S	177°26.75 E	2252
MC-122F	36°11.91 S	176°53.35 E	2541

## 3.2 Sediment core age models

### 3.2.1 Age model of sediment core MD02-2588

The chronostratigraphic framework of sediment core MD02-2588 was developed by Ziegler *et al.*, (2013) but is summarised here for completeness. The upper section of the core (<40 kyr BP) was constrained by 15 calibrated accelerator mass spectrometry (AMS) carbon-14 ( $^{14}\text{C}$ ) dates from measurements made on monospecific samples of the planktonic foraminifera *Globigerina bulloides* and *Globorotalia inflata*. Measurements were carried out at the Scottish Universities Environmental Research Centre (SUERC) Accelerator Mass Spectrometer laboratory. The AMS  $^{14}\text{C}$  ages were reservoir corrected by 800 years and then converted to calendar ages using the calibration curve of Fairbanks *et al.*, (2005). Conventional radiocarbon ages between 115 and 130 m in the core were older than ~ 40 kyr BP and were thus not included as control points in the age model construction.

For the lower section of the core (>40 kyr BP), between 105 and 1070 cm, the age model was developed by graphically tuning the core's benthic foraminiferal stable isotope record to the European Project for Ice Coring in Antarctica (EPICA) Dome C (EDC)  $\delta\text{D}$  record on the EDC3 timescale (Parrenin *et al.*, 2007). The complete age model yields an average sedimentation rate of 3.4 cm kyr<sup>-1</sup>. A table of radiocarbon ages and graphical tuning control points can be found in Ziegler *et al.*, (2013).

### 3.2.2 Age model of sediment core CD154 23-16P

An initial age model was constructed by tuning the Ca/Fe ratio derived from XRF scanning of sediment core CD154-23-16P (Hall, 2003; unpublished dataset) to the Chinese speleothem oxygen isotope record from the Sanbao and Hulu Caves (Wang *et al.*, 2001). This initial tuning allowed the identification of 10 sediment intervals that were subsequently sampled for radiocarbon dating of planktonic foraminifera consisting principally *Globigerinoides ruber (sensu lato)* but supplemented by tests of *G. ruber (sensu stricto)* when the former was not abundant enough. Picked samples weighed 12-13 mg and had a carbon content of ~ 10 % by weight. The samples were prepared to graphite at the Natural Environment Research Council (NERC) Radiocarbon Facility (East Kilbride) and underwent  $^{14}\text{C}$ -analysis at the Scottish Universities Environmental Research Centre (SUERC) AMS Laboratory. The radiocarbon ages were reported as conventional radiocarbon years BP (relative to AD 1950). The

chronostratigraphic framework of sediment core CD154-23-16P is developed and discussed in more detail in Chapter 7 of this thesis.

### **3.3 X-ray fluorescence (XRF) core-scanning**

#### *3.3.1 MD02-2588 XRF core-scanning*

(measured by Ian Hall and Martin Ziegler)

XRF scanning on sediment core MD02-2588 was performed using the ITRAX™ XRF Core scanner at the British Ocean Sediment Core Research Facility (BOSCORF), Southampton. Measurements were made at 1 cm intervals, with the count rate per sample set to 30 s and the XRF voltage and current set at 45 kV and 20 mA, respectively. Prior to scanning, the core surface was lightly sprayed with deionised water and smoothed with a plastic scraper to remove irregularities in the sediment that could have impacted the scanning operation. Cracks along the surface of the desiccated core resulted in the inclusion of analytical artefacts in the raw XRF scanning data. These analytical artefacts were identified in the raw data by monitoring the downcore records of total kilo-counts-per-second (kcps), calcium normalised with the total kilo-counts-per-second (Ca/kcps) and calcium normalised with iron (Ca/Fe). Cracks along the core were identified by substantial reduction in counts. Where these reductions were observed to also impact the Ca/kcps and Ca/Fe records, the data were labelled as corrupted and removed from the dataset. The Ca/kcps and Ca/Fe data were used so that cracks that did not affect the final records were not removed unnecessarily; calcium (Ca) and iron (Fe) were chosen because of their high abundance along the core. The data at each side of these artefacts were assumed to have originally been adjacent to each other. As such, the removal of the corrupted data associated with the cracks would have resulted in a shortening of the total core section length. This was corrected by leaving the top and bottom of each core section at their original depths and ‘stretching’ all the data between these two points. Thus, instead of shortening the core section length, the length of each sample became longer, allowing better comparison of the XRF core scanning data with the other datasets extracted from discrete samples along the core.

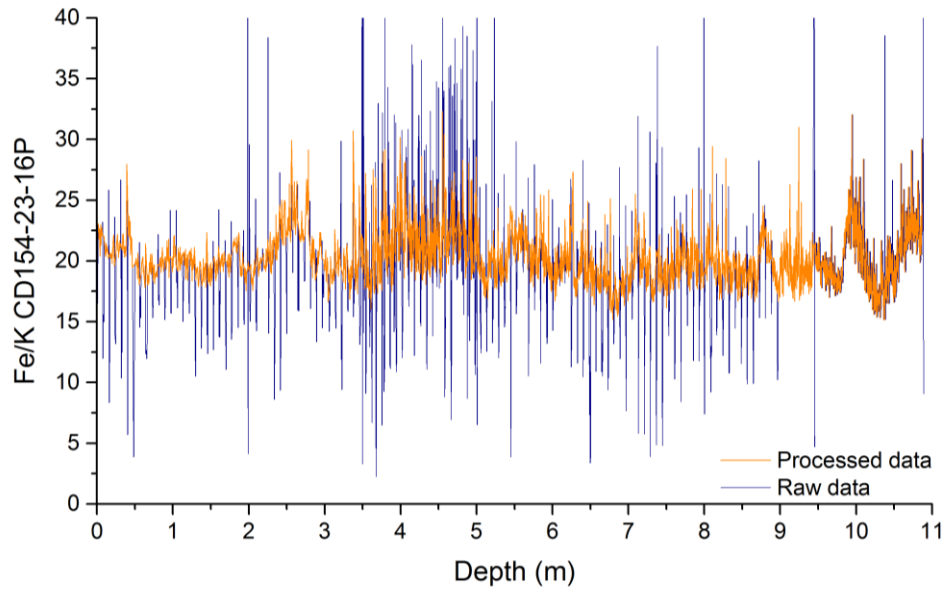


**Figure 3.4.** Raw and processed Fe/K XRF scanning data along sediment core CD154-23-16P. Processing in this case refers to the removal of the sampling artefacts in the elemental scanning records associated with the presence of gaps along the sediment core from where samples were extracted.

### 3.3.2 CD154-23-16P XRF core-scanning

XRF scanning on sediment core CD154-23-16P was also performed using the ITRAX™ XRF Core scanner at BOSCORF, Southampton. Measurements were made at variable resolutions along the core with a 0.5 cm resolution in the upper 3.5 m, a 0.1 cm resolution between 3.5 and 5 m and a 0.2 cm resolution for the remainder of the core. Count time per sample was set to 30 s and the XRF voltage and current were set at 30 kV and 50mA, respectively. Prior to scanning, the core surface was lightly sprayed with deionised water and smoothed with a plastic scraper to remove any irregularities in the sediment that could have impacted the scanning operation. We note that scanning was performed on the working half of the core (i.e., the same half from which samples had been taken) because of the bad condition of the archive half. This resulted in the inclusion of analytical artefacts in the raw XRF scanning data like those introduced by the cracks along MD02-2588. These were processed in a similar way to the method presented above and were removed for the final presentation of the data (for example, see Fig. 3.4 which demonstrates the pre- and post-processed Fe/K data). The only difference in processing relative to MD02-2588, was that the gaps in the CD154-23-16P record were not due to desiccation and shortening. Rather they reflected the removal of discreet sediment samples that had subsequently been infilled with plastic/polystyrene fillers. Thus, the position of each XRF data point was assumed to be in its original position and no ‘stretching’ was required.

The downcore XRF-scanning record of Fe from sediment core CD154-23-16P may be susceptible to the effects of diagenetic remobilisation of Fe and the precipitation of Mn-Fe oxides as micronodules within the sediment and as coatings on sedimentary particles (e.g., Burdige, 1993; Calvert and Pedersen, 1996). Such effects could ultimately impact the application of the Fe/K elemental ratio as a proxy for the deposition of terrigenous material from the African continent. We therefore examined the covariation between Fe and Mn counts derived from the XRF scans along this core to assess the potential impacts from diagenetic processes (Fig. 3.5). This comparison reveals the absence of major peaks in either Mn counts or Fe Counts that could be associated with diagenetic processes. For example, the upper sections of comparable records from sediment cores CD154-10-06P and CD154-17-17K are characterised by peaks with values of normalised Mn (i.e., Mn/total counts per second) that exceed

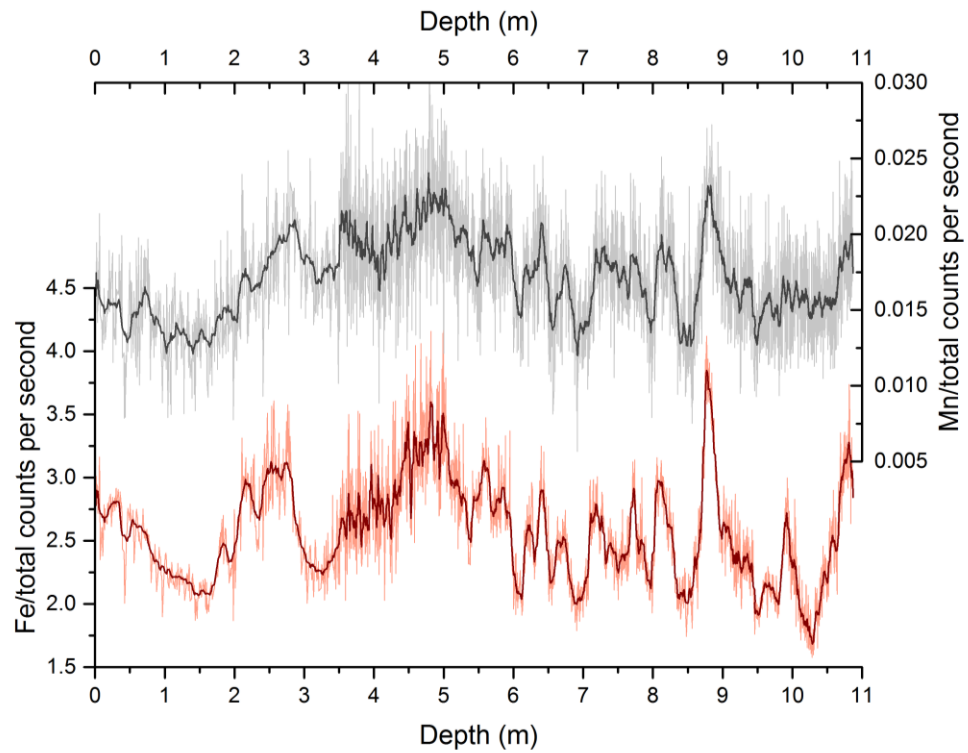


**Figure 3.5.** Upper panel (grey) shows the XRF scanning downcore profile of normalised Mn (Mn/total counts per second) from CD154-23-16P. Lower panel (red) shows the corresponding XRF scanning profile of normalised Fe (Fe/total counts per second) from the same core.

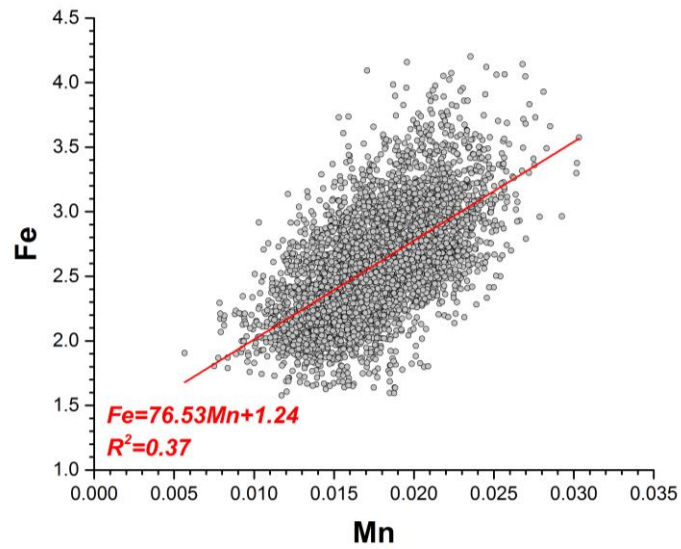


**Figure 3.6.** Scatter plot of downcore Fe vs downcore Mn from sediment core CD154-23-16P with line of best fit (red) through the data. Linear equation is also displayed along with the coefficient of determination ( $R^2$ ).

0.1, and in some cases, reach values close to 1 (Ziegler *et al.*, 2013; Simon *et al.*, 2015); in the case of CD154-23-16P, normalised Mn values are all within the range of 0.005-0.03 (Fig. 3.5). We do however note a strong similarity in the patterns of variability of the normalised Fe (i.e., Fe/total counts per second) and Mn records; simple linear regression of the two records returns an  $r^2$  value of 0.37 (Fig. 3.6). In the absence of evidence for a diagenetic or local hydrothermal source of Fe and Mn, we believe that the most likely explanation for the observed co-variation of these two elements is their common continental source and their input into the ocean via a common fluvial pathway from southeastern Africa (Martin and Meybeck, 1979). This reinforces the applicability of the Fe/K record in CD154-23-16P as a proxy of local changes in the fluvial input of terrigenous material.

### **3.4 Sediment sampling and processing**

The entire 1070 cm of sediment recovered in core MD02-2588 had been previously sampled at 1 cm intervals and processed at Cardiff University prior to the initiation of the work presented in this thesis. Samples had been washed over a wet sieve using a fine spray of deionised water and dried in an oven at 40°C. The fine (<63 µm) and coarse (>63 µm) fractions were then weighed for the calculation of the weight % of coarse and fine fractions (Hall and Diz, unpublished data). A split of the dried fine fraction material was processed for sortable silt mean grain size measurements while the dried coarse fraction material was used to pick foraminifera samples for stable isotope and elemental ratio analysis. Bulk sediment samples were also taken for nitrogen isotope analysis.

The full length of this core has been shown to extend back to ~350 kyr BP (Ziegler *et al.*, 2013). The sampling for the work presented in this thesis focused on the interval between 0 and 460 cm which corresponds to the last 150 kyr BP. We took splits from a total of 204 separate sediment intervals, with an approximate sampling resolution of 1 cm in the 0-100 cm depth interval, 1-2 cm resolution in the 360-460 cm depth interval, and an average sampling resolution of 5-6 cm for the section in between. This sampling strategy was intended to allow a more detailed investigation of the last two major glacial-interglacial transitions (i.e., the transitions between Marine Isotope Stage (MIS) 2 and MIS 1, and between MIS 6 and MIS 5). The bulk sediment samples for nitrogen isotope analysis were taken throughout the upper 450 cm of the core at approximately 5 cm intervals.

Sediment processing of core CD154-23-16P was identical to the procedure described above although the sampling resolution was lower. Our sampling focussed on the upper 897 cm out of the total 1103 cm of recovered sediment. Samples were taken every 8 cm, resulting in a total of 113 samples. These were supplemented by ten additional samples from which planktonic foraminifera were picked for radiocarbon dating.

The six core top samples (0-1 cm slice) from the multicores retrieved in the south west Pacific during cruise RR05-03 were processed at Rutgers University (Yair Rosenthal's laboratory) prior to the initiation of the current study. The coarse fraction samples were shipped to Cardiff University for planktonic foraminifera stable isotope analysis.

### **3.5 Stable isotope analysis of foraminiferal calcite**

To measure the stable isotopic composition of foraminiferal calcite during this study, the coarse fraction of each sediment sample was dry-sieved into narrow size fractions and foraminifera tests were carefully picked under a light microscope using a fine paint brush. We visually inspected each sample and selected the best preserved and cleanest individual foraminifera tests. The picked foraminifera samples were then transferred to a glass vial with a small amount of trace-grade methanol and were lightly ultrasonicated. The aim of this gentle cleaning step was to dislodge any contaminating carbonate material (e.g., small/juvenile foraminifera, coccoliths or detrital carbonate) which may have been adhering to the surface of individual foraminifera tests or which may have been trapped within the foraminifera test apertures.

The foraminifera samples from sediment core MD02-2588 were intended for paired stable isotope and elemental ratio analysis. Following the picking of foraminifera tests and their ultrasonication in methanol, the foraminifera samples were crushed between two clean glass plates, homogenised, and then split into two aliquots for the respective stable isotope and elemental ratio analyses. Approximately a third of the original volume was used for stable isotope analysis and the remaining two thirds were used for elemental analysis. Samples which were intended for replicate elemental analyses were split into three aliquots of  $1/3^{\text{rd}}$  each (i.e.,  $1/3^{\text{rd}}$  for stable isotope measurements and two separate samples of  $1/3^{\text{rd}}$  each for elemental ratio analysis).

The stable oxygen and carbon isotope analysis in sediment core MD02-2588 was performed on the deep-dwelling planktonic foraminifera species *Globorotalia truncatuli*

*noides (sinistral)* ( $\delta^{18}\text{O}_{G.trunc(s)}$  and  $\delta^{13}\text{C}_{G.trunc(s)}$ ) (n=171) and on the benthic foraminifera species *Cibicidoides wuellerstorfi* ( $\delta^{18}\text{O}_{C.wuell}$  and  $\delta^{13}\text{C}_{C.wuell}$ ) (n=132). For the planktonic foraminifera samples, approximately 50 individual tests were picked from the 250-315  $\mu\text{m}$  size fraction; for intervals where we intended to perform replicate measurements we picked 60-70 tests. In the case of the benthic foraminifera samples, where the number of picked tests was generally lower and more variable from sample to sample, it was sometimes necessary to increase the size fraction range to  $>250 \mu\text{m}$ . Generally, samples for paired stable isotope and elemental ratio analysis were composed of 20-25 individual *C. wuellerstorfi* tests. In samples of  $<15$  tests, we prioritised the elemental analysis; replicate elemental analyses were performed on samples containing  $>30$  tests.

In the case of the samples from CD154-23-16P, the stable isotope measurements were performed on the surface-dwelling planktonic foraminifera species *Globigerinoides ruber (sensu lato)* ( $\delta^{18}\text{O}_{G.ruber}$  and  $\delta^{13}\text{C}_{G.ruber}$ ) (n=112) and on the deep-dwelling planktonic species *G. truncatulinoides (s.)* (n=113). Foraminifera tests were picked from the 250-315  $\mu\text{m}$  size fraction. Each sample consisted of 15-30 individual tests of *G. ruber (s.l.)* and 8-20 tests of *G. truncatulinoides (s.)*. The foraminifera samples from this core were not crushed.

For the core-top samples from the six RR05-03 multicores, we picked *G. truncatulinoides* from various narrow size-fraction ranges and further separated the picked tests according to their coiling direction (i.e., sinistral and dextral). This sampling strategy extended the total sample number to 25 with duplicate measurements performed for all but three of these. Our initial intention was to also measure the elemental composition of these samples so the picked foraminifera tests were crushed and homogenised as described above for the foraminifera samples from sediment core MD02-2588.

Stable isotopes were measured at Cardiff University using either a Thermo Finnigan MAT 253 mass spectrometer linked to a Carbo Kiel-II carbonate preparation device or a Thermo Scientific Delta V Advantage mass spectrometer coupled with a Gas Bench III automated preparation device. The spectrometers were calibrated through the international carbonate standard NBS-19 and all isotopic results are reported as a per mille deviation from the Vienna Pee Dee Belemnite scale ( $\text{‰ VPDB}$ ). The long-term external precision of the Thermo Finnigan MAT 253 mass spectrometer, based on an internal laboratory carbonate standard (Carrara Marble), was better than  $\pm 0.04$

‰ and  $\pm 0.02$  ‰ for  $\delta^{18}\text{O}$  and  $\delta^{13}\text{C}$ , respectively ( $\pm 1\sigma$ ). For the Thermo Scientific Delta V Advantage mass spectrometer the long-term precision was better than  $\pm 0.06$  ‰ and  $\pm 0.03$  ‰ for  $\delta^{18}\text{O}$  and  $\delta^{13}\text{C}$ , respectively ( $\pm 1\sigma$ ).

The stable oxygen and carbon isotopes measurements of *C. wuellerstorfi* and *G. truncatulinoides* (*s.*) samples from sediment core MD02-2588 replicate some of the previously published data of Ziegler *et al.*, (2013). The new measurements made for the study presented herein ( $n=132$  and  $n=171$  for *C. wuellerstorfi* and *G. truncatulinoides* (*s.*), respectively), are combined with the previously published data ( $n=453$  and  $n=454$ , for the benthic and planktonic species, respectively; Ziegler *et al.*, 2013). The pooled standard deviation from the replicated  $\delta^{18}\text{O}_{C.wuell}$  measurements is  $0.09$ ‰, which is twice the long-term external instrumental precision ( $0.045$ ‰). The pooled standard deviation from the replicated  $\delta^{13}\text{C}_{C.wuell}$  measurements is  $0.07$ ‰, which is again more than twice the long-term external instrumental precision of  $0.02$ ‰. Combining the two *G. truncatulinoides* (*s.*) datasets from MD02-2588 yields a pooled standard deviation of  $0.16$  ‰ for  $\delta^{18}\text{O}_{G.trunc(s)}$  and  $0.09$  ‰ in the case of  $\delta^{13}\text{C}_{G.trunc(s)}$ .

This doubling of the pooled standard deviation relative to the instrumental error most likely results from the combined effect of instrumental offsets, methodological inconsistency between this study and that of Ziegler *et al.*, (2013) and the natural variability of the chemistry of the individual tests present in the same sediment intervals. Nonetheless, comparison of the data from each study indicates that there is a strong correlation between the datasets. For the  $\delta^{18}\text{O}_{C.wuell}$ , the correlation between the datasets is characterised by  $\rho=0.93$  and  $r^2=0.86$  ( $n=130$ ) while for  $\delta^{13}\text{C}_{C.wuell}$  the correlation is described by  $\rho=0.94$  and  $r^2=0.88$  (Fig. 3.7a). In the case of the *G. truncatulinoides* (*s.*) data, the correlation between the two  $\delta^{18}\text{O}_{G.trunc(s)}$  datasets is  $\rho=0.80$  and  $r^2=0.64$  ( $n=165$ ) and between the  $\delta^{13}\text{C}_{G.trunc(s)}$  datasets it is characterised by  $\rho=0.92$  and  $r^2=0.86$  ( $n=165$ ) (Fig. 3.7b).

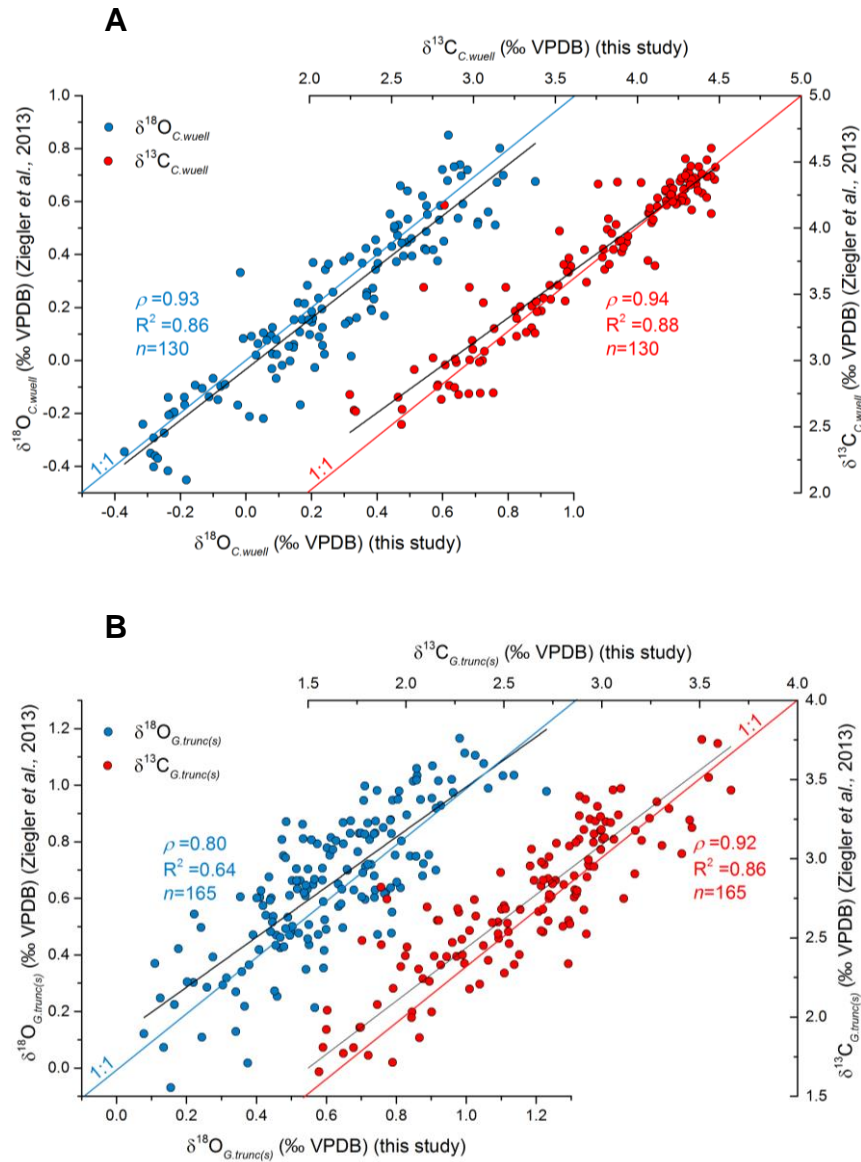


**Figure 3.7.** Comparison of stable oxygen (blue) and carbon isotope (red) ratios measured in (A) the benthic foraminifera species *Cibicoides wuellerstorfi* ( $\delta^{18}\text{O}_{C.wuell}$  and  $\delta^{13}\text{C}_{C.wuell}$ , respectively) and (B) the planktonic species *Globorotalia truncatulinoides* (*sinistral*) from sediment core MD02-2588. Data are from this study versus those of Ziegler et al., (2013). Measurements were performed on samples from the same depth intervals in sediment core MD02-2588. The 1:1 lines of each isotope are shown as the blue ( $\delta^{18}\text{O}_{C.wuell}$ ) and red ( $\delta^{13}\text{C}_{C.wuell}$ ) lines and the lines of best fit through the data are shown as black lines in both cases. Also displayed are the Pearson's r ( $\rho$ ) and the coefficient of determination ( $R^2$ ) for each dataset.

### 3.6 Estimating the stable oxygen isotope composition of seawater ( $\delta^{18}\text{O}_{\text{sw}}$ ) from benthic foraminiferal $\delta^{18}\text{O}$

The  $\delta^{18}\text{O}$  composition of foraminiferal tests ( $\delta^{18}\text{O}_{\text{foram}}$ ) is dependent on: (i) the  $\delta^{18}\text{O}$  composition of the seawater ( $\delta^{18}\text{O}_{\text{sw}}$ ) in which the tests are biogenically precipitated, and (ii) the temperature-dependent fractionation of oxygen isotopes between water and calcium carbonate during shell formation. A large component of the downcore variability of  $\delta^{18}\text{O}_{\text{foram}}$  observed in sediment cores is due to past variations of whole-ocean  $\delta^{18}\text{O}_{\text{sw}}$  because of the growth and decay of large ice sheets during glacial-interglacial cycles (Shackleton, 1967). However, downcore records of  $\delta^{18}\text{O}_{\text{foram}}$  can be corrected for the effects of changing ice volume with the use of contemporaneous sea level records (e.g., Waelbroeck *et al.*, 2002; Siddall *et al.*, 2003). This correction was applied to the stratigraphic series of  $\delta^{18}\text{O}_{G.\text{trunc}(s)}$  and  $\delta^{18}\text{O}_{C.\text{wuell}}$  generated from sediment core MD02-2588 to derive the ice-volume corrected  $\delta^{18}\text{O}_{\text{foram}}$  ( $\delta^{18}\text{O}_{\text{ivc-foram}}$ ) for the intermediate and bottom waters at this core site (Fig. 3.8).

The ice-volume correction was estimated by converting the available sea level records to an equivalent  $\delta^{18}\text{O}$  value ( $\delta^{18}\text{O}_{\text{sea level}}$ ). This was achieved by first assuming that a  $128\pm 5$  m sea level lowering during the LGM (18-30 kyr BP) (Lambeck *et al.*, 2004), would result in a  $^{18}\text{O}$  enrichment of the global ocean of  $0.008\pm 0.001\text{‰}$  (in units of Vienna Standard Mean Ocean Water, VSMOW) per meter of sea level lowering (Schrag *et al.*, 2002). Using this value in combination with the estimated sea level (ESL) reconstruction from Lambeck *et al.*, (2004) for the 0-34 kyr BP interval and the Red Sea relative sea level (RSL) reconstruction from Grant *et al.*, (2012) for the 34-150 kyr interval, we computed the global contribution of changes in ice volume to the global mean ocean value of  $\delta^{18}\text{O}_{\text{sw}}$  ( $\delta^{18}\text{O}_{\text{sea level}}$ ) using the relationship:

$$\delta^{18}\text{O}_{\text{sea level}} = -0.008\pm 0.001\text{‰ ESL\&RSL} + 0.27\text{‰}$$

Eq. 3.1

where ESL&RSL represents the estimated and relative sea level for the 0-34 kyr BP (Lambeck *et al.*, 2004) and 34-150 kyr Grant *et al.*, (2012) intervals, respectively. The addition of  $0.27\text{‰}$  accounts for the conversion of  $\delta^{18}\text{O}_{\text{sea level}}$  from VSMOW to VPDB (Hut, 1987).

The downcore records of  $\delta^{18}\text{O}_{G.\text{trunc}(s)}$  and  $\delta^{18}\text{O}_{C.\text{wuell}}$  from MD02-2588 were converted to a chronostratigraphic framework using to the age model of Ziegler *et al.*,

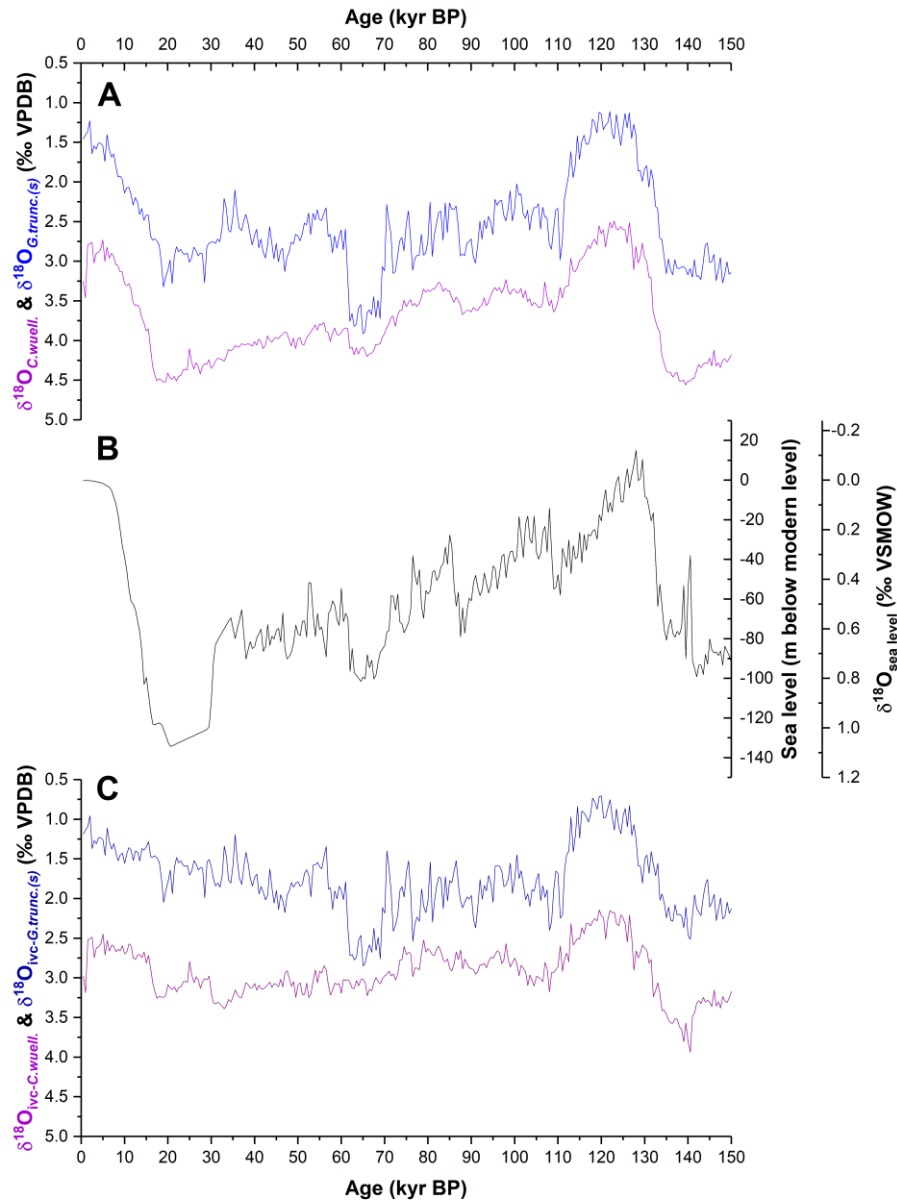


**Figure 3.8.** A) MD02-2588 oxygen isotope stratigraphic series generated from *Globorotalia truncatulinoides* (*sinistral*) ( $\delta^{18}\text{O}_{G.trunc(s)}$ ; blue line) and *Cibicidoides wuellerstorfi* ( $\delta^{18}\text{O}_{C.wuell.}$ ; purple line) incorporating data from this study and that of Ziegler *et al.*, (2013). Note inverted y-axis. VPDB: Vienna Pee Dee Belemnite. B) Global sea level change and corresponding time-series of global ocean  $\delta^{18}\text{O}$  ( $\delta^{18}\text{O}_{sea level}$ ; i.e., the ice volume component in the  $\delta^{18}\text{O}_{C.wuell.}$  record). The Sea level record incorporates the estimated and relative sea level data (ESL and RSL, respectively). ESL data are from Lambeck *et al.*, (2014) and cover the 0-34.5 kyr BP interval whereas the RSL data which cover the interval 35-150 kyr BP are from Grant *et al.*, (2012). C) Ice-volume corrected seawater  $\delta^{18}\text{O}$  ( $\delta^{18}\text{O}_{IVC-sw}$ ) based on subtracting  $\delta^{18}\text{O}_{sea level}$  from  $\delta^{18}\text{O}_{G.trunc(s)}$  (blue line) and  $\delta^{18}\text{O}_{C.wuell.}$  (blue line). All records have been interpolated onto an evenly spaced scale with a resolution of 500 years per sample).

(2013) and all the records were then interpolated onto an evenly spaced 500-year grid using piecewise linear interpolation. This was done to account for the uneven sampling along sediment core MD02-2588 and to align the MD02-2588 data points to those of the published sea level records. The  $\delta^{18}\text{O}_{\text{sea level}}$  record was subsequently subtracted from the  $\delta^{18}\text{O}_{\text{foram}}$  records to produce the  $\delta^{18}\text{O}_{\text{ivc-foram}}$  reconstructions for the MD02-2588 core site:

$$\delta^{18}\text{O}_{\text{ivc-foram}} (\text{VPDB}) = \delta^{18}\text{O}_{\text{foram}} - \delta^{18}\text{O}_{\text{sea level}}$$

Eq. 3.2

Full propagation of the errors associated with  $\delta^{18}\text{O}_{G.\text{trunc}(s)}$ ,  $\delta^{18}\text{O}_{C.\text{wuell}}$ , ESL, RSL, and  $\delta^{18}\text{O}_{\text{sea level}}$  yields pooled errors of 0.18‰ and 0.12‰ for the downcore records of  $\delta^{18}\text{O}_{\text{ivc-foram}}$  from *G. truncatulinoides* (*s.*) ( $\delta^{18}\text{O}_{\text{ivc-}G.\text{trunc}(s)}$ ) and *C. wuellerstorfi* ( $\delta^{18}\text{O}_{\text{ivc-}C.\text{wuell}}$ ), respectively.

### 3.7 Elemental ratio sample processing and analysis by Inductively Coupled Plasma Mass Spectrometry

Inductively Coupled Plasma Mass Spectrometry (ICP-MS) elemental ratio analyses in sediment core MD02-2588 were performed on samples composed of tests the deep-dwelling planktonic foraminifera species *G. truncatulinoides* (*s.*) (247 measurements, including 24 replicated samples) and on the epibenthic species, *C. wuellerstorfi* (227 measurements, including 24 replicated samples). Where possible, we used aliquots from samples that were split for paired stable isotope analysis. Where the volume of material was insufficient to allow paired measurements, we prioritised the elemental ratio analysis. We also picked 11 samples of the infaunal benthic foraminifera *Uvigerina spp.* in the upper section of MD02-2588 to compare the elemental ratio results between this species with those from samples of *C. wuellerstorfi*.

#### 3.7.1 Foraminifera sample processing and elemental ratio analysis

Following the crushing, mixing and splitting of the foraminifera samples from sediment core MD02-2588, the aliquots for elemental ratio analysis were prepared and cleaned following the protocol originally developed by Boyle (1981) and later modified by Boyle and Keigwin (1985/1986) and Boyle and Rosenthal (1996). This protocol is typically referred to as the ‘Cd-cleaning protocol’ and differs from the ‘Mg-cleaning protocol’ of Barker *et al.*, (2003) in that it includes a reductive step aimed at removing Mn-Fe-oxide coatings from the surface of the foraminifera tests. The fully

detailed cleaning protocol for the removal of potential contaminants from the surface of the foraminifera shell fragments adapted specifically to the laboratories at Cardiff University is presented in the appendix of this thesis. The procedure is summarised as follows:

- (i) Removal of fine clays by repeated rinsing of the samples with deionised water (18.2 M $\Omega$ ) and methanol, and agitation in an ultrasonic bath.
- (ii) Removal of metal oxide coatings from the foraminifera tests using a solution of ammonia, citric acid and hydrous hydrazine. The reaction was aided by heating the solution in a water bath and by repeatedly ultrasonically treating the samples. Samples then underwent two further water rinses and were transferred to clean vials.
- (iii) Removal of organic material with a heated solution of 0.1 M NaOH (sodium hydroxide) and H<sub>2</sub>O<sub>2</sub> (hydrogen peroxide), followed by two water rinses. This step was varied slightly depending on whether the samples were composed of planktonic or benthic foraminifera. In the former case, the vials were replenished with fresh solution halfway through the step.
- (iv) Finally, a dilute acid leach was performed to remove any contaminants that may have become adsorbed onto the surfaces of the foraminifera shell fragments during the cleaning process. This involved the addition of 0.002M HNO<sub>3</sub> (nitric acid) and ultrasonication, followed by a final rinsing with deionised water. Prior to analysis the cleaned samples were dissolved in 120  $\mu$ l of 0.065M HNO<sub>3</sub> and centrifuged to remove any remaining small silicate particles.

Elemental ratio analyses were performed using a Thermo Element XR High Resolution Inductive Coupled Plasma Mass Spectrometer (HR-ICPMS) at Cardiff University. As this instrument measures intensity, rather than concentration, the elemental concentration ratios are calculated by applying the relationship: [Sample ratio/Standard ratio] = [Sample concentration/Standard concentration]. This allows instrumental intensity ratios (i.e., element counts per second / calcium counts per second) to be converted to concentration ratios (i.e., mols of element / mols of calcium).

Prior to calculating the elemental concentration ratios, the dissolved samples were run for the measurement of Ca intensity and concentration to enable matrix matching of the standards with the foraminifera samples. These Ca concentration analyses were performed to determine the appropriate dilution of 'matrix-matched standards' that are

necessary for each elemental ratio analysis. The ‘matrix-matched standards’ ensure that the Ca concentration in each standard is equal (within the limits of analytical uncertainty) to the Ca concentration of each respective sample. The matrix-matching method ensures that the target element concentration (calculated from the sample intensity ratio) is a function of the variation of the concentration of the element of interest for each dissolved sample, rather than variations in Ca concentration.

Long-term instrumental precision of the element ratio measurements on this device was monitored by replicate analyses of two internal consistency standard solutions. The accepted values for the elemental ratios of ‘consistency standard 1’ are: Mg/Ca = 1.24 mmol mol<sup>-1</sup>, Cd/Ca = 1.25 μmol mol<sup>-1</sup> and B/Ca = 13.40 μmol mol<sup>-1</sup>; the accepted value for ‘consistency standard 2’ are Mg/Ca = 7.15 mmol mol<sup>-1</sup>, Cd/Ca = 1.56 μmol mol<sup>-1</sup> and B/Ca = 221.95 μmol mol<sup>-1</sup>. The replicate analyses of these two internal consistency standards during the measurement of the data presented in this thesis (37 analyses) yielded the following mean values and standard deviations ( $\pm 1\sigma$ ): (i) for ‘consistency standard 1’, Mg/Ca = 1.25  $\pm$  0.03 mmol mol<sup>-1</sup>, Cd/Ca = 1.19  $\pm$  0.02 μmol mol<sup>-1</sup> and B/Ca = 13.35  $\pm$  0.47 μmol mol<sup>-1</sup>; (ii) for ‘consistency standard 2’, the replicate analyses yielded values of Mg/Ca = 7.15  $\pm$  0.05 mmol mol<sup>-1</sup>, Cd/Ca = 1.53  $\pm$  0.04 μmol mol<sup>-1</sup> and B/Ca = 229.09  $\pm$  5.95 μmol mol<sup>-1</sup>.

The replicate elemental ratio measurements of the *C. wuellerstorfi* samples from MD02-2588 (n=20) yield pooled errors of  $\pm 0.03$  mmol mol<sup>-1</sup>,  $\pm 0.01$  μmol mol<sup>-1</sup> and  $\pm 4.04$  μmol mol<sup>-1</sup> for Mg/Ca, Cd/Ca and B/Ca, respectively. For the *G. truncatulinoides* (s.) samples from MD02-2588, the replicate Mg/Ca measurements (n=24) yield a pooled error of  $\pm 0.07$  mmol mol<sup>-1</sup>.

### **3.8 Elemental ratio sample processing and analysis by Laser Ablation ICP-MS**

(measured by Lennart de Nooijer, Royal Netherlands Institute for Sea Research)

Laser ablation ICP-MS (LA-ICP-MS) elemental ratio analyses in sediment core MD02-2588 were performed on twelve samples from three separate intervals along sediment core MD02-2588 (i.e., four samples at each interval). Each sample was composed of an individual *G. truncatulinoides* (s.) test picked from the > 315 μm size fraction. The whole foraminifera tests (i.e., uncrushed tests) were treated with the clay removal cleaning step listed above; all other cleaning steps were omitted.

The samples were measured at the Royal Netherlands Institute for Sea Research using a NWR193UC (New Wave Research) laser connected to a quadrupole ICP-MS (iCAP-Q, Thermo Scientific).

### **3.9 Elemental ratio data quality evaluation I - contamination from detrital material and diagenetic coatings**

#### *3.9.1 Procedural quality control*

Three procedural blanks were included in each cleaning batch and were carried through all the cleaning steps. The procedural blanks were subsequently analysed to test for potential contamination during the cleaning process. None of these had elemental concentrations above that of the analytical blank of each run.

Ten samples of the total 247 *G. truncatulinoides* (*s.*) elemental ratio measurements were rejected due to operational uncertainties that arose during the sample cleaning procedure. These ten samples were part of the first replicate batch to be processed and measured at the beginning of this PhD project. These samples had consistently elevated Mn/Ca and Cd/Ca ratios relative to the corresponding ratios in subsequent repeat analyses conducted on a different day. This systematic offset was investigated further by making additional measurements on foraminifera samples from the same depth intervals of the sediment core. The results of these replicated measurements demonstrated that the ten suspicious samples from the first cleaning batch had elevated Mn/Ca and Cd/Ca relative to all the subsequent measurements. This led to the suspicion that the samples were compromised in some way during the reductive cleaning step. For this reason, the ten samples from the first cleaning batch are discarded from all subsequent data analysis and discussion. This brings the total number of *G. truncatulinoides* (*s.*) samples from sediment core MD02-2588 down to 237.

An additional eight *G. truncatulinoides* (*s.*) samples measured during the same HR-ICP-MS run returned negative Al/Ca ratios (i.e.,  $Al/Ca < 0$ ). Several other samples from a different study that were run within that analytical batch also returned negative Al/Ca ratios. It was concluded that these data were compromised by an analytical failing and, to avoid any impacts on the quality of the MD02-2588 *G. truncatulinoides* (*s.*) dataset, the eight samples with negative Al/Ca were also discarded.

#### *3.9.2 Contaminant screening*

To screen the foraminifera samples from MD02-2588 against contamination from detrital material (i.e., clays) and diagenetic coatings (i.e., Mn-Fe oxides), we also determined the Al/Ca, Fe/Ca and Mn/Ca ratios of each sample (Boyle, 1983; Barker *et al.*, 2003; Pena *et al.*, 2005) (Fig. 3.9 and 3.10). We rejected samples that had values above the critical thresholds of  $100 \mu\text{mol mol}^{-1}$  in any of the three contaminant monitoring ratios (Boyle, 1983; Barker *et al.*, 2003). In addition to these traditional tracers of detrital and diagenetic contamination, the redox sensitive U/Ca ratio was also measured to monitor for the precipitation of authigenic uranium ( $U_{\text{authigenic}}$ ) on the foraminifera tests during early diagenesis (Mangini *et al.*, 2001; McManus *et al.*, 2005; Boiteau *et al.*, 2012) (Fig. 3.9 and 3.10). It is not known if elevated values of authigenic U/Ca affect the Mg/Ca, Cd/Ca and B/Ca records presented in this thesis and no threshold has been suggested above which samples should be rejected; calcite lattice-bound uranium values in modern planktonic and benthic foraminifera are typically in the range of  $1\text{-}30 \text{ nmol mol}^{-1}$  (Russell *et al.*, 1994, 1996, 2004; Yu *et al.*, 2008; Raitzsch *et al.*, 2011).

Based on these quality control criteria, we discarded five out of the 229 samples of *G. truncatulinoides* (*s.*) with Al/Ca, Fe/Ca, and/or Mn/Ca  $>100 \mu\text{mol mol}^{-1}$ , and an additional two samples with Al/Ca and Fe/Ca  $>80 \mu\text{mol mol}^{-1}$ . Nine additional samples with Mg/Ca greater than the  $2\sigma$  of the remaining *G. truncatulinoides* (*s.*) dataset (i.e., for  $n=222$ ,  $0.79 \text{ mmol mol}^{-1} > \text{Mg/Ca} > 1.57 \text{ mmol mol}^{-1}$ ) were also rejected. In the case of *C. wuellerstorfi*, of the total 227 samples, 20 of these had Al/Ca, Fe/Ca, and/or Mn/Ca  $>90 \mu\text{mol mol}^{-1}$ . A further 12 samples with B/Ca, Cd/Ca, and/or Mg/Ca  $>2\sigma$  of the remaining dataset were also rejected. We also excluded one additional sample with an anomalously high value of Li/Ca.

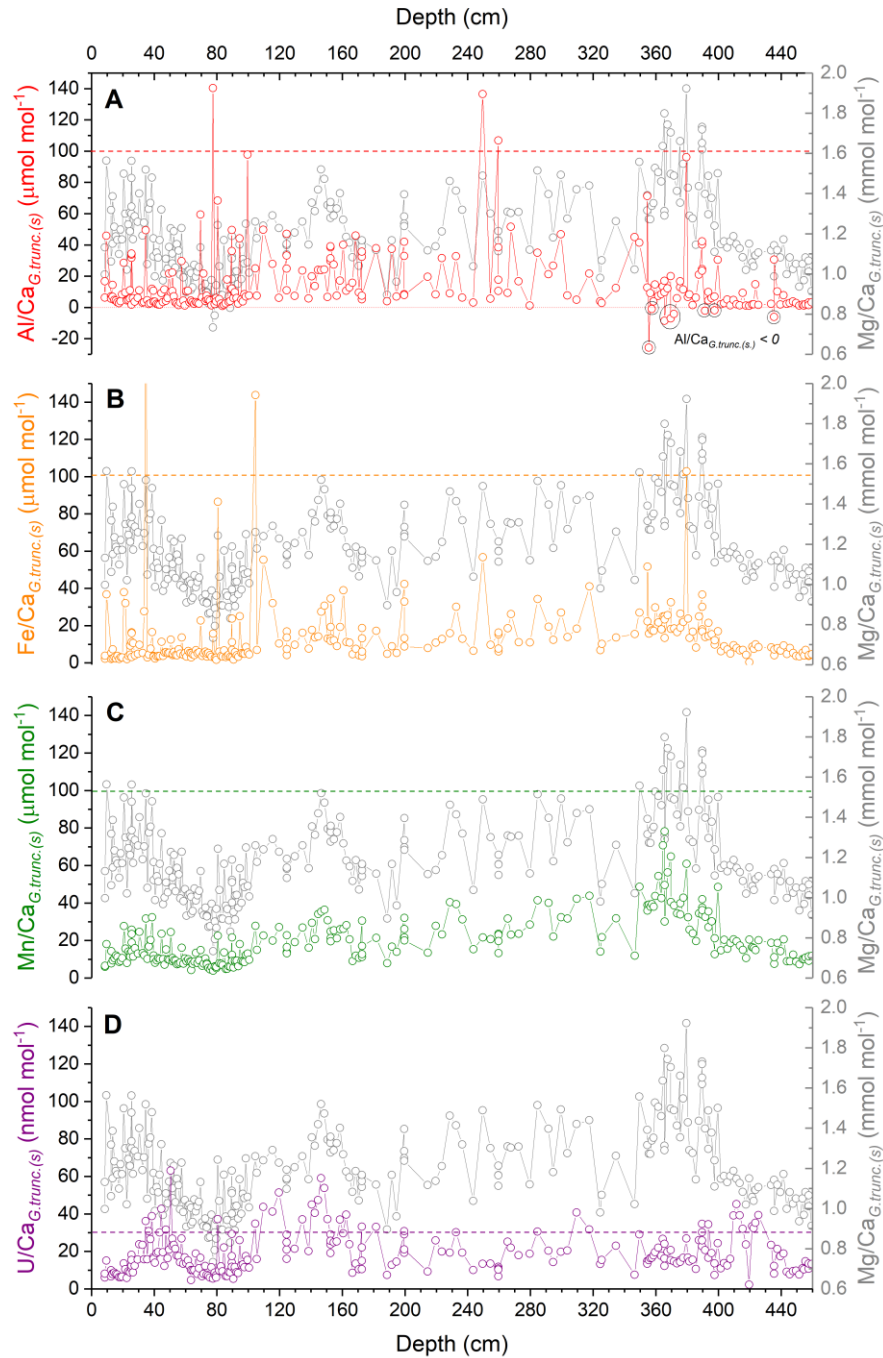


**Figure 3.9.** Comparison of *G. truncatulinoides* (*s.*) Mg/Ca record (grey line, open grey circles) from MD02-2588 with corresponding (A) Al/Ca (red line, open red circles), (B) Fe/Ca (orange line, open orange circles), (C) Mn/Ca (green line, open green circles) and (D) U/Ca (purple line, open purple circles). Panels A, B and C also show the suggested thresholds for likely detrital and diagenetic contamination (Boyle, 1983; Barker *et al.*, 2003) for Al/Ca (dashed red line at 100  $\mu\text{mol mol}^{-1}$ ), Fe/Ca (dashed orange line at 100  $\mu\text{mol mol}^{-1}$ ) and Mn/Ca (dashed green line at 100  $\mu\text{mol mol}^{-1}$ ). The upper limit of typical lattice-bound U/Ca is also marked in panel D (dashed purple line at 30  $\text{nmol mol}^{-1}$ ) (Russell *et al.*, 1994, 1996, 2004; Yu *et al.*, 2008; Raitzsch *et al.*, 2011).

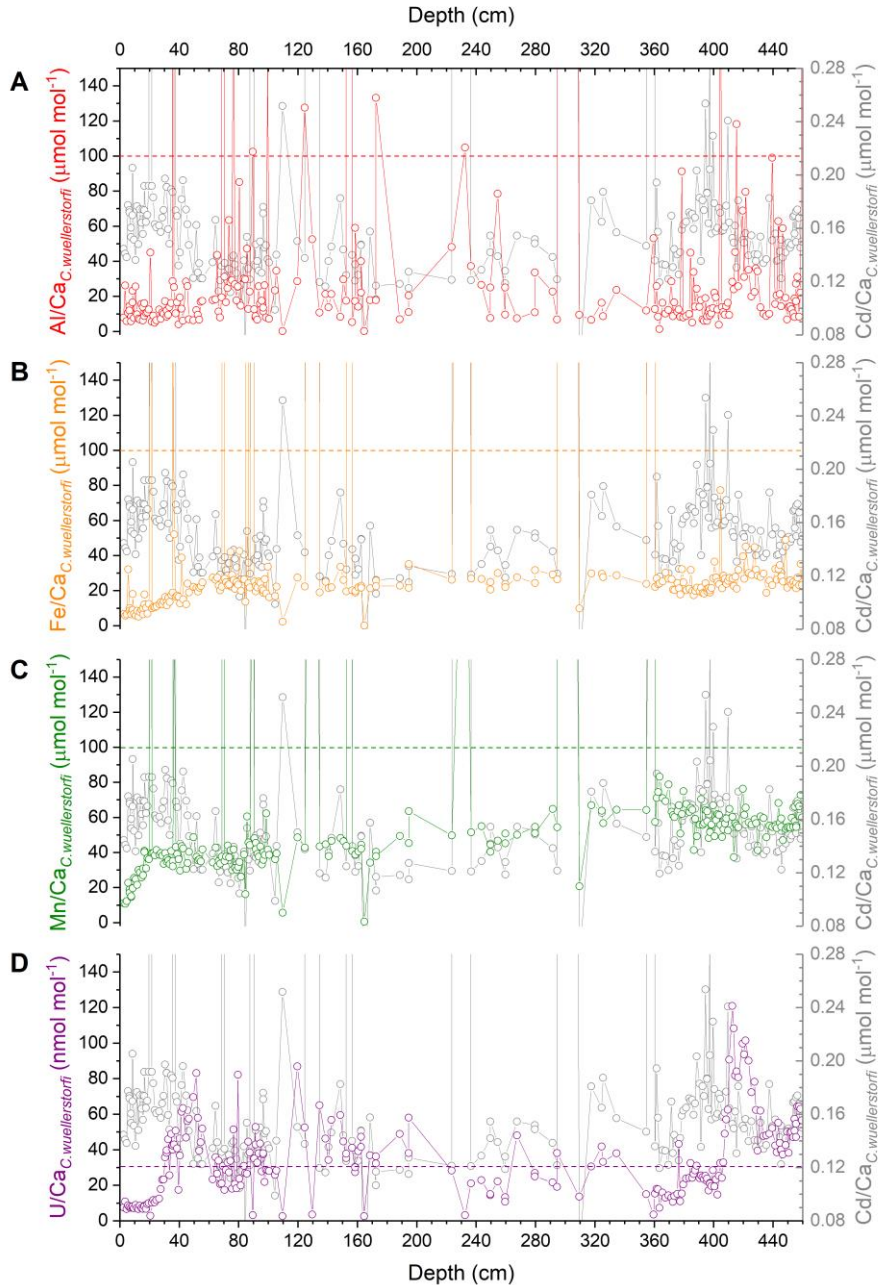


**Figure 3.10.** Comparison of *C. wuellerstorfi* Cd/Ca record (grey line, open grey circles) from MD02-2588 with corresponding (A) Al/Ca (red line, open red circles), (B) Fe/Ca (orange line, open orange circles), (C) Mn/Ca (green line, open green circles) and (D) U/Ca (purple line, open purple circles). Panels A, B and C also show the suggested thresholds for likely detrital and diagenetic contamination (Boyle, 1983; Barker *et al.*, 2003) for Al/Ca (dashed red line at 100  $\mu\text{mol mol}^{-1}$ ), Fe/Ca (dashed orange line at 100  $\mu\text{mol mol}^{-1}$ ) and Mn/Ca (dashed green line at 100  $\mu\text{mol mol}^{-1}$ ). The upper limit of typical lattice-bound U/Ca is also marked in panel D (dashed purple line at 30  $\text{nmol mol}^{-1}$ ) (Russell *et al.*, 1994, 1996, 2004; Yu *et al.*, 2008; Raitzsch *et al.*, 2011).

### 3.9.3 Contaminant monitoring elemental ratios versus target elemental ratios

These strict thresholds for sample rejection aim to minimise the impacts of sedimentary and diagenetic contamination on the datasets produced for this project. Nonetheless, we further examine these impacts by assessing the relationships that occur between the contaminant element ratios and the target ratios (Figures 3.11-3.13). In the first instance, these relationships are examined on the entire processed datasets.

The B/Ca and Cd/Ca of *C. wuellerstorfi* ( $B/Ca_{C.wuell.}$  and  $Cd/Ca_{C.wuell.}$ , respectively) show no correlations with any of the contaminant ratios (including U/Ca). In the case of Mg/Ca of *C. wuellerstorfi* ( $Mg/Ca_{C.wuell.}$ ) there appears to be a weak positive correlation with the corresponding Mn/Ca ratios (Pearsons'  $r(\rho) = 0.55$ ,  $r^2 = 0.30$ ). Likewise, the Mg/Ca of *G. truncatulinoides* ( $Mg/Ca_{G.trunc.}$ ) also displays a positive correlation with Mn/Ca ( $\rho = 0.82$ ,  $r^2 = 0.67$ ) and a weaker, but nonetheless apparent, positive correlation with Fe/Ca ( $\rho = 0.66$ ,  $r^2 = 0.43$ ). Equally, the downcore comparisons indicate that the pattern of  $Mg/Ca_{G.trunc.}$  variability is very similar to the pattern of variability observed in the corresponding Mn/Ca and Fe/Ca records (Fig. 3.12). For  $Mg/Ca_{C.wuell.}$ , its likeness to the corresponding Mn/Ca record is less apparent (Fig. 3.13C); nevertheless, there are similarities in their patterns of variability through certain sections of the record, as well as in their long-term trends.

The cross-plots of  $Mg/Ca_{G.trunc.}$  versus  $Al/Ca_{G.trunc.}$ ,  $Fe/Ca_{G.trunc.}$ ,  $Mn/Ca_{G.trunc.}$  and, to a lesser degree, versus  $U/Ca_{G.trunc.}$ , reveal a clustering of data at the lower end of the 'contaminant monitor' ratio range (i.e., the abscissa in figure 3.11a-d). For  $Al/Ca_{G.trunc.}$  and  $Fe/Ca_{G.trunc.}$ , this clustering occurs in the 0-15  $\mu\text{mol}\cdot\text{mol}^{-1}$  range, whereas for  $Mn/Ca_{G.trunc.}$  and  $U/Ca_{G.trunc.}$ , the data are clustered in the 0-25  $\mu\text{mol}\cdot\text{mol}^{-1}$  and 0-25  $\text{nmol}\cdot\text{mol}^{-1}$  ranges, respectively. The observed correlations between  $Mg/Ca_{G.trunc.}$  and the 'contaminant monitor' ratios are dominated by the data in these clusters within the lower range. This observation is important because it demonstrates that even at values well below the accepted thresholds for contamination (i.e.,  $<100 \mu\text{mol}\cdot\text{mol}^{-1}$  for  $Al/Ca_{G.trunc.}$ ,  $Fe/Ca_{G.trunc.}$  and  $Mn/Ca_{G.trunc.}$ ), the correlations with  $Mg/Ca_{G.trunc.}$  are a persistent feature of the dataset.

The above relationships and correlations were also examined in more detail along shorter sections of the MD02-2588 core to determine if the trends and relationships observed between the element ratios are consistent throughout the entire core section

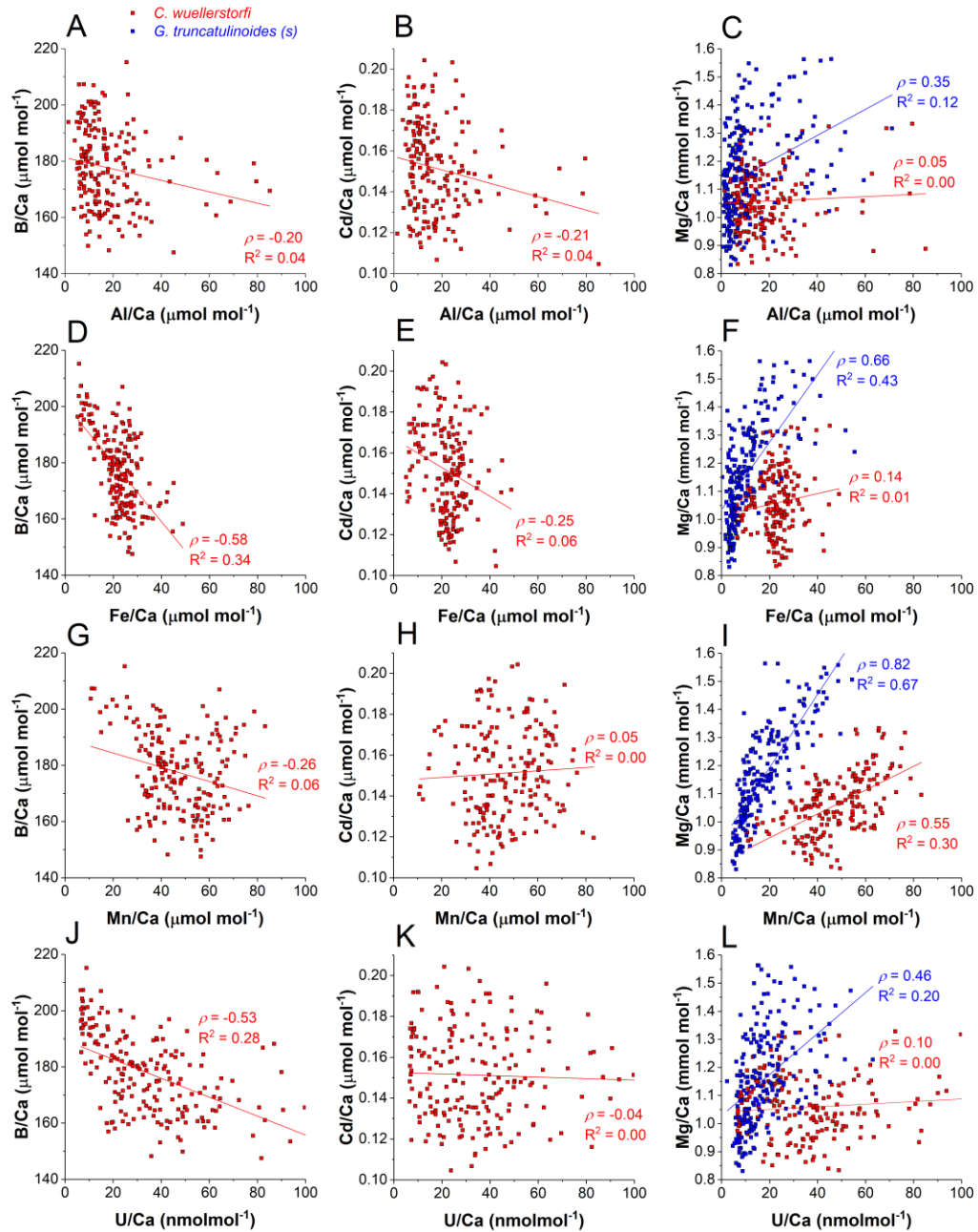


**Figure 3.11.** Scatter plots of *C. wuellerstorfi* B/Ca, Cd/Ca and Mg/Ca vs corresponding Al/Ca, Fe/Ca, Mn/Ca and U/Ca (shown in red) from MD02-2588. Scatter plots of *G. truncatulinoides* (s) Mg/Ca vs corresponding Al/Ca, Fe/Ca, Mn/Ca and U/Ca (shown in blue) from MD02-2588. Also shown are the lines of best fit through the datasets and the corresponding Pearson's  $r$  value ( $\rho$ ) and the coefficient of determination ( $R^2$ ) of each linear equation (not shown). Elemental ratio data with values above the suggested contamination thresholds have been removed.

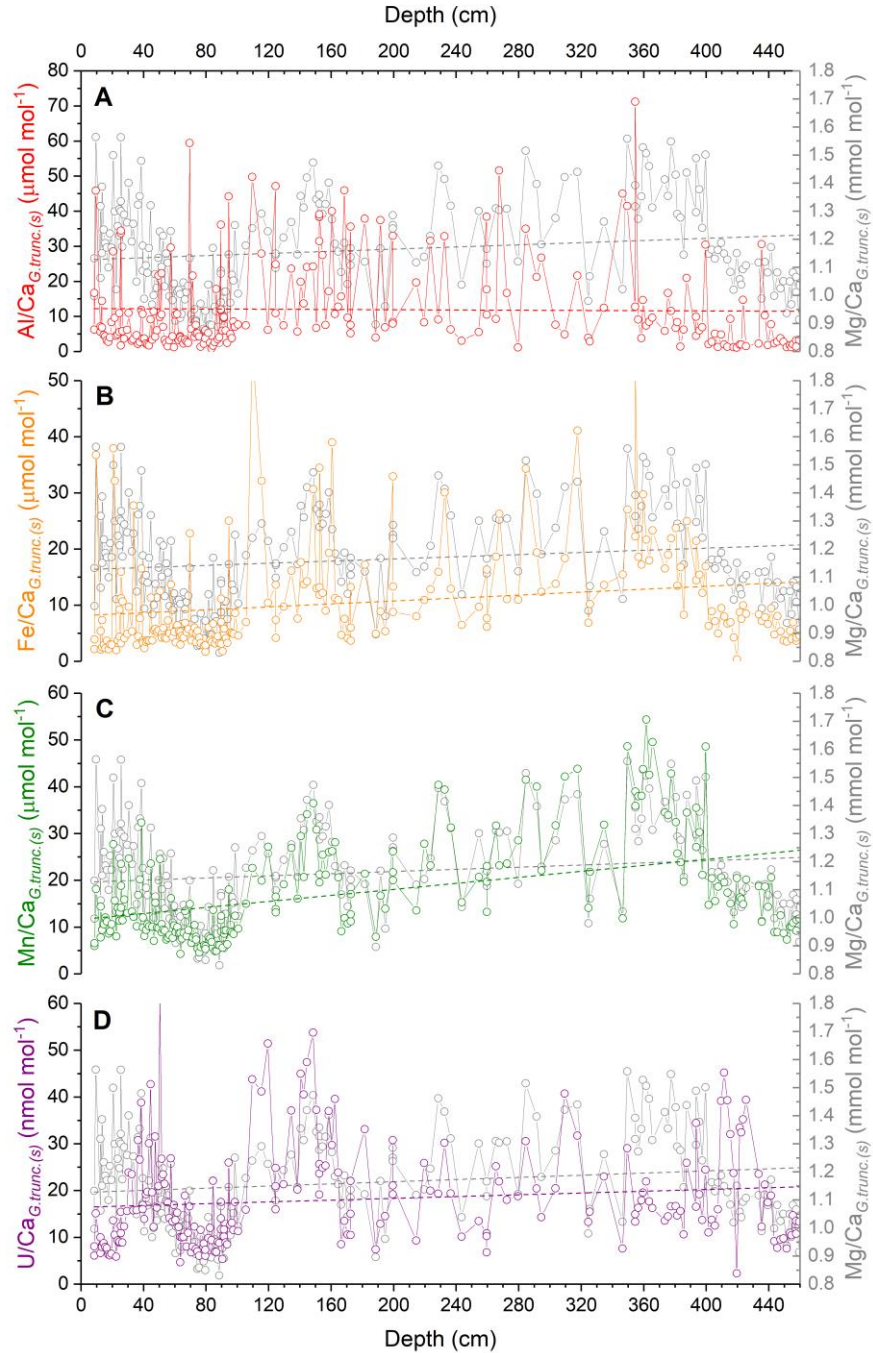


**Figure 3.12.** Comparison of processed *G. truncatulinoides* (*s.*) Mg/Ca record (grey line, open grey circles) from MD02-2588 with corresponding (A) Al/Ca (red line, open red circles), (B) Fe/Ca (orange line, open orange circles), (C) Mn/Ca (green line, open green circles) and (D) U/Ca (purple line, open purple circles). Elemental ratio data with values above the suggested contamination thresholds have been removed. Dashed lines show the average trend through the downcore elemental ratio data (colours of dashed lines correspond to each data set).

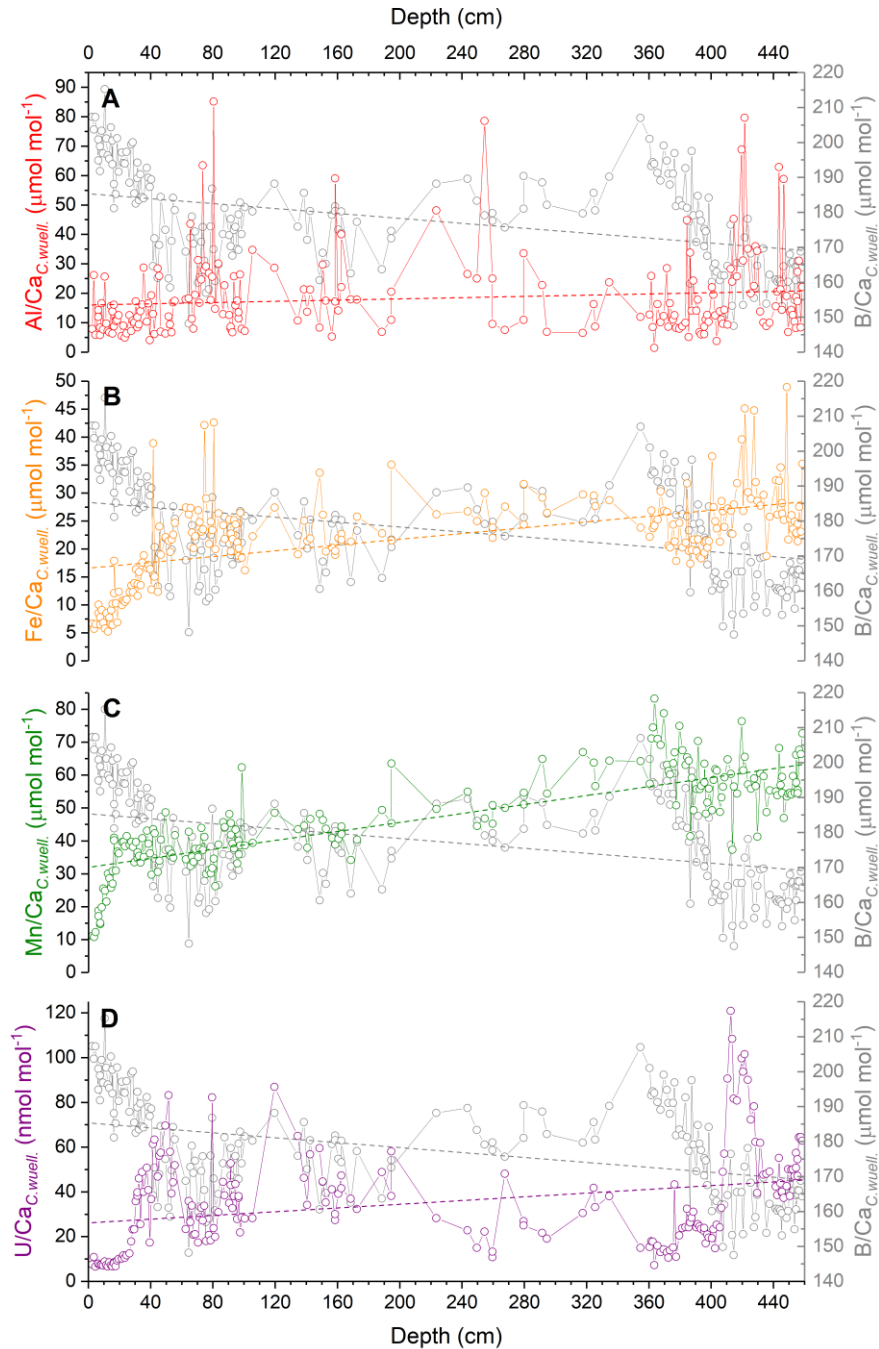


**Figure 3.13.A.** Comparison of processed *C. wuellerstorfi* B/Ca record (grey line, open grey circles) from MD02-2588 with corresponding (A) Al/Ca (red line, open red circles), (B) Fe/Ca (orange line, open orange circles), (C) Mn/Ca (green line, open green circles) and (D) U/Ca (purple line, open purple circles). Elemental ratio data with values above the suggested contamination thresholds have been removed. Dashed lines show the average trend through the downcore elemental ratio data (colours of dashed lines correspond to each data set).

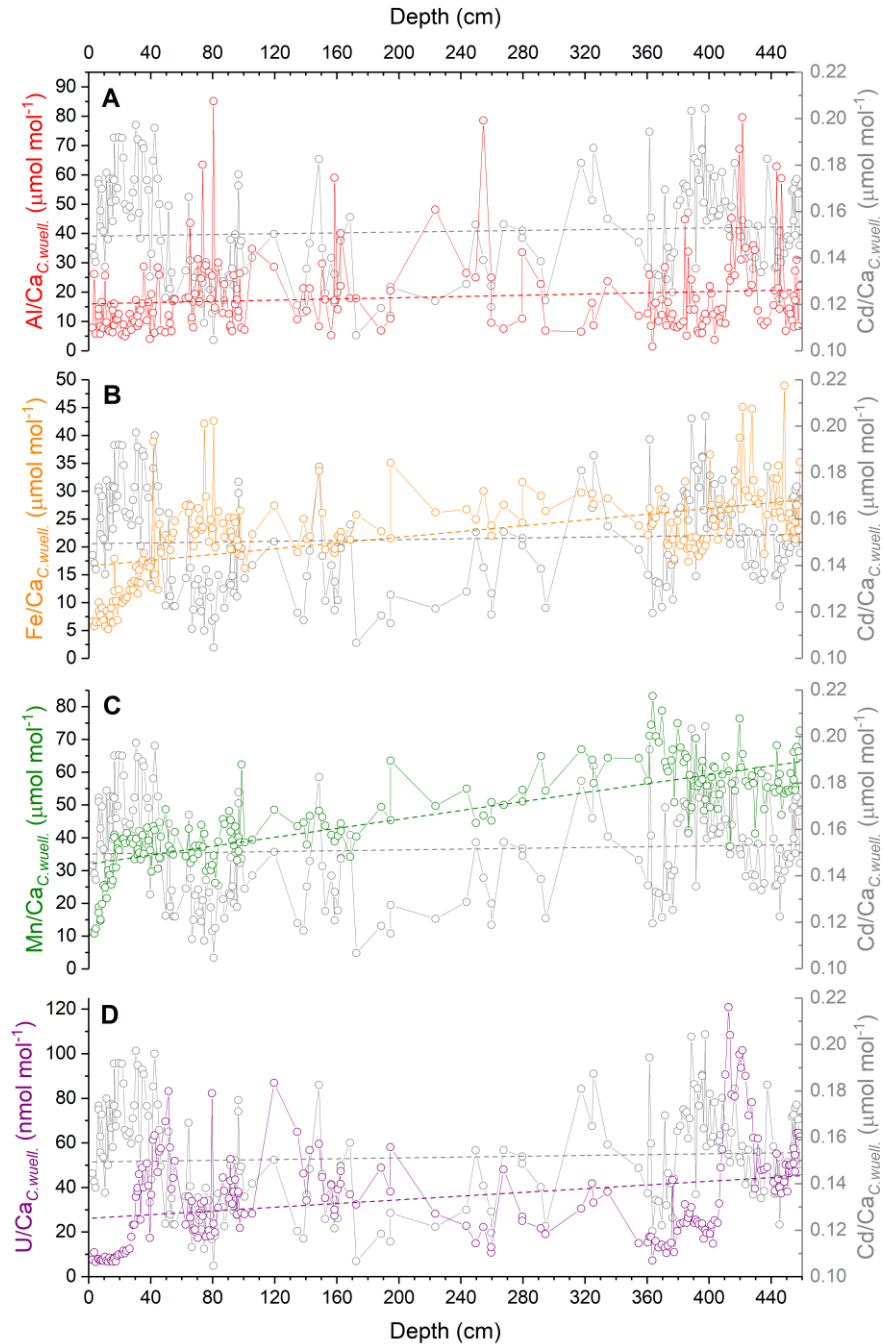


**Figure 3.13.B.** Comparison of processed *C. wuellerstorfi* Cd/Ca record (grey line, open grey circles) from MD02-2588 with corresponding (A) Al/Ca (red line, open red circles), (B) Fe/Ca (orange line, open orange circles), (C) Mn/Ca (green line, open green circles) and (D) U/Ca (purple line, open purple circles). Elemental ratio data with values above the suggested contamination thresholds have been removed. Dashed lines show the average trend through the downcore elemental ratio data (colours of dashed lines correspond to each data set).

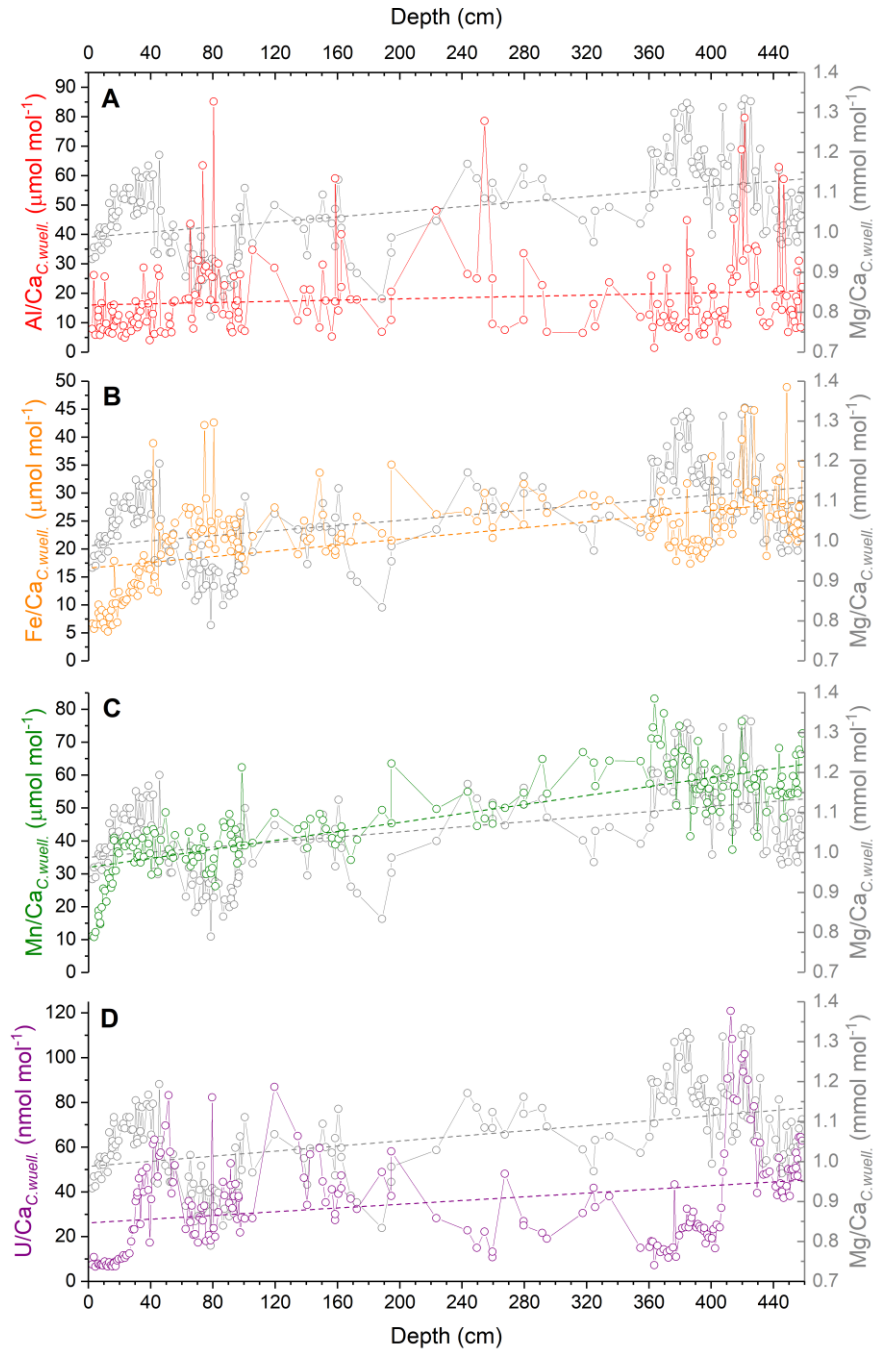


**Figure 3.13.C.** Comparison of processed *C. wuellerstorfi* Mg/Ca record (grey line, open grey circles) from MD02-2588 with corresponding (A) Al/Ca (red line, open red circles), (B) Fe/Ca (orange line, open orange circles), (C) Mn/Ca (green line, open green circles) and (D) U/Ca (purple line, open purple circles). Elemental ratio data with values above the suggested contamination thresholds have been removed. Dashed lines show the average trend through the downcore elemental ratio data (colours of dashed lines correspond to each data set).

under investigation in this study (i.e., the upper 460 cm). The downcore records from MD02-2588 were divided into six sections which correspond to Marine Isotope Stages (MIS) 1-6 according to the age-depth relationship determined by Ziegler *et al.*, (2013) (see Appendix Table 3.1). The division of the record into Marine Isotope Stages (Lisiecki and Raymo, 2005) provides a basic framework for examining the data in the context of global climate conditions (i.e., glacial vs interglacial) but it should be kept in mind that the uneven sampling of the sediment core introduces a ‘weighting effect’ to the results because each MIS division contains a different number of data points. Despite this caveat, we find that the relationships between the contaminant element ratios and the target ratios are more complex than is apparent from the examination of the downcore datasets in their entirety.

In the case of the relationship between  $Mg/Ca_{G.trunc.}$  and  $Mn/Ca_{G.trunc.}$ , a strong positive correlation is observed in all six subsections (Appendix Fig. 3.1-3.7) (MIS 1,  $\rho=0.83$ ,  $r^2=0.67$ ,  $n=29$ ; MIS 2,  $\rho=0.83$ ,  $r^2=0.68$ ,  $n=51$ ; MIS 3,  $\rho=0.91$ ,  $r^2=0.82$ ,  $n=37$ ; MIS 4,  $\rho=0.75$ ,  $r^2=0.53$ ,  $n=16$ ; MIS 5,  $\rho=0.85$ ,  $r^2=0.72$ ,  $n=45$ ; MIS 6,  $\rho=0.93$ ,  $r^2=0.86$ ,  $n=35$ ), reinforcing the suspicion that  $Mg/Ca_{G.trunc.}$  may be compromised by diagenetic contamination. Though weaker, the consistent positive correlation between  $Mg/Ca_{G.trunc.}$  and  $Fe/Ca_{G.trunc.}$  in all the subsections supports this position (Appendix Fig. 3.1-3.7) (MIS 1,  $\rho=0.63$ ,  $r^2=0.37$ ,  $n=29$ ; MIS 2,  $\rho=0.56$ ,  $r^2=0.30$ ,  $n=51$ ; MIS 3,  $\rho=0.61$ ,  $r^2=0.36$ ,  $n=37$ ; MIS 4,  $\rho=0.51$ ,  $r^2=0.21$ ,  $n=16$ ; MIS 5,  $\rho=0.61$ ,  $r^2=0.36$ ,  $n=45$ ; MIS 6,  $\rho=0.85$ ,  $r^2=0.72$ ,  $n=35$ ).

The relationships between contaminant monitoring element ratios and  $B/Ca_{C.wuell.}$  is also more complex than is apparent from the examination of the dataset in its entirety (Appendix Fig. 3.8-3.14).  $B/Ca_{C.wuell.}$  displays relatively strong negative correlations with  $Mn/Ca_{C.wuell.}$  and  $Fe/Ca_{C.wuell.}$  during the MIS 1 interval ( $\rho=-0.59$ ,  $r^2=0.33$ ,  $n=36$  and  $\rho=-0.72$ ,  $r^2=0.51$ ,  $n=36$ , respectively) and with  $Mn/Ca_{C.wuell.}$  during the MIS 5 interval ( $\rho=0.53$ ,  $r^2=0.27$ ,  $n=36$ ), although in the latter interval the correlation is positive. In the remaining sections, the correlations are weak and the sign of the relationship between  $B/Ca_{C.wuell.}$  and  $Mn/Ca_{C.wuell.}$  is inconsistent from section to section. The correlation between  $Cd/Ca_{C.wuell.}$  and  $Mn/Ca_{C.wuell.}$  is weak in all sections except for the MIS 1 interval (MIS 1,  $\rho=0.56$ ,  $R^2=0.30$ ,  $n=36$ ; MIS 2,  $\rho=0.26$ ,  $R^2=0.04$ ,  $n=33$ ; MIS 3,  $\rho=0.10$ ,  $r^2=0.04$ ,  $n=23$ ; MIS 4,  $\rho=-0.27$ ,  $r^2=-0.03$ ,  $n=11$ ; MIS 5,  $\rho=0.10$ ,  $r^2=0.02$ ,  $n=36$ ; MIS 6,  $\rho=-0.05$ ,  $r^2=0.00$ ,  $n=55$ ) (Appendix Fig. 3.15-3.21).

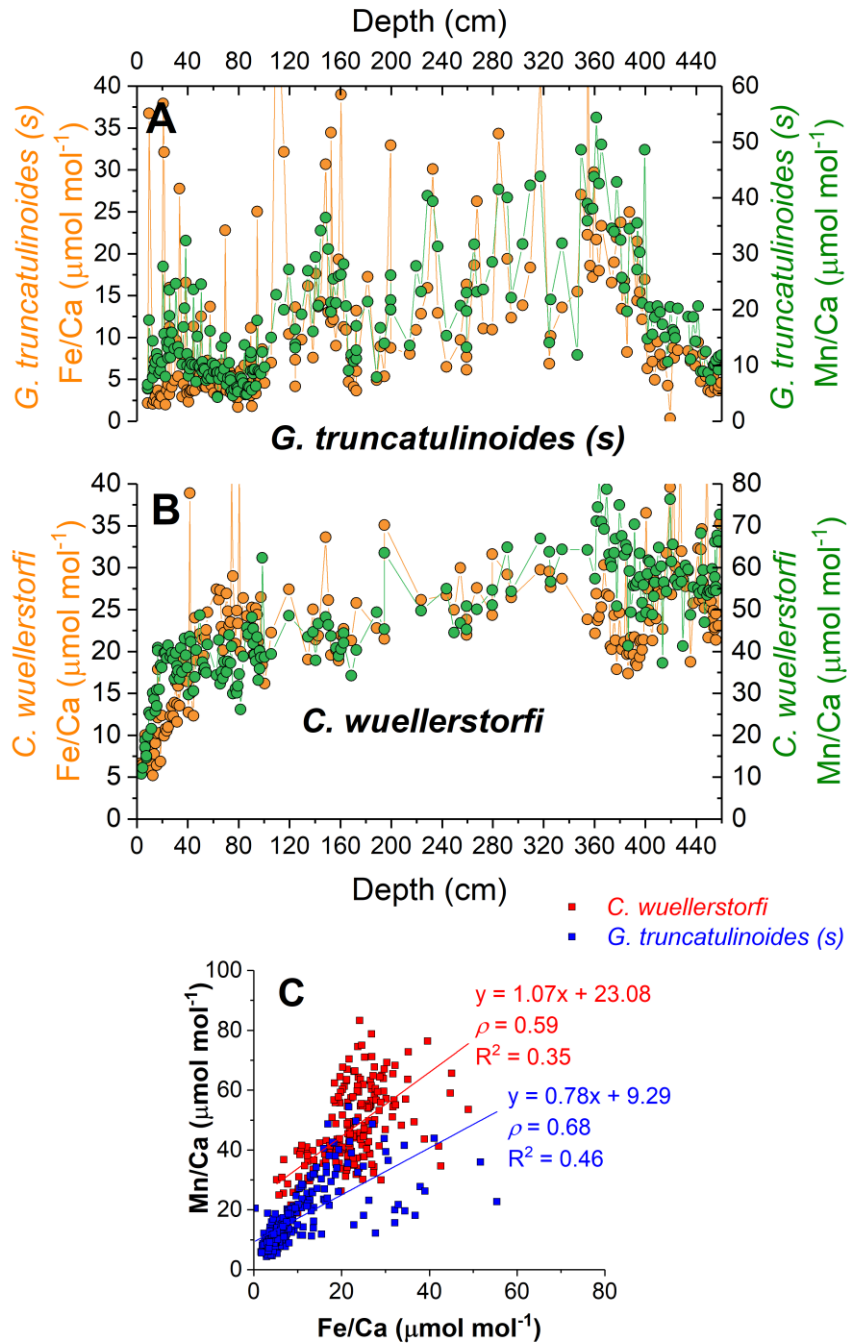


**Figure 3.14.** Downcore records of Fe/Ca (orange) and Mn/Ca (green) in (A) *G. truncatulinoides (s)* and (B) *C. wuellerstorfi* from MD02-2588. (C) Scatterplot of Mn/Ca vs Fe/Ca for *G. truncatulinoides (s)* (blue) *C. wuellerstorfi* (red) with lines of best fit. Also shown are the linear equations and the corresponding Pearson's r value ( $\rho$ ) and the coefficient of determination ( $R^2$ ) for each species.

The correlation between  $\text{Mg}/\text{Ca}_{C.wuell.}$  and  $\text{Mn}/\text{Ca}_{C.wuell.}$  is also weak in all sections except for the MIS 1 interval (MIS 1,  $\rho=0.87$ ,  $r^2=0.74$ ,  $n=36$ ; MIS 2,  $\rho=0.31$ ,  $r^2=0.07$ ,  $n=33$ ; MIS 3,  $\rho=0.14$ ,  $r^2=0.03$ ,  $n=23$ ; MIS 4,  $\rho=-0.12$ ,  $r^2=-0.10$ ,  $n=11$ ; MIS 5,  $\rho=0.22$ ,  $r^2=0.02$ ,  $n=36$ ; MIS 6,  $\rho=0.37$ ,  $r^2=0.12$ ,  $n=55$ ) (Appendix Fig. 3.22-3.28). The coincidence of relatively strong correlations for both  $\text{Mg}/\text{Ca}_{C.wuell.}$  and  $\text{Cd}/\text{Ca}_{C.wuell.}$  with  $\text{Mn}/\text{Ca}_{C.wuell.}$  during MIS 1 is highly suspicious and indicates that this interval may be compromised by diagenetic contamination. It is curious that the MIS 1 interval contains the lowest  $\text{Mn}/\text{Ca}_{C.wuell.}$  values in the record ( $\sim 10\text{-}40 \mu\text{mol mol}^{-1}$  for the MIS 1 interval compared to  $\sim 30\text{-}75 \mu\text{mol mol}^{-1}$  in the rest of the record).

The correlations between  $\text{Mn}/\text{Ca}$  and the target element ratios (particularly  $\text{Mg}/\text{Ca}_{G.trunc.}$ ,  $\text{Mg}/\text{Ca}_{C.wuell.}$ , and  $\text{Cd}/\text{Ca}_{C.wuell.}$ ) raises the possibility that these records are affected by diagenetic Fe-Mn oxide coatings that were not completely removed during the foraminifera cleaning procedure. Indeed, plotting the  $\text{Fe}/\text{Ca}$  ratios from the two species against  $\text{Mn}/\text{Ca}$  reveals a strong resemblance in the downcore pattern of variability and a positive correlation ( $\rho = 0.59$ ,  $r^2=0.35$ , for *C. wuellerstorfi*;  $\rho = 0.68$ ,  $r^2=0.46$  for *G. truncatulinoides (s)*) (Fig. 3.14). The absolute values of these element ratios are offset in the two species but the similarity in the slopes of the linear regressions between  $\text{Mn}/\text{Ca}$  and  $\text{Fe}/\text{Ca}$  may suggest that Mn-Fe-oxide coatings were not fully removed from the shell fragments during the sample cleaning process (Fig. 3.14c).

#### 3.9.4 LA-ICP-MS results of *G. truncatulinoides (s)* elemental ratios

The results of the LA-ICP-MS elemental ratio analysis reveal that the  $\text{Mg}/\text{Ca}$  and  $\text{Mn}/\text{Ca}$  of individual foraminifera from within the three discrete sampling intervals are characterised by large ranges of values (Fig. 3.15a and 3.15b). For the single-specimen  $\text{Mg}/\text{Ca}$  measurements at 20-21 cm, 57-58 cm and 365-366 cm, these ranges are  $1.27\text{-}3.54 \text{ mmol.mol}^{-1}$ ,  $0.88\text{-}2.08 \text{ mmol.mol}^{-1}$  and  $0.66\text{-}2.42 \text{ mmol.mol}^{-1}$ , respectively. The ranges for the corresponding  $\text{Mn}/\text{Ca}$  measurements are  $25\text{-}124 \mu\text{mol.mol}^{-1}$ ,  $21\text{-}61 \mu\text{mol.mol}^{-1}$  and  $7\text{-}78 \mu\text{mol.mol}^{-1}$  at the three respective depth intervals. Generally, the results of the LA-ICP-MS measurements are offset from the equivalent ICP-MS values at the equivalent sampling depths.

As was outlined in the methodology section above (Section 3.8), the laser-ablated foraminifera were picked from the  $>315 \mu\text{m}$  size fraction and the complete (i.e.,

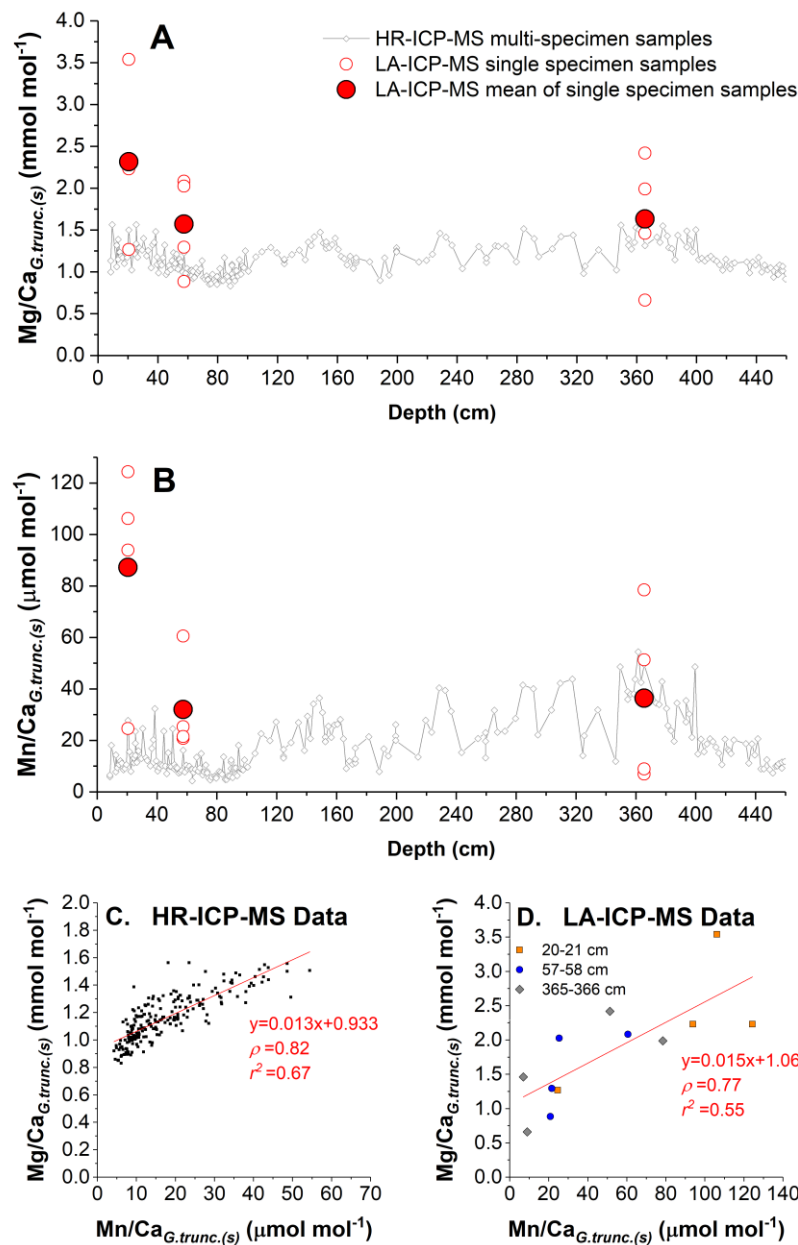


**Figure 3.15.** A) Comparison of processed *G. truncatulinoides* (*s.*) Mg/Ca record generated with HR-ICP-MS (grey line, open grey circles) from MD02-2588 with corresponding Mg/Ca in single specimens of *G. truncatulinoides* (*s.*) at three intervals determined by LA-ICP-MS (open red circles, individual single specimen Mg/Ca, closed red circles is average of single specimen results). B) Same as panel A, but for Mn/Ca. C) Cross plot of *G. truncatulinoides* (*s.*) Mg/Ca vs corresponding Mn/Ca data from HR-ICP-MS analysis, with linear regression equation and corresponding Pearson's  $r$  value ( $\rho$ ) and the coefficient of determination ( $R^2$ ). D) Same as panel C, but for LA-ICP-MS analyses. The measurements from each sediment interval are colour coded. Also shown is the linear regression through all data point and corresponding  $\rho$  and  $R^2$ .

uncrushed) tests only underwent the clay removal cleaning step (i.e., multiple rinses with deionised water). In the case of the measurements made by ICP-MS, foraminifera were picked from the 250-315  $\mu\text{m}$  size fraction, they were then crushed and homogenised and underwent the complete cleaning procedure (i.e., water rinses, reductive and oxidative treatment and acid leaching). This difference in methodology is expected to have introduced some variation in the results. However, the offset between the LA-ICP-MS results and the solution-based ICP-MS results are striking. Equally striking is the large range of Mg/Ca and Mn/Ca values that occur among the individual LA-ICP-MS measurements for each depth interval. This clearly demonstrates the large natural variability of the elemental ratios of individual foraminifera tests and highlights the need for constraining the size fraction and collecting numerous individual tests in order to gain a reliable indication of the average elemental ratios in multi-specimen samples.

Beyond this, the LA-ICP-MS data provide valuable clues as to the possibility of contamination by ferromanganese oxide coatings and the success of the reductive cleaning of the multi-specimen samples. In all the LA-ICP-MS profiles there are some signs of surface contamination (indicated by elevated counts for Mn, Al, Mg, etc.), but those peaks are relatively short and avoided when selecting the integration windows for the data output (Appendix figure 3.29). Therefore, the results of the LA-ICP-MS measurements should represent the elemental concentrations occurring in the main wall of the foraminiferal shell and should not include any contaminant phases that may be present on the inner and outermost surfaces of the shells.

Despite the large offsets between the results from the two analytical techniques, the relationship between the Mg/Ca and Mn/Ca in the two datasets is visibly similar. The slopes of the two relationships are almost parallel and their respective intercepts are comparable (Fig.3.15c and 3.15b). If the LA-ICP-MS data reflect the elemental ratios in the test wall of *G. truncatulinoides* (*s*), it could be inferred that the relationship between Mg/Ca and Mn/Ca is a feature of the calcite test of the foraminifera and is, therefore, not caused by diagenetic coatings on the inner and outer surfaces of the test. This would suggest that the ICP-MS data are unaffected by diagenetic contamination and that some other environmental or biological process is causing the correlation between Mg and Mn in the tests of foraminifera.

On the other hand, though the LA-ICP-MS method avoids measuring the inner and outer coatings on the foraminifera shells, it does not consider that such coatings can

permeate through the pores in the foraminiferal test wall. Work with electron microprobe mapping (EMP) of contaminated planktonic foraminifera has highlighted the importance of the foraminifera test texture and porosity in the distribution and formation of contaminant phases (Pena *et al.*, 2008). For example, in the case of *Neogloboquadrina dutertrei*, Mn phases have been shown to form a continuous thin layer in the inner part of the chambers, whereas for *Globigerinoides ruber*, Mn phases have been shown to have a patchy distribution and are usually found within pores. Among modern planktonic foraminifera *G. truncatulinoides* is considered to have an intermediate porosity (Bé, 1968). Generally, these pores penetrate the shell wall vertically but may bend and branch in various directions and may occur in various shapes (Takayanagi *et al.*, 1968). As such, the shell wall structure of *G. truncatulinoides* (*s*) may increase its susceptibility to the accumulation of contaminant phases within pores and may therefore be responsible for the correlation between Mg/Ca and Mn/Ca observed in both the ICP-MS and LA-ICP-MS data. However, as can be seen in the LA-ICP-MS profiles, the major contaminant peaks clearly occur on the outer surfaces of the shells (Appendix figure 3.29). This would suggest that any intrapore contamination must be less concentrated than the phases occurring on the outer shell. It also proposes that the cleaning procedure applied to the foraminifera samples may not adequately remove the intrapore contaminants.

### 3.9.5 Planktonic versus benthic elemental ratios

The impact of Mn-Fe oxide coatings on downcore foraminiferal B/Ca, Mg/Ca and Cd/Ca can be understood further by examining the relationships that occur between elemental ratios measured in planktonic and benthic foraminifera from the same sediment samples (Fig.3.16). *G. truncatulinoides* (*s*) and *C. wuellerstorfi* occupy very different habitats during their life cycles; the former is a deep-dwelling planktonic species that calcifies in the main thermocline, while the latter is an epibenthic species that lives on the seafloor. If the elemental ratios measured in the calcite tests of these two species preserve primary environmental signals derived from the ambient conditions of their individual habitats, we would expect to observe clear differences in their values. If, on the contrary, the values and the downcore patterns of variability of the elemental ratios in these two species are comparable, it is reasonable to suspect

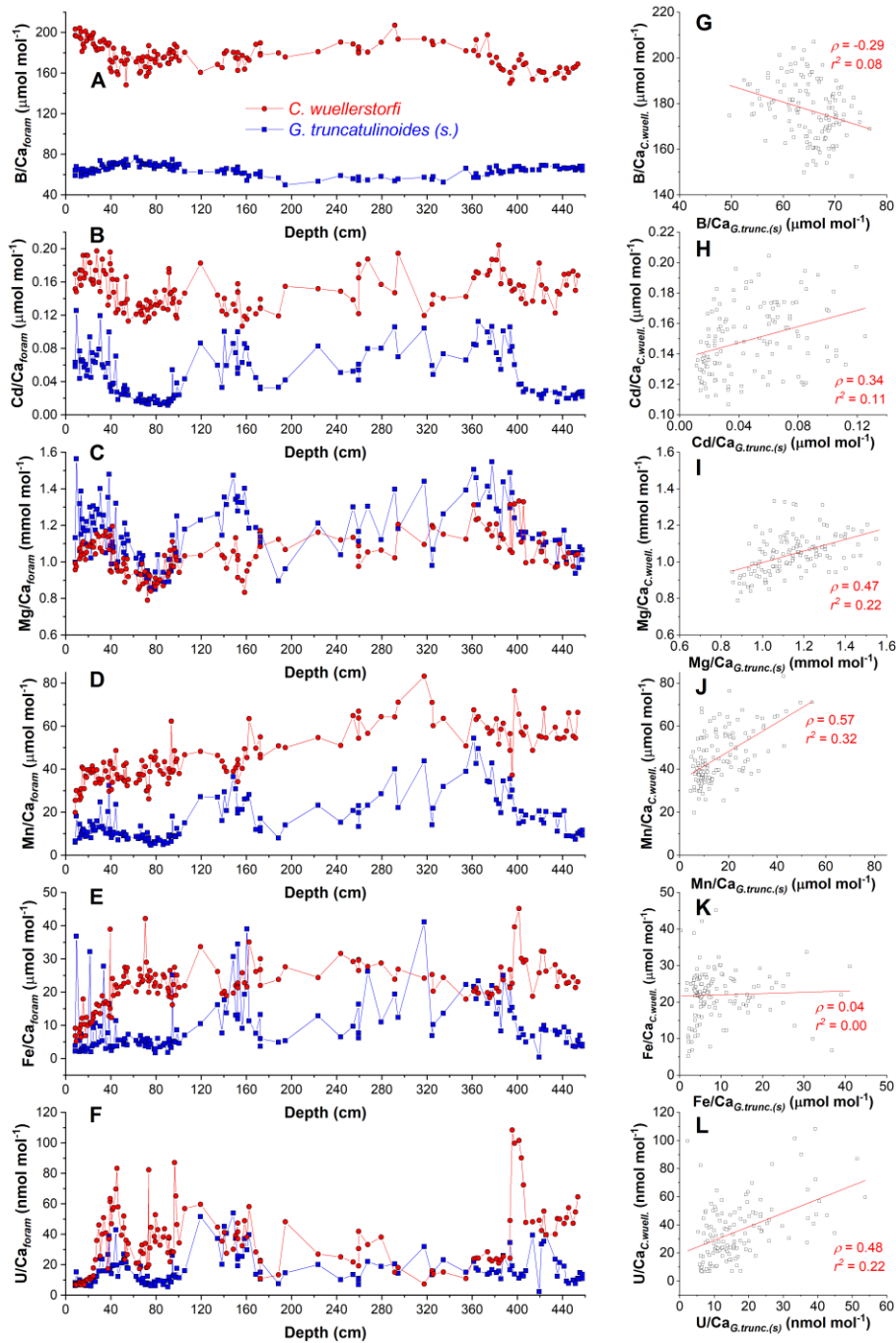


**Figure 3.16.** Panels on left-hand side show the downcore records of (A) B/Ca, (B) Cd/Ca, (C) Mg/Ca, (D) Mn/Ca, (E) Fe/Ca, and (F) U/Ca in *G. truncatulinoides* (s) (blue) and *C. wuellerstorfi* (red) from MD02-2588. Panels on the right are scatter plots of the downcore data of (G) B/Ca, (H) Cd/Ca, (I) Mg/Ca, (J) Mn/Ca, (K) Fe/Ca, and (L) U/Ca ratios from *C. wuellerstorfi* versus the corresponding ratios in *G. truncatulinoides* (s). The scatter plots include the lines of best fit with the details of the Pearson's r value ( $\rho$ ) and the coefficient of determination ( $R^2$ ) for each relationship.

that they represent post-depositional processes that occurred within the sediment, and which, therefore, may have impacted the calcite tests of the two species to a comparable extent.

Our examination reveals that the strongest correlations between co-registered planktonic and benthic elemental ratios are shown for Mg/Ca, Mn/Ca and U/Ca; generally, however, these correlations are weak ( $\rho=0.47$ ,  $r^2=0.22$ ;  $\rho=0.57$ ,  $r^2=0.33$ ;  $\rho=0.48$ ,  $r^2=0.22$ , respectively) (Fig. 3.16). Some similarity is also apparent in the broader trends of Cd/Ca in the two species ( $\rho=0.34$ ,  $r^2=0.11$ ).

Dividing the datasets into MIS-equivalent depth intervals allows these relationships to be probed in more detail (Appendix Fig. 3.30-3.35). Once divided, the data suggest that Mg/Ca in planktonic and benthic foraminifera is weakly correlated along parts of the sediment core (e.g., the MIS 2, MIS 3 and MIS 4 depth intervals) and uncorrelated along others (e.g., the MIS 1, MIS 5 and MIS 6 depth intervals). In contrast, planktonic and benthic Mn/Ca data are uncorrelated in all the MIS intervals, except for MIS 5. The strongest correlations are observed between planktonic and benthic U/Ca along the MIS 1 and MIS 3 intervals. However, as in the cases of Mg/Ca and Mn/Ca, this relationship is not consistent along the core. The correlation between planktonic and benthic Cd/Ca is strongest along the MIS 2 and MIS 6 intervals. During MIS 1, 3, 4 and 5, planktonic and benthic Cd/Ca are weakly correlated. The B/Ca and Fe/Ca data suggest that there is no correlation between planktonic and benthic records for these two elemental ratios. In conclusion, the analysis of the divided data does not reveal any clear and consistent patterns regarding the relationships between the planktonic and benthic foraminifera elemental ratio records that are not apparent in the analysis of the entire dataset (i.e., covering the entire upper 460 cm of sediment core MD02-2588).

Further to the strength of correlations between planktonic and benthic foraminiferal elemental ratios, the offsets in absolute values between the two species are also informative (Fig. 3.16). *C. wuellerstorfi* samples generally display higher concentrations than the corresponding *G. truncatulinoides* (*s*) samples. This is particularly apparent in the series of B/Ca, Cd/Ca, Mn/Ca and Fe/Ca. The offset is less apparent in the series of U/Ca, while in Mg/Ca, the relationship is reversed, such that the Mg/Ca of *G. truncatulinoides* (*s*) is higher than that of *C. wuellerstorfi* throughout most parts of the studied core section.

The occurrence of *C. wuellerstorfi* B/Ca concentrations that are ~100-150  $\mu\text{mol mol}^{-1}$  higher than the corresponding *G. truncatulinoides* (*s*) values is consistent with previous studies that have indicated lower B/Ca in planktonic foraminifera relative to benthic species (e.g., Yu *et al.*, 2007 and Rae *et al.*, 2011, respectively) (Fig. 3.16a). Studies have shown that B/Ca in benthic (Yu and Elderfield, 2007) and planktonic foraminifera (Yu *et al.*, 2007) is linked to the carbonate saturation state of seawater. However, without a calibration for *G. truncatulinoides* (*s*) it is difficult to assess whether the B/Ca offset between *C. wuellerstorfi* and *G. truncatulinoides* (*s*) in sediment core MD02-2588 is a consequence of the ambient seawater conditions in which each species calcified.

Similarly, the lack of a calibration for Cd/Ca in *G. truncatulinoides* (*s*) hampers any firm conclusions being drawn regarding the offset of Cd/Ca between the benthic and planktonic foraminifera in sediment core MD02-2588. The higher Cd/Ca concentrations in the benthic species cannot, therefore, be unambiguously explained in terms of ambient seawater nutrient content. The existing evidence suggests that unlike the lack of a significant temperature influence on the incorporation of Cd into the tests of *C. wuellerstorfi* (Marchitto, 2004), there does appear to be a potential temperature dependence of the incorporation of Cd into planktonic foraminifera (e.g., *Globigerinoides bulloides* and *Neogloboquadrina pachyderma* (*sinistral*)) (Rickaby and Elderfield, 1999; Yu *et al.*, 2013). The strong positive correlation between Mg/Ca and Cd/Ca in *G. truncatulinoides* (*s*) from MD02-2588 may suggest that this is also likely to be the case for this species ( $r^2=0.74$ ) (see following section). On the other hand, the correlation between  $\text{Mg}/\text{Ca}_{G.\text{trunc.}}$  and  $\text{Cd}/\text{Ca}_{G.\text{trunc.}}$  may be a consequence of contamination by Mn-Fe coatings, resulting in comparable alterations to both  $\text{Mg}/\text{Ca}_{G.\text{trunc.}}$  and  $\text{Cd}/\text{Ca}_{G.\text{trunc.}}$ , relative to the ‘pure’ foraminiferal calcite ratios.

Notwithstanding the potential temperature dependence of Cd incorporation into *G. truncatulinoides* (*s*) and alteration by a diagenetic overprint, the large offset between the planktonic and benthic records ( $\sim 0.1 \mu\text{mol mol}^{-1}$ ) may partly reflect a seawater nutrient signal. Specifically, the offset could indicate lower nutrient concentration in the thermocline waters above the core site relative to the higher nutrient content of deep waters bathing the Agulhas Plateau. Alternatively, the higher Cd/Ca in benthic foraminifera may be a function of the higher degree of diagenetic contamination relative to that observed in the planktonic record. Indeed, this interpretation is compatible

with the occurrence of planktonic-benthic offsets in the Mn/Ca and Fe/Ca records in which the benthic values are 10-30  $\mu\text{mol mol}^{-1}$  greater than the corresponding planktonic values. If Mn-Fe diagenetic coatings are indeed present on the foraminifera shell fragments, the offset in Cd/Ca, Mn/Ca and Fe/Ca may arise from differences in the morphology and surface chemistry of the calcite tests of the two species. For example, it is possible that the foraminifera used in this study have different surface area to mass ratios, different surface textures and/or different shell chemistries that promote increased precipitation of diagenetic coatings on the benthic foraminifera tests relative to those of the planktonic species. Likewise, the higher values of U/Ca in the benthic record relative to the planktonic record possibly indicate the preferential precipitation of authigenic uranium ( $U_{\text{authigenic}}$ ) on the tests of *C. wuellerstorfi*, relative to those of *G. truncatulinoides (s)*.

This is contrary to the relationship observed for Mg/Ca where higher Mg/Ca ratios (and a greater range) occur in *G. truncatulinoides (s)* samples relative to *C. wuellerstorfi* along most of the core. The reversed offset observed for Mg/Ca may be due to differences in the sensitivity of the temperature-dependent incorporation of Mg into the calcite tests of each species (e.g., calibrations of Elderfield and Ganssen, 2000 versus Cappelli *et al.*, 2015 for planktonic and benthic species, respectively). If the Mg/Ca ratios measured in the two foraminifera species are solely driven by calcification temperature, it is possible that the offset is coincidental. If, on the other hand, the Mg/Ca ratios were impacted by a diagenetic overprint, it would be reasonable to expect  $\text{Mg/Ca}_{C.wuell.}$  values to be greater than  $\text{Mg/Ca}_{G.trunc.}$ , in line with the higher values of benthic Mn/Ca, Fe/Ca and U/Ca; that is, analogous to the relationships observed between these ratios and the Cd/Ca data.

Yet, it could be argued that the contribution of Mg/Ca from the precipitation of secondary phases is insufficient to completely overprint the Mg/Ca signal derived from the primary calcite. Such a situation may have occurred if, for example, the Mg/Ca ratio of the primary calcite of *G. truncatulinoides (s)* was notably higher than that of *C. wuellerstorfi*. In such a case, even the preferential precipitation of authigenic coatings on the tests of the latter - as is seen in the case of Cd/Ca - may not have been sufficient to completely mask the signal derived from the primary calcite.

The average Mg/Mn ratios in manganese nodules/micronodules and manganese encrustations from data collected from the global ocean ranges between approximately

0.1 mol mol<sup>-1</sup> and 0.3 mol mol<sup>-1</sup> (Cronan, 1975; Baturin, 1988; de Lange *et al.*, 1992; Pattan, 1993). If the composition of Mn coatings that precipitate on the tests of foraminifera are comparable to the composition of manganese nodules and encrustations, it is reasonable to assume that the Mn-oxide coatings on foraminifera will also have Mg/Mn ratios of 0.1-0.3 mol mol<sup>-1</sup>. The Mg/Mn ratios of the samples from sediment core MD02-2588 range between 26 and 215 mol mol<sup>-1</sup> for *G. truncatulinoides (s)* and between 13 and 89 mol mol<sup>-1</sup> for *C. wuellerstorfi*; that is, the bulk foraminiferal Mg/Mn ratios are notably higher than the ratios observed in nodules and encrustations. Accordingly, the contribution of Mg from Mn-oxide coatings to the corresponding Mg/Mn ratio of the bulk samples from MD02-2588 range between 0.05% and 0.38% in *G. truncatulinoides (s)* samples and between 0.11% and 0.76% in *C. wuellerstorfi* samples. In other words, the contribution of Mg from Mn-oxide coatings to the total Mg/Ca ratio of the samples from sediment core MD02-2588 would be no more 1%. This mass balance calculation suggests that the contribution of the Mg/Ca signal from the coating should be masked by the Mg/Ca signal of the primary foraminiferal calcite. In practice, however, the coating signal may have a stronger influence than the above result would suggest because the dilute acid leaching and reductive cleaning steps may have partially dissolved the samples and altered the apparent Mg/Ca ratio (e.g., Barker *et al.*, 2003, Rosenthal *et al.*, 2004; Yu *et al.*, 2007; Yu and Elderfield, 2008; Bian and Martin, 2010). Nonetheless, the above analysis seems to suggest that the coating signal could not completely mask the Mg/Ca signal of the foraminiferal calcite.

### 3.9.6 U/Mn of authigenic coatings on foraminiferal tests

The mass-balance estimate presented above suggests that the occurrence of coatings makes a negligible contribution to the overall Mg/Ca composition of the sample. Nonetheless, it is vital to determine whether the correlation between Mg/Ca and Mn/Ca, particularly in *G. truncatulinoides (s.)*, is a feature of the foraminiferal calcite test or whether it reflects the ‘bulk’ composition of the sample (i.e., the combined composition of both the shell and the authigenic coating). In this section, we use the downcore records of U/Ca and Mn/Ca from sediment core MD02-2588 to further examine the occurrence of authigenic coatings on, and within, the foraminifera shells.

The removal of U from pore waters and its precipitation as authigenic foraminiferal coatings occurs below the oxygen penetration depth in the sediment column where organic matter is consumed by iron and sulphate reduction (Cochran *et al.*, 1986;

McManus *et al.*, 2005). Conversely, the precipitation of Mn coatings on foraminifera occurs when Mn is dissolved into pore waters under reductive sedimentary conditions (Boiteau *et al.*, 2012). The accumulation of authigenic U and Mn is, therefore, ultimately determined by the oxygen concentration of the overlying bottom waters and the deposition of organic matter on the seafloor.

The U/Ca of foraminifera from culturing experiments and sediment trap samples have been shown to range between 3 and 23 nmol mol<sup>-1</sup> (Russell *et al.*, 2004; Raitzsch *et al.*, 2011). In contrast, the U/Ca of foraminifera tests from downcore samples can reach concentrations of 300-700 nmol mol<sup>-1</sup>, much higher than the range found in the shell lattice (Boiteau *et al.*, 2012; Gottschalk *et al.*, 2016; Chen *et al.*, 2017). The co-occurrence of high Mn/Ca (>100 μmol mol<sup>-1</sup>) in downcore samples with high U/Ca indicates that the measured ratios reflect the bulk composition of the samples, incorporating both the contribution from the foraminiferal shell and the associated coatings.

The U/Ca of foraminifera from sediment core MD02-2588 range between 2 nmol mol<sup>-1</sup> and 63 nmol mol<sup>-1</sup> in the *G. truncatulinoides* (*s.*) samples and between 7 nmol mol<sup>-1</sup> and 121 nmol mol<sup>-1</sup> in the *C. wuellerstorfi* samples (Fig. 3.17). The lower U/Ca values of the foraminifera samples from MD02-2588 relative to those from previous studies (e.g., Boiteau *et al.*, 2012; Gottschalk *et al.*, 2016; Chen *et al.*, 2017) reflects the effectiveness of the reductive cleaning step in removing a notable proportion of authigenic coatings from the foraminifera shells. Nevertheless, the occurrence of U/Ca > ~30 nmol mol<sup>-1</sup> shows that the coatings have not been completely removed.

The offsets in values between the benthic and planktonic downcore records of both U/Ca and Mn/Ca from MD02-2588 suggests that differences in the structure, texture and/or chemical composition of the two types of foraminifera shell lead to variance in the precipitation of authigenic coatings and the effectiveness of their removal by reductive cleaning. The absolute concentration ratios of U/Ca and Mn/Ca are higher in the samples of *C. wuellerstorfi* (Fig. 3.17). This may indicate that the shell morphology of this species is more susceptible to the precipitation of authigenic coatings, or that U and Mn occur in higher concentrations within the calcite test of this species.

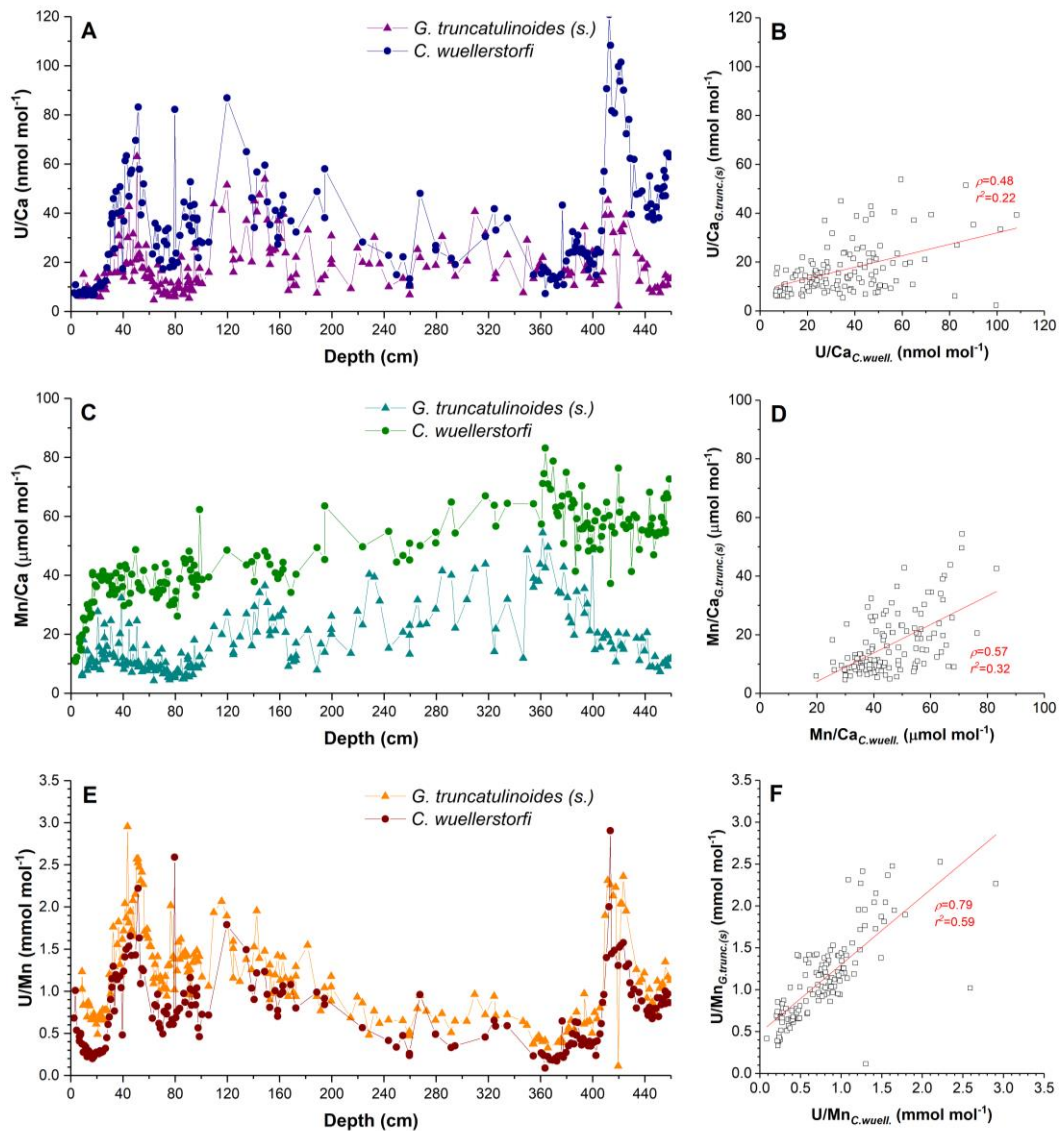


**Figure 3.17.** A) Downcore records of U/Ca measured in *G. truncatulinoides* (s.) (purple) and *C. wuellerstorfi* (blue) from MD02-2588. B) Cross plot of U/Ca measured in *G. truncatulinoides* (s.) versus and U/Ca of *C. wuellerstorfi*. C) Downcore records of Mn/Ca measured in *G. truncatulinoides* (s.) (cyan) and *C. wuellerstorfi* (green) from MD02-2588. D) Cross plot of Mn/Ca measured in *G. truncatulinoides* (s.) versus and Mn/Ca of *C. wuellerstorfi*. E) Downcore records of U/Mn measured in *G. truncatulinoides* (s.) (orange) and *C. wuellerstorfi* (red) from MD02-2588. F) Cross plot of U/Mn measured in *G. truncatulinoides* (s.) versus and U/Mn of *C. wuellerstorfi*.

The much stronger correlation between Mg/Ca and Mn/Ca in the planktonic species has already lead us to suggest that the porous structure of the *G. truncatulinoides* (*s.*) test possibly results in a higher susceptibility to authigenic coatings or, at least, results in less effective removal of such coatings during the reductive cleaning process. This interpretation would indicate that the higher U/Ca and Mn/Ca in *C. wuellerstorfi* are the consequence of higher concentrations of these elements in the calcite test of this species.

The bias introduced to the U/Ca and Mn/Ca records from variations in the structure, texture and/or chemical composition of the two types of foraminifera shell can be eliminated by normalising the coating-bound uranium concentrations to the corresponding coating-bound manganese concentrations (Gottschalk *et al.*, 2016). This normalisation process assumes that the downcore variability in Mn/Ca arises predominantly from variations in the Mn-Fe oxide coatings attached to the foraminiferal shell (as is supported by the correlation between Mn/Ca and Fe/Ca). By calculating the U/Mn ratio of each sample, the ‘shared’ shell-bound component of U/Ca and Mn/Ca is cancelled out and, theoretically, changes in downcore U/Mn should solely reflect variations in the concentration of coating-bound U and Mn.

The downcore records of U/Mn from *G. truncatulinoides* (*s.*) and *C. wuellerstorfi* in sediment core MD02-2588 reveal a striking resemblance to each other and a strong correlation (Fig. 3.17;  $\rho=0.79$ ,  $r^2=0.59$ ). These U/Mn records clearly indicate that the tests of both *G. truncatulinoides* (*s.*) and *C. wuellerstorfi* have been impacted by common early diagenetic processes and that the composition of the authigenic coatings that occur on the tests of the two species is almost identical. The U/Mn of the authigenic coatings ( $U/Mn_{\text{coat}}$ ;  $U/Mn_{G.\text{trunc.}-\text{coat}}$  and  $U/Mn_{C.\text{wuell.}-\text{coat}}$ , for coatings on *G. truncatulinoides* (*s.*) and *C. wuellerstorfi*, respectively) has been proposed to be a reliable indicator of redox conditions in marine sediments that is independent of variations of shell morphology and shell chemistry (Gottschalk *et al.*, 2016; Chen *et al.*, 2017). The close agreement of the planktonic and benthic foraminifera downcore records of U/Mn along MD02-2588 suggests that this parameter varies with diagenetic redox-processes occurring within the sediment and is consistent with previous findings (Boiteau *et al.*, 2012). We note however, that the samples from MD02-2588 have been reductively cleaned; therefore, they may not reflect the true magnitude of the variations of the sedimentary redox conditions. Even so, the fact that  $U/Mn_{G.\text{trunc.}-\text{coat}}$  and  $U/Mn_{C.\text{wuell.}-}$

$_{\text{coat}}$  are so similar despite having undergone the reductive cleaning step emphasises the ineffectiveness of the cleaning protocol in completely removing the authigenic coatings. Despite the potential implications this has for the quality of the elemental ratio data from MD02-2588, the  $U/Mn_{\text{coat}}$  records from this core may provide a tentative proxy for changes in the sedimentary redox conditions at the core site. Consequently, the  $U/Mn_{\text{coat}}$  records can be used to elucidate the impact sedimentary redox conditions on the quality of the elemental ratio data generated for the paleoenvironmental reconstruction of the Agulhas Plateau.

The stratigraphic records of  $U/Mn$  from MD02-2588 are not correlated with the corresponding records of  $Mg/Ca_{G.trunc.(s)}$  ( $\rho=0.35$ ,  $R^2=0.12$ ),  $B/Ca_{C.wuell.}$  ( $\rho=0.43$ ,  $R^2=0.18$ ),  $Cd/Ca_{C.wuell.}$  ( $\rho=0.09$ ,  $R^2=0.01$ ) or  $Mg/Ca_{C.wuell.}$  ( $\rho=0.15$ ,  $R^2=0.02$ ) (Fig. 3.18). The lack of correlation between  $U/Mn$  and these elemental ratios is also evident when the data are divided into MIS-equivalent depth sections (Appendix fig. 3.36-3.41). Taken at face value, this suggests that these elemental ratios are not impacted by changes in the sedimentary redox conditions at the MD02-2588 core site. Consequently, it can be argued that the correlations between  $Mn/Ca$  and  $Mg/Ca$ , particularly in the *G. truncatulinoides (s.)* records, is not driven by redox processes. This would suggest that the covariance of  $Mn/Ca$  with  $Mg/Ca$  is not controlled by the concentrations of these elements in the authigenic coatings on the tests of the foraminifera, but rather, that the correlation is a feature of the foraminiferal shell chemistry.

### 3.9.7 *Cd/Mn and Cd/U of authigenic coatings on foraminiferal tests*

From the above discussion, it is reasonable to assume that  $U_{\text{authigenic}}$  and Mn-oxide coatings are present on and within the cleaned foraminiferal shell fragments sampled from sediment core MD02-2588. In this section, we apply Gottschalk *et al.*, 's (2016) theoretical normalisation method to the  $Cd/Ca$ ,  $Mn/Ca$  and  $U/Ca$  data from MD02-2588. In this instance, the aim is to normalise the coating-bound Cd concentration to the corresponding coating-bound concentrations of manganese and uranium. In theory, this should allow us to assess how the coating-bound Cd concentration varies along the core and how this variation may impact the 'bulk'  $Cd/Ca$  data in both the planktonic and benthic downcore records from MD02-2588.

As was mentioned above, the data from this core reveal a very strong positive correlation between  $Mg/Ca$  and  $Cd/Ca$  in *G. truncatulinoides (s)* ( $\rho=0.86$ ,  $r^2=0.74$ ) but

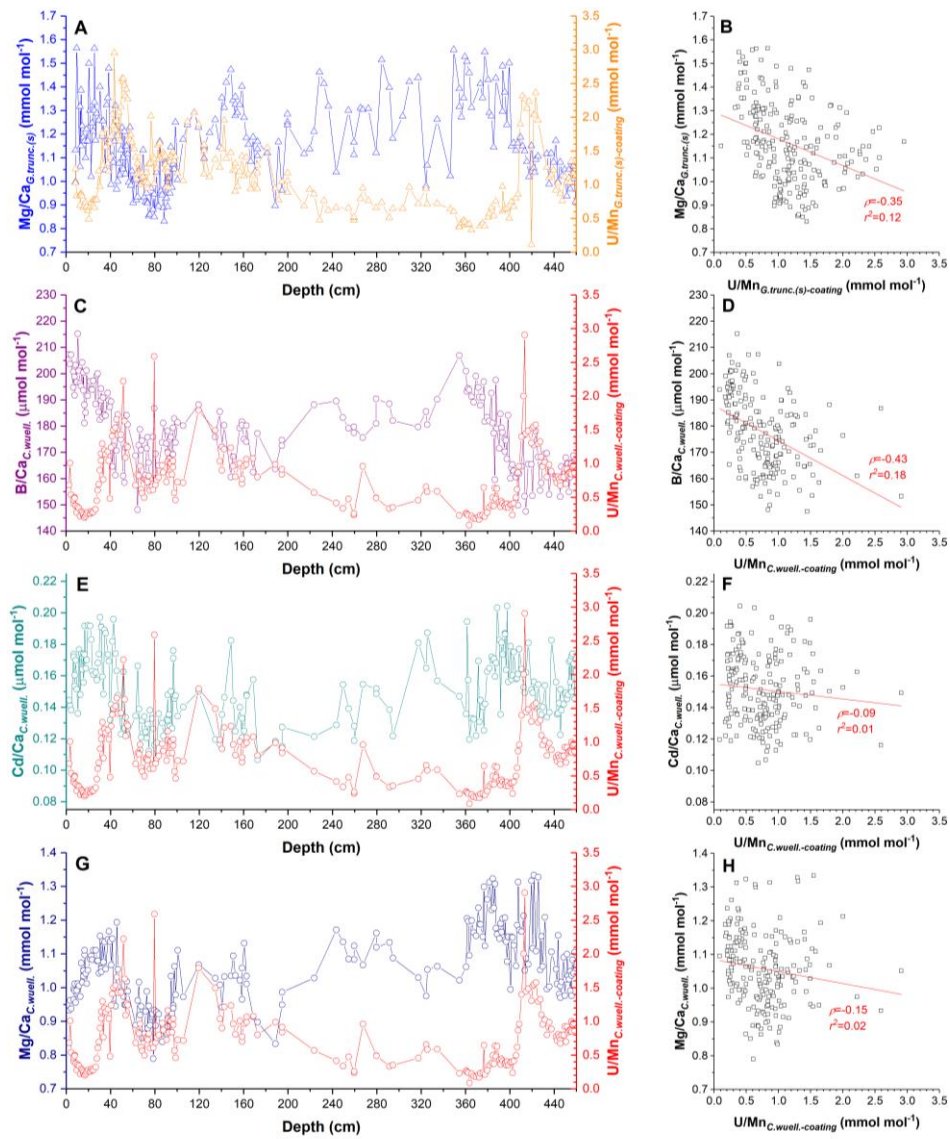


**Figure 3.18.** A) Downcore record of Mg/Ca measured in *G. truncatulinoides* (*s*) (light blue) from MD02-2588 plotted with corresponding downcore record of U/Mn from *G. truncatulinoides* (*s*) (orange). B) Cross plot of Mg/Ca measured in *G. truncatulinoides* (*s*) versus and U/Mn of *G. truncatulinoides* (*s*). C) Downcore records of B/Ca measured in *C. wuellerstorfi* (purple) from MD02-2588 plotted with corresponding downcore record of U/Mn from *C. wuellerstorfi* (red). D) Cross plot of B/Ca measured in *C. wuellerstorfi* versus and U/Mn of *C. wuellerstorfi*. E) Downcore records of Cd/Ca measured in *C. wuellerstorfi* (cyan) from MD02-2588 plotted with corresponding downcore record of U/Mn from *C. wuellerstorfi* (red). F) Cross plot of Cd/Ca measured in *C. wuellerstorfi* versus and U/Mn of *C. wuellerstorfi*. G) Downcore records of Mg/Ca measured in *C. wuellerstorfi* (dark blue) from MD02-2588 plotted with corresponding downcore record of U/Mn from *C. wuellerstorfi* (red). H) Cross plot of Mg/Ca measured in *C. wuellerstorfi* versus and U/Mn of *C. wuellerstorfi*.

only a weak correlation in the corresponding *C. wuellerstorfi* ratios ( $\rho=0.41$ ,  $r^2=0.16$ ) (Fig. 3.19a-3.19d). In the absence of a diagenetic overprint, the correlation between  $Mg/Ca_{G.trunc.}$  and  $Cd/Ca_{G.trunc.}$  may have been attributed to a temperature-dependent distribution coefficient for the incorporation of Cd into the calcite test of planktonic foraminifera (e.g., Rickaby and Elderfield, 1999; Yu *et al.*, 2013). However, the evidence presented thus far suggests that some degree of authigenic contamination has indeed impacted the samples from this core site. If we accept that part of the correlation between Cd/Ca and Mg/Ca is due to the presence of authigenic contaminants, we would expect the downcore variation of coating-bound Cd to be similar in the planktonic and benthic records.

To examine the downcore variation of foraminiferal coating-bound Cd we assume that downcore U/Ca and Mn/Ca predominantly reflect variations in the authigenic coatings on the shells. To quantify the downcore variability of foraminiferal coating-bound Cd we simply divide Cd/Ca in both foraminifera species by the corresponding Mn/Ca and U/Ca concentrations to determine Cd/Mn and Cd/U, respectively. This exercise reveals a striking resemblance between the downcore records of planktonic and benthic Cd/Mn and Cd/U (Fig. 3.19e and 3.19g). Strong positive correlations are observed between the planktonic versus benthic Cd/Mn records ( $\rho=0.73$ ,  $r^2=0.53$ ) (Fig. 3.19f) and between the planktonic versus benthic Cd/U records ( $\rho=0.82$ ,  $r^2=0.67$ ) (Fig. 3.19h). The range of values for Cd/Mn are very similar between the planktonic and benthic records along most of the core length, while for Cd/U the values are similar along most of the core except for the topmost 30 cm and between approximately 340 cm and 380 cm.

The strong correlations of Cd/Mn and Cd/U between the benthic and planktonic records suggests that part of the downcore variations of bulk Cd/Ca in both *G. truncatulinoides* (*s*) and *C. wuellerstorfi* can be attributed to variations in the concentration of coating-bound Cd. Therefore, the variability of Cd/Ca in both species cannot be regarded as reflecting solely an ambient seawater nutrient concentration signal.

One caveat in this analysis is that the magnitude of the Cd/Mn values measured in the foraminifera samples (between  $1 \text{ mmol mol}^{-1}$  and  $10 \text{ mmol mol}^{-1}$ ) is three times greater than the typical Cd/Mn ratio of manganese nodules ( $\sim 0.05 \text{ mmol mol}^{-1}$ ; based on global ocean data from de Lange *et al.*, 1992). If the Cd/Mn composition of the coatings that precipitate on the tests of foraminifera have comparable compositions

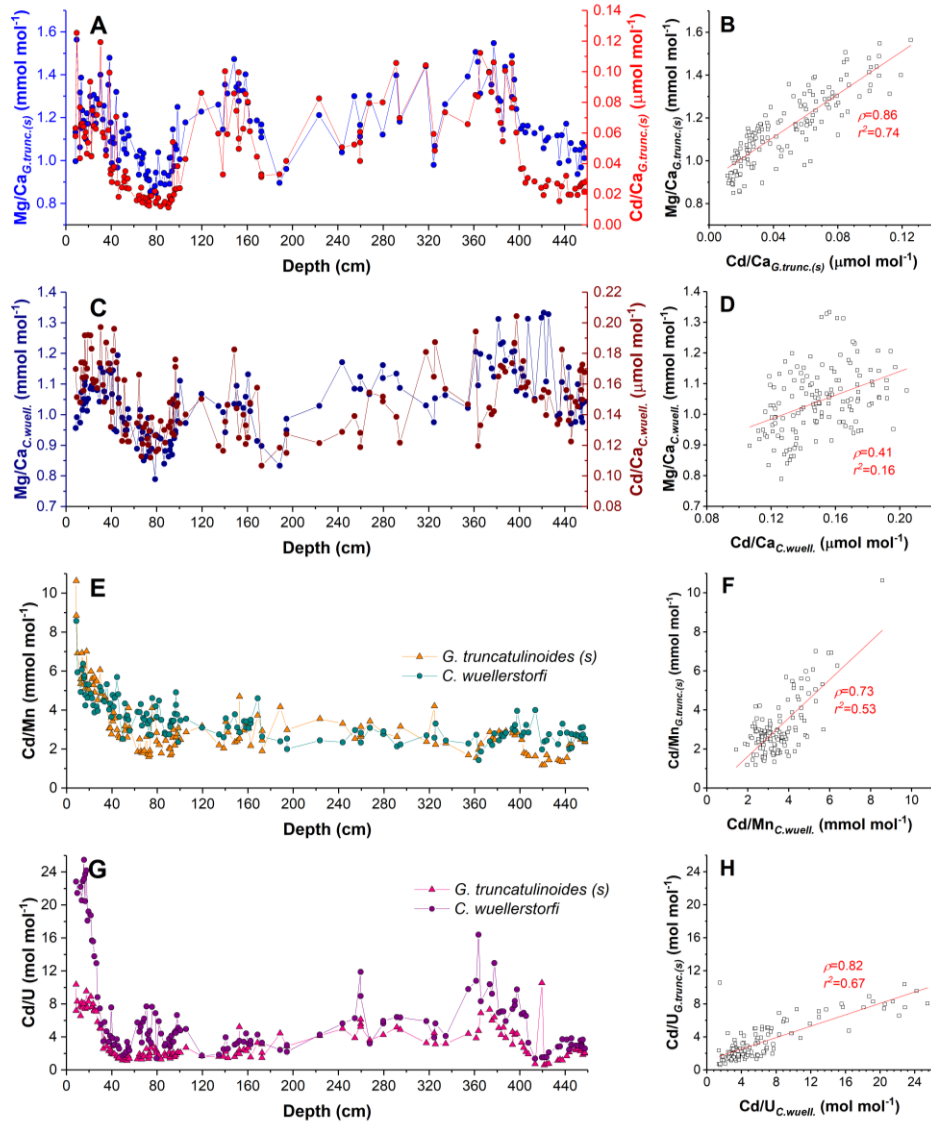


**Figure 3.19.** A) Downcore record of Mg/Ca measured in *G. truncatulinoides* (*s*) (light blue) from MD02-2588 plotted with corresponding downcore record of Cd/Ca from *G. truncatulinoides* (*s*) (red). B) Cross plot of Mg/Ca measured in *G. truncatulinoides* (*s*) versus and Cd/Ca of *G. truncatulinoides* (*s*). C) Downcore records of Mg/Ca measured in *C. wuellerstorfi* (dark blue) from MD02-2588 plotted with corresponding downcore record of Cd/Ca from *C. wuellerstorfi* (dark red). D) Cross plot of Mg/Ca measured in *C. wuellerstorfi* versus and Cd/Ca of *C. wuellerstorfi*. E) Downcore records of Cd/Mn measured in *C. wuellerstorfi* (cyan) from MD02-2588 plotted with corresponding downcore record of Cd/Mn from *G. truncatulinoides* (*s*) (orange). F) Cross plot of Cd/Mn measured in *C. wuellerstorfi* versus and Cd/Mn of *G. truncatulinoides* (*s*). G) Downcore records of Cd/U measured in *C. wuellerstorfi* (purple) from MD02-2588 plotted with corresponding downcore record of Cd/U from *G. truncatulinoides* (*s*) (pink). H) Cross plot of Cd/U measured in *C. wuellerstorfi* versus and Cd/U of *G. truncatulinoides* (*s*).

to manganese nodules, this would suggest that only ~1% of the Cd/Mn variability in the foraminifera records can be accounted for by variations in the composition of coatings. Accordingly, the remaining ~99% of the variability must be dependent on the variability of lattice-bound Cd and Mn. This interpretation would indicate that the normalisation method applied to the Cd/Ca and Mn/Ca does not reliably isolate the coating-bound Cd signal as was intended at the outset of the analysis. Taken at face value, this would suggest that the covariation observed between Cd/Mn in the planktonic and benthic series does not result from a common authigenic signal, but rather a common signal arising from lattice-bound covariations of Cd and Mn. It is unclear what process could have led to this coincidental or mechanistic covariation in both the planktonic and benthic foraminifera records. The downcore pattern of variability, at least, argues against a climate-driven process.

Alternatively, the composition of Cd/Mn of foraminiferal coatings at the MD02-2588 core site may differ from the average Cd/Mn composition of manganese nodules. Indeed, large deviations are reported to occur in the global averaged elemental composition of manganese nodules (de Lange *et al.*, 1992).

Overall, the analysis does not reveal convincing evidence that the Cd records from MD02-2588 have been detrimentally impacted by the presence of authigenic coatings. Unlike Cd/Mn and Cd/U, a similar analysis performed with the planktonic and benthic Mg/Mn and Mg/U data (not shown) does not reveal particularly convincing correlations. Again, this may reflect a notable lattice-bound contribution of both Mg, Mn and U to the overall signals of Mg/Ca, Mn/Ca and U/Ca.

### 3.9.8 Foraminiferal elemental ratios versus stable oxygen isotopic composition

The  $\delta^{18}\text{O}$  composition of foraminiferal tests ( $\delta^{18}\text{O}_{\text{foram}}$ ) is controlled by two main parameters: (i) the ambient  $\delta^{18}\text{O}$  composition of the seawater in which the test is biogenically precipitated, and (ii) the temperature-dependent fractionation of oxygen isotopes between water and calcium carbonate during shell formation. Certain ‘vital effects’ may cause  $\delta^{18}\text{O}_{\text{foram}}$  to deviate from these parameters but, on the whole,  $\delta^{18}\text{O}_{\text{foram}}$  is accepted as a reliable recorder of ambient  $\delta^{18}\text{O}_{\text{sw}}$  and temperature (e.g., Ravelo and Hillaire-Marcel, 2007).

This temperature dependency of  $\delta^{18}\text{O}_{\text{foram}}$  provides an additional measure with which to inspect the potential impacts of post-depositional contamination on  $\text{Mg}/\text{Ca}_{\text{foram}}$

measured along sediment core MD02-2588. The downcore records of  $\delta^{18}\text{O}_{G.trunc.(s)}$  and  $\text{Mg}/\text{Ca}_{G.trunc.(s)}$  from this core reveal a relatively weak negative correlation ( $\rho=-0.54$ ,  $r^2=0.29$ ) and even weaker correlation between  $\delta^{18}\text{O}_{C.wuell.}$  and  $\text{Mg}/\text{Ca}_{C.wuell.}$  ( $\rho=-0.34$ ,  $r^2=0.11$ ) (Fig. 3.20). The most robust correlation is observed between  $\delta^{18}\text{O}_{C.wuell.}$  and  $\text{B}/\text{Ca}_{C.wuell.}$  ( $\rho=-0.77$ ,  $r^2=0.60$ );  $\delta^{18}\text{O}_{C.wuell.}$  and  $\text{Cd}/\text{Ca}_{C.wuell.}$ , on the other hand, displays the weakest correlation ( $\rho=-0.25$ ,  $r^2=0.05$ ) (Fig. 3.20). The correlation between downcore  $\delta^{18}\text{O}_{G.trunc.(s)}$  and  $\text{Mg}/\text{Ca}_{G.trunc.(s)}$ , though weak, may suggest that the isotopic and elemental composition of the foraminiferal tests are partly effected by changes in intermediate water temperature at the core site. This is supported by the relatively small effect of global ice-volume change on planktonic foraminiferal  $\delta^{18}\text{O}$ . The relative weakness of the correlation could arise from the entanglement of various signals in the recorded isotopic composition of  $\delta^{18}\text{O}_{G.trunc.(s)}$ . Equally, the weak correlation could arise from the ‘masking effect’ of contaminant phases on bulk  $\text{Mg}/\text{Ca}_{G.trunc.(s)}$ . These effects could also explain the lack of a correlation between the downcore records  $\delta^{18}\text{O}_{C.wuell.}$  and  $\text{Mg}/\text{Ca}_{C.wuell.}$ . The strong correlation between the downcore records of  $\delta^{18}\text{O}_{C.wuell.}$  and  $\text{B}/\text{Ca}_{C.wuell.}$  may result from a connection between changes in bottom water carbonate ion concentration and changes in the local hydrography. Alternatively, the relationship between  $\delta^{18}\text{O}_{C.wuell.}$  and  $\text{B}/\text{Ca}_{C.wuell.}$  may be due to a link between bottom water carbonate ion concentration and global ice-volume changes. A caveat of the above observations is that various inconsistencies become apparent with these relationships when the records are separated into MIS-equivalent depth sections) (Appendix Fig. 3.42-3.47).

Notwithstanding these downcore inconsistencies, it is potentially useful to compare the downcore elemental ratio datasets with the ice volume corrected foraminiferal oxygen isotope compositions. Comparison of the downcore record of  $\text{Mg}/\text{Ca}_{G.trunc.(s)}$  with the record of ice-volume corrected  $\delta^{18}\text{O}_{G.trunc.(s)}$  ( $\delta^{18}\text{O}_{ivc-G.trunc.(s)}$ ) reveals a weaker correlation than was observed with the uncorrected isotopic record ( $\rho=-0.30$ ,  $r^2=0.08$  for  $\delta^{18}\text{O}_{ivc-G.trunc.(s)}$  vs  $\text{Mg}/\text{Ca}_{G.trunc.(s)}$ ) (Fig. 3.21a). This potentially indicates that intermediate water temperature change may be a less important factor than global ice volume change in explaining the correlation between the two parameters. A weaker correlation is also observed between  $\text{Mg}/\text{Ca}_{C.wuell.}$  and  $\delta^{18}\text{O}_{ivc-C.wuell.}$  ( $\rho=-0.26$ ,  $r^2=0.06$ ) relative to that observed with the uncorrected isotopic record (Fig. 3.21d). Interestingly, the correlation between  $\delta^{18}\text{O}_{ivc-C.wuell.}$  and  $\text{B}/\text{Ca}_{C.wuell.}$  does not change

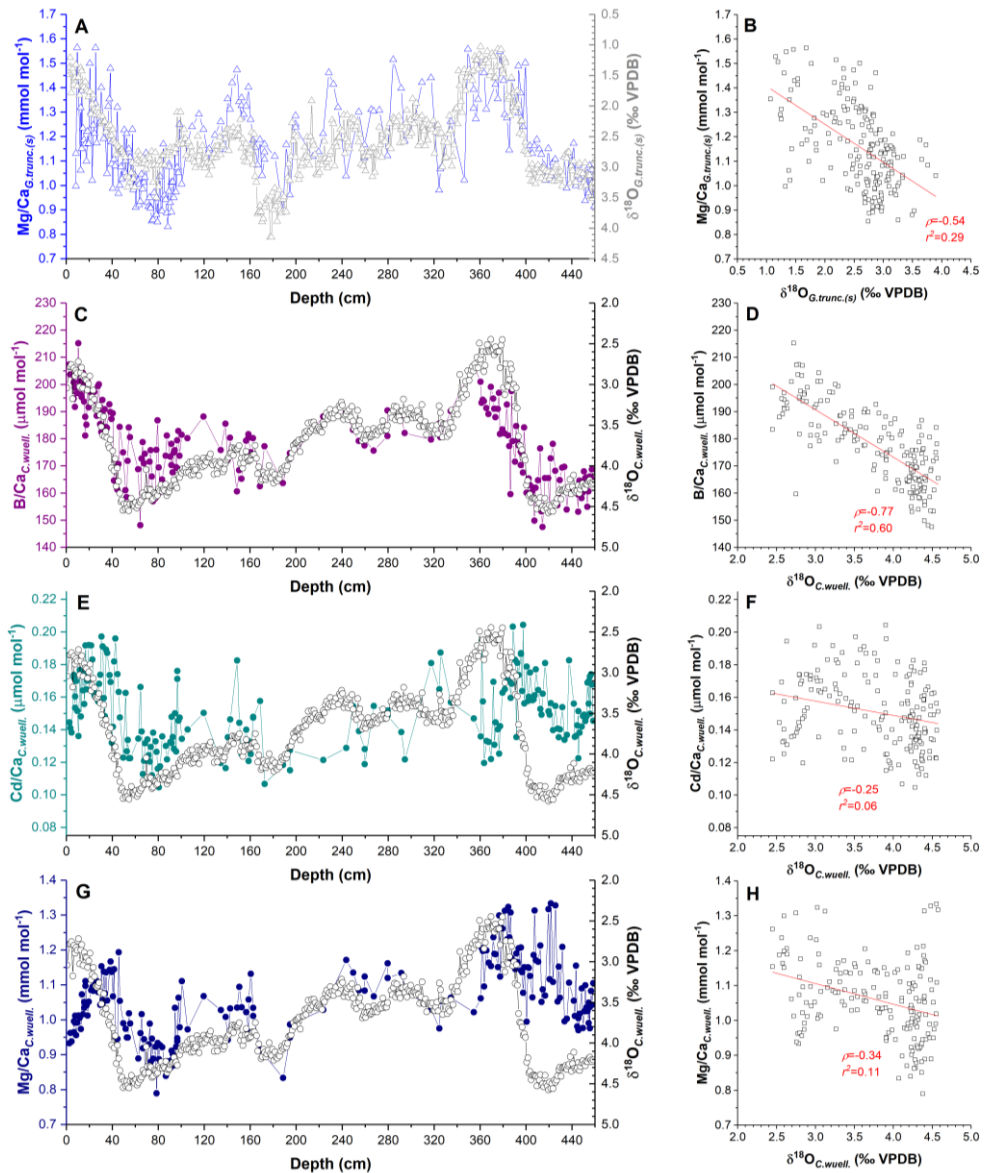


**Figure 3.20.** A) Downcore record of Mg/Ca measured in *G. truncatulinoides* (s) (light blue) from MD02-2588 plotted with corresponding downcore record of *G. truncatulinoides* (s)  $\delta^{18}\text{O}$  (grey symbols). B) Cross plot of Mg/Ca measured in *G. truncatulinoides* (s) versus  $\delta^{18}\text{O}$  of *G. truncatulinoides* (s). C) Downcore records of B/Ca measured in *C. wuellerstorfi* (purple) from MD02-2588 plotted with corresponding downcore record of *C. wuellerstorfi*  $\delta^{18}\text{O}$  (grey symbols). D) Cross plot of B/Ca measured in *C. wuellerstorfi* versus  $\delta^{18}\text{O}$  of *C. wuellerstorfi*. E) Downcore records of Cd/Ca measured in *C. wuellerstorfi* (cyan) from MD02-2588 plotted with corresponding downcore record of *C. wuellerstorfi*  $\delta^{18}\text{O}$  (grey symbols). F) Cross plot of Cd/Ca measured in *C. wuellerstorfi* versus  $\delta^{18}\text{O}$  of *C. wuellerstorfi*. G) Downcore records of Mg/Ca measured in *C. wuellerstorfi* (dark blue) from MD02-2588 plotted with corresponding downcore record of *C. wuellerstorfi*  $\delta^{18}\text{O}$  (grey symbols). H) Cross plot of Mg/Ca measured in *C. wuellerstorfi* versus  $\delta^{18}\text{O}$  of *C. wuellerstorfi*.

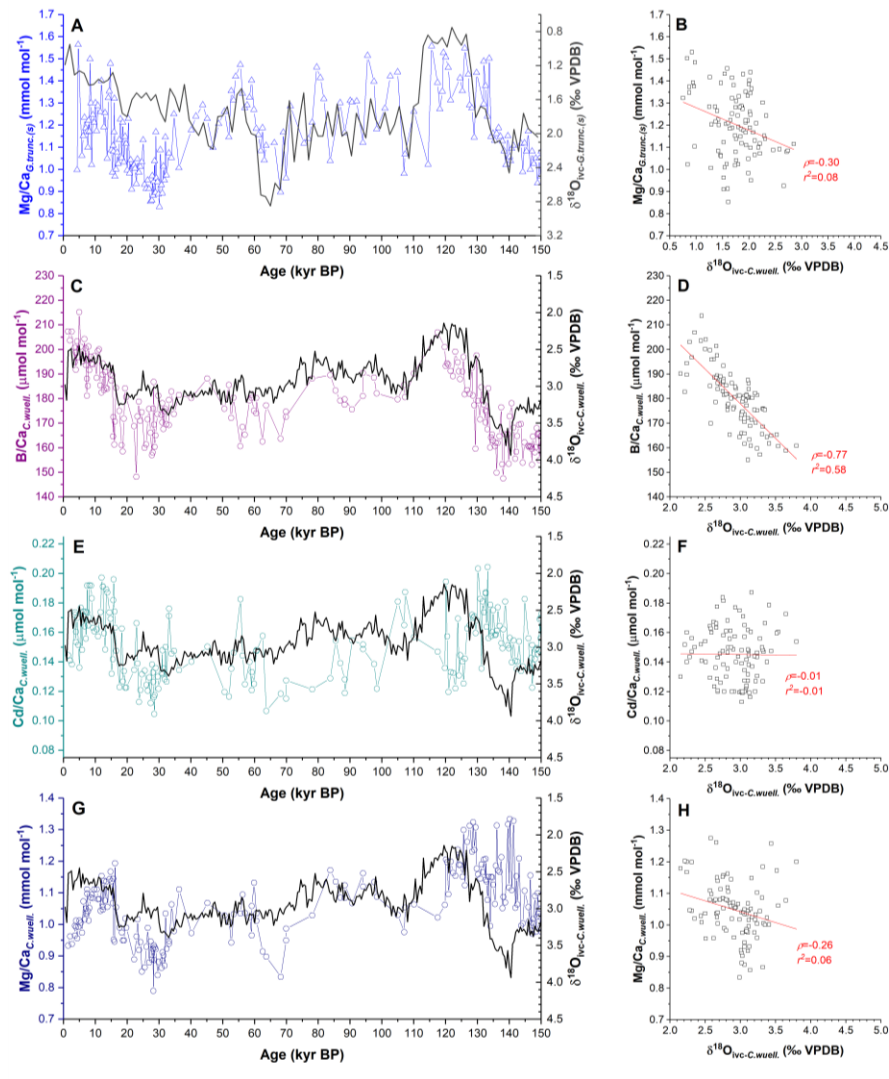


**Figure 3.21.** A) Downcore record of Mg/Ca measured in *G. truncatulinoides* (*s*) (light blue) from MD02-2588 plotted with corresponding downcore record of ice volume corrected  $\delta^{18}\text{O}$  from *G. truncatulinoides* (*s*) (grey line). B) Cross plot of Mg/Ca measured in *G. truncatulinoides* (*s*) versus and ice volume corrected  $\delta^{18}\text{O}$  of *G. truncatulinoides* (*s*). C) Downcore records of B/Ca measured in *C. wuellerstorfi* (purple) from MD02-2588 plotted with corresponding downcore record of ice volume corrected  $\delta^{18}\text{O}$  from *C. wuellerstorfi* (black line). D) Cross plot of B/Ca measured in *C. wuellerstorfi* versus ice-volume corrected  $\delta^{18}\text{O}$  of *C. wuellerstorfi*. E) Downcore records of Cd/Ca measured in *C. wuellerstorfi* (cyan) from MD02-2588 plotted with corresponding downcore record of ice volume corrected  $\delta^{18}\text{O}$  from *C. wuellerstorfi* (black line). F) Cross plot of Cd/Ca measured in *C. wuellerstorfi* versus ice volume corrected  $\delta^{18}\text{O}$  of *C. wuellerstorfi*. G) Downcore records of Mg/Ca measured in *C. wuellerstorfi* (dark blue) from MD02-2588 plotted with corresponding downcore record of ice volume corrected  $\delta^{18}\text{O}$  from *C. wuellerstorfi* (black line). H) Cross plot of Mg/Ca measured in *C. wuellerstorfi* versus ice volume corrected  $\delta^{18}\text{O}$  of *C. wuellerstorfi*.

( $\rho=-0.77$ ,  $r^2=0.58$ ) (Fig. 3.21b). This could indicate that the relationship between variations in the carbonate ion concentration of the waters bathing the Agulhas Plateau core site is more closely associated with local hydrographic changes rather than global ice-volume change. In the case of  $Cd/Ca_{C.wuell.}$ , there appears to be no relationship to the isotopic composition of the foraminiferal calcite whether the latter is corrected for global ice volume change or not (Fig. 3.21c). Again, the details of these relationships are more complex when the datasets are divided into MIS-equivalent depth sections so these observations should be considered tentatively (Appendix Fig. 3.48-3.53).

### 3.9.9 XRF core-scanning evidence of diagenetic contamination

The elemental concentration series obtained from XRF core scanning of sediment core MD02-2588 provide a further line of enquiry for determining the impacts of diagenetic contamination on the foraminiferal elemental ratio datasets. The downcore XRF core-scanned stratigraphic series of Mn and Fe may be susceptible to the effects of diagenetic remobilisation of Mn and Fe below the sediment-water interface which leads to the precipitation of Mn-Fe oxides as micromodules within the sediment and/or as coatings on sedimentary particles (e.g., Burdige, 1993; Calvert and Pedersen, 1996). Covariation between Mn and Fe counts derived from the XRF scans along sediment core MD02-2588 may, therefore, be an indicator of the impact of diagenetic processes on the elemental ratio records derived from foraminifera.

The normalised downcore records of Mn and Fe (i.e., Mn/counts per second (cps) and Fe/ counts per second, respectively) show very different patterns of downcore variation and no correlation to each other ( $\rho=-0.1$ ,  $r^2=0.01$ ) (Fig. 3.22a and 3.22b). Normalised Mn has a range between  $1.5 \times 10^{-5}$  and  $3 \times 10^{-5}$  below ~20 cm depth and is characterised by a peak centred on ~ 10 cm that reaches approximately  $1.75 \times 10^{-4}$  (i.e., almost an order of magnitude greater than the baseline value). The presence of this peak agrees with the occurrence of a maximum Mn-oxide precipitation zone below the sediment-water interface that should roughly coincide with the depth at which sedimentary oxygen is completely depleted. The lack of a similar peak in the downcore record of normalised Fe suggests that the variability of Fe, as determined by XRF core-scanning, is probably controlled by a different process. The strong correlation between normalised Fe and Ti suggests that the downcore Fe series most likely reflects the variability in deposition and erosion of terrigenous material by

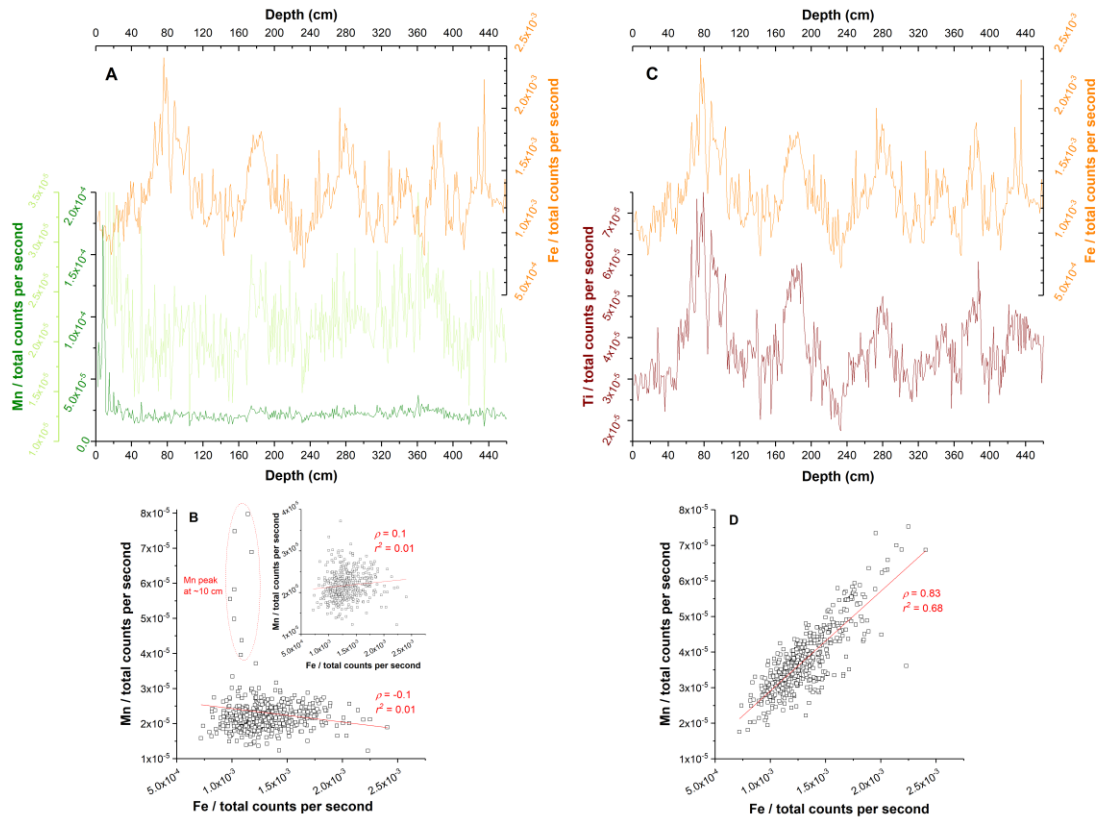


**Figure 3.22.** A) Upper panel (orange) shows the XRF scanning downcore profile of normalised Fe (Fe/total counts per second) from MD02-2588. Lower panel shows the corresponding XRF scanning profile of normalised Mn (Mn/total counts per second) (dark green for full range, light green shows baseline range) from the same core. B) Scatter plot of downcore Fe vs downcore Mn from MD02-2588 with line of best fit (red) through the data. Inset shows correlation with ‘Mn peak’ data removed. C) Upper panel (orange) shows the XRF scanning downcore profile of normalised Fe (Fe/total counts per second) from MD02-2588. Lower panel shows the corresponding XRF scanning profile of normalised Ti (Ti/total counts per second) (red) from the same core. D) Scatter plot of downcore Fe vs downcore Ti from MD02-2588 with line of best fit (red) through the data.

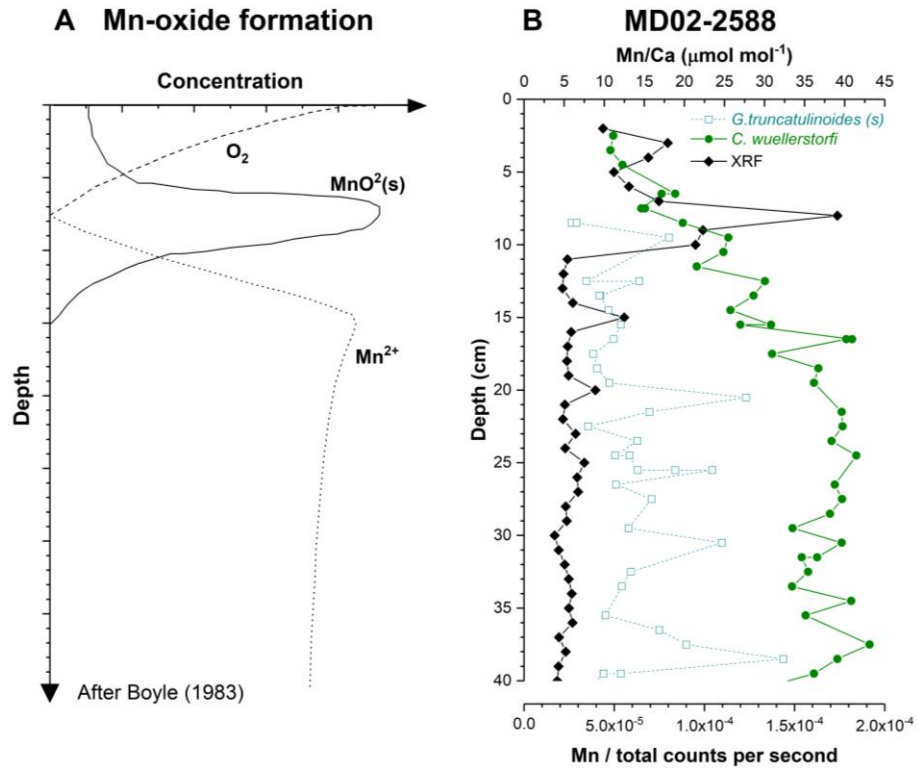


**Figure 3.23.** A) Schematic diagram indicating known manganese recycling processes (Boyle, 1983). B) MD02-2588 downcore records of normalised Mn (Mn/total counts per second) (black) derived from XRF core scanning and Mn/Ca in *G. truncatulinoides* (s) (cyan) and *C. wuellerstorfi* (green).

aeolean and nepheloid layer processes at the core site (Fig. 3.22c and 3.22d). As such, the XRF-derived Mn/Fe record cannot be compared with the foraminiferal Mn/Fe records.

Nonetheless, the Mn peak at ~10 cm agrees with known manganese cycling processes whereby reduced Mn (i.e.,  $\text{Mn}^{2+}$ ) diffuses up through the sediment column until it encounters oxygen and reprecipitates as Mn-oxides (Li *et al.*, 1969; Bender *et al.*, 1977; Froelich *et al.*, 1979) (Fig. 3.23a). When compared to the corresponding *C. wuellerstorfi* record of Mn/Ca in sediment core MD02-2588, it appears that the XRF-derived Mn peak at ~10 cm coincides with the decreasing Mn/ $\text{Ca}_{C.wuell.}$  trend in the upper 25 cm of the core (Fig. 3.23b). This raises the possibility that part of the  $\text{Mn}^{2+}$  that contributes to the Mn peak at ~10 cm is derived from Mn-oxides that had previously precipitated on foraminifera tests in the sediment. As has already been seen, however, the downcore Mn/ $\text{Ca}_{G.trunc(s)}$  data do not display a comparable decreasing trend over this topmost section of the sediment core and, in addition, are offset from the Mn/ $\text{Ca}_{C.wuell.}$  record by  $\sim 20 \mu\text{mol mol}^{-1}$  arguing against substantial alteration by Mn-oxide contamination on this basis (Fig. 3.23b). Furthermore, the complete lack of Mn/Ca peaks in either of the foraminiferal records at ~10 cm implies that the original foraminiferal calcite records are not substantially altered by the precipitation of Mn-oxides within the topmost layers of sediment. The same can be said of the data below 20 cm in the core, where normalised Mn ranges between  $1.5 \times 10^{-5}$  and  $3 \times 10^{-5}$  and displays a more regular variability on decimetre to metre scales. In the 20-460 cm interval of the core, the correlation between normalised Mn and Mn/ $\text{Ca}_{G.trunc(s)}$  and between normalised Mn and Mn/ $\text{Ca}_{C.wuell.}$  is very poor ( $\rho = -0.23$ ,  $R^2 = 0.05$  and  $\rho = -0.23$ ,  $R^2 = 0.05$ , respectively) (Fig. 3.24). If the variability of the XRF-derived Mn series is driven by the changes in the authigenic precipitation of manganese nodules and micronodules within the sediment, the lack of a correlation between it and the foraminiferal Mn/Ca records would argue against substantial alteration of the primary foraminiferal calcite signal. However, the XRF-derived Mn series most likely represents a mixed signal driven by both early diagenetic processes and changes in the deposition of aeolean-derived Mn on the seafloor (Baker *et al.*, 2017).

### 3.9.10 Elemental ratio data evaluation for contamination: summary & conclusion

Based on the evidence presented above, the foraminifera-derived elemental ratio records from sediment core MD02-2588 appear to be somewhat impacted by

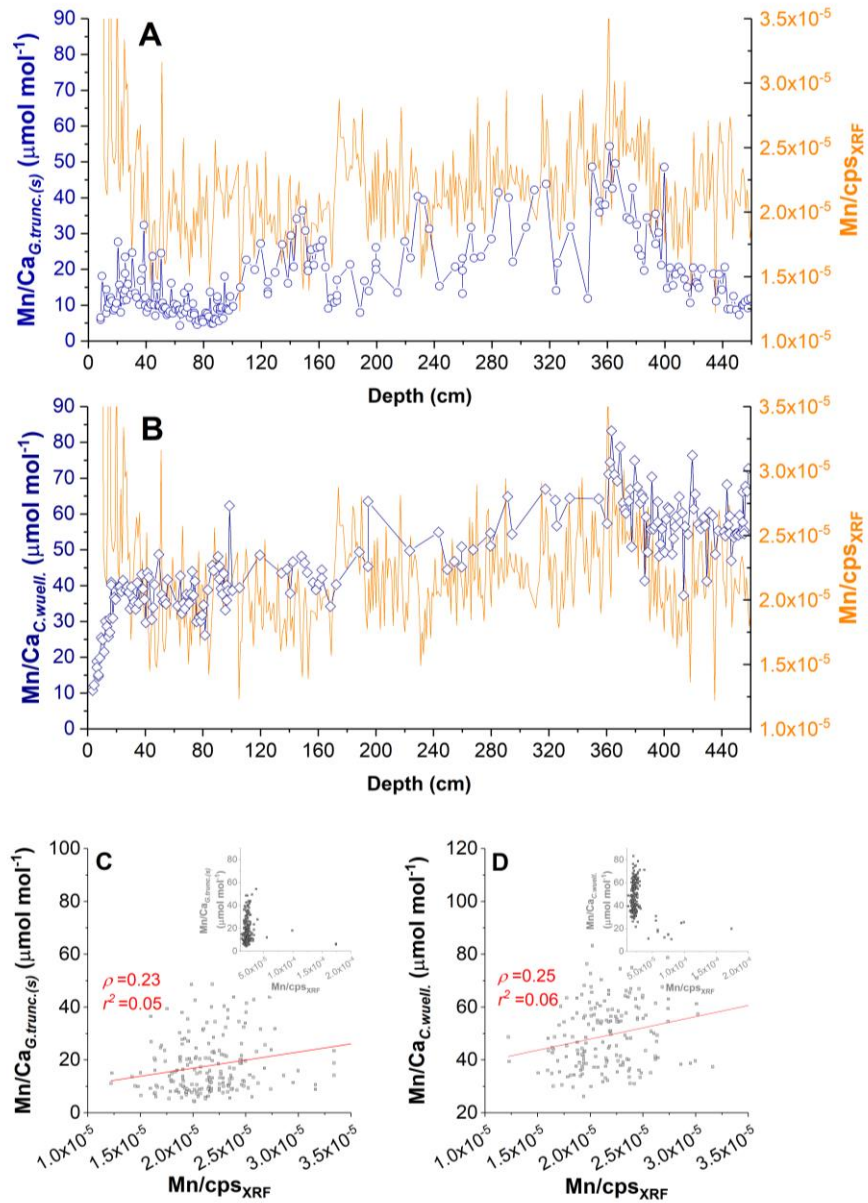


**Figure 3.24.** A) Downcore record of Mn/Ca measured in *G. truncatulinoides (s)* (light blue) from MD02-2588 plotted alongside normalised Mn (Mn/total counts per second) (black) derived from XRF core scanning. B) Downcore records of Mn/Ca measured in *C. wuellerstorfi* (dark blue) from MD02-2588 plotted alongside normalised Mn (Mn/total counts per second) (black) derived from XRF core scanning. C) Cross plot of Mn/Ca measured in *G. truncatulinoides (s)* versus normalised Mn. D) Cross plot of Mn/Ca measured in *C. wuellerstorfi* versus normalised Mn.

contamination from Mn-Fe-oxide coatings. This introduces uncertainties regarding the utility of foraminiferal Mg/Ca, Cd/Ca and B/Ca from this core site as proxies of temperature, nutrient concentration, and carbonate ion saturation state, respectively. What is important for this study, however, is whether the incomplete removal of diagenetic coatings significantly alters the primary environmental signals. Below, we summarise the evidence and determine whether the foraminiferal elemental ratios from sediment core MD02-2588 can be used to reconstruct the paleoceanographic conditions in the waters overlying the Agulhas Plateau.

Summary of evidence:

- (i) the Mn/Ca and Fe/Ca values from both *G. truncatulinoides* (*s*) and *C. wuellerstorfi* are, for the most part, well below the recommended thresholds for likely contamination from Mn-Fe-oxide coatings and manganese carbonate overgrowths (i.e.,  $<100 \mu\text{mol mol}^{-1}$ ) (Boyle, 1983; Barker *et al.*, 2003),
- (ii) Taking the B/Ca<sub>C.wuell.</sub> and Cd/Ca<sub>C.wuell.</sub> data in their entirety, there appear to be no correlations with any of the contaminant ratios (i.e., with Mn/Ca<sub>C.wuell.</sub> or Fe/Ca<sub>C.wuell.</sub>). Mg/Ca<sub>C.wuell.</sub>, on the other hand, appears to be weakly correlated with Mn/Ca<sub>C.wuell.</sub> ( $\rho=0.55$ ,  $r^2=0.30$ ). Likewise, Mg/Ca<sub>G.trunc.</sub> also displays a positive correlation with Mn/Ca<sub>G.trunc.</sub> ( $\rho=0.82$ ,  $r^2=0.67$ ) and a weaker, but nonetheless apparent, positive correlation with Fe/Ca ( $\rho=0.66$ ,  $r^2=0.43$ ).
- (iii) The observed correlations between Mg/Ca<sub>G.trunc.</sub> and the ‘contaminant monitor’ ratios are heavily influenced by the clustering of data within the lower ranges of the elemental ratios (0-15  $\mu\text{mol.mol}^{-1}$  for Al/Ca<sub>G.trunc.</sub> and Fe/Ca<sub>G.trunc.</sub>, and 0-25  $\mu\text{mol.mol}^{-1}$  and 0-25  $\text{nmol.mol}^{-1}$ , for Mn/Ca<sub>G.trunc.</sub> and U/Ca<sub>G.trunc.</sub> respectively). This demonstrates that even at values well below the accepted thresholds for contamination (i.e.,  $<100 \mu\text{mol.mol}^{-1}$  for Al/Ca<sub>G.trunc.</sub>, Fe/Ca<sub>G.trunc.</sub> and Mn/Ca<sub>G.trunc.</sub>), the correlations with Mg/Ca<sub>G.trunc.</sub> are a persistent feature of the dataset.
- (iv) Dividing the data into MIS-equivalent subsections reveals that the strong positive correlation between Mg/Ca<sub>G.trunc.</sub> and Mn/Ca<sub>G.trunc.</sub> (and to a lesser degree between Mg/Ca<sub>G.trunc.</sub> and Fe/Ca<sub>G.trunc.</sub>) is a persistent feature of the dataset.
- (v) In the benthic records, the correlations between Mg/Ca<sub>C.wuell.</sub> and Mn/Ca<sub>C.wuell.</sub>, and between Cd/Ca<sub>C.wuell.</sub> and Mn/Ca<sub>C.wuell.</sub>, are weak in all MIS sections except

for the interval equivalent to MIS 1. This may suggest that the MIS 1 interval is compromised by diagenetic contamination, although we note that the MIS 1 interval contains the lowest  $\text{Mn}/\text{Ca}_{C.wuell.}$  values in the entire record.

- (vi)  $\text{B}/\text{Ca}_{C.wuell.}$  displays relatively strong negative correlations with  $\text{Mn}/\text{Ca}_{C.wuell.}$  and  $\text{Fe}/\text{Ca}_{C.wuell.}$  during the MIS 1 interval and a relatively strong positive correlation with  $\text{Mn}/\text{Ca}_{C.wuell.}$  during the MIS 5 interval. In the remaining MIS sections, the correlations are weak and the sign of the relationship between  $\text{B}/\text{Ca}_{C.wuell.}$  and  $\text{Mn}/\text{Ca}_{C.wuell.}$  is inconsistent from section to section.
- (vii) The downcore  $\text{Fe}/\text{Ca}$  records from the two foraminifera species are moderately correlated with the corresponding  $\text{Mn}/\text{Ca}$  records. Though the benthic and planktonic  $\text{Mn}/\text{Ca}$  and  $\text{Fe}/\text{Ca}$  records are offset from each other in terms of absolute values, the slopes of the linear regressions in the relationship between the two ratios for both species are similar.
- (viii) Single specimen samples of *G. truncatulinoides* (*s.*) measured by LA-ICP-MS at three distinct sediment intervals along core MD02-2588 reveal large offsets in their elemental ratios relative to the multi-specimen samples measured by ICP-MS. Pertinent to the discussion of contamination by diagenetic coatings is the relationship that is observed between  $\text{Mg}/\text{Ca}_{G.trunc}$  and  $\text{Mn}/\text{Ca}_{G.trunc}$  measured by LA-ICP-MS. The relationship between these two elements in the LA-ICP-MS data is comparable to the relationship observed between the two elemental ratios in the ICP-MS data. This suggests that the strong correlation between  $\text{Mg}/\text{Ca}_{G.trunc}$  and  $\text{Mn}/\text{Ca}_{G.trunc}$  may be a feature of the chemistry of the shell wall of foraminifera and not of the authigenic coatings present on the inner and outer surfaces of the test. Instead, it may be possible that the observed correlation between  $\text{Mg}/\text{Ca}_{G.trunc}$  and  $\text{Mn}/\text{Ca}_{G.trunc}$  in both the LA-ICP-MS and the ICP-MS data is the result of the presence of low concentration contaminant phases which have permeated the shell walls through the pores in the shell structure.
- (ix) Our examination of the relationships between planktonic elemental ratio records and the corresponding benthic records reveals that the strongest correlations between co-registered planktonic and benthic elemental ratios occur for  $\text{Mg}/\text{Ca}$ ,  $\text{Mn}/\text{Ca}$  and  $\text{U}/\text{Ca}$ ; generally, however, these correlations are weak ( $\rho=0.47$ ,

$r^2=0.22$ ;  $\rho=0.57$ ,  $r^2=0.33$ ;  $\rho=0.48$ ,  $r^2=0.22$ , respectively). Some similarity is also apparent in the broader trends of Cd/Ca in the two species ( $\rho=0.34$ ,  $r^2=0.11$ ).

- (x) *C. wuellerstorfi* samples generally display higher concentrations than the corresponding *G. truncatulinoides* (*s*) samples. This is particularly apparent in the series of B/Ca, Cd/Ca, Mn/Ca and Fe/Ca. The offset is less apparent in the series of U/Ca, while in Mg/Ca, the relationship is reversed such that the Mg/Ca of *G. truncatulinoides* (*s*) is higher than that of *C. wuellerstorfi* throughout most parts of the studied core section.
- (xi) The contribution of Mg from Mn-Fe oxide coatings to the Mg/Ca ratio of the samples from MD02-2588 is approximately 1%. This would suggest that the contribution of the Mg/Ca signal from the coating should be masked by the Mg/Ca signal of the primary foraminiferal calcite.
- (xii) The strong correlation between the stratigraphic records of benthic and planktonic U/Mn from MD02-2588 suggests that authigenic coatings are present on the foraminiferal samples. However, the records of U/Mn are not correlated with the corresponding records of Mg/Ca<sub>*G.trunc.(s.)*</sub> ( $\rho=0.35$ ,  $r^2=0.12$ ), B/Ca<sub>*C.wuell.*</sub> ( $\rho=0.43$ ,  $r^2=0.18$ ), Cd/Ca<sub>*C.wuell.*</sub> ( $\rho=0.09$ ,  $r^2=0.01$ ) and Mg/Ca<sub>*C.wuell.*</sub> ( $\rho=0.15$ ,  $r^2=0.02$ ). The lack of correlation between U/Mn and these elemental ratios is also evident when the data are divided into MIS-equivalent depth sections. This would suggest that these elemental ratios are not impacted by changes in the sedimentary redox conditions at the MD02-2588 core site and that the measured values of these ratios do not reflect the coating-bound concentrations of Mn and U but rather the shell-bound concentrations of these elements.
- (xiii) A striking resemblance is evident between the planktonic and benthic records of Cd/Mn and Cd/U, potentially suggesting that the Cd/Ca records from MD02-2588 are influenced by the presence of coating-bound Cd. However, a mass balance calculation based on estimates of Cd/Mn in manganese nodules reveals that only 1% of the variability in downcore Cd/Mn variation at the MD02-2588 core site can be accounted for by authigenic Cd variations. Although it is not known how accurately the average composition of manganese nodules reflects the composition of authigenic coatings at the core site.

- (xiv) Comparison of the foraminiferal oxygen isotopic composition with the corresponding elemental ratio values from the same samples hints at a potential temperature influence on the record of  $\text{Mg}/\text{Ca}_{G.trunc}$  but not on  $\text{Mg}/\text{Ca}_{C.wuell.}$ .
- (xv) When compared to the corresponding *C. wuellerstorfi* record of  $\text{Mn}/\text{Ca}$  in sediment core MD02-2588, it appears that the XRF-derived Mn peak at ~10 cm coincides with the decreasing  $\text{Mn}/\text{Ca}_{C.wuell.}$  trend in the upper 25 cm of the core. This raises the possibility that part of the  $\text{Mn}^{2+}$  that contributes to the Mn peak at ~10 cm is derived from Mn-oxides that had previously precipitated on foraminifera test in the sediment. As has already been seen, however, the downcore  $\text{Mn}/\text{Ca}_{G.trunc(s)}$  data do not display a comparable decreasing trend over this topmost section of the sediment core and, in addition, are offset from the  $\text{Mn}/\text{Ca}_{C.wuell.}$  record by  $\sim 20 \mu\text{mol mol}^{-1}$  arguing against substantial alteration by Mn-oxide contamination, at least on this basis. Furthermore, the complete lack of Mn/Ca peaks in either of the foraminiferal records at ~10 cm would imply that the original foraminiferal calcite records are not substantially altered by the precipitation of Mn-oxides within that depth in the sediment column.
- (xvi) In the 20-460 cm interval of the core, the correlation between normalised Mn and  $\text{Mn}/\text{Ca}_{G.trunc(s)}$  and between normalised Mn and  $\text{Mn}/\text{Ca}_{C.wuell.}$  is very poor ( $\rho=-0.23$ ,  $R^2=0.05$  and  $\rho=-0.23$ ,  $R^2=0.05$ , respectively). If the variability of the XRF-derived Mn series is driven by the changes in the authigenic precipitation of manganese nodules and micronodules within the sediment, the lack of a correlation between it and the foraminiferal Mn/Ca records would argue against substantial alteration of the primary foraminiferal calcite signal.

From these observations, several arguments are relevant to the evaluation of the data in terms of the impacts of contamination by the presence of authigenic phases.

Though the suggested ‘critical’ thresholds for monitoring contamination are a somewhat arbitrary criterion for the evaluation of data quality (Boyle, 1983), we emphasise that the Mn/Ca values in this study are very low, especially when compared to those in other published studies. For example, at core sites in the North Atlantic, planktonic and benthic foraminiferal Mn/Ca can reach values of up to  $500 \mu\text{mol mol}^{-1}$  (Yu *et al.*, 2013; Lear *et al.*, 2016). In Mn-rich sediments from the Antarctic Southern Ocean,

foraminiferal Mn/Ca can be  $>1 \text{ mmol mol}^{-1}$  (Hasenfratz *et al.*, 2017) and in the Panama Basin, values as high as  $8 \text{ mmol mol}^{-1}$  have been measured (Pena *et al.*, 2005, 2008).

Likewise, as has been previously suggested for correlated downcore Mn/Ca and Mg/Ca data from the South Pacific, the similarity between the two elemental ratios may reflect ‘climate related diagenetic reorganisation of Mn rather than an imprint affecting Mg’ (Elderfield *et al.*, 2012). As was highlighted in that study, the actual contribution of Mg from any potential diagenetic coatings would be minimal when compared to the Mg content of the entire sample. In the case of the data from MD02-2588, the contribution of Mg from Mn-Fe oxide coatings to the Mg/Ca ratio of the samples is approximately 1% of the total signal. This would suggest that the coating-derived signal is masked by the Mg/Ca signal derived from the primary foraminiferal calcite.

Notwithstanding these qualifications, the relationship between Mn/Ca and Mg/Ca in *G. truncatulinoides* (*s*) is striking and highly suspicious. Furthermore, the observation of a similar relationship between Mn/Ca and Mg/Ca in the LA-ICP-MS results suggests that the correlation could be the result of ineffective removal of authigenic contaminant phases present within the pore system that permeates the shell wall structure of *G. truncatulinoides* (*s*) (e.g., Pena *et al.*, 2005, 2008; Hasenfratz *et al.*, 2017). Though there are no LA-ICP-MS data for *C. wuellerstorfi*, it could be hypothesised that the weaker correlation between Mn/Ca and Mg/Ca in this species is due to its low porosity such that contaminant phases occur predominantly as layers on the internal and external chamber walls which are more easily removed than contaminants located within pores (Pena *et al.*, 2005, 2008).

Differences in the morphology, structure and texture of the tests of *G. truncatulinoides* (*s*) relative to those *C. wuellerstorfi* may explain why the correlation between the downcore records of elemental ratios in planktonic and benthic are weak. For example, the occurrence of higher concentrations of Mn/Ca in *C. wuellerstorfi* relative to the corresponding concentrations in *G. truncatulinoides* (*s*) does not necessarily indicate that the former is more contaminated. Indeed, based on the correlation of  $\text{Mn}/\text{Ca}_{C.wuell.}$  with  $\text{Mg}/\text{Ca}_{C.wuell.}$  and  $\text{Cd}/\text{Ca}_{C.wuell.}$ , the data, arguably, indicate a lower level of diagenetic contamination of the benthic records. This may suggest that the Mn in *C. wuellerstorfi*, whether of diagenetic origin or not, has less impact on the corresponding  $\text{Mg}/\text{Ca}_{C.wuell.}$  and  $\text{Cd}/\text{Ca}_{C.wuell.}$  records. The one exception to this interpretation is the

uppermost section of core MD02-2588 which is equivalent to the MIS 1 interval. In that interval,  $Mn/Ca_{C.wuell.}$  is strongly correlated both with  $Mg/Ca_{C.wuell.}$  and with  $Cd/Ca_{C.wuell.}$ . It was noted above that although the benthic elemental ratios showed the strongest correlation during this interval, the concentration of  $Mn/Ca_{C.wuell.}$  was at its lowest. Therefore, it seems that high values of Mn/Ca do not necessarily indicate that samples are negatively impacted by Mn-Fe oxides, possibly because certain contaminant phases are not as compromising to Mg/Ca and Cd/Ca as others.

Despite the common diagenetic environment of benthic and planktonic foraminifera tests, the latter record appears to have been more severely compromised by contaminant phases than the former. This evaluation argues against the use of the Mg/Ca record of *G. truncatulinoides* (*s*) from sediment core MD02-2588 as a paleotemperature proxy in this study. As has been alluded to various times above, the MIS 1 section of the  $Mg/Ca_{C.wuell.}$  and  $Cd/Ca_{C.wuell.}$  records may also have been compromised. However, at this stage, we opt not to eliminate this section from the subsequent discussion of the data. This decision is principally based on the observation that the patterns of  $Mg/Ca_{C.wuell.}$  and  $Cd/Ca_{C.wuell.}$  variability during the last two glacial-interglacial transitions are very similar despite having very different relationships with the corresponding  $Mn/Ca_{C.wuell.}$  record. During MIS 1,  $Mn/Ca_{C.wuell.}$  displays a decreasing trend paralleling the  $Mg/Ca_{C.wuell.}$  and  $Cd/Ca_{C.wuell.}$  records, while during the early MIS 5 interval,  $Mn/Ca_{C.wuell.}$  displays an opposite trend to  $Mg/Ca_{C.wuell.}$  and  $Cd/Ca_{C.wuell.}$ .

### **3.10 Elemental ratio data quality evaluation II – post-depositional dissolution**

#### *3.10.1 Evaluation of post-depositional dissolution of C. wuellerstorfi samples*

The potential impacts of partial post-depositional dissolution of foraminifera tests on the downcore records of  $B/Ca_{C.wuell.}$ ,  $Cd/Ca_{C.wuell.}$  and  $Mg/Ca_{C.wuell.}$  can be evaluated by using the downcore record of average *C. wuellerstorfi* shell weights. The average shell weight was estimated by dividing the total weight of the picked foraminifera by the number of individual tests in each sample. The number of shells picked in each sample varied between 5 and 60 individual specimens with a corresponding range of total sample weight of 54-691  $\mu\text{g}$ . If the foraminiferal calcite deposited at core site MD02-2588 has undergone partial dissolution, a positive correlation between the elemental ratios and the average shell weights would be expected. Comparison of the average *C.*

*wuellerstorfi* shell weights with the corresponding downcore records of elemental ratios reveals a weak positive correlation with  $B/Ca_{C.wuell.}$  ( $\rho=0.52$ ,  $r^2=0.27$ ) and no correlation with  $Cd/Ca_{C.wuell.}$  ( $\rho=0.03$ ,  $r^2=0.00$ ) and  $Mg/Ca_{C.wuell.}$  ( $\rho=0.00$ ,  $r^2=0.00$ ) (Fig. 3.25). The lack of a correlation between the downcore records of average shell weights and  $Cd/Ca_{C.wuell.}$  and  $Mg/Ca_{C.wuell.}$  suggests that there has been no significant post-depositional dissolution of the calcite tests, or at least, that any post-depositional dissolution that has occurred, has not impacted these elemental ratio records. Conversely, the positive correlation between the average shell weight record and  $B/Ca_{C.wuell.}$ , though weak, suggests that these two parameters may be associated in some way. Indeed, benthic foraminiferal B/Ca has been shown to be related with bottom water carbonate ion saturation state (e.g., Yu and Elderfield, 2007). This parameter is inherently linked to the dissolution of carbonate deposits on the seafloor because it determines how oversaturated or undersaturated the seawater is with respect to carbonate ( $CO_3$ ) at any specific location in the ocean. The weak positive correlation between the average shell weight record and  $B/Ca_{C.wuell.}$  may, therefore, indicate that both these parameters are responding to changes in the carbonate ion saturation state at the core site. This supports the utility of  $B/Ca_{C.wuell.}$  as a proxy of carbonate ion saturation state along sediment core MD02-2588. Furthermore, the lack of correlation between the average shell weight record and either  $Cd/Ca_{C.wuell.}$  or  $Mg/Ca_{C.wuell.}$  potentially indicates that any partial post-depositional dissolution that has occurred at the site was not significant enough to impact the latter two elemental ratio records.

The downcore variability of the bulk carbonate content measured along sediment core MD02-2588 (Romero *et al.*, 2015) may provide additional information regarding the partial post-depositional dissolution of foraminiferal calcite deposited on the southern Agulhas Plateau. The downcore variability of bulk carbonate content is dependent on the combined influences of calcium carbonate ( $CaCO_3$ ) deposition and dissolution on the seafloor, and dilution from the other sedimentary components such as biogenic opal and terrigenous material (Romero *et al.*, 2015). As such, it may be considered as a supplementary proxy for the dissolution of  $CaCO_3$  on the seafloor.

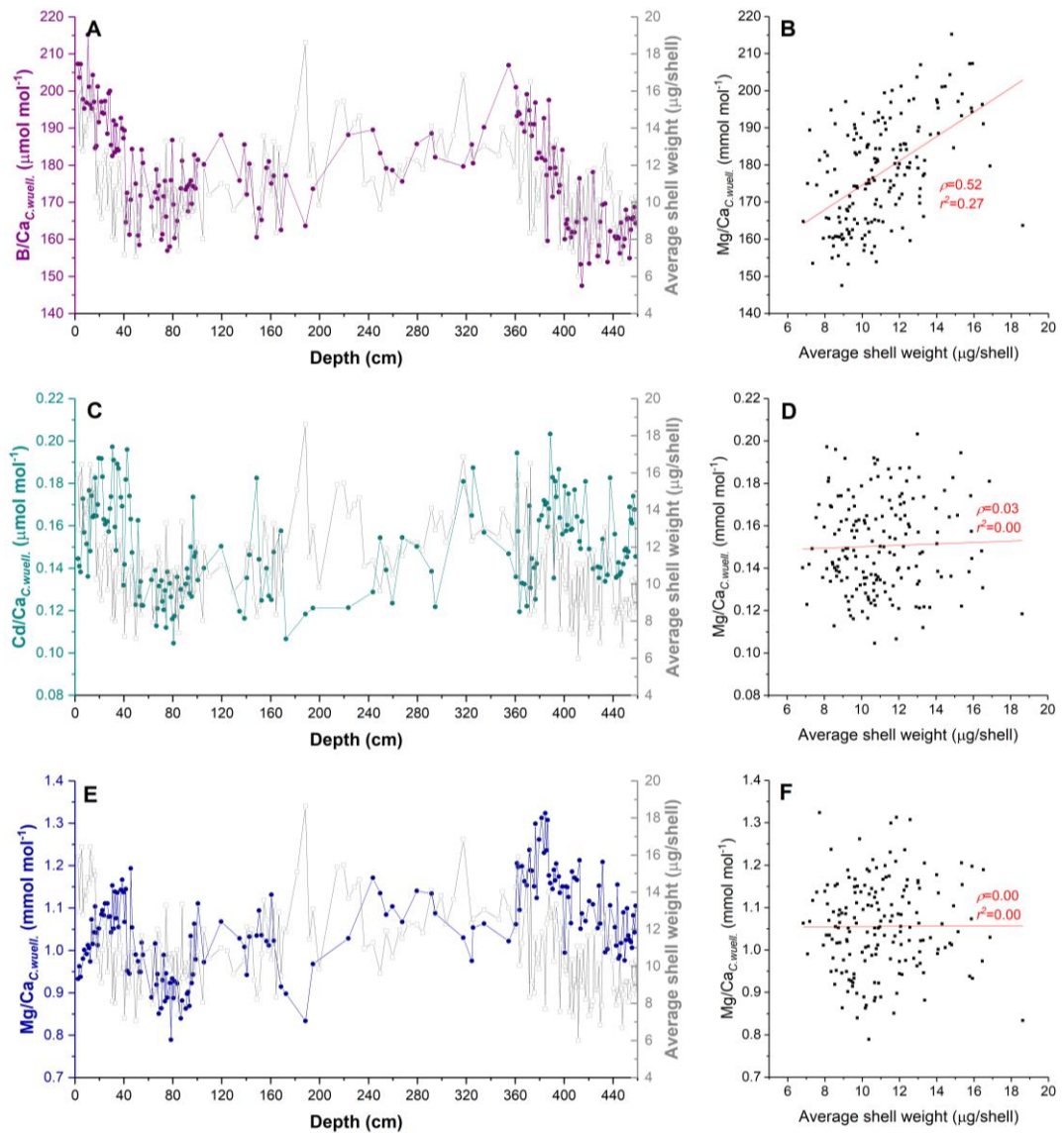


**Figure 3.25.** A) Downcore record of B/Ca measured in *C. wuellerstorfi* (purple) from MD02-2588 plotted with corresponding downcore record of average *C. wuellerstorfi* shell weight (grey line). B) Cross plot of B/Ca measured in *C. wuellerstorfi* versus average *C. wuellerstorfi* shell weight. C) Downcore records of Cd/Ca measured in *C. wuellerstorfi* (cyan) from MD02-2588 plotted with corresponding downcore record of average *C. wuellerstorfi* shell weight (grey line). D) Cross plot of Cd/Ca measured in *C. wuellerstorfi* versus average *C. wuellerstorfi* shell weight. E) Downcore records of Mg/Ca measured in *C. wuellerstorfi* (dark blue) from MD02-2588 plotted with corresponding downcore record of average *C. wuellerstorfi* shell weight (grey line). F) Cross plot of Mg/Ca measured in *C. wuellerstorfi* versus average *C. wuellerstorfi* shell weight.

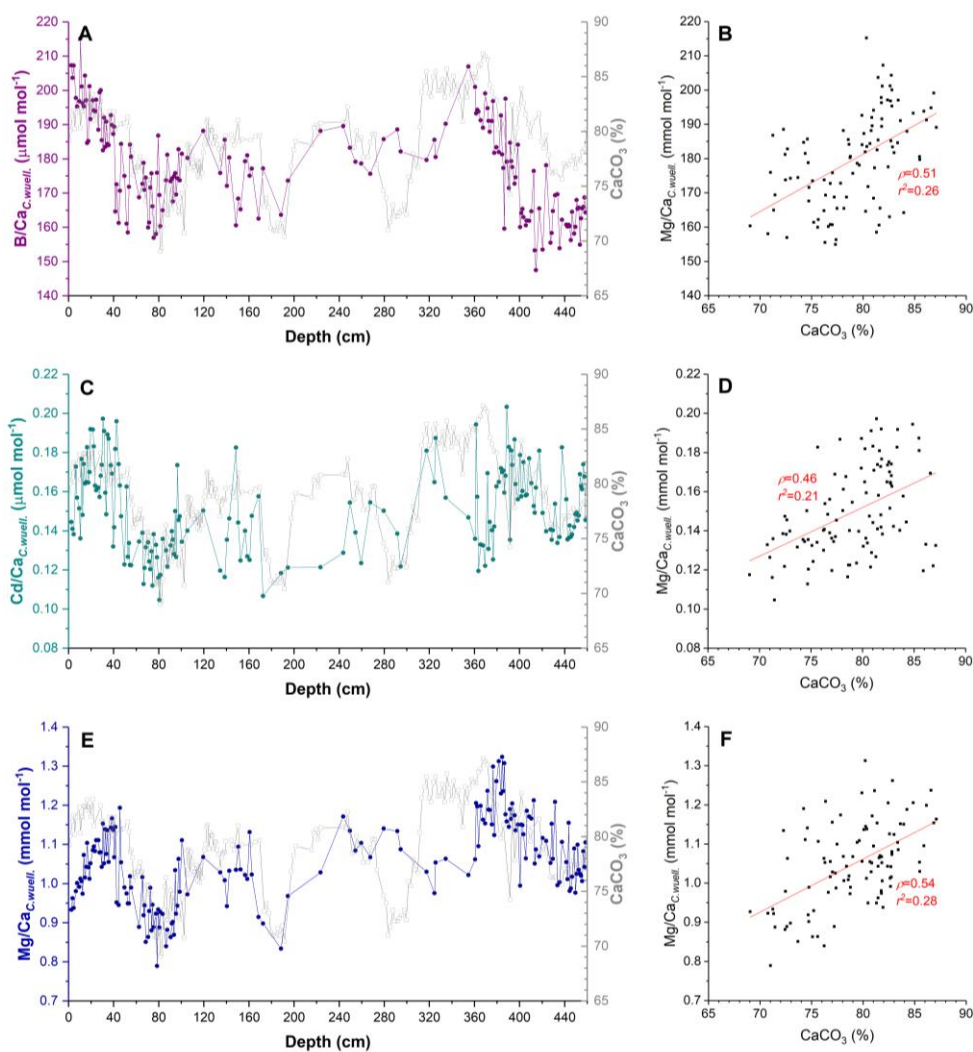


**Figure 3.26.** A) Downcore record of B/Ca measured in *C. wuellerstorfi* (purple) from MD02-2588 plotted with corresponding downcore record of  $\text{CaCO}_3$  percentage weight (grey line). B) Cross plot of B/Ca measured in *C. wuellerstorfi* versus  $\text{CaCO}_3$  percentage weight. C) Downcore records of Cd/Ca measured in *C. wuellerstorfi* (cyan) from MD02-2588 plotted with corresponding downcore record of  $\text{CaCO}_3$  percentage weight (grey line). D) Cross plot of Cd/Ca measured in *C. wuellerstorfi* versus  $\text{CaCO}_3$  percentage weight. E) Downcore records of Mg/Ca measured in *C. wuellerstorfi* (dark blue) from MD02-2588 plotted with corresponding downcore record of  $\text{CaCO}_3$  percentage weight (grey line). F) Cross plot of Mg/Ca measured in *C. wuellerstorfi* versus  $\text{CaCO}_3$  percentage weight.

However, comparison of the downcore record of bulk carbonate content from sediment core MD02-2588 with the corresponding record of average *C. wuellerstorfi* shell weights reveals that the two parameters are not correlated (Appendix figure 3.54;  $\rho=0.22$ ,  $r^2=0.04$ ). This suggests that the record of bulk carbonate content from MD02-2588 may not be a reliable indicator of post-depositional dissolution of foraminiferal calcite, most likely because the bulk carbonate content is controlled by a complex combination of the various drivers mentioned above. Bearing this caveat in mind, we observe that weak correlations occur between the record of bulk carbonate content and all elemental ratios ( $\rho=0.51$ ,  $r^2=0.26$ ,  $\rho=0.46$ ,  $r^2=0.21$ , and  $\rho=0.54$ ,  $r^2=0.28$  for  $B/Ca_{C.wuell.}$ ,  $Cd/Ca_{C.wuell.}$  and  $Mg/Ca_{C.wuell.}$ , respectively) (Fig. 3.26).

Overall, considering the association between  $B/Ca_{C.wuell.}$  and average shell weights, it appears that partial post-deposition dissolution has taken place at the core site, but the clear lack of correlation between the average shell weight record and either  $Cd/Ca_{C.wuell.}$  or  $Mg/Ca_{C.wuell.}$ , leads us to assume that the latter two elemental proxies are not impacted by post-depositional dissolution.

### 3.10.2 Evaluation of post-depositional dissolution of *G. truncatulinoides* (s.) samples

The average shell weights of the *G. truncatulinoides* (s.) samples from MD02-2588 were not measured. This prevents an assessment of the relationship between the downcore record of  $Mg/Ca_{G.trunc(s)}$  and possible post-depositional dissolution of the calcite tests of this foraminifera species. Instead, the downcore record of  $Mg/Ca_{G.trunc(s)}$  is compared to the corresponding record of  $B/Ca_{C.wuell.}$ . As has been mentioned above,  $B/Ca_{C.wuell.}$  is a reliable proxy of bottom water carbonate ion saturation state (e.g., Yu and Elderfield, 2007). In theory, the saturation state of bottom waters with respect to calcite should determine the dissolution rate of calcite deposited on the seafloor.

Comparison of the downcore record of  $Mg/Ca_{G.trunc(s)}$  with the corresponding  $B/Ca_{C.wuell.}$  record reveals a degree of similarity and a weak positive correlation between the two ( $\rho=0.43$ ,  $r^2=0.18$ ) (Fig. 3.27a). This may indicate that a small amount of post-depositional dissolution - driven by changes in bottom water carbonate ion saturation state - may have impacted the downcore record of  $Mg/Ca_{G.trunc(s)}$  at the

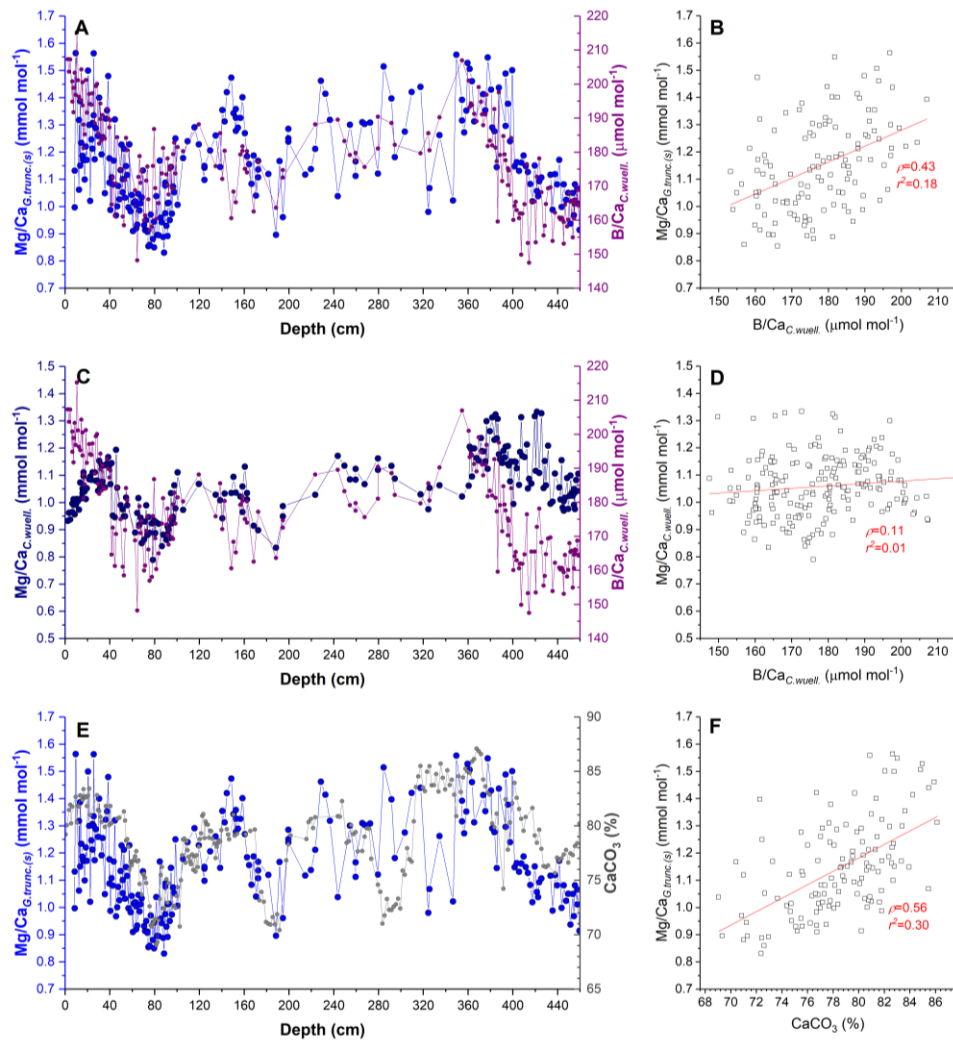


**Figure 3.27.** A) Downcore record of Mg/Ca measured in *G. truncatulinoides* (s) (light blue) from MD02-2588 plotted with corresponding downcore record of B/Ca measured in *C. wuellerstorfi* (purple). B) Cross plot of Mg/Ca measured in *G. truncatulinoides* (s) versus B/Ca measured in *C. wuellerstorfi*. C) Downcore record of Mg/Ca measured in *C. wuellerstorfi* (dark blue) from MD02-2588 plotted with corresponding downcore record of B/Ca measured in *C. wuellerstorfi* (purple). D) Cross plot of Mg/Ca measured in *C. wuellerstorfi* versus B/Ca measured in *C. wuellerstorfi*. E) Downcore record of Mg/Ca measured in *G. truncatulinoides* (s) (light blue) from MD02-2588 plotted with corresponding downcore record of CaCO<sub>3</sub> percentage weight (grey line). F) Cross plot of Mg/Ca measured in *G. truncatulinoides* (s) versus CaCO<sub>3</sub> percentage weight.

MD02-2588 core site. In detail, however, the downcore correlation between  $\text{Mg}/\text{Ca}_{G.\text{trunc.}(s)}$  and  $\text{B}/\text{Ca}_{C.\text{wuell.}}$  varies along the core. The section equivalent to MIS 4 shows the strongest correlation ( $\rho=0.61$ ,  $r^2=0.26$ ), while the section equivalent to MIS 3 shows a weak, but negative correlation ( $\rho=-0.26$ ,  $r^2=0.02$ ). All other sections display only very weak positive correlations ( $\rho=0.28$ ,  $r^2=0.03$ ,  $\rho=0.33$ ,  $r^2=0.08$ ,  $\rho=0.33$ ,  $r^2=0.06$ , and  $\rho=0.42$ ,  $r^2=0.13$ , for MIS 1, MIS 2, MIS 5 and MIS 6, respectively) (Appendix figure 3.55-3.60, Panels A).

Though the correlation between  $\text{Mg}/\text{Ca}_{G.\text{trunc.}(s)}$  and  $\text{B}/\text{Ca}_{C.\text{wuell.}}$  is generally weak, it is nonetheless stronger than the correlation observed between  $\text{Mg}/\text{Ca}_{C.\text{wuell.}}$  and  $\text{B}/\text{Ca}_{C.\text{wuell.}}$  when the downcore records are analysed in their entirety ( $\rho=0.11$ ,  $r^2=0.01$ ) (Fig. 3.27b). More detailed analysis of the correlation between  $\text{Mg}/\text{Ca}_{C.\text{wuell.}}$  and  $\text{B}/\text{Ca}_{C.\text{wuell.}}$  reveals that the reason for the relatively weaker correlation is largely driven by the moderately strong negative correlation in the depth section equivalent to MIS 1 ( $\rho=-0.66$ ,  $r^2=0.43$ ), and the weighing effect associated with the larger number of data points in this section (Appendix figure 3.55-3.60, Panels B).

A stronger correlation is observed between the downcore records of  $\text{Mg}/\text{Ca}_{G.\text{trunc.}(s)}$  and the  $\text{CaCO}_3$  content of the sediment ( $\rho=0.56$ ,  $r^2=0.30$ ) (Fig. 3.27c). However, as has already been mentioned, the relationship between  $\text{CaCO}_3$  content and post-depositional dissolution is more ambiguous and probably reflects a complex interaction between the production of  $\text{CaCO}_3$  in the surface ocean, its deposition on the seafloor and the dissolution of the deposited  $\text{CaCO}_3$  at the seafloor and within the sediment column.

Overall, the evidence suggests that post-depositional dissolution may have had a small impact on  $\text{Mg}/\text{Ca}_{G.\text{trunc.}(s)}$  but there are no grounds on which to conclusively argued that the dissolution has resulted in a large alteration of the downcore record of  $\text{Mg}/\text{Ca}_{G.\text{trunc.}(s)}$ .

### 3.11 Reconstructing bottom water carbonate ion saturation state from benthic foraminiferal B/Ca

$\text{B}/\text{Ca}$  measured in *C. wuellerstorfi* ( $\text{B}/\text{Ca}_{C.\text{wuell.}}$ ) is used to reconstruct the variability of bottom water carbonate ion saturation state ( $\Delta[\text{CO}_3^{2-}]$ ) at the MD02-2588 core site. Carbonate saturation state is defined as

$$\Delta[\text{CO}_3^{2-}] = [\text{CO}_3^{2-}]_{\text{in situ}} - [\text{CO}_3^{2-}]_{\text{sat}}$$

Eq. 3.3

where  $[\text{CO}_3^{2-}]_{\text{sat}}$  is the calcite saturation concentration and is calculated by

$$[\text{CO}_3^{2-}]_{\text{sat}} = [\text{CO}_3^{2-}] / \Omega$$

Eq. 3.4

$\Omega$ , in turn, is the solubility ratio of calcite. Downcore B/Ca<sub>C.wueller</sub> data from MD02-2588 are converted to  $\Delta[\text{CO}_3^{2-}]$  using the species-specific relationship of Yu and Elderfield, (2007) (Fig. 3.28):

$$\text{B/Ca}_{C.wueller} = 1.14 \pm 0.048 \Delta[\text{CO}_3^{2-}] + 177.1 \pm 1.41$$

Eq. 3.5

Full propagation of the errors associated with the B/Ca<sub>C.wueller</sub> data from MD02-2588, and the slope and intercept errors in Yu and Elderfield's calibration (2007), yields a pooled  $\Delta[\text{CO}_3^{2-}]$  error of 3.79  $\mu\text{mol kg}^{-1}$ . However, Yu and Elderfield (2007) reported that the uncertainty associated with reconstructing bottom water  $\Delta[\text{CO}_3^{2-}]$  using B/Ca in *C. wuellerstorfi* is  $\pm 9 \mu\text{mol kg}^{-1}$ .

The modern  $\Delta[\text{CO}_3^{2-}]$  value for the MD02-2588 core site was calculated using the CO2Calc (Version 4.0.9) (Robbins *et al.*, 2010). The equilibrium constants  $K_1$  and  $K_2$  are those from Mehrbach *et al.*, (1973), refitted by Dickson and Millero (1987),  $K_{\text{SO}_4}$  is from Dickson (1990) and we use the total boron value of Lee *et al.*, (2010). Hydrographic variables were taken from the Global Ocean Data Analysis Project (GLODAP) Bottle Data (version 2) (Olsen *et al.*, 2016). For the calculation of the modern  $\Delta[\text{CO}_3^{2-}]$  we used the following variables: Salinity=34.8 practical salinity units, temperature=1.9°C, pressure=2941 dbars, total alkalinity=2348  $\mu\text{mol kg}^{-1}$ , total  $\text{CO}_2$ =2220  $\mu\text{mol kg}^{-1}$ . Based on this input the CO2Calc software gives an  $\Omega$  of 1.23 and a  $[\text{CO}_3^{2-}]_{\text{in situ}}$  of 92.99  $\mu\text{mol kg}^{-1}$ . Using the relationships in equations 3.3 and 3.4, the modern  $\Delta[\text{CO}_3^{2-}]$  for core site MD02-2588 is estimated to be 17.45  $\mu\text{mol kg}^{-1}$ . No correction was made for the post-industrial anthropogenic  $\text{CO}_2$  contribution. Nonetheless, the modern  $\Delta[\text{CO}_3^{2-}]$  value is similar to the MD02-2588 core top (2.5 cm depth) value of  $\sim 26.51 \mu\text{mol kg}^{-1}$ , particularly when considering the  $\pm 9 \mu\text{mol kg}^{-1}$  uncertainty estimated by Yu and Elderfield's (2007) B/Ca<sub>C.wueller</sub>-to- $\Delta[\text{CO}_3^{2-}]$  calibration (Fig. 3.28). The average  $\Delta[\text{CO}_3^{2-}]$  value for the entire Holocene section of the

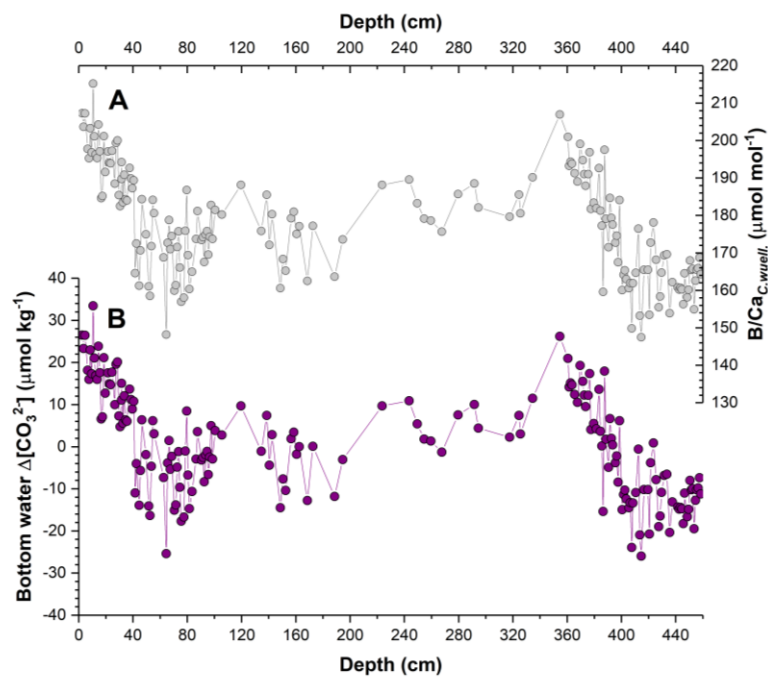


**Figure 3.28.** A) Downcore record of B/Ca measured in *C. wuellerstorfi* (grey) from MD02-2588. B) Downcore record of bottom water carbonate saturation state (purple) derived from B/Ca measured in *C. wuellerstorfi* from MD02-2588.

MD02-2588 core (0-30 cm) is  $17.96 \mu\text{mol kg}^{-1}$ , which is almost identical to modern bottom water  $\Delta[\text{CO}_3^{2-}]$ .

### 3.12 Evaluation of *C. wuellerstorfi* Mg/Ca as a paleotemperature proxy

It has been shown that at bottom water temperatures (BWT)  $< 3 \text{ }^\circ\text{C}$  the Mg/Ca ratio measured in the calcite tests of *C. wuellerstorfi* is significantly affected by changes in carbonate ion saturation state (Elderfield *et al.*, 2006). This proposed threshold behaviour has raised doubts about the use of Mg/Ca in this species as a proxy for BWT at temperatures typical of the deep ocean; see, for example, the technical comment by Yu and Broecker (2010) in response to the study by Sosdian and Rosenthal (2009). Despite these reservations, for deep sea temperatures  $> \sim 3^\circ\text{C}$ , where waters are typically oversaturated with respect to calcite, the  $\text{Mg}/\text{Ca}_{C.wuell}$  has been shown to be positively and significantly correlated with BWT (Cappelli *et al.*, 2015). In this section we examine whether the record of  $\text{Mg}/\text{Ca}_{C.wuell}$  from sediment core MD02-2588 can be used as a proxy for reconstructing the past variability of BWT at the southern Agulhas Plateau core site.

To isolate the temperature component of  $\text{Mg}/\text{Ca}_{C.wuell}$  and reconstruct the BWT variability at the core site, we corrected the raw  $\text{Mg}/\text{Ca}_{C.wuell}$  data from core MD02-2588 for the so-called ‘carbonate ion effect’ (Fig. 3.29). Following the estimation of downcore carbonate ion saturation state from  $\text{B}/\text{Ca}_{C.wuell}$  (see section 3.11 of this chapter), the  $\Delta[\text{CO}_3^{2-}]$  component of  $\text{Mg}/\text{Ca}_{C.wuell}$  ( $\text{Mg}/\text{Ca}_{\Delta[\text{CO}_3^{2-}]}$ ) was isolated by applying the relationships reported by Elderfield *et al.*, (2006) and Raitzsch *et al.*, (2008), based on correlations between the temperature-corrected  $\text{Mg}/\text{Ca}_{C.wuell}$  from Holocene sediment core-tops and modern bottom water  $\Delta[\text{CO}_3^{2-}]$ . Elderfield *et al.*, (2006) report the linear relationship:

$$\text{Mg}/\text{Ca}_{\Delta[\text{CO}_3^{2-}]} = 0.0086 \pm 0.0006 \Delta[\text{CO}_3^{2-}] - 0.15 \pm 0.02$$

Eq. 3.6

between  $\text{Mg}/\text{Ca}_{\Delta[\text{CO}_3^{2-}]}$  and bottom water  $\Delta[\text{CO}_3^{2-}]$  from a global database. The slope and constant of the relationship are reported in units of  $\text{mmol mol}^{-1} \mu\text{mol}^{-1} \text{kg}^{-1}$  and

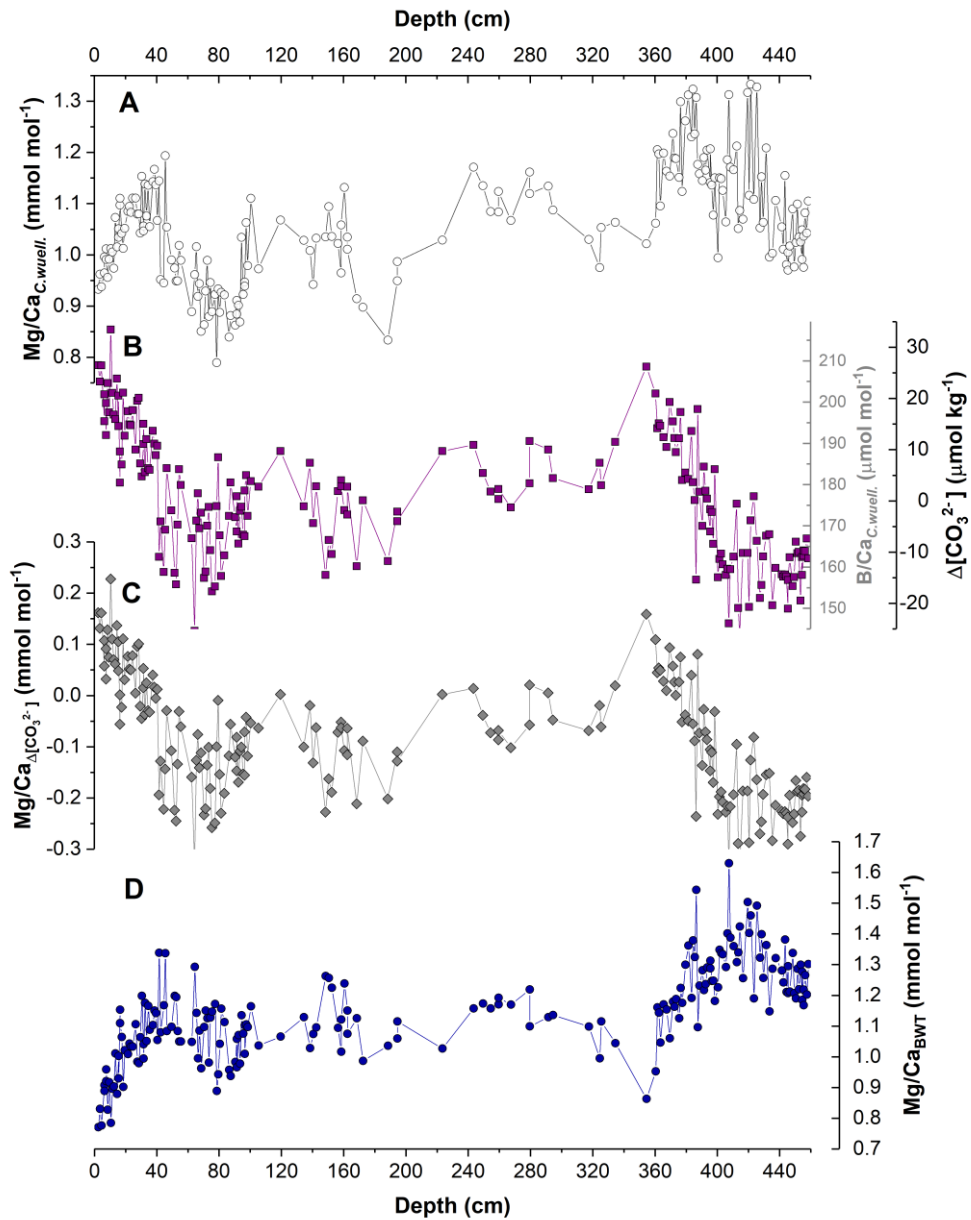


**Figure 3.29.** A) Downcore record of Mg/Ca measured in *C. wuellerstorfi* from MD02-2588 (grey, open circles). B) Downcore record of bottom water carbonate saturation state (purple, filled squares) derived from B/Ca measured in *C. wuellerstorfi* from MD02-2588. C) Downcore record of bottom water carbonate saturation state component of Mg/Ca in *C. wuellerstorfi* (dark grey, filled triangles). D) Downcore record of bottom water temperature component of Mg/Ca in *C. wuellerstorfi* (blue, filled circles).

mmol mol<sup>-1</sup>, respectively. Raitzsch *et al.*, (2008), on the other hand, report the linear relationship

$$\text{Mg/Ca}_{\Delta[\text{CO}_3^{2-}]} = 0.010 \pm 0.002 \Delta[\text{CO}_3^{2-}] - 0.03 \pm 0.08$$

Eq. 3.7

from a South Atlantic core-top calibration. We separately estimated  $\text{Mg/Ca}_{\Delta[\text{CO}_3^{2-}]}$  for MD02-2588 using each of these relationships and averaged the two solutions. Next, the  $\text{Mg/Ca}_{\Delta[\text{CO}_3^{2-}]}$  was subtracted from the raw  $\text{Mg/Ca}_{C.wuell}$  data. The difference should, in theory, represent the temperature component of the Mg/Ca record (i.e.,  $\text{Mg/Ca}_{bwt}$ ), which can subsequently be used to calculate BWT. Full error propagation through the above calculations yields pooled errors of 0.05 mmol mol<sup>-1</sup> for both  $\text{Mg/Ca}_{\Delta[\text{CO}_3^{2-}]}$  and  $\text{Mg/Ca}_{bwt}$ .

However, prior to calculating BWT from  $\text{Mg/Ca}_{bwt}$ , we repeat certain data quality evaluation steps. Particularly, we examine the impacts of detrital and diagenetic contamination, and partial post-depositional dissolution on the downcore  $\text{Mg/Ca}_{bwt}$  record (Fig. 3.30 and Appendix figures 3.61-3.66). The correlations between  $\text{Mg/Ca}_{bwt}$  and  $\text{Fe/Ca}_{C.wuell}$ ,  $\text{Mn/Ca}_{C.wuell}$ , and average shell weight are all stronger than the correlations observed between the latter records and the raw  $\text{Mg/Ca}_{C.wuell}$  data. The linear regressions between  $\text{Mg/Ca}_{bwt}$  and  $\text{Fe/Ca}_{C.wuell}$  and between  $\text{Mg/Ca}_{bwt}$  and  $\text{Mn/Ca}_{C.wuell}$  yield  $r^2$  values of 0.31 and 0.35, respectively (Fig. 3.30c-f). This compares to  $r^2$  values of 0.01 and 0.30 for the linear regressions between  $\text{Mg/Ca}_{C.wuell}$  and  $\text{Fe/Ca}_{C.wuell}$  and between  $\text{Mg/Ca}_{C.wuell}$  and  $\text{Mn/Ca}_{C.wuell}$ , respectively. The correlation to the  $\text{Mn/Ca}_{C.wuell}$  data is only marginally improved when  $\text{Mg/Ca}_{C.wuell}$  is corrected for  $\Delta[\text{CO}_3^{2-}]$ , but in the case of  $\text{Fe/Ca}_{C.wuell}$ , the  $\Delta[\text{CO}_3^{2-}]$  correction has a more notable effect. It is unclear why the correlation strengthens drastically for  $\text{Fe/Ca}_{C.wuell}$  but only marginally for  $\text{Mn/Ca}_{C.wuell}$ . Nonetheless, the improved  $r^2$  of the linear regression between the  $\Delta[\text{CO}_3^{2-}]$ -corrected  $\text{Mg/Ca}$  and  $\text{Fe/Ca}_{C.wuell}$  may indicate that the temperature component of the  $\text{Mg/Ca}_{C.wuell}$  is affected by the presence of Fe-Mn oxide coatings. The notably lower correlation between  $\text{Mg/Ca}_{C.wuell}$  and  $\text{Fe/Ca}_{C.wuell}$  may have resulted from a masking effect by the  $\Delta[\text{CO}_3^{2-}]$  component of the  $\text{Mg/Ca}$  data.

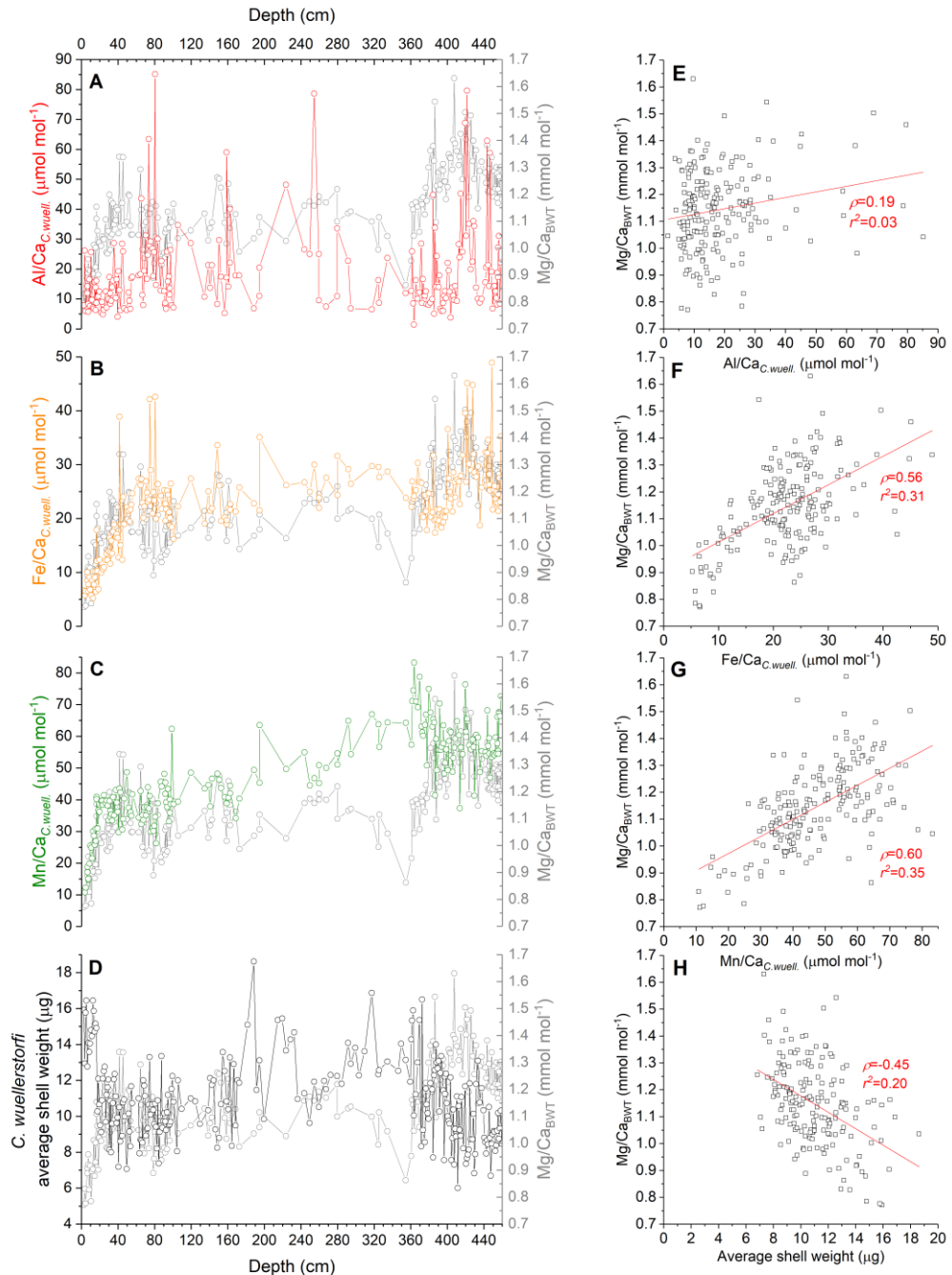


**Figure 3.30.** Comparison downcore record of bottom water temperature component of Mg/Ca in *C. wuellerstorfi* ( $Mg/Ca_{BWT}$ ) (grey line, open circles) from MD02-2588 with corresponding (A) Al/Ca (red line, open red circles), (B) Fe/Ca (orange line, open orange circles), (C) Mn/Ca (green line, open green circles) and (D) average *C. wuellerstorfi* shell weight (dark grey). E) Cross plot of  $Mg/Ca_{BWT}$  versus Al/Ca. F) Cross plot of  $Mg/Ca_{BWT}$  versus Fe/Ca. G) Cross plot of  $Mg/Ca_{BWT}$  versus Mn/Ca. H) Cross plot of  $Mg/Ca_{BWT}$  versus average *C. wuellerstorfi* shell weight.

In the case of the correlation between Mg/Ca and average shell weights, the  $\Delta[\text{CO}_3^{2-}]$ -correction reveals a negative correlation between  $\text{Mg}/\text{Ca}_{\text{bwt}}$  and average shell weight (Fig. 3.30g and 3.30h). This could indicate that high-Mg calcite is preferentially dissolved in the foraminifera shells in agreement with the expectation that high-Mg calcite is more susceptible to the effects of dissolution than lower-Mg calcite. A further explanation for the observed negative correlation between  $\text{Mg}/\text{Ca}_{\text{bwt}}$  and average shell weight is that the correlation between the two parameters reflects a bottom water signal, whereby the occurrence of colder waters at the core site coincides with the presence of a more corrosive water mass, and vice versa when bottom water temperatures are higher.

To complete this section, the downcore record of  $\text{Mg}/\text{Ca}_{\text{bwt}}$  is used to estimate bottom water temperature using the available calibrations. This provides an additional data quality control criterion, as the derived core-top and interglacial bottom water temperatures can be examined in relation to modern hydrographic data.

Numerous calibrations are available for the transformation of  $\text{Mg}/\text{Ca}_{\text{C.wuell}}$  to bottom water temperature and are expressed in the form:

$$\text{Mg}/\text{Ca} = a \exp (b \times \text{BWT})$$

Eq. 3.8

which is rearranged to:

$$\text{BWT} = \ln (\text{Mg}/\text{Ca} / a) / b$$

Eq. 3.9

The published calibrations include:

- (i) Martin *et al.*, (2002)

$$\text{Mg}/\text{Ca}_{\text{bwt}} = 1.22 \pm 0.08 \exp (0.109 \pm 0.007 \times \text{BWT})$$

Eq. 3.10

(ii) Lear *et al.*, (2002)

$$\text{Mg/Ca}_{\text{bwt}} = 0.867 \pm 0.049 \exp (0.109 \pm 0.007 \times \text{BWT})$$

Eq. 3.11

(iii) Elderfield *et al.*, (2006)

$$\text{Mg/Ca}_{\text{bwt}} = 0.90 \pm 0.037 \exp (0.11 \pm 0.003 \times \text{BWT})$$

Eq. 3.12

(iv) Raitzsch *et al.*, (2008)

$$\text{Mg/Ca}_{\text{bwt}} = 0.830 \exp (0.145 \times \text{BWT})$$

Eq. 3.13

(v) Healey *et al.*, (2008)

$$\text{Mg/Ca}_{\text{bwt}} = 0.781 \pm 0.023 \exp (0.23 \pm 0.013 \times \text{BWT})$$

Eq. 3.14

(vi) Tisserand *et al.*, (2013)

$$\text{Mg/Ca}_{\text{bwt}} = 0.82 \pm 0.04 \exp (0.19 \pm 0.01 \times \text{BWT})$$

Eq. 3.15

(vii) Kubota *et al.*, (2015)

$$\text{Mg/Ca}_{\text{bwt}} = 0.85 \pm 0.02 \exp (0.082 \pm 0.003 \times \text{BWT})$$

Eq. 3.16

(viii) Cappelli *et al.*, (2015)

$$\text{Mg/Ca}_{\text{bwt}} = 0.80 \pm 0.03 \exp(0.19 \pm 0.009 \times \text{BWT})$$

Eq. 3.17

(ix) Yu and Elderfield, (2008), whose relationship for reductively cleaned Mg/Ca also accounts for  $\Delta[\text{CO}_3^{2-}]$ :

$$\text{Mg/Ca}_{\text{C.wuell.}} = 0.85 \pm 0.03 + 0.0092 \pm 0.0007 \times \Delta[\text{CO}_3^{2-}] + 0.033 \pm 0.01 \times \text{BWT}$$

Eq. 3.18

Applying these calibrations to the downcore record of  $\text{Mg/Ca}_{\text{bwt}}$  from sediment core MD02-2588 provides a range of stratigraphic series of bottom water temperature for the core site (Fig. 3.31). The fully propagated errors associated with each calibration is listed in the figure caption. We exclude the bottom water temperature series obtained from the application of Yu and Elderfield's (2008) relationship (Eq. 18) because its excessive range plots off the scale of the figure. In addition, the values obtained at both ends of the range from that series are inconsistent with the expected modern and glacial bottom water temperature of the deep ocean; also, the propagated error associated with this series is unacceptably high ( $\sigma = \pm 1.87^\circ\text{C}$ , or  $\pm 30\%$ ). The BWT series obtained from the Martin *et al.*, (2002) relationship is also notably offset from the other timeseries. In a few sections of that record (e.g., ~0-10 kyr BP and 110-120 kyr BP), the estimated temperatures are lower than the typical freezing point of seawater (i.e.,  $< 2^\circ\text{C}$ ) and, therefore, we also consider Martin *et al.*, 's (2002) calibration as unsuitable for the MD02-2588 core site. The calibration of Kubota *et al.*, (2015) appears to overestimate the bottom water temperatures range of the site and although not as dramatic as the range obtained with the Yu and Elderfield (2008) calibration, the values at the upper and lower limits are nonetheless beyond the expected bottom water temperature range of the deep ocean.

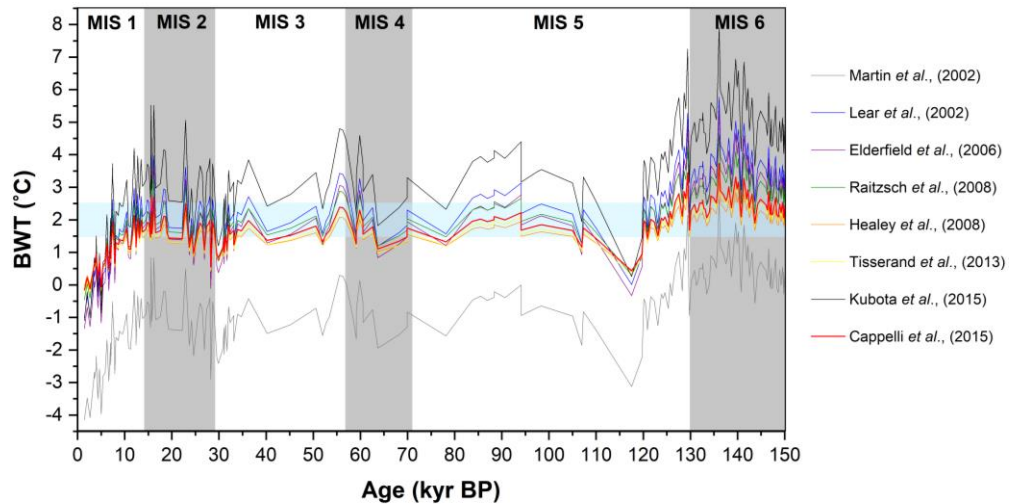


**Figure 3.31.** Downcore record of bottom water temperature (BWT) for sediment core MD02-2588 based on *C. wuellerstorfi* Mg/Ca after correcting for the carbonate ion effect. Application of the published Mg/Ca-to-BWT calibrations to the corrected *C. wuellerstorfi* Mg/Ca data from MD02-2588 produces a range of possible BWT records for this site. Available Mg/Ca-to-BWT calibrations are shown on right-hand side of plot. The data are plotted on the age scale of Ziegler *et al.*, (2013). Vertical grey bars delineate marine isotope stages (MIS) 1 through 6. Horizontal blue bar indicates the modern BWT for the MD02-2588 core site.

The range of bottom water temperatures obtained from the remaining calibrations are generally in agreement with typical deep ocean temperatures. Of these, the calibrations that yield the most reasonable temperature range for the core site (~1.5-2.5°C) are those of Healey *et al.*, (2008), Tisserand *et al.*, (2013) and Cappelli *et al.*, (2015). Cappelli *et al.*, 's (2015) calibration is perhaps the most applicable because it integrates all the previously published *C. wuellerstorfi* core top data from the 0 to 10 °C range.

Notwithstanding the reasonable bottom water temperature range obtained by this calibration, there are numerous sections of the record that raise serious suspicion about the applicability of  $Mg/Ca_{C.wuell.}$  - even in its 'corrected'  $Mg/Ca_{bwt}$  form - as a paleotemperature indicator at this core site.

The BWT record resulting from the calibration of Cappelli *et al.*, (2015) does not display a clear pattern of glacial-interglacial variability throughout the entire studied section of core MD02-2588 (Fig. 3.32). Between approximately 110 kyr BP and 14 kyr BP, the apparent BWT variability at the core site remains within a narrow range of 1-2°C, but overall displays a general pattern of colder glacial temperatures relative and slightly warmer interglacial temperatures. For examples, BWTs during MIS 5 and MIS 3 are slightly warmer than those of MIS 4 and MIS 2.

The most unexpected variations occur during the intervals at 115-150 kyr BP and 0-15 kyr BP. For example, the highest BWTs of ~ 2-3°C are recorded during MIS 6 and are followed by a gradual 2°C decrease at the MIS 5/6 boundary that occurs over approximately an 10 kyr interval. A similar pattern is observed in the upper-most section of the core where BWT again gradually decreases by ~2°C over the 10 kyr interval following the MIS 1/2 boundary, reaching the coldest BWT of the entire record at ~0 kyr BP. Comparing the BWT from MD02-2588 to the corresponding records of  $Mn/Ca_{C.wuell.}$  and  $Fe/Ca_{C.wuell.}$ , highlights the possible impact of contamination by Mn-Fe oxides (Fig. 3.32c versus 3.32a,b). This impact is most evident in the MIS 1 interval where the unexpected decrease in BWT during the Holocene is coincident with marked decreases of both  $Mn/Ca_{C.wuell.}$  and  $Fe/Ca_{C.wuell.}$ . The most pronounced drop in BWT during MIS 1 occurs at 8 kyr BP and is synchronous with the pronounced decrease in  $Fe/Ca_{C.wuell.}$ . The same pattern does not occur during the 115-130 kyr BP interval. In fact, the BWT decrease registered over that interval coincides with increasing trends in  $Mn/Ca_{C.wuell.}$  and  $Fe/Ca_{C.wuell.}$ .

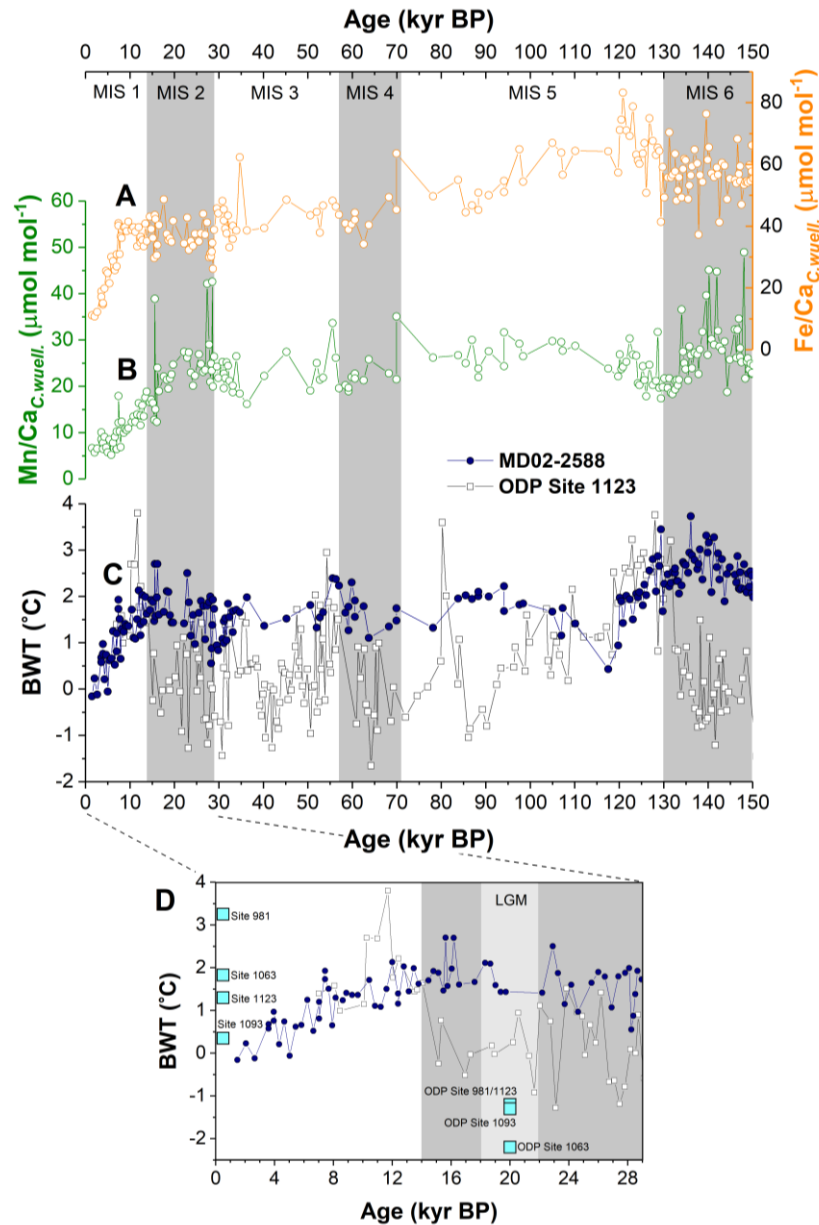


**Figure 3.32.** A) Downcore record of Fe/Ca in *C. wuellerstorfi* from MD02-2588 (orange, open circles). B) Downcore record of Mn/Ca in *C. wuellerstorfi* from MD02-2588 (green, open circles). C) Downcore record of bottom water temperature (BWT) for sediment core MD02-2588 based on *C. wuellerstorfi* Mg/Ca after correcting for the carbonate ion effect (blue, filled circles). Mg/Ca data were converted to BWT using the calibration of Cappelli *et al.*, (2015). The bottom water temperature record from ODP Site 1123 is shown for comparison (Elderfield *et al.*, 2012) (grey line, open circles). D) Same as C with the addition of BWT data from Adkins *et al.*, (2002). Vertical grey bars delineate marine isotope stages; the LGM is highlighted in panel D.

Considered in its entirety, the BWT from MD02-2588 is not compatible with the existing evidence of colder BWT during glacial stages and warmer BWT during interglacial stages (Adkins *et al.*, 2002; Elderfield *et al.*, 2012) (Fig. 3.32 c, d). The spurious trends between the BWT and the contaminant monitor ratios during MIS 1 and early MIS 5 complicate the application of this record. We, therefore, choose not to use the downcore record of Mg/Ca from sediment core MD02-2588 to reconstruct the BWT history of the core site.

### 3.13 Evaluation of *G. truncatulinoides* (s) Mg/Ca as a paleotemperature proxy

We have already concluded that the downcore record of  $Mg/Ca_{G.trunc.(s)}$  from sediment core MD02-2588 has been impacted by authigenic contamination, but it is nonetheless informative to convert the raw data into intermediate water temperatures (IWT). The resultant IWT series can be compared to the modern and ancient oceanographic conditions at the core site to assess how compatible the reconstructed temperatures are relative to the existing evidence.

As with *C. wuellerstorfi*, numerous calibrations are also available for the transformation of  $Mg/Ca_{G.trunc.(s)}$  to IWT. These include the following:

- (i) Elderfield and Ganssen's (2000) multispecies calibration,

$$Mg/Ca = 0.52 \pm 0.0085 \exp(0.10 \times IWT)$$

Eq. 3.19

- (ii) Anand *et al.*'s (2003) multispecies calibration,

$$Mg/Ca = 0.38 \pm 0.02 \exp(0.090 \pm 0.003 \times IWT)$$

Eq. 3.20

- (iii) Anand *et al.*'s (2003) *G. truncatulinoides* calibration,

$$Mg/Ca = 0.359 \pm 0.008 \exp(0.090 \pm 0.003 \times BWT)$$

Eq. 3.21

- (iv) McKenna and Prell's (2004) linear relationship,

$$\text{Mg/Ca} = 0.684 \pm 0.122 + 0.165 \pm 0.008 \times \text{IWT}$$

Eq. 3.22

- (v) McKenna and Prell's (2004) exponential relationship,

$$\text{Mg/Ca} = 0.355 \pm 0.053 \exp(0.098 \pm 0.008 \times \text{IWT})$$

Eq. 3.23

- (vi) Cléroux *et al.*'s (2008) mixed deep-dwelling planktonic foraminifera relationship,

$$\text{Mg/Ca} = 0.78 \pm 0.04 \exp(0.052 \pm 0.003 \times \text{IWT})$$

Eq. 3.24

- (vii) Cléroux *et al.*'s (2008) *G. truncatulinoides* relationship,

$$\text{Mg/Ca} = 0.88 \pm 0.022 \exp(0.045 \pm 0.016 \times \text{IWT})$$

Eq. 3.25

- (viii) Regenberg *et al.*'s (2009) *G. truncatulinoides (d.)* relationship,

$$\text{Mg/Ca} = 1.32 \pm 0.12 \exp(0.05 \pm 0.009 \times \text{IWT})$$

Eq. 3.26

- (ix) Regenberg *et al.*'s (2009) mixed deep-dwelling foraminifera relationship,

$$\text{Mg/Ca} = 0.84 \pm 0.06 \exp(0.083 \pm 0.005 \times \text{IWT})$$

Eq. 3.27

- (x) Cléroux *et al.*'s (2013) *G. truncatulinoides (d)* relationship for all data in that study,

$$\text{Mg/Ca} = 0.938 \pm 0.03 \exp(0.066 \pm 0.007 \times \text{IWT})$$

Eq. 3.28

- (xi) Cléroux *et al.*'s (2013) *G. truncatulinoides (d)* relationship for cores located shallower than 4 km water depth (assumed to be unaffected by dissolution),

$$\text{Mg/Ca} = 0.975 \pm 0.007 \exp(0.060 \pm 0.007 \times \text{IWT})$$

Eq. 3.29

Applying these calibrations to the downcore record of  $\text{Mg/Ca}_{G.trunc.(s)}$  from sediment core MD02-2588 results in a range of IWT stratigraphic series for the core site (Fig. 3.33a). The fully propagated errors associated with each calibration is listed in the figure caption.

The most apparent feature of this collection of stratigraphic series of IWT is that the calibrations listed above result in a very large range of possible scenarios. According to these calibrations the IWT at the core site during MIS 1 ranges between anything from  $\sim 13^\circ\text{C}$  to as low as  $\sim -3^\circ\text{C}$ . Regenberg *et al.*, 's (2009) calibration for *G. truncatulinoides (d.)* (equation 3.26) results in the lowest IWT, which are mostly below  $0^\circ\text{C}$  and achieve unrealistic values (i.e., well below the freezing point of seawater). Though not as extreme, a number of other calibrations also result in interglacial IWT that are lower the modern range of temperatures for the 100-400 m depth intervals in the waters overlying the southern Agulhas Plateau (i.e.,  $\sim 5\text{-}15^\circ\text{C}$ ) (Fig. 3.33b). These include Regenberg *et al.*, 's (2009) calibration for mixed deep-dwelling planktonic foraminifera (equation 3.27), the two calibrations from Cl eroux *et al.*, (2013) (equations 3.28 and 3.29) and McKenna and Prell's (2004) linear relationship (equation 3.22). The two calibrations of Cl eroux *et al.*, (2008) (equations 3.24 and 3.25) yield interglacial IWTs that are in reasonable agreement with modern values at the core site but the associated glacial values appear to be too cold ( $0\text{-}2^\circ\text{C}$ ) and the glacial-interglacial IWT differences in these two records are excessive.

The two calibrations of Anand *et al.*, (2003) and the linear calibration of McKenna and Prell (2004), yield downcore records of IWT that are quite similar. Generally, the application of these three calibrations to the  $\text{Mg/Ca}_{G.trunc.(s)}$  from sediment core MD02-2588 results in interglacial IWTs that are at the higher end of the range of modern IWT at the site, but that are nonetheless reasonable. Equally, the glacial-interglacial IWT differences in these downcore records are not as excessive as the differences observed in other records. However, because these three records result in IWTs that are at the higher end of the modern range we remain wary regarding their application to the  $\text{Mg/Ca}_{G.trunc.(s)}$  data from MD02-2588.

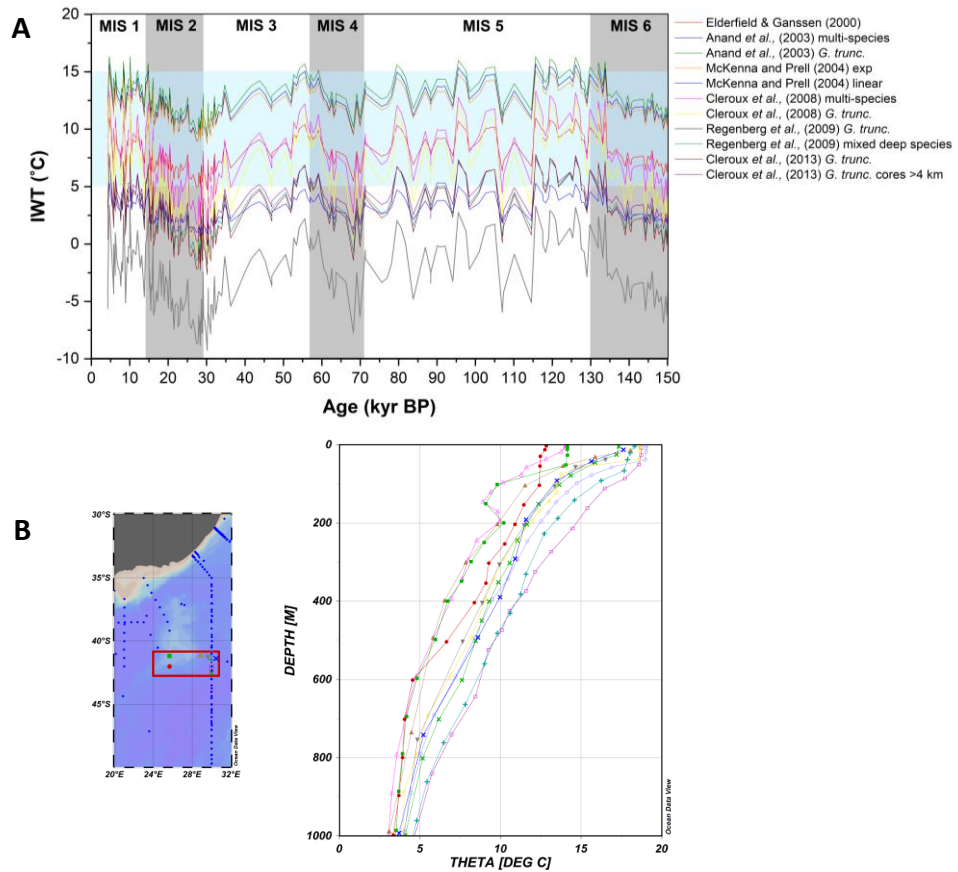


**Figure 3.33.** A) Range of downcore records of intermediate water temperature (IWT) for sediment core MD02-2588. Mg/Ca of *G. truncatulinoides* (*s.*) was converted to IWT using the available calibrations listed on the right-hand side of the plot. Vertical grey lines delineate marine isotope stages. Horizontal line indicates the modern temperature range at the 200-400 m depth interval. B) Modern temperature profiles from the southern Agulhas Plateau.

The calibration of Elderfield and Ganssen (2000) possibly represents the most suitable calibration for the conversion of  $\text{Mg}/\text{Ca}_{G.trunc.(s)}$  from sediment core MD02-2588 to a downcore record of IWT. Interglacial IWT estimates based on this calibration are in good agreement with modern conditions and the observed glacial-interglacial IWT differences along the core are not extreme. In this part of the ocean, the sea surface temperature is thought to have been approximately  $2^\circ\text{C}$  lower during the LGM than it was during the Holocene (MARGO Project Members, 2009). Therefore, the approximately  $5^\circ\text{C}$  glacial-interglacial IWT differences that result from Elderfield and Ganssen's (2000) calibration, though not excessive, may still be overestimating the true variance in the ocean. Of course, we cannot rule out that part of the observed glacial-interglacial IWT difference arises from a vertical shift in the average depth habitat of *G. truncatulinoides* (s.) on glacial-interglacial timescales (Feldmeijer *et al.*, 2015).

The numerous empirical calibrations available for the conversion of  $\text{Mg}/\text{Ca}_{G.trunc.(s)}$  to IWT result in a diverse set of stratigraphic records. This emphasises the need for careful selection of the most suitable calibration and also highlights the potential uncertainty arising from the application of a single calibration. In the case of the downcore record of  $\text{Mg}/\text{Ca}_{G.trunc.(s)}$  from sediment core MD02-2588, a number of these calibrations yield reasonable temperature estimates. This suggests that, as a whole, the absolute  $\text{Mg}/\text{Ca}_{G.trunc.(s)}$  values recorded at this site may not be excessively altered by early diagenetic processes. However, as the quality evaluation of this dataset has shown, there is a possibility that the downcore record of  $\text{Mg}/\text{Ca}_{G.trunc.(s)}$  has been effected by diagenetic processes that may be masking the primary temperature-controlled component of the  $\text{Mg}/\text{Ca}_{G.trunc.(s)}$  variations. Therefore the apparent pattern of variability in  $\text{Mg}/\text{Ca}_{G.trunc.(s)}$  cannot be reliably applied as an indicator of the IWT history of this part of the ocean.

### **3.14 Reconstruction of seawater Cd concentration from foraminiferal Cd/Ca**

The record of Cd/Ca measured in *C. wuellerstorfi* from sediment core MD02-2588 is converted to seawater Cd concentration ( $\text{Cd}_{\text{sw}}$ ) in order to facilitate the comparison to modern conditions at this site and to other published records. The distribution coefficient for the incorporation of Cd into benthic foraminifera ( $D_{\text{Cd}}$ ) is given by

$$D_{Cd} = (Cd/Ca)_{\text{foram}} / (Cd/Ca)_{\text{seawater}}$$

Eq. 3.30

The  $D_{Cd}$  of benthic foraminifera has been determined empirically and has been found to vary with depth (Boyle, 1992). For depths < 1150 m  $D_{Cd}$  is 1.3 and for depths > 3000 m  $D_{Cd}$  is 2.9; for depths between 1150 m and 3000 m,

$$D_{Cd} = 1.3 + (\text{core site depth} - 1150) (1.6/1850)$$

Eq. 3.31

Based on the MD02-2588 core site water depth of 2907 m we apply a  $D_{Cd}$  of 2.82. The seawater Ca concentration is assumed to remain constant at 0.01 mol.kg<sup>-1</sup> (Boyle, 1992). Published Cd/Ca records referred to in this study are converted to Cd<sub>sw</sub> in the same way.

To account for the uncertainty of the Cd<sub>sw</sub> conversion, we consider the error ( $\sigma$ ) in the Cd/Ca<sub>C.wuell.</sub> data to be  $\pm 0.01 \mu\text{mol mol}^{-1}$ , and we assume a  $\pm 10\%$  error in  $D_{Cd}$  (Boyle, 1992) and negligible error in seawater Ca concentration. Thus, computation of Cd<sub>sw</sub> along sediment core MD02-2588, yields a pooled error of  $\pm 0.06 \text{ nmol kg}^{-1}$ . Core-top Cd<sub>sw</sub> (sampled at 2.5 cm) is 0.51 nmol kg<sup>-1</sup> and average Cd<sub>sw</sub> from the entire Holocene section of the MD02-2588 core (0-30 cm) yields a value of 0.59 nmol kg<sup>-1</sup> (Fig. 3.34). These compares well to the modern Cd<sub>sw</sub> range of 0.47-0.58 nmol kg<sup>-1</sup> at ~3000 m water depth, based on observations from nearby GEOTRACES stations (Mawji *et al.*, 2017).

### 3.15 Estimating the air-sea fractionation signature of $\delta^{13}\text{C}_{\text{DIC}}$ from paired benthic foraminiferal Cd/Ca- $\delta^{13}\text{C}$

In this study we produce a stratigraphic series of the  $\delta^{13}\text{C}$  signature due to air-sea fractionation during the exchange of CO<sub>2</sub> ( $\delta^{13}\text{C}_{\text{as}}$ ) from the paired foraminiferal Cd/Ca- $\delta^{13}\text{C}$  measurements made along MD02-2588.  $\delta^{13}\text{C}_{\text{as}}$  is derived by separating the nutrient signal of seawater  $\delta^{13}\text{C}_{\text{DIC}}$  from the effect of carbon isotope fractionation

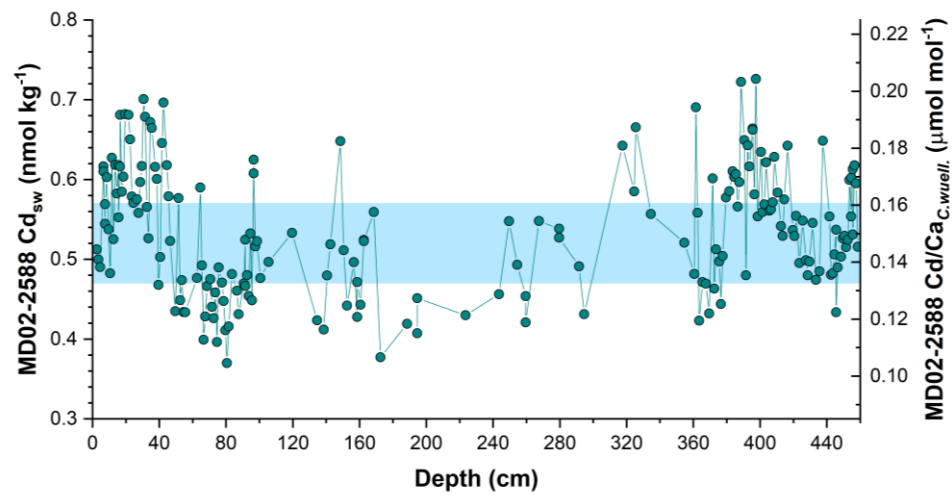


**Figure 3.34.** Downcore record of the concentration of dissolved Cd in seawater ( $Cd_{sw}$ ) based on Cd/Ca measured in *C. wuellerstorfi* along MD02-2588. Cd/Ca data were converted to  $Cd_{sw}$  using the relationship developed by Boyle (1992). Horizontal blue lines indicates the approximate modern range of  $Cd_{sw}$  values at the core site.

during air-sea gas exchange and the effect of variations in the marine carbon reservoir (Lynch-Stieglitz and Fairbanks, 1994; Lynch-Stieglitz *et al.*, 1996; Marchitto and Broecker, 2006).

Broecker and Maier-Reimer (1992) argue that in the absence of air-sea fractionation the distribution of  $\delta^{13}\text{C}_{\text{DIC}}$  in the ocean should be closely correlated with phosphate ( $\text{PO}_4^{3-}$ ) concentration according to the relationship:

$$\delta^{13}\text{C}_{\text{bio}} - \delta^{13}\text{C}_{\text{MO}} = \frac{\Delta\text{photo}}{\Sigma\text{CO}_2} \cdot \left(\frac{\text{C}}{\text{P}}\right)_{\text{org}} \cdot (\text{PO}_4^{3-} - \text{PO}_4^{3-}\text{MO})$$

Eq. 3.32

where MO stands for mean ocean,  $\Delta\text{photo}$  is the carbon isotope separation during marine photosynthesis and  $(\text{C}/\text{P})_{\text{org}}$  is the carbon to phosphorous ratio in marine organic matter. Boyle (1988) demonstrated the existence of a strong correlation between  $\text{Cd}_{\text{sw}}$  and  $\text{PO}_4^{3-}$  and developed the following relationships:

$$\text{Cd}_{\text{sw}} = 0.4 \cdot \text{PO}_4^{3-} - 0.25 \quad \text{for } \text{PO}_4^{3-} > 1.3 \mu\text{mol.kg}^{-1}$$

Eq. 3.33

$$\text{Cd}_{\text{sw}} = 0.21 \cdot \text{PO}_4^{3-} \quad \text{for } \text{PO}_4^{3-} < 1.3 \mu\text{mol.kg}^{-1}$$

Eq. 3.34

Lynch-Stieglitz and Fairbanks (1994) and Lynch-Stieglitz *et al.*, (1996) combined these relationships and proposed the following equations for estimating  $\delta^{13}\text{C}_{\text{as}}$  in the modern ocean:

$$\delta^{13}\text{C}_{\text{as}} = \delta^{13}\text{C} - \delta^{13}\text{C}_{\text{bio}} = \delta^{13}\text{C} + 2.75 \cdot \text{Cd}_{\text{sw}} - 2$$

Eq. 3.35

for  $\text{Cd}_{\text{sw}} > 0.28 \text{ nmol.kg}^{-1}$

$$\delta^{13}C_{as} = \delta^{13}C - \delta^{13}C_{bio} = \delta^{13}C + 5.29 \cdot Cd_{sw} - 2.7$$

Eq. 3.36

for  $Cd_{sw} < 0.28 \text{ nmol.kg}^{-1}$

For the LGM these equations were modified to account for a 2‰ increase in the  $\delta^{13}C$  of organic matter (Rau *et al.*, 1991), a 0.3‰ decrease in mean ocean  $\delta^{13}C$  (Curry *et al.*, 1988; Boyle, 1992) and a corresponding increase in total inorganic carbon of 4%. The oceanic  $Cd_{sw}$  and  $PO_4^{3-}$  inventories were assumed to be unchanged relative to modern values and the modern relationship between the two is also assumed to hold in the glacial ocean (Lynch-Stieglitz and Fairbanks, 1994; Lynch-Stieglitz *et al.*, 1996). The resulting LGM equations are:

$$\delta^{13}C_{as} = \delta^{13}C - \delta^{13}C_{bio} = \delta^{13}C + 2.375 \cdot Cd_{sw} - 1.46$$

Eq. 3.37

for  $Cd_{sw} > 0.28 \text{ nmol.kg}^{-1}$

$$\delta^{13}C_{as} = \delta^{13}C - \delta^{13}C_{bio} = \delta^{13}C + 4.57 \cdot Cd_{sw} - 2.05$$

Eq. 3.38

for  $Cd_{sw} < 0.28 \text{ nmol.kg}^{-1}$

These can be written in the general form:

$$\delta^{13}C_{as} = \delta^{13}C - \delta^{13}C_{bio} = \delta^{13}C + a \cdot Cd_{sw} - b$$

Eq. 3.39

These relationships were been built on further by Martínez-Méndez *et al.*, (2008, 2009) in order to produce a continuous  $\delta^{13}\text{C}_{\text{as}}$  time-series back to 345 kyr BP. The lack of independent estimates of past changes of marine  $\delta^{13}\text{C}_{\text{MO}}$  and the absence of reliable data on the ocean's carbon and nutrient inventory for pre-LGM times was overcome by the production of a synthetic time-series of the parameters *a* and *b*. This was achieved by fixing the Holocene and LGM values of these parameters to a benthic stack of  $\delta^{13}\text{C}$  ( $\delta^{13}\text{C}_{\text{stack}}$ ; Stüber, 1999; Zahn and Stüber, 2002) which was assumed to represent  $\delta^{13}\text{C}_{\text{MO}}$ . Shifts in  $\delta^{13}\text{C}$  of organic matter, changes of total inorganic carbon and variations in the oceanic carbon pool were assumed to be linearly related. The time-series of the parameters *a* and *b* are presented in Martínez-Méndez *et al.*, (2009). Despite the simplistic approach involved in its construction, the synthetic time-series of *a* and *b* allows first order estimations of  $\delta^{13}\text{C}_{\text{as}}$  to be made in continuous down-core records that are free of the influences arising from whole ocean changes in  $\delta^{13}\text{C}_{\text{DIC}}$ .

The  $\delta^{13}\text{C}_{\text{stack}}$  record from Zahn and Stüber (2002) used by Martínez-Méndez *et al.*, (2009) to produce the time-series of parameters *a* and *b* was constructed by combining the benthic foraminifera  $\delta^{13}\text{C}$  records of eight sediment cores from the Atlantic Ocean, one record from the Indian Ocean and two records from the Pacific Ocean (see Martínez-Méndez *et al.*, 2008, Supplementary information S2 for details). These records were combined and averaged into a  $\delta^{13}\text{C}_{\text{MO}}$  profile that was normalized to the Holocene  $\delta^{13}\text{C}$  level ( $\Delta_{\text{HOL}}\delta^{13}\text{C}$ ) and the Holocene-to-LGM amplitude was set to 0.32‰ (i.e., the value presented by Duplessy *et al.*, 1988). The small number of cores used to construct this  $\delta^{13}\text{C}_{\text{stack}}$  clearly does not provide a full representation of the global marine carbon reservoir but the structure of the record represents a crude indication of  $\delta^{13}\text{C}_{\text{MO}}$  changes through time.

In the present study we follow the method of Martínez-Méndez *et al.*, (2009) to produce a new time-series of parameters *a* and *b* using the more recent and more holistic  $\delta^{13}\text{C}$  record synthesis presented by Oliver *et al.*, (2010). In particular, we use the authors' data synthesis of Atlantic Ocean  $\delta^{13}\text{C}$  anomalies relative to the LGM ( $\Delta_{\text{LGM}}\delta^{13}\text{C}_{\text{AO}}$ ), where the LGM is defined as the interval between 19 and 23 kyr BP.

We follow the recommendation of Oliver *et al.*, (2010) to use  $\Delta_{\text{LGM}}\delta^{13}\text{C}_{\text{AO}}$  rather than the absolute  $\delta^{13}\text{C}$  stack for the Atlantic because there are smaller errors associated with the former data synthesis. Also, the expression of the compiled  $\delta^{13}\text{C}$  data as an

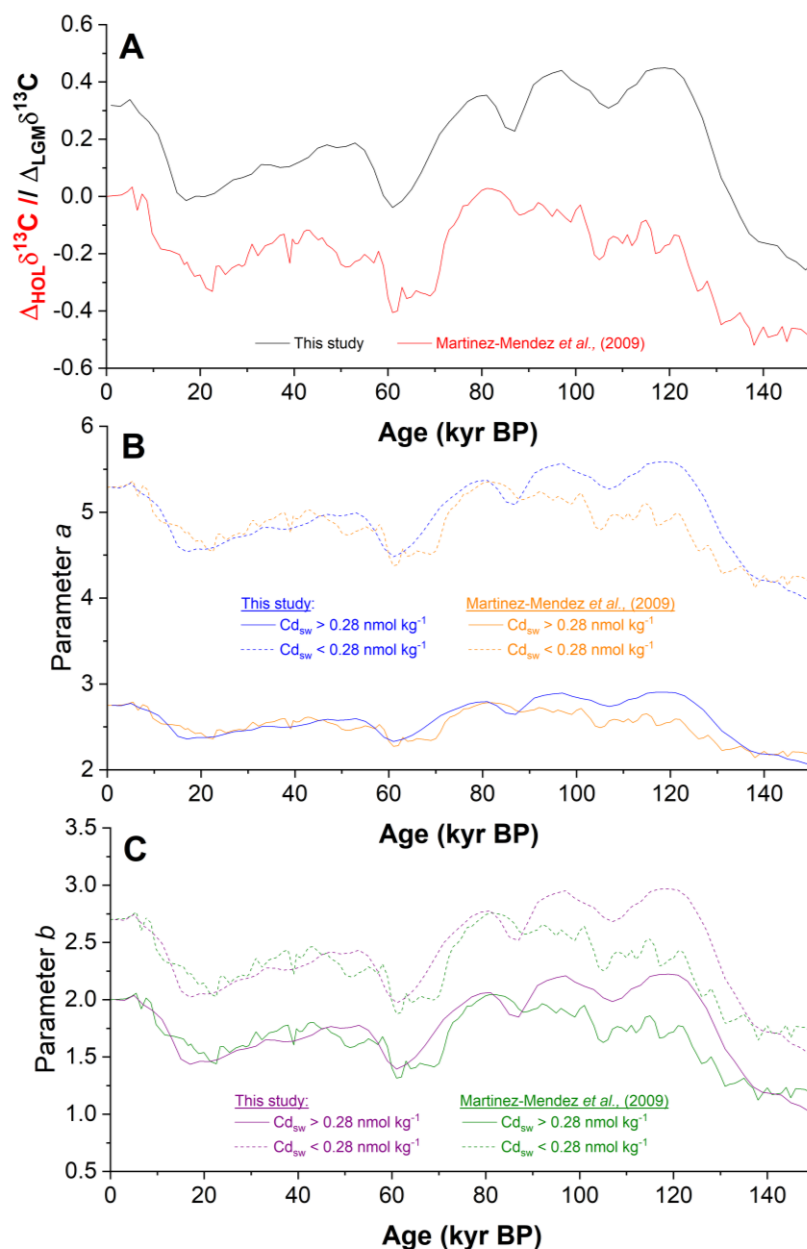


**Figure 3.35.** A) Comparison of the benthic stacks of  $\delta^{13}\text{C}$  used in this study (black) (from Oliver *et al.*, 2013) and in Martínez-Méndez *et al.*, (2009) (red) to construct parameters  $a$  and  $b$  (see main text for detailed explanation). The benthic stacks are presented as  $\delta^{13}\text{C}$  anomalies relative to the LGM and the Holocene, respectively. B) Comparison of parameters  $a$  time series produced using the two different benthic stacks presented in panel A, i.e., blue lines represent the times series produced based on the benthic stack of Oliver *et al.*, (2013) and orange lines represent the time series of parameter  $a$  produced by Martínez-Méndez *et al.*, (2009). C) same as in pane B, but for parameter  $b$ . Purple lines are the time series produced in this study, while green lines are the time series of Martínez-Méndez *et al.*, (2009).

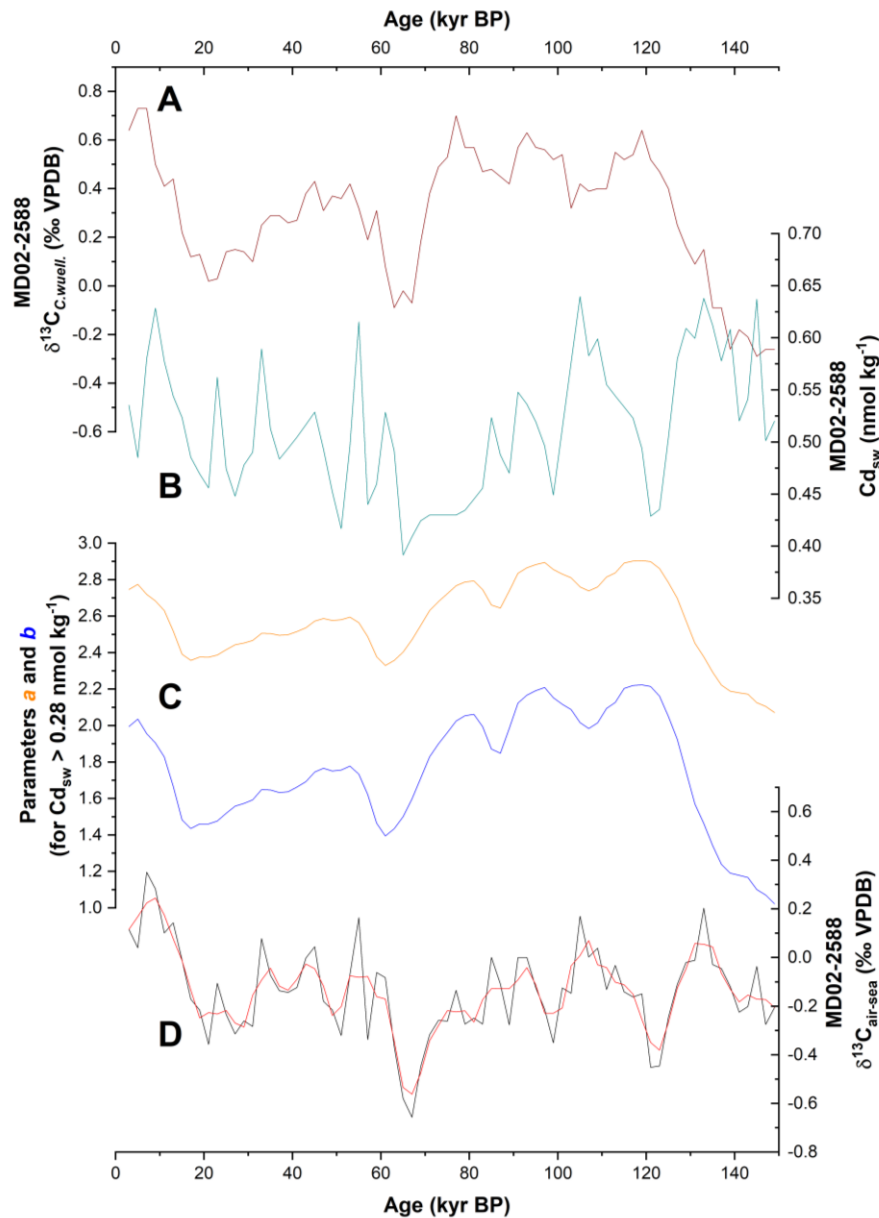


**Figure 3.36.** A) Benthic  $\delta^{13}\text{C}$  measured in *C. wuellerstorfi* ( $\delta^{13}\text{C}_{C.wuell}$ ) plotted on an inverted axis. B)  $\text{Cd}_{sw}$  derived from measurement of  $\text{Cd}/\text{Ca}$  in *C. wuellerstorfi* and application of the benthic calibration of Boyle (1992). C) Synthetic time series of parameters *a* and *b* generated from the benthic stack of  $\delta^{13}\text{C}$  (Oliver *et al.*, 2013). Refer to main text for details. D) Stratigraphic series of the  $\delta^{13}\text{C}$  signature due to air-sea fractionation during the exchange of  $\text{CO}_2$  ( $\delta^{13}\text{C}_{as}$ ) based on paired foraminiferal  $\text{Cd}/\text{Ca}$ - $\delta^{13}\text{C}$  measurements made along MD02-2588 (black line shows data at 2-kyr resolution; red line represent smoothing with a 3-point adjacent averaging filter). The raw stratigraphic-series and time-series presented in this figure have been placed onto an evenly sampled 2-kyr scale using piecewise linear interpolation; this was performed using the R software package ‘astrochron’ (Meyers, 2014).

anomaly relative to the LGM (i.e.,  $\Delta_{\text{LGM}}\delta^{13}\text{C}_{\text{AO}}$ ) is essentially equivalent to Zahn and Stüber's (2002) normalisation to the Holocene  $\delta^{13}\text{C}$  level (Fig. 3.35A).  $\Delta_{\text{LGM}}\delta^{13}\text{C}_{\text{AO}}$  is offset from  $\Delta_{\text{HOL}}\delta^{13}\text{C}$  by  $\sim 0.3\%$ , reflecting the Holocene-to-LGM difference in  $\delta^{13}\text{C}_{\text{MO}}$  (Duplessy *et al.*, 1988). The overall pattern of change is similar but there are differences during the early and mid MIS 5. The new parameterisation of  $a$  and  $b$  produces similar results to those presented in Martínez-Méndez *et al.*, (2009), again with some differences during the early and mid MIS 5 (Fig. 3.35B and C).

Finally, we use the timeseries of parameters  $a$  and  $b$  ( $\text{Cd}_{\text{sw}} > 0.28 \text{ nmol kg}^{-1}$ ) to calculate down-core  $\delta^{13}\text{C}_{\text{as}}$  along sediment core MD02-2588 using equation 3.39 (Fig. 3.36).  $\delta^{13}\text{C}_{\text{C.wuell}}$  is used as a proxy of  $\delta^{13}\text{C}_{\text{DIC}}$  (Mackensen *et al.*, 2001) and  $\text{Cd}_{\text{sw}}$  is calculated from  $\text{Cd}/\text{Ca}$  in *C. wuellerstorfi*. Due to the differences in temporal resolution between the various parameters used in the calculation of  $\delta^{13}\text{C}_{\text{as}}$ , the stratigraphic-series and time-series were placed onto an evenly sampled 2-kyr time series using piecewise linear interpolation; this was performed using the R software package 'astrochron' (Meyers, 2014). We note that the age modelling of the  $\Delta_{\text{LGM}}\delta^{13}\text{C}_{\text{AO}}$  record from which parameters  $a$  and  $b$  have been estimated was ascribed a  $2\sigma$  error of 6 kyr (Oliver *et al.*, 2010). As such, it is important that the  $\delta^{13}\text{C}_{\text{as}}$  is used only as an indicator of the changes on orbital timescales.

### 3.16 Sortable silt mean grain size

(Processed and measured by Ian R. Hall; Cardiff University)

The mean grain size of the 10-63  $\mu\text{m}$  fraction of terrigenous material was measured at 1 cm intervals over the entire length of sediment core MD02-2588. In this study we report only the results for the upper 460 cm ( $\sim 150$  kyr BP). The sediment samples were processed to remove the carbonate and biogenic opal components following the method outlined in McCave *et al.*, (1995). This involved placing 2-4 g of the fine fraction material (i.e.,  $< 63 \mu\text{m}$ ) into a glass jar with 2M acetic acid, stirring well, and then leaving the suspended material to settle overnight. Once settled, the acid was siphoned off and the step was repeated. The excess acid was siphoned off a second time and the samples were rinsed by filling the jar with deionised water. The samples were then treated with 0.2% sodium carbonate ( $\text{Na}_2\text{CO}_3$ ) at  $85^\circ\text{C}$  for five hours and were stirred every two hours. Samples were then left to cool and the material was again allowed to settle out of suspension. The  $\text{Na}_2\text{CO}_3$  was then siphoned off, replaced with deionised

water and left for 1-2 days to settle. Once the material had completely settled, the water was siphoned off and the rinsing step was repeated a second time. After this final rinse the material was left to settle for approximately a week. Once all the material had completely settled the water was siphoned off and the samples were suspended in 0.2% sodium hexametaphosphate (Calgon) dispersant in 60 ml Nalgene bottles. To ensure that the samples were fully disaggregated they were placed on a rotating wheel for a minimum of 24 hours. Immediately prior to analysis each sample was ultrasonicated for 3 minutes.

Grain size measurements were performed on a *Beckman Multisizer III Coulter Counter* at Cardiff University. Operating settings during each run were set as follows: aperture size=140  $\mu\text{m}$ ; particle sizing threshold=8  $\mu\text{m}$ ; counting threshold=10  $\mu\text{m}$ ; size bins=256; total counts=70,000 particles; size range=10-63  $\mu\text{m}$ . Individual samples were analysed three times and the averaged size distribution was calculated.

A preliminary calibration of the  $\overline{SS}$  proxy to bottom-water scalar geostrophic flow speed ( $U_g$ ) suggests that although it may prove difficult to extract absolute flow speeds from grain size data there is some indication that the  $\overline{SS}$  proxy may provide quantitative estimates of changes in flow speed ( $\Delta U_g$ ) (McCave *et al.*, 2017). According to this preliminary calibration, the application of a Reduced Major Axis regression through 12 calibration data points yields the following relationship between  $\overline{SS}$  and  $U_g$  ( $\text{cm s}^{-1}$ ):

$$\overline{SS} = 0.808 \pm 0.094 U_g + 15.46$$

Eq. 3.40

with a coefficient of correlation,  $r=0.928$  and standard errors ( $2\sigma$ ) for the calibration reported as  $\pm 12.5\%$  for  $U_g$  and  $\pm 5.6\%$  for  $\overline{SS}$  (McCave *et al.*, 2017). Applying equation 3.40 to the downcore  $\overline{SS}$  data from MD02-2588 results in a range of  $U_g$  between 3 and 19  $\text{cm s}^{-1}$ ; that is, a five-fold increase in  $U_g$  between the lowest recorded flow speed and the fastest (Fig. 3.37).

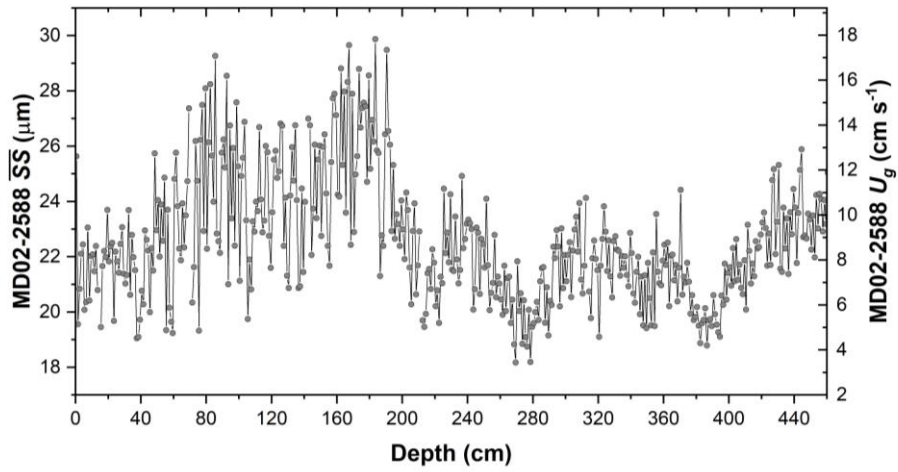


**Figure 3.37.** Downcore record of geostrophic scalar flow speed ( $U_g$ ) based on the mean grain size of sortable silt ( $\overline{SS}$ ) from MD02-2588.  $\overline{SS}$  data were converted to  $U_g$  using the relationship developed by McCave *et al.*, (2017).

### 3.17 Nitrogen isotopes in bulk sediment

(Processed and measured by Markus Kienast; Dalhousie University)

Eighty-four bulk sediment samples from core MD02-2588 underwent nitrogen isotopic analyses at the Pacific Centre for Isotopic and Geochemical Research, University of British Columbia. Prior to analysis the samples were freeze dried, ground in an agate mortar and packed in tin cups. The samples were then measure by combustion using a Carlo Erba NC 2500 elemental analyser coupled to a Finnigan Mat Delta Plus mass spectrometer, via a Finnigan Mat ConFlo III interface. Values were normalised to the international  $\delta^{15}\text{N}_{\text{air}}$  scale by running four replicates of an internal laboratory standard (Acetanilide [4.0]) and one international isotope reference (IAEA-N1 [0.4] or IAEA-N2 [20.3]) with every batch of samples. The  $\delta^{15}\text{N}_{\text{bulk}}$  isotopic result are reported as a per mille deviation from the  $\delta^{15}\text{N}$  isotopic composition of atmospheric  $\text{N}_2$  (‰ air). The reproducibility of  $\delta^{15}\text{N}_{\text{bulk}}$  was better than  $\pm 0.2\%$ .

---

## 4 Deep water variability on the southern Agulhas Plateau: implications for ocean circulation in the mid-depth South Atlantic and Southern Ocean during the past 150 kyr BP

---

### 4.1 Chapter Outline

In this chapter, we present downcore records of stable isotopes and elemental ratios measured in benthic foraminifera, and the mean grain size of sortable silt ( $\overline{SS}$ ) from sediment core MD02-2588. These stratigraphic-series reconstruct the history of mid-depth ocean circulation on the southern Agulhas Plateau during the past 150 kyr BP. A multi-proxy approach was applied to reconstruct and derive a range of physical and chemical bottom water parameters. These include the carbonate saturation state of seawater ( $\Delta[\text{CO}_3^{2-}]$ ), the concentration of dissolved Cd in seawater ( $\text{Cd}_{\text{sw}}$ ), and relative changes in near-bottom flow speeds. Additionally, we quantify the air-sea fractionation component of the carbon isotopes in benthic foraminifera ( $\delta^{13}\text{C}_{\text{as}}$ ) and present a qualitative reconstruction of past sediment pore-water oxygen concentration ( $[\text{O}_2]$ ). All stratigraphic series display prominent orbital modulation and where the sampling resolution is high enough, millennial-scale variability is also evident. However, no systematic correlation is identified between millennial-scale climate events and the high-frequency variability observed in the downcore record. Therefore, this chapter only discusses changes on glacial-interglacial timescales, with a particular focus on the last two deglaciations.

In broad terms, glacial stages are characterised by relatively low values of  $\Delta[\text{CO}_3^{2-}]$ ,  $\text{Cd}_{\text{sw}}$ ,  $\delta^{13}\text{C}_{\text{as}}$ , and  $[\text{O}_2]$ , while the  $\overline{SS}$  record indicates relatively high bottom-water flow speeds. During interglacials the situation is reversed, with relatively high values of  $\Delta[\text{CO}_3^{2-}]$ ,  $\text{Cd}_{\text{sw}}$ ,  $\delta^{13}\text{C}_{\text{as}}$ , and  $[\text{O}_2]$ , and slower bottom-water flow speeds. The higher sampling resolution of the elemental ratio records in the core sections that correspond to the last two deglaciations, allow additional complexities in the variability to be assessed.

We conclude that, during glacial stages, the southern Agulhas Plateau and the wider mid-depth South Atlantic Ocean came under increased influence of Lower Southern

Component Water (LSCW) as the Antarctic Circumpolar Current (ACC) shifted to a more equatorward position, in agreement with published geochemical evidence from the deep South Atlantic.

The lower  $\Delta[\text{CO}_3^{2-}]$  suggests that the mid-depth South Atlantic experienced an increase in the storage of respired carbon, as  $\text{CO}_2$  was sequestered from the glacial atmosphere. Despite the inferred increase in the relative volume of LSCW bathing the Agulhas Plateau during glacial stages, the contribution of Northern Component Water (NCW) is not thought to have diminished completely. In fact, the relative diminution in the relative volume of NCW bathing the MD02-2588 core site, appears to be counterbalanced by the lower nutrient content of northern-sourced water mass during glacial stages. The glacial lowering of seawater nutrient concentration in the mid-depth South Atlantic was possibly also affected by an increase in the formation of lower-nutrient mid-depth waters by open ocean convection in polynyas within the expanded circum-Antarctic sea ice zone.

The recurrent  $\text{Cd}_{\text{sw}}$  maxima recorded during glacial terminations are interpreted as resulting from the upward mixing of nutrient-rich bottom waters from the deepest and most isolated waters in the Southern Ocean following the deglacial breakdown of stratification in the ocean interior. The increases in  $\text{Cd}_{\text{sw}}$  recorded during deglaciations occur in tandem with increases in  $\Delta[\text{CO}_3^{2-}]$  on the southern Agulhas Plateau and increases of  $p\text{CO}_2$  in Antarctic ice cores. The covariation of these parameters supports the premise of increased outgassing of carbon from the deep Southern Ocean during deglaciations. This interpretation is also consistent with the inference of increased  $[\text{O}_2]$  in the bottom waters of the southern Agulhas Plateau which suggests that, during deglaciations, the deep South Atlantic experienced transient episodes of enhanced ventilation.

## 4.2 Introduction

The Atlantic meridional overturning circulation (AMOC) is a critical component of the global ocean circulation system and strongly influences climate through the transport of heat and freshwater (Talley, 2013; Buckley and Marshall, 2016). The AMOC is composed of an “upper” and “lower” cell. The “upper cell” originates from deep water formation sites in the North Atlantic and ventilates the upper 2.5 km of the Atlantic basin. The “lower cell” emanates from deep water formation sites close to

Antarctica and ventilates the abyssal ocean. The upper cell involves the northward flow of surface and intermediate waters toward the North Atlantic and their transformation into southward-flowing North Atlantic Deep Water (NADW); the lower cell on the other hand involves the formation of Antarctic Bottom Water (AABW) which flows northward into the Atlantic basin at abyssal depths and subsequently mixes with the overlying NADW to produce a southward return flow back toward the Southern Ocean.

Past variations of the AMOC are believed to have affected Pleistocene climate change by altering the patterns of oceanic heat transport (e.g., Rahmstorf, 1994, 2002; Lynch-Stieglitz *et al.*, 2007; Adkins, 2013) and by changing the quantity of respired carbon stored in the deep ocean (e.g., Knox and McElroy, 1984; Sarmiento and Toggweiler, 1984; Siegenthaler and Wenk, 1984). During glacial intervals, well-ventilated northern-sourced deep waters in the Atlantic Ocean (equivalent to NADW) appear to have shoaled, while poorly-ventilated southern-sourced deep waters (equivalent to AABW) expanded to fill a larger proportion the abyssal and deep ocean (e.g., Boyle and Keigwin, 1987; Duplessy *et al.*, 1988; Sarnthein *et al.*, 1994; Curry and Oppo, 2005; Marchitto and Broecker, 2006; Martínez-Méndez *et al.*, 2009; Freeman *et al.*, 2016).

The available paleoceanographic records from the deep and abyssal North Atlantic consistently indicate that during the LGM, poorly-ventilated (and nutrient-rich) southern-sourced waters replaced well-ventilated northern-sourced waters. At intermediate depths, a water-mass akin to NADW – often referred to in the literature as Glacial North Atlantic Intermediate Water (GNAIW) - continued to dominate. This reorganization of the glacial North Atlantic water-mass geometry has been inferred from studies of deep water chemical composition derived from sedimentary nutrient proxies, such as  $\delta^{13}\text{C}$  (e.g., Curry and Oppo, 2005) and Cd/Ca (e.g., Marchitto and Broecker, 2006) measured in benthic foraminifera, as well as deep-water carbonate ion concentration ( $[\text{CO}_3^{2-}]$ ) proxies such as foraminiferal B/Ca (Yu *et al.*, 2008). Estimates of deep water renewal rates (i.e., ventilation age) based on paired planktonic-benthic foraminiferal  $^{14}\text{C}$  age differences (e.g., Freeman *et al.*, 2016) and sedimentary  $^{231}\text{Pa}/^{230}\text{Th}$  ratio records (e.g., Gherardi *et al.*, 2009) have provided further support for the existence of an altered water-mass geometry in the North Atlantic.

In the South Atlantic the evidence regarding the variable contribution of northern- and southern-sourced deep waters on glacial-interglacial timescales is more complex. During glacial stages the Atlantic sector of the Southern Ocean above approximately 2.5 km water depth appears to have been filled with a water mass characterised by low  $\delta^{13}\text{C}$  which resulted in the development of a mid-depth chemical divide (or “chemocline”) comparable to that observed in the North Atlantic (Mackensen *et al.*, 2001; Ninnemann and Charles, 2002; Hodell *et al.*, 2003; Curry and Oppo, 2005). However, the available benthic foraminiferal Cd/Ca data from the deep South Atlantic do not show an obvious increase (Boyle, 1992; Martínez-Méndez *et al.*, 2009) suggesting that the development of this vertical  $\delta^{13}\text{C}$  gradient does not result from changes in deep-water nutrient concentration, but rather that it indicates changes in the isotopic fractionation of carbon during the exchange of  $\text{CO}_2$  between the Southern Ocean and the atmosphere (Broecker and Maier-Reimer, 1992). The development of the  $\delta^{13}\text{C}$  chemocline between the deep and mid-depth waters of the glacial South Atlantic is particularly pronounced south of  $43^\circ\text{S}$  (Martínez-Méndez *et al.*, 2009). This latitude coincides with the approximate position of the Subantarctic Front (SAF) during the LGM ( $\text{SAF}_{\text{LGM}}$ ) (Kohfeld *et al.*, 2013). South of the  $\text{SAF}_{\text{LGM}}$ , the deep waters of the South Atlantic outcrop at the surface and interact with the atmosphere; north of the  $\text{SAF}_{\text{LGM}}$ , the  $\delta^{13}\text{C}$  gradient between upper and lower water masses is more gradual with little evidence of a sharp chemocline (Martínez-Méndez *et al.*, 2009). This spatial variability appears to indicate enhanced mid-depth ventilation north of the  $\text{SAF}_{\text{LGM}}$  and reduced ventilation to the south.

Downcore records of  $\delta^{13}\text{C}$  that extend beyond the LGM also suggest that mid-depth waters (~2000 to ~3500 m) in the South Atlantic are characterised by small glacial-interglacial variations whereas in deep waters (> 3500 m) these variations are distinctly larger (Hodell *et al.*, 2003). This may indicate a less variable mid-depth circulation on glacial-interglacial timescales with a continuous contribution of Northern Component Water (NCW; equivalent to NADW or GNAIW) to the South Atlantic during the Late Pleistocene climate cycles. On the contrary, at greater depths, the South Atlantic appears to have experienced large glacial-interglacial changes in the mixing ratio between NCW and Lower Southern Component Waters (LSCW; i.e., the glacial equivalent of AABW). This interpretation is corroborated by studies of neodymium (Nd) isotope ratios ( $\epsilon\text{Nd}$ ) which suggest that, during glacial stages, the deep and bottom

waters of the South Atlantic acquired an isotopic signature increasingly indicative of a southern provenance (Rutberg *et al.*, 2000; Piotrowski *et al.*, 2004, 2005). Likewise, LGM radiocarbon-based ventilation age reconstructions indicate the presence of very ‘old’ waters in the deep South Atlantic, consistent with the shoaling of well-ventilated northern-sourced waters and their replacement by poorly-ventilated southern-sourced waters (Barker *et al.*, 2010; Skinner *et al.*, 2010).

The zonal and vertical complexity apparent from the available deep-water proxy records of the South Atlantic highlights the importance of generating paleoceanographic records from the full range of water depths and latitudes in this part of the Southern Ocean (see Martínez-Méndez *et al.*, 2009). This is particularly important if a better understanding of the role of the AMOC in the Late Pleistocene climate change is to be gained (e.g., Adkins, 2013). Studies based on sediment cores retrieved from around southern Africa have generated more detailed records of the variability of mid-depth ocean circulation in the South Atlantic paving the way towards a better understanding of the mid-depth circulation history in the Indian-Atlantic Ocean Gateway (I-AOG) (Molyneux *et al.*, 2007; Martínez-Méndez *et al.*, 2008, 2009).

We complement these studies by presenting additional multi-proxy records of deep water variability from a sediment core recovered from the southern flank of the Agulhas Plateau to reconstruct the paleoceanographic history of the mid-depth South Atlantic circulation. The core site is located at the transition zone between NADW and Circumpolar Deep Water (CDW) within the upper cell of the AMOC. This allows us to investigate the relative contribution of northern- and southern-sourced deep waters to the I-AOG during the last glacial-interglacial cycle. We consider the implications of these variations in the context of climate change on orbital timescales.

### **4.3 Regional deep water oceanographic setting**

The I-AOG off southern Africa refers to the oceanic region connecting the Indian and Atlantic Ocean and represents a key component of the global meridional overturning circulation (MOC) (Gordon, 1986; Gordon *et al.*, 1992; Weijer *et al.*, 1999) (Fig. 4.1). In this region, warm and saline surface waters from the Indian Ocean are transported westwards to the South Atlantic and provide a source of heat and salt to the Atlantic thermocline, potentially contributing to the formation of NADW in the

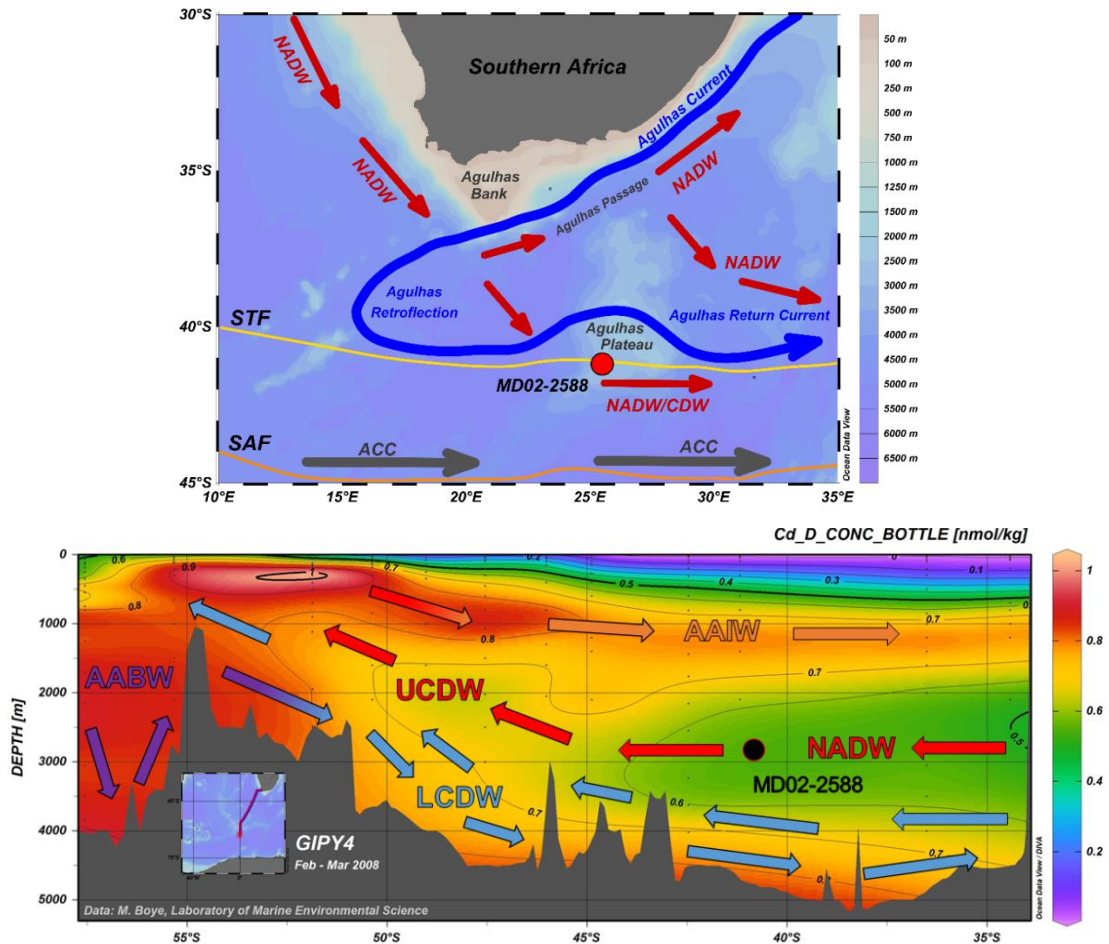


**Figure 4.1.** Upper panel: Map showing study area and position of core MD02-2588 on the southern Agulhas Plateau, together with the present-day position of the oceanic fronts and generalised ocean circulation (Peterson and Stramma, 1991; Orsi *et al.*, 1995; Arhan *et al.*, 2003). Blue continuous arrow shows the approximate pathway of the Agulhas Current along the African continental margin, the Agulhas Retroflection and the eastward flowing Agulhas Return Current. The red arrows show the pathway of North Atlantic Deepwater (NADW) exiting the South Atlantic and entering the Indian Ocean. The grey arrows indicate the flow of the Antarctic Circumpolar Current (ACC). The yellow and orange lines are the approximate positions of the Subtropical Front (STF) and the Subantarctic Front (SAF), respectively. The position of the sediment core MD02-2588 is indicated by the red circle. Lower panel: Modern oceanographic section of dissolved Cd concentration in the Atlantic Sector of the Southern Ocean (modified from Schlitzer, 2015) showing the positions of modern water masses and generalised meridional overturning circulation (e.g., Sarmiento *et al.*, 2004, Talley, 2013). AAIW, Antarctic Intermediate Water; NADW, North Atlantic Deep Water; UCDW, Upper Circumpolar Deep Water; LCDW, Lower Circumpolar Deep Water; AABW, Antarctic Bottom Water. The position of sediment core MD02-2588 is indicated by the black circle.

north of the basin (Weijer, 2000; Weijer *et al.*, 2002; Knorr and Lohmann, 2003; Van Sebille *et al.*, 2009; Biastoch *et al.*, 2008, 2009a). The westward surface flow in the I-AOG is compensated at depth by the eastward flow of NADW exiting the South Atlantic (Gordon, 1996; Lutjeharms, 1996; Arhan *et al.*, 2003) (Fig. 4.1). A branch of this eastward flowing NADW is transported around the southern tip of the Agulhas Bank and enters the South Indian Ocean through the Agulhas Passage that lies between the south eastern African continental margin and the northern Agulhas Plateau. A second branch of the southward propagating NADW that exits the South Atlantic extends further poleward enabling it to mix with Circumpolar Deep Water (CDW) and to flow around the southern edge of Agulhas Plateau as it joins the eastward-flowing Antarctic Circumpolar Current (ACC). This eastward flow of NADW/CDW along the southern flank of the Agulhas Plateau has led to the deposition of contourite sediment drifts from which the core used in this study (core MD02-2588) was recovered (Tucholke and Carpenter, 1977; Uenzelmann-Neben, 2001) (Fig. 4.1). Today the MD02-2588 core site is positioned in the transition zone between NADW and CDW and offers the opportunity to reconstruct past variations in the mixing between NCW and LSCW in the mid-depth South Atlantic at a water depth and latitude where detailed deep water records are currently lacking.

#### **4.4 Materials and methods**

Full methodological details are given in Chapter 3. The following is a brief summary of the materials and methods relevant to the data presented in this chapter.

The CASQ (Calypso square-corer) sediment core MD02-2588 was recovered from a contourite drift located on the southwestern flank of the Agulhas Plateau (41°19.90'S, 25°49.40'E, 2907 m water depth) during RV Marion Dufresne cruise MD128 (Girardeau, 2002) (Fig. 4.1). At this water depth, the core site is presently located in the transition zone between NADW and CDW (Fig. 4.1).

The chronostratigraphic framework of sediment core MD02-2588 was developed by Ziegler *et al.*, (2013). Fifteen calibrated accelerator mass spectrometry (AMS) <sup>14</sup>C dates are used for constructing the age model between 0 and 40 kyr BP. For the remainder of the core, the age model is constructed by graphical correlation of the downcore record of benthic foraminiferal oxygen isotopes to the European Project for

Ice Coring in Antarctica (EPICA) Dome C  $\delta D$  record (Jouzel *et al.*, 2007). See Ziegler *et al.*, 2013 and Section 3.2.1 of this thesis for more details.

Stable oxygen and carbon isotopes were measured on the benthic foraminifera *Cibicides wuellerstorfi* ( $\delta^{18}O_{C.wuell.}$  and  $\delta^{13}C_{C.wuell.}$ , respectively). The benthic foraminiferal stable isotope records presented in this chapter combine previously published data (n=453; Ziegler *et al.*, 2013) with new measurements made for this study (n=132). These records were replicated because we intended to generate stratigraphic series of paired stable isotope and elemental ratios measured from same benthic foraminiferal samples. A detailed description of the sample preparation and analysis associated with these datasets is given in sections 3.4-3.7.

In this chapter we present stratigraphic series of Cd/Ca and B/Ca measured in samples of *C. wuellerstorfi* ( $Cd/Ca_{C.wuell.}$  and  $B/Ca_{C.wuell.}$ , respectively); the majority of these measurements were made on aliquots of the samples also analysed for stable isotopes.  $Cd/Ca_{C.wuell.}$  was used to estimate seawater Cd concentration ( $Cd_{sw}$ ) (e.g., Boyle, 1988, 1992) (see Section 3.14), and  $B/Ca_{C.wuell.}$  was used to estimate bottom water carbonate ion saturation ( $\Delta[CO_3^{2-}]$ ) (e.g., Yu and Elderfield, 2007) (see Section 3.11). The paired measurements of  $\delta^{13}C_{C.wuell.}$  and  $Cd/Ca_{C.wuell.}$  on the same samples allowed the derivation of the air-sea fractionation signature of the deep-water  $\delta^{13}C_{DIC}$  ( $\delta^{13}C_{as}$ ) (e.g., Lynch-Stieglitz and Fairbanks, 1994) (see Section 3.15). The downcore record of U/Mn from *C. wuellerstorfi* ( $U/Mn_{C.wuell.}$ ) is used as a first-order indicator of changes in redox conditions preserved along sediment core MD02-2588 (see Section 3.9.6).

In addition, the sortable silt mean grain size ( $\overline{SS}$ ) proxy was used to reconstruct the variability of the past relative speed of the near-bottom currents at the MD02-2588 core site (e.g. McCave and Hall, 2006) (see Section 3.16).  $\overline{SS}$  was converted to bottom-water scalar geostrophic flow speed ( $U_g$ ) using the calibration of McCave *et al.*, (2017).

## 4.5 Results

### 4.5.1 Benthic foraminiferal oxygen and carbon isotope records

The stratigraphic record of  $\delta^{18}O_{C.wuell.}$  displays a prominent orbital modulation with additional variability on millennial timescales (Fig. 4.2a). The largest fluctuations are observed during Terminations I (TI) and II (TII), with decreases of 1.83‰ and 2.13‰, respectively, which are both well in excess of the mean ocean glacial-interglacial shift

of 0.8-1.1‰ (Schrag *et al.*, 2002; Waelbroeck *et al.*, 2002). This indicates that in addition to global ice volume change, the isotopic composition of benthic foraminiferal at this site also includes a component driven by changes in deep-water temperature and/or local seawater isotopic composition ( $\delta^{18}\text{O}_{\text{sw}}$ ).

The published  $\delta^{13}\text{C}_{C.wucll}$  data from MD02-2588 have already been described in detail (Ziegler *et al.*, 2013) and were shown to display fluctuations similar to those observed in the benthic foraminiferal  $\delta^{13}\text{C}$  stacks from the mid-depth and deep Atlantic Ocean (Lisiecki *et al.*, 2008). The largest fluctuations are observed across TI and TII, at which times  $\delta^{13}\text{C}_{C.wucll}$  displays changes of 0.99‰ and 1.12‰, respectively (Fig. 4.2b). A strong  $\delta^{13}\text{C}_{C.wucll}$  depletion is also observed during the MIS 5/MIS 4 transition.  $\delta^{13}\text{C}_{C.wucll}$  during this MIS 4 reaches values similar to those observed during MIS 2 and MIS 6, although the subsequent shift during the MIS 3/4 transition is only 0.61‰, approximately half that of TI and TII.

#### 4.5.2 Downcore variations of $\delta^{13}\text{C}_{\text{as}}$

The stratigraphic series of the carbon isotopic signature due to air-sea fractionation during the exchange of  $\text{CO}_2$  ( $\delta^{13}\text{C}_{\text{as}}$ ) was constructed for MD02-2588 from the paired foraminiferal Cd/Ca- $\delta^{13}\text{C}$  measurements over the past 150 kyr BP (Fig. 4.2b).  $\delta^{13}\text{C}_{\text{as}}$  was derived by separating the nutrient signal of seawater  $\delta^{13}\text{C}_{\text{DIC}}$  from the effect of the carbon isotope fractionation signal acquired during air-sea gas exchange and the effect of variations in the marine carbon reservoir (Lynch-Stieglitz and Fairbanks, 1994; Lynch-Stieglitz *et al.*, 1996; Marchitto and Broecker, 2006, Oliver *et al.*, 2010). The methodology is described in detail in Section 3.15.

The down-core  $\delta^{13}\text{C}_{\text{as}}$  record along MD02-2588 displays a prominent orbital timescale modulation indicating notable fluctuations either in the mixing of water masses of varying provenance, or fluctuations of the thermodynamic imprint of the waters bathing the Agulhas Plateau (Fig. 4.2b). Comparing the amplitude of the downcore records of  $\delta^{13}\text{C}_{C.wucll}$  and  $\delta^{13}\text{C}_{\text{as}}$  reveals that the latter accounts for a large proportion of the total isotopic signal preserved within the shells of benthic foraminifera at the core site. From MIS 4 onwards, the magnitude of  $\delta^{13}\text{C}_{\text{as}}$  variations closely track the variations of  $\delta^{13}\text{C}_{C.wucll}$ , suggesting that in this part of the record, air-sea fractionation processes are the main driver of  $\delta^{13}\text{C}_{C.wucll}$  changes. Prior to MIS 4,  $\delta^{13}\text{C}_{C.wucll}$  and

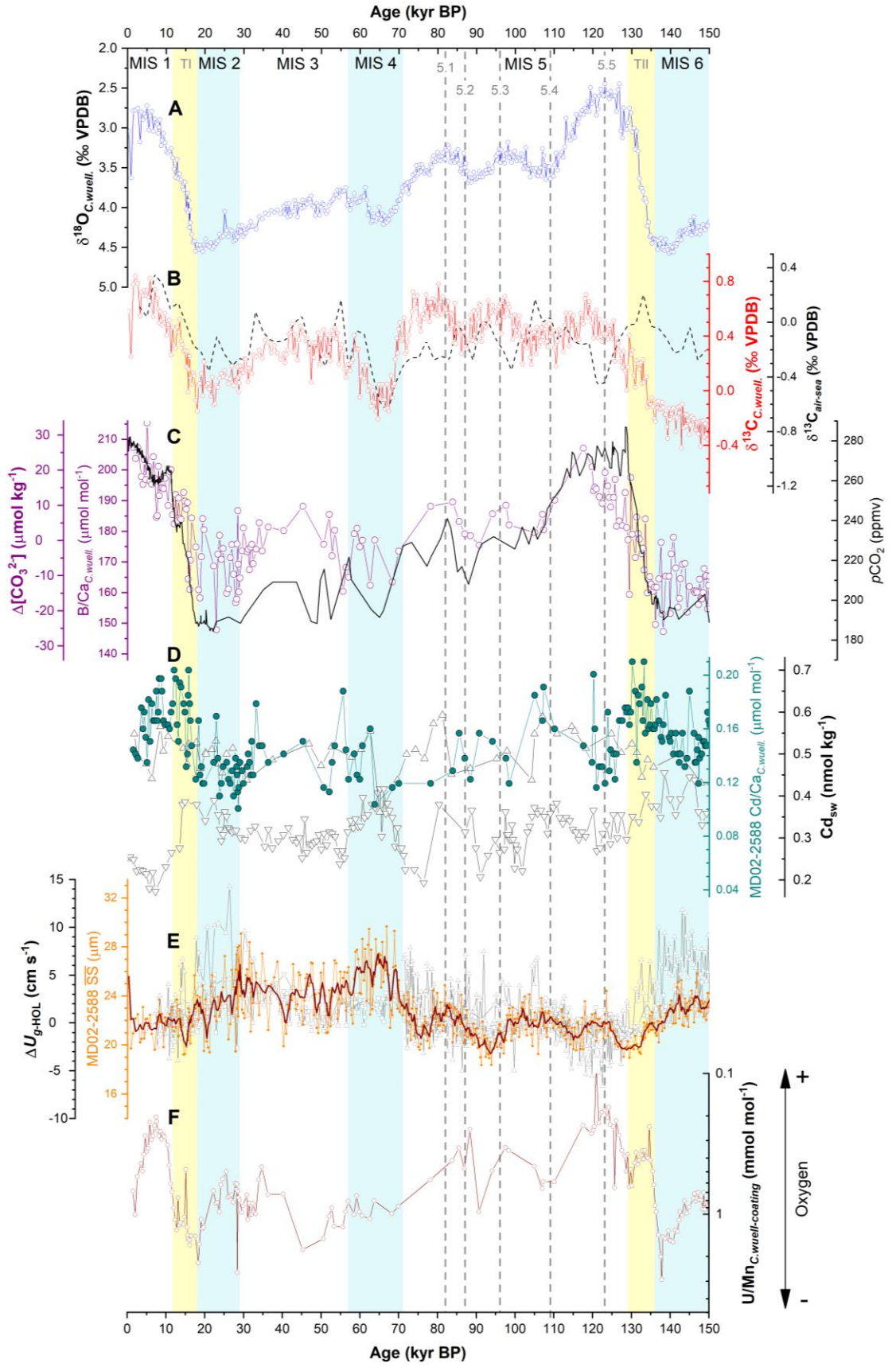


**Figure 4.2.** Deep-water stratigraphic records from sediment core MD02-2588 from the southern Agulhas Plateau. A) Oxygen isotopes measured in *Cibicides wuellerstorfi* ( $\delta^{18}\text{O}_{C.wuell}$ ), incorporating data from this study and Ziegler *et al.*, (2013) (blue line, open circles). Note inverted y-axis. VPDB is Vienna Pee Dee Belemnite. B) Carbon isotopes measured in *C. wuellerstorfi* ( $\delta^{13}\text{C}_{C.wuell}$ ), incorporating data from this study and Ziegler *et al.*, (2013) (red line, open circles). Also shown is the time-series of the air-sea fractionation component of the  $\delta^{13}\text{C}_{C.wuell}$  record ( $\delta^{13}\text{C}_{as}$ ) (dashed black line). See main text and chapter 3 for details of  $\delta^{13}\text{C}_{as}$  calculation. C) Downcore record of bottom-water carbonate saturation state ( $\Delta[\text{CO}_3^{2-}]$ ) reconstructed using the B/Ca of *C. wuellerstorfi* ( $\text{B}/\text{Ca}_{C.wuell}$ ) from MD02-2588 (purple line, open circles).  $\Delta[\text{CO}_3^{2-}]$  is calculated according to the relationship of Yu and Elderfield, (2007). Also shown is the atmospheric  $p\text{CO}_2$  record from Antarctic ice cores (Monin *et al.*, 2001; Petit *et al.*, 1999; Pepin *et al.*, 2001) (black line). D) Seawater Cd concentration ( $\text{Cd}_{sw}$ ) determined from the Cd/Ca ratio of *C. wuellerstorfi* samples (cyan line with solid circles). Also shown are the  $\text{Cd}_{sw}$  records from core CHN82-24-4 in the North Atlantic (grey line with downward-pointing triangles; 43°N, 33°W, 3427 m; Bolye and Keigwin, 1985/86; Keigwin and Boyle, 1985) and core RC13-229 from the Cape basin in the South Atlantic (grey line with upward-pointing triangles; 26°S, 11°E, 4194 m; Oppo and Fairbanks, 1987; Oppo *et al.*, 1990; Boyle, 1992; Oppo and Rosenthal, 1994). E) Change in geostrophic scalar flow speed relative to the Holocene ( $\Delta U_{g-HOL}$ ) estimated from the mean grain size of the 10-63  $\mu\text{m}$  size fraction of terrigenous material (sortable silt). Downcore record of  $\Delta U_{g-HOL}$  from MD02-2588 (orange line, closed circles, with 5-pt adjacent averaging smoothing filter shown in red). Note inverted y-axis. Also shown are the  $\Delta U_{g-HOL}$  records from MD02-2589 (grey line, open squares; 41°26.03'S; 25°15.30'E; 2660 m water depth; Molyneux *et al.*, 2007), MD96-2080 (grey line, upward-pointing triangles; 36°19.2'S; 19°28.2'E; 2488 m water depth; Martinez-Mendez *et al.*, 2008) and ODP Site 1123 (downward-pointing triangles; 41°47.2' S, 171° 29.9' W, 3290 m water depth; Hall *et al.*, 2001). F) U/Mn of authigenic coatings on *C. wuellerstorfi* ( $\text{U}/\text{Mn}_{C.wuell-coat}$ ) from sediment core MD02-2588 (wine red, open circles). Plotted on logarithmic scale with inverted axis. Marine Isotope Stages (MIS) are taken from Lisiecki and Raymo, (2005). Glacial stages are shown with vertical blue bars; MIS 5 substage peaks are shown with the vertical grey bars. Glacial terminations TI and TII are shown with vertical yellow bars and their ages are taken from Stern & Lisiecki, (2014) and Landais *et al.*, (2013), respectively. All records are plotted on their published age models. In the case of MD02-2588, we use the age model of Ziegler *et al.*, (2013).

$\delta^{13}\text{C}_{\text{as}}$  do not appear to vary in tandem, suggesting that processes other than air-sea fractionation have a more prominent role in the variability of the local  $\delta^{13}\text{C}_{\text{DIC}}$ , such as changes in the marine carbon reservoir and nutrient cycling.

In the modern ocean, NADW is characterised by negative  $\delta^{13}\text{C}_{\text{as}}$ , whereas LCDW and AABW plot around 0‰ and 0.4‰, respectively; Antarctic Intermediate Water (AAIW)  $\delta^{13}\text{C}_{\text{as}}$  is generally characterised by values of 0.8-1.0‰ (Charles *et al.*, 1993; Lynch-Stieglitz *et al.*, 1994; Marchitto and Broecker, 2006; Makou *et al.*, 2010; Mackensen, 2012). During MIS 1,  $\delta^{13}\text{C}_{\text{as}}$  ranges between 0.1 and 0.35‰, suggesting a dominant influence of southern-sourced deep waters at the MD02-2588 core site. During the glacial stages of MIS 2, MIS 4 and MIS 6, mean  $\delta^{13}\text{C}_{\text{as}}$  for each stage is generally characterised by negative values (-0.2‰, -0.4‰, and -0.1‰, respectively). During MIS 3, mean  $\delta^{13}\text{C}_{\text{as}}$  is -0.1‰, and during MIS 5 it is -0.2‰. The latter stage is characterised by a large magnitude oscillation between 110 kyr BP and 130 kyr BP, reaching values as low as -0.4‰. Curiously, this negative excursion occurs during the peak interglacial phase, when conditions are expected to have been similar to those occurring during late MIS 1.

The overall negative  $\delta^{13}\text{C}_{\text{as}}$  that characterises the downcore record from MD02-2588 argues for a continuous influence of northern-sourced waters on the Agulhas Plateau throughout the past 150 kyr BP. MIS 1 appears to be exceptional interval in the record, with consistently positive  $\delta^{13}\text{C}_{\text{as}}$  which suggests a stronger influence from southern-sourced waters during that time.

#### 4.5.3 Benthic foraminiferal B/Ca and carbonate saturation state of seawater

The  $\text{B}/\text{Ca}_{\text{C.wuell}}$  record from MD02-2588 is characterised by average interglacial values of 195  $\mu\text{mol mol}^{-1}$ , 176  $\mu\text{mol mol}^{-1}$  and 187  $\mu\text{mol mol}^{-1}$  for MIS 1, MIS 3 and MIS 5 respectively. During glacial stages, values of 172  $\mu\text{mol mol}^{-1}$ , 173  $\mu\text{mol mol}^{-1}$  and 166  $\mu\text{mol mol}^{-1}$  are respectively recorded during MIS 2, MIS 4 and MIS 6; the largest changes in  $\text{B}/\text{Ca}_{\text{C.wuell}}$  occur during glacial terminations TI and TII (Fig. 4.2c). Maximum values are observed during MIS 5.5 (207  $\mu\text{mol mol}^{-1}$ ) and during the late Holocene (215  $\mu\text{mol mol}^{-1}$ ).  $\text{B}/\text{Ca}_{\text{C.wuell}}$  values for MIS 3 and MIS 5.1-5.4 are intermediate between those of interglacial maxima and glacial minima (Fig. 4.2c).

Downcore  $\text{B}/\text{Ca}_{\text{C.wuell}}$  data from MD02-2588 were converted to  $\Delta[\text{CO}_3^{2-}]$  using the species-specific relationship of Yu and Elderfield, (2007). The reconstructed MD02-

2588 core-top (2.5 cm depth)  $\Delta[\text{CO}_3^{2-}]$  is  $26.51 \mu\text{mol kg}^{-1}$ . This is in good agreement with the modern bottom water value of  $17.45 \mu\text{mol kg}^{-1}$ , particularly when considering the  $\pm 9 \mu\text{mol kg}^{-1}$  uncertainty estimated by Yu and Elderfield's (2007)  $\text{B}/\text{Ca}_{\text{C.wuell}}$ -to- $\Delta[\text{CO}_3^{2-}]$  calibration (see section 3.11 and Fig. 3.28 from previous chapter). The average  $\Delta[\text{CO}_3^{2-}]$  value for the entire Holocene section of the MD02-2588 core (0-30 cm) is  $17.96 \mu\text{mol kg}^{-1}$ , which is almost identical to modern bottom water  $\Delta[\text{CO}_3^{2-}]$ . The downcore range of bottom water  $\Delta[\text{CO}_3^{2-}]$  observed along core MD02-2588 ( $-26$  to  $33 \mu\text{mol kg}^{-1}$ ) is within the range of modern deep ocean values (e.g. Elderfield *et al.*, 2006) (Fig. 4.2c). Note that the modern bottom water  $\Delta[\text{CO}_3^{2-}]$  listed above was estimated without accounting for the post-industrial contribution of anthropogenic  $\text{CO}_2$  to the oceans.

The downcore pattern of  $\Delta[\text{CO}_3^{2-}]$  variability at the MD02-2588 core site is characterised by undersaturated conditions ( $< 0 \mu\text{mol kg}^{-1}$ ) during glacial stages and oversaturated conditions ( $> 0 \mu\text{mol kg}^{-1}$ ) during interglacial stages. The lowest glacial values occur during MIS 6 and the most oversaturated conditions observed during the latest part of the Holocene and during MIS 5.5 (Fig. 4.2c).  $\Delta[\text{CO}_3^{2-}]$  values during the rest of MIS 5 are intermediate between glacial maximum values and peak interglacial values but on the whole remain oversaturated. Within the more resolved parts of the MIS 3 section, values fluctuate between undersaturated and oversaturated on millennial timescales, as they do during MIS 2. The millennial-scale variability is significant in the most resolved sections of MD02-2588, i.e. 0-30 kyr BP and 120-150 kyr BP, with fluctuations as large as  $20 \mu\text{mol kg}^{-1}$ , i.e., almost half the magnitude of the shifts that occur during TI and TII (Fig. 4.2c).

#### 4.5.4 Benthic foraminiferal Cd/Ca and dissolved Cd concentration in seawater

$\text{Cd}/\text{Ca}_{\text{C.wuell}}$  displays variability characterised by minimum values during early glacial stages (MIS 2, 4 and 6) and maximum values during the beginning of interglacial stages (MIS 1, 3 and 5) (Fig. 4.2d). Peak interglacial  $\text{Cd}/\text{Ca}_{\text{C.wuell}}$  values for MIS 1, MIS 3 and MIS 5 are  $0.20 \mu\text{mol mol}^{-1}$ ,  $0.18 \mu\text{mol mol}^{-1}$  and  $0.20 \mu\text{mol mol}^{-1}$ , respectively (Fig. 4.2d). Minimum glacial stage values for MIS 2, MIS 4 and MIS 6 are  $0.10 \mu\text{mol mol}^{-1}$ ,  $0.11 \mu\text{mol mol}^{-1}$  and  $0.12 \mu\text{mol mol}^{-1}$ . The most significant increases in  $\text{Cd}/\text{Ca}_{\text{C.wuell}}$  are observed during TI ( $0.07 \mu\text{mol mol}^{-1}$ ) and TII ( $0.05 \mu\text{mol mol}^{-1}$ ) as well as during the MIS 4/3 transition ( $0.06 \mu\text{mol mol}^{-1}$ ). During the Holocene the record is characterised by a decreasing trend of  $\text{Cd}/\text{Ca}_{\text{C.wuell}}$  from  $0.19 \mu\text{mol mol}^{-1}$  to  $0.14$

$\mu\text{mol mol}^{-1}$  over the 10 kyr interval following TI; this pattern is similar to that observed during the early phase of MIS 5 when  $\text{Cd}/\text{Ca}_{\text{C.wuell}}$  decreases from  $0.17 \mu\text{mol mol}^{-1}$  to  $0.12 \mu\text{mol mol}^{-1}$  following TII. In addition, high amplitude  $\text{Cd}/\text{Ca}_{\text{C.wuell}}$  fluctuations occur during MIS 3 and during the MIS 5 substage transitions (e.g., 5.5/5.4 and 5.4/5.3); these are as large as the changes observed during full glacial terminations.

To allow the  $\text{Cd}/\text{Ca}_{\text{C.wuell}}$  record from MD02-2588 to be compared with the modern regional hydrography, the data are converted to  $\text{Cd}_{\text{sw}}$ . The distribution coefficient for the incorporation of Cd into benthic foraminifera ( $D_{\text{Cd}}$ ) is given by  $D_{\text{Cd}} = (\text{Cd}/\text{Ca})_{\text{foram}} / (\text{Cd}/\text{Ca})_{\text{seawater}}$  (Boyle, 1988, 1992). A  $D_{\text{Cd}}$  of 2.82 was applied to the MD02-2588 data and the seawater Ca concentration was assumed to have remained constant at  $0.01 \text{ mol kg}^{-1}$  (Boyle, 1992). Using this calibration, the range of  $\text{Cd}/\text{Ca}_{\text{C.wuell}}$  values at MD02-2588 correspond to minimum glacial  $\text{Cd}_{\text{sw}}$  values of  $0.36 \text{ nmol kg}^{-1}$ ,  $0.37 \text{ nmol kg}^{-1}$  and  $0.42 \text{ nmol kg}^{-1}$  for MIS 2, MIS 4 and MIS 6, respectively and peak interglacial  $\text{Cd}_{\text{sw}}$  values of  $0.68 \text{ nmol kg}^{-1}$ ,  $0.62 \text{ nmol kg}^{-1}$  and  $0.70 \text{ nmol kg}^{-1}$  for MIS 1, MIS 3 and MIS 5 (Fig. 4.2d). The downcore range of  $\text{Cd}_{\text{sw}}$  at MD02-2588 exceeds the modern mid-depth range by  $\pm 0.10 \text{ nmol kg}^{-1}$  (i.e.,  $\pm 20\%$ ) (e.g., Mawji *et al.*, 2015; Fig. 4.1), suggesting small, but perceptible changes in nutrient concentration during the last 150 kyr BP. On orbital timescales  $\text{Cd}_{\text{sw}}$  has remained relatively stable for the duration of this record; average  $\text{Cd}_{\text{sw}}$  for Marine Isotope Stages 1 through 6 are  $0.60 \text{ nmol kg}^{-1}$ ,  $0.48 \text{ nmol kg}^{-1}$ ,  $0.50 \text{ nmol kg}^{-1}$ ,  $0.46 \text{ nmol kg}^{-1}$ ,  $0.53 \text{ nmol kg}^{-1}$  and  $0.56 \text{ nmol kg}^{-1}$ .

#### 4.5.5 Sortable silt mean grain size and changes in bottom-water flow speed

The sortable silt mean grain size ( $\overline{SS}$ ) record at MD02-2588 displays a clear orbital-timescale variability (Fig. 4.2e). The highest  $\overline{SS}$  are observed during MIS 4 where values reach  $\sim 27 \mu\text{m}$ . During MIS 6,  $\overline{SS}$  is  $\sim 23 \mu\text{m}$  and then begins to decrease at  $\sim 140$  kyr BP until it reaches minimum values of  $\sim 19 \mu\text{m}$  during TII. Peak  $\overline{SS}$  of  $\sim 25 \mu\text{m}$  during MIS 2 are recorded at the onset of the stage and then gradually decrease until  $\overline{SS}$  reaches minimum values of  $\sim 21 \mu\text{m}$  during TI. A comparable decrease in  $\overline{SS}$  occurs at the MIS 4/3 transition where values decrease from  $\sim 27 \mu\text{m}$  to  $23 \mu\text{m}$  at 50 kyr BP. The largest shift occurs during the glacial inception at the MIS 5/4 transition where  $\overline{SS}$  increase from  $\sim 20 \mu\text{m}$  to  $\sim 27 \mu\text{m}$ . Notable multi-millennial timescale (5-10 kyr) fluctuations are also recorded during MIS 5 and MIS 3 with amplitudes of 1-3  $\mu\text{m}$ . The

record is also characterised by pervasive millennial-scale variability that varies in magnitude through the studied interval. For example, the millennial-scale variability during MIS 6 and MIS 5 is characterised by amplitudes of  $\sim 0.5\text{-}3\ \mu\text{m}$  whereas during MIS 3 and MIS 2 the amplitude range increases to  $2\text{-}6\ \mu\text{m}$  (Fig. 4.2e).

Preliminary calibration of the  $\overline{SS}$  proxy to bottom-water scalar geostrophic flow speed ( $U_g$ ) suggests that it is possible to extract quantitative estimates of changes in flow speed ( $\Delta U_g$ ) at specific sites from grain size data (McCave *et al.*, 2017). The downcore  $\overline{SS}$  data from MD02-2588 are converted to  $U_g$  using the relationship presented by McCave *et al.*, (2017). The record of  $U_g$  was subsequently normalised to the Holocene (0-11 kyr BP) level to produce stratigraphic series of  $\Delta U_g$  at the core sites relative to average Holocene  $U_g$  (expressed as  $\Delta U_{g\text{-HOL}}$ ). This parameter is a convenient way of expressing the relative trends in the records and facilitates comparison between downcore records of  $\overline{SS}$ .

#### 4.5.6 *U/Mn of benthic foraminiferal coatings and bottom water oxygen concentration*

The U/Mn of the authigenic coatings on foraminifera has been proposed as an indicator of redox conditions in marine sediments (see Gottschalk *et al.*, 2016, Chen *et al.*, 2017, and discussion in section 3.9.6 of this thesis). The precipitation of authigenic uranium ( $U_{\text{authigenic}}$ ) as coatings on foraminifera occurs below the oxygen penetration depth in the sediment column where organic matter is consumed by iron and sulphate reduction (Cochran *et al.*, 1986; McManus *et al.*, 2005). Conversely, the precipitation of Mn coatings on foraminifera occurs when Mn is dissolved into pore waters under reductive sedimentary conditions (Boiteau *et al.*, 2012). As such, high U/Mn indicates low oxygen concentration in sediment pore waters and vice versa.

The U/Mn of authigenic coatings on *C. wuellerstorfi* ( $U/Mn_{C.wuell.-coat}$ ) from sediment core MD02-2588 is used here as a qualitative indicator of relative changes in the sedimentary redox conditions at the core site. The late phases of MIS 2 and MIS 6 are characterised by the occurrence of  $U/Mn_{C.wuell.-coat}$  maxima, which are preceded by increasing trend throughout the glacial stages and followed by rapid ( $< 5$  kyr) decreasing trends during the transitions to the respective interglacial stages. This suggests that pore water oxygen concentrations ( $[O_2]$ ) gradually decreased throughout MIS 2 and MIS 6 and reached their lowest values immediately prior to deglaciation. During the

deglaciations, pore water [O<sub>2</sub>] then increased rapidly and reached their highest levels during the early part of MIS 1 and during MIS 5.5, for each respective deglaciation. Subsequently, U/Mn<sub>C.wuell.-coat</sub> increases throughout the remainder of MIS 1 and during the transition to MIS 5.4, respectively. This indicates that following the pore water [O<sub>2</sub>] maxima, oxygen levels subsequently decreased.

In the less resolved section of the record (30-120 kyr BP), only the broad trends of U/Mn<sub>C.wuell.-coat</sub> variability can be identified. MIS 5 is characterised by a series of fluctuations on 5-10 kyr timescales that are broadly aligned with the MIS 5 substages. Between MIS 5.1 and the middle of MIS 3 the record displays a gradual increasing trend of U/Mn<sub>C.wuell.-coat</sub>. No notable excursions are observed during the transition into and out of MIS 4. A further U/Mn<sub>C.wuell.-coat</sub> maximum is reached during the middle of MIS 3, before subsequently increasing in the latter half of this glacial stage.

## 4.6 Discussion

### 4.6.1 $\Delta[\text{CO}_3^{2-}]$ variability at the MD02-2588 core site

Benthic foraminiferal B/Ca records from sediment cores in the Pacific and Indian Oceans have revealed a long-term (>100 kyr) increase of [CO<sub>3</sub><sup>2-</sup>] during glaciations that occurs in tandem with long-term decreases in atmospheric *p*CO<sub>2</sub> and global sea level (Kerr *et al.*, 2017). The long-term glacial increase in deep sea [CO<sub>3</sub><sup>2-</sup>] in the Pacific and Indian Ocean is thought to be driven by the reduction of carbonate deposition on shelves due to sea level decline which shifts the accumulation of alkalinity from shelf areas of the ocean to the deep ocean. Additionally, these records reveal the occurrence of transient excursions of deep sea [CO<sub>3</sub><sup>2-</sup>] from the long-term trend. These excursions are thought to result from carbonate compensation processes that operate on shorter timescales (<100 kyr) and which are linked to changes in deep ocean carbon storage (Kerr *et al.*, 2017).

During the last glacial inception, between ~80 and 65 kyr BP, [CO<sub>3</sub><sup>2-</sup>] in the deep Atlantic is estimated to have decreased by approximately 25 μmol kg<sup>-1</sup> (Yu *et al.*, 2016). This has been proposed to reflect increased sequestration of carbon into the deep Atlantic associated with the shoaling of the AMOC (Yu *et al.*, 2016). Similarly, a record of [CO<sub>3</sub><sup>2-</sup>] from the deep South Atlantic found that changes in the storage of

respired carbon in the abyssal ocean was possibly linked to the release of CO<sub>2</sub> from the Southern Ocean during the most recent deglaciation (Yu *et al.*, 2014).

The downcore record of  $\Delta[\text{CO}_3^{2-}]$  from MD02-2588 is expected to predominantly reflect transient changes in deep sea  $[\text{CO}_3^{2-}]$  that are linked to variations in the transfer of carbon between the upper and deep oceans. Decreases in  $[\text{CO}_3^{2-}]$  are associated with the addition of carbon to the deep ocean and increases in  $[\text{CO}_3^{2-}]$  are associated with the transfer of carbon to the upper ocean and atmosphere. In addition, the variability of  $\Delta[\text{CO}_3^{2-}]$  at the MD02-2588 core site is expected to be influenced by changes in the mixing ratio between CO<sub>3</sub><sup>2-</sup>-depleted southern-sourced deep waters and CO<sub>3</sub><sup>2-</sup>-enriched northern-sourced deep waters.

The downcore record of  $\Delta[\text{CO}_3^{2-}]$  from MD02-2588 is aligned to the corresponding  $\delta^{18}\text{O}_{\text{C.wuell.}}$  record and also closely tracks the broad variations observed in the atmospheric  $p\text{CO}_2$  record from the Antarctic ice cores (Monin *et al.*, 2001; Petit *et al.*, 1999; Pepin *et al.*, 2001). This potentially indicates that the variability of  $\Delta[\text{CO}_3^{2-}]$  at the MD02-2588 core site is linked to the glacial-interglacial transfer of carbon between the deep ocean and the upper ocean and atmosphere. If this is the case, the  $\Delta[\text{CO}_3^{2-}]$  record suggests that the mid-depth waters of the I-AOG act as a repository of respired carbon during glacial stages. At this stage, it is difficult to estimate if the decrease in  $\Delta[\text{CO}_3^{2-}]$  at the Agulhas Plateau during glacial stages is associated with the basin-wide accumulation of respired carbon (e.g. Yu *et al.*, 2016), or whether it is linked to changes in the mixing ratio between CO<sub>3</sub><sup>2-</sup>-depleted southern-sourced deep waters and CO<sub>3</sub><sup>2-</sup>-enriched northern-sourced deep waters. To resolve this issue it is necessary to understand reconstruct the relative contribution of northern- versus southern-sourced deep water masses to the bottom water mixture that has bathed the Agulhas Plateau over the past 150 kyr BP.

#### 4.6.2 $C_{\text{dsw}}$ variability at the MD02-2588 core site

Modern values of  $C_{\text{dsw}}$  in the southern South Atlantic at water depths between 2000 m and 3500 m (0.5-0.6 nmol kg<sup>-1</sup>) are elevated relative to unaltered NADW (0.2-0.3 nmol kg<sup>-1</sup>; Mawji *et al.*, 2015). This is a consequence of a combination of water mass aging during the southward advection of NADW from its source region in the North Atlantic as well as mixing of NADW with nutrient-rich CDW in the Southern Ocean

(e.g., Orsi *et al.*, Talley, 2013). Core-top  $Cd_{sw}$  at MD02-2588 is  $0.51 \text{ nmol kg}^{-1}$  confirming that the core site is currently located in the transition zone between NADW and CDW (Mawji *et al.*, 2015) (Fig. 4.1 and 4.2d).

Core CHN82-24-4PC from the deep central North Atlantic ( $41^{\circ}72'N$ ,  $32^{\circ}85'W$ , 3427 m; Bolye and Keigwin, 1985/86; Keigwin and Boyle, 1985) provides a record of Cd/Ca and  $Cd_{sw}$  variability of predominantly northern component deep water (NCW), equivalent to modern NADW; (Boyle and Keigwin, 1985/6). Cd/Ca in this core was measured in *Uvigerina spp* except in the upper section where *Cibicides kullenbergi* is used (Boyle and Keigwin, 1985/6). The Cd/Ca data from this core were converted to  $Cd_{sw}$  using the calibration of Boyle (1992). Down-core  $Cd_{sw}$  in MD02-2588 remains well above that of NCW during the last 150 kyr except for a very brief episode around 65 kyr BP when a peak in  $Cd_{sw}$  in CHN82-24-4PC coincides with a minimum in MD02-2588 (Fig. 4.2d).

Core RC13-229 from the deep Cape Basin in the South Atlantic ( $25^{\circ}30'S$ ,  $11^{\circ}20'E$ , 4191 m; Oppo and Fairbanks, 1987; Oppo *et al.*, 1990; Boyle, 1992; Oppo and Rosenthal, 1994) is presently overlain by waters containing approximately 80% CDW and 20% NADW (Oppo and Fairbanks, 1987; Fig. 4.2d). The down-core Cd/Ca record in RC113-229 was measured mainly in *C. wuellerstorfi* and has been interpreted as reflecting variations in the mixing ratio between northern and southern component deep waters (Oppo and Rosenthal, 1994). After conversion of RC113-229 Cd/Ca data to  $Cd_{sw}$  (Boyle, 1992) it is evident that  $Cd_{sw}$  in this record and in MD02-2588 display a similar range in values throughout the studied interval. This demonstrates the common CDW/altered-NADW influence at the two sites (Fig. 4.1 and Fig. 4.2d; Oppo and Rosenthal, 1994).

For the last glacial-interglacial transition (0-30 kyr BP) a further comparison can be made with three additional Cd/Ca records: two cores located on the southeast Indian Ridge (SIR; core MD88-768,  $45^{\circ}45'S$ ,  $82^{\circ}56'E$ , 3330 m and core MD88-769,  $46^{\circ}04'S$ ,  $90^{\circ}07'E$ , 3420 m; Rosenthal *et al.*, 1997) and a core from the Björn drift in the North Atlantic ( $61^{\circ}29'910''N$ ,  $24^{\circ}10'330''W$ , 1627 m; Rickaby and Elderfield, 2005) (Fig. 4.3). Sediment core NEAP 4K is located close to the present-day source of NADW, while the SIR cores are located at the distal edge of the NADW tongue as it propagates around the Southern Ocean via the Antarctic Circumpolar Current (ACC). Cd/Ca data generated from the SIR cores represent averaged measurements

of three benthic species (*Uvigerina spp.*, *Cibicidoides kullenbergi*, and *Melonis barleeanum*);  $Cd_{sw}$  values for these Cd/Ca data are also calculated according to Boyle (1992). The SIR  $Cd_{sw}$  records show glacial values which are notably lower than those of MIS 1. Furthermore, the overall trend over this 30 kyr interval is very similar to the Agulhas Plateau  $Cd_{sw}$  record, although there is an offset in absolute values which is possibly due to the use of different benthic foraminifera species in each of the records (Fig. 4.3). Despite this offset the similarity of the  $Cd_{sw}$  histories of these three mid-depth Southern Ocean sites suggests that they could be recording a response to a common process.

$Cd_{sw}$  values from NEAP 4K are calculated using the calibration for the high-latitude North Atlantic of Bertram *et al.*, (1995) with  $D_{Cd} = 2.2$  (as presented by Rickaby and Elderfield, 2005). This record reveals that  $Cd_{sw}$  at intermediate depth in the high-latitude North Atlantic remained below those of the Agulhas Plateau during the last 30 kyr BP (Fig. 4.3). However, during the abrupt North Atlantic cooling events of the last deglaciation (i.e., Heinrich 1 and the Younger Dryas),  $Cd_{sw}$  increases markedly, reaching values almost as high as those of the southern Agulhas Plateau during the youngest event (Fig. 4.3). Rickaby and Elderfield (2005) attributed these  $Cd_{sw}$  spikes to the penetration of AAIW to the high-latitude North Atlantic as a consequence of a transient instability in the density balance between northern- and southern-sourced intermediate waters. The proposed relative increase in the density of the latter would have allowed it to sink beneath NCW and penetrated northwards to all latitudes in the Atlantic. We note, that the two  $Cd_{sw}$  spikes observed in the NEAP 4K record correspond to two peaks in  $Cd_{sw}$  from MD02-2588 raising the possibility that the Agulhas Plateau was also influenced by the proposed transient density instability of intermediate waters. However, the clear transient nature of these events in the NEAP 4K record limit the ability of this mechanism to explain the more enduring shifts observed in MD02-2588. As is pointed out by Rickaby and Elderfield (2005), the density reversals between northern- and southern-sourced intermediate waters during the last deglaciation require ‘unprecedented volumes of freshwater influx to the North Atlantic’. Such large influx of freshwater to the North Atlantic is only thought to have occurred during the relatively short-lived Heinrich stadials and the Younger Dryas.

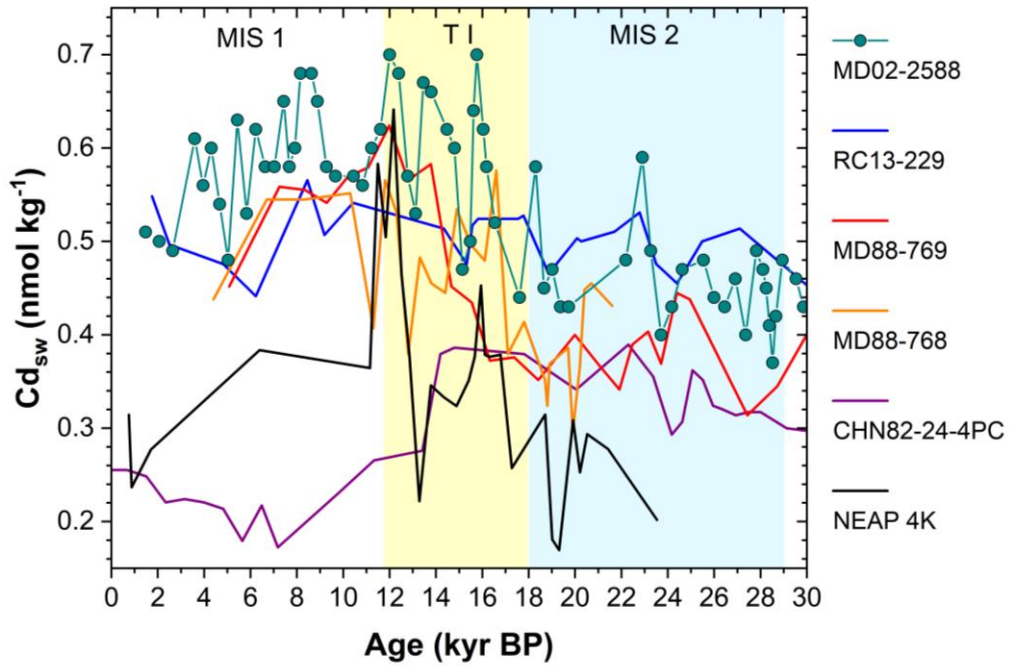


**Figure 4.3.** Downcore record of seawater Cd concentration ( $Cd_{sw}$ ) along sediment core MD02-2588 (cyan line with solid circles). Also shown are the  $Cd_{sw}$  records from: core CHN82-24-4 in the deep North Atlantic (purple line; 43°N, 33°W, 3427 m; Bolye and Keigwin, 1985/86; Keigwin and Boyle, 1985), core RC13-229 from the deep South Atlantic (blue line; 26°S, 11°E, 4194 m; Oppo and Fairbanks, 1987; Oppo *et al.*, 1990; Boyle, 1992; Oppo and Rosenthal, 1994), cores MD88-768 and MD88-769 from the mid-depth Southern Ocean (located on the southeast Indian Ridge (SIR) at 45°45'S, 82°56'E, 3330 m and core MD88-769, 46°04'S, 90°07'E, 3420 m, respectively; Rosenthal *et al.*, 1997) and core NEAP-4K from the intermediate-depth North Atlantic (61°29'910''N, 24°10'330''W, 1627 m; Rickaby and Elderfield, 2005). Cd/Ca data from MD02-2588 and NEAP-4K were determined on multi-specimen samples of *C. wuellerstorfi*; Cd/Ca data from CHN82-24-4 were determined on samples composed of *Uvigerina spp* except in the upper section where *Cibicides kullenbergi* was used (Boyle and Keigwin, 1985/6); Cd/Ca data from RC13-229 were also determined on samples of *Uvigerina spp* and supplemented by measurements on *C. wuellerstorfi*; SIR cores represent averaged values of measurements on the three benthic species, *Uvigerina spp.*, *C. kullenbergi*, and *Melonis barleanum*). Marine Isotope Stages (MIS) are taken from Lisiecki and Raymo, (2005). MIS 2 is shown with the vertical blue bar; glacial terminations TI is shown with the vertical yellow bar (age according to Stern & Lisiecki, (2014)). All records are plotted on their published age models. In the case of MD02-2588, we use the age model of Ziegler *et al.*, (2013).

#### 4.6.3 $\overline{SS}$ and $\Delta U_{g-HOL}$ variability at the MD02-2588 core site

The general pattern of orbital-timescale variability of  $\overline{SS}$  at MD02-2588 is consistent with other published records from the Southern Ocean (Fig. 4.2e). This includes records from the Chatham Rise, east of New Zealand (ODP Site 1123, 41°47.2' S, 171°29.9' W, 3290 m water depth; Hall *et al.*, 2001), the western slope of the Agulhas Bank, off South Africa (MD96-2080, 36°19.2'S; 19°28.2'E; 2488 m water depth; Martinez-Mendez *et al.*, 2008) and another core from southern Agulhas Plateau at a slightly shallower water depth (MD02-2589, 41°26.03'S; 25°15.30'E; 2660 m water depth; Molyneux *et al.*, 2007). The  $\overline{SS}$  grain size range in MD02-2588 of 18 to 30  $\mu\text{m}$  is slightly larger than that recorded from the shallower Agulhas Plateau (19-24  $\mu\text{m}$ ; Molyneux *et al.*, 2007) but is smaller than that from the Agulhas Bank (17-37  $\mu\text{m}$ ; Martinez-Mendez *et al.*, 2008) and larger than that measured in the southwest Pacific (13-19  $\mu\text{m}$ ; Hall *et al.*, 2001).

The downcore record of  $\Delta U_{g-HOL}$  from MD02-2588 reveals that the timing and magnitude of flow speed changes on the Agulhas Plateau are in excellent agreement with the published records from the Southern Ocean (Fig. 4.2e). The trends of  $\Delta U_{g-HOL}$  at MD02-2588 are particularly well-aligned to the trends recorded at MD02-2589, located approximately 300 m shallower on the Agulhas Plateau. The only exception occurs during MIS 4 when  $\Delta U_{g-HOL}$  at MD02-2588 is about 6  $\text{cm s}^{-1}$  greater, suggesting that flow speeds increased by a greater proportion at the deeper site. Also, the magnitude of the millennial-scale variability of  $\Delta U_{g-HOL}$  is greater along the downcore record from MD02-2588 relative to that observed along MD02-2589. This could be a sedimentological feature associated with the greater spread of grain size values in the former record or it could reflect a more variable flow speed pattern (e.g., due to a more turbulent flow at the deeper core site). Either way it is evident that the downcore variations of flow speed at the two core sites on the southern flank of the Agulhas Plateau controlled by the same process, at least on orbital timescales.

The eastward flow of the ACC, with its estimated total transport of 100-130 Sv (1 Sv=10<sup>6</sup> m<sup>3</sup> s<sup>-1</sup>) (Whitworth and Peterson, 1985; Cunningham *et al.*, 2003), is concentrated along a number of fronts that extend throughout the water column (Orsi *et al.*, 1995; Sokolov and Rintoul, 2002, 2009) and the majority of the transport is thought to occur within narrow jets at these fronts; specifically, the Antarctic Polar Front (APF) and the Subantarctic Front (SAF), at a mean water depth of 3000 m (Nowlin

and Klinck, 1986; Gille, 1994; Orsi *et al.*, 1995). We follow the reasoning of Molyneux *et al.*, (2007) and argue that the variability in  $\overline{SS}$  and flow speeds recorded at MD02-2588 may therefore indicate changes in the influence of the ACC on the southern Agulhas Plateau. The northward migration of the surface expression of the APF and STF during glacial intervals (e.g., Kohfeld *et al.*, 2013) could have brought the MD02-2588 and MD02-2589 core sites within closer proximity to the ACC and its faster flowing deep current jets. Equally the minima in  $\overline{SS}$  and flow speeds recorded at MD02-2588 during TI and TII and the subsequent interglacial stages (i.e., MIS 1 and MIS 5, respectively) potentially suggest the return of these fronts to their southward position.

The good agreement of the downcore records of  $\Delta U_{g-HOL}$  from MD02-2588 and ODP site 1123 in the south-western Pacific provides further supports the premise of a link between the flow speed variability on the Agulhas Plateau and changes in the strength of the ACC. The  $\Delta U_{g-HOL}$  variability at ODP Site 1123 is thought to result from intensified inflow of bottom waters to the Pacific Ocean during the glacial periods associated with increased production of AABW, which in turn could be linked to increased wind strengths in the Southern Ocean and a faster ACC. The similarity in the flow speed trends between the Agulhas Plateau sites and those recorded at the Chatham Rise suggests that there is a link between the two oceanic regions controlled by processes operating in the Southern Ocean.

The location of the MD96-2080 core site on the western slope of the Agulhas Bank also exposes this site to the increased influence of LSCW and faster flow speeds associated with the northward migration of the ACC during glacial stages. Of the four records discussed here, MD96-2080 displays the largest  $\Delta U_{g-HOL}$  variability with the increase in flow speeds during glacial stages appearing particularly pronounced relative to the Holocene conditions. MD96-2080 is located further away from the main flow path of the ACC so it is likely that Holocene flow speeds at this site are smaller than those of the southern Agulhas Plateau. If the baseline flow speeds were lower on the Agulhas Bank relative to those on the Agulhas Plateau, then the northward migration of the ACC during glacial stages could have resulted in a greater relative increase at the former site.

#### 4.6.4 *U/Mn and bottom water oxygen variability at the MD02-2588 core site*

The occurrence of sediment pore water [O<sub>2</sub>] minima during the peak glacial conditions of MIS 6 and at the end of MIS 2 could be driven by an increase in respiration of organic carbon at the seafloor, a decrease in bottom-water [O<sub>2</sub>], or both of these processes together. The higher levels of export production in the Sub-Antarctic Zone (SAZ) of the Atlantic during glacial stages is expected to have increased the flux of organic carbon to the seafloor (Martínez-García *et al.*, 2014; Jaccard *et al.*, 2016; Gottschalk *et al.*, 2016). This, in turn, could have caused an increase in the respiration of organic carbon at the seafloor and a diminishing of pore water [O<sub>2</sub>]. This mechanism could explain the occurrence of [O<sub>2</sub>] minima recorded in sediment core MD02-2588 during the peak glacial conditions. Similarly, the apparent increase in [O<sub>2</sub>] during deglaciations agrees with the reduction in export production that has been observed in sedimentary records from the SAZ (Martínez-García *et al.*, 2014; Jaccard *et al.*, 2016; Gottschalk *et al.*, 2016).

However, this pattern of low [O<sub>2</sub>] during glacial stages and high [O<sub>2</sub>] during interglacial stages could equally be explained by changes in bottom-water ventilation linked to deep-water convection and air-sea gas exchange. If this is the case, the downcore pattern of [O<sub>2</sub>] variability recorded in sediment core MD02-2588 suggests that the bottom-waters bathing the Agulhas Plateau were poorly ventilated during full glacial stages and well ventilated during peak interglacial conditions.

#### 4.6.5 *Glacial versus interglacial bottom water characteristics on the Agulhas Plateau*

The combined Cd<sub>sw</sub> and δ<sup>13</sup>C<sub>DIC</sub> estimates from Cd/Ca and δ<sup>13</sup>C in *C. wuellerstorfi* are used to characterise the bottom waters of the Agulhas Plateau in terms of water mass provenance, ventilation age and mixing history. Mean Cd<sub>sw</sub> and δ<sup>13</sup>C<sub>DIC</sub> were calculated for the six marine isotope stages and the two glacial terminations recorded in MD02-2588, with MIS 1 being divided into an early and late interval (see Table 4.1 for details of mean values of Cd<sub>sw</sub> and δ<sup>13</sup>C<sub>DIC</sub> (±1σ) and the age ranges used for each MIS).

The paired Cd<sub>sw</sub>-δ<sup>13</sup>C<sub>DIC</sub> data from MD02-2588 are plotted alongside the characteristic Cd<sub>sw</sub>-δ<sup>13</sup>C<sub>DIC</sub> of water mass end-members and the available Holocene and LGM data from 65 sediment cores retrieved from the North, Central and South Atlantic (Fig.

4.4). Sediment core sites and hydrographic station locations and water depths are presented in Tables 4.1, 4.2 and 4.3.  $Cd_{sw}-\delta^{13}C_{DIC}$  coordinates are plotted together with  $\delta^{13}C_{as}$  fractionation isolines to allow the distinction between changes due to biogeochemical aging, air-sea fractionation and water mass mixing (Lynch-Stieglitz and Fairbanks, 1994; Lynch-Stieglitz *et al.*, 1996). The water mass end-members used here are estimates for the Holocene and LGM (Table 4.3).  $\delta^{13}C_{as}$  isolines are computed using a modern and LGM parameterisation in order to account for glacial-interglacial differences between  $\delta^{13}C_{DIC}$  and nutrient stoichiometry (Lynch-Stieglitz and Fairbanks, 1994; Lynch-Stieglitz *et al.*, 1996). In the ‘termination’ plot, both glacial and interglacial  $\delta^{13}C_{as}$  isolines are presented to account for the uncertainties regarding mean ocean  $\delta^{13}C_{DIC}$  during these transient events (Fig. 4.4c).

The late MIS 1  $Cd_{sw}-\delta^{13}C_{DIC}$  coordinates plot along the mixing line between NADW and AABW (Fig. 4.4a). These coordinates reveal an approximate mixing ratio between the two end-members of 40%:60%, respectively, indicating an excellent match to modern conditions. The early MIS 1 coordinates, on the other hand, indicate lower  $\delta^{13}C_{DIC}$  and higher  $Cd_{sw}$  which results in a displacement from the late MIS 1 coordinate along the ‘biology’ or water mass ‘aging’ line. This suggests the presence of a less ventilated and more nutrient-rich water mass in during early MIS 1 but with an air-sea imprint that is almost identical to late MIS 1. This potentially implies a persistent source of water mass production throughout the entire interval but with increased aging due to a slower rate of overturning during early MIS 1. The MIS 5  $Cd_{sw}-\delta^{13}C_{DIC}$  relationship is offset vertically from the NADW and AABW mixing line, and from the late MIS 1  $Cd_{sw}-\delta^{13}C_{DIC}$  relationship, suggesting a clear difference in the isotopic imprint of air-sea fractionation at this time. This is interpreted as signifying either a difference in the prevailing oceanographic and atmospheric conditions at the water mass formation site during the last interglacial or the increased influence of water masses with different properties compared to those of MIS 1. The early and late MIS 1 are characterised by  $\delta^{13}C_{as}$  values of  $\sim 0.25\%$ , consistent with an oceanographic scenario of mixing between negative NADW and positive AABW end-members (e.g., Marchitto and Broecker, 2006). The slightly more negative  $\delta^{13}C_{as}$  value of  $\sim -0.1\%$  observed during MIS 5 probably arises from the mixing of northern and southern-sourced water masses with slightly different end-member  $\delta^{13}C_{as}$  values relative to MIS 1 or due to slightly different mixing rates.

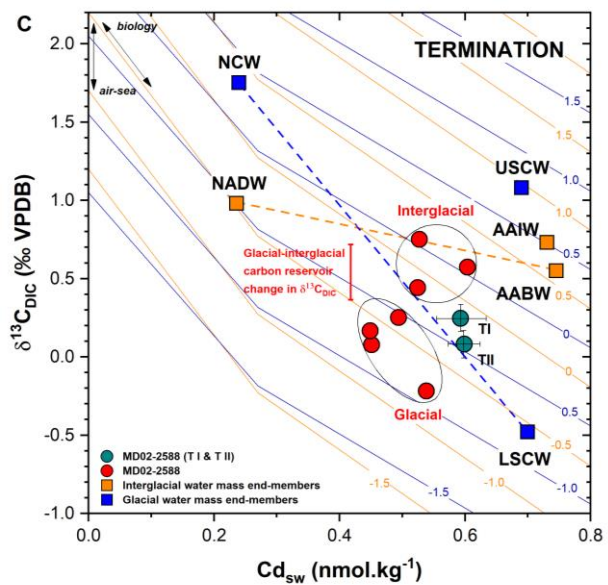
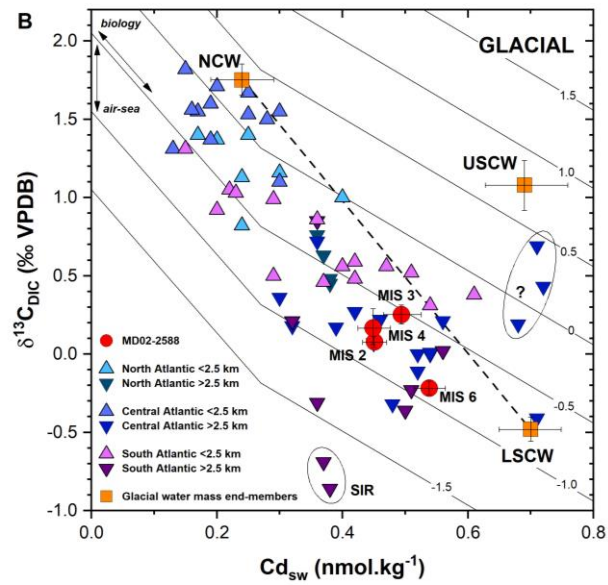
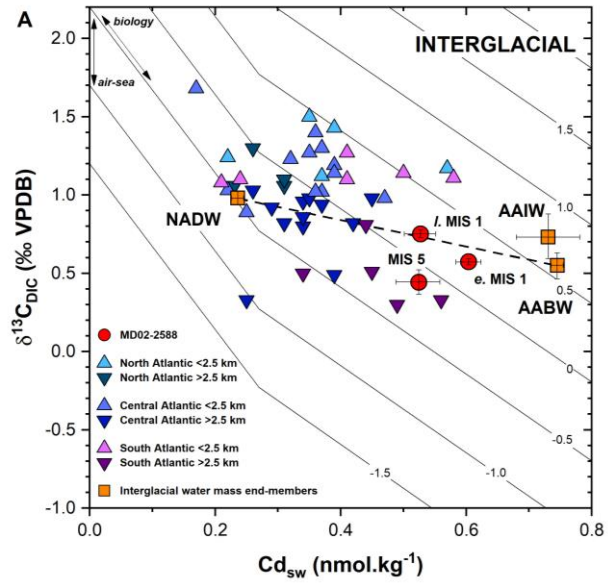


**Figure 4.4.** Proxy-proxy diagram displaying  $Cd_{sw}$  and  $\delta^{13}C_{DIC}$  data from sediment core MD02-2588 and reference cores from the Atlantic Ocean.  $\delta^{13}C_{as}$  isolines are computed using a modern and LGM parameterisation in each case in order to account for glacial-interglacial differences between the  $\delta^{13}C_{DIC}$  and nutrient stoichiometry (Lynch-Stieglitz and Fairbanks, 1994; Lynch-Stieglitz *et al.*, 1996). Dashed lines indicate the possible mixing lines between northern and southern sourced deep waters. A) Mean  $Cd_{sw}$  versus mean  $\delta^{13}C_{DIC}$  of core MD02-2588 for the late Marine Isotope Stage (MIS) 1, early MIS 1 and MIS 5 (red circles) (Table 4.1), plotted versus reference cores (Table 4.2) from the North Atlantic, Central Atlantic and South Atlantic. Upward-pointing triangles represent cores located at water depths shallower than 2500 m water depth while inverted triangles are cores located deeper than 2500 m. Orange squares indicate modern water mass end-members (Table 4.3). B) Same as in figure 4.4A, but for glacial marine isotope stages. The three sites circled with a question mark that do not fall on the mixing line between Northern Component Water (NCW) and Lower Southern Component Water (LSCW) are from the Sierra Leone Rise in the eastern tropical North Atlantic (Boyle, 1992). These have been previously highlighted as not being easily explained by mixing and aging of water masses (Marchitto and Broecker, 2006). The two sites circled and labelled SIR are from the southeast Indian Ridge (Rosenthal *et al.*, 1997). Water mass end-member values are for NCW, LSCW and Upper Southern Component Water (USCW) (see Table 4.3). C) Glacial termination mean  $Cd_{sw}$  versus mean  $\delta^{13}C_{DIC}$  from core MD02-2588, indicated by cyan circles (Table 4.1), are plotted with the Holocene and LGM water mass end-member values and the glacial and interglacial data from MD02-2588. Also indicated are the water mass mixing lines and the glacial-interglacial  $\delta^{13}C_{DIC}$  offset due to changes in the mean ocean carbon reservoir ( $\sim 0.35\%$ ). Note that no corrections are applied to the data to account for this glacial to interglacial reservoir change because this shift will affect all water masses more-or-less equally in each time-slice. In the case of the glacial plot, this results in an artificial offset between the  $Cd_{sw}$ - $\delta^{13}C_{DIC}$  data and the computed isolines. Accounting for this effect would not alter our interpretation. Mixing of two different water masses in different proportions moves data along a line connecting the two end-member compositions (dashed lines). Changes due to “aging” or increased biological input will move data along a gradient indicated by the “biology” arrow in the top left-hand corner. Variations due to air-sea fractionation at the source region will shift the data vertically by changing the carbon isotope signature but not the nutrient content as shown by the “air-sea” arrow.

**Table 4.1.** Average  $Cd_{sw}$  and  $\delta^{13}C_{C.wuell}$  values for marine isotope stages and glacial terminations.

Late MIS 1 (0-5 kyr BP)	Late MIS 1 (0-5 kyr BP)	Early MIS 1 (5-11.7 kyr BP)	Early MIS 1 (5-11.7 kyr BP)	MIS 5 (71-129 kyr BP)	MIS 5 (71-129 kyr BP)		
$Cd_{sw} \pm 1\sigma, n$ (nmol.kg <sup>-1</sup> )	$\delta^{13}C_{DIC} \pm 1\sigma, n$ (‰ VPDB)	$Cd_{sw} \pm 1\sigma, n$ (nmol.kg <sup>-1</sup> )	$\delta^{13}C_{DIC} \pm 1\sigma, n$ (‰ VPDB)	$Cd_{sw} \pm 1\sigma, n$ (nmol.kg <sup>-1</sup> )	$\delta^{13}C_{DIC} \pm 1\sigma, n$ (‰ VPDB)		
0.53±0.05, 7	0.75±0.05, 7	0.60±0.04, 16	0.57±0.13, 16	0.52±0.07, 31	0.44±0.15, 31		
MIS 2 (18-29 kyr BP)	MIS 2 (18-29 kyr BP)	MIS 3 (29-57 kyr BP)	MIS 3 (29-57 kyr BP)	MIS 4 (57-71 kyr BP)	MIS 4 (57-71 kyr BP)	MIS 6 (136-150 kyr BP)	MIS 6 (136-150 kyr BP)
$Cd_{sw} \pm 1\sigma, n$ (nmol.kg <sup>-1</sup> )	$\delta^{13}C_{DIC} \pm 1\sigma, n$ (‰ VPDB)	$Cd_{sw} \pm 1\sigma, n$ (nmol.kg <sup>-1</sup> )	$\delta^{13}C_{DIC} \pm 1\sigma, n$ (‰ VPDB)	$Cd_{sw} \pm 1\sigma, n$ (nmol.kg <sup>-1</sup> )	$\delta^{13}C_{DIC} \pm 1\sigma, n$ (‰ VPDB)	$Cd_{sw} \pm 1\sigma, n$ (nmol.kg <sup>-1</sup> )	$\delta^{13}C_{DIC} \pm 1\sigma, n$ (‰ VPDB)
0.45±0.04, 22	0.08±0.07, 22	0.49±0.06, 21	0.25±0.12, 21	0.45±0.05, 7	0.17±0.23, 7	0.54±0.05, 32	-0.22±0.09, 32
Termination I (11.7-18 kyr BP)	Termination I (11.7-18 kyr BP)	Termination II (129-136 kyr BP)	Termination II (129-136 kyr BP)				
$Cd_{sw} \pm 1\sigma, n$ (nmol.kg <sup>-1</sup> )	$\delta^{13}C_{DIC} \pm 1\sigma, n$ (‰ VPDB)	$Cd_{sw} \pm 1\sigma, n$ (nmol.kg <sup>-1</sup> )	$\delta^{13}C_{DIC} \pm 1\sigma, n$ (‰ VPDB)				
0.59±0.08, 16	0.25±0.17, 16	0.60±0.05, 17	0.08±0.18, 17				

**Table 4.2.** Published Holocene and LGM benthic  $\delta^{13}C$  and  $Cd_{sw}$  values for the Atlantic Ocean.

*North Atlantic (from 65°N to 41°N) published Holocene and LGM benthic  $\delta^{13}C$  (‰ VPDB) and  $Cd_{sw}$  (nmol.kg<sup>-1</sup>); from benthic Cd/Ca).*

Core	Lat. (°)	Long. (°)	Depth (m)	Hol. $\delta^{13}C$ (‰)	LGM $\delta^{13}C$ (‰)	Hol. $Cd_{sw}$ (nmol.kg <sup>-1</sup> )	LGM $Cd_{sw}$ (nmol.kg <sup>-1</sup> )	Ref.
NEAP-4K	61.48	-24.17	1627	1.5	1.5	0.35	0.28	15, 3
BOFS14K	58.62	-19.44	1756	1.02	1.4	0.37	0.17	1
V29-204	61.18	-23.02	1849	1.24	1.37	0.22	0.2	11
V28-14	64.78	-29.57	1855		1.13		0.24	3
BOFS11K	55.19	-20.35	2004	1.43	1.4	0.39	0.25	1
V28-73	57.18	-20.87	2063	1.17	1.16	0.57	0.3	11
ODP 980	55.48	-14.70	2168		0.82		0.24	11
M23414	53.54	-20.29	2196	1.12	1	0.37	0.4	17
V29-202	60.38	-20.97	2658	1.06	0.45	0.31	0.38	11
CHN82-20	43.50	-29.87	3070	1.3	0.76	0.26	0.36	3, 11
V29-179	44.00	-24.53	3331	1.1	0.63	0.31	0.37	3
CHN82-24	41.71	-32.85	3427	1.06	0.48	0.23	0.38	4

*Central Atlantic (from 41°N to 10°S) published Holocene and LGM benthic  $\delta^{13}\text{C}$  (‰ VPDB) and  $\text{Cd}_{\text{sw}}$  (nmol.kg<sup>-1</sup>; from benthic Cd/Ca).*

Core	Lat. (°)	Long. (°)	Depth (m)	Hol. $\delta^{13}\text{C}$ (‰)	LGM $\delta^{13}\text{C}$ (‰)	Hol. $\text{Cd}_{\text{sw}}$ (nmol.kg <sup>-1</sup> )	LGM $\text{Cd}_{\text{sw}}$ (nmol.kg <sup>-1</sup> )	Ref.
OC205-2-149JPC	26.26	-77.67	423	1.68	1.82	0.17	0.15	10
OC205-2-106GGC	25.98	-78.18	654	1.19	1.67	0.39	0.25	10
OC205-2-108GGC	25.98	-78.18	743	1.14	1.71	0.39	0.2	10
OC205-2-33GGC	26.22	-77.69	783	1.02	1.55	0.37	0.17	10
OC205-2-103GGC	26.07	-78.06	965	1.27	1.56	0.35	0.16	10
OC205-2-100GGC	26.06	-78.03	1057	1.4	1.5	0.36	0.28	14
SO75-26KL	37.82	-9.50	1099	1.02	1.6	0.36	0.19	17
OC205-2-97JPC	26.94	-77.85	1183	1.23	1.53	0.32	0.25	9
M35003	12.08	-61.25	1299	0.98	1.55	0.47	0.3	18
OC205-2-7JPC	26.14	-77.74	1320	1.3	1.37	0.37	0.19	10
M16004	29.98	-10.65	1512	1.03	1.1	0.22	0.3	17
KNR64-5	16.52	-74.80	1800	0.89	1.31	0.25	0.13	13
M12392	25.17	-16.83	2573		0.36		0.3	3
V22-174	10.07	-12.82	2630	0.8	0.72	0.34	0.36	3
M12328	21.00	-19.00	2778	0.92	0.27	0.29	0.42	2
KNR110-82	4.34	-43.49	2816		0.21		0.32	3
EN66-38	4.92	-20.50	2931	0.98	0.69	0.45	0.71	3
V30-49	18.43	-21.08	3093		0.21		0.56	3, 12
EN66-16	5.47	-21.13	3152	0.94	0.43	0.37	0.72	3
V22-197	14.17	-18.58	3167	0.49	0.17	0.39	0.39	3
BOFS31K	19.00	-20.00	3330	0.96	0.22	0.34	0.46	2
EN66-10	6.65	-21.90	3527	0.82	0.19	0.42	0.68	3
V30-40	0.20	-23.13	3706		-0.11		0.52	3
V25-59	1.37	-39.48	3824	1.03	0.07	0.26	0.45	3, 16
V26-176	36.00	-72.00	3942		0.18		0.32	3
BOFS29K	20.00	-21.00	4000	0.82	0	0.31	0.54	2
EN120-GGC1	33.67	-57.62	4450	0.33	-0.41	0.25	0.71	5
V23-100	22.68	-21.30	4579		0		0.52	3
BOFS28K	24.00	-22.00	4900	0.98	0.01	0.35	0.54	2
EN66-32	2.47	-19.73	5003	0.86	-0.32	0.34	0.48	3

*South Atlantic (south of 22°S) published Holocene and LGM benthic  $\delta^{13}\text{C}$  (‰ VPDB) and  $\text{Cd}_{\text{sw}}$  (nmol.kg<sup>-1</sup>; from benthic Cd/Ca).*

Core	Lat. (°)	Long. (°)	Depth (m)	Hol. $\delta^{13}\text{C}$ (‰)	LGM $\delta^{13}\text{C}$ (‰)	Hol. $\text{Cd}_{\text{sw}}$ (nmol.kg <sup>-1</sup> ) <sup>1)</sup>	LGM $\text{Cd}_{\text{sw}}$ (nmol.kg <sup>-1</sup> )	Ref.
KNR 159-5 14 GGC	-26.68	-46.44	441		1.05		0.22	8
KNR 159-5 137 GGC	-26.69	-46.34	462		1.31		0.15	8
KNR 159-5 10 GGC	-26.48	-45.93	630		1.03		0.23	8
KNR 159-5 99 GGC	-27.37	-46.84	790		0.5		0.29	8
KNR 159-5 153 JPC	-26.39	-45.69	898		0.46		0.37	8
KNR 159-5 38 JPC	-27.27	-46.63	936		0.52		0.51	8
KNR 159-5 90GGC	-27.35	-46.63	1105	1.27	0.38	0.41	0.61	7, 8, 13
KNR 159-5 105 JPC	-27.35	-46.63	1108	1.11	0.31	0.58	0.54	7, 8, 13
KNR 159-5 36 GGC	-27.25	-46.47	1268		0.59		0.42	8
KNR159-5 36 GGC	-27.25	-46.47	1268	1.14	0.56	0.5	0.4	6
KNR 159-5 95 JPC	-27.53	-46.55	1485		0.86		0.36	8
RC16-119	-27.70	-46.52	1567	1.1	0.99	0.41	0.29	6
KNR 159-5 17 JPC	-27.00	-46.49	1627		0.92		0.2	8
V24-253	-26.95	-44.68	2069	1.1	0.48	0.24	0.42	13
RC16-84	-26.70	-43.33	2438	1.08	0.56	0.21	0.47	13
KNR110-82	4.34	-43.49	2816		0.21		0.32	3
AII107-131	-30.88	-38.05	2925		0.85		0.36	3
V19-240	-30.58	-13.28	3103		0.02		0.56	3
RC13-228	-22.33	11.20	3204	0.5	-0.31	0.34	0.36	3, 16
RC12-294	-37.27	-10.10	3308	0.81	-0.23	0.44	0.51	3, 16
MD88-768*	-45.75	82.93	3330	0.51	-0.86	0.45	0.38	16
MD88-769*	-46.06	90.11	3420	0.33	-0.69	0.56	0.37	16
RC13-229	-25.50	11.33	4191	0.30	-0.36	0.49	0.5	3, 16

Reference details: (1) Bertram *et al.*, (1995); (2) Beveridge *et al.*, (1995); (3) Boyle, (1992); (4) Boyle and Keigwin (1985/86); (5) Boyle and Keigwin, (1987); (6) Came *et al.*, (2003); (7) Curry and Oppo, (2005); (8) Makou *et al.*, (2010); (9) Marchitto and Broecker (2006); (10) Marchitto *et al.*, (1998); (11) Marchitto *et al.*, (2002); (12) Martin and Lea, (1998); (13) Oppo and Horowitz (2000); (14) Oppo and Rosenthal (1994); (15) Rickaby *et al.*, (2000); (16) Rosenthal *et al.*, (1997); (17) Willamowski and Zahn, (2000); (18) Zahn, *et al.*, (1987).

**Table 4.3.**  $\delta^{13}\text{C}_{\text{DIC}}$  and  $\text{Cd}_{\text{sw}}$  values of modern and glacial Atlantic water mass endmembers.

Water mass	$\delta^{13}\text{C}_{\text{DIC}}$ $\pm 1\sigma$ , n (‰ VPDB)	Data source	$\text{Cd}_{\text{sw}} \pm 1\sigma$ , n (nmol.kg <sup>-1</sup> )	Data source	Refs
Modern					
NADW	0.98±0.09, 36	Atlantic GEOSECS Stations 60-50°N; 19°E-43°W; 1500- 3000 m water depth	0.24±0.02, 49	Geotraces GA02 64- 51°N; 46-34°W; 1500-4040km water depth	1, 2
AAIW	0.73±0.29, 10	Atlantic GEOSECS Stations 33-55°S; 21-55°W; 750-1100 m water depth	0.73±0.10, 31	Geotraces GA02, GPY4, GPY5 34- 55°N; 39°W-14°E; 750-1100 m depth	1, 2
AABW	0.55±0.16, 14	Atlantic GEOSECS Stations 45-60°S; 11°E-66°W; 4000- 6500 m water depth	0.75±0.02, 15	Geotraces GA02, GPY5 47-56°S; 47°W-4°E; 4000- 5800 m water depth	1, 2
Glacial					
NCW	1.75±0.20, 11	Benthic foraminif- eral isotope data from 20°–65°N; 1000–2000 m water depth	0.24±0.10, 12	Benthic foraminif- eral Cd/Ca data from 20°–65°N; 1000– 2000 m water depth	3-8
USCW	1.08±0.31, 4	Benthic foraminif- eral isotope data off Tasmania, 800-1500 m water depth	0.69±0.13, 4	Benthic foraminif- eral Cd/Ca data off Tasmania, 800-1500 m water depth	9
LSCW	-0.48 ±0.15, 8	Benthic foraminif- eral isotope data from Southern Ocean, >3000 m wa- ter depth	0.70±0.10	Data extrapolation of South Atlantic ben- thic foraminiferal Cd/Ca data	10, 8

Reference details: (1) Ostlund *et al.*, (1987), as compiled by Martinez-Mendez *et al.*, (2008); (2) Mawji *et al.*, (2015); (3) Boyle (1992); (4) Bertram *et al.*, (1995); (5) Willamowski and Zahn (2000); (6) Marchitto *et al.*, (1998); (7) Rickaby *et al.*, (2000); (8) Marchitto and Broecker (2006); (9) Lynch-Stieglitz *et al.*, (1996); (10) Ninnemann and Charles (2002).

The glacial  $Cd_{sw}-\delta^{13}C_{DIC}$  coordinates do not plot on the mixing line between NCW and LSCW (the latter being equivalent to AABW and LCDW in the modern ocean), but the mean values from the glacial sections in MD02-2588 are consistent with LGM cores from the deep central and South Atlantic (Fig. 4.4b). Despite the offset from the mixing line, the approximate mixing ratio between the NCW and LSCW glacial water mass end-members of 40%:60%, resembles the mixing conditions during the interglacial stages. The MIS 2 and MIS 4  $Cd_{sw}-\delta^{13}C_{DIC}$  coordinates are in close proximity to each other suggesting comparable bottom water conditions during these times. The slight vertical offset between MIS 2 and MIS 4 potentially arises from differences in the air-sea fractionation of  $\delta^{13}C$  and probably reflects slightly variable conditions at the site of water mass formation during these stages. This difference in air-sea fractionation of  $\delta^{13}C$  could be driven by variations in the temperature of equilibration during gas exchange between the ocean and atmosphere, differences in upper ocean stratification and/or reduced exchange due to differences in the extent of sea ice cover.

MIS 3 has a marginally higher  $\delta^{13}C_{DIC}$  value and a somewhat higher  $Cd_{sw}$  value relative to MIS 2 and MIS 4, but generally this lies within the same  $Cd_{sw}-\delta^{13}C_{DIC}$  cluster. MIS 6 on the other hand exhibits a more pronounced difference and plots closer to the LSCW end-member. The offset between MIS 6 and the MIS 2-4 cluster seems to be due to an increased nutrient concentration of the water mass bathing the site while the  $\delta^{13}C_{as}$  signature remains roughly constant. The glacial stages in MD02-2588 are generally characterised by  $\delta^{13}C_{as}$  values between -1.0 and -0.5‰, consistent with a stronger influence of a LSCW during the LGM (Marchitto and Broecker, 2006; Mackensen, 2012).

In figure 4.4c we plot the glacial  $Cd_{sw}-\delta^{13}C_{DIC}$  coordinates alongside interglacial coordinates to allow a clearer comparison of the differences between the two climate states. We also plot the  $\delta^{13}C_{as}$  isolines for both the Holocene and the glacial parameterisation.  $0.32\pm 0.20\%$  of the  $\delta^{13}C_{DIC}$  shift between the two climate states can be accounted for by glacial-interglacial changes in the global ocean carbon reservoir (Gebbie *et al.*, 2015).  $Cd_{sw}$  is slightly higher for the cluster of interglacial coordinates although overall the values during glacials and interglacials remain within the range observed for aged NADW in the modern ocean, i.e., 0.4-0.6 nmol kg<sup>-1</sup> (Mawji *et al.*, 2015). The highest  $Cd_{sw}$  values occur during the last two glacial terminations and during the late Holocene (Fig. 4.4c). TI and TII  $Cd_{sw}-\delta^{13}C_{DIC}$  coordinates plot on the

glacial mixing line between NCW and LSCW and are characterised by  $\delta^{13}\text{C}_{\text{as}}$  between  $\sim 0\text{‰}$  and  $\sim -0.5\text{‰}$  depending on whether the glacial or the Holocene parameterisation is applied. The resulting TI and TII coordinates stand out from both glacial and interglacial clusters suggesting that the conditions during these two transient climate events should be considered separately.

Examining the relationships between all the quantitative deep water proxy data from MD02-2588 reveals a clear distinction between glacial and interglacial conditions (Fig. 4.5). The higher  $\delta^{13}\text{C}_{\text{DIC}}$  and slightly higher  $\text{Cd}_{\text{sw}}$  recorded during in the Agulhas Plateau bottom waters during interglacial stages, coincides with positive values of  $\Delta[\text{CO}_3^{2-}]$  (i.e., waters oversaturated with respect to calcite) and decreasing trends of bottom water flow speeds. During glacial stages, the relatively low  $\delta^{13}\text{C}_{\text{DIC}}$  and  $\text{Cd}_{\text{sw}}$  coincided with the occurrence of negative values of  $\Delta[\text{CO}_3^{2-}]$  and increasing trends of bottom water flow speeds. During glacial terminations, the values of each of these parameters are generally intermediate between those that occur during glacial and interglacial stages (Fig. 4.5). The  $\text{Cd}_{\text{sw}}$  data is exceptional in this respect. Rather than observing intermediate values during glacial terminations,  $\text{Cd}_{\text{sw}}$  appears to peak during these transient events.

#### 4.6.6 Processes driving the glacial-interglacial variability of bottom waters on the Agulhas Plateau

The key observations arising from the  $\text{Cd}_{\text{sw}}-\delta^{13}\text{C}_{\text{DIC}}$  crossplots are the following: (i) both  $\text{Cd}_{\text{sw}}$  and  $\delta^{13}\text{C}_{\text{DIC}}$  values are lower during glacials relative to interglacials; (ii) the highest  $\text{Cd}_{\text{sw}}$  values are recorded during glacial terminations and (iii)  $\delta^{13}\text{C}_{\text{as}}$  is negative during glacial stages and positive during interglacial stages.

Assuming  $\text{Cd}_{\text{sw}}$  is a more conservative nutrient tracer than  $\delta^{13}\text{C}_{\text{DIC}}$ , the glacial-interglacial shift recorded in MD02-2588 suggests that  $\delta^{13}\text{C}_{\text{DIC}}$  is decoupled from nutrient stoichiometry (Boyle, 1988; Broecker and Maier-Reimer, 1992). Available estimates suggest that 0.3-0.4‰ of the total glacial-interglacial  $\delta^{13}\text{C}_{\text{DIC}}$  change is due to the transfer of carbon between the oceanic and terrestrial reservoirs (Shackleton, 1977; Curry *et al.*, 1988; Oliver *et al.*, 2010), but previous studies have shown that such changes cannot account for the total glacial-interglacial shift of 0.6-0.7‰ observed at MD02-2588 (Sigman and Boyle, 2000). The decoupling between  $\text{Cd}_{\text{sw}}$

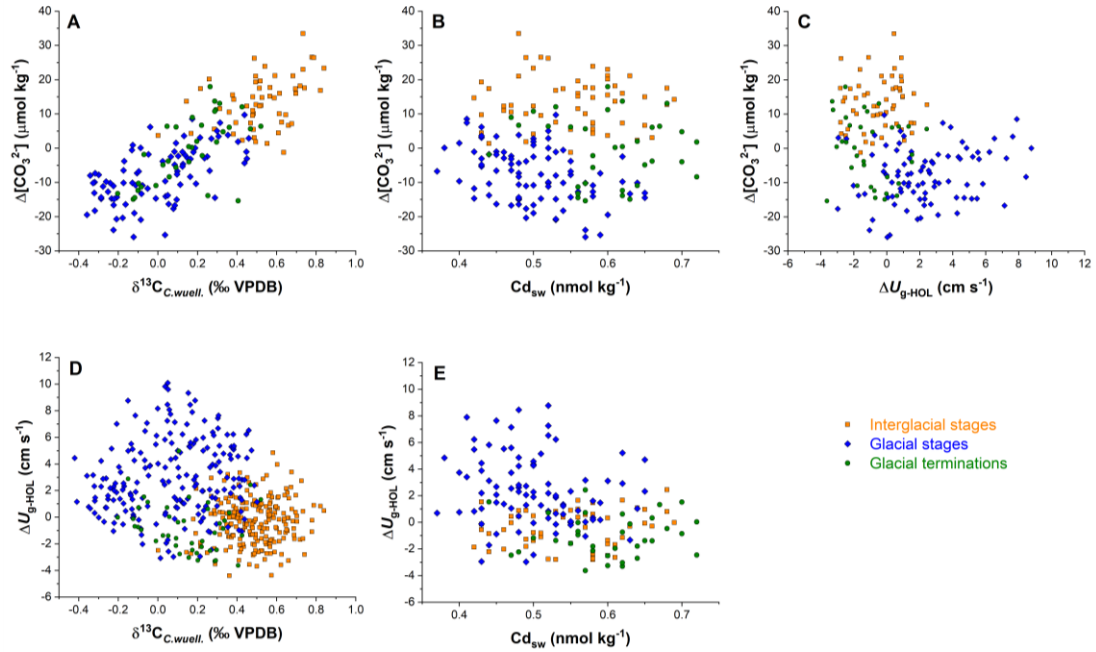


**Figure 4.5.** Proxy-proxy cross plots of data from sediment core MD02-2588. A) Bottom-water carbonate saturation state ( $\Delta[\text{CO}_3^{2-}]$ ) reconstructed using the B/Ca of *C. wuellerstorfi* ( $\text{B}/\text{Ca}_{C.wuell.}$ ) from MD02-2588 versus corresponding carbon isotopes also measured in *C. wuellerstorfi* ( $\delta^{13}\text{C}_{C.wuell.}$ ). B)  $\Delta[\text{CO}_3^{2-}]$  versus seawater Cd concentration ( $\text{Cd}_{sw}$ ) determined from the Cd/Ca ratio of *C. wuellerstorfi* samples. C)  $\Delta[\text{CO}_3^{2-}]$  versus change in geostrophic scalar flow speed relative to the Holocene ( $\Delta U_{g-HOL}$ ) estimated from the mean grain size of the 10-63  $\mu\text{m}$  size fraction of terrigenous material (sortable silt). D)  $\Delta U_{g-HOL}$  versus  $\delta^{13}\text{C}_{C.wuell.}$ . E)  $\Delta U_{g-HOL}$  versus  $\text{Cd}_{sw}$ . Data are divided into three age categories: data from interglacial marine isotope stages (i.e., MIS 1 and MIS 5, shown as orange squares), data from glacial marine isotope stages (i.e., MIS 2, MIS 3, MIS 6, shown as blue diamonds) and data from glacial terminations (i.e., TI and TII, shown as green circles). The age boundaries for each grouping are listed in table 4.1.

and  $\delta^{13}\text{C}_{\text{DIC}}$  is most likely caused by changes in air-sea gas exchange and the associated thermodynamic imprint on carbon isotope fractionation (Broecker and Maier-Reimer, 1992). During the LGM, NCW appears to have acquired a high  $\delta^{13}\text{C}_{\text{as}}$  signature due to increased air-sea gas exchange at cold temperatures (Lynch-Stieglitz and Fairbanks, 1994). LSCW on the other hand acquired a low  $\delta^{13}\text{C}_{\text{as}}$  signature as a consequence of reduced ventilation during its formation. This was most likely due to more extensive sea-ice cover around Antarctica during the LGM (Stephens and Keeling, 2000; Keeling and Stephens, 2001; Adkins *et al.*, 2002; Gersonde *et al.*, 2005). In addition, the higher  $\delta^{13}\text{C}_{\text{as}}$  NCW would have had a more limited effect on the LSCW  $\delta^{13}\text{C}_{\text{as}}$  signal as northern-sourced waters are not thought to have contributed significantly to the LSCW feed waters in the glacial ocean (Ninnemann and Charles, 2002; Lund *et al.*, 2011; Adkins, 2013). In sediment core MD02-2588, the  $\delta^{13}\text{C}_{\text{as}}$  value  $\sim -0.5\text{‰}$  observed during glacial stages (Fig. 4.2b) is in good agreement with the estimated LSCW end-member value of  $-0.75\text{‰}$  (Fig. 4.4b). It is also consistent with other LGM data from sediment cores in the deep Central and South Atlantic (Fig. 4.4b). The glacial  $\delta^{13}\text{C}_{\text{as}}$  estimates therefore would suggest that core site MD02-2588 was under greater influence of LSCW during these times. Interglacial  $\delta^{13}\text{C}_{\text{as}}$  values recorded in MD02-2588 are between  $\sim -0.25$  and  $0.25\text{‰}$ . This is approximately half-way between the NADW value of  $-0.5\text{‰}$  and the AABW value of  $0.5\text{‰}$  which suggests that during interglacial stages the core site is occupied by a mixture of these two water masses in roughly equal proportion.

The glacial-interglacial  $\text{Cd}_{\text{sw}}$  variability at MD02-2588 does not appear to be consistent with an interpretation of an admixture of NCW and LSCW bathing the site during interglacials and the dominance of LSCW during glacials. Though the difference in  $\text{Cd}_{\text{sw}}$  between glacial and interglacial stages is small relative to the range of  $\text{Cd}_{\text{sw}}$  observed in the modern ocean, there is nonetheless a definite shift toward lower  $\text{Cd}_{\text{sw}}$  values in the bottom waters bathing the Agulhas Plateau site during glacial stages (Fig. 4.2d and Fig. 4.4). This is contrary to observations from the deep northern and central Atlantic where a significant increase in  $\text{Cd}_{\text{sw}}$  is observed during the LGM due to the penetration of  $\text{Cd}_{\text{sw}}$ -rich LSCW into the northern reaches of the basin (Marchitto and Broecker, 2006). Conversely,  $\text{Cd}_{\text{sw}}$  data from the deep South Atlantic, although sparse, do not generally show a large glacial-interglacial difference, nor do they show

a consistent increase or decrease where data are available (Marchitto and Broecker, 2006).

This raises an important question: if the  $\delta^{13}\text{C}_{\text{as}}$  estimates from MD02-2588 point to a stronger glacial influence of LSCW at the site, why are  $\text{Cd}_{\text{sw}}$  values lower? We discuss two potential mechanisms that could explain this observation and attempt to reconcile the evidence.

The first mechanism involves a scenario that has already been elaborated by Rosenthal *et al.*, (1997) in light of observations from two sediment cores recovered from the southeast Indian Ridge. The LGM  $\text{Cd}_{\text{sw}}$  values from these two cores (MD88-768 and MD88-769, from 3330 m and 3420 m water depth, respectively; Fig. 4.3) are among the lowest of the deep glacial ocean, comparable with  $\text{Cd}_{\text{sw}}$  levels recorded above 2.5 km water depth in the Atlantic ( $\sim 0.4 \text{ nmol kg}^{-1}$ ) (Fig. 4.4b). This, however, is in contrast to their very low glacial  $\delta^{13}\text{C}_{\text{DIC}}$  ( $\sim -0.8 \text{ ‰}$ ) which consequently results in an extremely negative  $\delta^{13}\text{C}_{\text{as}}$  signature ( $\sim -1.75 \text{ ‰}$ ). Rosenthal *et al.*, (1997) proposed that these southeast Indian Ridge core sites were occupied by a nutrient-depleted deep water mass during the LGM which had a unique glacial mode of formation. Specifically, the authors argue that under glacial conditions, deep ocean convection in polynyas within the sea-ice zone may have been a more important mode of deep-water formation than it is today (Mackensen *et al.*, 1994, 1996). At present, deep waters originating from the Southern Ocean are enriched in nutrients as a result of the high nutrient concentrations of Antarctic surface waters. However, there is evidence, based on the nitrogen isotopic composition of diatoms, that nutrient concentrations were lower in the waters around Antarctica during glacial stages (Robinson and Sigman, 2008). This is consistent with the proposal that the southeast Indian Ridge sediment cores were bathed by a nutrient-depleted southern-sourced water mass during the LGM (Rosenthal *et al.*, 1997). It is therefore possible that these hypothetical deep waters, which would have formed by open ocean convection, could have also contributed to the mid-depth waters that fed the MD02-2588 core site on the Agulhas Plateau during glacial stages.

There are however two major complications with this hypothesis. As is acknowledged by Rosenthal *et al.*, (1997), the rate of production of this hypothetical nutrient-depleted glacial water mass would have been relatively low. It was therefore probably

only detectable close to the source, which Rosenthal *et al.*, (1997) suggest was somewhere within the southeast Indian sector of the Southern Ocean, although it is possible that there may have been multiple formation sites within and in front of the LGM circum-Antarctic sea-ice zone. Reconstructions of the sea ice distribution during the LGM suggest that the winter sea ice zone extended northward by an additional 10° of latitude (relative to its modern position) to reach approximately 50°S in the Indian Sector of the Southern Ocean (Gersonde *et al.*, 2005). The increased proximity of cores MD88-768 and MD88-769 (located at 45°S) to the northern edge of the winter sea ice zone during the LGM may indeed have brought these core sites under a stronger influence of a nutrient-depleted glacial water mass formed by open ocean convection in polynyas within the sea-ice zone (Rosenthal *et al.*, 1997). The main limitation of this hypothesis is whether a large enough volume of this water mass could have reached the Agulhas Plateau before its distinctive properties were lost through mixing in the ACC. This would especially be the case if the formation site (or sites) were indeed limited to locations downstream of the Agulhas Plateau. A further point against this mechanism is the large (~ 1‰) difference of the  $\delta^{13}\text{C}_{\text{as}}$  signatures between the southeast Indian Ridge cores and MD02-2588; it could, however, be argued that this discrepancy is due to a different end-member mixing model (e.g., between southeast Indian Ridge waters and LSCW; Fig. 4.4b). These limitations lead us to propose an alternative scenario to explain the glacial-interglacial  $\text{Cd}_{\text{sw}}$  variability in MD02-2588.

The volume of northern-sourced waters exiting the South Atlantic around southern Africa has likely waxed and waned throughout the glacial-interglacial cycles of the Late Pleistocene (e.g., Rutberg *et al.*, 2000). However, we propose that core site MD02-2588, which is presently located immediately downstream of the eastward-flowing NADW that exits the South Atlantic (e.g., Bailey and Rogers, 1997; Arhan *et al.*, 2003), has been under the continuous influence of northern-sourced waters for at least the past 150 kyr BP. The inferred  $\delta^{13}\text{C}_{\text{as}}$  estimates from MD02-2588 suggest a more dominant influence of the nutrient-rich LSCW during glacials, relative to the approximately 1:1 mixture of NCW-LSCW that occurs during interglacial stages (Fig. 4.4a). However, the lower  $\text{Cd}_{\text{sw}}$  values observed during glacial stages appear to contradict the above inference.

Mixing between northern and southern-sourced deep water masses is thought to have been dramatically reduced in the glacial ocean (Lund *et al.*, 2011). Part of this decrease has been attributed to thermodynamic processes that reduce mixing along isopycnals in the ocean interior (Lund *et al.*, 2011; Adkins, 2013). In addition, the shoaling of the glacial water mass boundary between NCW and LSCW may have reduced the mechanical mixing of these two water masses due to the diminished influence of the rough seafloor topography that is believed to be critical for mixing in the modern ocean (Polzin *et al.*, 1997; Ferrari *et al.*, 2014).

Despite the overall reduction of mixing in the glacial ocean interior, mixing between NCW and LSCW may not have abated completely. Though the glacial sections in MD02-2588 are characterised by a stronger influence of southern-sourced waters (based on  $\Delta[\text{CO}_3^{2-}]$  and  $\delta^{13}\text{C}_{\text{as}}$ ), this does not necessitate the presence of pure LSCW. As we have already pointed out, the glacial  $\text{Cd}_{\text{sw}}\text{-}\delta^{13}\text{C}_{\text{DIC}}$  coordinates in Fig. 4.4b are close enough to the mixing line between NCW and LSCW to support the idea that some mixing between these two water masses continued to take place. In fact, the location of the southern Agulhas Plateau, close to the northern boundary of the ACC, suggests that the site was occupied by a CDW-like water mass as opposed to pure LSCW. If the Southern Ocean fronts, and by extension the ACC, did indeed migrate northwards during glacial maxima, as is suggested by a suite of paleodata (see review by Kohfeld *et al.*, 2013), then the southern Agulhas Plateau would have likely come under an even greater influence of CDW. In addition, the more northerly position of the ACC would have potentially allowed greater entrainment and mixing of NCW into CDW along the frontal boundary. This, in turn, would increase the likelihood that northern-sourced waters would be traceable at the southern Agulhas Plateau.

In the modern ocean and during late MIS 1, where a NADW-like water mass bathes the MD02-2588 core site, the  $\text{Cd}_{\text{sw}}$  concentration is somewhat higher than the glacial values; compare for example the MIS 2 value of  $\sim 0.45 \text{ nmol kg}^{-1}$  with the modern value of  $\sim 0.53 \text{ nmol kg}^{-1}$  (Mawji *et al.*, 2015; Fig. 4.1, 4.2d, and 4.4). The available glacial  $\text{Cd}_{\text{sw}}$  data from depths shallower than 2500 m in the North and Central Atlantic indicate that the  $\text{Cd}_{\text{sw}}$  of NCW was lower than its modern equivalent (Marchitto and Broecker, 2006; Fig. 4.4). This could have been due to the occurrence of lower nutrient concentrations at the site of NCW formation and/or a decrease in the biogeochemical aging of this water mass along its southwards advection path (i.e., an enhancement

of NCW ventilation). Indeed,  $^{231}\text{Pa}/^{230}\text{Th}$  studies from the subtropical western and eastern Atlantic Ocean suggest that during the LGM, the NCW circulation above  $\sim 3000$  m water depth was characterised by a more vigorous overturning relative to the circulation of the Holocene (Gherardi *et al.*, 2009). We therefore propose that the implied reduction in the proportion of NCW bathing the southern Agulhas Plateau, was counterbalanced by the enhanced ventilation rate of the Atlantic Ocean above  $\sim 3$  km water depth. Therefore, the inferred increase in the relative volume of LSCW bathing the site, was compensated by the lower nutrient content of glacial NCW at water depths  $>3$ km.

Our proposed mechanism to explain the lower glacial  $\text{Cd}_{\text{sw}}$  at MD02-2588 is complementary to the mechanism of Rosenthal *et al.*, (1997). The continued incorporation of NCW into CDW in the Southern Ocean is likely to have partially contributed to the lower  $\text{Cd}_{\text{sw}}$  values observed on the southeast Indian Ridge. This would relax the requirement for a significantly nutrient depleted ‘open-ocean deep-water mass’. Equally, our mechanism does not exclude the possibility that the lower  $\text{Cd}_{\text{sw}}$  recorded on the Agulhas Plateau during glacial stages may have also been partly due to mixing with a nutrient-depleted deep water mass forming within the Antarctic sea-ice zone, particularly if this was a widespread mode of glacial deep water formation.

#### 4.6.7 *Interpretation of the glacial-interglacial bottom water variability on the Agulhas Plateau*

Geochemical reconstructions of the glacial Atlantic Ocean show increased storage of respired DIC and nutrients in the deep ocean below  $\sim 2.5$  km water depth, supporting the idea that the deep ocean became more isolated from the atmosphere during glacials (Boyle, 1988; Hodell *et al.*, 2003; Curry and Oppo, 2005; Marchitto and Broecker, 2006; Gebbie, 2014). Over the course of the deglaciation, changes in the Southern Ocean are proposed to have released trapped  $\text{CO}_2$  to the atmosphere (Martínez-Botí *et al.*, 2015) through a combination of diminished nutrient utilisation (Martin, 1990), increased vertical mixing (Toggweiler, 1999), and enhanced air-sea gas exchange (Stephens and Keeling, 2000). During deglaciations, the chemical stratification between the deep and intermediate depth ocean is thought to have weakened, allowing  $\text{CO}_2$  to be upwelled and released to the atmosphere. Though the exact cause of this chemical destratification remains uncertain, a number of mechanisms have been identified to explain it. One mechanism invokes an increase in air-sea gas exchange

through a reduction in sea-ice extent (Stephens and Keeling, 2000) and/or a reduction in surface ocean stratification (Francois *et al.*, 1997). A second mechanism suggests that destratification resulted from a decrease in the density difference between the poorly ventilated waters of the deep ocean (>2.5 km water depth) and the better-ventilated waters of the upper ocean (>2.5 km water depth) (Sigman *et al.*, 2010).

The bottom-water records of  $\Delta[\text{CO}_3^{2-}]$ ,  $\text{Cd}_{\text{sw}}$  and  $\delta^{13}\text{C}_{\text{DIC}}$  presented in this study, along with the previously published record of  $\delta^{13}\text{C}$  from the deep-dwelling planktonic foraminifera species *Globorotalia truncatulinoides (sinistral)* ( $\delta^{13}\text{C}_{G.\text{trunc.}(s)}$ ) - also measured in MD02-2588 (Ziegler *et al.*, 2013) - reveals a striking concurrence of events throughout the past 150 kyr BP (Fig. 4.6). The identification of two prominent carbon isotope minimum events (CIMEs) in the  $\delta^{13}\text{C}_{G.\text{trunc.}(s)}$  record of MD02-2588 during each of the last two glacial terminations (Ziegler *et al.*, 2013) is in agreement with the relatively widespread occurrence of such features in carbon isotopic records from the Indo-Pacific, sub-Antarctic, and South Atlantic (Spero and Lea, 2002). CIMEs during glacial terminations are thought to represent a response to the breakdown of surface water stratification, renewed CDW upwelling, and advection of low  $\delta^{13}\text{C}_{\text{DIC}}$  waters to the convergence zone at the SAF. These waters subsequently advect throughout the low-latitude Southern Hemisphere oceans, including the region overlying the Agulhas Plateau (Ziegler *et al.*, 2013). The CIMEs in MD02-2588 occur synchronous to significant changes in the bottom-water proxies presented in this chapter. Specifically, CIMEs coincide with bottom-water maxima of  $\text{Cd}_{\text{sw}}$  and increases in  $\Delta[\text{CO}_3^{2-}]$  and  $p\text{CO}_2$  (Fig. 4.6).

The almost concurrent incidence of  $\text{Cd}_{\text{sw}}$  maxima during CIMEs suggest a notable increase in the nutrient content of the waters bathing the MD02-2588 core site at these times;  $\text{Cd}_{\text{sw}}$  reaches values almost as high as  $0.7 \text{ nmol kg}^{-1}$ . In the modern Southern Ocean, such values are associated with CDW which forms by the mixing of northern and southern-sourced waters in the ACC (e.g., Orsi *et al.*, 1995); LCDW forms from mixing between AABW and NADW, whereas Upper CDW (UCDW) forms from mixing between AAIW and NADW (Orsi *et al.*, 1995). We have already argued that the glacial values of  $\text{Cd}_{\text{sw}}$  recorded on the southern Agulhas Plateau result from the continued –though diminished- influence of NCW that is has a lower nutrient content relative to modern NADW. The increase in  $\text{Cd}_{\text{sw}}$  during glacial terminations could therefore have resulted from one of two processes, or a combination

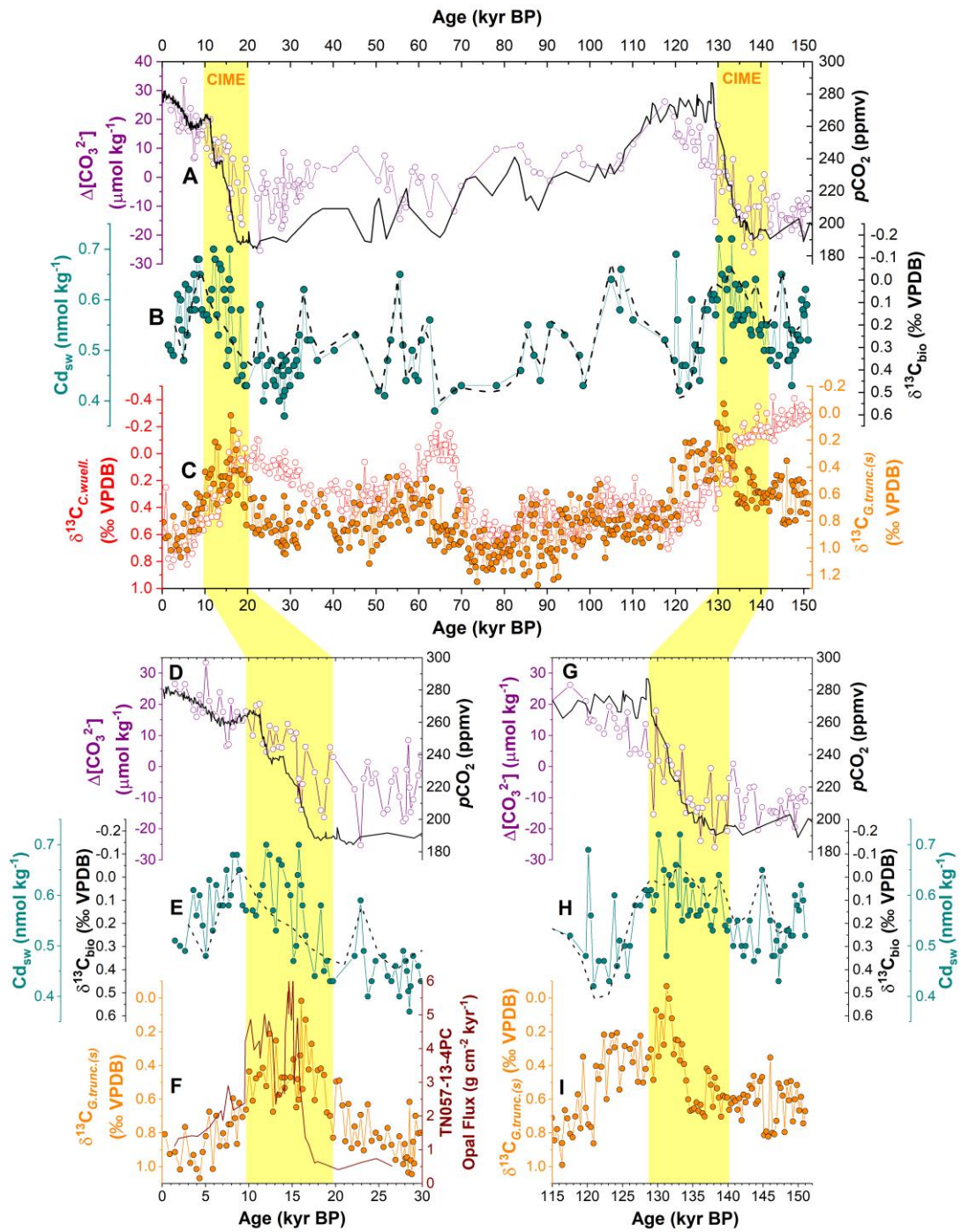


**Figure 4.6.** A) Downcore record of bottom-water carbonate saturation state ( $\Delta[\text{CO}_3^{2-}]$ ) reconstructed using the B/Ca of *C. wuellerstorfi* ( $\text{B/Ca}_{C.wuell.}$ ) from MD02-2588 (purple line, open circles). Also shown is the atmospheric  $p\text{CO}_2$  record from Antarctic ice cores (Monin *et al.*, 2001; Petit *et al.*, 1999; Pepin *et al.*, 2001) (black line). B) Seawater Cd concentration ( $\text{Cd}_{\text{sw}}$ ) determined from the Cd/Ca ratio of *C. wuellerstorfi* samples from MD02-2588 (cyan line with solid circles). Also shown is the biological component of the benthic foraminiferal  $\delta^{13}\text{C}$  record ( $\delta^{13}\text{C}_{\text{bio}}$ ) from MD02-2588 plotted on an inverted axis (black dashed line). See main text and chapter 3 for details. C) Downcore carbon isotope record measured in *C. wuellerstorfi* ( $\delta^{13}\text{C}_{C.wuell.}$ ), incorporating data from this study and Ziegler *et al.*, (2013) (red line, open circles), and corresponding record of  $\delta^{13}\text{C}$  measured in the deep-dwelling planktonic foraminifera *Globorotalia truncatulinoides (sinistral)* ( $\delta^{13}\text{C}_{G.trunc.(s)}$ ) in sediment core MD02-2588 (Ziegler *et al.*, 2013) (orange line, filled circles). Plots in the lower panels (i.e., D, E, F, G, H, I) display a more detailed view of the stratigraphic series for the intervals 0-30 kyr BP and 120-150 kyr BP, where the sampling resolution is higher than the rest of the core. Plot F also includes the opal flux record from sediment core TN057-13-4PC in the Atlantic sector of the Southern Ocean (53.2°S 5.1°E) plotted on its published age model. Vertical yellow bars indicate the carbon isotope minimum events (CIME) during Terminations I and II. The position of the two CIME are delineated according to  $\delta^{13}\text{C}_{G.trunc.(s)}$  minima in MD02-2588.

of these. First, mixing between northern and southern-sourced waters could have remained relatively stable during deglaciation, while the nutrient content of NCW increased as it evolved to increasingly resemble modern NADW. Alternatively, the MD02-2588 core site could have experienced a short-lived interval of increased mixing with high-nutrient bottom waters that had previously been isolated at abyssal depths in the Southern Ocean.

The first scenario could certainly have contributed to the increasing  $Cd_{sw}$  values during terminations as glacial NCW appears to have been as low as 0.2-0.3  $nmol\ kg^{-1}$  in the North and Central Atlantic, as opposed to NADW which has concentrations closer to 0.3-0.4  $nmol\ kg^{-1}$  (Fig. 4.4). Despite the deglacial increase in nutrient concentration of NCW, northern-sourced waters never approach the glacial termination values of 0.6-0.7  $nmol\ kg^{-1}$  (Fig. 4.4 and 4.6). We therefore suggest that a more likely scenario to explain the  $Cd_{sw}$  peaks during glacial terminations is that MD02-2588 was bathed by nutrient-rich bottom-waters that originated from the deepest and most isolated parts of the glacial Southern Ocean. At 2907 m water depth, core site MD02-2588 is located in an intermediate position relative to the nutrient-rich LSCW and the nutrient-poor NCW. The mid-depth waters in the South Atlantic sector of the Southern Ocean have been shown to have evolved differently from the deep waters in this basin during the Pleistocene (Hodell *et al.*, 2003). The records from the deepest sites exhibit large glacial-interglacial variations in benthic  $\delta^{13}C$  and are characterised by the lowest values of the entire glacial ocean. Though these extremely low glacial values are probably partly due to fractionation during air-sea gas exchange, it is still likely that a portion of the signal observed in abyssal benthic  $\delta^{13}C$  records reflects an increase in respired DIC and nutrients in the deep ocean (Hodell *et al.*, 2003).

In the modern Southern Ocean, the most Cd-rich waters are found in the deepest basins (Mawji *et al.*, 2015). This probably results from the accumulation of respired DIC and nutrients within very dense waters that are not easily mixed into the upper layers of LCDW. The accumulation of respired DIC and nutrients in deep basins is likely to have been exacerbated during glacials, where sedimentological and geochemical evidence indicate a slower overturning circulation in the southern deep cell (Hall and McCave, 2000; Gherardi *et al.*, 2009). Modelling results also suggest that deepwater ventilation in the Southern Ocean was reduced during the LGM (Toggweiler, 1999). We thus propose that the peaks in  $Cd_{sw}$  recorded during glacial terminations in MD02-

2588 are analogous to the CIMEs observed in the stratigraphic series of  $\delta^{13}\text{C}_{G.trunc.(s)}$ . As has already been stated, the CIMEs represents the expansion of deepwater ventilation and upwelling of  $\delta^{13}\text{C}_{\text{DIC}}$ -depleted water south of the APF in the postglacial ocean which then feed the intermediate-depth waters (500-1500 m water depth) of the Southern Hemisphere ocean (Spero and Lea, 2002; Anderson *et al.*, 2009). The resumption of more vigorous deepwater ventilation during glacial terminations, possibly linked to increased mixing of the ACC over the complex seafloor topography of the Southern Ocean (Garabato *et al.*, 2007), would have allowed respired DIC and nutrients from the deepest basins to be more effectively mixed into glacial LCDW. This could have consequently lead to the increases of  $\text{Cd}_{\text{sw}}$  concentration observed at sites such MD02-2588. The deglacial rise in  $\text{Cd}_{\text{sw}}$  in the southeast Indian Ridge cores (Rosenthal *et al.*, 1997) is also in agreement with this mechanism (Fig. 4.3), as is the slight increase in  $\text{Cd}_{\text{sw}}$  recorded in the deeper Cape Basin record (Oppo and Rosenthal, 1994) (Fig. 4.2); the more muted signal in the Cape Basin could be due to its more northerly location.

The mixing of these Cd- and respired DIC-rich bottom waters into LCDW during glacial terminations would explain the peaks in  $\text{Cd}_{\text{sw}}$  on the Agulhas Plateau site. Subsequent entrainment and eventual upwelling of these waters in the destratified Antarctic Zone of the Southern Ocean would lead to the carbon isotope minima that are observed in the  $\delta^{13}\text{C}_{G.trunc.(s)}$  record of MD02-2588 (Fig. 4.6c).

One of the limitations of this mechanism is the absence of notable CIMEs in the  $\delta^{13}\text{C}_{C.wuell}$  record of MD02-2588 (Fig. 4.6c). If the peak  $\text{Cd}_{\text{sw}}$  concentrations during glacial terminations do indeed represent the increased influence of high nutrient waters then we would also expect increased concentrations of respired DIC and associated minima in  $\delta^{13}\text{C}_{C.wuell}$ . What we see instead is a divergence of  $\text{Cd}_{\text{sw}}$  and  $\delta^{13}\text{C}_{C.wuell}$  and an associated abrupt increase in  $\delta^{13}\text{C}_{\text{as}}$  (Fig. 4.2b and 4.6). Even though a large component of the  $\delta^{13}\text{C}_{C.wuell}$  signal seems to be driven by changes in  $\delta^{13}\text{C}$  fractionation during air-sea gas exchange (Fig. 4.2b), the isolated biological component of  $\delta^{13}\text{C}_{C.wuell}$  ( $\delta^{13}\text{C}_{\text{bio}}$ ) does in fact indicate modest depletions of 0.2-0.35‰ associated with an increased concentration of respired DIC (Fig. 4.6b).

The increases in  $\text{Cd}_{\text{sw}}$  and corresponding decreases in  $\delta^{13}\text{C}_{\text{bio}}$  recorded during the CIMEs occur in tandem with increases in  $\Delta[\text{CO}_3^{2-}]$  on the southern Agulhas Plateau and

increases of  $p\text{CO}_2$  in Antarctic ice cores (Fig. 4.6). The covariation of these parameters supports the premise of increased outgassing of carbon from the deep Southern Ocean during deglaciations, as a result of the breakdown of stratification in the ocean interior (Sigman *et al.*, 2010). The decreases in  $\text{U}/\text{Mn}_{\text{C.wuell.-coat}}$  observed during deglaciations (Fig. 4.2) are also consistent with increased  $[\text{O}_2]$  in the waters bathing the southern Agulhas Plateau which suggests that the deep South Atlantic experienced an interval of enhanced ventilation.

#### 4.7 Conclusion

In this chapter, we present downcore records of stable isotopes and elemental ratios measured in benthic foraminifera, and the mean grain size of sortable silt from sediment core MD02-2588. These stratigraphic-series reconstruct the history of mid-depth ocean circulation on the southern Agulhas Plateau during the past 150 kyr BP. A multiproxy approach was applied to reconstruct and derive a range of physical and chemical bottom water parameters. These include the carbonate saturation state of seawater, the concentration of dissolved Cd in seawater, and relative changes in near-bottom flow speeds. Additionally, we isolate the various components that constitute the carbon isotopic composition preserved in benthic foraminifera and present a qualitative reconstruction of past sediment pore-water oxygen concentration. All stratigraphic series display prominent orbital modulation and where the sampling resolution is high enough, millennial-scale variability is also evident. However, no systematic correlation is identified between millennial-scale climate events and the high-frequency variability observed in the downcore record. Therefore, this chapter only discusses changes on glacial-interglacial timescales, with a particular focus on the last two deglaciations.

In broad terms, glacial stages are characterised by relatively low values of  $\Delta[\text{CO}_3^{2-}]$ ,  $\text{Cd}_{\text{sw}}$ ,  $\delta^{13}\text{C}_{\text{as}}$ , and  $[\text{O}_2]$ , while the  $\overline{\text{SS}}$  record indicates relatively high bottom-water flow speeds. During interglacials the situation is reversed, with relatively high values of  $\Delta[\text{CO}_3^{2-}]$ ,  $\text{Cd}_{\text{sw}}$ ,  $\delta^{13}\text{C}_{\text{as}}$ , and  $[\text{O}_2]$ , and slower bottom-water flow speeds. The higher sampling resolution of the elemental ratio records in the core sections that correspond to the last two deglaciations, allow additional complexities in the variability to be assessed.

We conclude that, during glacial stages, the southern Agulhas Plateau and the wider mid-depth South Atlantic Ocean came under increased influence of LSCW as the ACC shifted to a more equatorward position, in agreement with published geochemical evidence from the deep South Atlantic (Oppo *et al.*, 1990; Oppo and Rosenthal, 1994; Charles *et al.*, 1996; Ninnemann and Charles, 2002; Hodell *et al.*, 2003; Piotrowski *et al.*, 2005; Barker *et al.*, 2010; Skinner *et al.*, 2010; Burke and Robinson, 2012; Barker and Diz; 2014). The lower  $\Delta[\text{CO}_3^{2-}]$  suggests that the mid-depth South Atlantic experienced an increase in the storage of respired carbon, as  $\text{CO}_2$  was sequestered from the glacial atmosphere. Despite the inferred increase in the relative volume of LSCW bathing the Agulhas Plateau during glacial stages, the contribution of NCW is not thought to have diminished completely. In fact, the relative diminution in the relative volume of NCW bathing the MD02-2588 core site, appears to be counterbalanced by the lower nutrient content of northern-sourced water mass during glacial stages. The glacial lowering of seawater nutrient concentration in the mid-depth South Atlantic was possibly also affected by an increase in the formation of lower-nutrient mid-depth waters by open ocean convection in polynyas within the expanded circum-Antarctic sea ice zone. The recurrent  $\text{Cd}_{\text{sw}}$  maxima recorded during glacial terminations are interpreted as resulting from the upward mixing of nutrient-rich bottom waters from the deepest and most isolated waters in the Southern Ocean following the deglacial breakdown of stratification in the ocean interior. The increases in  $\text{Cd}_{\text{sw}}$  recorded during deglaciations occur in tandem with increases in  $\Delta[\text{CO}_3^{2-}]$  on the southern Agulhas Plateau and increases of  $p\text{CO}_2$  in Antarctic ice cores. The covariation of these parameters supports the premise of increased outgassing of carbon from the deep Southern Ocean during deglaciations. This interpretation is also consistent with the inference of increased  $[\text{O}_2]$  in the bottom waters of the southern Agulhas Plateau which suggests that, during deglaciations, the deep South Atlantic experienced transient episodes of enhanced ventilation.

---

## 5 Changes in upper ocean nutrient supply on the Agulhas Plateau linked to meridional migrations of the subtropical front during the past 150 kyr BP

---

### 5.1 Chapter outline

In this chapter, we examined how the position of the subtropical front (STF) within the Indian-Atlantic Ocean Gateway (I-AOG) migrated over the past 150 ky BP and considered how these changes may have impacted the nutrient supply to the surface waters of the southern Agulhas Plateau. The record of bulk sediment nitrogen isotope composition ( $\delta^{15}\text{N}_{\text{Bulk}}$ ) from sediment core MD02-2588 suggests that the northward migration of the STF during glacials is associated with increases in nutrient supply relative to interglacial levels. Enhanced nutrient supply to the surface waters of the southern Agulhas Plateau is thought to be due to increased northward advection of relatively nutrient-rich Subantarctic surface waters to the MD02-2588 core site, along with weaker upper ocean stratification which facilitated vertical mixing of nutrients from the thermocline. During interglacial intervals, when the STF was located further south, nutrient supply was lower. The lower nutrient levels observed during interglacial are thought to reflect reduced northward advection of Subantarctic surface waters relative to the advection of nutrient-poor Subtropical waters. In addition, the southward shift of the STF during interglacial stages may have reduced the vertical mixing of nutrients from the thermocline due to the enhanced upper ocean stratification that is characteristic of the subtropical zone.

The likeness of the  $\delta^{15}\text{N}_{\text{Bulk}}$  record from MD02-2588 with analogous records from the eastern equatorial Pacific (EEP) may suggest that the temporal variability of  $\delta^{15}\text{N}_{\text{nitrate}}$  within these two regions is linked on glacial-interglacial timescales. We suggest that the correlation of these records is due to independent responses to glacial-interglacial changes in the position of the Southern Ocean fronts. On the Agulhas Plateau, changes in the position of the STF determines the local nutrient supply, whereas in the EEP, changes in the position of the Southern Ocean fronts regulate the oxygen supply to the

eastern tropical Pacific oxygen minimum zone with in turn determines the level of denitrification.

## 5.2 Introduction

In the Indian-Atlantic Ocean Gateway (I-AOG), the STF represents the hydrographic boundary that separates the Southern Ocean waters from the warmer and saltier subtropical waters (Orsi *et al.*, 1995; Belkin and Gordon, 1996) (Fig. 5.1). South of the STF, the Antarctic Circumpolar Current (ACC), driven by the Southern Hemisphere westerly winds and steered by the Southern Ocean seafloor ridge system, flows as one continuous current around Antarctica with a total eastward transport of 100-130 Sv (1 Sv= $10^6 \text{ m}^3 \text{ s}^{-1}$ ) (Whitworth and Peterson, 1985; Cunningham *et al.*, 2003). Its flow is concentrated along a number of fronts characterised by enhanced meridional gradients of water properties that extend throughout the water column (Orsi *et al.*, 1995; Peterson and Stramma; 1991; Sokolov and Rintoul, 2002, 2009). To the north of the STF the circulation in the I-AOG is characterised by the Agulhas Current Retroflexion (Lutjeharms *et al.*, 2006) (Fig. 5.1). Here, the westward-flowing Agulhas Current detaches from the African continental shelf and, driven by its own inertia, retroflects back toward the Indian Ocean as the Agulhas Return Current (Lutjeharms and Van Ballegooyen, 1988; Peterson and Stramma, 1991). Instabilities in the retroflexion cause Agulhas Rings to spin off, carrying warm and saline waters into the South Atlantic as so called ‘Agulhas Leakage’, which is important for the transfer of water between the Indian and Atlantic Oceans (Gordon, 1986; Gordon *et al.*, 1992; de Ruijter *et al.*, 1999; Weijer *et al.*, 1999; Lutjeharms *et al.*, 2006).

Changes in the position of the STF have been suggested to play an important role in Agulhas Leakage with implications for global ocean circulation and climate variability on a range of timescales (Beal *et al.*, 2011). The reconstruction of the past position and dynamics of the STF within the I-AOG is therefore paramount to improving our understanding of Agulhas Leakage and its potential impact on climate change. Previous studies have revealed evidence of meridional migrations of the STF within this region on glacial-interglacial and millennial timescales (Flores *et al.*, 1999; Rau *et al.*, 2002; Peeters *et al.*, 2004; Bard and Rickaby, 2009; Martínez-Méndez *et al.*, 2010; Marino *et al.*, 2013; Simon *et al.*, 2013; Dyez *et al.*, 2014; Romero *et al.*, 2015). However, it still remains unclear what the implications of these migrations are

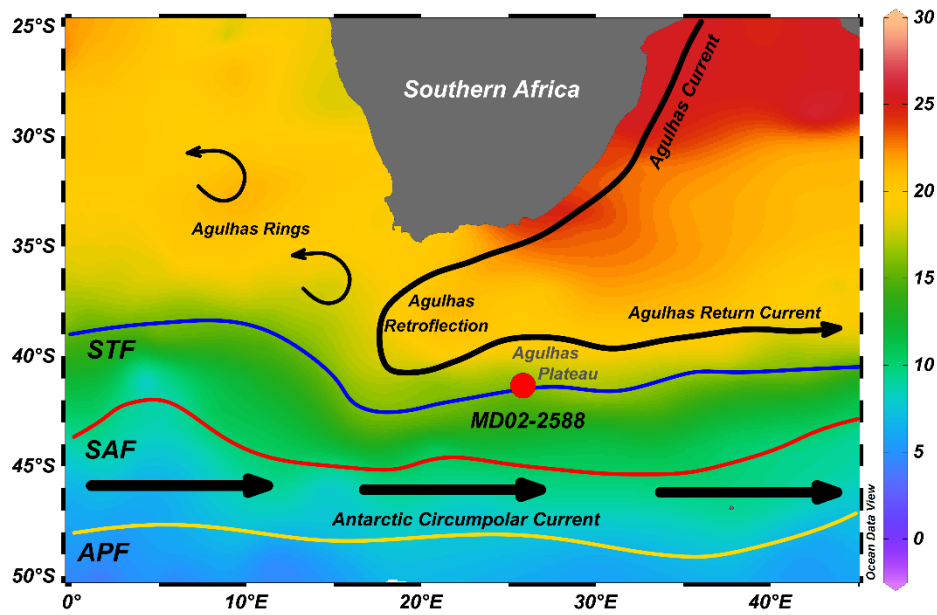


**Figure 5.1.** Modern sea surface temperature (SST) map showing the study area and the location of sediment core MD02-2588 on the southern Agulhas Plateau, together with the present day position of the Southern Ocean fronts and the generalised regional surface ocean circulation (Peterson and Stramma, 1991; Orsi *et al.*, 1995). Black continuous arrow shows the approximate pathway of the Agulhas Current along the African continental margin, the Agulhas Retroflection and the eastward flowing Agulhas Return Current, with Agulhas Rings in the South Atlantic. The thick black discontinuous arrows indicate the flow of the Antarctic Circumpolar Current (ACC). The blue, red and yellow lines show the approximate positions of the Subtropical Front (STF), the Subantarctic Front (SAF), and the Antarctic Polar Front (APF), respectively. The position of the sediment core MD02-2588 is indicated by the red circle. SST is in degrees Celsius. Map produced and edited in Ocean Data View (Schlitzer, 2016).

for the past variability of Agulhas Leakage, and consequences for the Atlantic meridional overturning circulation (AMOC).

Recent observational and modelling studies have suggested that the positions of the Southern Hemisphere westerly wind system may not be the main determinant of the position and dynamics of the STF (Graham and De Boer, 2013; De Boer *et al.*, 2013; Durgadoo *et al.*, 2013) which brings into question the theory that the latitude of the STF regulates the volume of Agulhas Leakage waters transported into the Atlantic Ocean. The uncertainty surrounding the importance of the westerlies and the position of the STF for Agulhas Leakage clearly demonstrates the need for continued analysis of observational data and ocean modelling experiments, and also highlights the potential for paleoceanographic studies to make a meaningful contribution to the resolution of this issue (Beal *et al.*, 2011).

In addition to the potential implications of changes in the position of the STF for Agulhas Leakage, the meridional migrations of the Southern Ocean fronts are also thought to impact the nutrient availability and biological productivity of the waters of the I-AOG. A survey of the Southwest Indian Ocean found that the distributions of nitrate, silicate and chlorophyll  $\alpha$  concentrations are strongly linked to the frontal and water mass structure of the I-AOG (Read *et al.*, 2000). Specifically, this survey showed that surface chlorophyll  $\alpha$  concentrations were elevated in the band of waters between the STF and the Subantarctic Front (SAF), but were low to the north and south of these two fronts. The low chlorophyll  $\alpha$  concentrations to the north of the STF were interpreted as being due to nitrate limitation (Fig. 5.2). In the region to the south of the SAF, silicate and nitrate were abundant and the surface layer was well-stratified, but the occurrence of low chlorophyll  $\alpha$  concentration was thought to suggest that biological productivity was limited, possibly due to low concentrations of Fe (e.g., Martin, 1990). The region in between the STF and SAF, where chlorophyll  $\alpha$  concentrations were at their highest, nitrate was found to be plentiful in the surface layer while silicate was depleted, suggesting that diatom growth must have been limited (Fig. 5.2). The low silicate concentration in the I-AOG probably arise as a consequence of the strong depletion of this nutrient south of the APF to the extent that little is left to be transported northwards across the SAF (Brzezinski *et al.*, 2002; Matsumoto *et al.*, 2002; Sarmiento *et al.*, 2004).

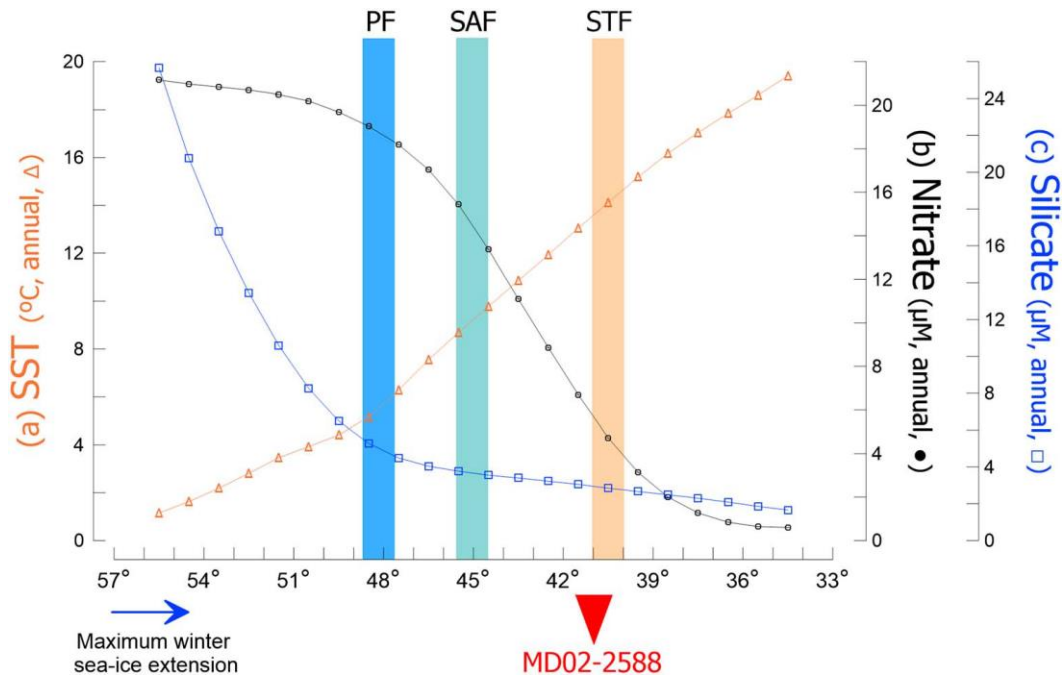


**Figure 5.2.** Modern, annual averaged latitudinal variability of sea surface temperature (SST) (orange line with triangle), nitrate (black line with circles) and silicate (blue line with squares) along 25°E in the Southern Ocean and the Indian-Atlantic Ocean Gateway between 57° and 33°S. Figure is taken from Romero *et al.*, (2015). Original data are from <http://iridl.ldeo.columbia.edu/SOURCES/.LEVITUS94/>. The blue arrow shows the maximum extension of the winter Antarctic sea ice cover between 23° and 27°E in the modern ocean. The inverted red triangle shows the location of the MD02-2588 core site. Also shown are the positions of the Subtropical Front (STF) (vertical orange bar), the Subantarctic Front (SAF) (vertical light blue bar) and the Antarctic Polar Front (PF) (vertical dark blue bar) (after Peterson and Stramma, 1991; Orsi *et al.*, 1995).

**Table 5.1.** Location of core sites referred to in Chapter 5.

Core	Latitude	Longitude	Water depth
<u>Indian-Atlantic Ocean Gateway sites</u>			
MD02-2588	41°19.9'S	25°49.7'E	2907 m
MD02-2589	41°26.0'S	25°15.3'E	2660 m
MD96-2077	33°10.1'S	31°14.8'E	3781 m
MD96-2080	36°19.2'S	19°28.2'E	2488 m
MD96-2081	35°35.0'S	17°41.0'E	3164 m
GeoB-3603-2	35°07.5'S	17°32.6'E	2840 m
ODP Site 1087	31°27.9'S	15°18.7'E	1371 m
PS2487-6	35°49.2'S	18°05.4'E	2950 m
<u>Eastern equatorial Pacific sites</u>			
ME0005A-24JC	0°01.3'N	86°27.8'W	2941 m
ME0005A-27JC	1°51.2'S	82°47.2'W	2203 m
TR163-19P	2°15.5'N	90°57.1'W	2348 m
TR163-31P	3°37.1'S	83°58.2'W	3205 m

Nutrient supply to the I-AOG occurs predominantly by the net northward transport of nutrient-rich surface waters from the Subantarctic and Polar Front Zones (SAZ and PFZ, respectively, where the former is the zone between the STF and SAF, and the latter is the zone between the SAF and APF) (Sigman *et al.*, 1999) as opposed to vertical nutrient supply from nutrient-rich subsurface waters such as Subantarctic Mode Water (SAMW) (e.g., Sarmiento *et al.*, 2004). As such, the nutrient supply and the biological productivity of this region is strongly linked to the position of the Southern Ocean fronts. Due to the prominent role of the Southern Ocean in the cycling of carbon between the ocean and the atmosphere, both at present and throughout the Pleistocene (see Section 1.3 of this thesis), it is vital that the interaction between the physical and biological processes operating in the wider region are mapped out and better understood. This chapter aims to address this question by examining how the position of the STF may have migrated over the past 150 ky BP and how these migrations may have impacted the nutrient supply to the I-AOG during this interval.

### 5.3 Previous work

The available evidence suggests that during the glacial stages of the late Pleistocene the STF was located further north in the I-AOG relative to its modern position. This is shown by fluctuations of coccolithophore and planktonic foraminifera assemblage data in sediment core PS2487-6 from the Agulhas Current Retroflexion area (35°49.2'S, 18°05.4'E, 2950 m depth; Table 5.1) (Flores *et al.*, 1999) and in sediment core MD96-2080 from the western flank of the Agulhas Bank (36°19.2'S, 19°28.2'E, 2488 m water depth; Table 5.1) (Rau *et al.*, 2002, 2006). Additional evidence for a more northerly position of the STF during glacials has come from SST reconstructions from foraminiferal Mg/Ca in MD96-2080 (Martínez-Méndez *et al.*, 2010) and from the  $U^{k}_{37}$  index in sediment core MD96-2077 (33°10'S, 31°15'E, 3781 m water depth; Table 5.1) (Bard and Rickaby, 2009). The record from MD96-2080 displays minimum SST at the onset of full-glacial conditions (i.e., at the beginning of Marine Isotope Stages (MIS) 2 and 6), followed by warming trends that continue into the ensuing interglacial stages (i.e., MIS 1 and 5, respectively). This has been suggested to indicate: (i) that the STF was at its northernmost position at the onset of full-glacial stages and (ii) that the Agulhas Bank SST warmed progressively throughout the glacial interval as the tropical/sub-tropical Agulhas waters became increasingly prevalent; this was possibly also com-

bined with a decreasing influence of cold Subantarctic surface waters due to a southward-migrating STF (Martínez-Méndez *et al.*, 2010). The  $U^{k'}_{37}$ -based SST record and marine productivity proxies in sediment core MD96-2077 indicate apparent northward shifts of the STF by up to  $7^\circ$  of latitude during the particularly intense glacials of MIS 10 and 12 (Bard and Rickaby, 2009). However, the continuous presence of the tropical/subtropical planktonic foraminifera species *Globorotalia menardii* in core MD96-2080 (Rau *et al.*, 2002, 2006) and at ODP Site 1087 ( $31^\circ 28'S$ ,  $15^\circ 19'E$ , 1371 m water depth; Table 5.1) in the southern Benguela region (Caley *et al.*, 2012) has been interpreted as suggesting that the exchange of water from the South Indian Ocean to the South Atlantic Ocean was never completely shut off during the past 1.3 million years (Myr) BP. This interpretation is corroborated by SST ( $U^{k'}_{37}$  index and dinoflagellate cyst assemblages) and sea surface salinity (SSS) reconstructions ( $\delta D$  of alkenones) from ODP Site 1087 (Petrick *et al.*, 2015).

The common feature seen in records from the I-AOG is the indication of less leakage during full glacial conditions compared to interglacial intervals and greatest leakage at glacial terminations. This is supported by the detailed foraminiferal assemblage work from the spliced Cape Basin record (CBR), constructed from sediment cores GeoB-3603-2 and MD96-2081 (retrieved from  $35^\circ 08'S$ ,  $17^\circ 33'E$ , 2840 m water depth and  $35^\circ 35'S$ ,  $17^\circ 41'E$ , 3164 m water depth, respectively; Table 5.1) in which a characteristic assemblages of planktonic foraminifera, termed Agulhas Leakage Fauna (ALF), was found to reach maximum proportions of the total assemblage during the past five glacial terminations (Peeters *et al.*, 2004). Quantitative estimates for the past 640 kyr BP suggest that Agulhas Leakage varied by  $\sim 10$  Sv during glacial-interglacial cycles, with maximum volume transport of 10-15 Sv occurring during glacial terminations (Caley *et al.*, 2014).

A number of previous studies have also examined how variations of the position of the STF in the I-AOG may have impacted the local nutrient supply and export productivity of the region. For example, the considerable fluctuations in the benthic foraminiferal assemblage composition over the last 150 kyr BP in sediment core MD02-2589 from the southern Agulhas Plateau ( $41^\circ 26.0'S$ ,  $25^\circ 15.3'E$ , 2660 m water depth) (Diz *et al.*, 2007). The variability of the foraminiferal assemblage in this core was interpreted as indicating changes in the supply of organic carbon to the seafloor in relation to changes in surface ocean productivity; increased delivery of organic matter to the ocean bottom

occurred during MIS 5.5 to MIS 5.3 and reduced delivery was observed during the glacial stages MIS 6, 4, 3 and 2 (Diz *et al.*, 2007). The intervals of greater organic matter supply to the seafloor observed in that study were interpreted as indicating northward migrations of the SAF and its confluence with the more stationary STF and Agulhas Front (associated with the Agulhas Return Current, Fig. 5.1). In support of this interpretation, Read *et al.*, (2000) suggest that, in the modern ocean, concentrations of chlorophyll *a* are elevated where the Agulhas Return Current, the STF, and the SAF are in close proximity, as this results in enhanced upwelling and cross-frontal leakage of nutrients.

Equally, reconstructions of biosiliceous productivity over the past 350 kyr BP from sediment core MD02-2588 reveal a clear glacial-interglacial cyclicality that has been interpreted as representing a response to changes in water mass dynamics, nutrient availability, and stratification of the upper ocean, all of which seem to be linked to the position of the STF over the Agulhas Plateau (Romero *et al.*, 2015).

Another example comes from the records of ocean productivity measured in sediment core MD96-2077 (Table 5.1). This record indicates that during cold stages, SST was up to 6°C cooler than its modern value and productivity at the core site peaked (Bard and Rickaby, 2009). As was mentioned previously, these data potentially indicate northward shifts of the STF by up to 7° of latitude during the particularly intense glacials of MIS 10 and 12. This not only leads to the observed severe cooling of the surface ocean, but also potentially increases the advection of the nutrient-rich surface waters from the PFZ and SAZ to the I-AOG.

#### **5.4 Materials and methods**

Full methodological details are given in Chapter 3. The following is a brief summary of the materials and methods relevant to the data presented in this chapter.

The CASQ (Calypso square-corer) sediment core MD02-2588 was recovered from a contourite drift located on the southwestern flank of the Agulhas Plateau (41°19.90'S, 25°49.40'E, 2907 m water depth) during RV Marion Dufresne cruise MD128 (Girardeau, 2002) (Fig. 5.1). The chronostratigraphic framework of sediment core MD02-2588 was developed by Ziegler *et al.*, (2013). Fifteen calibrated accelerator mass spectrometry (AMS) <sup>14</sup>C dates are used for constructing the age model between 0 and 40

kyr BP. For the remainder of the core, the age model is constructed by graphical correlation of the downcore record of benthic foraminiferal oxygen isotopes to the European Project for Ice Coring in Antarctica (EPICA) Dome C  $\delta D$  record (Jouzel *et al.*, 2007). See Ziegler *et al.*, 2013 and Section 3.2.1 of this thesis for more details.

In this chapter, we present downcore records of stable oxygen isotopes measured on the deep-dwelling planktonic foraminifera *G. truncatulinoides* (*s.*) ( $\delta^{18}O_{G.trunc(s)}$ ), a record of bulk sediment nitrogen isotope composition ( $\delta^{15}N_{Bulk}$ ) and a record of U/Mn ratios measured on samples of *G. truncatulinoides* (*s.*).

## 5.5 Results

### 5.5.1 Planktonic foraminiferal oxygen isotope record

The  $\delta^{18}O_{G.trunc(s)}$  displays a prominent orbital modulation with additional variability on millennial timescales (Fig. 5.3a). Values range between 1.0‰ and 4.2‰, with high  $\delta^{18}O_{G.trunc(s)}$  values occurring during glacial stages and low  $\delta^{18}O_{G.trunc(s)}$  values occurring during interglacial stages. Maximum recorded  $\delta^{18}O_{G.trunc(s)}$  during glacial stages MIS 2, 4 and 6 are 3.5‰, 4.2‰ and 3.3‰, respectively (Fig. 5.5a). Minimum recorded values during interglacial stages MIS 1 and 5.5 are 1.2‰ and 1.0‰, respectively. During MIS 3 and MIS 5.1 to 5.4, values are intermediate between the two climate extremes;  $\delta^{18}O_{G.trunc(s)}$  fluctuates between ~2‰ and ~3‰ during these intervals. The largest  $\delta^{18}O_{G.trunc(s)}$  shifts are observed during glacial to interglacial transitions with variations of 2.1‰ and 2.2‰, for the MIS 2/1 and MIS 6/5 transitions respectively. These major transitions in the  $\delta^{18}O_{G.trunc(s)}$  record during the last two glacial terminations (TI and TII) are well in excess of the mean ocean shift of 0.8-1.1‰ (Shrag *et al.*, 2002; Waelbroeck *et al.*, 2002). This indicates that in addition to global ice volume change, the isotopic composition of the deep-dwelling planktonic foraminifera at this site also include a component driven by changes in intermediate water temperature and/or local seawater  $\delta^{18}O$  values. During MIS 1 a continued decreasing trend is observed toward the top of the core. During MIS 5,  $\delta^{18}O_{G.trunc(s)}$  reaches a minimum value at peak interglacial conditions (MIS 5.5, at ~123 kyr BP) and then rises by ~1.6‰ over an approximately 10 kyr interval until at MIS 5.4 values reach similar levels to those of the preceding full-glacial (i.e., MIS 6). For the remainder of MIS 5, fluctuations of 0.5-1.0‰ are observed on 5-10 kyr timescales. Prominent shifts of 1.5‰ also occur during the transitions into and out of MIS 4 which occur

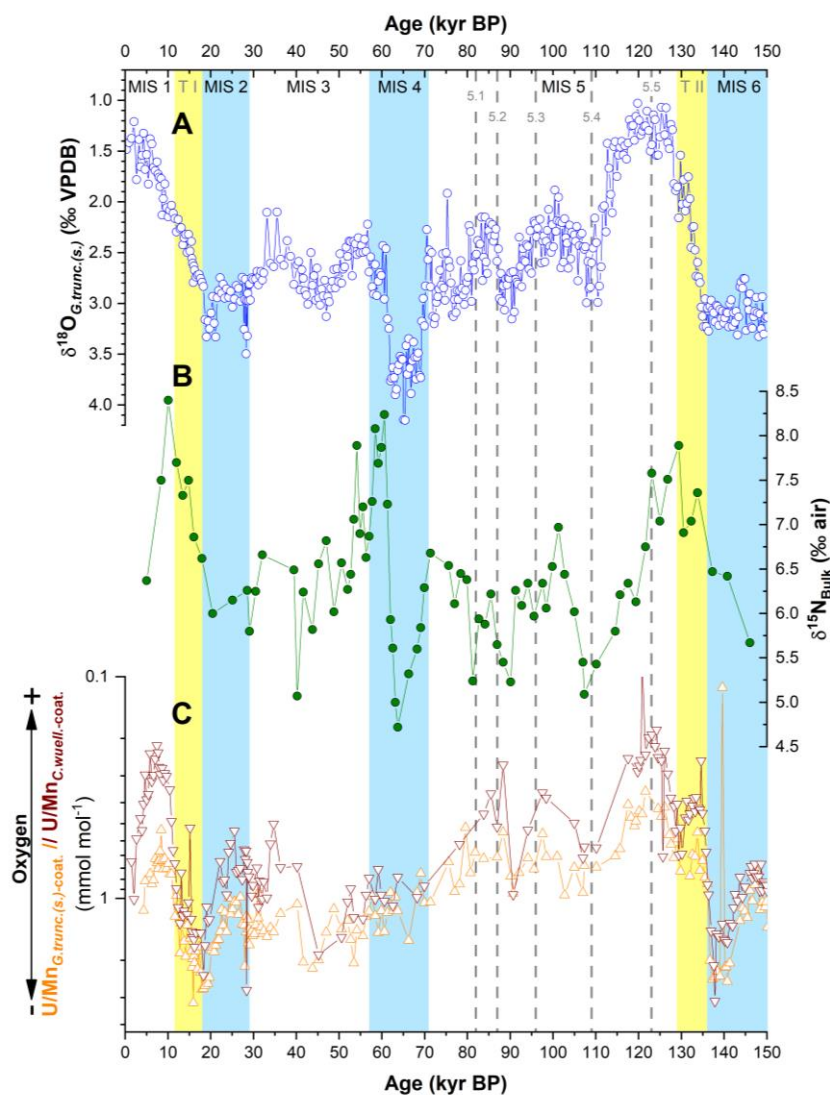


**Figure 5.3.** A) Oxygen isotope stratigraphic series from sediment core MD02-2588 generated from *Globorotalia truncatulinoides (sinistral)* ( $\delta^{18}\text{O}_{G.trunc(s)}$ ) which incorporates data from this study and from Ziegler *et al.*, (2013). Note inverted y-axis. VPDB is Vienna Pee Dee Belemnite. B) Bulk sediment nitrogen isotope ( $\delta^{15}\text{N}_{\text{Bulk}}$ ) stratigraphic series from MD02-2588 measured in per mille versus air. C) U/Mn of authigenic coatings on *G. truncatulinoides (s.)* ( $\text{U/Mn}_{G.trunc(s).-coat}$ ) (orange, upward-pointing triangles) and *C. wuellerstorfi* ( $\text{U/Mn}_{C.wuell.-coat}$ ) (red, downward-pointing triangles) from sediment core MD02-2588. U/Mn is Plotted on logarithmic scale with an inverted axis. Marine Isotope Stages (MIS) are taken from Lisiecki and Raymo, (2005). Glacial stages are shown with vertical blue bars; MIS 5 substage peaks are shown with the vertical grey dashed lines. Glacial terminations TI and TII are shown with vertical yellow bars and their ages are taken from Stern & Lisiecki, (2014) and Landais *et al*, (2013), respectively.

within a 1-2 kyr timeframe; this makes them two of the most abrupt large-amplitude fluctuations in the  $\delta^{18}\text{O}_{G.trunc(s)}$  record of the past 150 kyr BP. Superimposed on these orbital-timescale oscillations is a well-defined millennial-scale variability that is generally expressed as oscillations of  $\delta^{18}\text{O}_{G.trunc(s)} < 0.5\text{‰}$ . A number of shifts in the  $\delta^{18}\text{O}_{G.trunc(s)}$  record coincide with well-known millennial-timescale climate events but this relationship does not appear to be systematic. For example, the cold North Atlantic Heinrich Events (HE) (Hemming, 2004) which correspond to coeval warm Antarctic Isotope Maxima (AIM) events in the Southern Hemisphere ((EPICA, 2006), occur synchronous with some shifts in the  $\delta^{18}\text{O}_{G.trunc(s)}$  record; specifically, small ( $< 0.5\text{‰}$ ) negative excursions in  $\delta^{18}\text{O}_{G.trunc(s)}$  occur during HE 4, 5 and 6. This, however, does not appear to be the case for younger HEs, raising doubts about the consistency of this relationship (N.B.: HEs are not demarcated on figure 5.3).

#### 5.5.2 Bulk sediment nitrogen isotope record ( $\delta^{15}\text{N}_{Bulk}$ )

The downcore record of  $\delta^{15}\text{N}_{Bulk}$  along sediment core MD02-2588 ranges between a minimum value of 4.7‰, recorded during MIS 4, and a maximum value of 8.4‰, recorded during the early part of MIS 1 (Fig. 5.3b). Glacial to interglacial transitions are characterised by increasing trends, with  $\delta^{15}\text{N}_{Bulk}$  variations of 2.4‰, 3.5‰ and 2.2‰ for the 2/1, 4/3 and 6/5 MIS transitions, respectively. MIS 5 shows a  $\delta^{15}\text{N}_{Bulk}$  decrease of 2.8‰ between MIS 5.5 and MIS 5.4, before increasing to 6-7‰ during MIS 5.3. This is followed by smaller fluctuations between values of 5‰ and 6‰ for the remainder of MIS 5 on multi-millennial timescales (1-5 kyr); the low resolution of the  $\delta^{15}\text{N}_{Bulk}$  record does not allow the identification of higher frequency variability. The transition into MIS 4 is recorded by a drop in  $\delta^{15}\text{N}_{Bulk}$  from 6.7‰ at the MIS 5/4 boundary, to the lowest recorded value of 4.7‰ in the middle of MIS 4. This is followed by the largest increase in the record from the minimum value at ~64 kyr BP to 8.1‰ at ~60 kyr BP (i.e., close to the MIS 4/3 boundary). During MIS 3 multi-millennial oscillations of 0.5-1‰ are superimposed on the overall decreasing trend toward values of ~6‰ during MIS 2. As was noted above,  $\delta^{15}\text{N}_{Bulk}$  increases during the last deglaciation to reach its maximum value of 8.4‰ at the end of Termination I. Throughout MIS 1,  $\delta^{15}\text{N}_{Bulk}$  displays a ~2‰ decrease over an approximately 5 kyr timescale. The magnitude and timing of changes during the last deglaciation are almost identical to those recorded during the penultimate deglaciation, (i.e., the transition from MIS 6 to MIS 5).

### 5.5.3 U/Mn ratios of authigenic coatings on foraminiferal tests

The U/Mn ratio of the authigenic coatings on foraminifera has been proposed as an indicator of redox conditions in marine sediments (see Gottschalk *et al.*, 2016, Chen *et al.*, 2017, and discussion in section 3.9.6 of this thesis). The precipitation of authigenic uranium ( $U_{\text{authigenic}}$ ) as coatings on foraminifera occurs below the oxygen penetration depth in the sediment column where organic matter is consumed by iron and sulphate reduction (Cochran *et al.*, 1986; McManus *et al.*, 2005). Conversely, the precipitation of Mn coatings on foraminifera occurs when Mn is dissolved into pore waters under reductive sedimentary conditions (Boiteau *et al.*, 2012). As such, high U/Mn indicates low oxygen concentration in sediment pore waters and vice versa. The U/Mn ratios of authigenic coatings on foraminiferal tests from sediment core MD02-2588 can therefore be used as a qualitative indicator of relative changes in the sedimentary redox conditions at the core site.

As was specified in Chapter 3 of this thesis (section 3.9.6), the downcore records of U/Mn of authigenic coatings on *G. truncatulinoides* (*s.*) ( $U/Mn_{G.trunc.(s).-coat}$ ) and *C. wuellerstorfi* ( $U/Mn_{C.wuell.-coat}$ ) from sediment core MD02-2588 display almost identical patterns of variability and very similar values. The offset in values is possibly due to differences in the test morphology and chemistry of each species.

The late phases of MIS 2 and MIS 6 are characterised by the occurrence of  $U/Mn_{G.trunc.(s).-coat}$  and  $U/Mn_{C.wuell.-coat}$  (collectively referred to as  $U/Mn_{\text{foram-coat}}$ ) maxima, which are preceded by increasing trend throughout the glacial stages and followed by rapid (< 5 kyr) decreasing trends during the transitions to the respective interglacial stages. This suggests that pore water oxygen concentrations ( $[O_2]$ ) gradually decreased throughout MIS 2 and MIS 6 and reached their lowest values immediately prior to deglaciation. During the deglaciations, pore water  $[O_2]$  then increased rapidly and reached their highest levels during the early part of MIS 1 and during MIS 5.5, for each respective deglaciation. Subsequently,  $U/Mn_{\text{foram-coat}}$  increases throughout the remainder of MIS 1 and during the transition to MIS 5.4, respectively. This indicates that following the pore water  $[O_2]$  maxima, oxygen levels subsequently decreased.

In the less resolved section of the record (30-120 kyr BP), only the broad trends of  $U/Mn_{\text{foram-coat}}$  variability can be identified. MIS 5 is characterised by a series of fluctuations on 5-10 kyr timescales that are broadly aligned with the MIS 5 substages.

Between MIS 5.1 and the middle of MIS 3 the record displays a gradual increasing trend of  $U/Mn_{\text{foram-coat}}$ . No notable excursions are observed during the transition into and out of MIS 4. A further  $U/Mn_{\text{foram-coat}}$  maximum is reached during the middle of MIS 3, before subsequently increasing in the latter half of this glacial stage.

## 5.6 Discussion

### 5.6.1 Evidence for migration of the subtropical front over the Agulhas Plateau

The STF in the I-AOG is thought to have migrated northward by between  $4^\circ$  (Rau *et al.*, 2002) and  $7^\circ$  of latitude (Bard and Rickaby, 2009) during glacial stages. In this section, we examine the available evidence for meridional migrations of the STF over the southern Agulhas Plateau.

The records of  $\delta^{18}O_{G.trunc(s)}$  and the alkenone-based SST reconstruction from sediment core MD02-2588 (Romero *et al.*, 2014) reveal a striking similarity to the Antarctic ice core record of the isotopic composition of deuterium ( $\delta D$ ) (European Project for Ice Coring in Antarctica (EPICA) Dome C (EDC);  $75^\circ 06'S$ ,  $123^\circ 21'E$ ; 3,233 m above sea level) (EPICA, 2004) (Fig. 5.4). This may suggest that changes in the temperature of surface and intermediate waters over the Agulhas Plateau are interconnected with the glacial-interglacial climatic variations occurring on the Antarctic continent and in the wider Southern Ocean. However, a notable portion of the variability in the  $\delta^{18}O_{G.trunc(s)}$  record is likely due to global ice-volume changes.

The alkenone-based SST record on the other hand is unaffected by global ice-volume change and represents a more truthful indicator of relative temperature changes in the surface waters of the Agulhas Plateau. The overestimation of SST from the alkenone-based record may suggest that the material deposited at the MD02-2588 core site includes a proportion of alkenones that may have been advected from the subtropical waters of the south west Indian Ocean. In spite of the impact this may have on the reconstruction of absolute SST changes, the alkenone-based SST record nonetheless provides an excellent indication of migrations of the STF. The lower SSTs recorded during glacial stages represent either a direct lowering of local SST, or a decrease in the advection of subtropical-sourced alkenones (Fig. 5.4c). Equally, the higher SST recorded during interglacial stages represent either a direct increase of local SST, or an increase in the advection of subtropical-sourced alkenones (Fig. 5.4c). Either way,

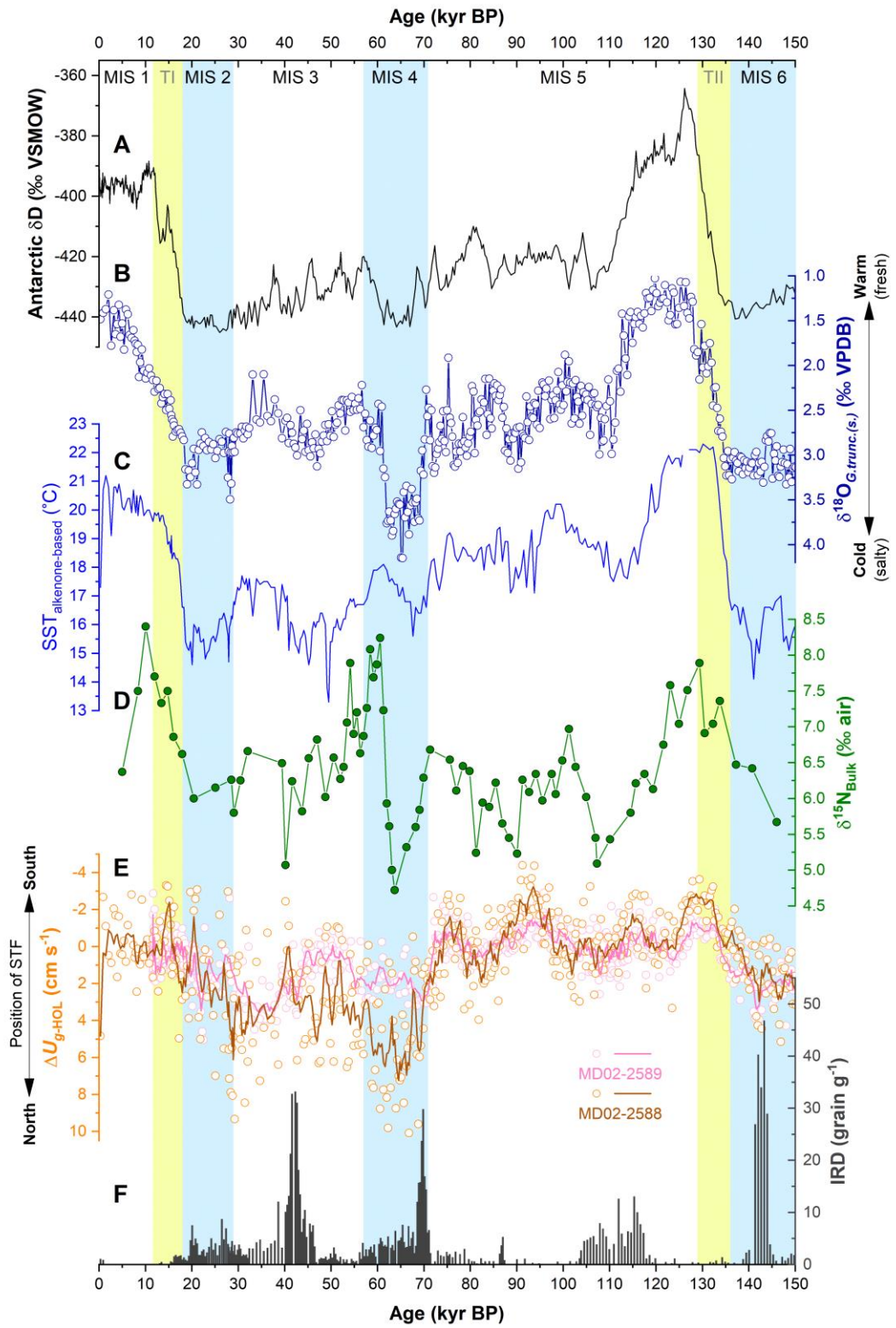


**Figure 5.4.** A) Antarctic record of the isotopic composition of deuterium ( $\delta D$ ) in ice versus Vienna Standard Mean Ocean Water (VSMOW) from the European Project for Ice Coring in Antarctica (EPICA) Dome C (EDC) (75°06' S, 123°21' E, 3233 m above sea level) (EPICA, 2004) (black line). B) Oxygen isotope stratigraphic series from sediment core MD02-2588 generated from *Globorotalia truncatulinoides* (*sinistral*) ( $\delta^{18}\text{O}_{G.trunc(s)}$ ) which incorporates data from this study and from Ziegler *et al.*, (2013) (dark blue line with open circles). C) Alkenone-based sea surface temperature (SST) from MD02-2588 (Romero *et al.*, 2015) (light blue line). D) Bulk sediment nitrogen isotope ( $\delta^{15}\text{N}_{\text{Bulk}}$ ) stratigraphic series from MD02-2588. E) Downcore record of change in geostrophic scalar flow speed relative to the Holocene ( $\Delta U_{g-HOL}$ ) estimated from the mean grain size of the 10-63  $\mu\text{m}$  size fraction of terrigenous material (sortable silt) from MD02-2588 (orange circles) and MD02-2589 (pink circles). 5-pt adjacent averaging smoothing filters were applied to each record (orange and pink lines for MD02-2588 and MD02-2589, respectively). Note inverted y-axis. F) Ice-rafted debris (IRD) in MD02-2588 (Marino *et al.*, 2013; Simon *et al.*, 2013) (grey bars). MD02-2588 records are plotted on the age model of Ziegler *et al.*, (2013); the  $\delta D$  record is plotted on its published scale (EPICA, 2004). Marine Isotope Stages (MIS) are taken from Lisiecki and Raymo, (2005). Glacial stages are shown with vertical blue bars; MIS 5 substage peaks are shown with the vertical grey dashed lines. Glacial terminations TI and TII are shown with vertical yellow bars and their ages are taken from Stern & Lisiecki, (2014) and Landais *et al.*, (2013), respectively.

the relative variations in the alkenone-based SST record are directly linked with meridional migrations of the STF.

The downcore records of sortable silt mean grain size ( $\overline{SS}$ ) from MD02-2588 and MD02-2589 were presented in chapters 3 and 4 of this thesis, and are used here as a qualitative indicator of relative meridional migrations of the ACC.  $\overline{SS}$  data were converted to bottom-water scalar geostrophic flow speeds ( $U_g$ ) using the relationship presented by McCave *et al.*, (2017). The records of  $U_g$  were subsequently normalised to the Holocene (0-11 kyr BP) level to produce stratigraphic series of  $\Delta U_g$  at the core sites relative to average Holocene  $U_g$  at each site (expressed as  $\Delta U_{g-HOL}$ ). This parameter is a convenient way of expressing the relative trends in the records and facilitates comparison between downcore records of  $\overline{SS}$ .

As was discussed in chapter 4 of this thesis, the downcore records of  $\Delta U_{g-HOL}$  from the southern Agulhas Plateau indicate a northward migration (or expansion) of the deep manifestation of the ACC during glacial stages. If this interpretation of the  $\Delta U_{g-HOL}$  is correct, it is reasonable to assume that the surface ocean fronts would have migrated in unison with the ACC, thus providing further evidence that the southern Agulhas Plateau came under a greater influence from Subantarctic waters during glacial stages (Fig. 5.4e). This is in agreement with observations from the modern ocean which indicate that the Southern Ocean fronts are characterised by enhanced meridional gradients of water properties that extend from the surface to the deep ocean (Orsi *et al.*, 1995; Sokolov and Rintoul, 2002, 2009).

Additional support for the northward expansion of Subantarctic waters during glacial stages has been provided by the MD02-2588 record of ice rafted debris (IRD) (Marino *et al.*, 2013; Simon *et al.*, 2013) that indicates episodes of enhanced IRD deposition coincident with intervals of relatively low SST (Fig. 5.4f). This is thought to reflect northward shifts of the regional oceanic fronts as a result of pronounced northward advection of polar waters during circum-Antarctic cold phases (Pahnke *et al.*, 2003). These cold phases are thought to have allowed icebergs to be transported as far north as the location of MD02-2588 at  $\sim 41^\circ S$  (Marino *et al.*, 2013; Simon *et al.*, 2013).

Though the trends in downcore records of SST,  $\Delta U_{g-HOL}$  and IRD concentration from sediment core MD02-2588 are in broad agreement regarding glacial-interglacial vari-

ations, the relationships are not linear nor do the fluctuations always occur synchronously (Fig. 5.4f). Each proxy record is affected by several processes that are not expected to operate consistently throughout the duration of the record. However, by examining the various lines of evidence presented above, and taking the published literature into consideration (e.g., MARGO, 2009; Kohfeld *et al.*, 2013), it is reasonable to interpret the downcore records from MD02-2588 as representing a response to migrations of the Southern Ocean fronts on glacial-interglacial timescales. The trends in the downcore record of  $\delta^{15}\text{N}_{\text{Bulk}}$  from MD02-2588 indicate that nutrient utilisation in the surface waters of the Agulhas Plateau co-varied with the expansion and contraction of Subantarctic waters on orbital timescales throughout the past 150 kyr BP.

### 5.6.2 Nutrient utilisation in the surface waters of the southern Agulhas Plateau

As well as determining the temperature variability of the waters overlying the southern Agulhas Plateau, the meridional migrations of the STF are also expected to have influenced the supply of nutrients to the surface ocean with important implications for local export production. The MD02-2588 core site is currently located very close to the modern position of the STF (Fig. 5.1). The more northerly position of this front during glacial stages is likely to have led to a shift to more Subantarctic-like conditions at the core site, with higher nutrient concentrations and a reduction of upper ocean stratification (Flores *et al.*, 1999; Rau *et al.*, 2002; Peeters *et al.*, 2004; Bard and Rickaby, 2009; Martínez-Méndez *et al.*, 2010; Marino *et al.*, 2013; Simon *et al.*, 2013; Dyez *et al.*, 2014; Romero *et al.*, 2015). Mixed layer depths (MLD) between 45°S and 60°S in the modern Southern Ocean are very deep and display a strong seasonal cycle. MLD varies between 300 m in winter and 70 m in summer; north of the STF, the MLD is notably shallower (Rintoul and Trull, 2001; de Boyer Montégut *et al.*, 2004). To this end, the  $\delta^{15}\text{N}_{\text{Bulk}}$  record from MD02-2588 can be used as a proxy of local nutrient utilisation to assess how the meridional migrations of the STF impacted the nutrient supply to the surface waters overlying the southern Agulhas Plateau during the past 150 kyr BP.

#### 5.6.2.1 Factors influencing the $\delta^{15}\text{N}_{\text{Bulk}}$ record in sediment core MD02-2588

As with all sedimentary records of  $\delta^{15}\text{N}_{\text{Bulk}}$ , the record from MD02-2588 represents a response to a combination of processes which determine the isotopic composition of nitrate ( $\delta^{15}\text{N}_{\text{nitrate}}$ ). These processes include: i) changes in the mean ocean isotopic

composition of nitrate ( $\delta^{15}\text{N}_{\text{MO}}$ ), ii) changes in regional  $^{15}\text{N}$  depletion or enrichment relative to  $\delta^{15}\text{N}_{\text{MO}}$ , iii) changes in the completeness of nitrate consumption in the local surface layer, and iv) post depositional alteration of organic matter (Galbraith *et al.*, 2008; Robinson *et al.*, 2012). Unfortunately, the global background signal linked to changes in  $\delta^{15}\text{N}_{\text{MO}}$  has not yet been resolved and cannot be explicitly accounted for in the  $\delta^{15}\text{N}_{\text{Bulk}}$  record from MD02-2588. To simplify the discussion of the  $\delta^{15}\text{N}_{\text{Bulk}}$  record from MD02-2588, we assume that changes in  $\delta^{15}\text{N}_{\text{MO}}$  have a negligible effect. Indeed, the small glacial-interglacial difference observed in many records of  $\delta^{15}\text{N}_{\text{Bulk}}$  (<0.5‰) from various ocean basins (e.g., Huon *et al.*, (2002) in the North Atlantic; François *et al.*, (1997) in the southern Indian Ocean and Horikawa *et al.*, (2006) in the Sulu Sea) has been proposed to imply that  $\delta^{15}\text{N}_{\text{MO}}$  did not vary significantly between glacials and interglacials despite very large variations in other parameters of the climate system on these timescales (Lisiecki and Raymo, 2005).

On the contrary, regional-scale effects, driven principally by changes in nitrate consumption in the SAZ are likely to have had a more notable impact on the  $\delta^{15}\text{N}_{\text{Bulk}}$  record from MD02-2588. The available evidence suggests that export production in the SAZ was higher during glacials relative to interglacials (Mortlock *et al.*, 1991; Kumar *et al.*, 1995; Chase *et al.*, 2003; Martínez-García *et al.*, 2014) whereas in the Antarctic Zone, the opposite is true, with lower export production during the LGM relative to the Holocene (François *et al.*, 1997; Kohfeld *et al.*, 2005). Despite the differences in export production between the Antarctic and Subantarctic zones,  $\delta^{15}\text{N}_{\text{Bulk}}$  records generally indicate higher values during the LGM in both zones which implies that nutrient utilisation increased throughout the entire Southern Ocean (François *et al.*, 1997; Kohfeld *et al.*, 2005). Downcore records of  $\delta^{15}\text{N}_{\text{Bulk}}$  are consistent with records of diatom-bound and planktonic foraminifera-bound  $\delta^{15}\text{N}$  ( $\delta^{15}\text{N}_{\text{DB}}$  and  $\delta^{15}\text{N}_{\text{FB}}$ , respectively) from the Antarctic (Sigman *et al.*, 1999; Crosta and Shemesh, 2002; Robinson *et al.*, 2004; Robinson and Sigman, 2008) and the Subantarctic (Crosta *et al.*, 2005; Robinson *et al.*, 2005; Martínez-García *et al.*, 2014). These microfossil-bound  $\delta^{15}\text{N}$  records are believed to be less susceptible to diagenetic alteration and therefore provide support for the use  $\delta^{15}\text{N}_{\text{Bulk}}$  as a nutrient utilisation proxy (Robinson *et al.*, 2012). The occurrence of elevated values of  $\delta^{15}\text{N}_{\text{nitrate}}$  in the Antarctic Zone during glacials, when export production was lower, has led to the suggestion that this zone was more strongly stratified during these times. This would have limited the supply of

nitrate from the deep ocean to the surface waters and would have resulted in more complete consumption of the available nutrients (François *et al.*, 1997). In the SAZ, the elevated  $\delta^{15}\text{N}_{\text{nitrate}}$  values recorded during glacials occur alongside increased deposition of opal and alkenones, and higher dust flux. Higher nutrient utilisation in SAZ during glacials is therefore interpreted as resulting from increased export production, possibly linked to enhanced iron supply from terrestrial dust sources (Ziegler *et al.*, 2013; Lamy *et al.*, 2014; Martínez-García *et al.*, 2014).

Glacial-interglacial and sub-orbital variations of nutrient utilisation in the surface waters of the Southern Ocean are therefore believed to determine the  $\delta^{15}\text{N}_{\text{nitrate}}$  of Subantarctic waters. These waters are subsequently advected northwards and entrained into intermediate and mode waters (principally SAMW) and their  $\delta^{15}\text{N}_{\text{nitrate}}$  signature is propagated throughout the entire Southern Hemisphere (e.g., Sarmiento *et al.*, 2004; Dubois *et al.*, 2011). These regional-scale processes are likely to constitute a key component of the signal recorded in the record of  $\delta^{15}\text{N}_{\text{Bulk}}$  from MD02-2588.

In addition to the regional-scale signals originating from the Antarctic and Subantarctic zones, local effects, driven by changes in the completeness of nitrate consumption in the surface mixed-layer over the Agulhas Plateau, are also likely to contribute to the downcore variations of  $\delta^{15}\text{N}_{\text{Bulk}}$  recorded in MD02-2588. Changes in local nutrient utilisation are most likely associated with variations in local export production and the supply of nutrients to the surface mixed-layer over the Agulhas Plateau.

As was alluded to above, the supply of nutrients to the surface waters of the Agulhas Plateau is determined by the balance between the advection of nutrient-rich Subantarctic surface waters from the south and advection of nutrient-poor Subtropical waters from the north which is regulated by meridional migrations of the STF on glacial-interglacial and shorter timescales (Flores *et al.*, 1999; Rau *et al.*, 2002; Peeters *et al.*, 2004; Bard and Rickaby, 2009; Martínez-Méndez *et al.*, 2010; Marino *et al.*, 2013; Simon *et al.*, 2013; Dyez *et al.*, 2014; Romero *et al.*, 2015). In addition, variations in upper ocean stratification (i.e., MLD) will determine the supply of nutrients from thermocline waters. An equatorward shift of the STF, would result in an increase of the MLD over the southern Agulhas Plateau (i.e. a weaker upper ocean stratification) and vice versa for a poleward shift of the front (de Boyer Montégut *et al.*, 2004). Weaker stratification would in turn cause an increase in the supply of nutrients from the thermocline.

All else being equal (e.g., export production, nutrient stoichiometry), a more equatorward position of the STF is expected to lead to a greater concentration of nutrients in the surface waters of the Agulhas Plateau by increasing the lateral advection of Subantarctic waters and causing a deepening of the MLD. This would cause a decrease in surface water  $\delta^{15}\text{N}_{\text{nitrate}}$  and  $\delta^{15}\text{N}_{\text{Bulk}}$ . On the contrary, a more poleward position of the STF would tend to limit lateral advection of Subantarctic waters and reduce the MLD. This, in turn, would lead to conditions similar to those that characterise the modern ocean over the core site, with relatively low nutrient concentrations in surface waters and an increase in relative nutrient utilisation. Under such conditions, surface water  $\delta^{15}\text{N}_{\text{nitrate}}$  and  $\delta^{15}\text{N}_{\text{Bulk}}$  are expected to increase.

Finally, it is important to consider the potential impact of diagenetic processes on the  $\delta^{15}\text{N}_{\text{Bulk}}$  record in sediment core MD02-2588. Comparisons of diatom-bound (Robinson *et al.*, 2005) and foram-bound (Martínez-García *et al.*, 2014)  $\delta^{15}\text{N}$  with  $\delta^{15}\text{N}_{\text{Bulk}}$  from the SAZ suggest that the downcore isotopic variability of  $\delta^{15}\text{N}_{\text{Bulk}}$  could be compromised by diagenetic alteration. The ‘diagenetic offset’ between microfossil-bound  $\delta^{15}\text{N}$  and  $\delta^{15}\text{N}_{\text{Bulk}}$  revealed in the downcore records from the SAZ are presumed to be a consequence of isotopic fractionation during the degradation of bulk organic matter in deep sea sediments (Altabet and François; Robinson *et al.*, 2012). Under conditions of higher N content and N burial flux, the diagenetic effect appears to be smaller. Under such condition, the  $\delta^{15}\text{N}$  of bulk sediment closely matches the isotopic composition of N exported from the surface ocean (Martínez-García *et al.*, 2014). Essentially, the diagenetic offset is lower in sediments with higher organic matter burial rates where the organic matter reaching the seafloor undergoes less degradation (Robinson *et al.*, 2012). The implication for the  $\delta^{15}\text{N}_{\text{Bulk}}$  from sediment core MD02-2588 is that the nutrient utilisation signal associated with the processes described above may be overprinted by diagenetic effects. Indeed,  $\delta^{15}\text{N}_{\text{Bulk}}$  records from open ocean settings such the Agulhas Plateau are more susceptible to these overprints and the results from the microfossil-bound  $\delta^{15}\text{N}$  from the SAZ suggest that  $\delta^{15}\text{N}_{\text{Bulk}}$  should be interpreted with caution (Robinson *et al.*, 2005; Martínez-García *et al.*, 2014). As such, the glacial-interglacial changes of  $\delta^{15}\text{N}_{\text{Bulk}}$  in sediment core MD02-2588 probably indicate maximum estimates of surface ocean nutrient utilisation variations.

#### 5.6.2.2 Interpretation of the $\delta^{15}\text{N}_{\text{Bulk}}$ record from sediment core MD02-2588

Taking the above regional and local controlling factors into account, we now attempt to interpret the  $\delta^{15}\text{N}_{\text{Bulk}}$  record in sediment core MD02-2588 (Fig. 5.5). We first consider the evidence of glacial-interglacial changes at the regional scale and the implications this has for the nutrient content and  $\delta^{15}\text{N}_{\text{nitrate}}$  in the surface waters of the southern Agulhas Plateau. This includes the contribution from laterally-advected Subantarctic surface waters and from vertically-mixed thermocline waters (Sigman *et al.*, 1999).

The lower vertical nutrient supply in the Antarctic Zone during glacials and the concurrent increase in dust-mediated export production in the SAZ (Ziegler *et al.*, 2013; Martínez-García *et al.*, 2014) would have resulted in an overall decrease of Southern Ocean surface water nutrient concentrations and an increase of  $\delta^{15}\text{N}_{\text{nitrate}}$  relative to interglacial levels (Fig. 5.5a and 5.5b). These waters would have subsequently been incorporated into SAMW and distributed throughout the thermocline waters of the Southern Hemisphere (Robinson and Sigman, 2008). Despite the overall lower nutrient content and higher  $\delta^{15}\text{N}_{\text{nitrate}}$  of the Antarctic and Subantarctic waters during glacials, nutrient utilisation in the waters overlying the Agulhas Plateau appears to have decreased; that is to say, a lower proportion of nutrients were consumed relative to the amount that was supplied (Fig. 5.5d). The lower glacial  $\delta^{15}\text{N}_{\text{Bulk}}$  in MD02-2588 therefore suggest that a mechanism was in operation that countered the effect of the increased source water  $\delta^{15}\text{N}_{\text{nitrate}}$ . The surface waters of the southern Agulhas Plateau must therefore have experienced either a decrease in local export production or an increase in nutrient supply (or a combination of the two) relative to interglacial values.

Productivity proxies from sediment core MD02-2588 reveal that export production on the southern Agulhas Plateau was higher during the full-glacial stages of the past 350 kyr BP, relative to interglacial levels (Romero *et al.*, 2015). This has been demonstrated by higher abundance of *Chaetoceros* resting spores, relatively higher percentage weights of bulk biogenic silica and total organic carbon (TOC), and higher total concentrations of diatoms (Romero *et al.*, 2015) (Fig. 5.5c). The more extensive sea ice cover in the Antarctic Zone during glacials relative to interglacials (Gersonde *et al.*, 2003, 2005; Crosta *et al.*, 2004) is believed to have impeded diatom productivity and Si consumption in that region, thus facilitating increased leakage of unutilised silicic acid ( $\text{H}_4\text{SiO}_4$ ) out of the Antarctic Zone and consequently increasing silicic acid concentration in the surface waters of the SAZ and in SAMW (Brzezinski *et al.*, 2002;

Matsumoto *et al.*, 2002; Sarmiento *et al.*, 2004). The increased biosiliceous productivity on the southern Agulhas Plateau during glacials has therefore been interpreted as a response to a greater supply of silicon (Si) from southern-sourced waters, enabled by the more northerly position of the STF in the I-AOG (Romero *et al.*, 2015). The concurrent alleviation of iron-limitation due to enhanced glacial dust fluxes in the wider SAZ (Martínez-García *et al.*, 2014) appears to have allowed diatoms living in the surface waters of the southern Agulhas Plateau to take maximum advantage of the relatively Si-rich waters from the south and from the thermocline (Romero *et al.*, 2015).

If the rate of nutrient supply to the surface waters of the Agulhas Plateau remained constant, the enhanced glacial biosiliceous productivity observed at the MD02-2588 core site would have caused an increase in the  $\delta^{15}\text{N}_{\text{nitrate}}$  of surface waters. The occurrence of lower values of  $\delta^{15}\text{N}_{\text{Bulk}}$  in sediment core MD02-2588 during glacials therefore suggests that the supply of nutrients to the surface waters overlying the site must have increased. The increase in the supply of nutrients must have been high enough to counteract the effects of higher export production on the southern Agulhas Plateau and increased sourced water  $\delta^{15}\text{N}_{\text{nitrate}}$ . In agreement with Romero *et al.*, (2015), we suggest that the increased nutrient supply during glacials was a consequence of the more northward position of the Southern Ocean fronts. This would have enabled increased northward advection of relatively nutrient-rich Antarctic and Subantarctic surface waters to the MD02-2588 core site whilst the weaker upper ocean stratification expected from the northward migration of these fronts would have increased the supply of nutrients from the thermocline.

A caveat to this interpretation is that the downcore records of  $\delta^{15}\text{N}_{\text{Bulk}}$  and percentage weight TOC, appear similar to the corresponding records of foraminiferal U/Mn (Fig. 5.5e). The downcore variability of TOC is broadly in agreement with the productivity proxies from this core (i.e., *Chaetoceros* resting spores, percentage weight of bulk biogenic silica); intervals of higher surface ocean productivity correlate with higher

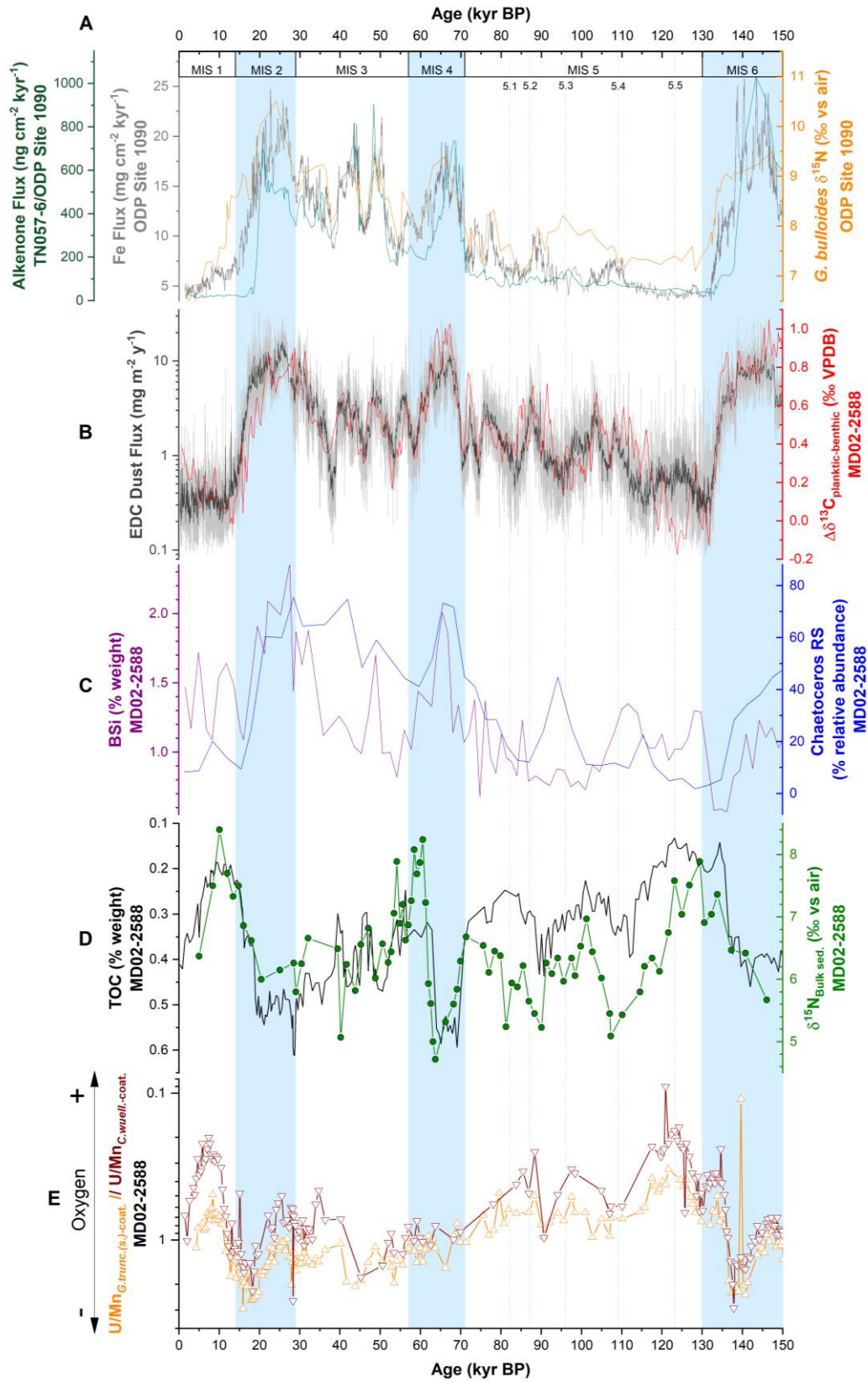


**Figure 5.5.** A)  $^{230}\text{Th}$ -normalized iron flux (grey line) and foraminifera-bound nitrogen isotopes ( $\delta^{15}\text{N}$ ) measured in the planktonic species *Globigerina bulloides* (orange line) from ODP Site 1090 (Martínez-García *et al.*, 2014).  $^{230}\text{Th}$ -normalized alkenone flux from TN057-6 (0 to 90 kyr BP) and ODP Site 1090 (90 to 160 kyr BP) (dark-green line). Data are from Sachs and Anderson, (2003) and Martínez-García *et al.*, (2014). B) Carbon isotope gradient between planktonic and benthic foraminifera ( $\Delta\delta^{13}\text{C}_{\text{plankton-benthic}}$ ) (red line with circles) measured in *Globorotalia truncatulinoides* (*sinistral*) and *Cibicidoides wuellerstorfi* in sediment core MD02-2588 which incorporates data from this study and Ziegler *et al.*, (2013). Also plotted is the European Project for Ice Coring in Antarctica (EPICA) Dome C (EDC) record of dust flux (light-grey line) with a with a 100-pt smoothing filter (equivalent to  $\sim 1$  kyr) using the adjacent averaging method (dark-grey line) (Lambert *et al.*, 2012). C) Concentration (% weight) of biogenic silica (BSi) (blue line) and relative abundance (%) of *Chaetoceros* resting spores from MD02-2588 (Romero *et al.*, 2015). D) Concentration (% weight) of total organic carbon (black line) (Romero *et al.*, 2015) and bulk sedimentary nitrogen isotopic composition ( $\delta^{15}\text{N}_{\text{Bulk}}$ ) (green line with filled circles) measured in MD02-2588. E) U/Mn of authigenic coatings on *G. truncatulinoides* (*s.*) ( $\text{U/Mn}_{G.\text{trunc}(s.).\text{-coat}}$ ) (orange, upward-pointing triangles) and *C. wuellerstorfi* ( $\text{U/Mn}_{C.\text{wuell.}\text{-coat}}$ ) (red, downward-pointing triangles) from sediment core MD02-2588. U/Mn is Plotted on logarithmic scale with an inverted axis. Marine Isotope Stages (MIS) are taken from Lisiecki and Raymo, (2005). Glacial stages are shown with vertical blue bars; MIS 5 substage peaks are shown with the vertical blue dashed lines. Glacial terminations TI and TII are shown with vertical yellow bars and their ages are taken from Stern & Lisiecki, (2014) and Landais *et al.*, (2013), respectively.

percentage weight of TOC, and vice versa. However, the occurrence of a symmetrical anti-correlation between  $\delta^{15}\text{N}_{\text{Bulk}}$  and TOC, and the similarity of these records with parts of the U/Mn series, raises the possibility that  $\delta^{15}\text{N}_{\text{Bulk}}$  has undergone a degree of post-depositional alteration. Higher pore-water  $[\text{O}_2]$ , inferred from low U/Mn, would lead to preferential degradation of isotopically-light organic matter and would result in an increase of  $\delta^{15}\text{N}_{\text{Bulk}}$ . In contrast, lower pore-water  $[\text{O}_2]$  would promote increased preservation of isotopically-light organic matter and would, therefore, result in a relative decrease of  $\delta^{15}\text{N}_{\text{Bulk}}$ .

The relationship observed between the downcore variability of  $\delta^{15}\text{N}_{\text{Bulk}}$  and the corresponding records of foraminiferal U/Mn reveals that, during certain intervals, this interpretation may be valid. The trends in  $\delta^{15}\text{N}_{\text{Bulk}}$  and U/Mn are comparable during the MIS 6/5 and MIS 2/1 intervals, but differ during MIS 4 and MIS 3 (Fig. 5.5e). The large variations of  $\delta^{15}\text{N}_{\text{Bulk}}$  observed during the transition into and out of MIS 4, occur in the absence of comparable changes in the records of U/Mn. This would suggest that the downcore variability of  $\delta^{15}\text{N}_{\text{Bulk}}$  is certainly not exclusively driven by post-depositional alteration. In fact, the covariation of  $\delta^{15}\text{N}_{\text{Bulk}}$  and U/Mn during deglaciations may be coincidental. The increase in pore-water  $[\text{O}_2]$  observed during deglaciations may result from reduced delivery of organic carbon to the seafloor, linked to the deglacial decline in export production at the MD02-2588 core site. A decrease in the deposition of organic carbon on the seafloor would reduce seafloor oxygen consumption, allowing pore-water  $[\text{O}_2]$  to increase. Such changes are likely to have occurred in tandem with the meridional migrations of the STF, and therefore, the correlation observed between  $\delta^{15}\text{N}_{\text{Bulk}}$  and U/Mn during deglaciations may simply reflect the common timing of changes in surface ocean nutrient supply and export production associated with the meridional migrations of the STF, as was discussed above. Nonetheless, it is clear that the interpretation of the downcore record of  $\delta^{15}\text{N}_{\text{Bulk}}$  as a nutrient utilisation proxy requires verification. The generation of a corresponding record of microfossil-bound  $\delta^{15}\text{N}$  from sediment core MD02-2588 will be particularly useful.

### 5.6.3 *Links between downcore $\delta^{15}\text{N}_{\text{Bulk}}$ variation on the Agulhas Plateau and the eastern equatorial Pacific*

The resemblance of the  $\delta^{15}\text{N}_{\text{Bulk}}$  record from sediment core MD02-2588 to analogous records from the eastern equatorial Pacific (EEP) (Table 5.1; Fig. 5.6) provides assurance that post-depositional processes on the seafloor of the southern Agulhas Plateau

may not have lead to significant alteration of downcore  $\delta^{15}\text{N}_{\text{Bulk}}$ . The likeness of the EEP records to the  $\delta^{15}\text{N}_{\text{Bulk}}$  record from MD02-2588 may suggest that the temporal variability of  $\delta^{15}\text{N}_{\text{nitrate}}$  within these two disparate regions is linked (Dubois *et al.*, 2011; Dubois and Kienast, 2011). The glacial-interglacial variability of the  $\delta^{15}\text{N}_{\text{Bulk}}$  records from the EEP has been interpreted as resulting from variations in the denitrification rates in the nearby oxygen minimum zones (OMZ) of the tropical eastern Pacific. Changes in denitrification are thought to have been determined by the variable supply of dissolved oxygen to intermediate depths; that is to say that the rates of denitrification fluctuated as a response to changes in the oxygen content of southern-sourced intermediate water (i.e., SAMW), rather than being due to in-situ oxygen consumption during the oxidation of sinking organic matter (Dubois *et al.*, 2011). However, differences between the four EEP records of  $\delta^{15}\text{N}_{\text{Bulk}}$ , especially during warmer intervals, have been suggested to indicate that additional local-scale changes also impact these records; these local effects are probably linked to variable patterns of upwelling and spatial shifts in surface nitrate utilization (Dubois and Kienast, 2011). For example, the positive offset of the northernmost site (core TR163-19, blue line in Fig. 5.6; Table 5.1) relative to the other three cores in the collection from the EEP (i.e., ME0005A-24JC, ME0005A-27JC and TR163-31P; Fig. 5.6; Table 5.1) is indicative of a greater degree of nitrate consumption due to its more distal location from the main zone of equatorial upwelling (Fig. 5.6) (Dubois and Kienast, 2011). It is interesting to note that the values of  $\delta^{15}\text{N}_{\text{Bulk}}$  recorded in MD02-2588 are also higher than those recorded in the three EEP cores from within the equatorial upwelling zone, indicating that nutrient utilisation – as a volumetric proportion of the supply of nutrients - was relatively higher in the surface waters of the southern Agulhas Plateau throughout the past 150 kyr BP.

Regardless of these local effects, the similarity of the temporal variability of the  $\delta^{15}\text{N}_{\text{Bulk}}$  record from the Agulhas Plateau with those from the EEP suggest that the two regions may be linked in one way or another on glacial-interglacial timescales. As has already been argued, in the absence of significant post-depositional alteration, the  $\delta^{15}\text{N}_{\text{Bulk}}$  record from MD02-2588 is thought to principally respond to changes in the supply of nutrients brought about by latitudinal shifts of the Southern Ocean fronts. The EEP records. On the other hand, are thought to respond to variations in

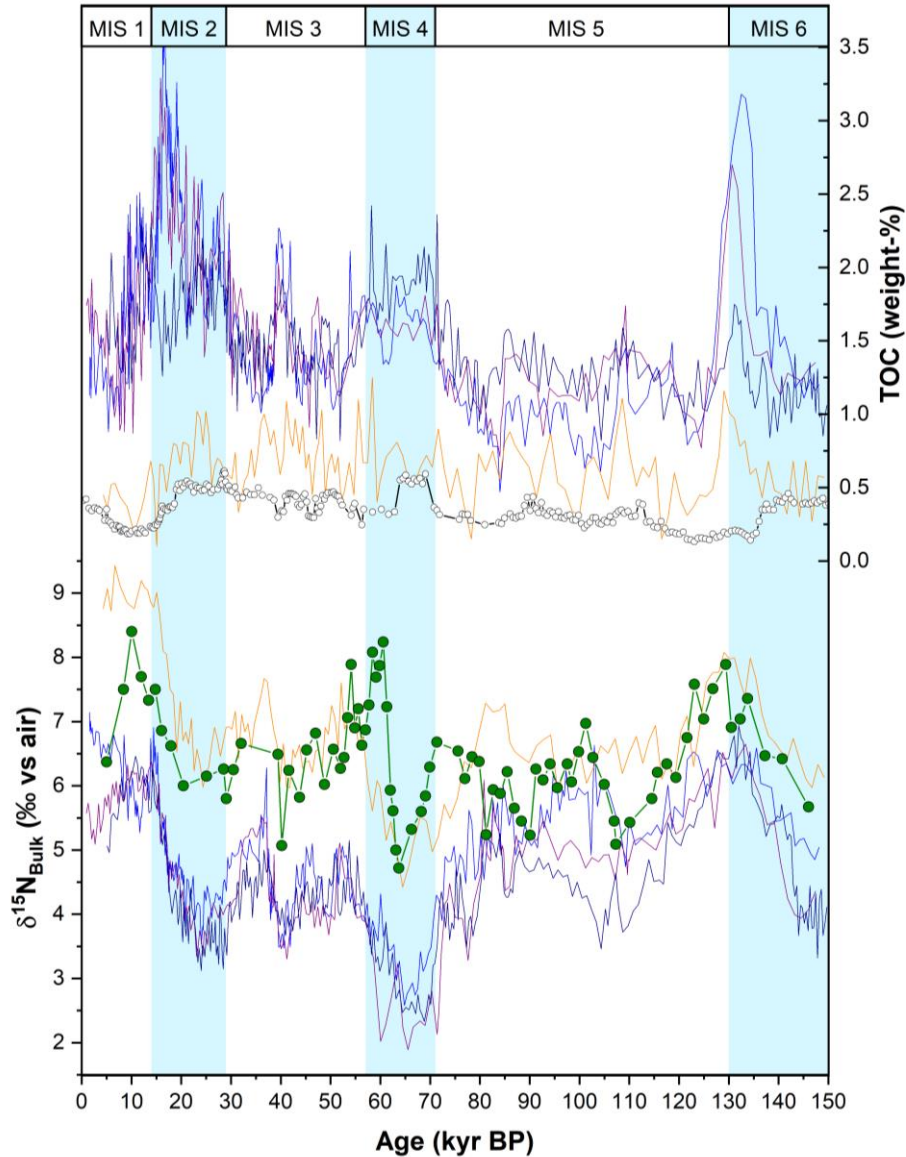


**Figure 5.6.** Down-core records of bulk sediment nitrogen isotopes ( $\delta^{15}\text{N}_{\text{Bulk}}$ ; bottom panel) and total organic carbon content (TOC; top panel) from the southern Agulhas Plateau (this study) and the eastern equatorial Pacific (EEP) (Dubois and Kienast, 2011) for the last 150 kyr BP. All cores are plotted on their published age models (i.e., Dubois and Kienast, 2011; Ziegler *et al.*, 2013). Details of core locations are given in Table 1.  $\delta^{15}\text{N}_{\text{Bulk}}$  from MD02-2588 is plotted as a green line with filled circles; the corresponding TOC record is plotted as a black line with open circles.  $\delta^{15}\text{N}_{\text{Bulk}}$  and TOC records from the EEP cores are plotted in the same style in both the upper and lower panels, with TR163-19P in orange, TR163-31P in navy blue, ME0005A-24JC in blue and ME0005A-27JC in medium purple. Marine Isotope Stages (MIS) are taken from Lisiecki and Raymo, (2005). Glacial stages are shown with vertical blue bars.

the rates of denitrification in the eastern Pacific OMZ (Dubois *et al.*, 2011; Dubois and Kienast, 2011). The greater proximity of the EEP cores to the OMZ, as well as the upstream location of MD02-2588 in terms of SAMW transport, would argue against a common response to water column denitrification. Instead, we suggest that the correlation of these records is due to independent responses to glacial-interglacial changes in the Southern Ocean.

The connection between the Southern Ocean and the biogeochemical history of the EEP is well documented in the sedimentary archive (e.g., Spero and Lea, 2002; Sarmiento *et al.*, 2004; Galbraith *et al.*, 2004; Anderson *et al.*, 2009; Dubois *et al.*, 2011; Martínez-Botí *et al.*, 2015). These records tend to highlight the importance of ‘oceanic tunnelling’, which involves the transfer of southern-sourced intermediate waters (AAIW and SAMW), and their geochemical and thermal signals, from the Southern Ocean to the equatorial Pacific (Liu and Yang, 2003). The records of  $\delta^{15}\text{N}_{\text{Bulk}}$  from the southern Agulhas Plateau and from the EEP demonstrate this connection through their response to glacial-interglacial changes in the Southern Ocean. On the Agulhas Plateau, the  $\delta^{15}\text{N}_{\text{Bulk}}$  record responds to changes in the position of the STF which determine local nutrient supply via the lateral advection of Subantarctic and Subtropical waters and via vertical mixing with SAMW. In the case of the EEP records, changes in the position of the Southern Ocean fronts regulate the oxygen supply to the eastern tropical Pacific OMZ by determining the temperature of intermediate waters (higher oxygen solubility at lower temperature) and the rate of thermocline ventilation due to changes in the strength and/or position of the Southern Hemisphere westerly winds (Galbraith *et al.*, 2004). Accordingly, the northward position of the Southern Ocean fronts during glacial stages, potentially combined with stronger westerly winds (Kohfeld *et al.*, 2013), may have resulted in an increased nutrient supply to the southern Agulhas Plateau and an increased oxygen supply to the eastern tropical Pacific. In the case of MD02-2588, the higher nutrient concentrations explains the lower levels of nutrient utilisation in the surface waters of the Agulhas Plateau. In the EEP, a decrease in water column denitrification due to higher oxygen concentration in SAMW would result in a decline of regional  $\delta^{15}\text{N}_{\text{nitrate}}$  (Galbraith *et al.*, 2008). Both these processes would have caused lower glacial  $\delta^{15}\text{N}_{\text{Bulk}}$ , thus providing a reasonable explanation of the variations observed on the Agulhas Plateau and in the EEP. During warmer intervals, the

more southward position of the Southern Ocean fronts and the potentially weaker westerly winds, could have caused a decrease in nutrient supply to the Agulhas Plateau and a decrease in oxygen supply to the eastern tropical Pacific (e.g., from lower oxygen solubility at warm temperatures and a lower rate of SAMW ventilation). This could explain the relatively higher  $\delta^{15}\text{N}_{\text{Bulk}}$  observed during interglacial stages in both regions. Local fluctuations in export productivity are of course likely to have modulated these broader signals (see TOC records in Fig. 5.6). This could account for the temporal discrepancies observed in the records, as well as differences in absolute the absolute values recorded at each site (e.g., higher  $\delta^{15}\text{N}_{\text{Bulk}}$  values in MD02-2588 and TR163-19 relative to  $\delta^{15}\text{N}_{\text{Bulk}}$  in TR163-31P, ME0005A-24JC and ME0005A-27JC; Table 5.1).

## 5.7 Conclusion

In this chapter, we examined how the position of the STF within the I-AOG may have migrated over the past 150 ky BP and considered how these changes may have impacted the nutrient supply surface waters of the southern Agulhas Plateau. The record of  $\delta^{15}\text{N}_{\text{Bulk}}$  from sediment core MD02-2588 suggests that the northward migration of the STF during glacials is associated with increases in nutrient supply relative to interglacial levels. This increase in nutrient supply to the surface ocean is thought to be due to increased northward advection of relatively nutrient-rich Subantarctic surface waters to the MD02-2588 core site along with weaker upper ocean stratification which would have facilitated vertical mixing of nutrients from the thermocline. During interglacial intervals, when the position of the STF was similar to its modern one, nutrient supply was lower. The lower interglacial nutrient levels are likely due to reduced northward advection of Subantarctic surface waters relative to the advection of nutrient-poor Subtropical waters. In addition, the southward shift of the STF may have reduced the vertical mixing of nutrients from the thermocline due to the enhanced upper ocean stratification that is characteristic of the subtropical zone.

The likeness of the  $\delta^{15}\text{N}_{\text{Bulk}}$  record from MD02-2588 with analogous records from the EEP may suggest that the temporal variability of  $\delta^{15}\text{N}_{\text{nitrate}}$  within these two regions is linked on glacial-interglacial timescales. We suggest that the correlation of these records is due to independent responses to glacial-interglacial changes in the position of the Southern Ocean fronts. On the Agulhas Plateau, changes in the position of the STF determines the local nutrient supply, whereas in the EEP, changes in the position of

the Southern Ocean fronts regulate the oxygen supply to the eastern tropical Pacific OMZ.

---

## 6 Carbon isotopic composition of *Globorotalia truncatulinoides*: application as a proxy of the soft-tissue biological pump and of air-sea gas exchange in the Southern Ocean

---

### 6.1 Chapter outline

In this chapter we present new data from a set of core-top samples collected around New Zealand in order to assess the utility of the deep-dwelling planktonic foraminifera species, *G. truncatulinoides*, as a recorder of the isotopic composition of dissolved inorganic carbon ( $\delta^{13}\text{C}_{\text{DIC}}$ ). From the results of this study, we conclude that this species is indeed a reliable tracer of thermocline chemical properties. Though, offsets between the values of  $\delta^{13}\text{C}$  measured in the calcite tests of this species ( $\delta^{13}\text{C}_{G.trunc(s)}$ ) and the corresponding water column  $\delta^{13}\text{C}_{\text{DIC}}$  highlights the importance of consistency in sample selection for down-core studies.

We then present a down-core assessment of the  $\delta^{13}\text{C}_{G.trunc(s)}$  using published data from sediment core MD02-2588 (Ziegler *et al.*, 2013) and new replicate data from the same core. Our aim is to build on the original evaluation conducted by Ziegler *et al.*, (2013) of how secondary effects that are not associated with nutrient and dissolved inorganic carbon (DIC) cycling impact  $\delta^{13}\text{C}_{G.trunc(s)}$ . We compare the  $\delta^{13}\text{C}_{G.trunc(s)}$  record from MD02-2588 with the record of isotopic composition of atmospheric carbon ( $\delta^{13}\text{C}_{\text{atm}}$ ) from Antarctic ice cores and find them to be strikingly similar in terms of their patterns of variability throughout the past 150 kyr BP. The same is found to be true for the biological component of the benthic  $\delta^{13}\text{C}$  ( $\delta^{13}\text{C}_{\text{benthic-bio}}$ ) record from MD02-2588 which reflects the nutrient and DIC characteristics of deep waters that upwell around Antarctica. These similarities demonstrate the importance of carbon transfer between the Southern Ocean and the atmosphere and highlights the potential of using records of  $\delta^{13}\text{C}_{\text{DIC}}$  from Southern Ocean to reconstruct the variability of  $\delta^{13}\text{C}_{\text{atm}}$  further back in time, possibly even allowing first-order estimations of relative changes of  $\delta^{13}\text{C}_{\text{atm}}$  to be extended beyond the scope of ice core records.

Furthermore, we show that the record the carbon isotope gradient between planktonic and benthic foraminifera ( $\Delta\delta^{13}\text{C}_{\text{plank-benthic}}$ ) from MD02-2588 is consistent with the suggestion that the Southern Ocean's soft-tissue biological pump plays a role in at least part of the variability of  $\delta^{13}\text{C}_{\text{atm}}$  recorded in Antarctic ice cores, although it remains difficult to quantify its exact contribution relative to other drivers of  $\delta^{13}\text{C}_{\text{atm}}$  variability. The most notable indication of the link between the biological pump and  $\delta^{13}\text{C}_{\text{atm}}$  is the occurrence of the three largest negative  $\delta^{13}\text{C}_{\text{atm}}$  excursions during glacial terminations and during Marine Isotope Stage 4, synchronous to the three largest negative shifts of  $\Delta\delta^{13}\text{C}_{\text{plank-benthic}}$ .

## 6.2 Introduction

The soft tissue biological pump refers to the biogenic flux of organic matter from the sunlit surface ocean to the ocean interior (Volk and Hoffert, 1985). It is the principal process controlling the vertical distribution of dissolved inorganic carbon (DIC) and nutrients in the ocean. The formation of organic matter during primary production in the euphotic zone removes DIC and nutrients from the surface ocean causing the partial pressure of  $\text{CO}_2$  ( $PCO_2^{\text{surface}}$ ) to decline. A fraction of this organic material sinks into the deep ocean where it is oxidised, thereby releasing DIC and nutrients and causing an increase in the partial pressure of  $\text{CO}_2$  at depth ( $PCO_2^{\text{deep}}$ ). The resultant vertical flux of  $\text{CO}_2$  from the surface ocean to the deep ocean promotes the sequestration of  $\text{CO}_2$  out of the atmosphere. The recognition that the atmospheric partial pressure of  $\text{CO}_2$  ( $pCO_2^{\text{atm}}$ ), as recorded in ice cores, was as much as 80 parts per million by volume (ppmv) lower during the last glacial maximum (LGM) (Delmas *et al.*, 1980; Neftel *et al.*, 1982) lead to the suggestion that changes in the strength of the soft tissue biological pump could have been the main cause of the decrease (Broecker 1982a, b). Since then, significant effort has been made to understand the role of the soft tissue biological pump in the glacial/interglacial variability of  $pCO_2^{\text{atm}}$  (e.g., Broecker 1982a, b; Sigman and Boyle, 2000; Archer *et al.*, 2000; Sigman and Haug, 2003; Kohfeld *et al.*, 2005; Sigman *et al.*, 2010; Hain *et al.*, 2014). Nonetheless, many questions and uncertainties still remain. The development of reliable and rigorously tested proxies of the soft tissue biological pump is paramount to improving our understanding of its relationship to glacial-interglacial  $pCO_2^{\text{atm}}$  variability.

Reconstructing the soft tissue biological pump from the carbon isotope gradient between planktonic and benthic foraminifera exploits the recognition that fractionation

processes associated with biological carbon cycling cause the vertical distribution of the  $\delta^{13}\text{C}$  of DIC ( $\delta^{13}\text{C}_{\text{DIC}}$ ) in the ocean to mirror the vertical distribution of the concentration of DIC and nutrients. Photosynthetic carbon fixation preferentially utilises  $^{12}\text{C}$  from the surface-layer reservoir of DIC, which causes an increase in surface ocean  $\delta^{13}\text{C}_{\text{DIC}}$ . As the exported organic material sinks out of the surface ocean and undergoes oxidation at depth, it returns to its dissolved inorganic form and releases  $^{12}\text{C}$ -enriched carbon to the ocean interior, thereby lowering deep ocean  $\delta^{13}\text{C}_{\text{DIC}}$ . The sequestration of  $^{12}\text{C}$ -rich DIC into the ocean interior thus results in the establishment of a  $\delta^{13}\text{C}_{\text{DIC}}$  gradient in the water column that is a function of the strength of the soft-tissue biological pump; that is, the stronger the soft-tissue biological pump, the greater the gradient will be. Broecker (1982a) and Shackleton *et al.*, (1983) were the first to exploit the relationship between the vertical gradient of  $\delta^{13}\text{C}_{\text{DIC}}$  ( $\Delta\delta^{13}\text{C}_{\text{DIC}}$ ) and the strength of the soft-tissue biological pump. They reconstructed  $\Delta\delta^{13}\text{C}_{\text{DIC}}$  from sediment core records using measurements of  $\delta^{13}\text{C}$  in planktonic and benthic foraminifera and found that the  $\Delta\delta^{13}\text{C}_{\text{DIC}}$  was greater during ice ages, which suggested that the biological pump may have been stronger at these times. More importantly, comparison of their  $\Delta\delta^{13}\text{C}_{\text{DIC}}$  reconstructions with the early ice core records of  $p\text{CO}_2^{\text{atm}}$  (Delmas *et al.*, 1980; Neftel *et al.*, 1982) led them to propose that an increase in the strength of the soft-tissue biological pump could potentially explain the lower  $p\text{CO}_2^{\text{atm}}$  of the last ice age.

Since these early studies, a number of complexities have been revealed regarding this approach. For example, the isotopic composition of certain foraminifera species is now known to be influenced by physiological processes such as respiration and symbiont photosynthesis (Spero *et al.*, 1991). In addition, foraminiferal calcite  $\delta^{13}\text{C}$  may respond to changes in seawater carbonate concentration ( $[\text{CO}_3^{2-}]$ ) (Spero *et al.*, 1997). Furthermore, air-sea fractionation processes have been found to significantly affect the distribution of carbon isotopes in the modern ocean (Charles and Fairbanks, 1990; Broecker and Maier-Reimer, 1992; Charles *et al.*, 1993; Lynch-Stieglitz *et al.*, 1995) and it is believed that this distribution is likely to have varied in the past (e.g., Marchitto and Broecker, 2006). Moreover, changes in ocean circulation and water-mass distribution (Curry and Oppo, 2005; Marchitto and Broecker, 2006; Lynch-Stieglitz *et al.*, 2007) further complicate the interpretation of oceanic  $\Delta\delta^{13}\text{C}_{\text{DIC}}$  reconstructions. Glacial-interglacial changes in the size of the terrestrial biosphere, however, do not impact the gradient (Shackleton, 1977; Curry *et al.*, 1988; Sigman and Boyle, 2000; Oliver *et al.*,

2010). Despite these complexities, the basic premise of using foraminiferal-based  $\Delta\delta^{13}\text{C}_{\text{DIC}}$  reconstructions as a proxy of the soft-tissue biological pump remains robust and continues to provide a viable approach (Ziegler *et al.*, 2013).

In addition to  $\delta^{13}\text{C}$  records from planktonic and benthic foraminifera, time series of the  $\delta^{13}\text{C}$  of atmospheric  $\text{CO}_2$  ( $\delta^{13}\text{C}_{\text{atm}}$ ) from Antarctic ice cores that now extend over the entire last glacial-interglacial cycle have provided additional important constraints on the exchange of  $\text{CO}_2$  between the ocean and the atmosphere (Leuenberger *et al.*, 1992; Francey *et al.*, 1999; Indermühle *et al.*, 1999; Smith *et al.*, 1999; Elsig *et al.*, 2009; Köhler *et al.*, 2010; Lourantou *et al.*, 2010a,b; Schmitt *et al.*, 2012; Schneider *et al.*, 2013; Eggleston *et al.*, 2016). The evidence from these ice core records generally suggests that a number of processes were probably involved in controlling the variability of  $\delta^{13}\text{C}_{\text{atm}}$  during the past 160 kyr BP. The principle drivers of  $\delta^{13}\text{C}_{\text{atm}}$  variability are thought to be: (i) fluctuations of sea surface temperature (SST), (ii) changes in the Atlantic meridional overturning circulation (AMOC), (iii) upwelling of deep water in the Southern Ocean, (iv) long-term trends in terrestrial carbon storage and (v) changes in marine biological export in the Southern Ocean, probably linked to variations in aeolian iron fluxes. Regarding this final mechanism, strong correlations have been shown to exist between proxies of aeolian iron flux and various proxies of productivity and nutrient utilisation in the Subantarctic Zone. These include radionuclide proxies of biogenic flux (Kumar *et al.*, 1995), the mass accumulation rate of total organic carbon and alkenones (Martínez-García *et al.*, 2009), foram-bound nitrogen isotopes (Martínez-García *et al.*, 2014) and the planktonic-to-benthic foraminiferal carbon isotope gradient ( $\Delta\delta^{13}\text{C}_{\text{plank-benthic}}$ ; Ziegler *et al.*, 2013).

Under conditions where all other parameters are kept constant, a stronger global soft-tissue biological pump is expected to result, not only in higher  $\delta^{13}\text{C}_{\text{DIC}}$  in the surface ocean, but also in higher  $\delta^{13}\text{C}_{\text{atm}}$  (e.g. Köhler and Fischer, 2006; Köhler *et al.*, 2010). The observations of significant decreases of  $\delta^{13}\text{C}_{\text{atm}}$  during the deglacial rises in  $p\text{CO}_2^{\text{atm}}$  over the last two glacial terminations, I and II (T I and T II, respectively), and during Marine Isotope Stage (MIS) 4, are therefore consistent with the soft tissue biological pump hypothesis for glacial-interglacial  $p\text{CO}_2^{\text{atm}}$  change (Smith *et al.*, 1999; Lourantou *et al.*, 2010a,b; Schmitt *et al.*, 2012; Schneider *et al.*, 2013; Eggleston *et al.*, 2016). Thus, the comparison of  $\Delta\delta^{13}\text{C}_{\text{plank-benthic}}$  (and its individual components)

with  $\delta^{13}\text{C}_{\text{atm}}$  could provide valuable clues to the role of the soft-tissue pump in past  $p\text{CO}_2^{\text{atm}}$  change.

Ziegler *et al.*, (2013) generated a 350-kyr record of the intermediate-to-deep  $\Delta\delta^{13}\text{C}_{\text{DIC}}$  along sediment core MD02-2588 from the southern Agulhas Plateau based on  $\delta^{13}\text{C}$  measurements in benthic (*Cibicidoides wuellerstorfi*) and deep-dwelling planktonic foraminifera (*Globorotalia truncatulinoides*, sinistral) extracted from single samples. *G. truncatulinoides* (s.), which inhabits thermocline-depth waters was used as a recorder of the  $\delta^{13}\text{C}_{\text{DIC}}$  of SAMW. *C. wuellerstorfi* was applied as a recorder of the  $\delta^{13}\text{C}_{\text{DIC}}$  of bottom-waters, which at the MD02-2588 core site are principally composed of Circumpolar Deep Water (CDW). CDW upwells around Antarctica and is subsequently converted to Antarctic Intermediate Water (AAIW) and Subantarctic Mode Water (SAMW) in the subantarctic zone (SAZ) (see Chapter 4). The  $\delta^{13}\text{C}_{\text{DIC}}$  reconstructed from *G. truncatulinoides* and *C. wuellerstorfi* therefore share a common preformed signal which is eliminated when calculating  $\Delta\delta^{13}\text{C}_{\text{plank-benthic}}$ . Similarly, processes that impact the whole-ocean  $\delta^{13}\text{C}_{\text{DIC}}$ , such as the transfer of relative low- $\delta^{13}\text{C}$  terrestrial organic material to the oceans during glacial intervals are also eliminated. The residual  $\Delta\delta^{13}\text{C}_{\text{plank-benthic}}$  therefore primarily reflects biological processes in the SAZ, with secondary effects related to air-sea fractionation at the sea surface.

In this chapter, we evaluate  $\Delta\delta^{13}\text{C}_{\text{plank-benthic}}$  as a proxy for the soft-tissue biological pump by assessing whether the foraminifera species used in the  $\Delta\delta^{13}\text{C}_{\text{plank-benthic}}$  reconstruction are reliable signal carriers of  $\delta^{13}\text{C}_{\text{DIC}}$ . Our focus is on *G. truncatulinoides* as the epibenthic species *C. wuellerstorfi* is generally known to secrete calcite close to the  $\delta^{13}\text{C}_{\text{DIC}}$  values of ambient bottom water (Mackensen *et al.*, 2001). In addition, we compare down-core  $\delta^{13}\text{C}_{\text{DIC}}$  reconstructions from MD02-2588 with the available  $\delta^{13}\text{C}_{\text{atm}}$  datasets to investigate oceanic-atmospheric  $\text{CO}_2$  exchange.

### 6.3 Materials and methods

In this chapter we use a combination of new and published data to evaluate the Southern Ocean vertical carbon isotope gradient as a proxy of the soft-tissue biological pump. We present a core-top assessment of the utility of the deep-dwelling planktonic foraminifera species *G. truncatulinoides* as a recorder of  $\delta^{13}\text{C}_{\text{DIC}}$ , wherein we present new data from a set of core-top samples from around New Zealand. We then present a down-core assessment of the *G. truncatulinoides*  $\delta^{13}\text{C}$  ( $\delta^{13}\text{C}_{G.\text{trunc}(s)}$ ) and  $\Delta\delta^{13}\text{C}_{\text{plank-}}$

benthic reconstruction along sediment core MD02-2588 using data from Ziegler *et al.*, (2013) and new replicate data.

### 6.3.1 *Globorotalia truncatulinoides*

#### 6.3.1.1 *Species description*

*Globorotalia truncatulinoides* (d'Orbigny, 1839) is a subsurface-dwelling, non-spinose, non-symbiotic, trochospiral planktonic foraminifera species. It has a conical test with five ventrally elongated chambers in the final whorl and a keel along the entire periphery in adult specimens (de Vargas *et al.*, 2001) (Fig.6.1). The spiral test may coil in a clockwise (right/dextral-coiling) or counter-clockwise (left/sinistral-coiling) direction. *G. truncatulinoides* has a wide biogeographic distribution that ranges from the Antarctic Polar Front (APF) to the Northern Transitional Zone, with a maximum abundance in subtropical and temperate regions (Bé and Tolderlund, 1971; Bé, 1977) (Fig. 6.2). It is one of the most intensively studied species of living planktonic foraminifera with an ecology and evolutionary history that is relatively well understood and is frequently utilised in paleoceanographic studies as a proxy of subsurface oceanographic conditions (e.g., Ericson *et al.*, 1954; Kennett, 1968; Erez and Honjo, 1981; Durazzi, 1981; Lohmann and Malmgren, 1983; Pharr and Williams, 1987; Lohmann, 1992; Martínez, 1994, 1997; Mulitza *et al.*, 1997; LeGrande *et al.*, 2004; Cléroux *et al.*, 2007, 2009; Martinez *et al.*, 2007; Steph *et al.*, 2009; Ziegler *et al.*, 2013; Feldmeijer *et al.*, 2015).

#### 6.3.1.2 *Evolution and migration*

*G. truncatulinoides* originated between 2.8 and 2.3 million years before present (Myr BP) in the subtropical south west Pacific as a descendant from the extant *Globorotalia crassaformis* via an extinct intermediate morphotype, *Globorotalia tosaensis* (Lazarus *et al.*, 1995; Spencer-Cervato and Thierstein, 1997) (Fig. 6.3). Differentiated morphotypes of *G. truncatulinoides* later migrated into the Indian and Atlantic Ocean in punctuated pulses between 2.3 and 1.9 Myr BP (Spencer-Cervato and Thierstein, 1997). Subsequent adaptation to colder environments in the Southern Ocean at ~500 thousand years ago (kyr BP) allowed colonisation of southern subpolar waters in two successive expansions at ~300 and ~200 kyr BP (Pharr and Williams, 1987). These adaptations and migrations are the reason for the asymmetrical geographic distribution

observed in today's ocean, where *G. truncatulinoides* is generally restricted to subtropical and tropical waters in the Northern Hemisphere, but extends into Subantarctic waters in the Southern Hemisphere (Kennett, 1968).

Detailed molecular and morphological studies have revealed a complex genetic and morphologic variability within the taxonomic unit of *G. truncatulinoides* (de Vargas *et al.*, 2001; Renaud and Schmidt, 2003; Ujiie and Lipps, 2009; Quillévéré *et al.*, 2013). Based on these studies the morphospecies *G. truncatulinoides* is now known to occur as five separate genotypes, Types I to V. Each genotype displays distinct morphological characteristics and a preference for particular oceanographic conditions (Quillévéré *et al.*, 2013). Type I appears to inhabit the warm (sub)tropical waters of the Southern Hemisphere. Types II and V are found in the warm (sub)tropical waters of the Atlantic and NW Pacific, respectively. Types III and IV appear to be restricted, to the productive subtropical and the cold subpolar frontal zones of the Southern Ocean, respectively. All species are left-coiling, except for Type II which display both left- and right-coiling directions (de Vargas, *et al.*, 2001).

#### 6.3.1.3 *Depth habitat and life cycle*

Early studies of *G. truncatulinoides* (Emiliani, 1954, Bé and Tolderlund, 1971; Bé, 1977) and in-situ observations (Fairbanks *et al.*, 1980; Deuser and Ross, 1989) classified this species as a deep-dwelling planktonic foraminifera, with living specimens having been found at depths of up to 1000 m in the western Atlantic (Durazzi, 1981; Hemleben *et al.*, 1985; Lohmann and Schweitzer, 1990). *G. truncatulinoides* is also known to have a complex life cycle involving large vertical migrations in the water column (Fig. 6.4). Like most planktonic foraminifera species, *G. truncatulinoides* begins its life in the upper few hundred meters of the water column, but unlike surface-dwelling species it continues to grow and calcify new chambers at greater depths until it reaches the adult stage. Its reproductive strategy involves an annual vertical migration of several hundred meters. Studies in the Sargasso Sea have revealed that neanic and juvenile specimens appear to develop during the winter to spring months in relatively shallow water (Fig. 6.4). At the end of spring, adults descend deeper in the water column, where they continue to calcify, and then migrate upwards in late autumn to reproduce (Vergnaud-Grazzini, 1976; Deuser and Ross,

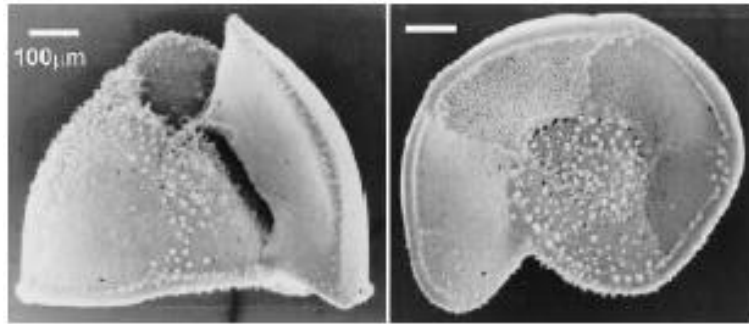


**Figure 6.1.** Morphology of *Globorotalia truncatulinoides*. Left coiled specimen from Bermuda. Image taken from de Vargas *et al.*, (2001).

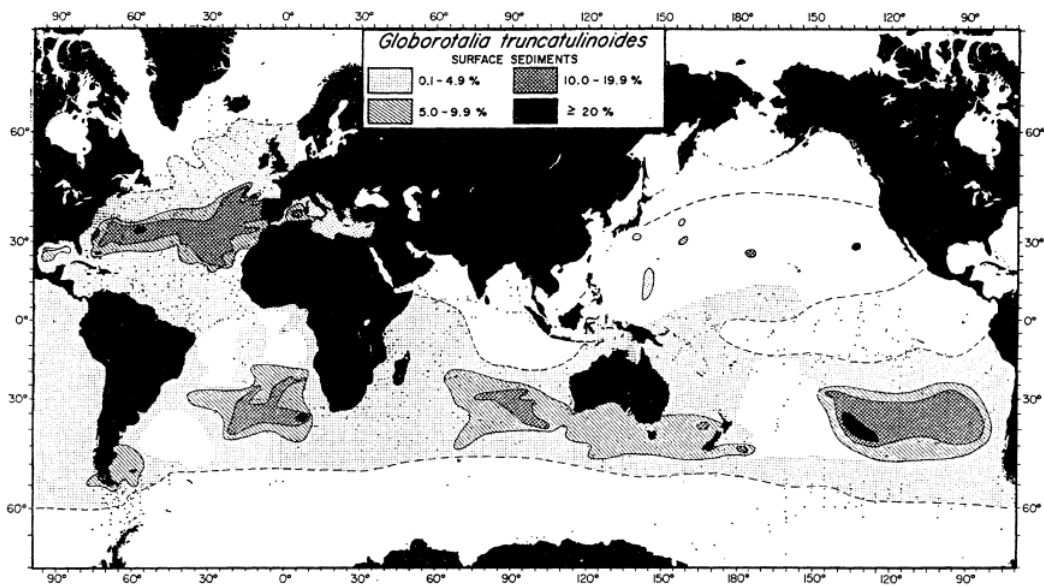


**Figure 6.2.** *Globorotalia truncatulinoides* in surface sediments of the world's oceans corresponding to the modern biogeography of the morphospecies (From Bé, 1977).

1989; Lohmann and Schweitzer, 1990) (Fig. 6.4). The occurrence of these vertical migrations at times of low stratification suggests that they are linked to the stability of the water column (Lohmann and Schweitzer, 1990; McKenna and Prell, 2004) (Fig. 6.4). Despite the large depth range of the *G. truncatulinoides* life cycle, studies of the oxygen isotope ( $\delta^{18}\text{O}$ ) composition of modern foraminifera shells and the temperature and  $\delta^{18}\text{O}$  composition of modern seawater suggest that *G. truncatulinoides* builds most of its test in the main thermocline (Deuser and Ross, 1989; Ganssen and Kroon, 2000; LeGrande *et al.*, 2004; Cléroux *et al.*, 2007).

#### 6.3.1.4 *G. truncatulinoides* in paleoceanography

*G. truncatulinoides* is thought to record the hydrography of the waters in which it calcified, i.e., from the surface, down to the permanent thermocline (Lohmann and Schweitzer, 1990; Ravelo and Fairbanks, 1992; Martínez, 1994, 1997; LeGrande *et al.*, 2004; Steph *et al.*, 2009). As such, this species is often utilised for the reconstruction of subsurface paleoceanographic conditions (Ericson *et al.*, 1955; Kennett, 1968; Erez and Honjo, 1981; Lohmann and Malmgren, 1983; Pharr and Williams, 1987; Lohmann, 1992; Martínez, 1994, 1997; Mulitza *et al.*, 1997; LeGrande *et al.*, 2004; Cléroux *et al.*, 2007, 2009; Martinez *et al.*, 2007; Steph *et al.*, 2009; Ziegler *et al.*, 2013; Feldmeijer *et al.*, 2015). The potential of *G. truncatulinoides* as a paleoceanographic indicator has been known since the mid-1950's when pioneering research first identified a relationship between North Atlantic provinces and the coiling ratio of *G. truncatulinoides* from surface sediments (Ericson *et al.*, 1955). This made it possible to use downcore variations in coiling ratio as a stratigraphic tool for correlating sediment cores. An example of the use of the coiling ratio of *G. truncatulinoides* as a paleoceanographic proxy can be found in a study of a South Atlantic sediment core where *G. truncatulinoides* was observed to have changed from the predominantly shallower-dwelling, right-coiling morphotype to the deeper-dwelling, left-coiling variety over the past 700 kyr (Lohmann, 1992). Shell development also shifted towards the rates normally associated with deep mixing (Lohmann, 1992). These changes were interpreted as reflecting a variation in the structure of the upper water column and a gradual increase in the seasonal upwelling of nutrients in the subtropical South Atlantic (Lohmann, 1992).

In addition to coiling ratios, the morphological characteristics of *G. truncatulinoides* were also found to vary with oceanographic conditions. Specifically, a relationship

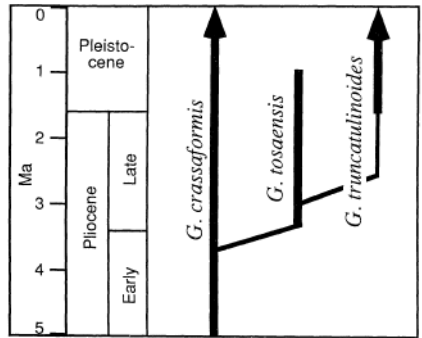


**Figure 6.3.** Phylogenetic tree of *Globorotalia crassaformis*, *G. tosaensis* and *G. truncatulinoides*. The narrow line of the *G. truncatulinoides* branch indicates its geographical restriction during the Pliocene. Image taken from Lazarus *et al.*, 1995; Original figure found in Kennett and Srinivasan (1983).

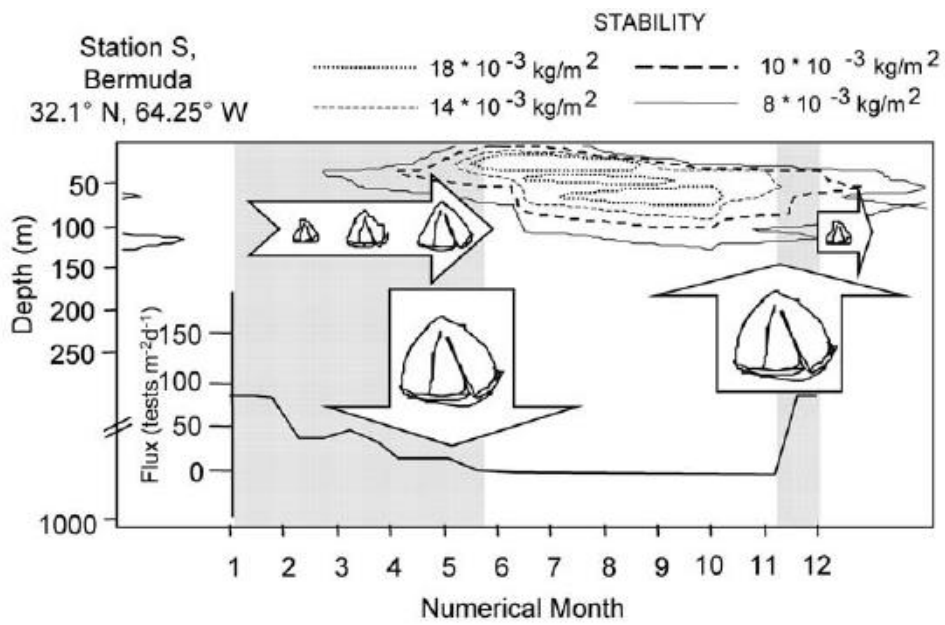


**Figure 6.4.** Life cycle of *G. truncatulinoides* (*dextral*) and its relation to water column properties. The reproductive cycle of *G. truncatulinoides* (*d.*) is synchronised to the annual variation of simple stability ( $\Delta\sigma_t/\Delta z$ ) in the upper water column. The annual flux of the species in sediment traps at Station S, Bermuda, occurs during those months when the water column stability is weakest (Deuser and Ross, 1989). Figure taken from McKenna and Prell, (2004).

was observed between test morphology and the latitudinal surface-water temperature gradient; highly conical forms were predominantly observed in tropical areas, whereas compressed, convex forms were associated with cold waters (Kennett, 1968). Investigation of the downcore morphological variability suggested that highly conical morphotypes were found at higher latitudes during the last 700 kyr BP when compared to their present distribution and migrated equatorward progressively (Lohmann and Malmgren, 1983).

Much of this early work based on coiling ratios and morphological characterisation has been superseded by detailed molecular and morphometric studies, which explain much of the variability and distribution of *G. truncatulinoides* in terms of the evolution and migration of 5 distinctive genotypes (de Vargas *et al.*, 2001; Renaud and Schmidt, 2003; Ujiié and Lipps, 2009; Quillévéré *et al.*, 2013). Nonetheless, *G. truncatulinoides* continues to be a valuable foraminifer for paleoceanographic reconstructions. It has been used successfully to reconstruct changes in the position of the Tasman Front (Martinez, 1994) during the Late Pleistocene and examine the influence of SAMW north of this front over the past 150 kyr (Martinez, 1997).

The application of stable isotope geochemistry to the tests of *G. truncatulinoides* has also been found to be a reliable technique in paleoceanographic reconstructions. The  $\delta^{18}\text{O}$  composition of the test of this planktonic foraminifera provides a means to investigate changes in the intermediate-depth water column density (LeGrande *et al.*, 2004) as well as changes in thermocline temperatures (Cléroux *et al.*, 2007). In addition, calcification depth reconstructions based on the  $\delta^{18}\text{O}$  of *G. truncatulinoides* have revealed large variations over the past 12 kyr in the waters of the western margin of the North Atlantic (Cléroux *et al.*, 2009). More recently, the depth of the permanent thermocline in the North Atlantic was reconstructed over Termination III based on changes in the morphology of *G. truncatulinoides* and the isotopic composition of single specimens of multiple size fractions (Feldmeijer *et al.*, 2015).

Stable isotope studies on the tests of *G. truncatulinoides* have also been used in conjunction with stable isotope measurements in other species to investigate vertical gradients of hydrographic and chemical properties (Mullitza *et al.*, 1997; Steph *et al.*, 2009; Ziegler *et al.*, 2013). For example, the oxygen isotope gradient ( $\Delta\delta^{18}\text{O}$ ) between *G. truncatulinoides* and *G. sacculifer* from a gravity core in the western equatorial Atlantic was shown to be significantly lower during MIS 2, suggesting that the glacial

temperature stratification of the surface waters in this region was significantly reduced relative to the Holocene (Mulitza *et al.*, 1997). The Southern Ocean  $\Delta\delta^{13}\text{C}_{\text{plank-benthic}}$  between *G. truncatulinoides* and *C. wuellerstorfi*, as used by Ziegler *et al.*, (2013) to reconstruct changes in the relative strength of the biological pump over the past 350 kyr provides another notable example.

### 6.3.2 Core-top materials and methodology

#### 6.3.2.1 Sampling strategy

We measured stable oxygen and carbon isotopes in the planktonic foraminifera *G. truncatulinoides* in six core tops (0-1 cm slice) from multicores retrieved in the south west Pacific during cruise RR05-03, 2005, *R/V Roger Revelle*. The multicore sites extend from the southern flank of the Chatham Rise, east of New Zealand's South Island, up to the Bay of Plenty, which extends northwards of North Island (Fig. 6.5; Table 6.1). To maximise the range of stable isotope values and hydrographic properties captured by this limited suite of core-top samples we picked *G. truncatulinoides* from various size fractions and separated them according to coiling direction (i.e., sinistral and dextral). This sampling strategy extended the total sample number to 25 with duplicate measurements performed for all but three of these.

#### 6.3.2.2 Estimating calcification depths

To estimate the calcification depth of each sample we compiled temperature and salinity data from hydrographic stations in the vicinity of each multicore site using the Southern Ocean Atlas dataset (Olbers *et al.*, 1992) (Fig. 6.6; Table 6.2). Salinity was converted to seawater  $\delta^{18}\text{O}$  ( $\delta^{18}\text{O}_{\text{sw}}$ ) using the regional salinity- $\delta^{18}\text{O}_{\text{sw}}$  relationship which was developed for this study using data from Craig and Gordon, (1965) and Ostlund *et al.*, (1987) (Fig. 6.7 and Table 6.3):

$$\delta^{18}\text{O}_{\text{sw}} = 0.55 * \text{Salinity} - 18.96$$

$$(r^2=0.91, n=33, p < 0.0001)$$

Equation (Eq.) 6.1

Next, the temperature and  $\delta^{18}\text{O}_{\text{sw}}$  profiles were used to calculate equilibrium  $\delta^{18}\text{O}$  ( $\delta^{18}\text{O}_{\text{eq}}$ ) profiles for each multicore site. Two commonly used  $\delta^{18}\text{O}$ -temperature equations were applied:

- (i) The Epstein *et al.*, (1953) equation, developed from molluscs at temperatures ranging from 7 to 29.5 °C:

$$T_{\text{water}} = 16.5 - 4.3 (\delta^{18}\text{O}_{\text{calcite}} - \delta^{18}\text{O}_{\text{sw}}) + 0.14 (\delta^{18}\text{O}_{\text{calcite}} - \delta^{18}\text{O}_{\text{sw}})^2$$

Eq. 6.2

- (ii) The inorganic equation of Kim and O'Neil (1997) calibrated across temperatures from 10 to 40 °C:

$$T_{\text{water}} = 16.1 - 4.64 (\delta^{18}\text{O}_{\text{calcite}} - \delta^{18}\text{O}_{\text{sw}}) + 0.09 (\delta^{18}\text{O}_{\text{calcite}} - \delta^{18}\text{O}_{\text{sw}})^2$$

Eq. 6.3

where  $T_{\text{water}}$  refers to seawater temperature and  $\delta^{18}\text{O}_{\text{calcite}}$  is assumed to be equivalent to  $\delta^{18}\text{O}_{\text{eq}}$ . These equations were rearranged and solved as follows:

- (i) Epstein *et al.*, (1953):

$$\delta^{18}\text{O}_{\text{eq}} = \frac{4.64 - \sqrt{21.53 - (16.1 - T)}}{0.18} + (\delta^{18}\text{O}_{\text{sw}} - 0.27)$$

Eq. 6.4

- (ii) Kim and O'Neil (1997)

$$\delta^{18}\text{O}_{\text{eq}} = \frac{4.3 - \sqrt{18.49 - (16.5 - T)}}{0.28} + (\delta^{18}\text{O}_{\text{sw}} - 0.27)$$

Eq. 6.

The subtraction of 0.27‰ from  $\delta^{18}\text{O}_{\text{sw}}$  is necessary for the conversion of  $\delta^{18}\text{O}_{\text{eq}}$  from the Vienna Standard Mean Ocean Water (VSMOW) scale to the standard Vienna Pee Dee Belemnite (VPDB) scale.

These two separate solutions result in two distinct  $\delta^{18}\text{O}_{\text{eq}}$  profiles. These were averaged to produce a unique  $\delta^{18}\text{O}_{\text{eq}}$  profile for each multicore site against which the measured *G. truncatulinoides*  $\delta^{18}\text{O}$  ( $\delta^{18}\text{O}_{G.\text{trunc}}$ ) could be matched, thus allowing a calcification depth assignment for each core-top sample (Fig. 6.6). The corresponding core-top *G. truncatulinoides*  $\delta^{13}\text{C}$  ( $\delta^{13}\text{C}_{G.\text{trunc}}$ ) values were then compared to seawater  $\delta^{13}\text{C}_{\text{DIC}}$  data from the Global Ocean Data Analysis Project version 2 (GLODAPv2) database in order to assess the reliability of this species as a  $\delta^{13}\text{C}_{\text{DIC}}$  signal carrier (Key *et al.*, 2015) (Fig. 6.8; Table 6.4).

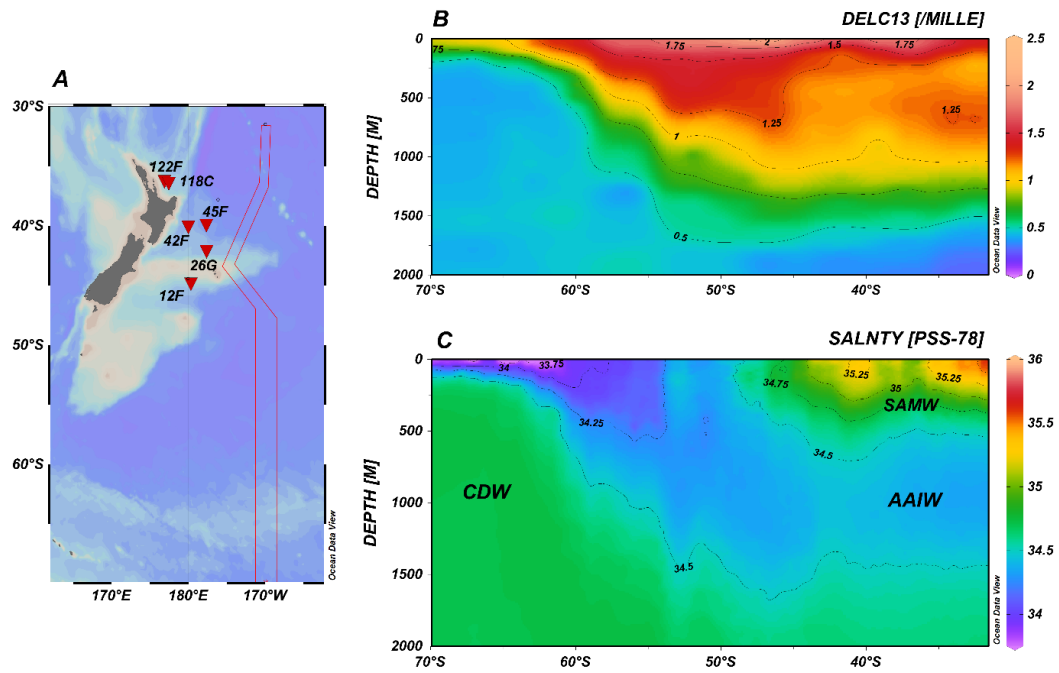


**Fig. 6.5.** A) Map showing the location of the core-top samples discussed in this work (inverted red triangles). The red lines highlight the area that defines the oceanographic cross sections in the adjacent panels and corresponds to World Ocean Circulation Experiment (WOCE) transect P15 (Talley, 2007). B) Latitudinal cross section of  $\delta^{13}\text{C}_{\text{DIC}}$  (‰ VPDB) in the upper 2000 m of the water column. C) Latitudinal cross section of salinity in the upper 2000 m of the water column. Also shown are the main water masses which are clearly distinguished by their salinity; Circumpolar Deep Water (CDW), Antarctic Intermediate Water (AAIW) and Subantarctic Mode Water (SAMW). Figure produced using Ocean Data View.

**Table 6.1** Core-top locations and water depths

Core-top name	Latitude	Longitude	Water Depth (m)
MC-12F	44°47.83 S	179°39.76 W	1335
MC-26G	42°04.47 S	177°37.56 W	2418
MC-42F	39°52.64 S	177°39.46 W	3575
MC-45F	40°01.97 S	179°59.75 W	2991
MC-118C	36°22.63 S	177°26.75 E	2252
MC-122F	36°11.91 S	176°53.35 E	2541

**Table 6.2.** Details of hydrographic stations

Core site	Station no.	Longitude (°E)	Latitude (°N)	Depth range (m)
MC-12F	9673	180	-45	0-1750
	9674	181	-45	0-1500
	10021	178	-45	0-2250
	10022	179	-45	0-2250
MC-26G	10720	182	-42	0-2500
	10721	183	-42	0-2500
	10722	184	-42	0-2500
	11068	182	-41	0-2750
	11069	183	-41	0-3500
	11070	184	-41	0-3750
MC-42F	11414	182	-40	0-3750
	11415	183	-40	0-3750
	11416	184	-40	0-4000
	11760	182	-39	0-3500
	11761	183	-39	0-4000
	11762	184	-39	0-4000
	12106	182	-38	0-3250
	12107	183	-38	0-4000
	12108	184	-38	0-4500
MC-45F	11066	180	-41	0-2750
	11067	181	-41	0-2750
	11068	182	-41	0-2750
	11412	180	-40	0-2750
	11413	181	-40	0-3500
	11414	182	-40	0-3750
	11758	180	-39	0-3500

	11759	181	-39	0-3500
	11760	182	-39	0-3500
MC-118C	12768	176	-37	0-20
	12769	177	-37	0-1500
	12770	178	-37	0-2000
	13101	176	-36	0-250
	13102	177	-36	0-2250
	13103	178	-36	0-2500
	13432	176	-35	0-1750
	13433	177	-35	0-2250
	13434	178	-35	0-3000
MC-122F	12768	176	-37	0-20
	12769	177	-37	0-1500
	13100	175	-36	0
	13101	176	-36	0-250
	13102	177	-36	0-2250
	13431	175	-35	0-900
	13432	176	-35	0-1750
	13433	177	-35	0-2250

---

Data source: Southern Ocean Atlas (Olbers *et al.*, 1992).

**Table 6.3.** Salinity and seawater  $\delta^{18}\text{O}$  ( $\delta^{18}\text{O}_{\text{sw}}$ ) data for the core-top study site.

Latitude (°S)	Longitude (°W)	Depth (m)	Salinity (psu)	$\delta^{18}\text{O}_{\text{sw}}$ (‰ VSMOW)	Reference
38°00'00	163°00'00	0	34.81	0.22	Craig and Gordon (1965)
36°00'00	162°00'00	1139	34.39	-0.13	Craig and Gordon (1965)
34°00'00	161°00'00	0	35.10	0.45	Craig and Gordon (1965)
36°31'12	179°36'00	7	35.67	0.56	GEOSECS Ostlund <i>et al.</i> , (1987)
44°57'00	166°39'36	3	34.71	0.18	GEOSECS Ostlund <i>et al.</i> , (1987)
“	“	1	34.87	0.27	“
38°22'48	170°04'12	2	34.93	0.34	GEOSECS Ostlund <i>et al.</i> , (1987)
“	“	43	34.93	0.37	“
“	“	82	35.05	0.48	“
“	“	102	35.06	0.45	“
“	“	399	34.69	0.22	“
“	“	497	34.59	0.19	“
“	“	597	34.50	0.11	“
“	“	696	34.45	0.09	“
“	“	892	34.40	0.04	“
“	“	1088	34.39	0.01	“
“	“	1243	34.39	0.01	“
“	“	1540	34.49	0.02	“
“	“	1834	34.58	0.04	“
35°40'12	166°46'48	1	35.31	0.53	GEOSECS Ostlund <i>et al.</i> , (1987)
“	“	12	35.30	0.52	“
“	“	57	35.35	0.57	“
“	“	112	35.39	0.49	“
“	“	188	35.13	0.42	“
“	“	287	34.93	0.36	“
“	“	496	34.53	0.12	“
“	“	645	34.43	0.04	“
“	“	787	34.37	0.00	“
“	“	886	34.37	0.02	“
“	“	1277	34.42	0.04	“
“	“	1421	34.49	-0.01	“
“	“	1582	34.54	0.00	“
“	“	1717	34.58	0.01	“

**Table 6.4.** Global Ocean Data Analysis Project version 2 (GLODAPv2) station details of bottle data used to produce the regional  $\delta^{13}\text{C}_{\text{DIC}}$  profile (Key *et al.*, 2015).

Cruise No.	Station	Longitude ( $^{\circ}\text{E}$ )	Latitude ( $^{\circ}\text{N}$ )	Depth range (m)
243	140	199.52	-32.50	21-5511
243	148	194.84	-32.51	63-6319
243	157	190.16	-32.50	18-5591
243	165	186.82	-32.49	2901-5817
243	171	184.26	-32.50	25-5858
243	175	182.35	-32.51	1195-6748
243	179	181.35	-32.50	600-3425
243	182	179.92	-32.51	18-1476
244	5	175.19	-34.83	2-1420
244	8	175.38	-33.70	2-2533
244	12	175.64	-32.18	2-3906
244	15	175.86	-30.88	1-4129
273	73	181.09	-32.50	3-1987
273	76	181.72	-32.50	4-5088
273	80	183.25	-32.50	4-5991
273	84	185.16	-32.50	4-1463
273	96	189.75	-32.50	29-5358
273	102	195.76	-32.50	85-5665
273	110	202.14	-32.50	4-5388
280	74	189.09	-46.72	9-5274
280	84	185.46	-43.65	10-779
280	90	186.06	-41.71	11-3112
280	97	187.87	-39.07	5-1016
280	101	189.11	-37.31	6-5126
280	109	190.00	-34.00	6-1339
280	112	190.00	-32.50	5-5538
335	14	189.98	-37.51	4-2465
335	23	189.99	-45.98	4-5166
486	55	177.01	-30.57	10-4280
486	61	179.92	-32.51	11-2833
486	69	182.74	-32.50	10-5636
486	75	185.67	-32.49	10-5836
486	81	188.09	-32.50	10-4130
486	86	190.00	-32.51	11-5499
486	93	193.50	-32.49	12-5253
486	97	196.17	-32.49	11-5518
486	101	198.85	-32.50	10-5121

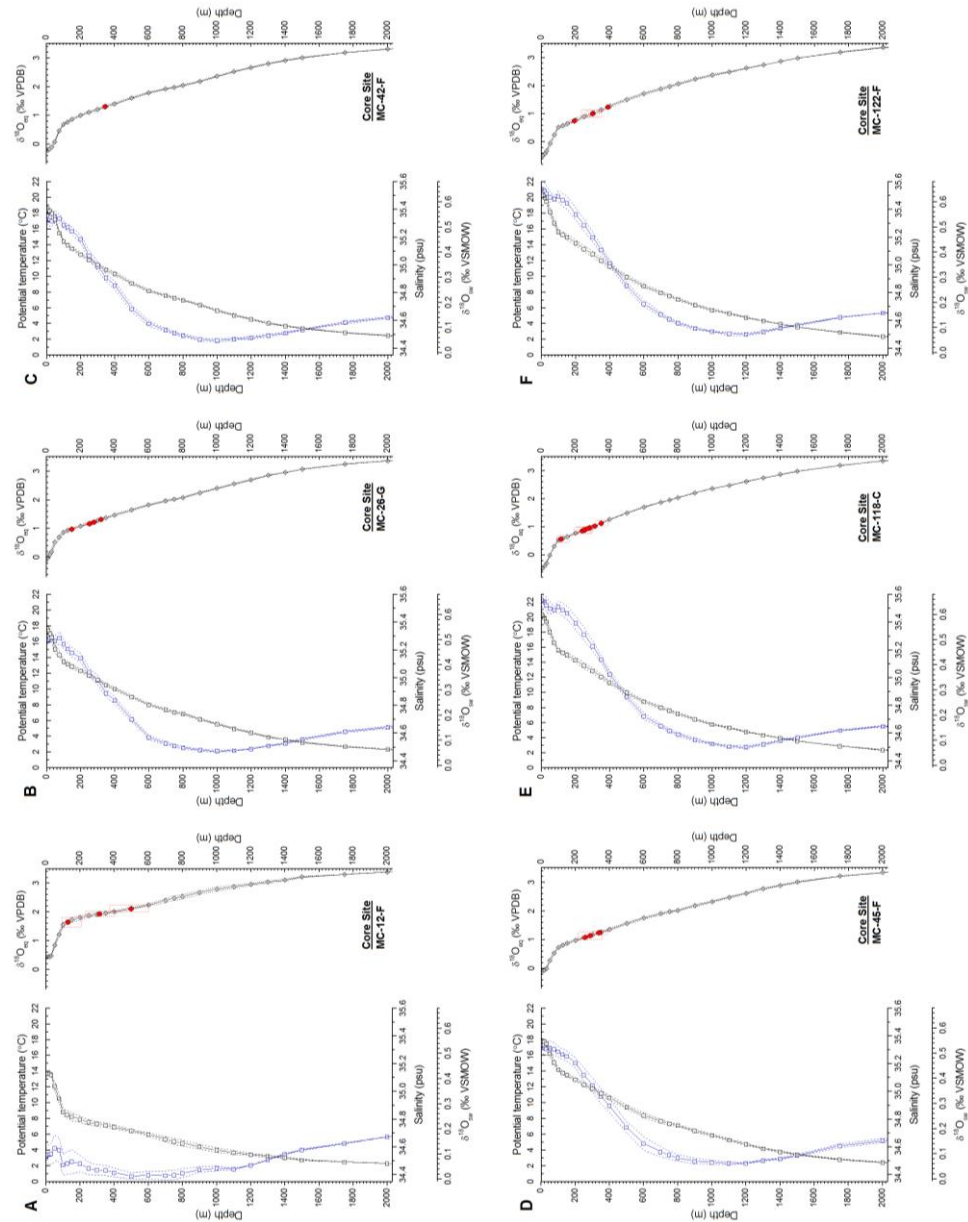


**Figure 6.6.** Vertical profiles of temperature (black line with open square symbols), salinity and seawater  $\delta^{18}\text{O}$  ( $\delta^{18}\text{O}_{\text{sw}}$ ; blue line with open square symbols) and equilibrium  $\delta^{18}\text{O}$  ( $\delta^{18}\text{O}_{\text{eq}}$ ; black line with grey diamond symbols) for each of the core-top sites used in this study. Error envelopes indicate the  $1\sigma$  values (dashed lines). Core-top *G. truncatulinoides*  $\delta^{18}\text{O}$  ( $\delta^{18}\text{O}_{G.\text{trunc.}}$ ) results are shown in relation to  $\delta^{18}\text{O}_{\text{eq}}$  profiles of each site (closed red circles). Dashed rectangles around  $\delta^{18}\text{O}_{G.\text{trunc.}}$  data points indicate  $1\sigma$  associated with isotope measurement and with the estimation of calcification depth. See tables 6.1 and 6.2 for locations of core-top sites and hydrographic stations. Calculation of the  $\delta^{18}\text{O}_{\text{sw}}$  and  $\delta^{18}\text{O}_{\text{eq}}$  profiles are discussed in main text. Core-top sample details including  $\delta^{18}\text{O}_{G.\text{trunc.}}$  and calcification depths are summarised in table 6.5.

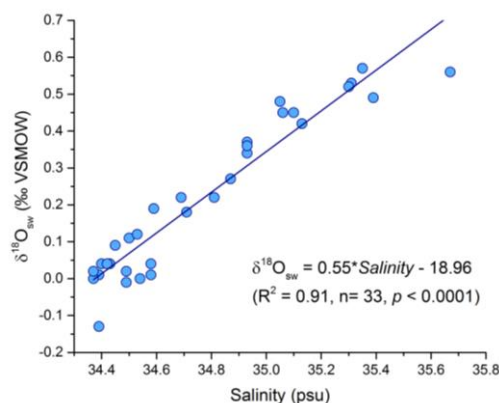


**Figure 6.7.** Salinity-seawater  $\delta^{18}\text{O}$  relationship for the calibration study site based on published hydrographic data from the region (Table 6.3).

### 6.3.3 Downcore materials and methodology

The downcore record of  $\delta^{13}\text{C}_{G.trunc}$  presented in this chapter is derived from sediment core MD02-2588 and incorporates data originally presented by Ziegler *et al.*, (2013), with the addition of replicate measurements made for the present study (see chapter 3 of this thesis).

## 6.4 Results and discussion

### 6.4.1 Core-top $\delta^{13}\text{C}_{G.trunc}$ results

The estimated calcification depths for the core-top samples range between 115 m and 500 m, with a mean value of 283 m and a first and third quartile value of 254 m and 330 m, respectively (Fig. 6.6 and Table 6.5). Overall, this suggests that the chemical composition of the calcite test of *G. truncatulinoides* is more representative of thermocline waters as opposed to SAMW. The estimated calcification depths are generally in agreement with the accepted view that *G. truncatulinoides* builds most of its calcite test in the main thermocline (Deuser and Ross, 1989; Ganssen and Kroon, 2000; LeGrande *et al.*, 2004; Cl  roux *et al.*, 2007; Steph *et al.*, 2009). Nonetheless, we consider this *G. truncatulinoides* to be a suitable signal carrier for approximating SAMW chemical properties as this water mass is typically considered to be the main source of nutrients and DIC to the thermocline in the Southern Hemisphere (Toggweiler *et al.*, 1991; Sarmiento *et al.*, 2004).

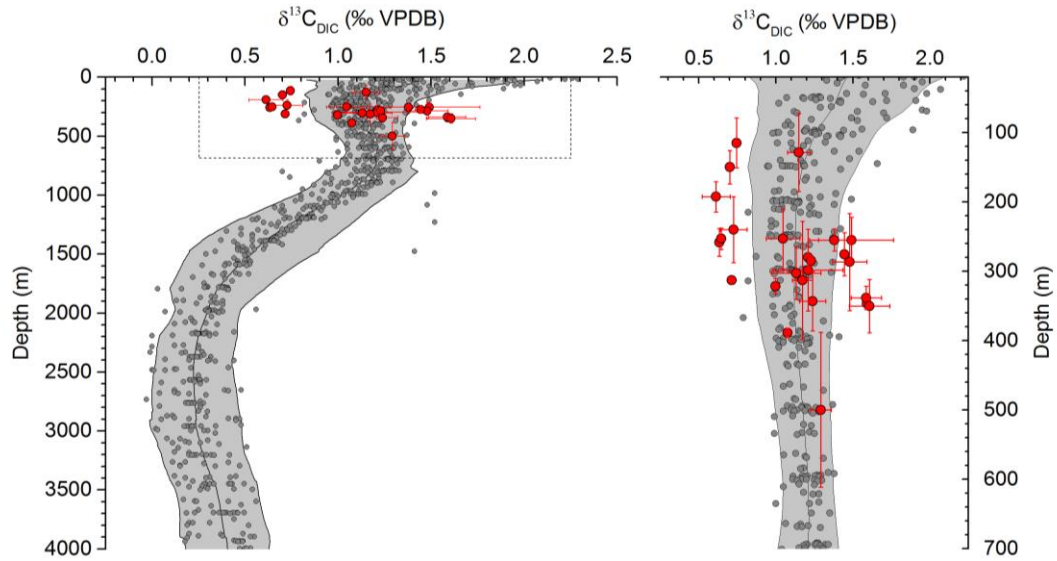


**Figure 6.8.** Vertical profile of the carbon isotope composition of dissolved inorganic carbon (DIC) produced by compiling all available data close to the core-top sites used in this study. The left panel shows data down to 4000 m below sea level. The right panel focusses on the area shown in the dashed rectangle. See table 6.3 for details of the stations used in the compilation. Grey circles are the individual data points and the black line is the average value. The area shaded in light grey indicates  $\pm 2\sigma$  of the available  $\delta^{13}\text{C}_{\text{DIC}}$  data. Core-top  $\delta^{13}\text{C}_{G.trunc}$  data are shown as closed red circles, with vertical error bars accounting for calcification depth estimation and horizontal bars accounting for  $\delta^{13}\text{C}_{G.trunc}$  measurement errors, both at  $1\sigma$ .

**Table 6.5.** Core-top sample details and foraminiferal stable isotope results.

No.	Site	Size ( $\mu\text{m}$ )	Coil	$\delta^{18}\text{O}$ (‰)	$1\sigma$	Average calci- fication depth (m)	Calcification depth range (m)	$\delta^{13}\text{C}$ (‰)	$1\sigma$
1	MC-12F	250-315	S	1.636	0.161	129	94-207	1.150	0.074
2	MC-12F	315-355	S	1.928	0.083	313	233-403	1.173	0.066
3	MC-12F	355-500	S	2.106	0.127	500	377-600	1.292	0.068
4	MC-26G	250-315	S	1.308	0.026*	322	309-332	0.997	0.014*
5	MC-26G	315-500	S	0.975	0.050	150	125-173	0.701	0.022
6	MC-26G	250-355	D	1.223	0.032*	280	265-395	1.209	0.017*
7	MC-26G	355-425	D	1.167	0.029	255	238-270	1.379	0.101
8	MC-26G	425-500	D	1.168	0.062	255	220-285	1.491	0.272
9	MC-42F	315-500	D	1.300	0.002	347	347-347	1.592	0.006
10	MC-45F	250-355	S	1.079	0.035*	258	235-275	0.633	0.020*
11	MC-45F	250-355	D	1.240	0.081	343	302-387	1.239	0.084
12	MC-45F	355-425	D	1.130	0.126	287	215-355	1.479	0.112
13	MC-45F	425-500	D	1.230	0.028	338	322-355	1.587	0.099
14	MC-118C	250-315	S	1.029	0.001	313	313-313	0.715	0.011
15	MC-118C	315-355	S	0.887	0.033	253	236-267	0.645	0.013
16	MC-118C	355-425	S	0.862	0.107	240	195-290	0.727	0.086
17	MC-118C	425-500	S	0.890	0.103	253	212-299	1.046	0.109
18	MC-118C	250-315	D	0.555	0.111	115	91-163	0.744	0.006
19	MC-118C	315-355	D	0.964	0.013	285	280-294	1.228	0.004
20	MC-118C	355-425	D	0.941	0.074	276	245-307	1.444	0.028
21	MC-118C	425-500	D	1.126	0.104	351	314-391	1.607	0.132
22	MC-122F	250-315	D	0.736	0.045	193	164-208	0.613	0.091
23	MC-122F	315-355	D	1.228	0.016	389	380-393	1.075	0.006
24	MC-122F	355-425	D	1.011	0.101	303	262-338	1.131	0.160
25	MC-122F	425-500	D	0.996	0.141	298	235-353	1.210	0.227

Core-top  $\delta^{13}\text{C}_{G.trunc}$  values vary between 0.61‰ and 1.61‰ and generally fall within the  $\delta^{13}\text{C}_{DIC}$  range typically associated with AAIW (i.e., 0.75–1.75‰), which in the southwest Pacific Ocean occupies depths between 600 and 1300 m (Bostock *et al.*, 2010). SAMW lies above AAIW at depths between 400 m and 600 m (McCartney, 1977) and according to the available data from this region, SAMW is characterised by a  $\delta^{13}\text{C}_{DIC}$  range between ~1 and 1.5 ‰ (Fig. 6.5 and Fig. 6.8). Core-top  $\delta^{13}\text{C}_{G.trunc}$  values generally plot close to their depth-equivalent  $\delta^{13}\text{C}_{DIC}$  values, suggesting that *G. truncatulinoides* is, on the whole, a reliable recorder of the chemical signature of the water in which it calcifies. However,  $\delta^{13}\text{C}_{G.trunc}$  values display a wider range than the equivalent  $\delta^{13}\text{C}_{DIC}$  of seawater in this region. Twelve of the 25 core-top samples plot well within of the  $\delta^{13}\text{C}_{DIC}$  profile ( $\pm 2\sigma$  of  $\delta^{13}\text{C}_{DIC}$ ), and all but 6 samples lie within 0.1‰ of the  $\pm 2\sigma$  levels. Three samples have  $\delta^{13}\text{C}_{G.trunc}$  values that are slightly  $>0.1\%$  compared to the corresponding  $\delta^{13}\text{C}_{DIC}$  ( $\pm 2\sigma$  of  $\delta^{13}\text{C}_{DIC}$ ) and 3 samples have  $\delta^{13}\text{C}_{G.trunc}$  values that are slightly  $<0.1\%$  than the corresponding  $\delta^{13}\text{C}_{DIC}$  ( $\pm 2\sigma$  of  $\delta^{13}\text{C}_{DIC}$ ). All samples have been scrutinised in detail to assess if coiling direction, size fraction and/or core-site can explain the offset between the  $\delta^{13}\text{C}_{G.trunc}$  and  $\delta^{13}\text{C}_{DIC}$  but no systematic relationships have been identified. The random nature of these relationships suggest that differences related to genotype, coiling direction, maturity, and preservation do not introduce specific and quantifiable biases. It does however highlight the need to select and measure  $\delta^{13}\text{C}_{G.trunc}$  as consistently as possible in down-core studies; that is to say, samples should consist of individual foraminifera tests that are well preserved, that are selected from a limited and consistent size fraction, and must consist of individual tests with the same coiling direction, and though differentiation of genotype is not always possible, this would provide further reliability (e.g., Feldmeijer *et al.*, 2015).

#### 6.4.2 Downcore $\delta^{13}\text{C}_{G.trunc}$ results

The carbon isotope stratigraphic series of  $\delta^{13}\text{C}_{G.trunc(s)}$  displays a pronounced orbital modulation with superimposed variability on millennial timescales (Fig. 6.9a). As has already been noted by Ziegler *et al.*, (2013) this pattern is similar to other planktonic  $\delta^{13}\text{C}$  stratigraphic series from the Subantarctic Zone (SAZ) of the Southern Ocean (Ninnemann and Charles, 1997) as well as records from further afield in the equatorial Atlantic (Curry and Crowley, 1987) and Pacific Ocean (Pena *et al.*, 2008), where the

thermocline is supplied by southern-sourced Subantarctic Mode Water (SAMW) (Sarmiento *et al.*, 2004). The most distinctive feature of the  $\delta^{13}\text{C}_{G.trunc(s)}$  record from MD02-2588, as is the case with all  $\delta^{13}\text{C}$  records that are sourced by SAMW, is the occurrence of carbon isotope minimum events (CIME) during glacial terminations (Spero and Lea, 2002). These features are thought to represent a response to the breakdown of surface water stratification in the Southern Ocean and renewed upwelling of Circumpolar Deep Water (CDW) with a low  $\delta^{13}\text{C}$  composition, followed by advection of these waters to the convergence zone at the Subantarctic front (SAF) and their propagation throughout the Southern Hemisphere thermocline (Luyten *et al.*, 1983).

Values of  $\delta^{13}\text{C}_{G.trunc(s)}$  in the MD02-2588 record range between 0.0‰ and 1.3‰, with minimum values occurring during the CIME at TI and TII, (centred around 0.4‰ and 0.2‰, for each termination respectively). A less pronounced  $\delta^{13}\text{C}_{G.trunc(s)}$  drop is also observed at the MIS 4/3 boundary, although values only drop as low as  $\sim$ 0.5‰. MIS 2 and MIS 4 are characterised by decreasing trends of  $\delta^{13}\text{C}_{G.trunc(s)}$ , whereas the part of MIS 6 captured in this section of the sediment core appears to remain relatively constant at  $\sim$ 0.6‰ (albeit with superimposed millennial-timescale fluctuations of  $\sim$ 0.2‰ either side of this value) (Fig. 6.9a). During MIS 1, the early part of MIS 3 and the interval between MIS 5.5 and 5.4,  $\delta^{13}\text{C}_{G.trunc(s)}$  displays increasing trends from the minimum values associated with the CIME and the MIS 4/3 boundary to approximately 0.9‰ over a period of about 10 kyr. The rest of MIS 5 displays a continued long-term ( $\sim$  30 kyr) increase from 0.7 to 1.1‰, superimposed with suborbital-timescale fluctuations of 0.3-0.6‰. Following the initial increase at the start of MIS 3, values fluctuate by  $\sim$ 0.3‰ on multi-millennial timescales.

#### 6.4.3 Thermodynamic influences on down-core $\delta^{13}\text{C}_{G.trunc(s)}$

The high  $\delta^{13}\text{C}_{\text{DIC}}$  that characterises AAIW and SAMW in the modern ocean is a consequence of  $^{13}\text{C}$  enrichment relative to global nutrient stoichiometry. This arises from isotopic fractionation during air-sea gas exchange with the atmosphere in the formation zones of these water masses. Wind-driven upwelling brings CDW to the surface south of the Antarctic Polar Front (APF) (Rintoul *et al.*, 2001) and part of this water is advected northwards by Ekman transport, driven by the prevailing westerly winds (Marshall and Speer, 2012) (Fig. 6.10). These waters mix with subtropical surface water and are converted to SAMW while the densest Antarctic surface waters are transformed into AAIW. The exchange of  $\text{CO}_2$  between the surface ocean and the

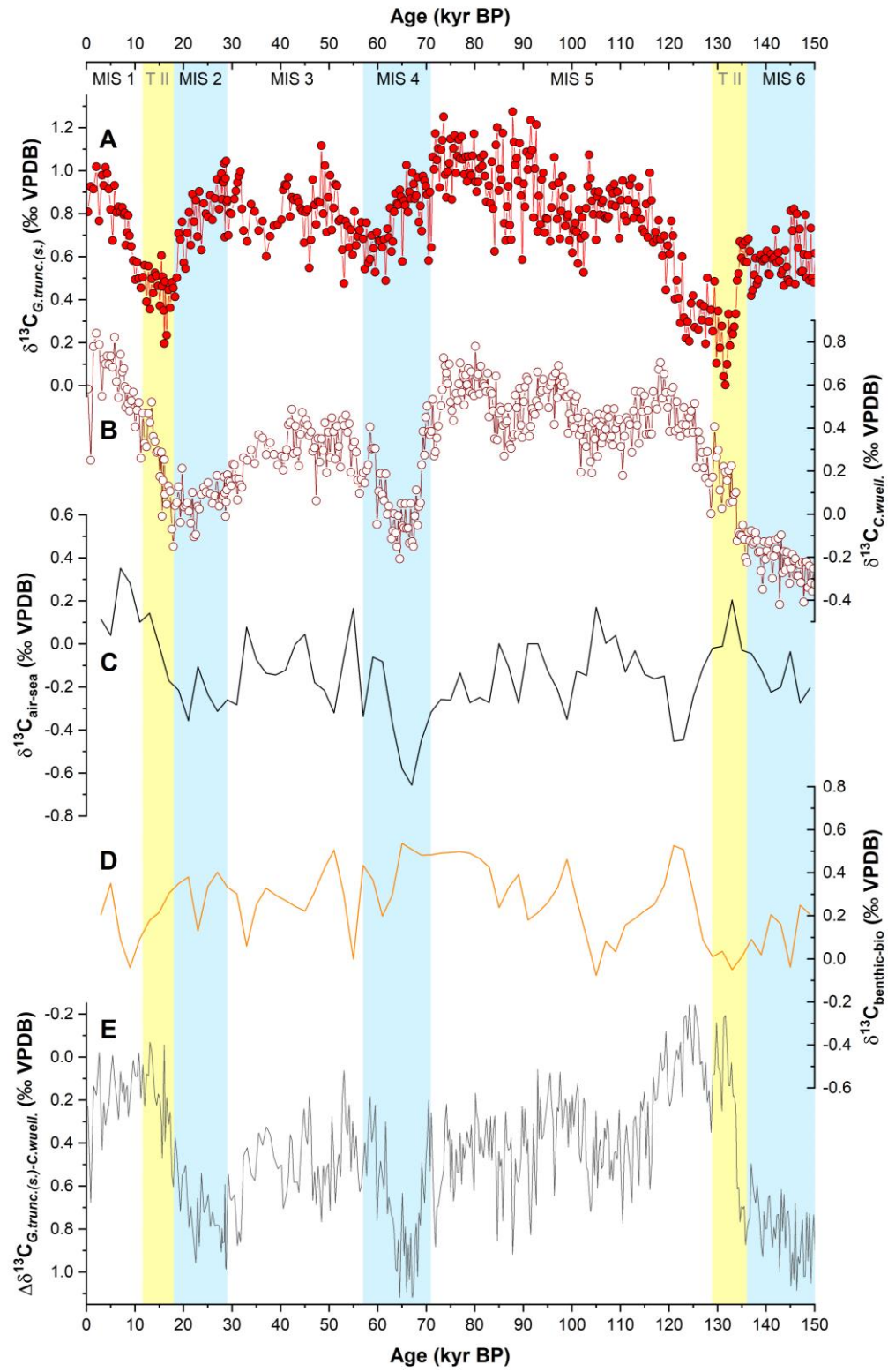


**Figure 6.9.** A) Downcore record of carbon isotopes measured in the deep-dwelling planktonic foraminifera *Globorotalia truncatulinoides (sinistral)* ( $\delta^{13}\text{C}_{G.trunc.(s)}$ ) in sediment core MD02-2588, which incorporates data from this study and Ziegler *et al.*, (2013) (red line with filled circles). B) Downcore carbon isotope record measured in *C. wuellerstorfi* ( $\delta^{13}\text{C}_{C.wuell}$ ) from MD02-2588, incorporating data from this study and Ziegler *et al.*, (2013) (red line, open circles). C) Reconstructed time-series of the air-sea fractionation component of the  $\delta^{13}\text{C}_{C.wuell}$  record from MD02-2588 ( $\delta^{13}\text{C}_{as}$ ) (dashed black line). See main text and chapter 3 for details of  $\delta^{13}\text{C}_{as}$  calculation. D) Biological component of the benthic foraminiferal  $\delta^{13}\text{C}$  record ( $\delta^{13}\text{C}_{bentic-bio}$ ) from MD02-2588. This record is derived by correcting  $\delta^{13}\text{C}_{C.wuell}$  for the effects of air-sea fractionation and mean ocean changes of  $\delta^{13}\text{C}_{DIC}$  (see chapters 3 and 4 for details). E) Carbon isotope gradient between *G. truncatulinoides (s)* and *C. wuellerstorfi* ( $\Delta\delta^{13}\text{C}_{G.trunc(s)-C.wuell}$ ) from MD02-2588, incorporating the data presented in this thesis and in Ziegler *et al.*, (2013) (grey line). Marine Isotope Stages (MIS) are taken from Lisiecki and Raymo, (2005). Glacial stages are shown with vertical blue bars. Glacial terminations TI and TII are shown with vertical yellow bars and their ages are taken from Stern & Lisiecki, (2014) and Landais *et al.*, (2013), respectively.

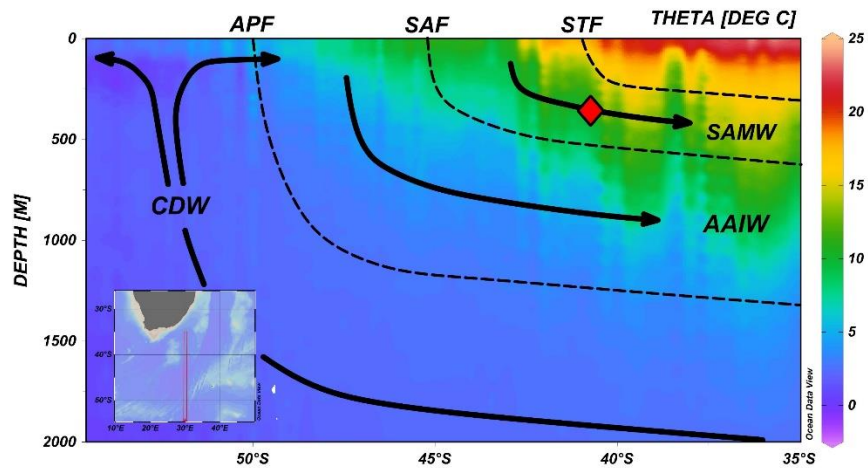


**Figure 6.10.** Meridional cross section of potential temperature ( $\theta$ ) in the Southern Ocean, between Antarctic and Africa (Schlitzer, 2012). Also shown schematically, is the upwelling of Circumpolar Deep Water (CDW) south of the Antarctic Polar Front (APF) and its northward advection to the polar front zone between the APF and the Subantarctic Front (SAF) where it is transformed into Antarctic Intermediate Water (AAIW). Further north, in the Subantarctic Zone between the SAF and the Subtropical Front (STF) surface waters originating from upwelled CDW are converted to Subantarctic Mode Water (SAMW). Red triangle indicates the approximate calcification depth of *Globorotalia truncatulinoides* (*sinistral*), within the core of SAMW in this part of the Southern Ocean.

atmosphere at cold ambient temperatures cause the  $^{13}\text{C}$  enrichment of DIC (Broecker and Maier-Reimer, 1992; Charles *et al.*, 1993; Lynch-Stieglitz *et al.*, 1995). It is possible that temperature changes of Antarctic surface waters in the past may have contributed to part of the variability of  $\delta^{13}\text{C}_{\text{DIC}}$  reconstructions of southern-sourced intermediate waters. Thus, down-core records of  $\delta^{13}\text{C}_{G.trunc(s)}$  may have deviated from nutrient stoichiometry to varying degrees depending on Southern Ocean SST variability with consequences for the application of  $\Delta\delta^{13}\text{C}_{\text{plank-benthic}}$  as a proxy of the soft-tissue biological pump.

The impact of variable air-sea gas exchange on the  $\delta^{13}\text{C}_{G.trunc(s)}$  record from MD02-2588 and its consequences for the  $\Delta\delta^{13}\text{C}_{\text{plank-benthic}}$  stratigraphic series were considered by Ziegler *et al.*, (2013) to be minimal as Southern Ocean surface water temperature variations are thought to have been small. Compiled proxy data from the Southern Ocean indicate a northward shift of the polar front during the LGM to a position at  $\sim 45^\circ\text{S}$  (Gersonde *et al.*, 2005; Kohfeld *et al.*, 2013) and an associated SST cooling between 2 to  $6^\circ\text{C}$  (MARGO Project Members, 2006). Assuming that  $\delta^{13}\text{C}_{\text{DIC}}$  increases by  $0.1\text{‰}$  per degree of cooling (Mook *et al.*, 1974), the temperature variation suggests that 0.2-0.6‰ of the total LGM  $\delta^{13}\text{C}_{\text{DIC}}$  value of Southern Ocean surface waters is driven by temperature changes and not by biological processes. At the lower estimate of temperature change this process would only have a small impact on the  $\delta^{13}\text{C}_{G.trunc(s)}$  record. On the other hand, an LGM cooling of  $6^\circ\text{C}$  would result in a more substantial impact.

Ziegler *et al.*, (2013) quantified the possible impact of temperature dependent changes on down-core  $\delta^{13}\text{C}_{G.trunc(s)}$  by using the  $\delta^{18}\text{O}$  gradient ( $\Delta\delta^{18}\text{O}$ ) between *G. truncatulinoides* (*s.*) and *C. wuellerstorfi* as a first order estimate of temperature variability at the site of SAMW formation. This approach assumes that benthic  $\delta^{18}\text{O}$  ( $\delta^{18}\text{O}_{C.wuell}$ ) principally responds to the effect of global ice volume changes on  $\delta^{18}\text{O}_{\text{sw}}$  with only a minor contribution from deep water temperature change. Thus, the subtraction of  $\delta^{18}\text{O}_{C.wuell}$  from the planktonic  $\delta^{18}\text{O}$  record ( $\delta^{18}\text{O}_{G.trunc(s)}$ ) eliminates the ice volume effect.  $\Delta\delta^{18}\text{O}$  should therefore mainly reflect the temperature variability in the planktonic record. The  $\Delta\delta^{18}\text{O}$  stratigraphic series was then converted to a temperature anomaly record by subtracting the mean Holocene (0-7 ka) value from the series and assuming a slope of  $0.25\text{‰}$  change in  $\delta^{18}\text{O}$  per  $1^\circ\text{C}$  change in temperature (Shackleton, 1974).

Based on that analysis, the resultant glacial-interglacial temperature anomaly was estimated to be  $\pm 2^\circ\text{C}$ , which indeed indicates only a minor impact of temperature-dependent carbon isotope fractionation on down-core  $\delta^{13}\text{C}_{G.trunc(s)}$  at MD02-2588.

#### 6.4.4 Southern Ocean air-sea gas exchange during the past 150 kyr BP

The transfer of carbon between the atmosphere and the oceans on glacial-interglacial and millennial timescales results not only in changes of  $p\text{CO}_2^{\text{atm}}$  but also in the  $\delta^{13}\text{C}$  of atmospheric  $\text{CO}_2$  ( $\delta^{13}\text{C}_{\text{atm}}$ ). Each process of carbon transfer between the various reservoirs, i.e., the atmosphere, the oceans, the terrestrial biosphere and sediments, results in isotopic fractionation of  $\delta^{13}\text{C}$ . Therefore, records of  $\delta^{13}\text{C}_{\text{atm}}$  represent a crucial piece of evidence for understanding changes in the global carbon cycle.

The records of  $\delta^{13}\text{C}_{\text{atm}}$  from measurements in Antarctic ice cores that now span the past 160 kyr BP, have revealed significant excursions at glacial terminations I and II, and during MIS 4 (Schneider, 2011; Schmitt *et al.*, 2012; Schneider *et al.*, 2013 Eggleston *et al.*, 2016). Complementary modelling studies (Köhler *et al.*, 2010; Menviel *et al.*, 2012), have identified a number of processes that likely contributed to these fluctuations, including: (i) changing sea surface temperatures, (ii) long-term trends in terrestrial carbon storage, (iii) changes in the AMOC, (iv) upwelling of deep water in the Southern Ocean, and (v) changes in marine biological export in the Southern Ocean due to variations in aeolian iron fluxes, (e.g., Laurantou *et al.*, 2010a, 2010b; Schmitt *et al.*, 2012; Schneider *et al.*, 2013 Eggleston *et al.*, 2016). These interpretations have highlighted the role that the Southern Ocean plays, not only in determining  $p\text{CO}_2^{\text{atm}}$ , but also  $\delta^{13}\text{C}_{\text{atm}}$  and have thus lent support to previous hypotheses that have emphasised the importance of the Southern Ocean in glacial-interglacial climate change (e.g., Sigman and Boyle, 2000; Archer *et al.*, 2000; Sigman *et al.*, 2010; Fischer *et al.*, 2010).

Here we compare the planktonic and benthic foraminiferal records of  $\delta^{13}\text{C}$  from MD02-2588 with the Antarctic ice core records of  $\delta^{13}\text{C}_{\text{atm}}$ . Our aim is to test whether the proxy evidence of variations in marine biological export and upwelling of deep waters in the Southern Ocean can indeed be reconciled with the record of  $\delta^{13}\text{C}_{\text{atm}}$ .

##### 6.4.4.1 Links between the downcore records of carbon isotopic composition of foraminifera from MD02-2588 and the ice core records of $\delta^{13}\text{C}_{\text{atm}}$

The variations of  $\delta^{13}\text{C}_{G.trunc(s)}$  in the downcore record from sediment core MD02-2588 closely follow the pattern of  $\delta^{13}\text{C}_{\text{atm}}$  change during the past 150 kyr BP (Fig. 6.11a).

The absolute values in each record are offset by  $\sim 7\text{‰}$  but both have a range very close to  $1\text{‰}$  and the general trends are in excellent agreement even on their independent age models (Fig. 6.11a). The negative excursions during TI, TII and MIS 4 are present in both records and with the exception of the latter excursion, they appear to be of similar magnitude. Moreover, a comparison of  $\delta^{13}\text{C}_{\text{atm}}$  with the biological component of the benthic  $\delta^{13}\text{C}$  record from MD02-2588 ( $\delta^{13}\text{C}_{\text{benthic-bio}}$ ) suggests a comparable coupling (Fig. 6.11b). The temporal lag between  $\delta^{13}\text{C}_{\text{benthic-bio}}$  variations and  $\delta^{13}\text{C}_{\text{atm}}$  (e.g., during the CIME of TI) may be related to differences in the age-models of each record. The record of  $\delta^{13}\text{C}_{\text{benthic-bio}}$  was presented and discussed in Chapter 4; briefly, it represents the component of the *C. wuellerstorfi*  $\delta^{13}\text{C}$  record from MD02-2588 that corresponds solely to nutrient variability, and is based on the  $\text{Cd}_{\text{sw}}$  reconstruction from Cd/Ca measurements made on the same foraminifera samples. Therefore, the record of  $\delta^{13}\text{C}_{\text{benthic-bio}}$  is assumed to exclude the variations associated with air-sea fractionation processes and mean ocean changes of  $\delta^{13}\text{C}_{\text{DIC}}$ . As such,  $\delta^{13}\text{C}_{\text{benthic-bio}}$  record is considered to represent the preformed nutrient and DIC signal that is upwelled to the Southern Ocean surface prior to being modified and incorporated into intermediate waters. The similarity of the general trends and the range of values in the  $\delta^{13}\text{C}_{\text{benthic-bio}}$  record with the  $\delta^{13}\text{C}_{\text{atm}}$  again suggests a link between the upwelling of CDW in the Southern Ocean and interaction of the deep carbon reservoir with the atmosphere. Southern Ocean surface waters are one of the principal sources of  $\text{CO}_2$  to the atmosphere and their carbon isotopic composition directly contributes to the isotopic signal of the atmosphere. The same is true of the  $\delta^{13}\text{C}_{\text{benthic-bio}}$  record which demonstrates the importance of the deep water contribution of DIC and nutrients to intermediate waters, as well as illustrating its importance as a source of carbon to the atmosphere. The similarity of these three records is therefore indicative of the transfer of carbon between the deep ocean and the atmosphere, and also highlights how the isotopic signal of Southern Ocean surface waters closely tracks the variability of  $\delta^{13}\text{C}_{\text{atm}}$ .

The modelling study of Köhler *et al.*, (2010) has demonstrated that the most important process for lowering glacial  $\delta^{13}\text{C}_{\text{atm}}$  is the decrease of ocean temperatures. According to their study, lower glacial ocean temperatures lead to an estimated

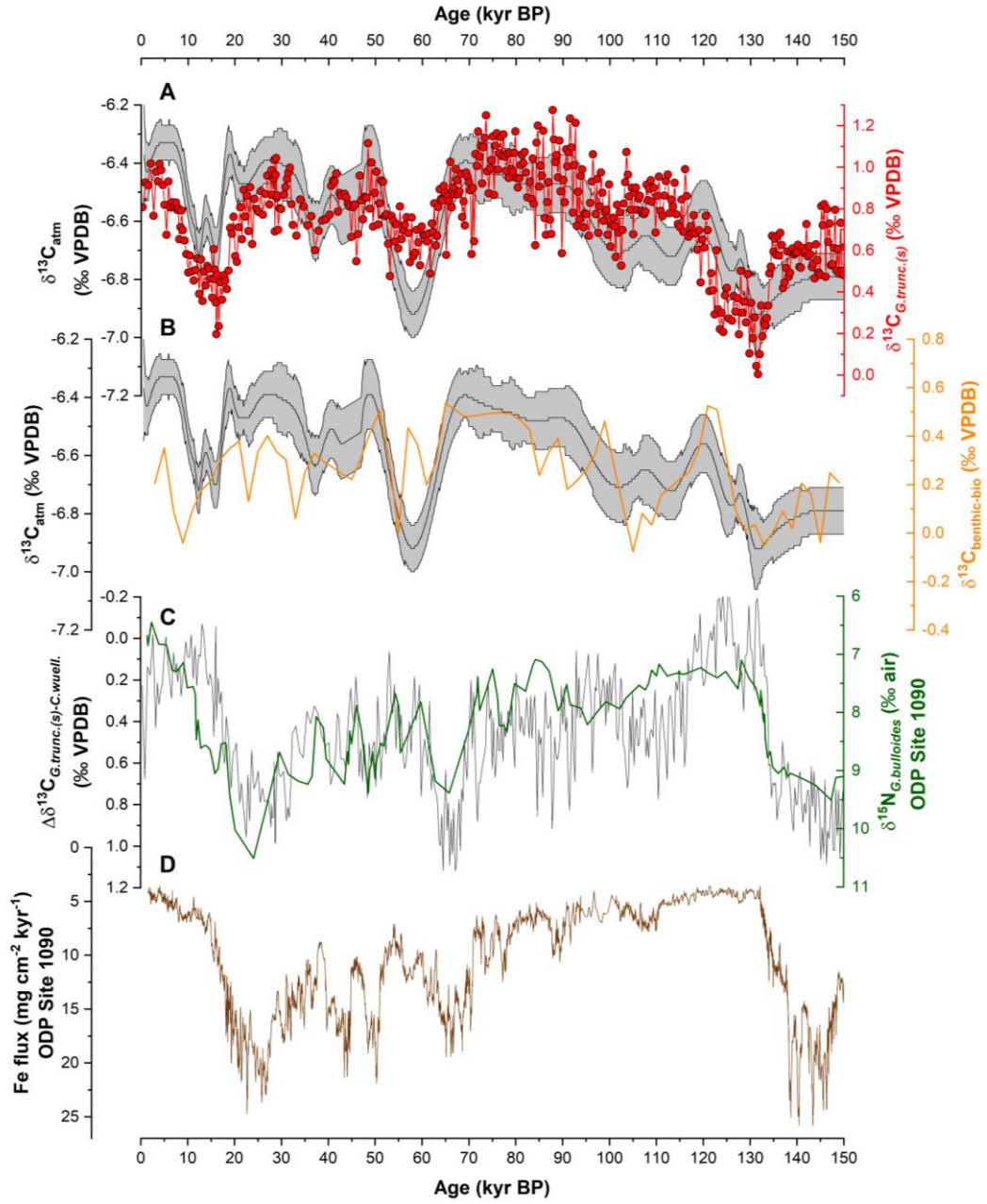


**Figure 6.11.** A) Downcore record of carbon isotopes measured in the deep-dwelling planktonic foraminifera *Globorotalia truncatulinoides (sinistral)* ( $\delta^{13}\text{C}_{G.trunc.(s)}$ ) in sediment core MD02-2588, which incorporates data from this study and Ziegler *et al.*, (2013) (red line with filled circles). Also shown is the Antarctic ice core record of atmospheric  $\delta^{13}\text{C}$  ( $\delta^{13}\text{C}_{\text{atm}}$ ) (black line) on its published age model (Schneider, 2011; Schmitt *et al.*, 2012; Schneider *et al.*, 2013 Eggleston *et al.*, 2016). The envelope around the  $\delta^{13}\text{C}_{\text{atm}}$  record is the  $2\sigma$  uncertainty bounds of the Monte Carlo cubic spline Average (MCA) (Eggleston *et al.*, 2016). See Schmitt *et al.*, (2012) for a detailed description of this method. B) Biological component of the benthic foraminiferal  $\delta^{13}\text{C}$  record ( $\delta^{13}\text{C}_{\text{bentic-bio}}$ ) from MD02-2588. This record is derived by correcting the *C. wuellerstorfi*  $\delta^{13}\text{C}$  for the effects of air-sea fractionation and mean ocean changes  $\delta^{13}\text{C}_{\text{DIC}}$  (see chapters 3 and 4 for details). Again, shown for comparison is the Antarctic ice core record of  $\delta^{13}\text{C}_{\text{atm}}$ . C) Carbon isotope gradient between *G. truncatulinoides (s)* and *C. wuellerstorfi* ( $\Delta\delta^{13}\text{C}_{G.trunc(s)-C.wuell}$ ) from MD02-2588, incorporating the data presented in this thesis and in Ziegler *et al.*, (2013) (grey line). Also shown is the foram-bound  $\delta^{15}\text{N}$  measured in *Globigerina bulloides* at ODP Site 1090 on its published age model (Martínez-García *et al.*, 2014) (green line). Note reversed y-axes. D)  $^{230}\text{Th}$ -normalized iron flux from ODP Site 1090 (brown line), calculated using the  $^{230}\text{Th}$ -normalized mass flux measured in the parallel core TN057-6 on its published age model (Martínez-García *et al.*, 2014). Note reversed y-axis.

$\delta^{13}\text{C}_{\text{atm}}$  reduction of 0.49‰. This is because reduced temperatures lead to a higher uptake of carbon via the so-called solubility pump (see Chapter 1 of this thesis). Preferential uptake of the heavier carbon isotope at lower ocean temperatures causes a depletion of  $\delta^{13}\text{C}_{\text{atm}}$  and a relative enrichment of  $\delta^{13}\text{C}_{\text{DIC}}$  in the ocean (Lynch-Stieglitz *et al.*, 1995). Our discussion of the impact of air-sea fractionation on  $\delta^{13}\text{C}_{\text{DIC}}$  in the previous section has already highlighted that a SST lowering of 2-6°C during the LGM (MARGO Project Members, 2009) would result in a  $\delta^{13}\text{C}_{\text{DIC}}$  increase of 0.2-0.6‰ (Mook *et al.*, 1974).

The second most important process for the lowering of  $\delta^{13}\text{C}_{\text{atm}}$  and  $\delta^{13}\text{C}_{\text{DIC}}$  is the reduction of terrestrial carbon storage. Estimates based on a release of 500 Pg C (that is,  $10^{15}$  g of carbon) of  $^{13}\text{C}$ -depleted carbon to the atmosphere during the LGM causes  $\delta^{13}\text{C}_{\text{atm}}$  to drop by 0.44‰ (Köhler *et al.*, 2010). This is comparable to the estimated 0.3-0.4‰ decrease of oceanic values caused by the transfer of terrestrial material to the ocean during the LGM, as estimated from  $\delta^{13}\text{C}$  measured in benthic foraminiferal calcite (Shackleton, 1977; Curry *et al.*, 1988; Oliver *et al.*, 2010).

The effects of temperature and the terrestrial biosphere are compensated by ocean circulation and the biological pump which tend to cause an increase in  $\delta^{13}\text{C}_{\text{atm}}$  during glacials (Köhler *et al.*, 2010). The AMOC determines the balance between carbon uptake in the region of the NADW formation and carbon release in the Southern Ocean, where deep waters return to the surface (Marshall and Speer, 2012). During the LGM, both  $\delta^{13}\text{C}_{\text{atm}}$  and the  $\delta^{13}\text{C}_{\text{DIC}}$  of Southern Ocean surface waters increase as a result of less upwelling of  $\delta^{13}\text{C}_{\text{DIC}}$ -depleted deep water (Köhler *et al.*, 2010). The same principle applies for an increase in Southern Ocean stratification and an expansion of sea ice around Antarctica during the LGM (e.g., François *et al.*, 1997; Stephens and Keeling, 2000). In both cases, a reduction in vertical exchange limits  $\delta^{13}\text{C}_{\text{DIC}}$ -depleted deep waters from reaching the surface ocean and thus causes both  $\delta^{13}\text{C}_{\text{DIC}}$  of surface waters and  $\delta^{13}\text{C}_{\text{atm}}$  to increase. Similarly, and as we have already discussed, an increase in the strength of the soft-tissue biological pump during glacials, possibly stimulated by increased aeolian iron deposition into the Southern Ocean (e.g., Martínez-García *et al.*, 2014), results in increased export of organic carbon depleted in  $^{13}\text{C}$  to the ocean interior, thus causing  $\delta^{13}\text{C}_{\text{DIC}}$  in the surface ocean and  $\delta^{13}\text{C}_{\text{atm}}$  to increase.

Regarding the role of the Southern Ocean's soft-tissue biological pump as a modifier of the carbon isotopic composition of the atmosphere, it is instructive to compare the

ice core record of  $\delta^{13}\text{C}_{\text{atm}}$  with the stratigraphic series of  $\Delta\delta^{13}\text{C}_{\text{plank-benthic}}$  from MD02-2588 (Fig. 6.11c). We note that the  $\Delta\delta^{13}\text{C}_{\text{plank-benthic}}$  record is in excellent agreement with the *Globigerina bulloides* nitrogen isotope ( $\delta^{15}\text{N}_{G.bulloides}$ ) record from ODP Site 1090, which is considered to be a robust proxy of nitrate consumption in the Subantarctic (Martínez-García *et al.*, 2014) (Fig. 6.11c). When compared to the reconstruction of iron burial flux from ODP Site 1090 (Fig. 6.11d), it appears that the increased dust flux that characterises peak glacial times and millennial-timescale cold events occurs in parallel with increases in  $\delta^{15}\text{N}_{G.bulloides}$  and  $\Delta\delta^{13}\text{C}_{\text{plank-benthic}}$  from MD02-2588. This indicates increased nitrate consumption and a larger water column gradient of  $\delta^{13}\text{C}_{\text{DIC}}$ , respectively. Further corroboration is provided by the record of alkenone flux in the Subantarctic which also suggests an increase in export productivity at these time (Sachs and Anderson, 2003; Martínez-García *et al.*, 2014). Taken together, these records indicate that the increased aeolian iron deposition into the Southern Ocean during cold intervals stimulated a strengthening of the Southern Ocean's soft tissue biological pump, at least within the Subantarctic zone. This has been suggested to be a significant mechanism for explaining the lowering of  $p\text{CO}_2^{\text{atm}}$  on both orbital and millennial time-scales, although there is still ambiguity as to whether this process is more important during the transition from mid-climate states to full glacial conditions (Martínez-García *et al.*, 2014), or during the initiation of glaciations (Ziegler *et al.*, 2013).

The record of  $\Delta\delta^{13}\text{C}_{\text{plank-benthic}}$  from MD02-2588 and the Subantarctic records of nitrate consumption, export productivity and iron flux are all consistent with the suggestion that the Southern Ocean's soft-tissue biological pump plays a role in at least part of the variability of  $\delta^{13}\text{C}_{\text{atm}}$ . The most notable indication of this is the occurrence of the three negative  $\delta^{13}\text{C}_{\text{atm}}$  excursions synchronous to the three largest negative shifts of  $\Delta\delta^{13}\text{C}_{\text{plank-benthic}}$ ,  $\delta^{15}\text{N}_{G.bulloides}$  and iron flux, namely during TI, TII and MIS 4 (Fig. 6.11). The same is true for some of the stronger shifts during MIS 3, e.g., at ~40 kyr BP and ~47 kyr BP, as well as for the longer-term trend during MIS 2. However, in all cases, it remains difficult to quantify the exact contribution of the soft-tissue biological pump to the respective shift in  $\delta^{13}\text{C}_{\text{atm}}$  relative to other influences.

#### 6.4.4.2 Southern Ocean carbon dioxide leakage and $\delta^{13}\text{C}_{G.\text{trunc}(s)}$

The similarity between the  $\delta^{13}\text{C}_{G.trunc(s)}$  record from MD02-2588 and the  $\delta^{13}\text{C}_{atm}$  from Antarctic ice cores clearly demonstrates the link between the atmosphere and the surface waters of the Southern Ocean. Ever since the series of ‘Harvardton Bear’ papers highlighted the potential dependence of  $p\text{CO}_2^{atm}$  on the balance between biological productivity and ventilation of the deep Southern Ocean, this region has been the main focus of studies that have attempted to explain the glacial/interglacial variability of  $p\text{CO}_2^{atm}$  (Knox and McElroy, 1984; Sarmiento and Toggweiler, 1984; Siegenthaler and Wenk, 1984). Although this variability still remains a major challenge to our understanding of the carbon cycle and the climate system, there appears to be little doubt that the Southern Ocean plays a key role (Sigman *et al.*, 2010; Hain *et al.*, 2014).

Particular effort has been placed on trying to understand the last glacial termination (TI) and the deglacial rise in  $p\text{CO}_2^{atm}$  observed in ice cores at this time (Denton *et al.*, 2010). This rise in  $p\text{CO}_2^{atm}$  is thought to result from the reconnection of the deep-ocean carbon reservoir with the atmosphere, though most evidence tends to be indirect – e.g., from reconstructions of nutrient cycling and ocean circulation, or from indications of changes ventilation history and  $\delta^{13}\text{C}_{atm}$  (Anderson *et al.*, 2009; Burke and Robinson, 2012; Schmitt *et al.*, 2012). Recently however, more direct evidence of ocean–atmosphere  $\text{CO}_2$  exchange has been provided by the boron isotope ( $\delta^{11}\text{B}$ ) pH proxy, which has shown that Subantarctic surface waters did indeed become a significant source of carbon to the atmosphere during the last deglaciation (Martínez-Botí *et al.*, 2014) (Fig. 6.12a).

Sediment core PS2498-1, from which the deglacial  $\delta^{11}\text{B}$  record referred to above was produced, is located in the Subantarctic Atlantic (44°09'S, 14°13.8'W), a few degrees southwest of MD02-2588 (41°19.90'S, 25°49.70'E). The pattern and amplitude of variability between  $\delta^{13}\text{C}$  records measured in planktonic foraminifera at the two sites is in excellent agreement (Fig. 6.12b); the offset of ~1.4‰ between the two records probably reflects species-specific physiological differences and minor modifications of  $\delta^{13}\text{C}_{DIC}$  between its formation area in the Subantarctic site and the more downstream location of the Agulhas Plateau. This provides further support that the variability of  $\delta^{13}\text{C}_{G.trunc(s)}$  recorded in MD02-2588 is directly associated with surface water variability in the Subantarctic, albeit with an offset. In addition, it demonstrates how

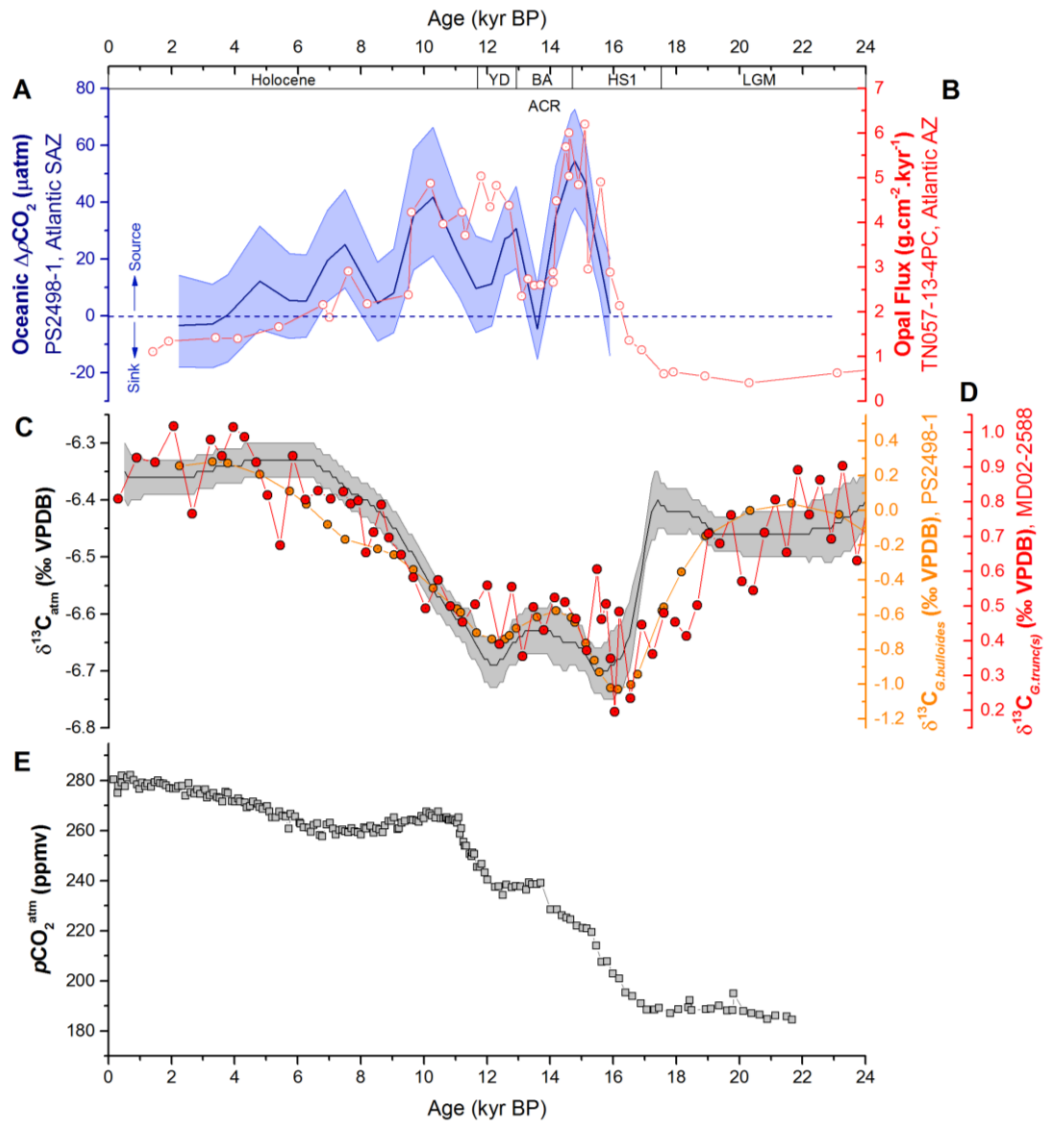


**Figure 6.12.** A) Difference in CO<sub>2</sub> concentration between the surface ocean and the atmosphere ( $\Delta p\text{CO}_2$ ) (blue line with shading) (Martínez-Botí *et al.*, 2014). Surface ocean CO<sub>2</sub> concentration was calculated using the boron isotope ( $\delta^{11}\text{B}$ ) pH proxy in planktonic foraminifera from the Subantarctic Atlantic sediment core PS2498-1 (44.15°S, 14.23°W, 3,783 m water depth) whilst atmospheric CO<sub>2</sub> concentration is from ice cores. The shaded envelopes show the 95% uncertainty bounds based on a LOESS regression of the  $\delta^{11}\text{B}$ -derived records using a Monte Carlo approach; thick line denotes the maximum-probability fit to the data (Martínez-Botí *et al.*, 2014). The dashed horizontal line denotes the equilibrium level of  $\Delta p\text{CO}_2$ ; values above this line indicate that the ocean was a source of CO<sub>2</sub> to the atmosphere, whereas values below indicate that the ocean was a sink of CO<sub>2</sub>. B) opal flux record from sediment core TN057-13-4PC in the Atlantic sector of the Southern Ocean (53.2°S 5.1°E) (red line with empty circles) (Anderson *et al.*, 2009). C) Antarctic ice cores record of atmospheric  $\delta^{13}\text{C}$  ( $\delta^{13}\text{C}_{\text{atm}}$ ) (black line) (Schneider, 2011; Schmitt *et al.*, 2012; Schneider *et al.*, 2013 Eggleston *et al.*, 2016). The envelope around the  $\delta^{13}\text{C}_{\text{atm}}$  record is the 1 $\sigma$  uncertainty bounds of the Monte Carlo cubic spline Average (MCA) (Eggleston *et al.*, 2016). See Schmitt *et al.*, (2012) for a detailed description of this method. D) *Globorotalia truncatulinoides* (*s*)  $\delta^{13}\text{C}$  ( $\delta^{13}\text{C}_{G.\text{trunc}(s)}$ ) from sediment core MD02-2588 (red line with filled circles) (Ziegler *et al.*, 2013; Chapter 5.2, this thesis) and *Globigerina bulloides*  $\delta^{13}\text{C}$  ( $\delta^{13}\text{C}_{G.\text{bulloides}}$ ) from sediment core PS2498-1 (orange line with filled circles) (Martínez-Botí *et al.*, 2014). E)  $p\text{CO}_2^{\text{atm}}$  from Antarctic ice core records (Grey circles) (Monnin *et al.*, 2001, 2004). All records are plotted on their published age models.

the  $\delta^{13}\text{C}_{G.trunc(s)}$  record is linked to the deglacial outgassing of  $\text{CO}_2$  from the Southern Ocean, providing direct evidence of the gas exchange processes that link planktonic foraminiferal  $\delta^{13}\text{C}$  (and thus, surface water  $\delta^{13}\text{C}_{\text{DIC}}$ ) to  $\delta^{13}\text{C}_{\text{atm}}$ , at least over the last glacial termination. Therefore, if we can assume that the connection between Subantarctic surface water  $\delta^{13}\text{C}_{\text{DIC}}$  and  $\delta^{13}\text{C}_{\text{atm}}$  was maintained beyond the last deglaciation, then this raises the prospect of using records such as  $\delta^{13}\text{C}_{G.trunc(s)}$  in MD02-2588 as a first order indicator of  $\delta^{13}\text{C}_{\text{atm}}$  back in time, possibly even allowing reconstructions of relative changes of  $\delta^{13}\text{C}_{\text{atm}}$  beyond the extent of ice core records.

## 6.5 Conclusion

In this chapter we presented new data from a set of core-top samples collected around New Zealand in order to assess the utility of the deep-dwelling planktonic foraminifera species, *G. truncatulinoides*, as a recorder of  $\delta^{13}\text{C}_{\text{DIC}}$ . From the results of this study, we concluded that this species is indeed a reliable tracer of thermocline chemical properties. Though, offsets between the values of  $\delta^{13}\text{C}$  measured in the calcite tests of this species and the corresponding water column  $\delta^{13}\text{C}_{\text{DIC}}$  highlights the importance of consistency in sample selection for down-core studies.

We then presented a down-core assessment of the  $\delta^{13}\text{C}_{G.trunc(s)}$  using published data from sediment core MD02-2588 (Ziegler *et al.*, 2013) and new replicate data from the same core. Our aim was to build on the original evaluation conducted by Ziegler *et al.*, (2013) of how secondary effects, not associated with nutrient and DIC cycling, impact  $\delta^{13}\text{C}_{G.trunc(s)}$ . We compared the  $\delta^{13}\text{C}_{G.trunc(s)}$  record from MD02-2588 with the record of  $\delta^{13}\text{C}_{\text{atm}}$  from Antarctic ice cores and found them to be strikingly similar in terms of their patterns of variability throughout the past 150 kyr BP. The same was found to be true for the biological component of the benthic  $\delta^{13}\text{C}$  ( $\delta^{13}\text{C}_{\text{benthic-bio}}$ ) record from MD02-2588 which reflects the nutrient and DIC characteristics of deep waters that upwell around Antarctica. These similarities demonstrate the importance of carbon transfer between the Southern Ocean and the atmosphere and highlights the potential of using records of  $\delta^{13}\text{C}_{\text{DIC}}$  from Southern Ocean to reconstruct the variability of  $\delta^{13}\text{C}_{\text{atm}}$  further back in time, possibly even allowing first-order estimations of relative changes of  $\delta^{13}\text{C}_{\text{atm}}$  to be extended beyond the scope of ice core records.

Furthermore, we show that the record  $\Delta\delta^{13}\text{C}_{\text{plank-benthic}}$  from MD02-2588 is consistent with the suggestion that the Southern Ocean's soft-tissue biological pump plays a role

in at least part of the variability of  $\delta^{13}\text{C}_{\text{atm}}$  recorded in Antarctic ice cores, although it remains difficult to quantify its exact contribution relative to other drivers of  $\delta^{13}\text{C}_{\text{atm}}$  variability. The most notable indication of the link between the biological pump and  $\delta^{13}\text{C}_{\text{atm}}$  is the occurrence of the three largest negative  $\delta^{13}\text{C}_{\text{atm}}$  excursions during TI, TII and MIS 4, synchronous to the three largest negative shifts of  $\Delta\delta^{13}\text{C}_{\text{plank-benthic}}$ .

---

## 7 Preliminary study of marine sediment core CD154-23-16P: elemental composition and initial stable isotope stratigraphy

---

### 7.1 Chapter outline

In the following chapter we present results from a preliminary study of sediment core CD154-23-16P retrieved from the flank of the Mallory Seamount, offshore southern Africa. We show the results of high-resolution X-ray fluorescence (XRF) core-scanning and the initial results of stable oxygen and carbon isotopes measured in surface- and deep-dwelling planktonic foraminifera. We develop an age model for this core using a combination of radiocarbon dating of planktonic foraminifera and graphical tuning techniques. We then exploit this chronostratigraphic framework to assess and discuss the XRF and stable isotope results in the context of past environmental changes in this region.

### 7.2 Introduction

The Agulhas Current is the western boundary current associated with the Indian Ocean subtropical gyre and is responsible for the transport of  $\sim 70$  Sverdrup (Sv) ( $1 \text{ Sv} = 10^6 \text{ m}^3 \text{ s}^{-1}$ ) of tropical and subtropical waters along the southeastern coast of Africa (Lutjeharms, 2006, 2007) (Fig. 7.1). This current flows southwestward as a narrow jet along the steep continental slope between approximately 28 to 34°S before diverging from the coast to continue its course along the Agulhas Bank (Gründlingh, 1983). Near 36°S it detaches from the continental shelf and in the region between 16 and 20°E it retroflects back toward the Indian Ocean as the Agulhas Return Current (Lutjeharms and Van Ballegooyen, 1988). A small proportion of the warm and salty Agulhas Current waters (2-15 Sv) are transported as Agulhas Leakage into the South Atlantic through the Indian-Atlantic Ocean Gateway (I-AOG) (de Ruijter *et al.*, 1999). Modeling studies have shown that this leakage can stimulate regional buoyancy anomalies in the Atlantic basin that can ultimately alter the Atlantic meridional overturning circulation (AMOC) and the climate of the North Atlantic region on various timescales

(Weijer, 2000; Weijer *et al.*, 2002; Knorr and Lohmann, 2003; Van Sebille *et al.*, 2009; Biastoch *et al.*, 2008, 2009).

The CD154-23-16P core site is presently located directly under the southernmost reach of the Agulhas Current, close to the region where it detaches from the continental shelf to become the Agulhas Current Retroflexion. This core forms part of a suite of sediment cores retrieved from the southeastern continental slope of southern Africa from within the main flow of the Agulhas Current (Hall and Zahn, 2004). These cores have enabled the first multi-proxy reconstructions of the upstream and midstream variability of the Agulhas Current during the last glacial interval at millennial-scale resolution (Simon *et al.*, 2013, 2015). Sediment core CD154-23-16P provides an opportunity to complement these studies by potentially allowing the reconstruction of millennial-scale variability from within the southernmost reach of the Agulhas Current. Furthermore, this collection of sediment cores has yielded important insights into the relative variability of river discharge from southeastern Africa on orbital and millennial time-scales which has been linked to regional terrestrial climatic variability (Simon *et al.*, 2015). The coincidence of abrupt climatic changes with intervals of technological and behavioural innovation within the Middle Stone Age of South Africa has also led to the suggestion that this climatic variability may have played a role in the development and cultural evolution of *Homo sapiens* in this region of Africa (Ziegler *et al.*, 2013). The addition of core CD154-23-16P to this latitudinal series of sites will therefore improve the spatial coverage of these reconstructions and will allow a more complete picture to be gained regarding the impact of climate change on early human populations.

### **7.3 Material and Methods**

Full methodological details are given in Chapter 3 of this thesis. The following is a summary of the materials and methods relevant to the data presented in this Chapter.

#### *7.3.1 Sediment core CD154-23-16P: retrieval and sampling*

Marine sediment core CD154-23-16P was retrieved from 3189 m water depth from the flank of the Mallory Seamount (36°49.08`S, 022°00.02`E) during *RRS Charles Darwin* cruise number 154 (Hall and Zahn, 2004). The core recovered 1103 cm of sediment composed of soft watery green and brown-green mud in the upper part with

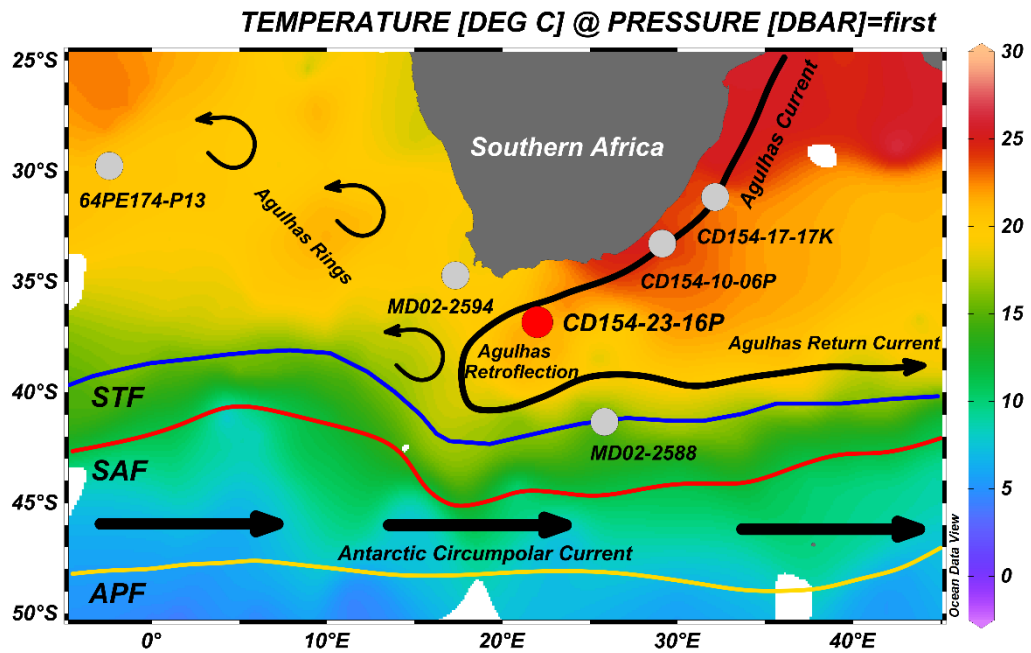


**Figure 7.1.** Modern sea surface temperature (SST) map showing the study area and the location of sediment core CD154-23-16P, together with the present day position of the Southern Ocean fronts and the generalised regional surface ocean circulation (Peterson and Stramma, 1991; Orsi *et al.*, 1995). Black continuous arrow shows the approximate pathway of the Agulhas Current along the African continental margin, the Agulhas Retroflection and the eastward flowing Agulhas Return Current, with Agulhas Rings in the South Atlantic. The thick black discontinuous arrows indicate the flow of the Antarctic Circumpolar Current (ACC). The blue, red and yellow lines show the approximate positions of the Subtropical Front (STF), the Subantarctic Front (SAF), and the Antarctic Polar Front (APF), respectively. The position of the sediment core CD154-23-16P is indicated by the red circle. The position of sediment cores discussed in this chapter are indicated by light grey circles (Table 7.4). Map produced and edited in Ocean Data View (Schlitzer, 2016).

abundant foraminifera, radiolaria and sponge spicules. In the lower part of the core sediments have a lower water content and are stiffer and are more green-grey in colour and lack the siliceous elements (radiolaria, sponge spicules).

For this study we took sediment samples every 8 cm throughout the upper 9 m of the core for stable oxygen and carbon isotope analysis of planktonic foraminiferal tests. Ten additional intervals were sampled for radiocarbon dating of planktonic foraminiferal carbonate. The latter sampling depths were selected based on an initial tuning of the Ca/Fe ratio derived from XRF scanning of sediment core CD154-23-16P (Hall, 2003; unpublished dataset) to the Chinese speleothem oxygen isotope record from the Sanbao and Hulu Caves (Wang *et al.*, 2001).

### 7.3.2 XRF core scanning

Core scanning for this study was performed using the ITRAX™ XRF Core scanner at the British Ocean Sediment Core Research Facility (BOSCORF, Southampton). Measurements were made at variable resolutions along the core with a 0.5 cm resolution in the upper 3.5 m, 0.1 cm resolution between 3.5 and 5 m and 0.2 cm resolution for the remainder of the core. Count time per sample was set to 30 s and the XRF voltage and current were set at 30 kV and 50mA, respectively. As the sampling of the core was performed prior to the XRF core scanning the data had to be processed to remove values associated with sediment gaps in the core.

### 7.3.3 Stable oxygen and carbon isotope analysis

Stable oxygen and carbon isotopes were measured in carbonate samples consisting of the calcite tests of the surface-dwelling planktonic foraminifera *Globigerinoides ruber* (*sensu lato*) (n=112) and the deep-dwelling planktonic foraminifera *Globorotalia truncatulinoides* (*sinistral*) (n=113). Foraminiferal tests were picked from the 250-315 µm size fraction and each sample consisted of 15-30 individual tests in the case of *G. ruber* (*s.l.*) and 8-20 tests in the case of *G. truncatulinoides* (*s.*). Picked samples were lightly ultrasonicated in methanol (~3 s) to dislodge any carbonate material that may have affected the isotopic composition of the samples (e.g., coccoliths). Stable isotope analysis was performed on whole-test samples.

Stable isotopes were measured at Cardiff University using either a Thermo Finnigan MAT 253 mass spectrometer linked online to a Carbo Kiel-II carbonate preparation device or a Thermo Scientific Delta V Advantage mass spectrometer coupled with a

Gas Bench III automated preparation device. Measurements of foraminiferal oxygen ( $\delta^{18}\text{O}_{G.ruber}$  and  $\delta^{18}\text{O}_{G.trunc(s)}$ ) and carbon isotopes ( $\delta^{13}\text{C}_{G.ruber}$  and  $\delta^{13}\text{C}_{G.trunc(s)}$ ) were determined relative to the Vienna Peedee Belemnite scale (VPDB) through calibration with the NBS-19 carbonate standard. The long-term external precision of the Thermo Finnigan MAT 253 mass spectrometer based on an internal laboratory carbonate standard (Carrara Marble) was better than  $\pm 0.04\text{‰}$  and  $\pm 0.02\text{‰}$  for  $\delta^{18}\text{O}$  and  $\delta^{13}\text{C}$ , respectively ( $\pm 1\sigma$ ). For the Thermo Scientific Delta V Advantage mass spectrometer these were  $\pm 0.03\text{‰}$  for  $\delta^{18}\text{O}$  and  $\pm 0.04\text{‰}$  for  $\delta^{13}\text{C}$  ( $\pm 1\sigma$ ).

#### 7.3.4 Age model

The age model for sediment core CD154-23-16P was developed using ten  $^{14}\text{C}$  accelerator mass spectrometry (AMS) dates measured in carbonate samples consisting principally *G. ruber* (*s.l.*) but supplemented by tests of *G. ruber* (*sensu stricto*) when the former was not abundant enough. Picked samples weighed 12-13 mg and had a carbon content of  $\sim 10\%$  by weight. The samples were prepared to graphite at the Natural Environment Research Council (NERC) Radiocarbon Facility (East Kilbride) and underwent  $^{14}\text{C}$ -analysis at the Scottish Universities Environmental Research Centre (SUERC) AMS Laboratory (Table 7.1).

The radiocarbon ages were reported as conventional radiocarbon years BP (relative to AD 1950) and show one age reversal at 230.5 cm which was rejected and is not included in the subsequent calibration of the radiocarbon ages (Table 7.1). This age reversal is presumably associated with the deposition of a turbidite composed of older material from an upslope region on the seamount flank. The two samples that bound this age reversal indicate that this interval is characterised by the deposition of approximately 30 cm of sediment over approximately 100 conventional radiocarbon years. The  $^{14}\text{C}$  AMS dating of the selected samples captures another interval where the deposition of approximately 30 cm of sediment occurs over a duration of about 100 conventional radiocarbon years (between 606.5 cm and 630.5 cm). In this case the dating does not show an age reversal but the rapid deposition of the material suggests that this interval may also be associated with a turbidite. Comparison of the percentage (by weight) coarse-fraction ( $>63\ \mu\text{m}$ ) shows rapid increases from  $\sim 20\%$  to about  $40\%$  close to these two intervals. This supports the suggestion that these intervals represent the deposition of higher-energy coarser material by a turbidity current (Fig. 7.2). Intriguingly, neither of these intervals stand out in colour spectral

**Table 7.1.** Uncalibrated <sup>14</sup>C dates for CD154 23-16P

<b>Species</b>	<b>Depth (cm)</b>	<b>Conven- tional <sup>14</sup>C AMS age (yrs BP)</b>	<b>+/- 1σ (<sup>14</sup>C yrs BP)</b>	<b><sup>14</sup>C AMS age +1σ (<sup>14</sup>C yrs BP)</b>	<b><sup>14</sup>C AMS age -1σ (<sup>14</sup>C yrs BP)</b>	<b>Laboratory Code</b>
<i>G. ruber</i>	1	2523	35	2558	2488	SUERC-50004
<i>G. ruber</i>	205.5	13756	45	13801	13711	SUERC-50005
<i>G. ruber</i>	230.5	14403*	48	14451	14355	SUERC-50006
<i>G. ruber</i>	238.5	13861	56	13917	13805	SUERC-50009
<i>G. ruber</i>	442.5	21281	90	21371	21191	SUERC-50010
<i>G. ruber</i>	537.5	25619	132	25751	25487	SUERC-50011
<i>G. ruber</i>	550	26157	136	26293	26021	SUERC-50012
<i>G. ruber</i>	606.5	29565	200	29765	29365	SUERC-50013
<i>G. ruber</i>	630.5	29632	220	29852	29412	SUERC-50014
<i>G. ruber</i>	1074	38310	594**	38904	37716	SUERC-50015
<i>G. ruber</i>	1085	41331	857**	42188	40474	SUERC-50016

\*Age reversal.

\*\* Large uncertainty in samples at the bottom of the core.

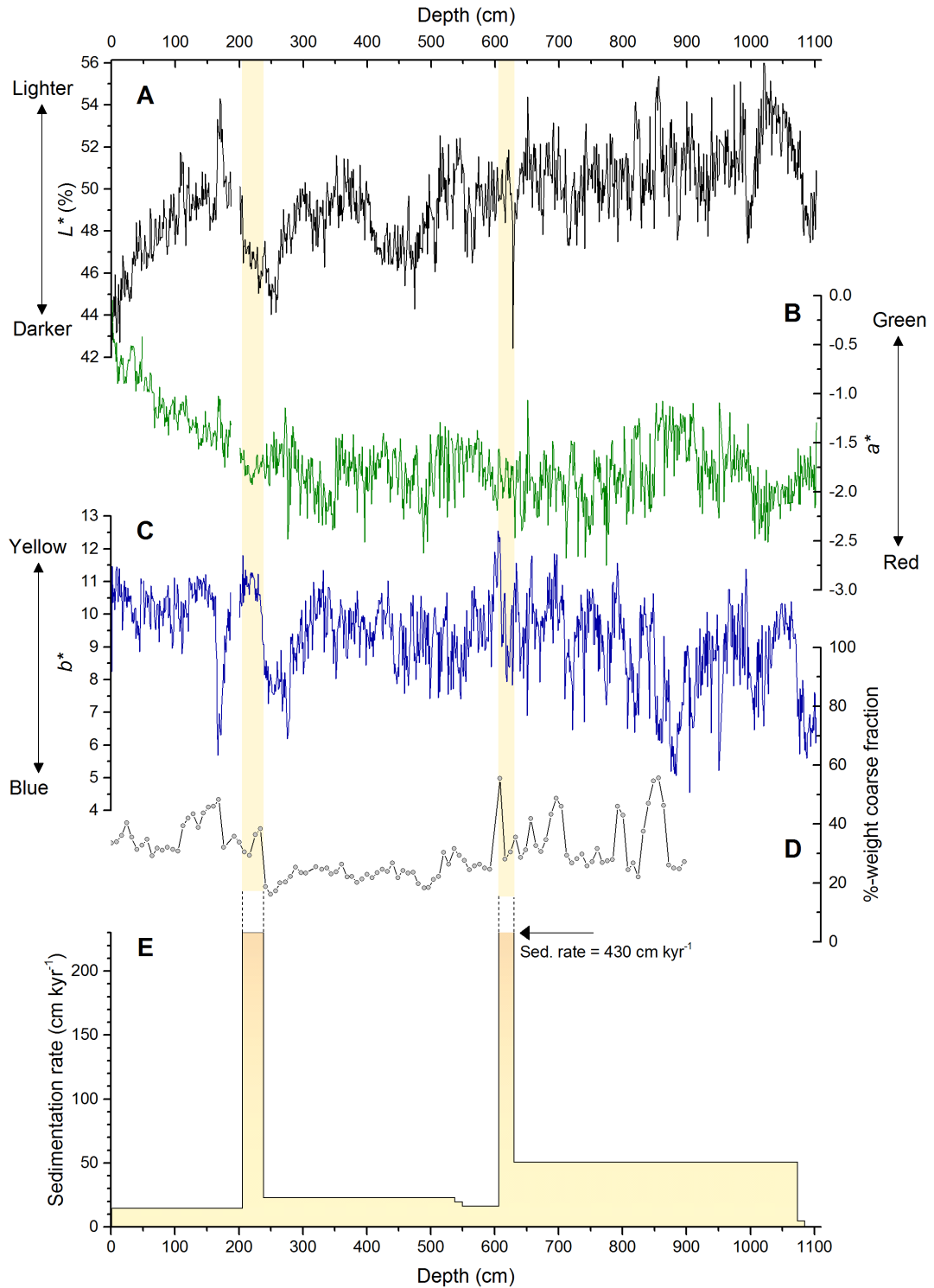


**Figure 7.2.** Colour spectral analysis scans of sediment core CD154-23-16P showing: A) the  $L^*$ , B) the  $a^*$ , and C) the  $b^*$  values. D) Percentage-weight of coarse fraction in along the core. E) Sedimentation rates using the calibrated radiocarbon ages (excluding the age-reversed sample; see main text). Note the two intervals of very high sedimentation rates highlighted by the vertical bars.

analysis scans. Two possible exceptions are the b\* record in which two large increases occur in the approximate position of these events and an L\* minimum at the onset of the older turbidite interval. Furthermore, the initial optical inspection of the core did not reveal the presence of sedimentological features associated with turbidite deposition.

Despite the possibility of the presence of these event deposits within sediment core CD154-23-16P we proceed to develop a calibrated age model with the available data and only reject the  $^{14}\text{C}$  AMS date at 230.5 cm that is associated with the age reversal. The conventional radiocarbon ages were converted to calendar years using the Marine13 radiocarbon age calibration curve which incorporates a time-dependent global ocean reservoir correction (R) of about 400 years (Reimer *et al.*, 2013). However, in order to accommodate local effects, the difference between the reservoir age of the local region and the global ocean mean of 400 years ( $\Delta\text{R}$ ) was also determined. The  $\Delta\text{R}$  for the most proximal site to CD154 23-16P is 224 years (Southon *et al.*, 2002). This value was therefore subtracted from the conventional radiocarbon ages of each sample in CD154-23-16P to account for the local reservoir-age offset from the global mean.

The calibration of the  $^{14}\text{C}$  AMS dates was performed using the R statistical package 'Bchron' (Parnell *et al.*, 2011) which calculates the highest density regions of the calibrated dates at the 95% level (Table 7.2). The  $^{14}\text{C}$ -based core chronology was also constructed using this statistical package by applying a function that uses a Bayesian approach to calculate the quantiles of the predicted ages by depth along the core (Fig. 7.3).

The chronology of the core based on radiocarbon dating alone yields ages for the deepest two samples that are 15-20 kyr younger than our initial estimates based on the tuning of the Ca/Fe XRF-scan (Hall, 2003, unpublished dataset) to the Chinese speleothem  $\delta^{18}\text{O}$  record (Wang *et al.*, 2001). This, and the large errors (600-850 years) associated with these two radiocarbon dates from the deepest samples of the core lead us to question their reliability as age control points in the construction of the chronostratigraphic framework. The estimated sedimentation rates for this age model provide a further indication that these two oldest dates may be erroneous (Fig. 7.1). With the exception of the potential turbidite deposits between approximately 2-2.4 m and 6-6.3 m, the sedimentation rates vary between 15-23 cm kyr<sup>-1</sup> in the upper

**Table 7.2.** Calibrated  $^{14}\text{C}$  dates for CD154 23-16P

Depth (cm)	Conven- tional $^{14}\text{C}$ AMS age (yrs BP)	+/- $1\sigma$ ( $^{14}\text{C}$ yrs BP)	$\Delta\text{R}$ cor- rec- tion (225 years )	Highest Density Re- gion (95%) Lower age limit (kyr BP)	Highest Density Re- gion (95%) Mid-point (kyr BP)	Highest Density Re- gion (95%) Upper age limit (kyr BP)
1	2523	35	2298	1.832	1.9085	1.985
205.5	13756	45	1353	15.634	15.76	15.886
230.5	14403*	48	Re- jected	Rejected	Rejected	Rejected
238.5	13861	56	1363	15.758	15.9035	16.049
442.5	21281	90	2105	24.569	24.8555	25.142
537.5	25619	132	2539	28.755	29.034	29.313
550	26157	136	2593	29.303	29.6755	30.048
606.5	29565	200	2934	32.652	33.124	33.596
630.5	29632	220	2940	32.691	33.18	33.669
1074	38310	594	3808	41.147	41.966	42.785
1085	41331	857	4110	42.909	44.2375	45.566

\*Age-reversed sample rejected.

**Table 7.3.** Age control points from graphical tuning of Fe/K series in CD154 23-16P to the Chinese speleothem  $\delta^{18}\text{O}$  record (Wang *et al.*, 2001).

<b>Depth (cm)</b>	<b>Age (kyr BP)</b>
7.12	39.3
8.77	48.1
9.92	55.1
10.74	60

6 m of the core. Using the calibrated  $^{14}\text{C}$  AMS date of the penultimate sample at 1074.5 cm results in a sedimentation rate of  $50 \text{ cm kyr}^{-1}$  for the lower 4 m of the core. This difference between the upper and lower section of the core implies either a dramatic shift in the sedimentary environment during this interval or an error with the  $^{14}\text{C}$  AMS dates in the deepest samples of the core. The largest differences in sedimentation rate are expected to have occurred between the Holocene and the Last Glacial Maximum (LGM), when relative sea level was lowered by  $\sim 130 \text{ m}$  (Lambeck *et al.*, 2014). Presumably this would have shifted intermediate waters to greater depths and would have moved the locus of maximum scour from the peak of the Mallory Seamount ( $\sim 800 \text{ m}$  water depth) to the flanks. This in turn could have resulted in increased slope instabilities and downslope sediment transport. The occurrence of the shift from higher sedimentation rates at the bottom of the core to lower rates at the LGM is not compatible with such a change. The relatively stable rates between the Holocene and LGM also imply that sediment deposition at the site is not impacted by glacial-interglacial sea level changes. This leads us to propose that the  $^{14}\text{C}$  AMS dates at the bottom of the core are not reliable and as such we opt for a different approach to tune the lower section of the core.

A remarkable similarity has been observed between elemental ratios of Fe/K (and Fe/Ca) derived from XRF-scanning of sediment cores along the southeastern continental margin of Africa, associated with riverine input to the ocean (Ziegler *et al.*, 2013; Simon *et al.*, 2015) and the structure of millennial-scale events in the precisely dated (U/Th) Chinese speleothem record of  $\delta^{18}\text{O}$  ( $\delta^{18}\text{O}_{\text{speleo}}$ ), which is related to the strength of the East Asian monsoon (Wang *et al.*, 2001, 2008; Yuan *et al.*, 2004; Cheng *et al.*, 2006). These records are believed to be dynamically connected by the interhemispheric signal propagation related to the antiphased terrestrial climatic conditions in each region, i.e., humid (dry) conditions in eastern South Africa during dry (wet) conditions in Central China (and vice versa).

We follow these previous studies and exploit this relationship to tune the lower section of core CD154-23-16P. This involves tuning the Fe/K stratigraphic series of CD154-23-16P to the combined Hulu-Sanbao  $\delta^{18}\text{O}_{\text{speleo}}$  record using the R software package ‘astrochron’ (Meyers, 2016). The individual speleothem records are adjusted in order to align them to a common  $\delta^{18}\text{O}$  scale by subtracting 1.6 from the Hulu Cave records in order to account for the difference in elevation and location compared to

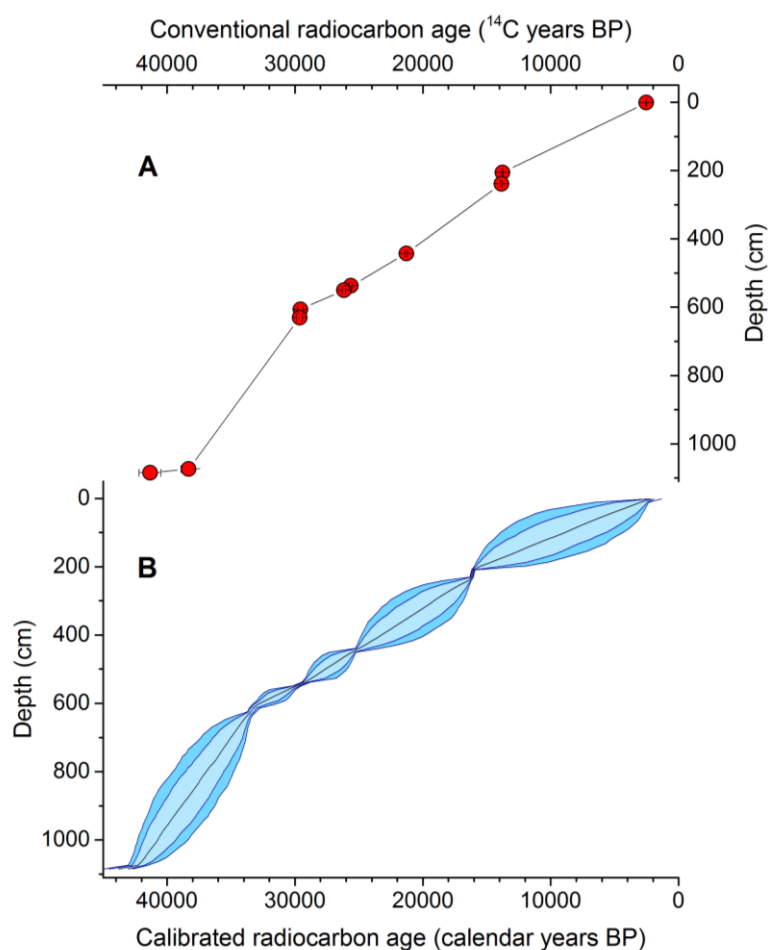


**Figure 7.3.** A) Conventional radiocarbon ages measured in samples composed of the surface-dwelling planktonic foraminifera *Globigerinoides ruber* versus depth in sediment core CD154-23-16P. B) Quantiles of predicted ages by depth according to the calibration of conventional radiocarbon ages in panel A above. The quantiles of the predicted ages are for the 2.5% level and the 10%, 50%, 90% and 97.5% levels. Conventional radiocarbon ages were converted to calendar years using the Marine13 radiocarbon age calibration curve which incorporates a time-dependent global ocean reservoir correction (R) of about 400 years (Reimer *et al.*, 2013). Prior to calibration the conventional radiocarbon ages are corrected for the local offset from the global reservoir age ( $\Delta R$ ) by the subtraction of 225 years according to the  $\Delta R$  for the most proximal site to CD154 23-16P is 224 years (Southon *et al.*, 2002). The calibration was performed using the R statistical package ‘Bchron’ (Parnell *et al.*, 2011).

the Sanbao Cave site (Wang *et al.*, 2008). In addition, prior to the graphical tuning we standardise the  $\delta^{18}\text{O}_{\text{speleo}}$  record, i.e., we subtract the mean and divide it by the standard deviation; this facilitates the identification of the millennial-scale variability. We do not remove the standardised Northern Hemisphere summer insolation curve (21st July at  $65^\circ\text{N}$ ) (Berger, 1978) from the standardised  $\delta^{18}\text{O}_{\text{speleo}}$  record as was suggested by Barker *et al.*, (2011) because the millennial-scale events are sufficiently evident for our purpose without this further modification.

We select a minimum of four age control points from within the bottom 4 m of the core (Table 7.3 and Fig. 7.4) and combine these with the seven calibrated  $^{14}\text{C}$  AMS dates from the upper 6.3 m (i.e., excluding the age-reversed sample at 230.5 cm and the two samples from the core bottom). Ages between each control point, including the calibrated  $^{14}\text{C}$  AMS dates, were estimated by linear interpolation. This chronostratigraphic framework yields sedimentation rates in the bottom of the core that are similar to the those in the upper section (Fig. 7.4). The consistency of sedimentation rates under this adjusted framework provides a strong validation for the rejection of the bottom two  $^{14}\text{C}$  AMS dates and supports our graphical tuning approach for the construction of this core's age model.

## 7.4 Preliminary results and discussion

### 7.4.1 Fe/K results

The spatial variability of Fe/K in sediment core-top samples from the margins of the Atlantic Ocean has been found to reflect the input of intensely weathered material from humid regions relative to input of less weathered particles from drier areas (Govin *et al.*, 2012). The high precipitation in humid, tropical climates promotes intense chemical weathering of bedrock (Middelburg *et al.*, 1988) which results in the production of highly weathered and Fe-rich soils. Potassium on the other hand is derived from potassium feldspar or illite, which are both associated with the lower the chemical weathering rates of drier regions (Zabel *et al.*, 2001). These geochemical signals are believed to be transported to marine sediments via river discharge into the ocean and as such, down-core changes in the Fe/K ratio of marine sediments close to ocean margins are thought to reflect relative changes of the hydrology and terrestrial climate in the adjoining continental region from which the sedimentary material is derived of the source region from which the material is derived. Relatively high Fe/K

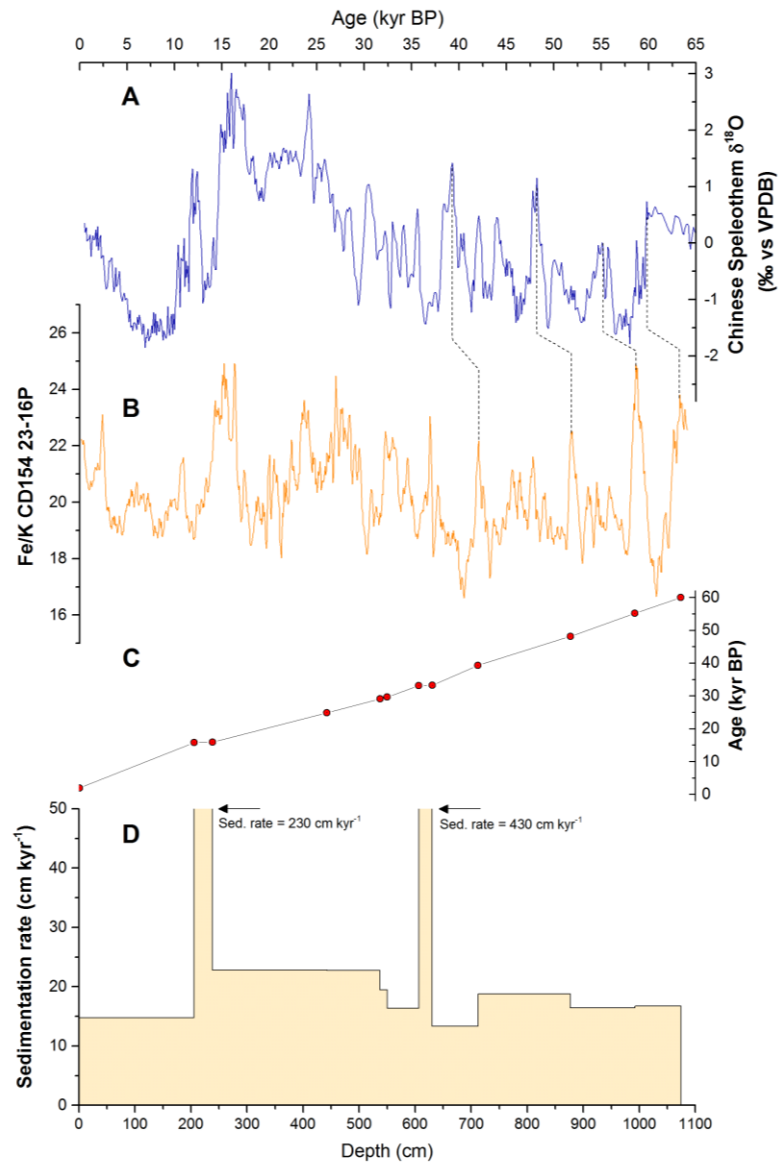


**Figure 7.4.** A) Standardised Chinese speleothem oxygen isotope record from the Hulu and Sambaos Caves on its published age model. B) Fe/K record derived from XRF scanning of sediment core CD154-23-16P. Dashed lines show the selected age control points used for tuning the lower section of the core. C) Age-depth plot for sediment core CD154-23-16P. The uppermost eight age control points are the calibrated radiocarbon ages, while the lowermost four points are the age control points derived from graphical tuning to the Chinese speleothem record (i.e., panels A and B). D) Sedimentation rates for CD154-23-16P derived by using the calibrated radiocarbon ages in the upper 7 m of the core (excluding the age-reversed sample) and the graphical tuning age control point in the lower 4 m of the core. Note the two intervals of very high sedimentation rates highlighted by the vertical bars which are off the scale.

values indicate the deposition of predominantly intensely-weathered material, whereas relatively low Fe/K values indicate the deposition of material that has only been slightly weathered and hence implies the delivery of material from relatively dry regions (Govin *et al.*, 2012). Calibrated down-core records of the Fe/K ratio in marine sediment cores from offshore southeastern Africa at 31°S and 33°S (Fig. 7.1; Table 7.4) have been successfully used to reconstruct relative changes of regional hydrological conditions in south east Africa (Ziegler *et al.*, 2013; Simon *et al.*, 2015). The Fe/K record from CD154-23-16P at 36°S thus allows us to expand the spatial coverage of these reconstructions in order to map out the millennial-scale changes of the south east African hydroclimate over an even broader area.

In agreement with these previous studies, the Fe/K record of sediment core CD154-23-16P display a prominent millennial-scale variability with a number of abrupt events towards more humid conditions (high Fe/K) throughout the past 60 kyr BP (Fig. 7.5). Most of the prominent peaks of Fe/K (i.e. humid events) can be traced to analogous Northern Hemisphere glacial stadials (GS) as documented in the Greenland ice core temperature record (NGRIP, 2004). In addition, these Fe/K peaks can also be traced to corresponding increases in the  $\delta^{18}\text{O}_{\text{speleo}}$  record from the Hulu-Sanbao caves which indicate drier conditions in Central China as a result of weakened East Asian monsoon intensity (Wang *et al.*, 2001,2008). In spite of the temporal offset during certain events within the radiocarbon-dated section of the core (e.g. GS 1, GS 2 and GS 3) there is a remarkable similarity in the structure of the millennial-scale variability of the Fe/K record from CD154-23-16P and the Hulu-Sanbao Cave  $\delta^{18}\text{O}_{\text{speleo}}$  record (Fig. 7.5). This pattern of humid (dry) south east African condition during dry (wet) conditions in Central China has also been reported for the Fe/K records for sediment cores CD154-17-17K and CD154-10-06P from along the southeast continental margin of Africa (Ziegler *et al.*, 2013; Simon *et al.*, 2015, respectively).

#### 7.4.2 Interpretation of the Fe/K record from CD154-23-16P

The abrupt changes to more humid conditions in southeastern Africa during Northern Hemisphere cooling events (i.e. Greenland stadials) are thought to be caused by southward shifts of the Intertropical Convergence Zone (ITCZ) as a result of changes in the mode of AMOC circulation and of changes in North Atlantic temperatures (Vellinga and Wood, 2002; Schefuß *et al.*, 2011). This shift of the ITCZ would have

**Table 7.4.** Core sites referred to in this chapter.

Core	Latitude	Longitude	Water depth
CD154-23-16P	36°49.08`S	022°00.02`E	3189 m
CD154-10-06P	33° 16.13`S	029°07.29`E	3333 m
CD154-17-17K	31° 10.36`S	032°08.91`E	3076 m
MD02-2588	41°19.9`S	025°49.7`E	2907 m
MD02-2594	34° 42.6`S	017°20.3`E	2440 m
64PE174-P13	29° 45.71`S	002° 24.10`S	2912 m

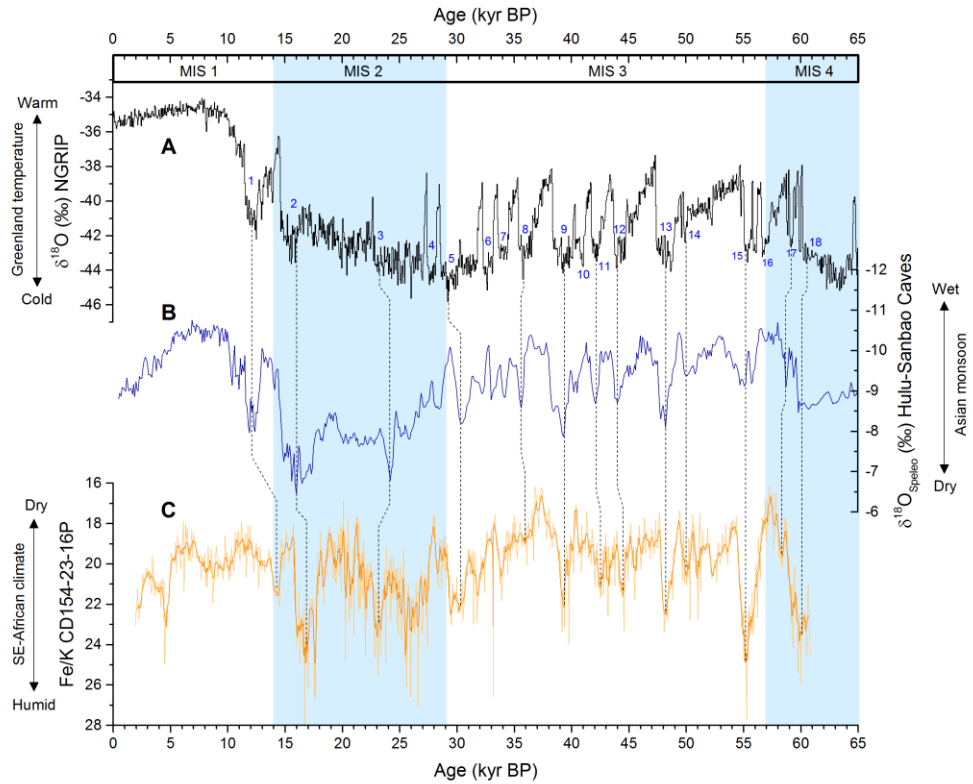


**Figure 7.5.** A) Oxygen isotope record from Greenland ice core NGRIP displaying abrupt temperature variability in the North Atlantic (NGRIP, 2004). The blue numbers are the Northern Hemisphere glacial stadials as defined by Rasmussen *et al.*, (2014). B) Standardised oxygen isotope record from Chinese speleothems constructed by alignment of the Hulu and Sanbao records (Wang *et al.*, 2001,2008). The record has been linearly interpolated at a resolution of 0.1 kyr to account for the variable sampling rate of individual speleothem deposits in the compiled series. C) Fe/K record of CD154-23-16P (lighter shade of orange) with a 5-point smoothing performed by adjacent averaging (darker shade of orange). Vertical blue bars highlight Marine Isotope Stages 2 and 4 and the dashed line trace the Fe/K maxima to corresponding and antiphased events in the Greenland temperature and Chinese speleothem records (panels A and B).

also pushed the Indian Ocean subtropical anticyclone southwards bringing southeast Africa more directly under the influence of the moist easterly winds blowing over the south west Indian Ocean, thus encouraging increased rainfall on the continent (Simon *et al.*, 2015). It has also been suggested that these wetter condition may have been exacerbated by concurrent warming of the Agulhas Current which is considered an additional source of moisture for rainfall along the southeast coast of southern Africa (Jury *et al.*, 1993; Simon *et al.*, 2015).

Not all proxy evidence however is in agreement regarding the antiphased relationship between the southeastern African hydroclimate and the Northern Hemisphere cooling events (e.g. Stager *et al.*, 2011); this disagreement has recently been highlighted by the synthesis and re-analysis of pollen records from South Africa (Chevalier and Bard, 2015). Specifically, the pollen data indicate that while the antiphased relationship may have existed in certain regions of the continent, the conditions south of  $\sim 20^{\circ}\text{S}$  imply an in-phase relationship with Northern Hemisphere climate during the last glacial. This has led to the proposition that while the southerly displacement of the ITCZ is consistent with some of the available data (Johnson *et al.*, 2002; Schefub *et al.*, 2011; Ziegler *et al.*, 2013; Simon *et al.*, 2015), the impact is not uniform over the entire region. Our Fe/K results from XRF-scanning of marine sediment core CD154-23-16P at a latitude of  $36^{\circ}\text{S}$  are consistent with similar records that extend along the southeast African continental margin from  $18^{\circ}\text{S}$  to  $33^{\circ}\text{S}$  (Schefub *et al.*, 2011; Ziegler *et al.*, 2013 and Simon *et al.*, 2015); all indicate an antiphasing of the southeast African hydroclimate with Northern Hemisphere cold events during the last glacial cycle (Fig. 7.5). The discrepancy between the African margin datasets and the pollen data from the continent highlights the complexity of the spatial variability of changes in the regional hydroclimate of south east Africa. It also emphasises the importance of increasing the spatial coverage of high-resolution records of both terrestrial climate as well records of the conditions in the adjoining oceanic region.

#### 7.4.3 *Stable oxygen and carbon isotope results*

Building on this need for a better understanding of how the past variability of the Agulhas Current interacts with the terrestrial climate of southeastern Africa we herein present an initial foraminiferal  $\delta^{18}\text{O}$  and  $\delta^{13}\text{C}$  stratigraphy for sediment core CD154-23-16P which spans the past 50 kyr BP.

The records of  $\delta^{18}\text{O}_{G.ruber}$  and  $\delta^{18}\text{O}_{G.trunc(s)}$  display typical patterns associated with orbital modulation; maximum glacial-interglacial amplitudes are 1.8‰ and 2.7‰ in each record, respectively (Fig. 7.6a). Minimum interglacial values of foraminiferal  $\delta^{18}\text{O}$  are recorded during the mid-Holocene in both records, whereas maximum glacial values occur asynchronously, with the peak  $\delta^{18}\text{O}_{G.trunc(s)}$  recorded at ~ 21 kyr BP, and at ~ 16 kyr BP in the case of  $\delta^{18}\text{O}_{G.ruber}$  (note coincidence with the timing of Heinrich Stadial (H) 1). Superimposed on the orbital-scale pattern is the higher frequency variability that indicates millennial-scale changes in the surface and intermediate water hydrography of the Agulhas Current. Overall, this higher frequency variability is less pronounced in the  $\delta^{18}\text{O}_{G.ruber}$  record relative to that of  $\delta^{18}\text{O}_{G.trunc(s)}$ , in agreement with the lower amplitude of glacial-interglacial changes in the former. The millennial-scale oscillations range between 0.2 and 0.5‰ in  $\delta^{18}\text{O}_{G.ruber}$  and between 0.2 and 0.9‰ in  $\delta^{18}\text{O}_{G.trunc(s)}$ . We cautiously note that a number of millennial-scale minima in the  $\delta^{18}\text{O}_{G.trunc(s)}$  record coincide with the timing of Northern Hemisphere Heinrich stadials (Hemming, 2004) which are analogous to the Southern Hemisphere warming events recorded as Antarctic isotope maxima (AIM) (EPICA, 2006). This coincidence with millennial-scale climatic events does not appear to apply to the  $\delta^{18}\text{O}_{G.ruber}$  record.

The records of  $\delta^{13}\text{C}_{G.ruber}$  and  $\delta^{13}\text{C}_{G.trunc(s)}$  display a pattern of relatively stable values during MIS 3 and during most of MIS 2, with values centred around 0.5‰; minimum values are reached during the last glacial termination before following an overall rising trend throughout the duration of MIS 1 (Fig. 7.6b). During the last glacial termination values decrease to ~0.2‰ in the  $\delta^{13}\text{C}_{G.ruber}$  record and to -0.05‰ in the  $\delta^{13}\text{C}_{G.trunc(s)}$  record. A single  $\delta^{13}\text{C}_{G.trunc(s)}$  data point reaches the lowest recorded value of -0.2‰ during H1. During MIS 1 values in both records rise from ~0.4‰ to ~0.8‰ at 2 kyr BP, although the youngest data point in the  $\delta^{13}\text{C}_{G.trunc(s)}$  record continues to increase to the maximum recorded carbon isotopic composition of 1.3‰. During the relative long-term stability in the glacial section of the record values fluctuate between 0.2 and 0.8‰ on millennial timescales. No clear systematic relationship is seen between the foraminiferal  $\delta^{13}\text{C}$  records and the timing of millennial-scale climate events although we cautiously note that a number of the larger excursions in the record do align with these events.

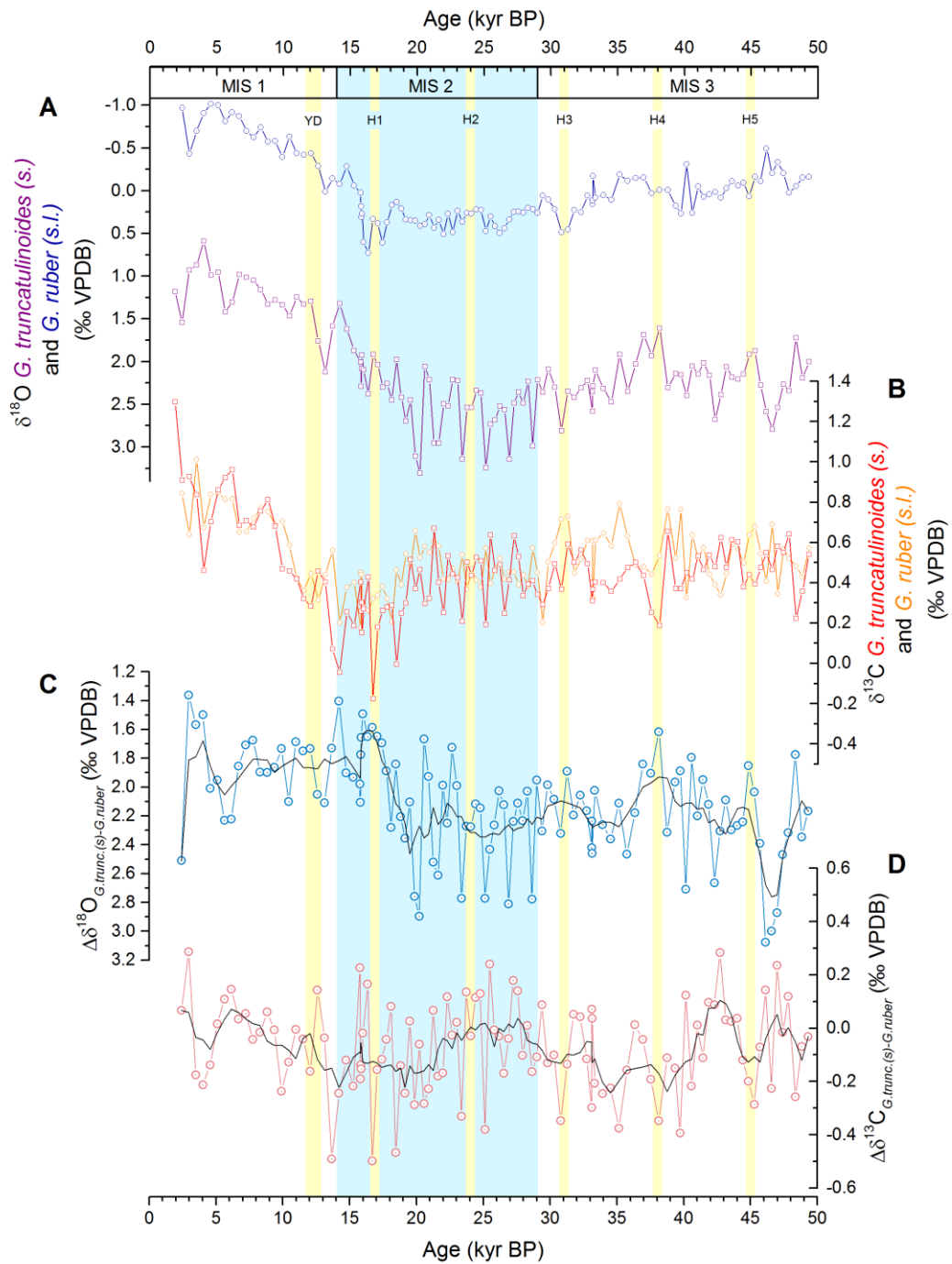


**Figure 7.6.** A) Oxygen isotope stratigraphic series generated from *Globigerinoides. ruber* (*sensu lato*) (blue) and *G. truncatulinoides* (*sinistral*) (purple) in sediment core CD154 23-16P. B) Carbon isotope stratigraphic series generated from *G. ruber* (*s.l.*) (orange) and *G. truncatulinoides* (*s.*) (red) in sediment core CD154 23-16P. C) Oxygen isotope gradient and D) carbon isotope gradient between *G. truncatulinoides* (*s.*) and *G. ruber* (*s.l.*). Black line in panels C and D shows a 5-point smoothing of the data series. Vertical blue bar highlights Marine Isotope Stage (MIS) 2 and yellow bars show the timing of Heinrich stadials (H) in the Northern Hemisphere, including the Younger Dryas (YD).

One of the most notable features of the foraminiferal stable isotope records is the disparity of the offset observed between the  $\delta^{18}\text{O}$  and  $\delta^{13}\text{C}$  records of each species: the  $\delta^{18}\text{O}$  records display a large offset from each other while the  $\delta^{13}\text{C}$  records show a much more minor offset (Fig. 7.6 a and b). The surface-to-intermediate gradients of the stable oxygen and carbon isotope records ( $\Delta\delta^{18}\text{O}_{G.t-G.r}$  and  $\Delta\delta^{13}\text{C}_{G.t-G.r}$ , respectively) reveal a number of further interesting features which are not evident in the individual records (Fig. 7.6 c and d). In the case of oxygen isotopes there appears to be a pattern of a higher values of  $\Delta\delta^{18}\text{O}_{G.t-G.r}$  in the glacial section of the core with a transition to relatively lower  $\Delta\delta^{18}\text{O}_{G.t-G.r}$  of MIS 1 taking place in the latter part of MIS 2 (Fig. 7.6c). There is also a notable peak between  $\sim 46$  and  $48$  kyr BP and in addition, the entire record exhibits high amplitude oscillations at the millennial-scale frequency. It also appears that the timing of Heinrich stadials (excluding the Younger Dryas (YD) event) correspond with millennial-scale minima in the  $\Delta\delta^{18}\text{O}_{G.t-G.r}$  record.

The minimal offset in the surface and intermediate water  $\delta^{13}\text{C}$  at orbital timescales manifests itself as a  $\Delta\delta^{13}\text{C}_{G.t-G.r}$  record that shows a relatively stable long-term trend around the 0‰ level (Fig. 7.6d). Superimposed on this long-term trend however are abrupt shifts at millennial timescales that range from 0.2 to 0.6‰. We observe that Heinrich stadials H1, H3, H4 and H5, as well as the YD event, are associated with negative excursions in the  $\Delta\delta^{13}\text{C}_{G.t-G.r}$  record.

#### 7.4.4 Assessment of the stable oxygen and carbon isotope records from CD154-23-16P

##### 7.4.4.1 Stable oxygen isotopes

The individual records of  $\delta^{18}\text{O}_{G.ruber}$  and  $\delta^{18}\text{O}_{G.trunc(s)}$ , as well as the gradient between the two (i.e.,  $\Delta\delta^{18}\text{O}_{G.t-G.r}$ ), provides an intriguing insight into the variability of the physical properties of surface and intermediate waters within the downstream reach of the Agulhas Current. Of particular interest is the difference in amplitude and timing of glacial-interglacial and millennial-scale changes in surface waters relative to intermediate waters. The  $\delta^{18}\text{O}$  composition in each foraminiferal species represents the response to three principal parameters: the global ice volume, the temperature of calcification and the isotopic composition of local seawater ( $\delta^{18}\text{O}_{sw}$ ) (Emiliani, 1955). As the ice volume effect impacts the whole ocean equally, the  $\Delta\delta^{18}\text{O}_{G.t-G.r}$  at any point along core CD154-23-16P will be exclusively controlled by the temperatures recorded

by each of the two foraminiferal species, with an additional component due to the difference between  $\delta^{18}\text{O}_{\text{sw}}$  which is dependent on local salinity. Therefore, the variability of  $\Delta\delta^{18}\text{O}_{G.t-G.r}$  can be used as a first-order indication of changes in the thermal and salinity profile of the upper water column overlying the core site. Furthermore, the direct proportionality of seawater density to salinity and the inverse proportionality between density and temperature allows  $\Delta\delta^{18}\text{O}_{G.t-G.r}$  to be applied as a qualitative estimate of variations in the density stratification of the permanent thermocline through time (Lynch-Stieglitz *et al.*, 1999). As such, the occurrence of a stronger gradient between surface and intermediate foraminiferal  $\delta^{18}\text{O}$  during the glacial interval of the record could suggest that the upper water column (i.e., the Agulhas Current) at the CD154-23-16P core site was generally more strongly stratified during this time. The higher frequency variability of the  $\Delta\delta^{18}\text{O}_{G.t-G.r}$  record could equally indicate changes in density stratification at millennial timescales.

However, the gradient record can only inform us of whether the foraminiferal  $\delta^{18}\text{O}$  composition of each species varied relative to the other; that is say that the  $\Delta\delta^{18}\text{O}_{G.t-G.r}$  record does not specify how the temperature and  $\delta^{18}\text{O}_{\text{sw}}$  signals varied within each depth habitat (i.e., surface vs thermocline). It is therefore instructive to remove the ice volume signal from each of the individual records in order to isolate the combined temperature and  $\delta^{18}\text{O}_{\text{sw}}$  variability of each record. This is achieved by estimating the  $\delta^{18}\text{O}$  value of the ice volume effect and subtracting it from the individual records of  $\delta^{18}\text{O}_{G.ruber}$  and  $\delta^{18}\text{O}_{G.trunc(s)}$ . The mean ocean  $\delta^{18}\text{O}_{\text{sw}}$  ( $\delta^{18}\text{O}_{\text{MO}}$ ) component which is linked to the ice volume effect is acquired by converting the available relative sea level records (Grant *et al.*, 2012; Lambeck *et al.*, 2004) to an equivalent  $\delta^{18}\text{O}_{\text{sw}}$  composition assuming an  $^{18}\text{O}$  enrichment of the global ocean by 0.008‰ per meter sea level lowering (Schrag *et al.*, 2002).

The results of this exercise reveal a number of interesting features (Fig. 7.7). The first observation is that the removal of the  $\delta^{18}\text{O}_{\text{MO}}$  value from the foraminiferal  $\delta^{18}\text{O}$  records clearly reveals that the glacial-interglacial  $\Delta\delta^{18}\text{O}_{G.t-G.r}$  variability is driven primarily by changes in  $\delta^{18}\text{O}_{G.trunc(s)}$ . The ice-volume corrected  $\delta^{18}\text{O}_{G.trunc(s)}$  record ( $\delta^{18}\text{O}_{\text{IVC-G.trunc(s)}}$ ) displays a clear distinction between higher values during MIS 3 and MIS 2 (~1.6‰) and relatively lower values during MIS 1 (~1.0‰), with the main transition between these two extremes occurring from ~20 to 15 kyr BP (Fig. 7.7c).

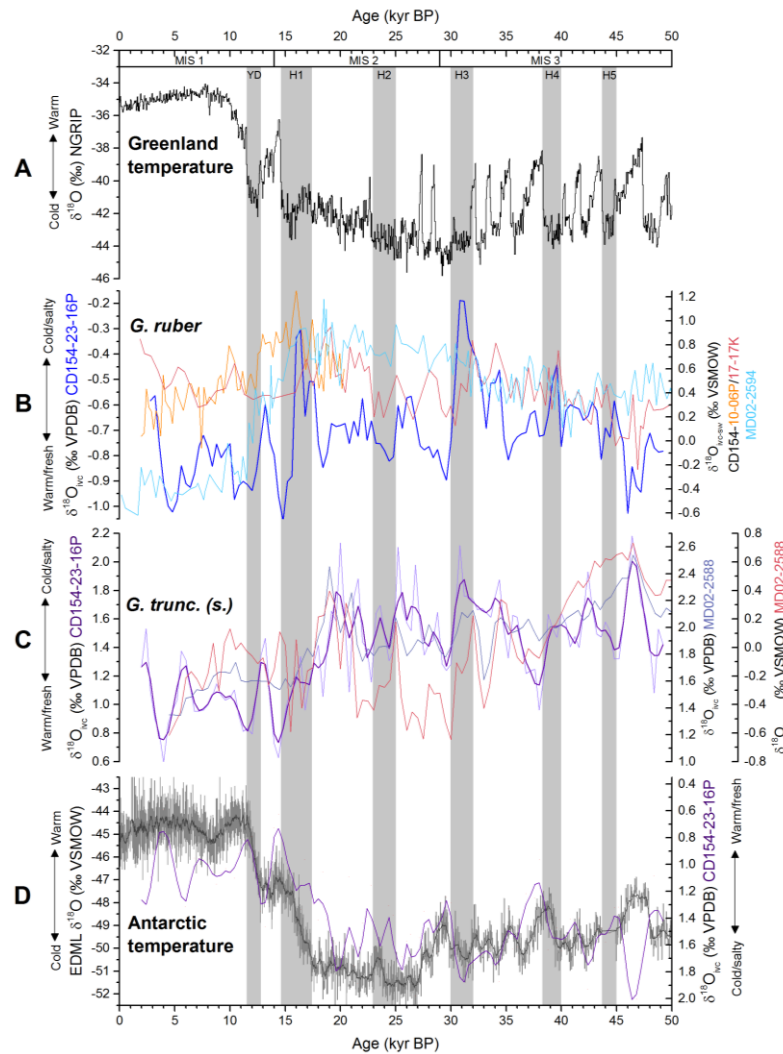


**Figure 7.7.** A) Oxygen isotope ( $\delta^{18}\text{O}$ ) record from Greenland ice core NGRIP displaying abrupt temperature variability in the North Atlantic (NGRIP, 2004). B) Oxygen isotope records of *Globigerinoides ruber*: Blue line is the record of ice-volume corrected *G. ruber*  $\delta^{18}\text{O}$  ( $\delta^{18}\text{O}_{\text{IVC}}$ ) from CD154-23-16P (this study); orange and red are the records of seawater  $\delta^{18}\text{O}$  from sediment cores CD154-10-06P and CD154-17-17K (Table 7.4), respectively (both are corrected for the ice-volume effect and calcification temperature) ( $\delta^{18}\text{O}_{\text{IVC-sw}}$ ) (Simon *et al.*, 2013, 2015); light blue line is the record of the  $\delta^{18}\text{O}_{\text{IVC-sw}}$  from sediment core MD02-2594 (Dyez *et al.*, 2014). C) Oxygen isotope records of *Globorotalia truncatulinoides* (*sinistral*): Purple line is the record of ice-volume corrected *G. truncatulinoides* (*s.*)  $\delta^{18}\text{O}$  ( $\delta^{18}\text{O}_{\text{IVC}}$ ) from CD154-23-16P (this study; darker shaded line is the 3-point smoothed record); lilac line is the ice-volume corrected *G. truncatulinoides* (*s.*)  $\delta^{18}\text{O}$  ( $\delta^{18}\text{O}_{\text{IVC}}$ ) from MD02-2588 (Chapter 5.2 of this thesis); red line is the  $\delta^{18}\text{O}_{\text{IVC-sw}}$  (i.e., ice-volume- and temperature-corrected) record from *G. truncatulinoides* (*s.*) in MD02-2588 (Chapter 5.2 of this thesis). D)  $\delta^{18}\text{O}$  record from the European Project for Ice Coring in Antarctica (EPICA) Dronning Maud Land (EDML) site (after correction for upstream and glacial–interglacial ice sheet altitude effects) compared to *G. truncatulinoides* (*s.*)  $\delta^{18}\text{O}_{\text{IVC}}$  from CD154-23-16P (panels C). Vertical grey bars highlight the timing of Heinrich stadials (H) in the Northern Hemisphere, including the Younger Dryas (YD).

The timing and the amplitude of the variations in the  $\delta^{18}\text{O}_{\text{IVC-G.trunc}(s)}$  record therefore imply that changes in the longer-term trends of water-column profile overlying the CD154-23-16P core site are driven principally by changes in the physical properties of intermediate waters. Unfortunately, the available data does not allow us to estimate what proportion of the signal is due to temperature versus salinity.

In the modern ocean the intermediate waters overlying the core site are a mixture of southern-sourced Subantarctic Mode Water and a blend of northern-sourced waters that are delivered to the site by the Agulhas Current (Gordon *et al.*, 1987); the northern-sourced intermediate waters include components from the tropical thermocline of the western Indian Ocean and a component of Red Sea water (RSW) at lower intermediate depths. Attributing the variability of the  $\delta^{18}\text{O}_{\text{IVC-G.trunc}(s)}$  record to changes in the properties of each of these sources is beyond the scope of the available dataset, but we note that this record displays similarities in its pattern of variability to records that are representative of the southern source region. For example, there is some similarity between the pattern of the  $\delta^{18}\text{O}_{\text{IVC-G.trunc}(s)}$  with the record of Antarctic temperature as well as with the ice volume corrected  $\delta^{18}\text{O}_{\text{sw}}$  ( $\delta^{18}\text{O}_{\text{IVC-sw}}$ ) record derived from paired Mg/Ca- $\delta^{18}\text{O}$  measurements in *G. truncatulinoides* (*s.*) in core MD02-2588 from the Agulhas Plateau (Chapter 5.2 of this thesis) (Fig. 7.7 c and d; Table 5.2.4).

Unlike  $\delta^{18}\text{O}_{\text{IVC-G.trunc}(s)}$ , the ice-volume corrected  $\delta^{18}\text{O}_{\text{G.ruber}}$  record ( $\delta^{18}\text{O}_{\text{IVC-G.ruber}}$ ) displays no clear glacial-interglacial pattern, with only a small difference between the average value of MIS 1 (~0.9‰) and that of MIS 2 and 3 (~0.8‰) (Fig. 7.7b). Again, this clearly implies that the glacial-interglacial variability of the  $\Delta\delta^{18}\text{O}_{\text{G.t-G.r}}$  record is principally driven by the intermediate-water signal. The  $\delta^{18}\text{O}_{\text{IVC-G.ruber}}$  record on the other hand reveals a very striking pattern of millennial-scale variability with two prominent peaks that are coeval with the timing of H1 and H3. Two smaller peaks occur during H4 and H5, while during H2 and the YD the record displays abrupt decreases. The peak values of  $\delta^{18}\text{O}_{\text{IVC-G.ruber}}$  during a number of these climate events indicate that the surface waters of the Agulhas Current experienced abrupt decreases in temperature or increases in salinity, or some combination of the two. Without further data of ambient seawater temperature from this site is not possible to estimate the separate temperature and salinity components associated with these  $\delta^{18}\text{O}_{\text{IVC-G.ruber}}$  changes. However, comparison of the  $\delta^{18}\text{O}_{\text{IVC-G.ruber}}$  record to published records of temperature- and ice-volume-corrected  $\delta^{18}\text{O}_{\text{G.ruber}}$  from sites within the Agulhas Current (CD154-17-

17K and CD154-10-06P; Simon *et al.*, 2013, 2015) and from the western slope of the Agulhas Bank (MD02-2594; Dyez *et al.*, 2014) reveal a number of similarities in the patterns of variability (Fig. 7.7b).

Firstly, the  $\delta^{18}\text{O}_{\text{IVC-G.ruber}}$  peak during H1 in CD154-23-16P is synchronous to the  $\delta^{18}\text{O}_{\text{IVC-sw}}$  maximum in sediment core CD154-10-06P. The latter has been interpreted as indicating a peak in salinity in the upstream waters of the Agulhas Current which may have been propagated downstream and into the Indian-Atlantic Ocean Gateway (I-AOG) (Simon *et al.*, 2015). Similar high-amplitude salinity oscillations have been reported from the I-AOG during the penultimate

glacial-interglacial cycle which manifest themselves as a series of millennial-scale salinification events (Marino *et al.*, 2013). The two major peaks in the  $\delta^{18}\text{O}_{\text{IVC-G.ruber}}$  from CD154-23-16P could represent analogous events in the downstream reach of the Agulhas Current. At a conceptual level, this would support, to a first order, the propagation of more saline waters from the upstream region of the Agulhas Current to its southernmost extent prior to retroflecting and shedding Agulhas rings into the South Atlantic. If this is indeed the case for the  $\delta^{18}\text{O}_{\text{IVC-G.ruber}}$  during H1, it may also be the case during H3 where an even more prominent increase occurs in CD154-23-16P (Fig. 7.7b). The smaller peaks of  $\delta^{18}\text{O}_{\text{IVC-G.ruber}}$  during H4 and H5 may equally represent such salinification events although we refrain from stipulating further until more data become available to allow the temperature and salinity signals in  $\delta^{18}\text{O}_{\text{IVC-G.ruber}}$  to be deconvolved. We do however note that these events are of almost equal magnitude to similar events in the  $\delta^{18}\text{O}_{\text{IVC-sw}}$  record of sediment core CD154-17-17K from the mid-stream reach of the Agulhas Current; this may suggest that the majority of the  $\delta^{18}\text{O}_{\text{IVC-G.ruber}}$  signal is a response to variations of salinity as opposed to temperature (Fig. 7.7b).

#### 7.4.4.2 Stable carbon isotopes

One of the most conspicuous features of the  $\delta^{13}\text{C}_{\text{G.ruber}}$  and  $\delta^{13}\text{C}_{\text{G.trunc(s)}}$  records is the occurrence of minimum values during the last glacial termination between ~20 and 15 kyr BP (Fig. 7.8). This feature, which is most apparent in  $\delta^{13}\text{C}_{\text{G.trunc(s)}}$  record but it is nonetheless also evident in  $\delta^{13}\text{C}_{\text{G.ruber}}$ , is a common characteristic in  $\delta^{13}\text{C}$  records associated with SAMW. The occurrence of these so-called ‘carbon isotope minimum events’ (CIME) during glacial terminations is thought to represent a response to the breakdown of surface water stratification in the Southern Ocean and renewed

upwelling of Circumpolar Deep Water (CDW) with a low  $\delta^{13}\text{C}$  value; this signal is then entrained to the convergence zone at the Subantarctic front (SAF) and is subsequently propagated throughout the Southern Hemisphere thermocline (Luyten *et al.*, 1983; Spero and Lea, 2002). The distinctive CIME in the  $\delta^{13}\text{C}_{G.trunc(s)}$  record of CD154-23-16P points towards a notable contribution of SAMW to the chemical signature of the thermocline waters overlying the core site. The occurrence of a CIME during the last deglaciation in the record of  $\delta^{13}\text{C}_{G.ruber}$  suggests that surface waters at the CD154-23-16P site (i.e., the Agulhas Current) were also influenced by this event although to a lesser degree than the thermocline waters. The more subdued expression in the surface waters of the site may indicate that the signal has been muted by local processes that affect the  $\delta^{13}\text{C}$  of dissolved inorganic carbon ( $\delta^{13}\text{C}_{DIC}$ ) in surface waters. For example, a degree of dilution of the signal would be expected during the vertical mixing of the thermocline waters with the tropical and subtropical waters that dominate the surface waters overlying the core site.

The presumption that the  $\delta^{13}\text{C}_{G.trunc(s)}$  record is more directly influenced by the presence of SAMW certainly accounts for the larger response during the CIME, where values are on average 0.2‰ lower than in the corresponding  $\delta^{13}\text{C}_{G.ruber}$  record. However, we find that the carbon isotopic signature in of thermocline waters is on average lower than the surface-water equivalent throughout almost the entire record (Fig. 7.8). This observation provides a valuable clue for the interpretation of the carbon isotope records from core CD154-23-16P. The  $\delta^{13}\text{C}_{DIC}$  of seawater represents a complex mixture of physically- and biologically-mediated processes. Thermocline and intermediate waters that are sourced from the Southern Ocean, i.e., SAMW and Antarctic Intermediate Water (AAIW), are typically characterised by  $\delta^{13}\text{C}_{DIC}$  values that deviate from nutrient stoichiometry due to a strong isotopic fractionation during exchange with the atmosphere at low ambient temperature (Broecker and Maier-Reimer, 1992; Charles *et al.*, 1993; Lynch-Stieglitz *et al.*, 1995). The component of the  $\delta^{13}\text{C}_{DIC}$  composition of seawater that is associated with these air-sea fractionation effects ( $\delta^{13}\text{C}_{as}$ ) is therefore expected to be higher in the southern-sourced thermocline waters relative to the surface waters at the site, which are sourced from the tropical and subtropical Indian Ocean. The fact that  $\delta^{13}\text{C}_{G.trunc(s)}$  remains lower than  $\delta^{13}\text{C}_{G.ruber}$

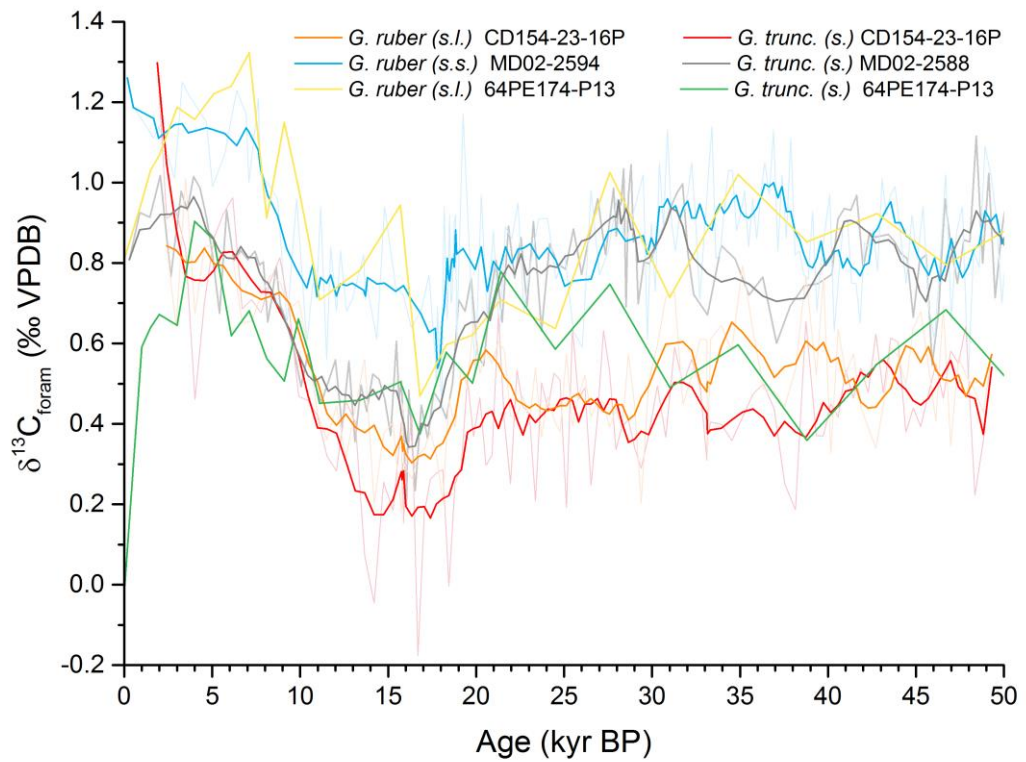


**Figure 7.8.** Carbon isotope stratigraphic series generated from *Globigerinoides. ruber* and *G. truncatulinoides (sinistral)* in the southwest Indian Ocean and the southeast Atlantic Ocean. See legend for details and Table. 7.4 for core location. All records except those from 64PE174-P13 are shown with a 5-point smoothing in bold; raw data series are shown in lighter shades.

for most of the record along CD154-23-16P suggests that despite the strong positive  $\delta^{13}\text{C}_{\text{as}}$  signal from the south, the  $\delta^{13}\text{C}_{\text{DIC}}$  composition of thermocline waters at the site was swamped by the nutrient signal; it suggests that thermocline waters remained richer in nutrients relative to surface waters throughout the studied interval. Interestingly, there appears to be a convergence of  $\delta^{13}\text{C}_{G.\text{trunc}(s)}$  and  $\delta^{13}\text{C}_{G.\text{ruber}}$  after the CIME which could suggest a decreased chemical stratification during MIS 1 which is in agreement with the relative decrease of  $\Delta\delta^{18}\text{O}_{G.t-G.r}$  during MIS 1 (Fig. 7.7). The implied decrease in density stratification during the interglacial stage, relative to MIS 2 and 3, may have been related to changes of the upper water column structure in the I-AOG as a result of meridional shifts of the Southern Ocean fronts on glacial-interglacial timescales (see Chapter 5.2 of this thesis). The convergence of  $\delta^{13}\text{C}_{G.\text{trunc}(s)}$  and  $\delta^{13}\text{C}_{G.\text{ruber}}$  between 28 and 24 kyr BP (Fig. 7.8), which is also evident in the  $\Delta\delta^{13}\text{C}_{G.t-G.r}$  record (Fig. 7.7), indicates another episode of decreased nutrient stratification, although in this case it occurs in the absence of a corresponding decrease in  $\Delta\delta^{18}\text{O}_{G.t-G.r}$ . Foraminiferal-based subantarctic temperature records indicate that the coldest conditions occur at the beginning of full-glacial stages (i.e., MIS 2) (e.g. Martínez-Méndez *et al.*, 2010; Chapter 5.2 this thesis). The higher thermocline  $\delta^{13}\text{C}_{\text{DIC}}$  compositions expected from carbon isotopic fractionation at these lower temperatures (Mook *et al.*, 1974; Chapter 5.3 this thesis) may thus have driven  $\delta^{13}\text{C}_{G.\text{trunc}(s)}$  toward values that were almost identical to those of the tropical and subtropical surface water signal, as recorded in  $\delta^{13}\text{C}_{G.\text{ruber}}$ .

To further aid our interpretation of the  $\delta^{13}\text{C}_{G.\text{trunc}(s)}$  and  $\delta^{13}\text{C}_{G.\text{ruber}}$  records from CD154-23-16P we compare them with similar records from the wider region. Specifically, we refer to the

$\delta^{13}\text{C}_{G.\text{trunc}(s)}$  records from sediment cores MD02-2588 from the Agulhas Plateau (Ziegler *et al.*, 2013, complemented by data presented in Chapter 5.2) and the 64PE174-P13 from the Walvis Ridge (Scussolini and Peeters, 2013) and the  $\delta^{13}\text{C}_{G.\text{ruber}}$  records from MD02-2594 (Dyez *et al.*, 2014) and 64PE174-P13 (Scussolini and Peeters, 2013) (Fig. 7.8; see Fig. 7.1 and Table 7.4 for core location details). This comparison reveals a number of interesting relationships that allow us to gain a better understanding of the regional context of the records from CD154-23-16P. We first note the similarity between the  $\delta^{13}\text{C}_{G.\text{ruber}}$  records from 64PE174-P13 and MD02-2594 throughout the past 50 kyr BP which may imply a common source of the  $\delta^{13}\text{C}_{\text{DIC}}$  signal reaching these

sites in surface waters. Alternatively, it may indicate that both sites were under the influence of regional-scale processes that impacted the  $\delta^{13}\text{C}_{\text{DIC}}$  composition of surface waters of the wider south east Atlantic - for example variations of the Benguela upwelling system (Garzoli and Gordon, 1996). The consistently lower values of  $\delta^{13}\text{C}_{G.ruber}$  in CD154-23-16P relative to these two records from the South Atlantic suggests that the processes controlling the  $\delta^{13}\text{C}_{\text{DIC}}$  of surface water may have been different on either side of the I-AOG. However, the relatively lower values of  $\delta^{13}\text{C}_{G.ruber}$  in CD154-23-16P is also compatible with the gradual loss of  $^{12}\text{C}$  from surface waters due to export production along the trajectory of the Agulhas Current and its leakage as Agulhas Rings into the South Atlantic (de Ruijter *et al.*, 1999).

The published  $\delta^{13}\text{C}_{G.trunc(s)}$  records from sediment cores MD02-2588 (Ziegler *et al.*, 2013) and 64PE174-P13 (Scussolini and Peeters, 2013) also provide insights to the interpretation of our record from CD154-23-16P. Of special interest is the general resemblance of the patterns of variability between MD02-2588 and CD154-23-16P, in particular as regards the orbital-timescale trends (Fig. 7.8). The difference of the absolute values of two records are in accord with the purer (i.e., less diluted) Subantarctic signal in the thermocline waters at the more upstream location of the Agulhas Plateau in regard to the northward flow of SAMW. The lower  $\delta^{13}\text{C}_{G.trunc(s)}$  values in CD154-23-16P on the Mallory Seamount may thus be the result of increased dilution of the original  $\delta^{13}\text{C}_{\text{DIC}}$  signal due to mixing with the surrounding waters along the trajectory of SAMW. Indeed, the occurrence of glacial  $\delta^{13}\text{C}_{G.trunc(s)}$  values in CD154-23-16P that resemble the corresponding surface-water values more than those of  $\delta^{13}\text{C}_{G.trunc(s)}$  from MD02-2588 supports the idea of increased dilution of SAMW at the Mallory Seamount; in essence the very positive  $\delta^{13}\text{C}_{\text{as}}$  signal from the Subantarctic may have been countered by the negative  $\delta^{13}\text{C}_{\text{as}}$  values associated with the tropical and subtropical Indian Ocean waters delivered to the CD154-23-16P core site by the northern-sourced thermocline waters entrained by the Agulhas Current. The dilution of the positive  $\delta^{13}\text{C}_{\text{as}}$  signal may have been amplified by the accumulation of biologically-respired  $^{12}\text{C}$  along the trajectory of both SAMW and northern-sourced thermocline waters advected to the Mallory Seamount thermocline. The combination of the dilution effect and the increased accumulation of low- $\delta^{13}\text{C}_{\text{DIC}}$  could therefore explain the oc-

currence of values of  $\delta^{13}\text{C}_{G.trunc(s)}$  in CD154-23-16P that are lower than both the corresponding  $\delta^{13}\text{C}_{G.ruber}$  from the surface waters as well as lower than the  $\delta^{13}\text{C}_{G.trunc(s)}$  values from the Agulhas Plateau.

Interestingly, following the CIME of the last deglaciation, the offset between  $\delta^{13}\text{C}_{G.trunc(s)}$  from CD154-23-16P and MD02-2588 is reduced for the duration of MIS 1, where both display a steady rise to equally high values. This possibly indicates the transition to a common southern-sourced signal during the Holocene (i.e., a reduction of dilution due to mixing with northern-sourced waters) or alternatively, it could indicate a reduction in the accumulation of biologically-respired  $^{12}\text{C}$  along the trajectories of both SAMW and northern-sourced thermocline waters. In the context of shifting Southern Ocean fronts, a northward position during glacial stages could be envisaged to bring the thermocline waters of the Mallory Seamount closer to the source of SAMW which would have led to a convergence of values which is the opposite of what is observed. As such, it may be more likely that the offset during the glacial stages was driven by processes originating in the upstream region of the Agulhas Current and that the convergence of  $\delta^{13}\text{C}_{G.trunc(s)}$  values from CD154-23-16P with those from MD02-2588 during MIS 1 may reflect a reduced influence from northern-sourced thermocline waters during interglacial stages.

## 7.5 Conclusion

In this chapter we have introduced and assessed the results of a preliminary study of sediment core CD154-23-16P retrieved from the flank of the Mallory Seamount, offshore southern Africa. We presented a high-resolution record of Fe/K derived from XRF core-scanning and an initial low-resolution record of stable oxygen and carbon isotopes measured in surface- and deep-dwelling planktonic foraminifera. We developed the age model for this core using a combination of radiocarbon dating of planktonic foraminifera and graphical tuning to the Chinese speleothem stable oxygen isotope record. Our findings from the initial assessment of these results revealed the following:

- (i) The age model indicates that this core represents a continuous sedimentary sequence that spans the past 60 kyr BP. The radiocarbon dates and age control points derived from our graphical tuning approach suggest that the core site is characterised by very high sedimentation rates that range between 15 and 23 cm kyr<sup>-1</sup>. We infer the

presence of two turbidite deposits based on two episodes where sedimentation rates increase by an order of magnitude (230 cm kyr<sup>-1</sup> between 2 and 2.4 cm depth along the core and 430 cm kyr<sup>-1</sup>, between 6 and 6.3 cm). The uppermost of the two inferred deposits is also associated with an age reversal. No systematic relationship is observed between these episodes of high sedimentation and the available colour spectral analysis scans, nor were they evident during the initial optical inspection of this core. We do however observe what appear to be sharp increases in the record of percentage coarse fraction during these high sedimentation intervals, although we cannot be certain that these peaks are the result of the deposition of turbidites.

(ii) The Fe/K record of sediment core CD154-23-16P was found to display a prominent millennial-scale variability throughout the past 60 kyr BP and reveals a remarkable similarity to the millennial-scale structure of the Hulu-Sanbao Cave  $\delta^{18}\text{O}_{\text{speleo}}$  record. The relationship between these two records reveals an antiphasing of the hydrological conditions between southeastern Africa and Central China. Most of the prominent peaks of Fe/K can be traced to corresponding Northern Hemisphere glacial stadials, although we note the occurrence of temporal offsets during certain events within the radiocarbon-dated section of the core (e.g. GS 1, GS 2 and GS 3). The antiphased relationship between the Northern Hemisphere records and Fe/K from CD154-23-16P is thought to be caused by latitudinal shifts of the Intertropical Convergence Zone (ITCZ) as a result of changes in the mode of AMOC circulation and of changes of North Atlantic temperatures.

(iii) The initial stable oxygen isotope stratigraphy developed for CD154-23-16P from measurements of surface and deep-dwelling planktonic foraminifera has permitted an intriguing insight to be gained regarding the physical variability of the upper ocean during the past 50 kyr BP. Specifically, the oxygen isotope records indicate an increased gradient of physical properties between the surface and thermocline waters overlying the core site during the glacial stages, relative to the interglacial gradient. Removal of the ice-volume component from the foraminiferal oxygen isotopic records allows us to attribute the glacial-interglacial changes in stratification to changes in the thermocline waters. The ice-volume correction also allows us to identify a number of prominent peaks in the surface water record coincident with Northern Hemisphere Heinrich stadials. We propose that these peaks are equivalent to the salinification events which have been identified as originating in the upstream region of the Agulhas

current during the last glacial stage and which have also been identified in the I-AOG during the penultimate deglaciation.

(iv) The corresponding carbon isotope stratigraphy from CD154-23-16P was used to make an initial assessment of the chemical variability of the upper ocean during the studied interval. The most distinctive feature of these records is the occurrence of minimum values during the last glacial termination between ~20 and 15 kyr BP. This minimum is more apparent in the thermocline waters but is nonetheless also evident in surface waters at this site. We identify this feature as a deglacial carbon isotope minimum event which is typical of Southern Hemisphere  $\delta^{13}\text{C}$  records that are fed by southern-sourced intermediate waters. Comparison of the carbon isotope records from CD154-23-16P to published records from the region also allowed us to recognise differences in the chemical history of both surface waters and intermediate waters in the wider I-AOG region. Specifically, we find a more-or less constant offset between the surface water signature at CD154-23-16P and sites on the Atlantic side of the I-AOG throughout the entire duration of our record which we propose as being due to differences in local export production or differences in source-water signals on either side of the African continent. In addition, we observe an offset between intermediate waters at the CD154-23-16P core site relative to a record from further south. Interestingly, in the case of the intermediate waters the offset is more prominent in the glacial section; within the Holocene section of the record these values tend to converge. We propose that this pattern is a response to a complex interaction between changes in northern vs southern-sourced carbon isotope signals as a result of variable mixing and dilution, compounded by changes in export production, both locally and along the trajectories of thermocline waters entrained to the core site.

Our assessment of the preliminary results from core CD154-23-16P leads us to propose a key direction for future work on this core. Firstly, we propose a more detailed sedimentological examination of the core and an evaluation of the proposed chronostratigraphic framework. If the age model developed in this study proves to be reliable and if the inferred sedimentation rates are not impacted greatly by repeated turbidite deposition, then this sediment core may provide a unique opportunity for very high resolution paleoceanographic reconstructions. With an average sedimentation rate of ~20 cm kyr<sup>-1</sup> (excluding the inferred turbidite intervals), a 1 cm sampling interval would equate to a temporal resolution of 50 years per sample. However, the occurrence

of the two inferred turbidite deposits may suggest that sedimentation rates are exaggerated by undetected turbidites. We therefore propose a detailed sedimentological analysis of the core to determine if such deposits can be identified and if so to assess their impact on the age model and the inferred sedimentation rates at this site. This assessment should involve detailed visual core-logging and comparison to the available datasets of XRF and colour spectral analysis scanning. Further sampling to examine changes in the proportion of coarse fraction may also be useful. Once these sedimentological assessments have been made conducted a detailed sampling strategy can be designed.

Based on our initial stable isotope stratigraphy from measurements in surface- and deep-dwelling planktonic foraminifera we propose that the most fruitful line of enquiry is a more detailed examination of the prominent oxygen isotope peaks identified in the ice-volume corrected surface water record. These features may correspond to the salinification events identified in the upstream region of the Agulhas Current which are propagated to the I-AOG and which may be responsible for buoyancy anomalies in the Atlantic with important implication for the AMOC.

---

## 8 Conclusions and future work

---

### 8.1 Deep water variability in the Indian-Atlantic Ocean Gateway during the past 150 kyr BP

In chapter 4 of this thesis, we presented downcore records of stable isotopes and elemental ratios in benthic foraminifera and mean grain sizes of sortable silt from sediment core MD02-2588. These stratigraphic-series reconstruct the history of mid-depth ocean circulation on the southern Agulhas Plateau during the past 150 kyr BP. A multiproxy approach was applied to derive a range of physical and chemical bottom water parameters from the stable isotopes, elemental ratios and grain size data. These include the carbonate saturation state of seawater, the concentration of dissolved Cd in seawater, and relative changes in near-bottom flow speeds. Additionally, we isolated the various components that constitute the carbon isotopic composition preserved in benthic foraminifera, and furthermore, we presented a qualitative reconstruction of past sediment pore-water oxygen concentration based on U/Mn ratios in foraminifera. All stratigraphic series display prominent orbital modulation and where the sampling resolution is high enough, millennial-scale variability is also evident. However, no systematic correlation was identified between millennial-scale climate events and the high-frequency variability observed in the downcore record. Therefore, this chapter only discussed changes on glacial-interglacial timescales, with a particular focus on the last two deglaciations.

In broad terms, glacial stages are characterised by relatively low values of  $\Delta[\text{CO}_3^{2-}]$ ,  $\text{Cd}_{\text{sw}}$ ,  $\delta^{13}\text{C}_{\text{as}}$ , and  $[\text{O}_2]$ , while the  $\overline{SS}$  record indicates relatively high bottom-water flow speeds. During interglacials the situation is reversed, with relatively high values of  $\Delta[\text{CO}_3^{2-}]$ ,  $\text{Cd}_{\text{sw}}$ ,  $\delta^{13}\text{C}_{\text{as}}$ , and  $[\text{O}_2]$ , while bottom-water flow speeds are slower. The higher sampling resolution of the elemental ratio records in the core sections that correspond to the last two deglaciations allowed additional complexities in the variability to be assessed.

We concluded that, during glacial stages, the southern Agulhas Plateau and the wider mid-depth South Atlantic Ocean came under increased influence of LSCW as the ACC shifted to a more equatorward position, in agreement with published geochemical evidence from the deep South Atlantic (Oppo *et al.*, 1990; Oppo and Rosenthal, 1994; Charles *et al.*, 1996; Ninnemann and Charles, 2002; Hodell *et al.*, 2003; Piotrowski *et*

*al.*, 2005; Barker *et al.*, 2010; Skinner *et al.*, 2010; Burke and Robinson, 2012; Barker and Diz; 2014). The lower  $\Delta[\text{CO}_3^{2-}]$  suggests that the mid-depth South Atlantic experienced an increase in the storage of respired carbon, as  $\text{CO}_2$  was sequestered from the glacial atmosphere. Despite the inferred increase in the relative volume of LSCW bathing the Agulhas Plateau during glacial stages, the contribution of NCW is not thought to have diminished completely. In fact, the decrease in the relative volume of NCW bathing the MD02-2588 core site, appears to be counterbalanced by the lower nutrient content of northern-sourced water masses during glacial stages. The glacial lowering of seawater nutrient concentration in the mid-depth South Atlantic was possibly also affected by an increase in the formation of lower-nutrient mid-depth waters by open ocean convection in polynyas within the expanded circum-Antarctic sea ice zone.

The recurrent  $\text{Cd}_{\text{sw}}$  maxima recorded during glacial terminations were interpreted as resulting from the upward mixing of nutrient-rich bottom waters from the deepest and most isolated layers in the Southern Ocean following the deglacial breakdown of stratification in the ocean interior. The increases in  $\text{Cd}_{\text{sw}}$  recorded during deglaciations occur in tandem with increases in  $\Delta[\text{CO}_3^{2-}]$  on the southern Agulhas Plateau and increases of  $p\text{CO}_2$  in Antarctic ice cores. The covariation of these parameters supports the premise of increased outgassing of carbon from the deep Southern Ocean during deglaciations. This interpretation is also consistent with the inference of increased  $[\text{O}_2]$  in the bottom waters of the southern Agulhas Plateau which suggests that during deglaciations, the deep South Atlantic experienced transient episodes of enhanced ventilation

## **8.2 Changes in surface ocean nutrient utilisation in the Indian-Atlantic Ocean Gateway during the past 150 kyr BP**

In Chapter 5 we examined how the position of the subtropical front (STF) within the Indian-Atlantic Ocean Gateway (I-AOG) migrated over the past 150 ky BP and considered how these changes may have impacted the nutrient supply to the surface waters of the southern Agulhas Plateau. The record of bulk sediment nitrogen isotope composition ( $\delta^{15}\text{N}_{\text{Bulk}}$ ) from sediment core MD02-2588 suggests that the northward migration of the STF during glacials is associated with increases in nutrient supply relative to interglacial levels. Enhanced nutrient supply to the surface waters of the southern Agulhas Plateau is thought to be due to increased northward advection of relatively nutrient-rich Subantarctic surface waters to the MD02-2588 core site, along with

weaker upper ocean stratification which facilitated vertical mixing of nutrients from the thermocline. During interglacial intervals, when the STF was located further south, nutrient supply was lower. The lower nutrient levels observed during interglacial are thought to reflect reduced northward advection of Subantarctic surface waters relative to the advection of nutrient-poor Subtropical waters. In addition, the southward shift of the STF during interglacial stages may have reduced the vertical mixing of nutrients from the thermocline due to the enhanced upper ocean stratification that is characteristic of the subtropical zone.

The likeness of the  $\delta^{15}\text{N}_{\text{Bulk}}$  record from MD02-2588 with analogous records from the eastern equatorial Pacific (EEP) may suggest that the temporal variability of  $\delta^{15}\text{N}_{\text{nitrate}}$  within these two regions is linked on glacial-interglacial timescales. We suggest that the correlation of these records is due to independent responses to glacial-interglacial changes in the position of the Southern Ocean fronts. On the Agulhas Plateau, changes in the position of the STF determines the local nutrient supply, whereas in the EEP, changes in the position of the Southern Ocean fronts regulate the oxygen supply to the eastern tropical Pacific oxygen minimum zone with in turn determines the level of denitrification.

### **8.3 Carbon isotopic composition of *Globorotalia truncatulinoides* and applications as a proxy of the soft-tissue biological pump and of air-sea gas exchange in the Southern Ocean**

In Chapter 6 we presented new data from a set of core-top samples collected around New Zealand in order to assess the utility of the deep-dwelling planktonic foraminifera species, *G. truncatulinoides*, as a recorder of  $\delta^{13}\text{C}_{\text{DIC}}$ . From the results of this study, we concluded that this species is indeed a reliable tracer of thermocline chemical properties. Though, offsets between the values of  $\delta^{13}\text{C}$  measured in the calcite tests of this species ( $\delta^{13}\text{C}_{G.\text{trunc}(s)}$ ) and the corresponding water column  $\delta^{13}\text{C}_{\text{DIC}}$  highlighted the importance of consistency in sample selection for down-core studies.

We then presented a down-core assessment of the  $\delta^{13}\text{C}_{G.\text{trunc}(s)}$  using published data from sediment core MD02-2588 (Ziegler *et al.*, 2013) and new replicate data from the same core. Our aim was to build on the original evaluation conducted by Ziegler *et al.*, (2013) of how secondary effects, not associated with nutrient and DIC cycling, impact  $\delta^{13}\text{C}_{G.\text{trunc}(s)}$ . We compared the  $\delta^{13}\text{C}_{G.\text{trunc}(s)}$  record from MD02-2588 with the record of

$\delta^{13}\text{C}_{\text{atm}}$  from Antarctic ice cores and found them to be strikingly similar in terms of their patterns of variability throughout the past 150 kyr BP. The same was found to be true for the biological component of the benthic  $\delta^{13}\text{C}$  ( $\delta^{13}\text{C}_{\text{benthic-bio}}$ ) record from MD02-2588 which reflects the nutrient and DIC characteristics of deep waters that upwell around Antarctica. These similarities demonstrate the importance of carbon transfer between the Southern Ocean and the atmosphere and highlights the potential of using records of  $\delta^{13}\text{C}_{\text{DIC}}$  from Southern Ocean to reconstruct the variability of  $\delta^{13}\text{C}_{\text{atm}}$  further back in time, possibly even allowing first-order estimations of relative changes of  $\delta^{13}\text{C}_{\text{atm}}$  to be extended beyond the scope of ice core records.

Furthermore, we showed that the record  $\Delta\delta^{13}\text{C}_{\text{plank-benthic}}$  from MD02-2588 is consistent with the suggestion that the Southern Ocean's soft-tissue biological pump plays a role in at least part of the variability of  $\delta^{13}\text{C}_{\text{atm}}$  recorded in Antarctic ice cores, although it remains difficult to quantify its exact contribution relative to other drivers of  $\delta^{13}\text{C}_{\text{atm}}$  variability. The most notable indication of the link between the biological pump and  $\delta^{13}\text{C}_{\text{atm}}$  is the occurrence of the three largest negative  $\delta^{13}\text{C}_{\text{atm}}$  excursions during TI, TII and MIS 4, synchronous to the three largest negative shifts of  $\Delta\delta^{13}\text{C}_{\text{plank-benthic}}$ .

#### **8.4 Preliminary study of marine sediment core CD154-23-16P**

In Chapter 7 we presented the results of a preliminary study of sediment core CD154-23-16P which was retrieved from the flank of the Mallory Seamount, offshore southern Africa. We presented a high-resolution record of Fe/K derived from X-Ray Fluorescence (XRF) core-scanning and an initial low-resolution record of stable oxygen and carbon isotopes measured in surface- and deep-dwelling planktonic foraminifera. We developed the age model for this core using a combination of radiocarbon dating of planktonic foraminifera and graphical tuning to the Chinese speleothem stable oxygen isotope record ( $\delta^{18}\text{O}_{\text{speleo}}$ ). Our findings from the initial assessment of these results revealed the following:

(v) The age model indicated that this core represents a continuous sedimentary sequence that spans the past 60 kyr BP. The radiocarbon dates and age control points derived from our graphical tuning approach suggest that the core site is characterised by very high sedimentation rates that range between 15 and 23 cm kyr<sup>-1</sup>. We infer the presence of two turbidite deposits based on two episodes where sedimentation rates

increase by an order of magnitude. The uppermost of the two inferred deposits is also associated with an age reversal. No systematic relationship is observed between these episodes of high sedimentation and the available colour spectral analysis scans, nor were they evident during the initial optical inspection of this core. We do however observe what appear to be sharp increases in the record of percentage coarse fraction during these high sedimentation intervals, although we cannot be certain that these peaks are the result of the deposition of turbidites.

(vi) The Fe/K record of sediment core CD154-23-16P was found to display a prominent millennial-scale variability throughout the past 60 kyr BP and reveals a remarkable similarity to the millennial-scale structure of the Hulu-Sanbao Cave  $\delta^{18}\text{O}_{\text{speleo}}$  record. The relationship between these two records reveals an antiphasing of the hydrological conditions between southeastern Africa and Central China. Most of the prominent peaks of Fe/K can be traced to corresponding Northern Hemisphere glacial stadials, although we note the occurrence of temporal offsets during certain events within the radiocarbon-dated section of the core (e.g. GS 1, GS 2 and GS 3). The antiphased relationship between the Northern Hemisphere records and Fe/K from CD154-23-16P is thought to be caused by latitudinal shifts of the Intertropical Convergence Zone (ITCZ) as a result of changes in the mode of AMOC circulation and of changes of North Atlantic temperatures.

(vii) The initial stable oxygen isotope stratigraphy developed for CD154-23-16P from measurements of surface and deep-dwelling planktonic foraminifera permitted a preliminary view to be gained regarding the physical variability of the upper ocean during the past 50 kyr BP. Specifically, the oxygen isotope records indicate an increased gradient of physical properties between the surface and thermocline waters overlying the core site during the glacial stages, relative to the interglacial gradient. Removal of the ice-volume component from the foraminiferal oxygen isotopic records allowed us to attribute the glacial-interglacial changes in stratification to changes in the thermocline waters. The ice-volume correction also allowed us to identify a number of prominent peaks in the surface water record coincident with Northern Hemisphere Heinrich stadials. We propose that these peaks were equivalent to the salinification events which have been identified as originating in the upstream region of the Agulhas current during the last glacial stage (Simon *et al.*, 2015) and which have also been identified in the I-AOG during the penultimate deglaciation (Marino *et al.*, 2013).

(viii) The corresponding carbon isotope stratigraphy from CD154-23-16P was used to make an initial assessment of the chemical variability of the upper ocean during the studied interval. The most distinctive feature of these records is the occurrence of minimum values during the last glacial termination between ~20 and 15 kyr BP. This minimum is more apparent in the thermocline waters but is nonetheless also evident in surface waters at this site. We identified this feature as a deglacial carbon isotope minimum event which is typical of Southern Hemisphere  $\delta^{13}\text{C}$  records that are fed by southern-sourced intermediate waters. Comparison of the carbon isotope records from CD154-23-16P to published records from the region also allowed us to recognise differences in the chemical history of both surface waters and intermediate waters in the wider I-AOG region. Specifically, we find a more-or less constant offset between the surface water signature at CD154-23-16P and sites on the Atlantic side of the I-AOG throughout the entire duration of our record which we propose as being due to differences in local export production or differences in source-water signals on either side of the African continent. In addition, we observe an offset between intermediate waters at the CD154-23-16P core site relative to a record from further south. Interestingly, in the case of the intermediate waters the offset is more prominent in the glacial section; within the Holocene section of the record these values tend to converge. We proposed that this pattern was a response to a complex interaction between changes in northern vs southern-sourced carbon isotope signals as a result of variable mixing and dilution, compounded by changes in export production, both locally and along the trajectories of thermocline waters entrained to the core site.

## 8.5 Future work

The work presented in this thesis has established the value of marine sediment cores MD02-2588 and CD154-23-16P for paleoceanographic reconstructions of the I-AOG. This work has also illustrated several issues regarding the quality of the data presented herein that require further attention.

Our assessment of the preliminary results from core CD154-23-16P leads us to propose a key direction for future work on this core. Firstly, we propose a more detailed sedimentological examination of the core and an evaluation of the proposed chronostratigraphic framework. If the age model developed in this study proves to be reliable, and if the inferred sedimentation rates are not impacted greatly by repeated turbidite deposition, then this sediment core may provide a unique opportunity for very high resolution paleoceanographic reconstructions. With an average sedimentation rate of  $\sim 20 \text{ cm kyr}^{-1}$  (excluding the inferred turbidite intervals), a 1 cm sampling interval would equate to a temporal resolution of 50 years per sample. However, the occurrence of the two turbidite deposits may suggest that sedimentation rates are exaggerated by undetected turbidites. We therefore propose a more detailed sedimentological analysis of the core to determine if such deposits can be identified and if so, to assess their impact on the age model and the inferred sedimentation rates at this site.

Based on our initial stable isotope stratigraphy for sediment core CD154-23-16P, based on measurements in surface- and deep-dwelling planktonic foraminifera, we propose that the most fruitful line of enquiry is a more detailed examination of the prominent oxygen isotope peaks identified in the ice-volume corrected surface water record. These features may correspond to the salinification events identified in the upstream region of the Agulhas Current which are propagated to the I-AOG and which may be responsible for buoyancy anomalies in the Atlantic with important implication for the AMOC. The excellent agreement between the variability of elemental profiles derived by XRF core scanning with previous studies at neighbouring sites along the eastern margin of southern Africa, suggest that these data can be incorporated into a regional-scale reconstruction of the terrestrial hydroclimate of south eastern Africa. Further development of the proxies of ocean changes can then be integrated with the terrestrial reconstructions to better understand the links between land and sea in this region on glacial to interglacial and millennial timescales.

The downcore records of stable isotopes, elemental ratios and grain size from sediment core MD02-2588 demonstrate how this core can help inform a number of pertinent questions regarding the paleoceanographic history of the I-AOG on orbital and millennial timescales. During the recent IODP Expedition 361 ‘Southern African climates’ (Hall *et al.*, 2015) the southern flank of the Agulhas Plateau was targeted for drilling and successfully recovered core material at a site in very close proximity to the location of MD02-2588 (IODP Site U1475; 41°25.61’S, 25°15.64’E). The initial age-depth relationships of the recovered core material suggest that this site extends to approximately 7 Myr BP (Hall *et al.*, 2015). An obvious direction for work would be to extend the records from MD02-2588 further back in time using the new material recovered from IODP Site U1475.

We propose to use samples from IODP Site U1475 to extend the gradient between stable carbon isotopes in deep-dwelling planktonic and benthic foraminifera ( $\Delta\delta^{13}\text{C}_{\text{plank-benthic}}$ ) record of Ziegler *et al.*, (2013) from MD02-2588 from 350 kyr BP, through the Middle Pleistocene Transition (MPT) to approximately 1.5 myr BP in order to reconstruct changes in the strength of the Subantarctic Zone (SAZ) soft tissue biological pump this critical time of Pleistocene climate history. This work could be coupled with the available record Fe and dust mass accumulation rates from ODP Site 1090 (Martinez-Garcia *et al.*, 2011) as well as with the XRF core scanning records which have been generated for IODP Site U1475. This will essentially allow the  $\Delta\delta^{13}\text{C}_{\text{plank-benthic}}$  record to be compared directly with the records of Southern Ocean dust deposition and in order to examine the potential role of dust-borne iron fertilisation of the Southern Ocean during the MPT. Associated with the development of a  $\Delta\delta^{13}\text{C}_{\text{plank-benthic}}$  through the MPT is the opportunity to further investigate the very enticing correlation that has been found between stable carbon isotopic composition of deep-dwelling planktonic foraminifera from MD02-2588 and the Antarctic ice core records of the atmospheric carbon isotopic composition over the past 150 kyr BP.

The mean grain size record of sortable silt from MD02-2588 also demonstrates how IODP Site U1475 may be used to generate a record of changes in the strength and/or position of the Antarctic Circumpolar Current throughout the Plio-Pleistocene. Equally, the robustness of the B/Ca data from MD02-2588 indicate that it should be possible to develop long proxy records of the carbonate saturation state history of the mid-depth I-AOG. The Cd/Ca data from MD02-2588 still require further evaluation

before they can conclusively be applied to reconstruct changes in the dissolved Cd concentration of mid-depth waters in the I-AOG, due to the possibility of post-depositional contamination by authigenic coatings.

The occurrence of such coatings on foraminifera from MD02-2588 has highlighted the potential inadequacy of the quality control criteria typically applied to foraminifera-based elemental ratio records. A very important outcome of the work presented in this thesis is that post-depositional alteration in such records may not always be apparent when examining records from individual species, or using individual proxies. Clearly, more work is required to develop robust quality control criteria for downcore records of elemental ratios in foraminifera. We propose that a review of post-depositional alteration of foraminifera-based elemental ratio records be carried out urgently.

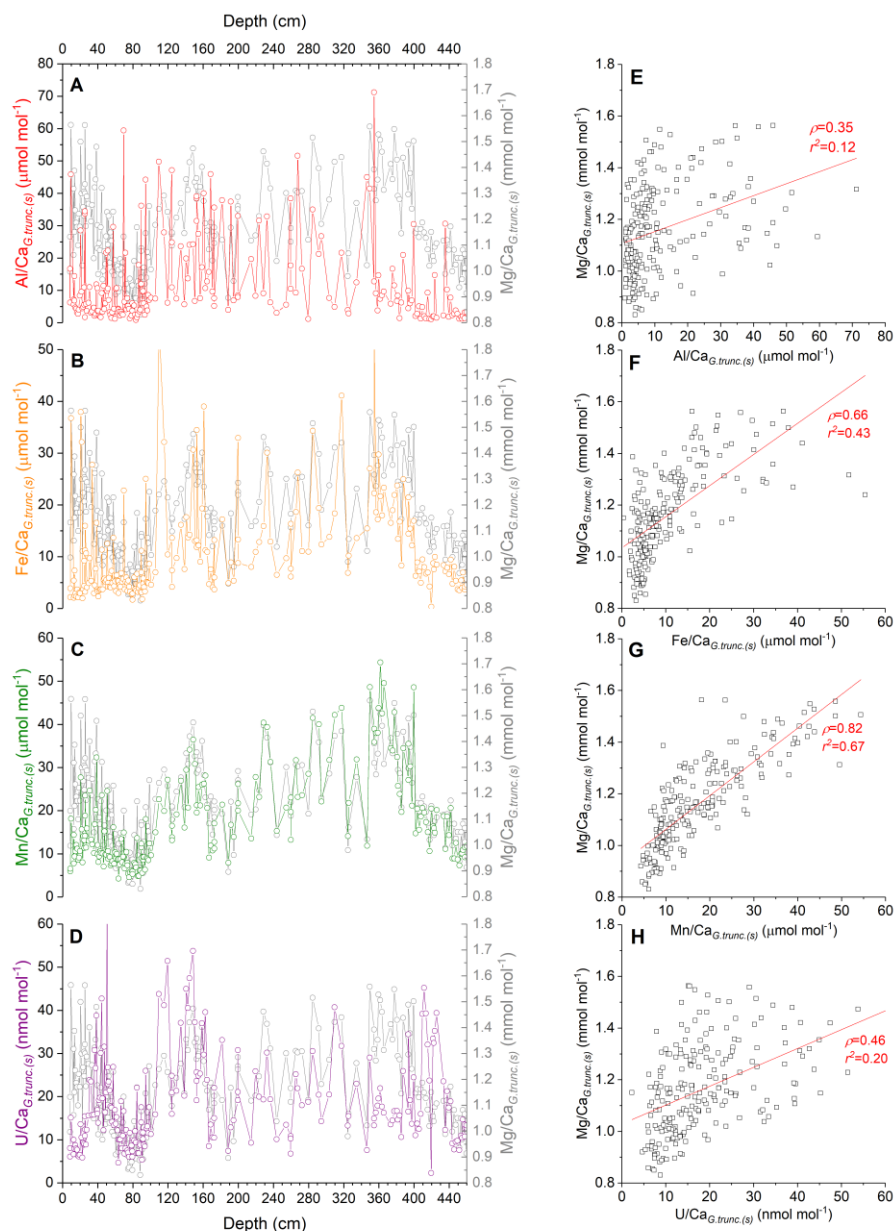
---

## Appendix

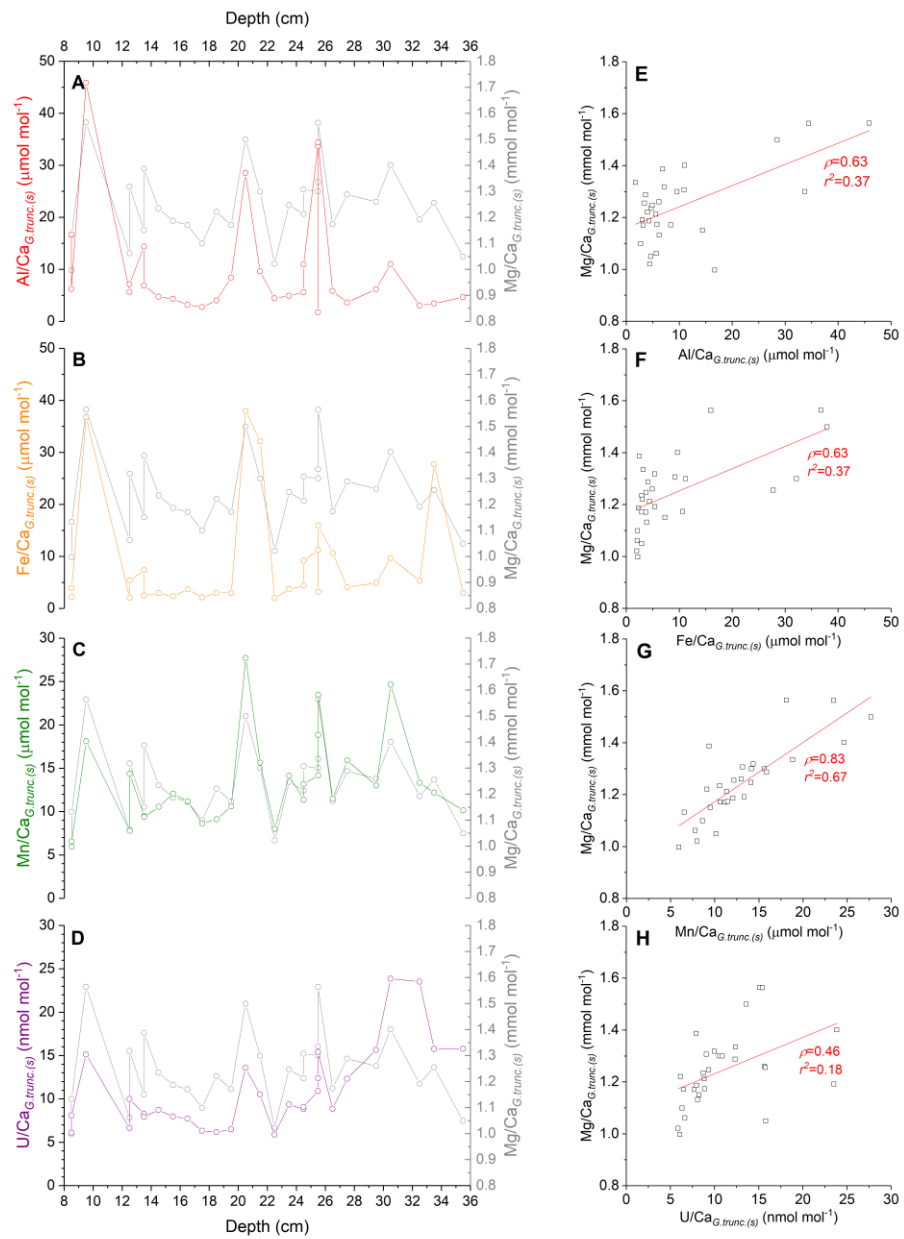
---

**Appendix table 3.1.** Depths of Marine Isotope Stages along sediment core MD02-2588

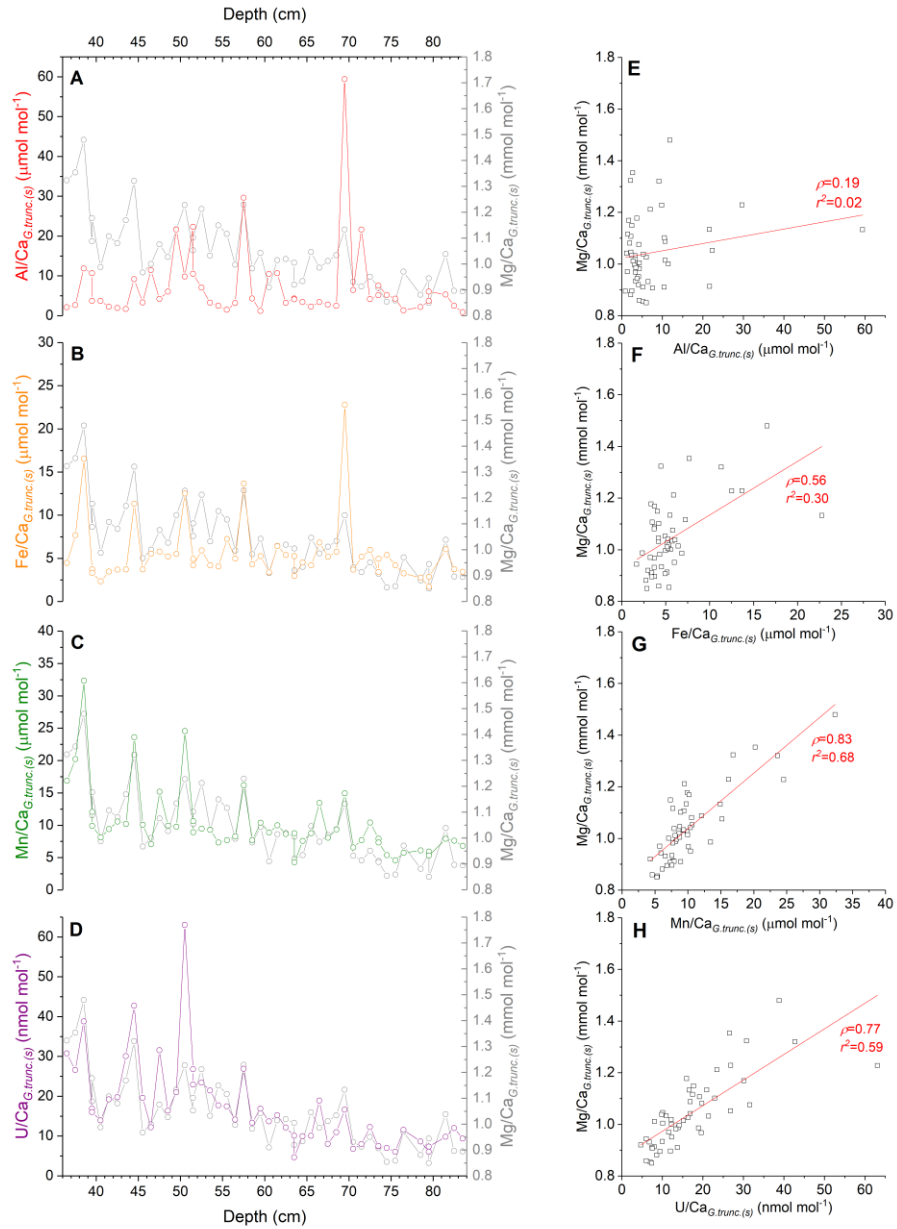
<b>Marine Isotope Stage</b>	<b>Age interval (kyr BP)</b>	<b>Sampling depth (cm)</b>
MIS 1	0-14	0.5-35.5
MIS 2	14-29	36.5-83.5
MIS 3	29-57	84.5-152.5
MIS 4	57-71	153.5-197.5
MIS 5	71-130	198.5-387.5
MIS 6 (incomplete)	130-150	388.5-455.5



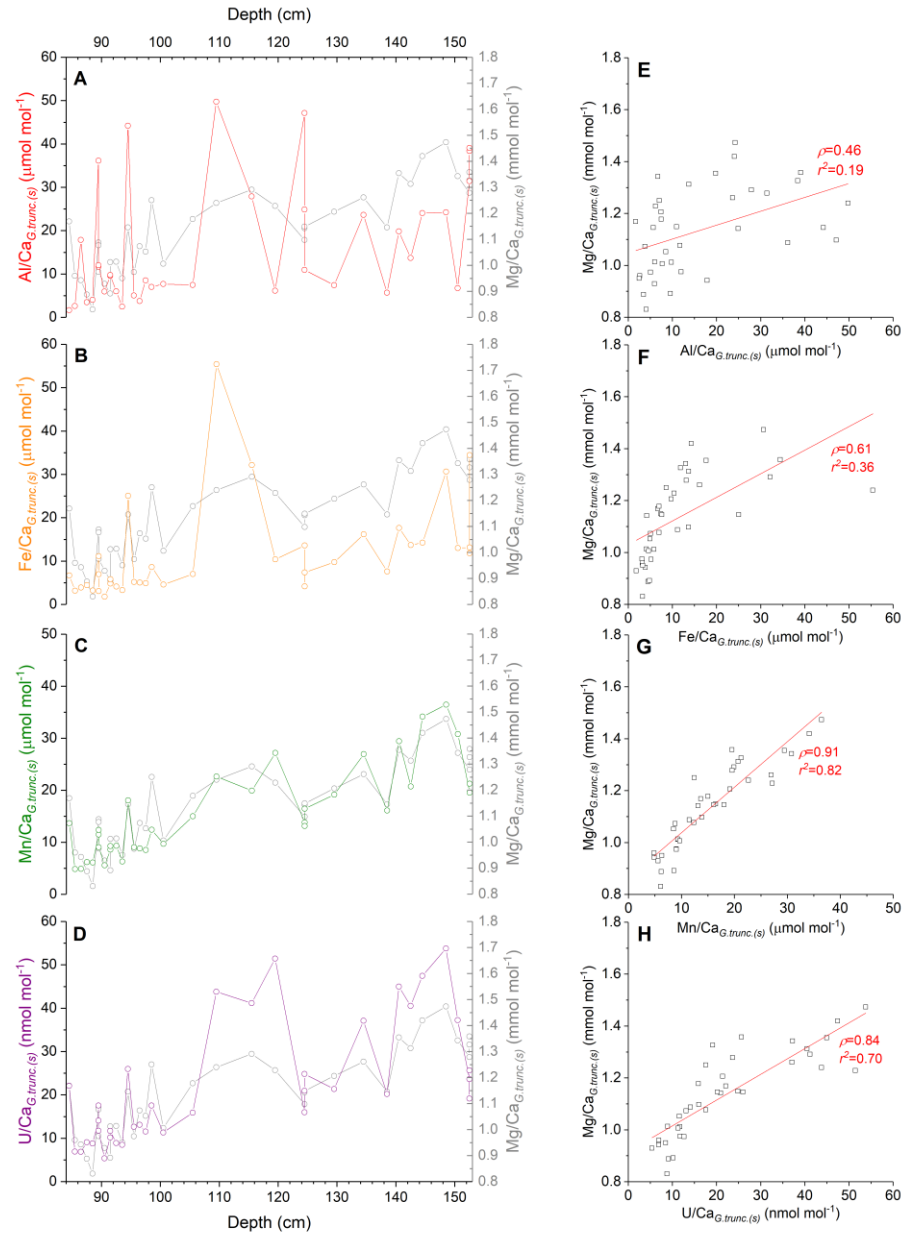
**Appendix Figure 3.1.** Comparison of *G. truncatulinoides (s.)* Mg/Ca record (grey line, open grey circles) from MD02-2588 with corresponding (A) Al/Ca (red line, open red circles), (B) Fe/Ca (orange line, open orange circles), (C) Mn/Ca (green line, open green circles) and (D) U/Ca (purple line, open purple circles). Corresponding cross plots of Mg/Ca versus (E) Al/Ca, (F) Fe/Ca, (G) Mn/Ca and (H) U/Ca in *G. truncatulinoides (s.)* samples. Also shown are the lines of best fit through the datasets and the corresponding Pearson's r value ( $\rho$ ) and the coefficient of determination ( $R^2$ ) of each linear equation (not shown). Elemental ratio data with values above the suggested contamination thresholds have been removed.



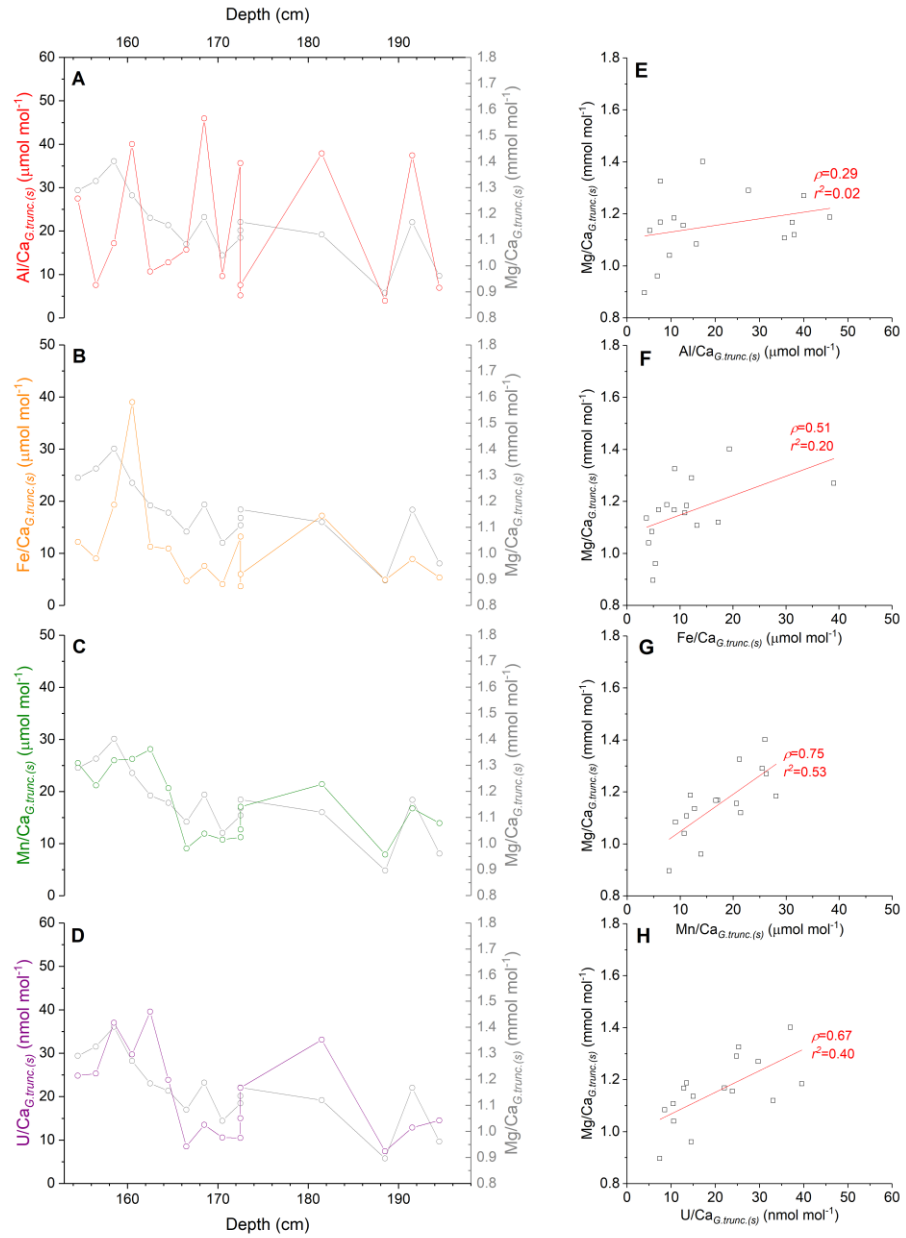
Appendix Figure 3.2. Detailed view of the MIS 1 section of appendix figure 3.1.



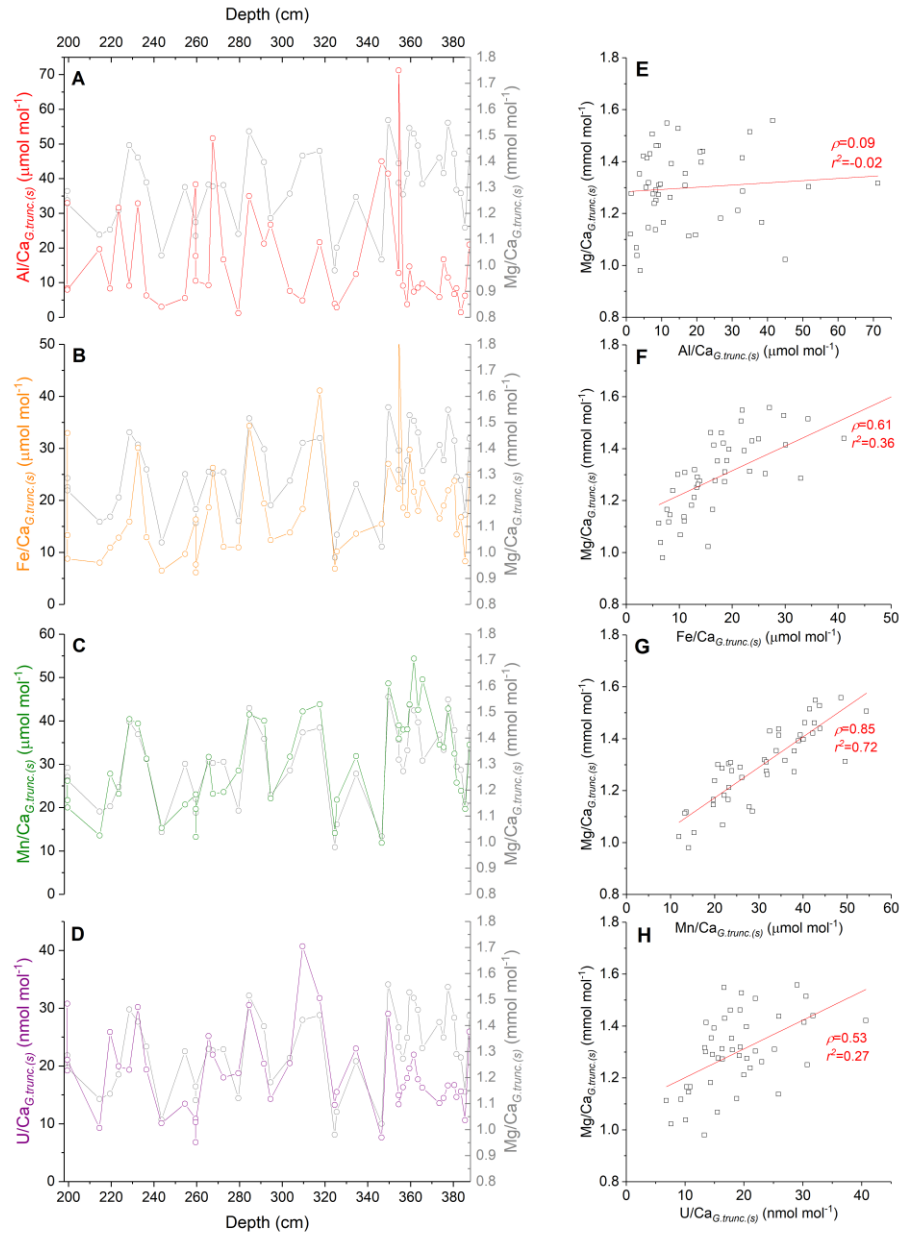
Appendix Figure 3.3. Detailed view of the MIS 2 section of appendix figure 3.1.



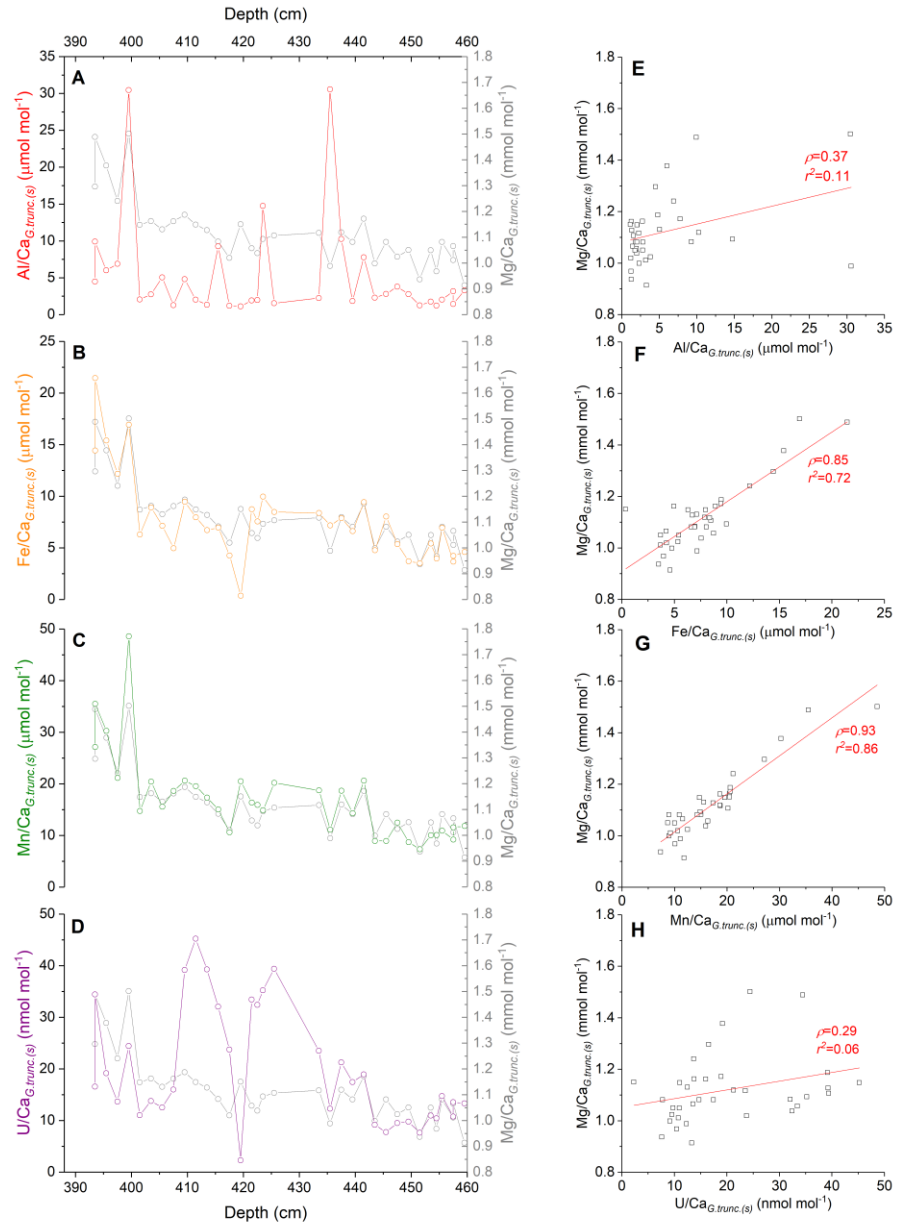
Appendix Figure 3.4. Detailed view of the MIS 3 section of appendix figure 3.1.



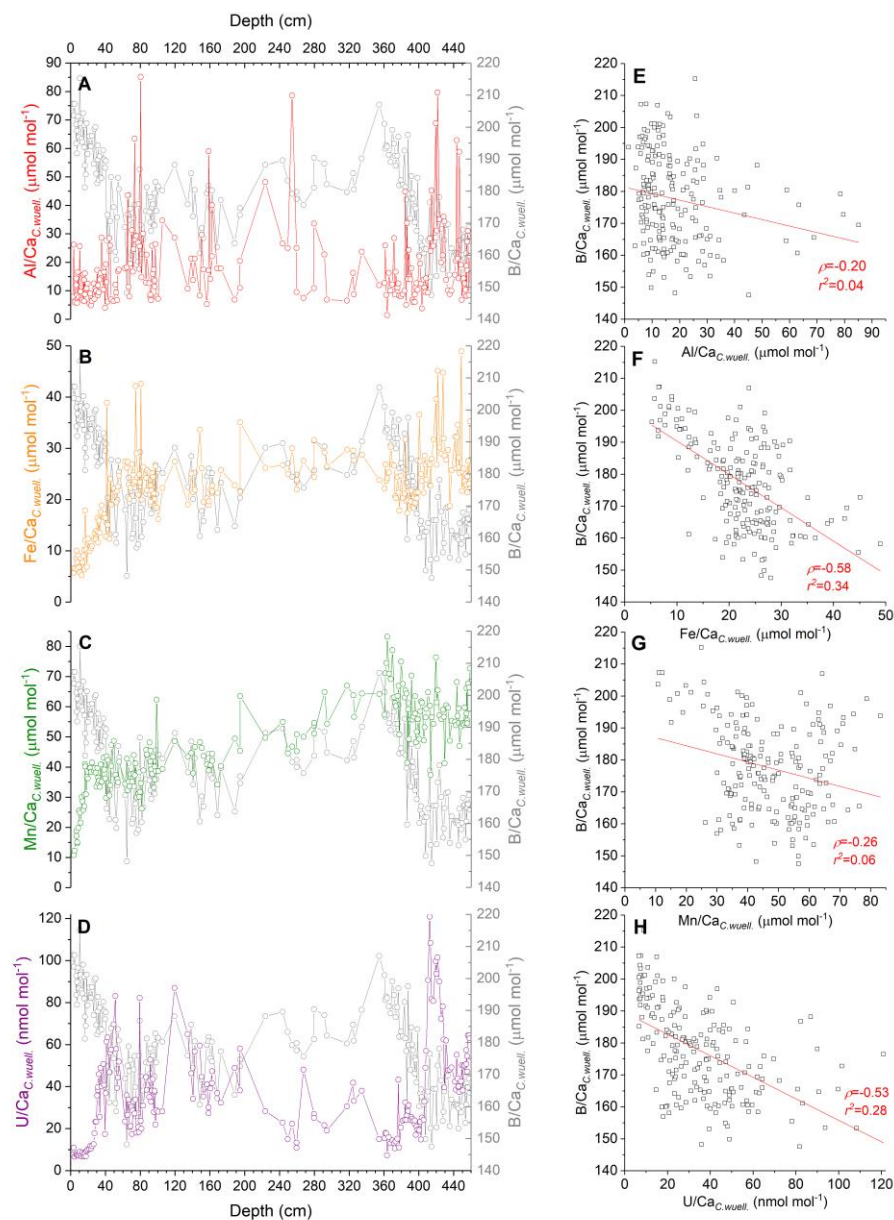
Appendix Figure 3.5. Detailed view of the MIS 4 section of appendix figure 3.1.



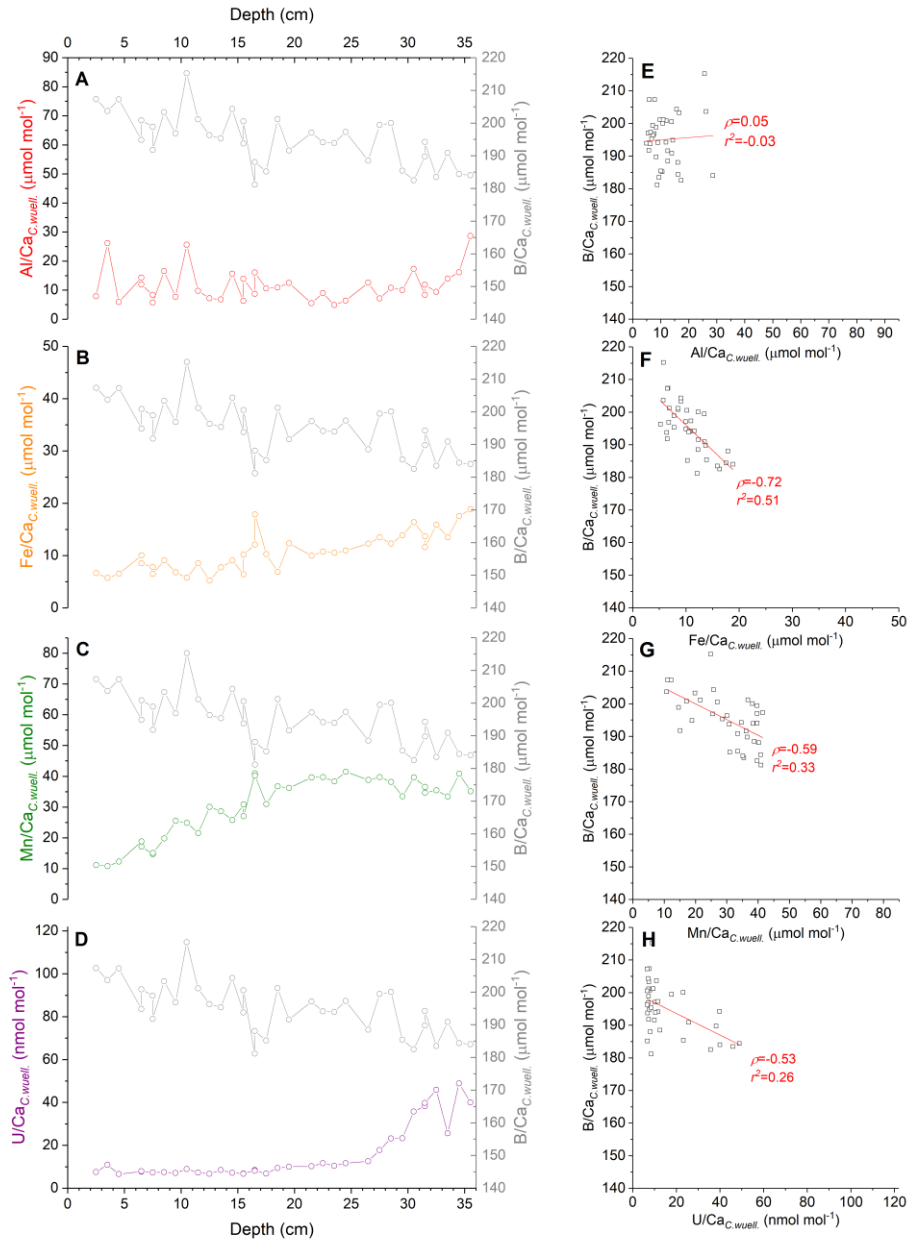
Appendix Figure 3.6. Detailed view of the MIS 5 section of appendix figure 3.1.



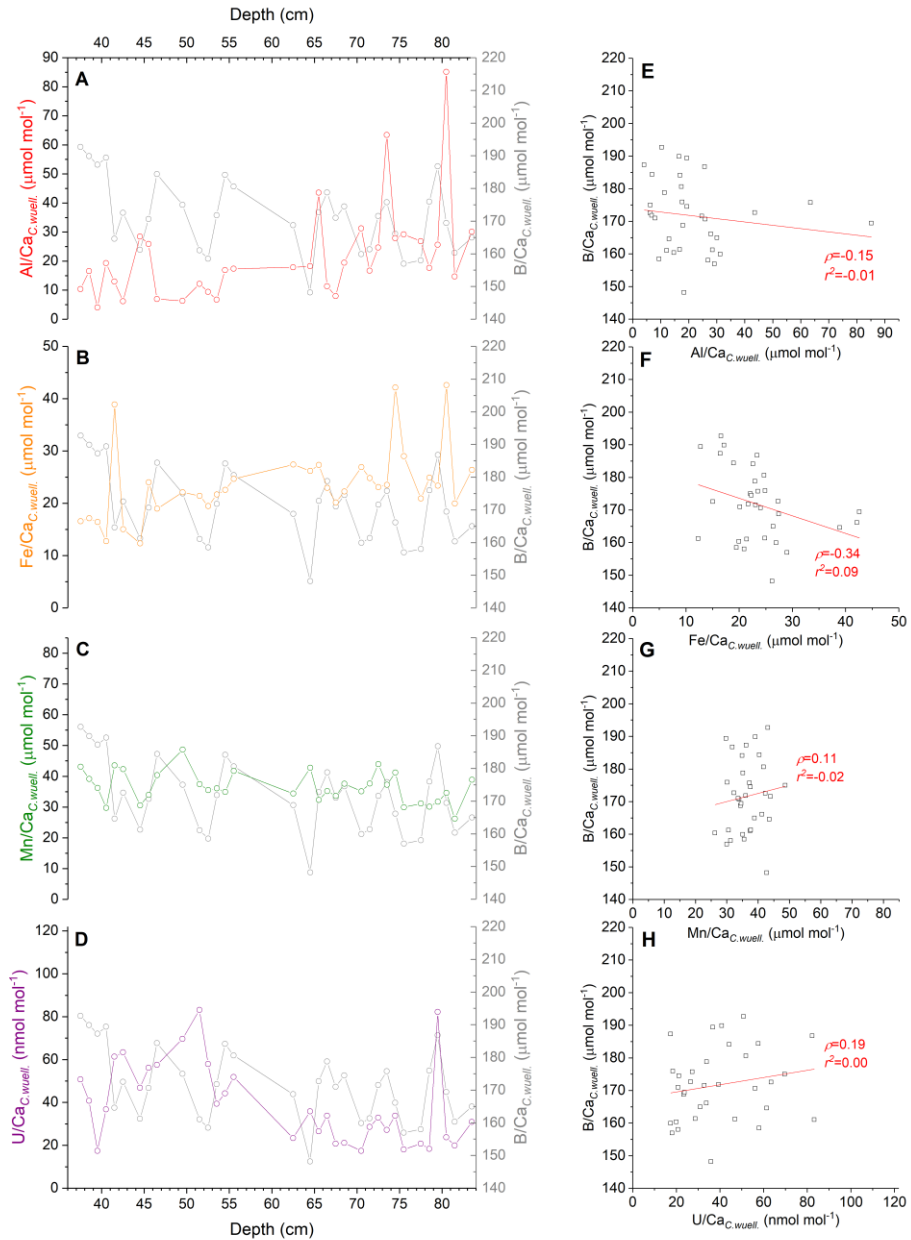
Appendix Figure 3.7. Detailed view of the MIS 6 section of appendix figure 3.1.



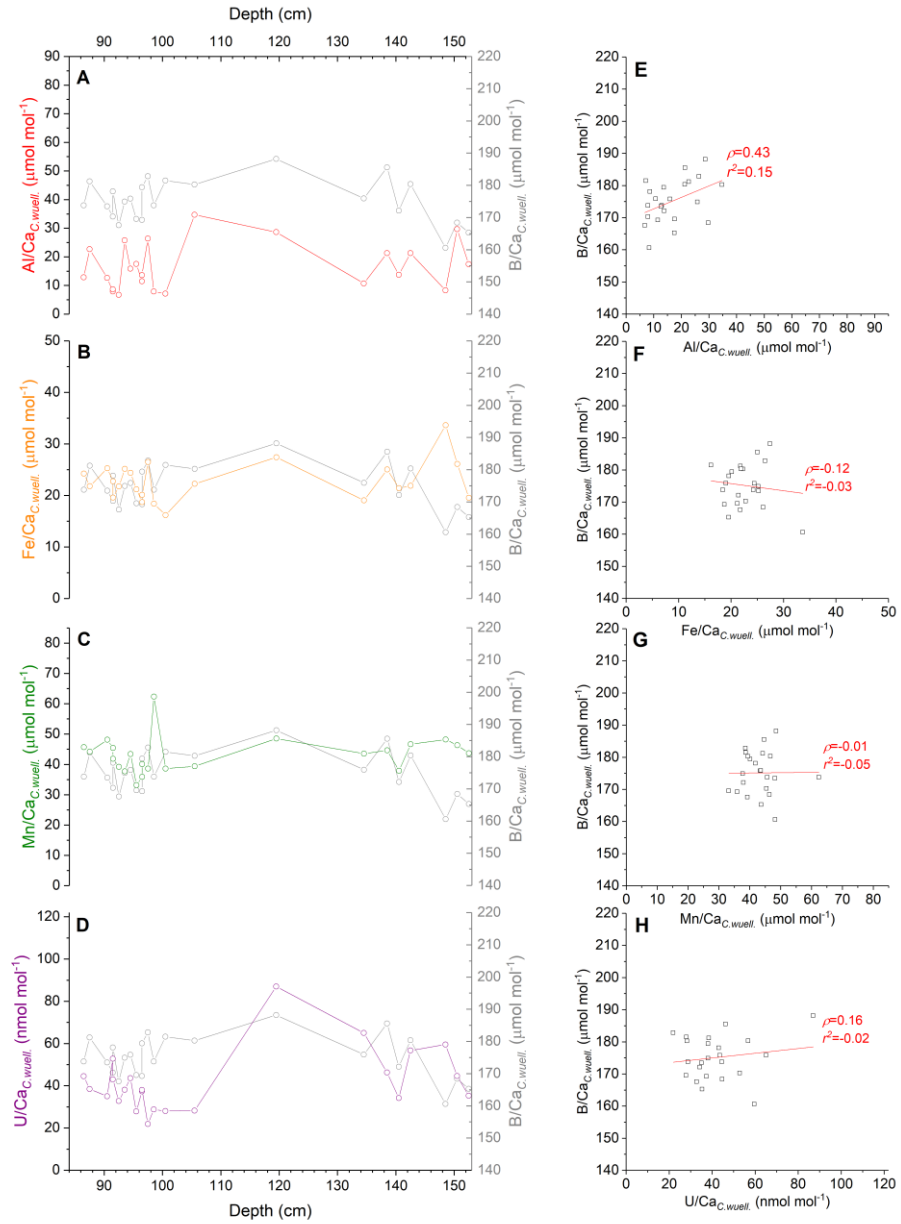
**Appendix Figure 3.8.** Comparison of *C. wuellerstorfi* B/Ca record (grey line, open grey circles) from MD02-2588 with corresponding (A) Al/Ca (red line, open red circles), (B) Fe/Ca (orange line, open orange circles), (C) Mn/Ca (green line, open green circles) and (D) U/Ca (purple line, open purple circles). Corresponding cross plots of B/Ca versus (E) Al/Ca, (F) Fe/Ca, (G) Mn/Ca and (H) U/Ca in *C. wuellerstorfi* samples. Also shown are the lines of best fit through the datasets and the corresponding Pearson's r value ( $\rho$ ) and the coefficient of determination ( $R^2$ ) of each linear equation (not shown). Elemental ratio data with values above the suggested contamination thresholds have been removed.



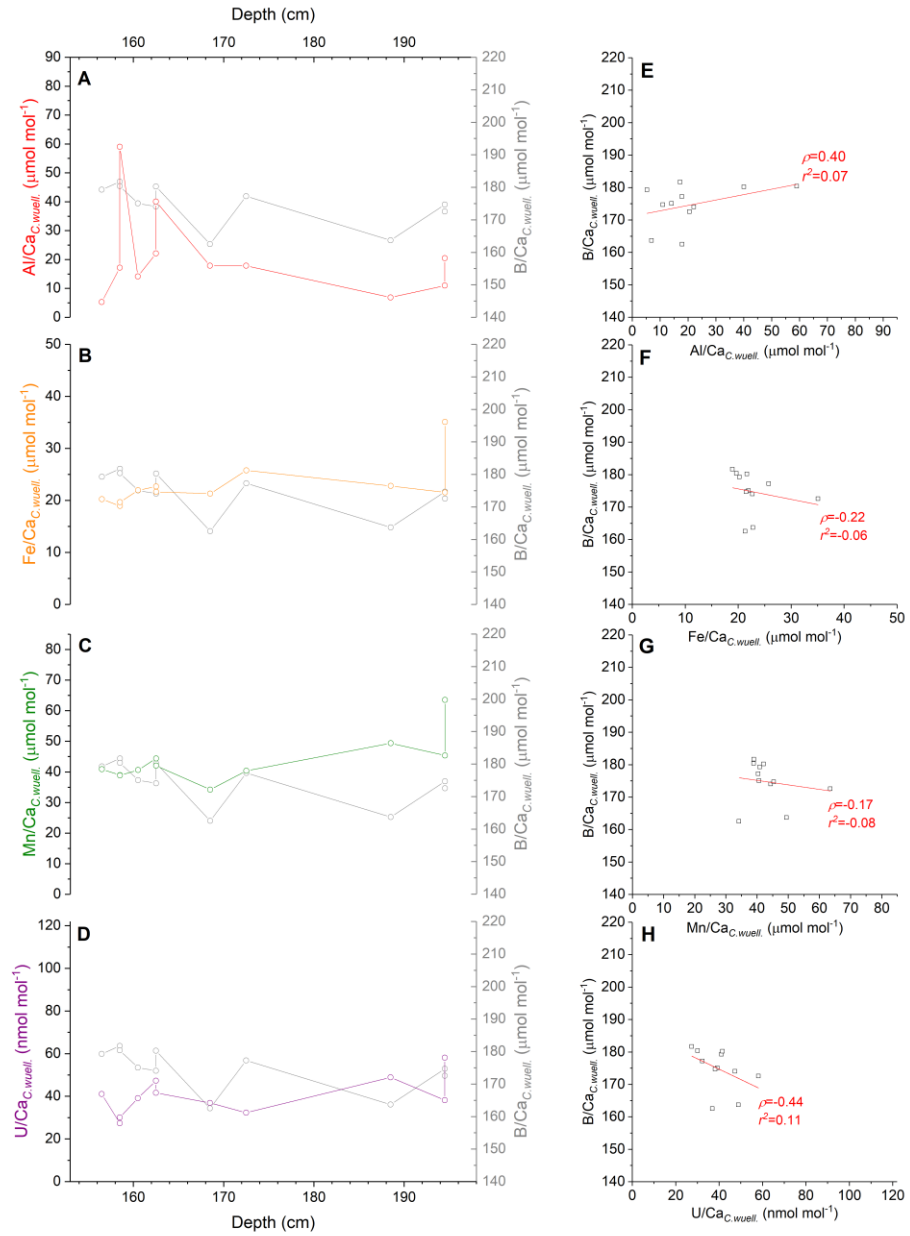
Appendix Figure 3.9. Detailed view of the MIS 1 section of appendix figure 3.8.



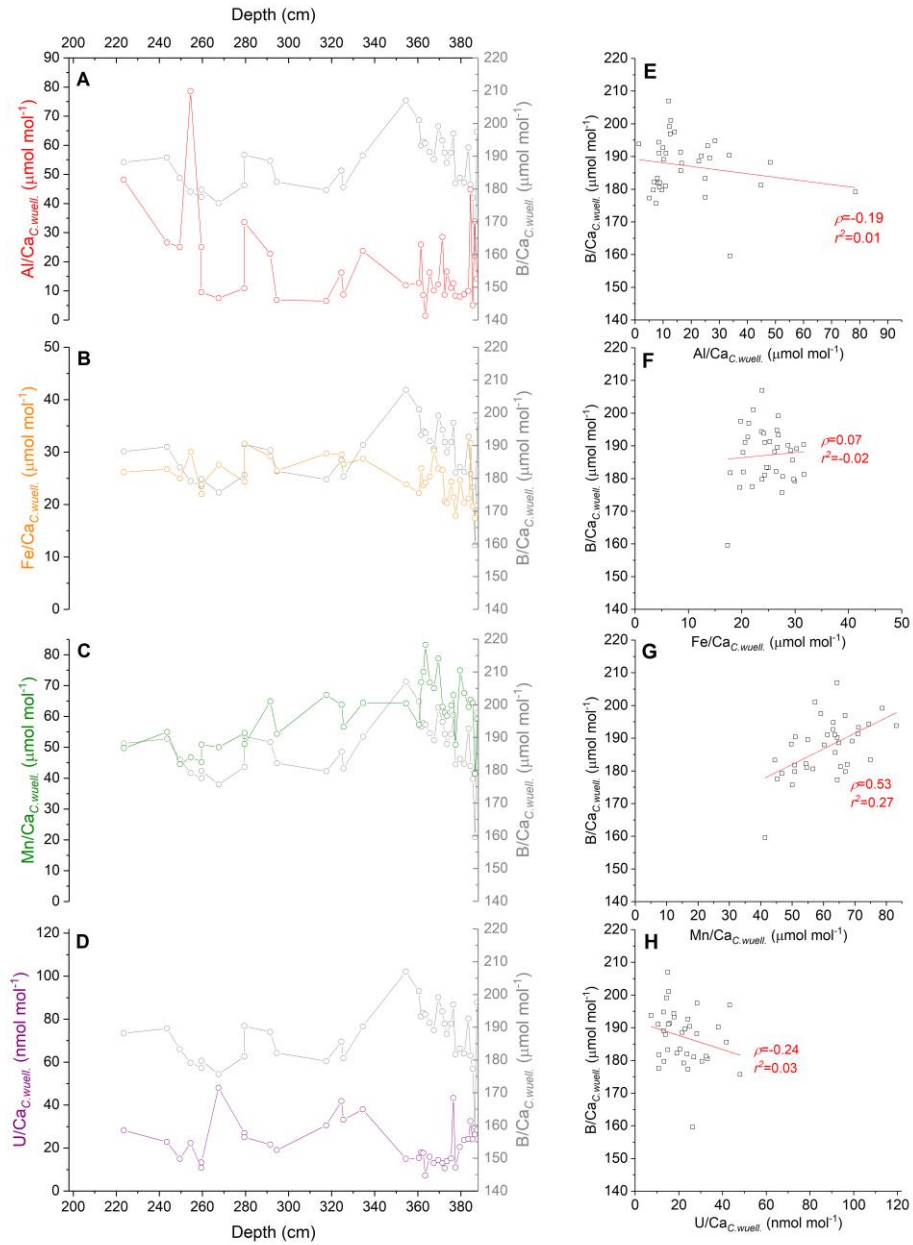
Appendix Figure 3.10. Detailed view of the MIS 2 section of appendix figure 3.8.



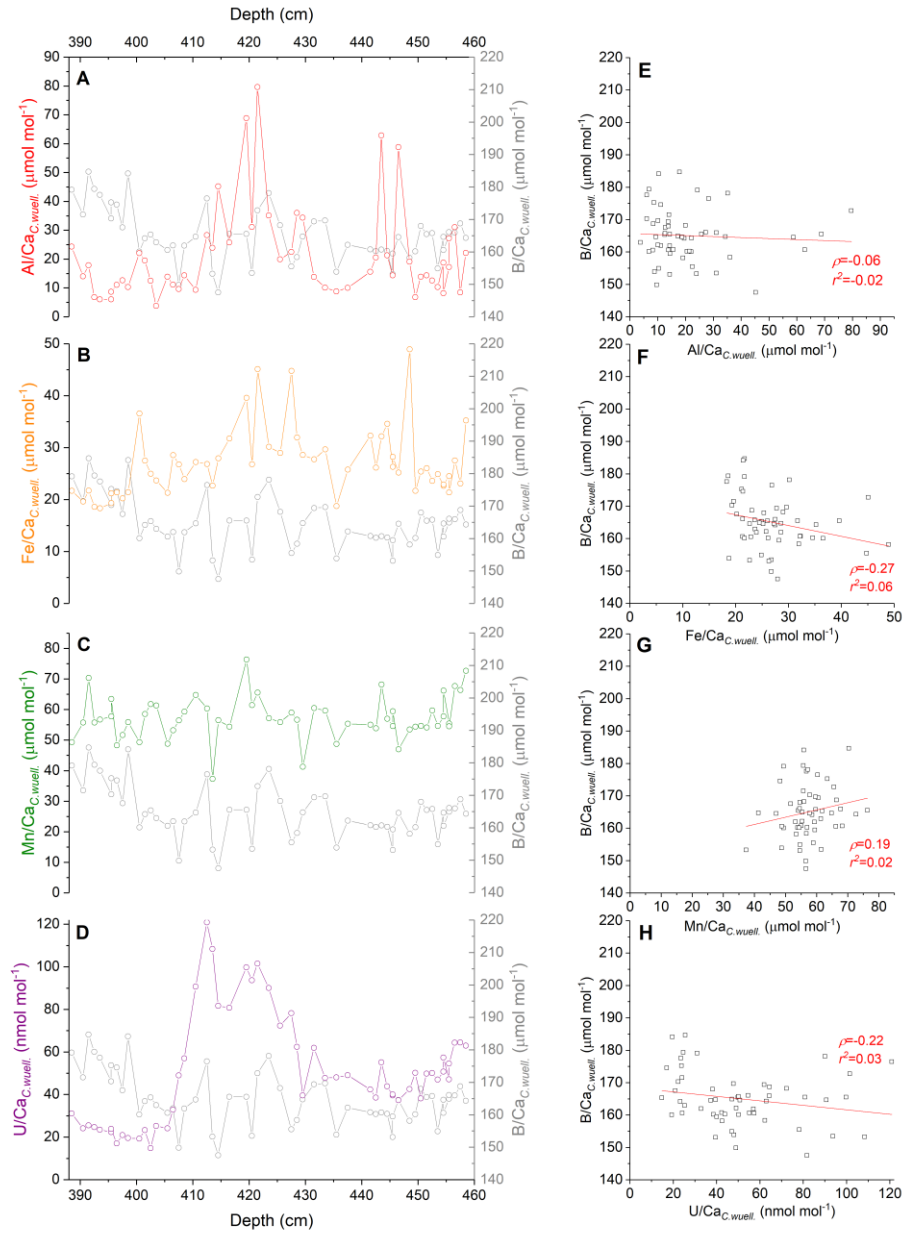
Appendix Figure 3.11. Detailed view of the MIS 3 section of appendix figure 3.8.



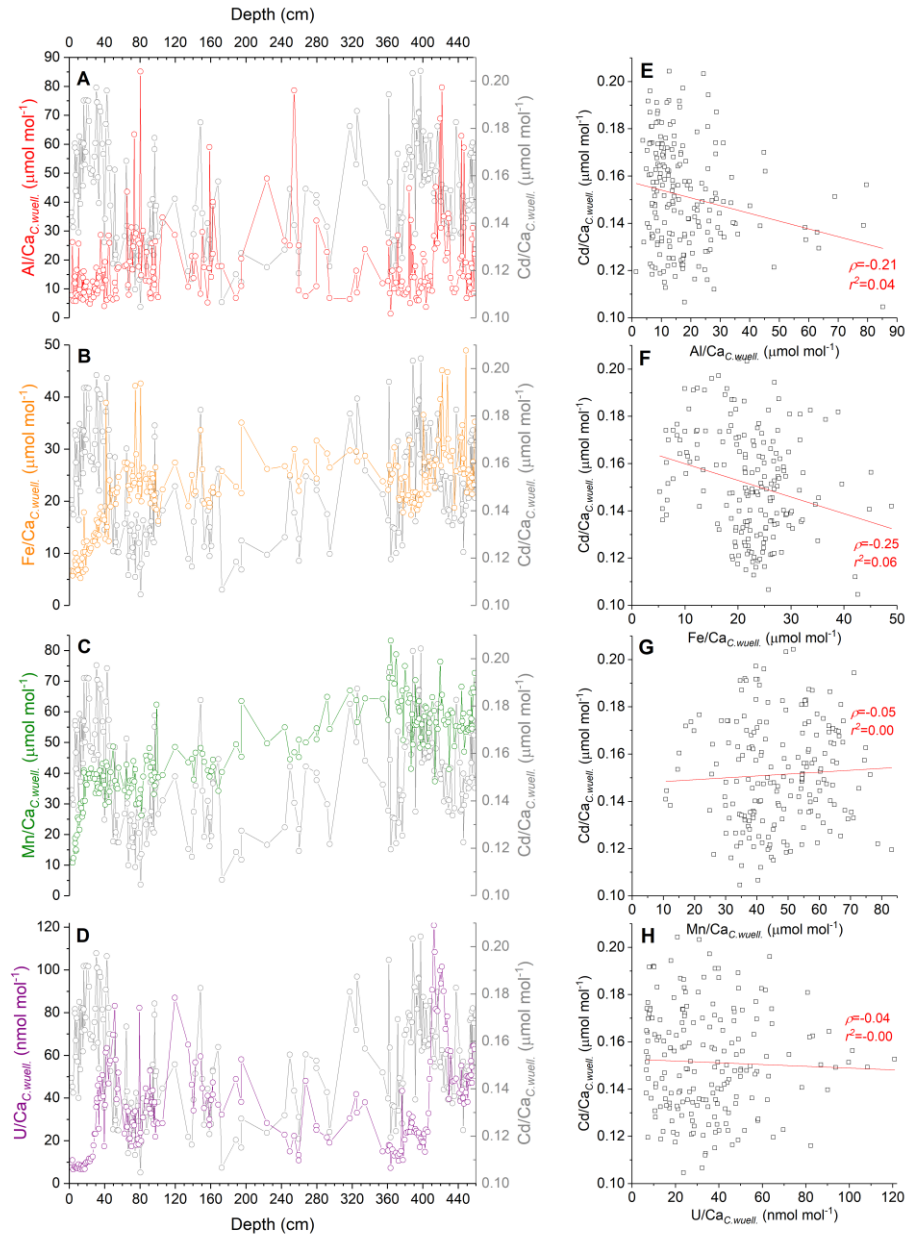
Appendix Figure 3.12. Detailed view of the MIS 4 section of appendix figure 3.8.



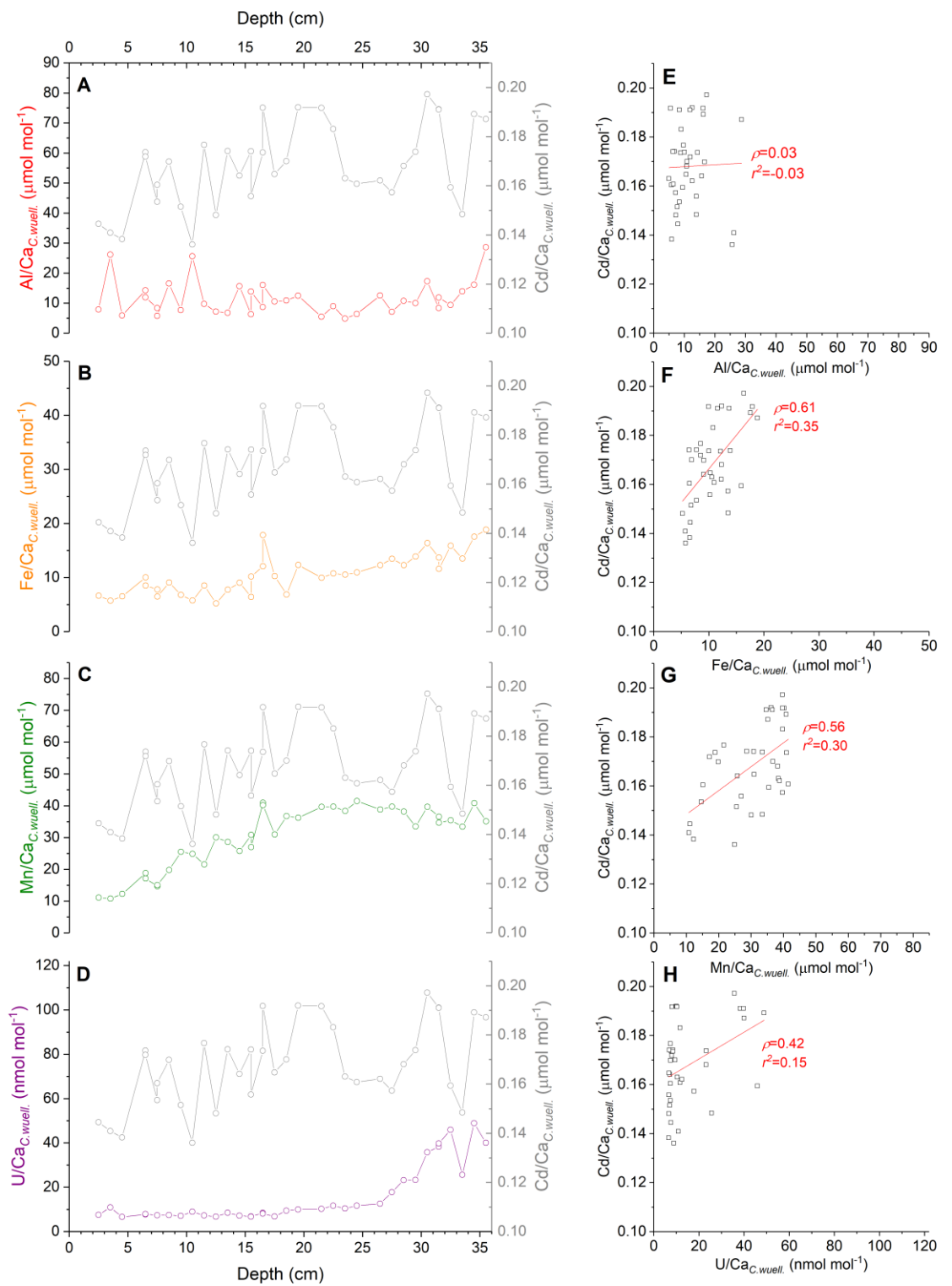
Appendix Figure 3.13. Detailed view of the MIS 5 section of appendix figure 3.8.



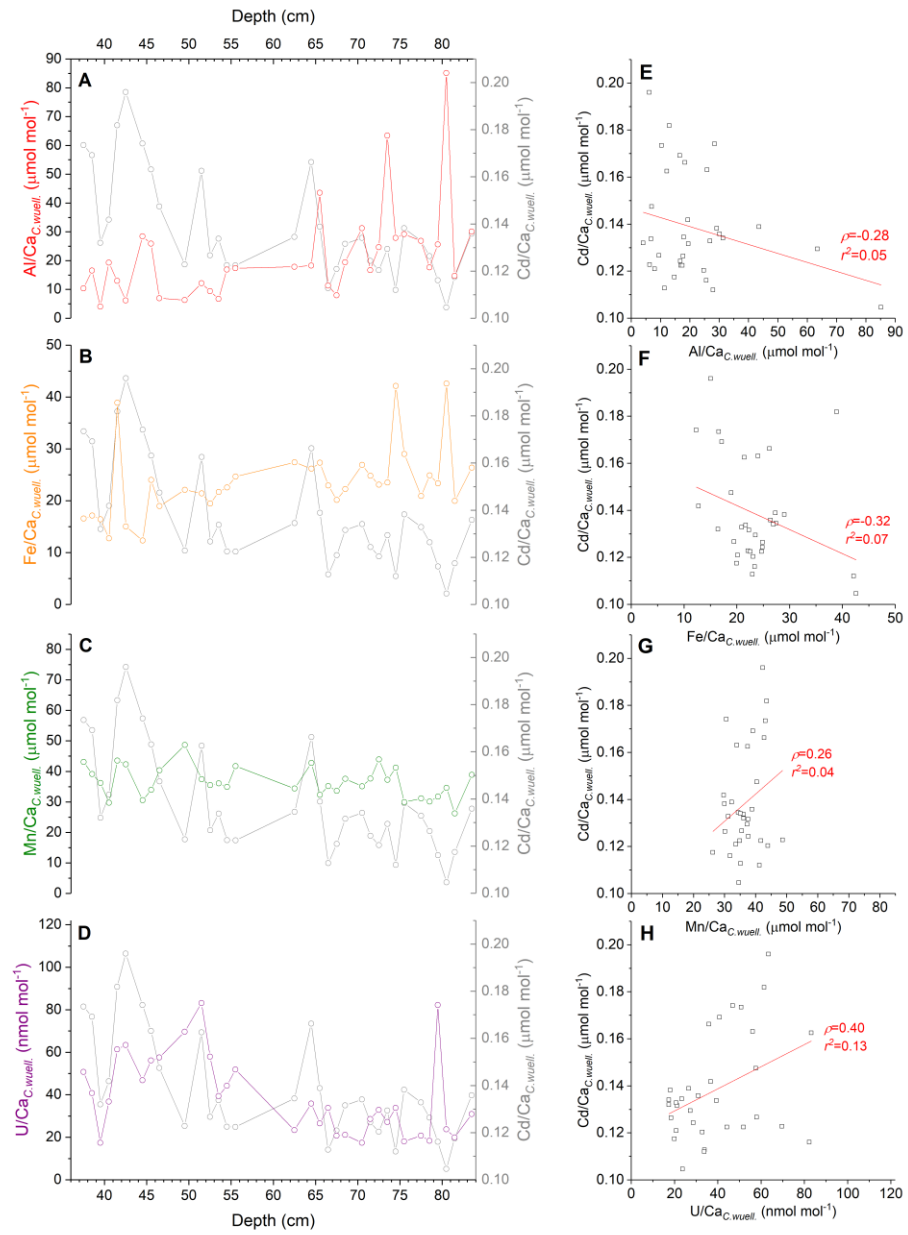
Appendix Figure 3.14. Detailed view of the MIS 6 section of appendix figure 3.8.



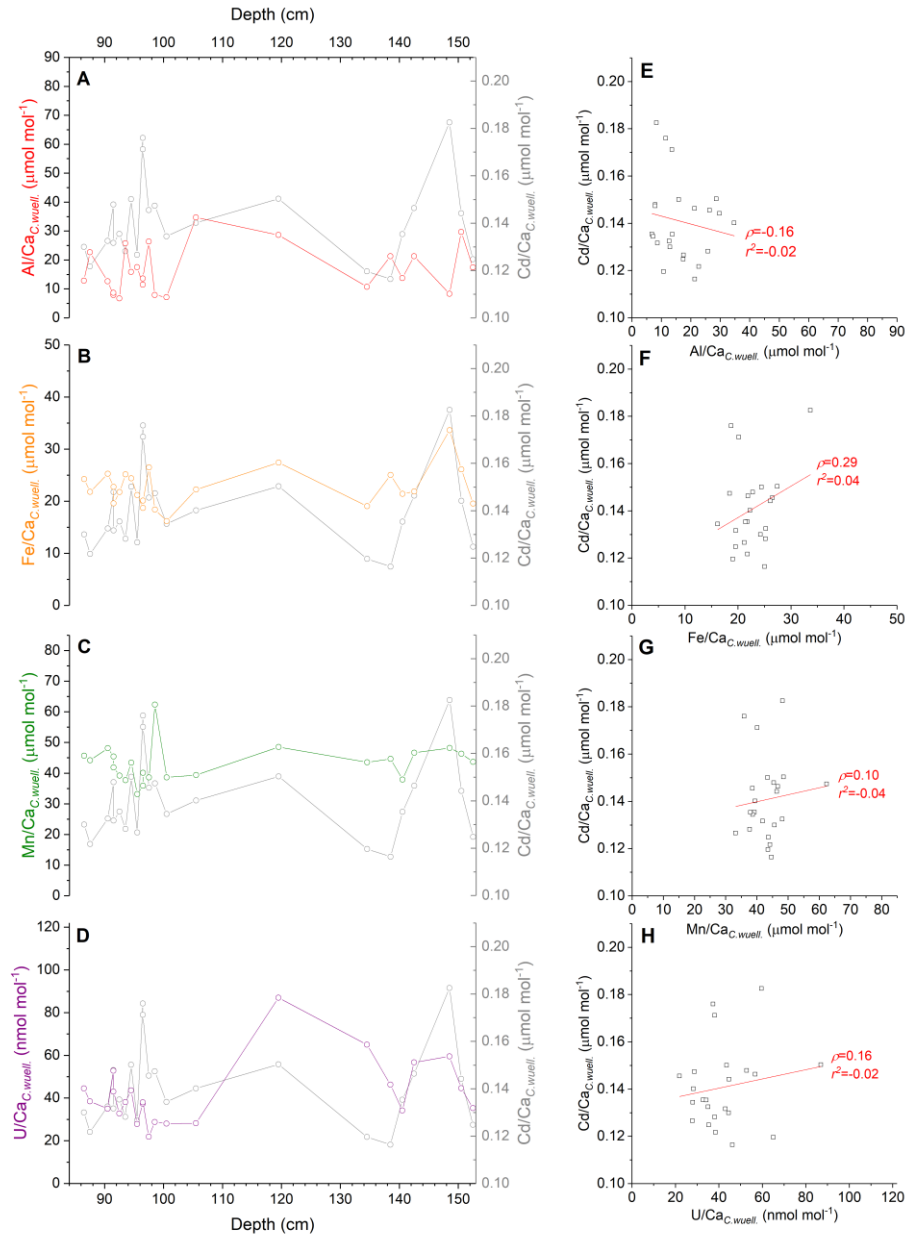
**Appendix Figure 3.15.** Comparison of *C. wuellerstorfi* Cd/Ca record (grey line, open grey circles) from MD02-2588 with corresponding (A) Al/Ca (red line, open red circles), (B) Fe/Ca (orange line, open orange circles), (C) Mn/Ca (green line, open green circles) and (D) U/Ca (purple line, open purple circles). Corresponding cross plots of Cd/Ca versus (E) Al/Ca, (F) Fe/Ca, (G) Mn/Ca and (H) U/Ca in *C. wuellerstorfi* samples. Also shown are the lines of best fit through the datasets and the corresponding Pearson's  $r$  value ( $\rho$ ) and the coefficient of determination ( $R^2$ ) of each linear equation (not shown). Elemental ratio data with values above the suggested contamination thresholds have been removed.



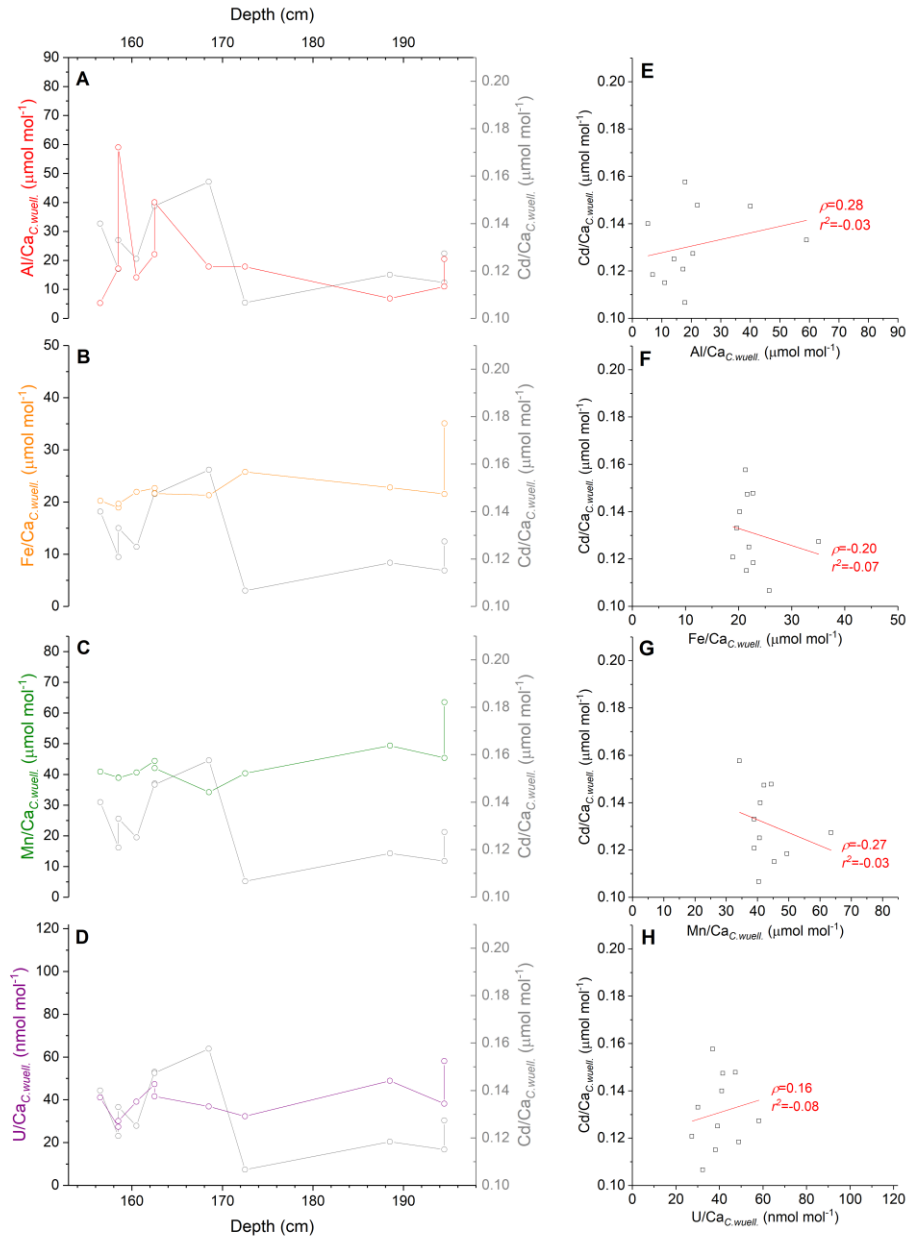
Appendix Figure 3.16. Detailed view of the MIS 1 section of appendix figure 3.15.



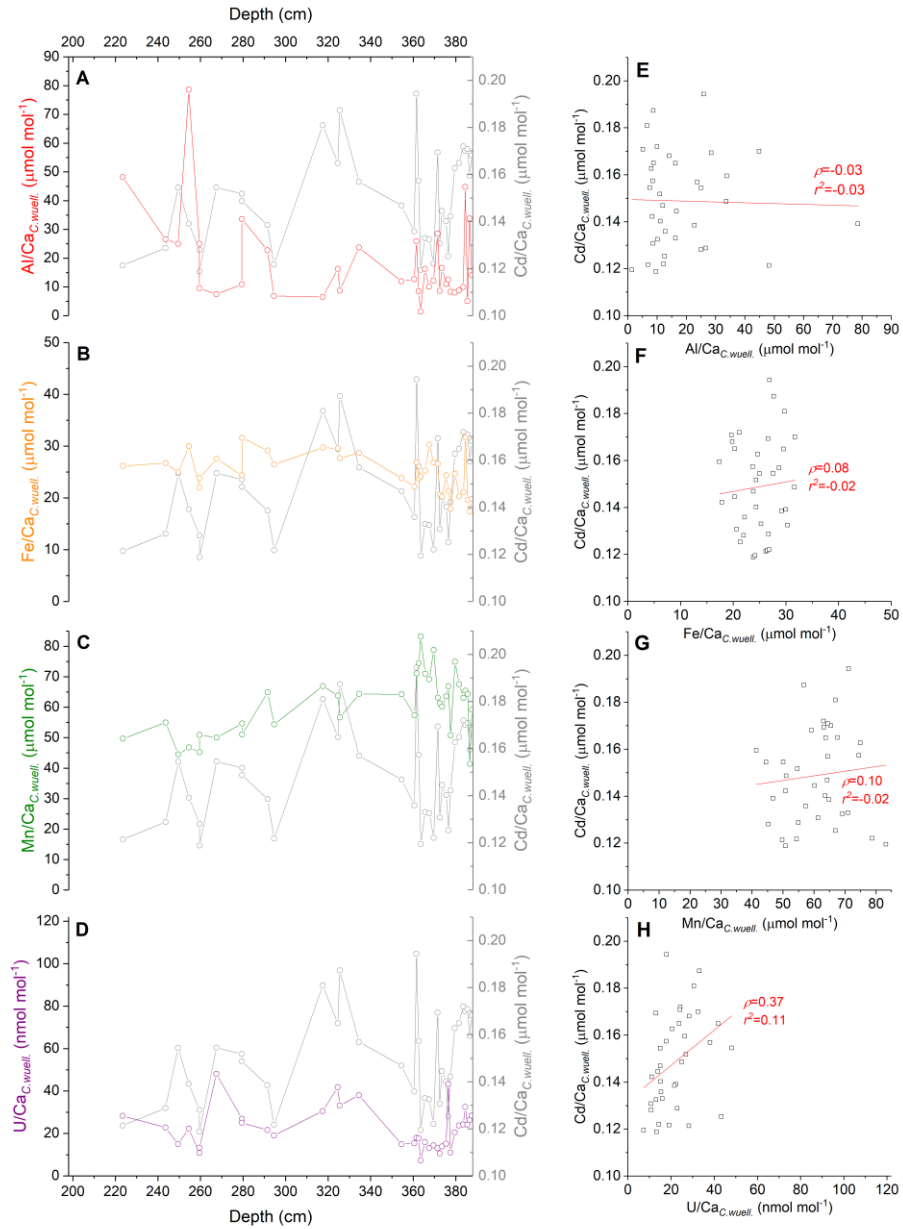
Appendix Figure 3.17. Detailed view of the MIS 2 section of appendix figure 3.15.



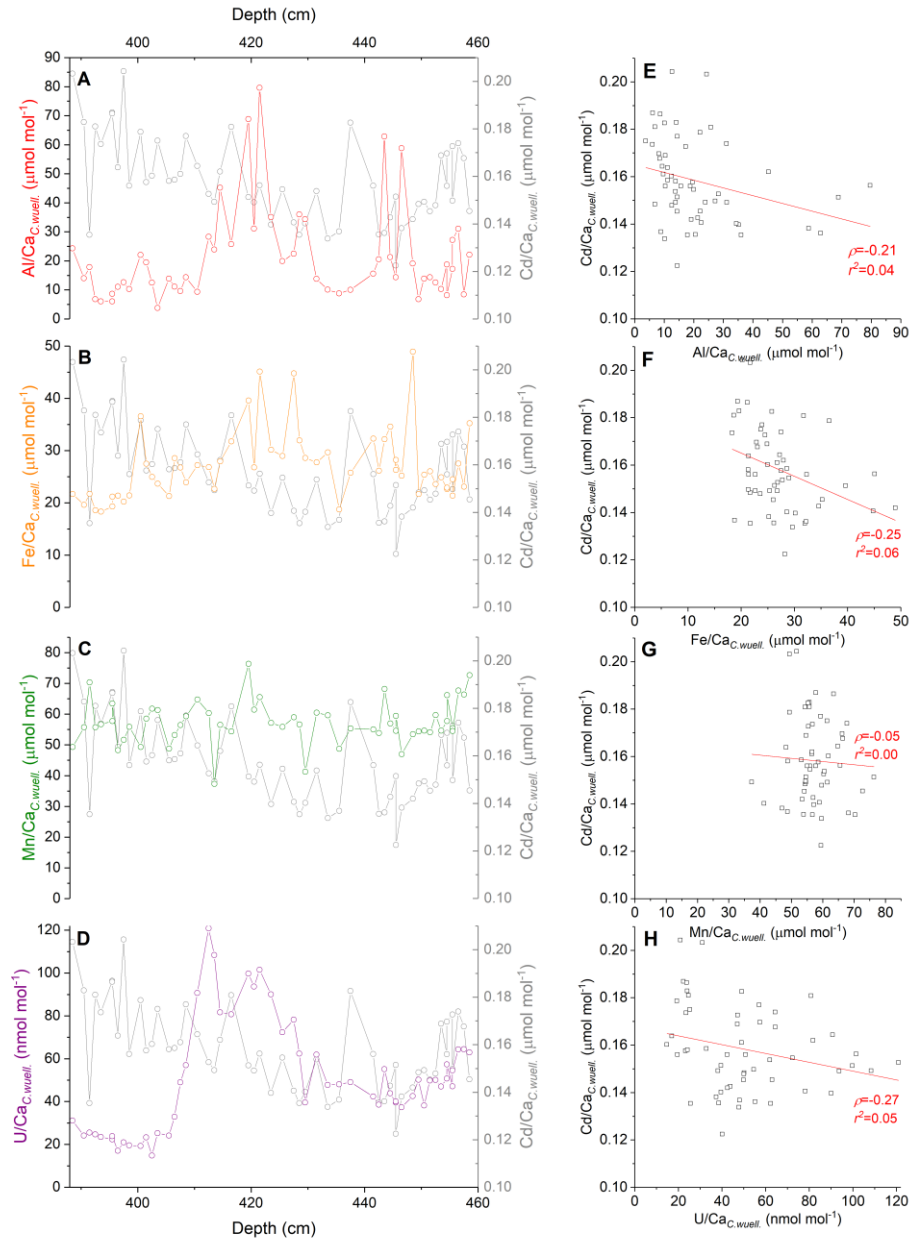
Appendix Figure 3.18. Detailed view of the MIS 3 section of appendix figure 3.15.



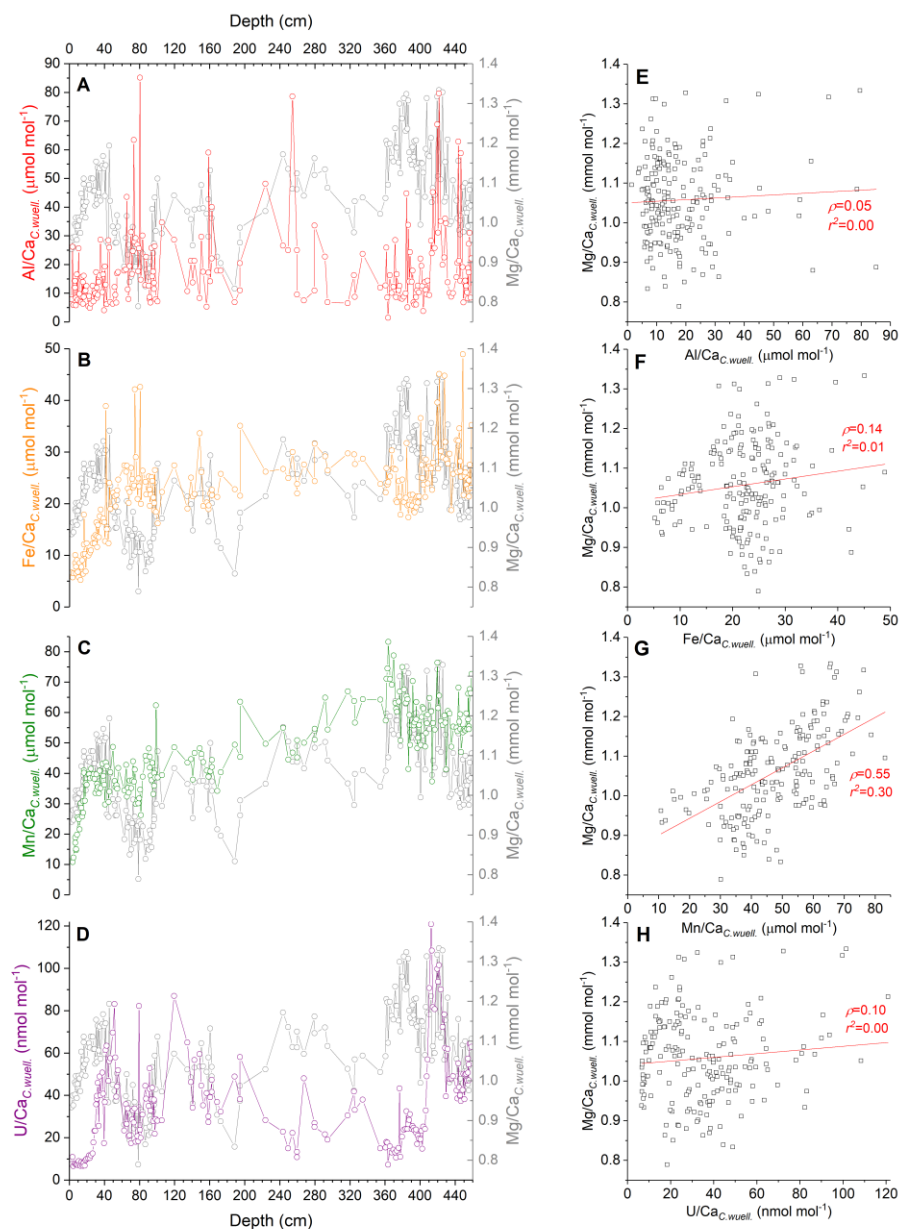
Appendix Figure 3.19. Detailed view of the MIS 4 section of appendix figure 3.15.



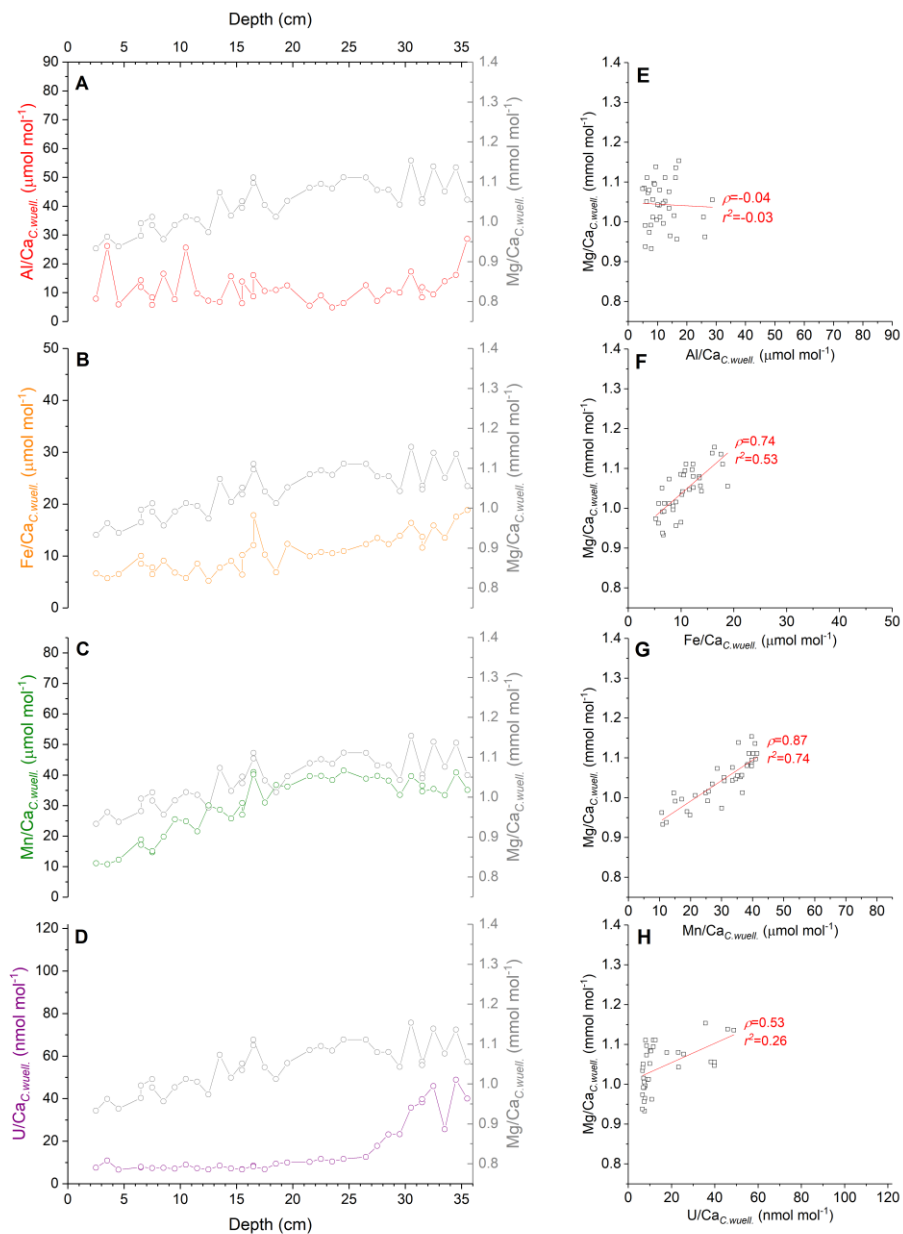
Appendix Figure 3.20. Detailed view of the MIS 5 section of appendix figure 3.15.



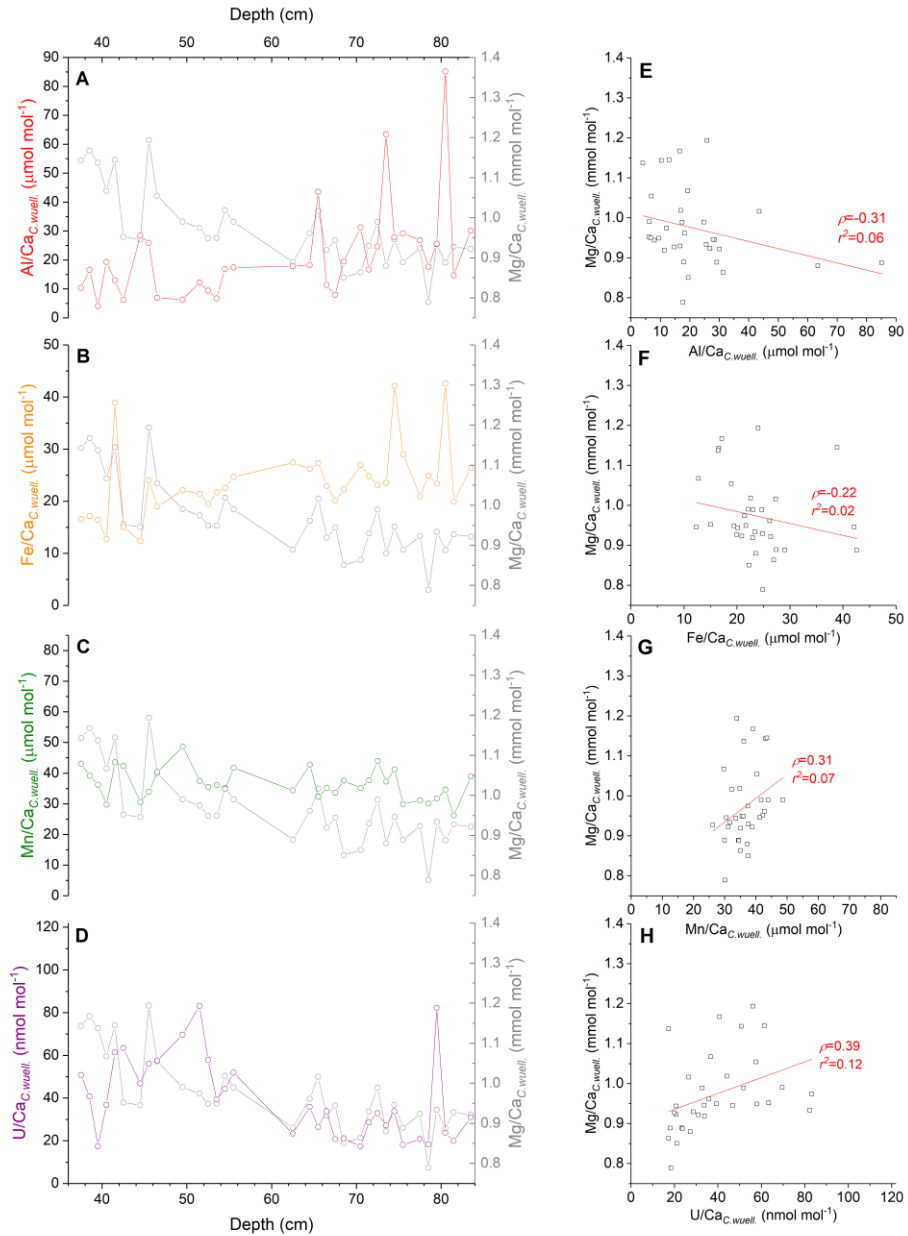
Appendix Figure 3.21. Detailed view of the MIS 6 section of appendix figure 3.15.



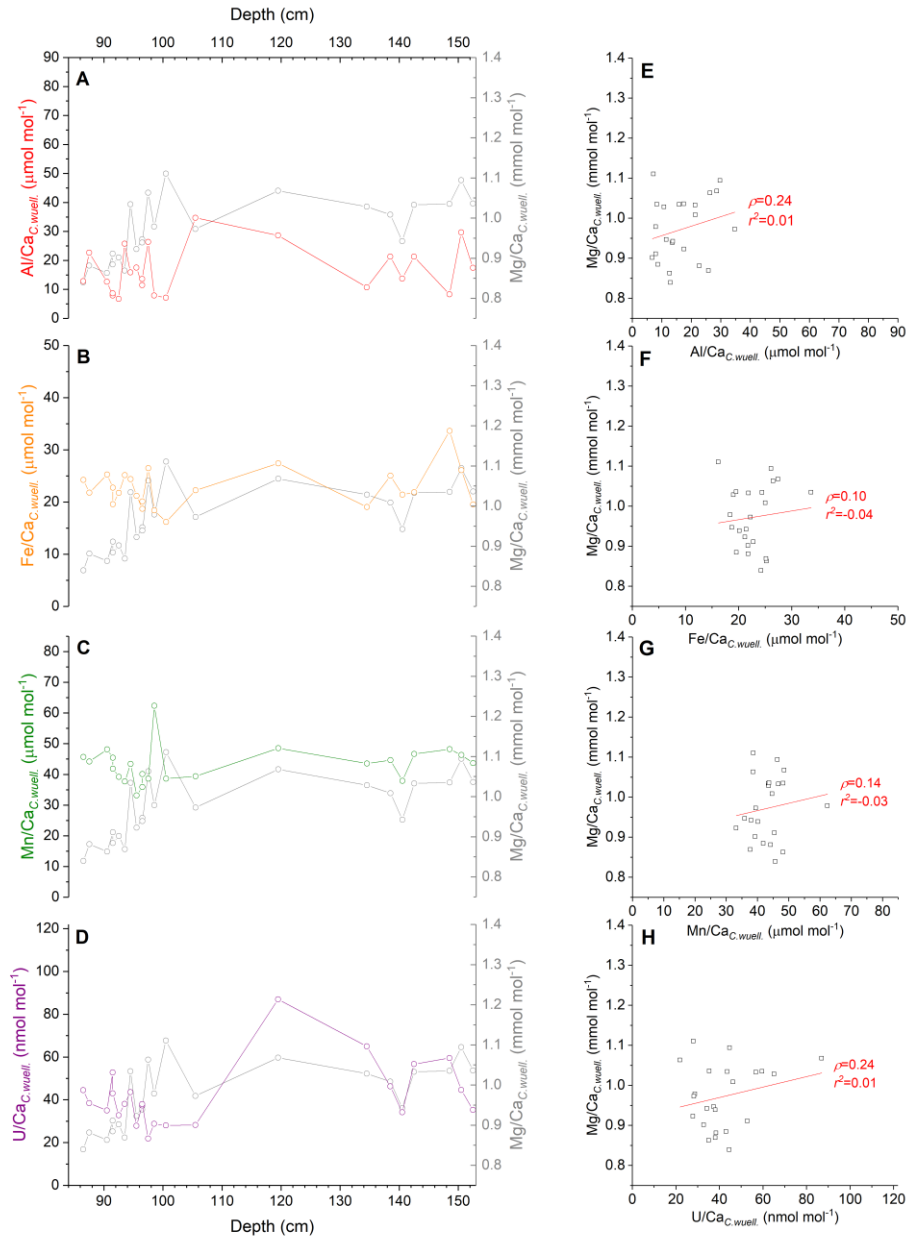
**Appendix Figure 3.22.** Comparison of *C. wuellerstorfi* Mg/Ca record (grey line, open grey circles) from MD02-2588 with corresponding (A) Al/Ca (red line, open red circles), (B) Fe/Ca (orange line, open orange circles), (C) Mn/Ca (green line, open green circles) and (D) U/Ca (purple line, open purple circles). Corresponding cross plots of Mg/Ca versus (E) Al/Ca, (F) Fe/Ca, (G) Mn/Ca and (H) U/Ca in *C. wuellerstorfi* samples. Also shown are the lines of best fit through the datasets and the corresponding Pearson's r value ( $\rho$ ) and the coefficient of determination ( $R^2$ ) of each linear equation (not shown). Elemental ratio data with values above the suggested contamination thresholds have been removed.



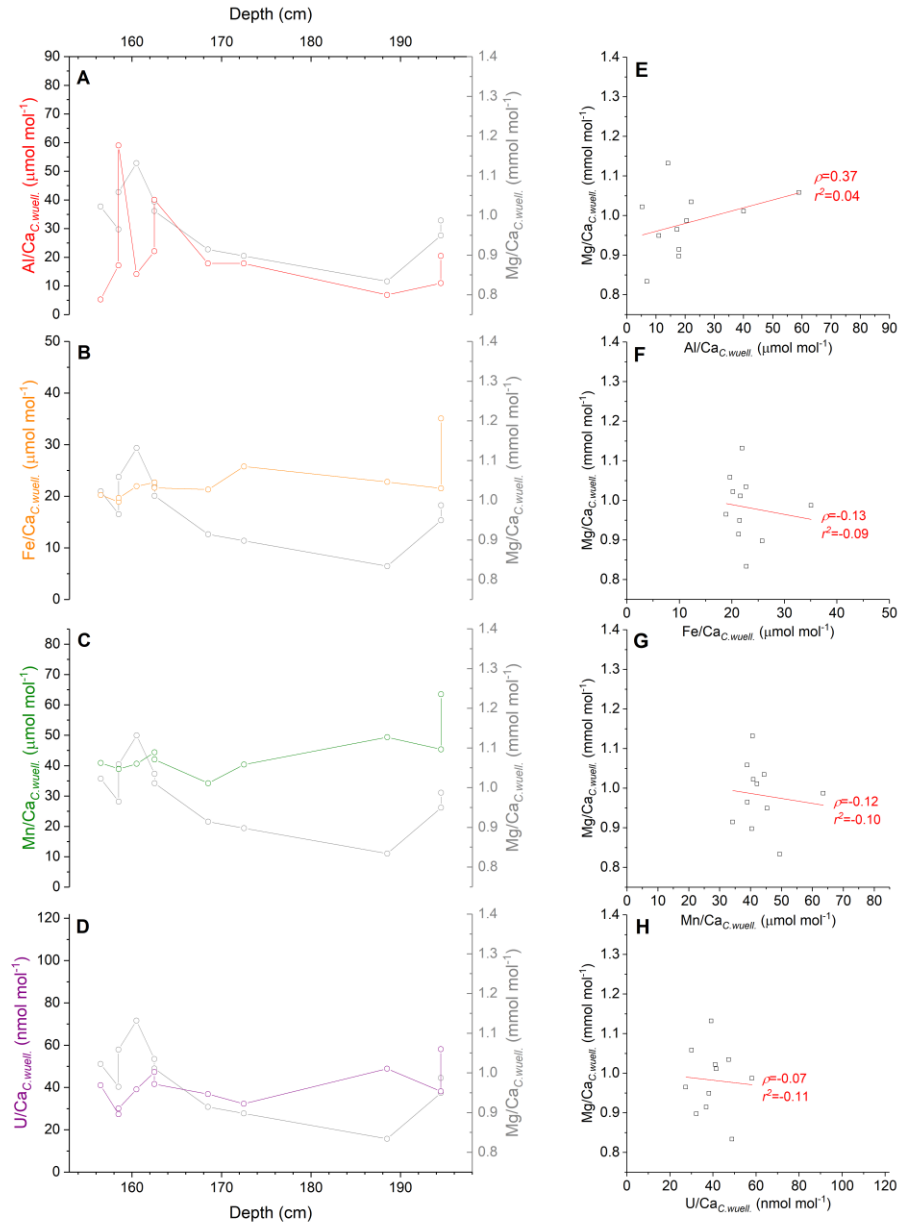
**Appendix Figure 3.23.** Detailed view of the MIS 1 section of appendix figure 3.22.



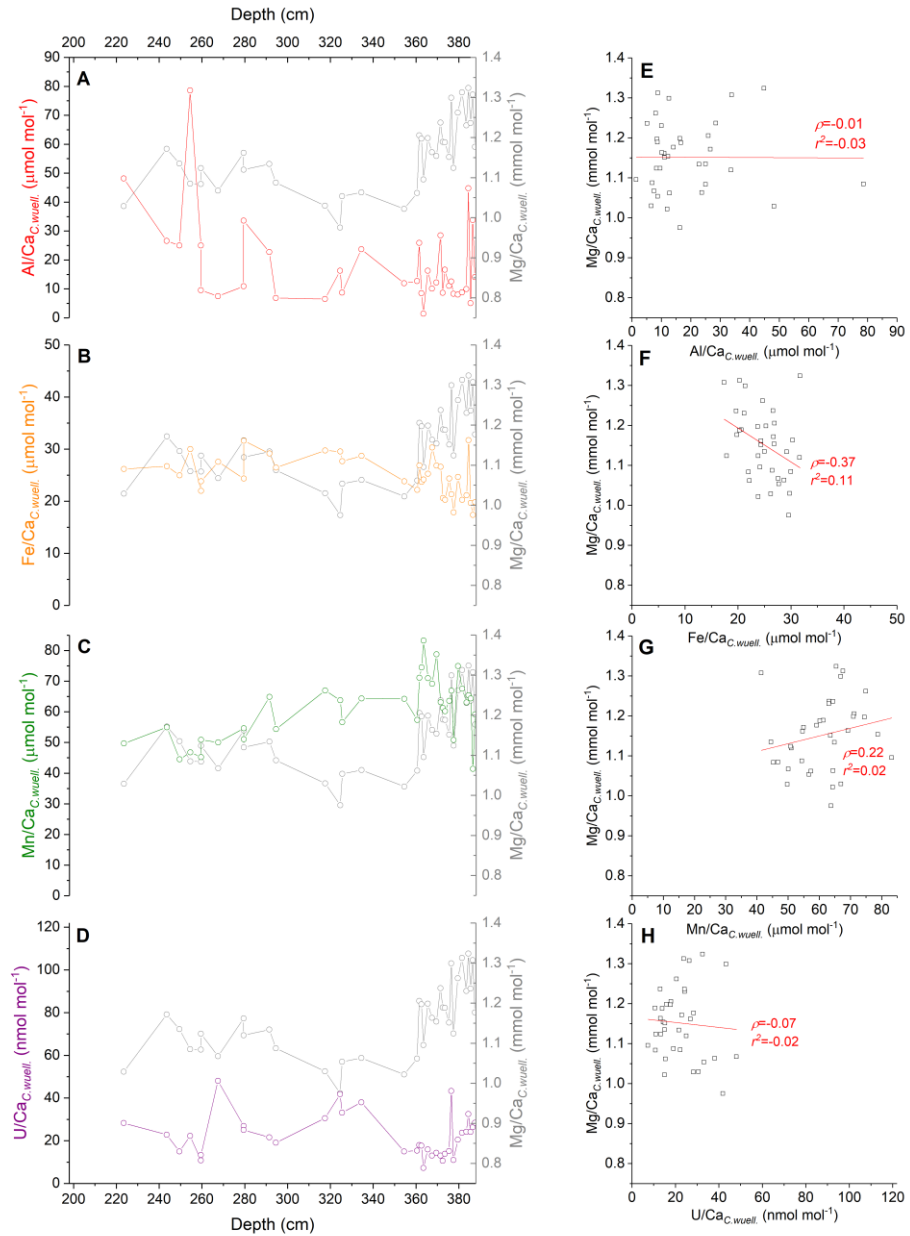
Appendix Figure 3.24. Detailed view of the MIS 2 section of appendix figure 3.22.



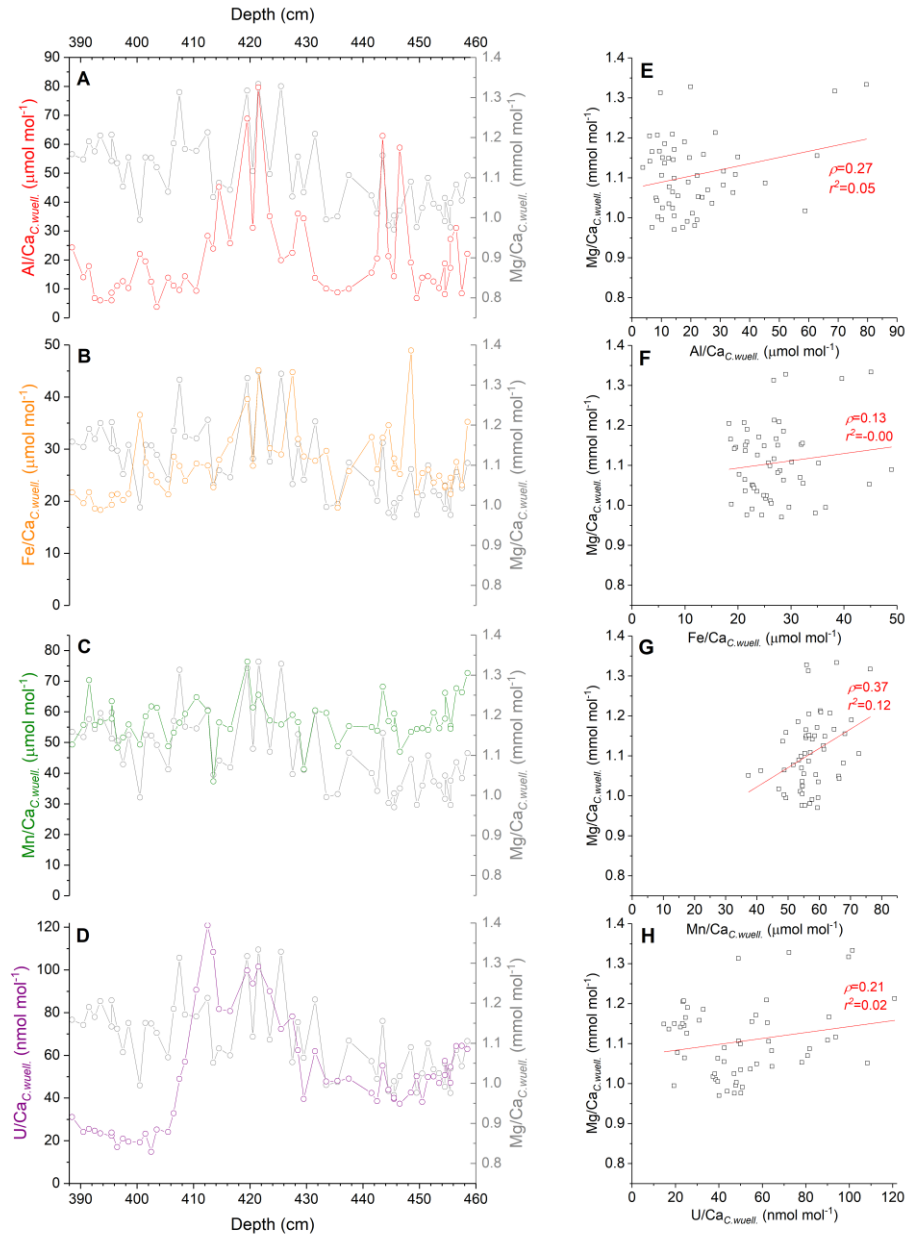
**Appendix Figure 3.25.** Detailed view of the MIS 3 section of appendix figure 3.22.



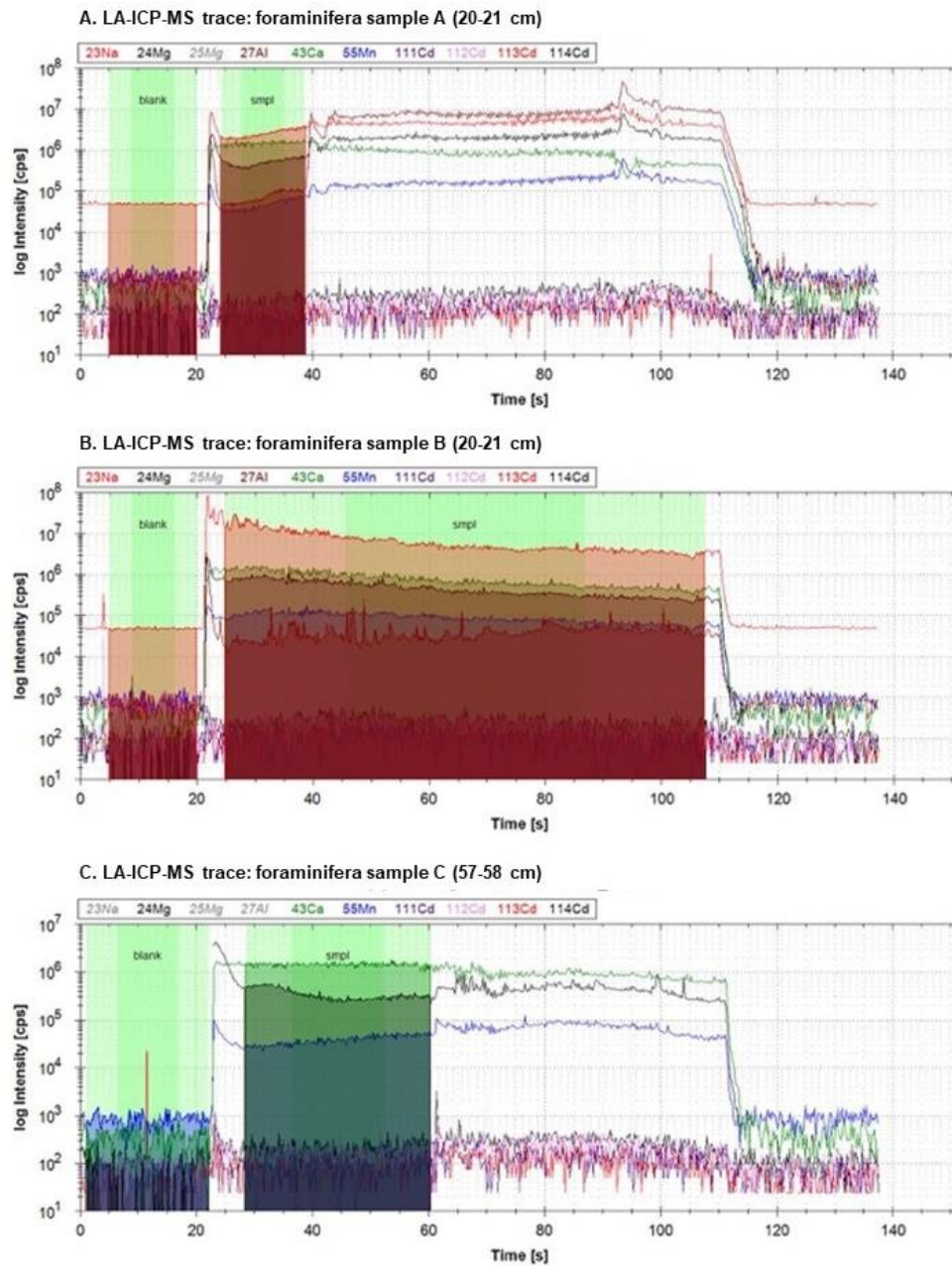
**Appendix Figure 3.26.** Detailed view of the MIS 4 section of appendix figure 3.22.



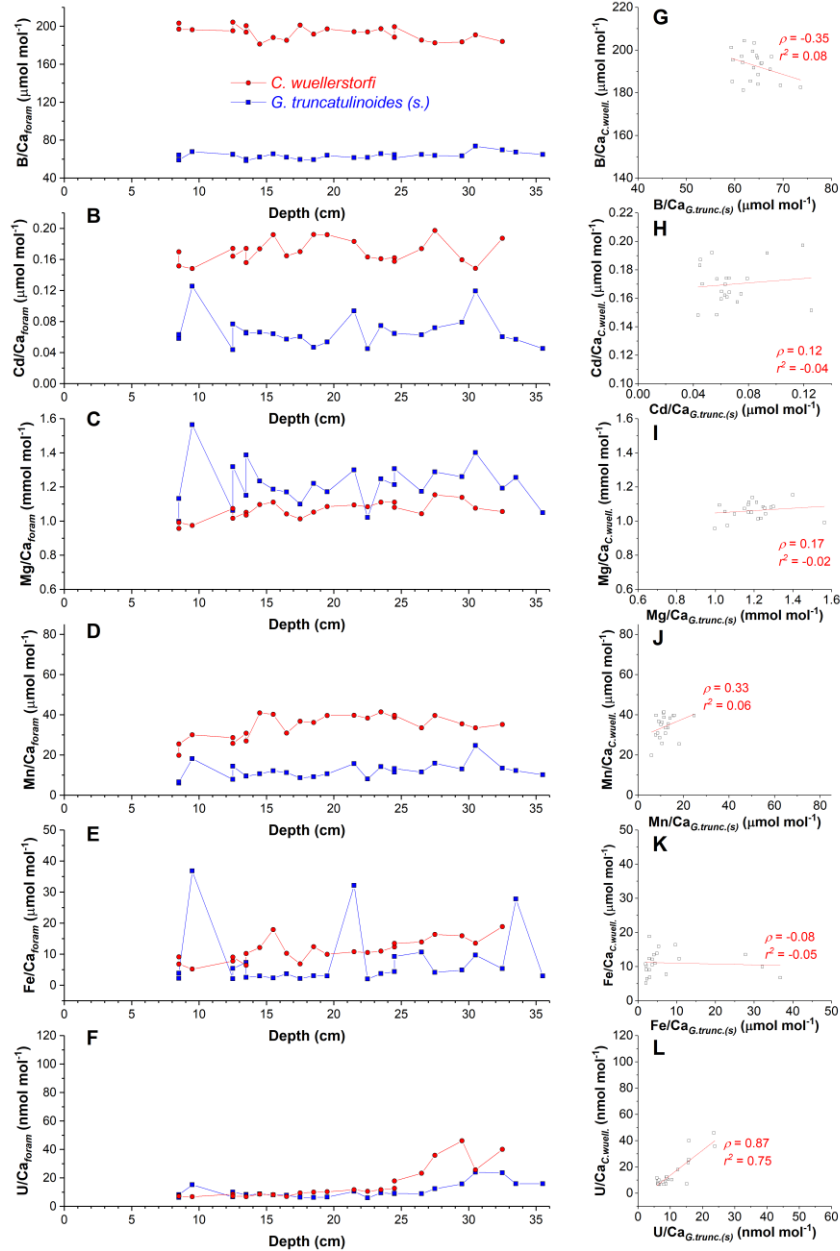
Appendix Figure 3.27. Detailed view of the MIS 5 section of appendix figure 3.22.



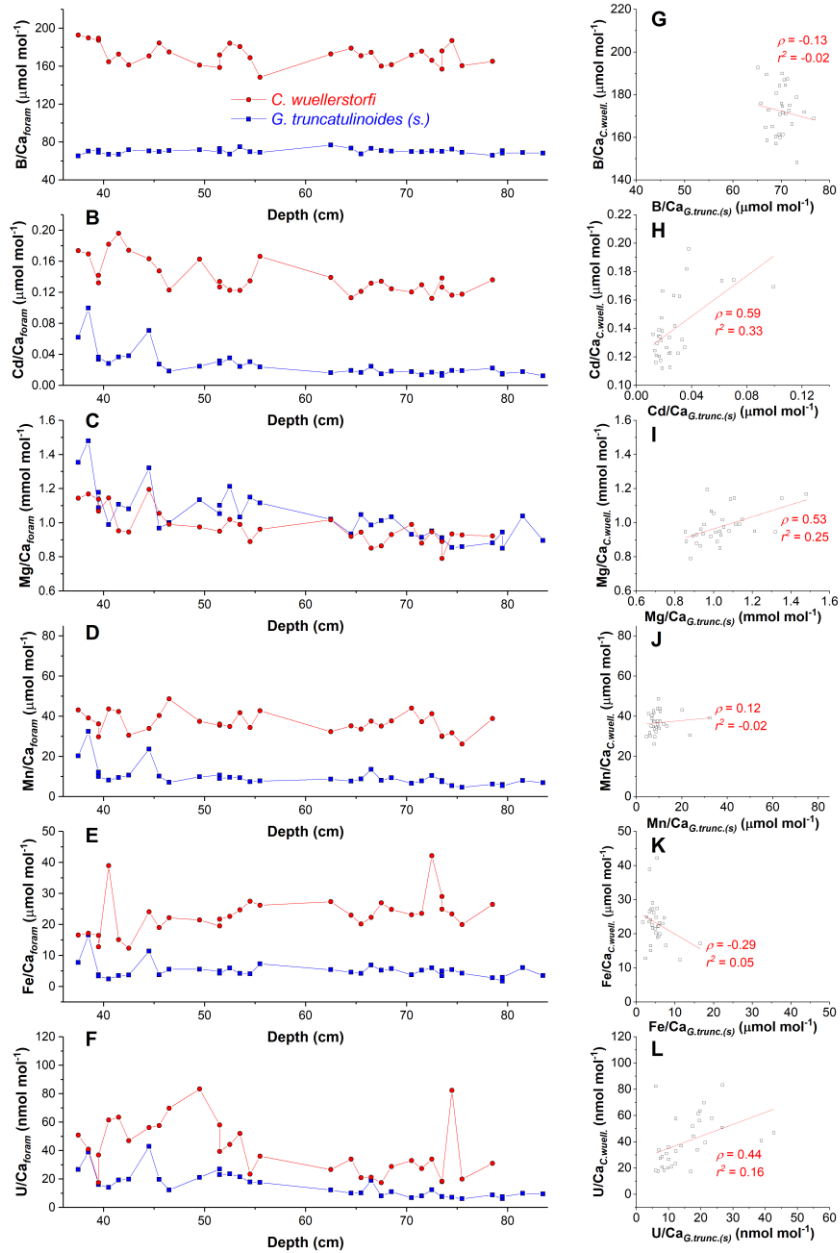
Appendix Figure 3.28. Detailed view of the MIS 6 section of appendix figure 3.22.



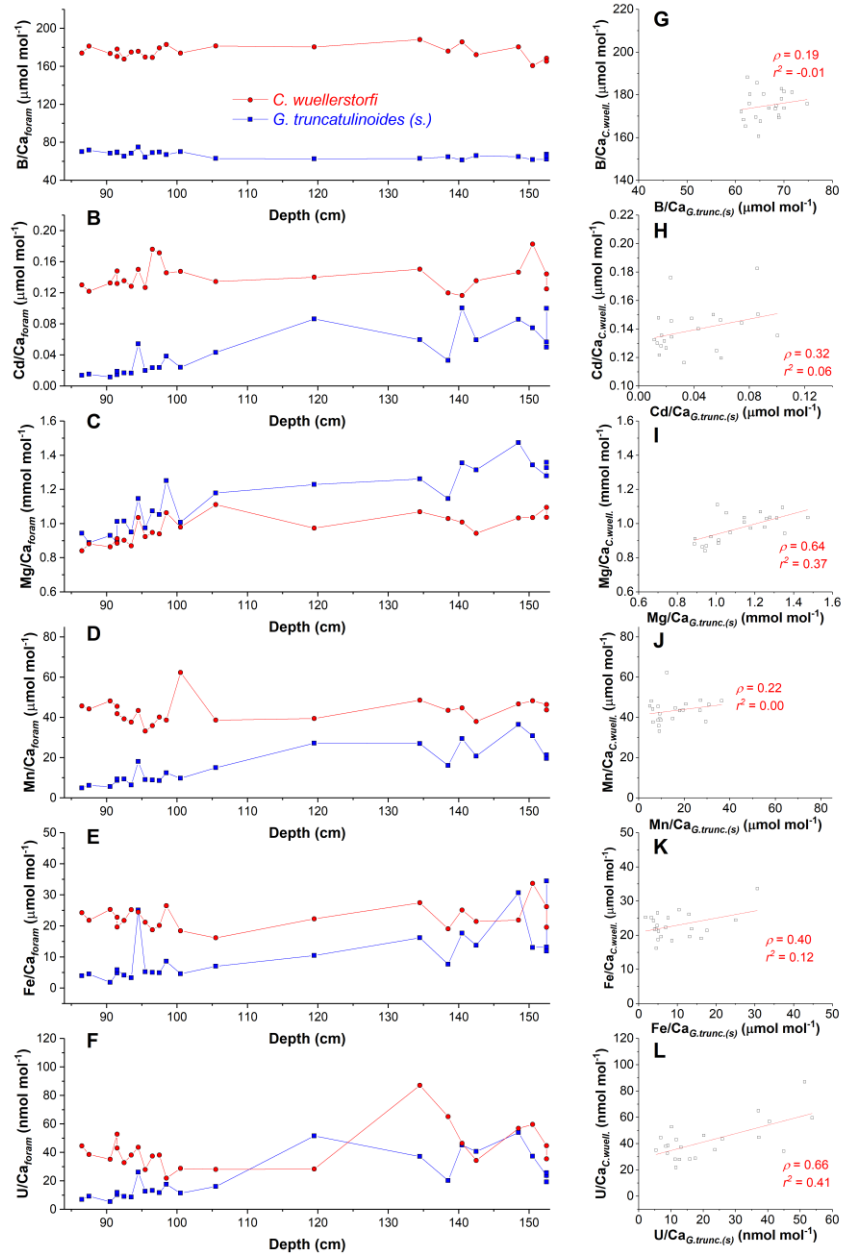
**Appendix Figure 3.29.** Laser Ablation ICP-MS traces through individual foraminifera tests in three samples from sediment core MD02-2588. Green shaded regions are the integration windows from which the final values are estimated.



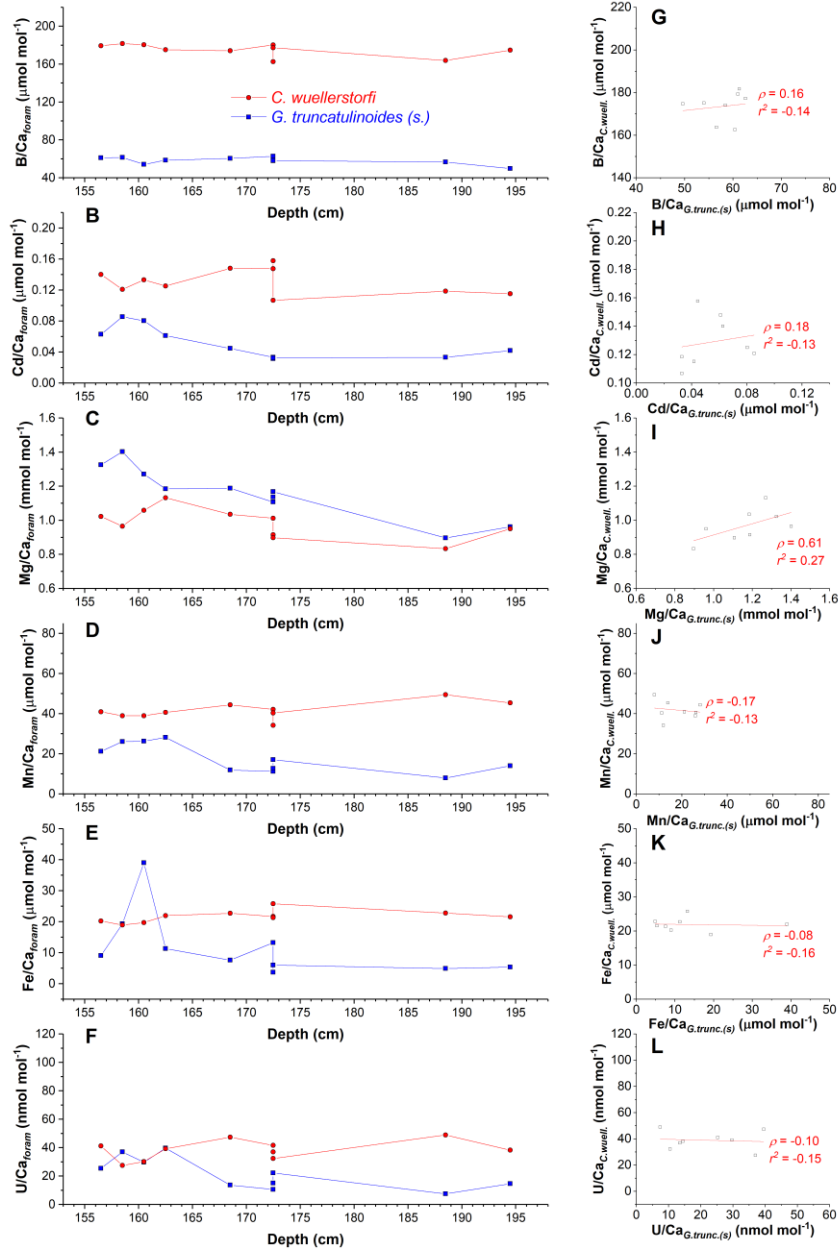
Appendix Figure 3.30. Detailed view of the MIS 1 section of figure 3.16 in Chapter 3.



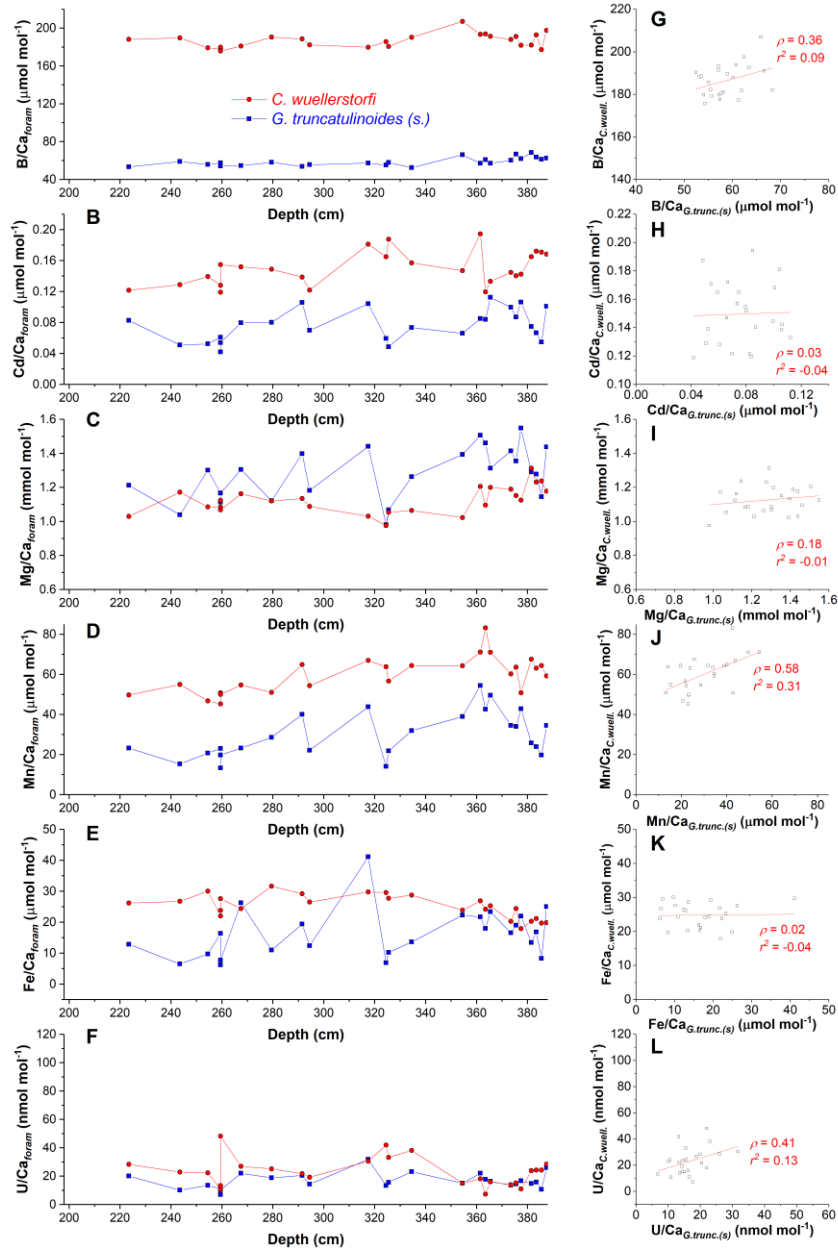
Appendix Figure 3.31. Detailed view of the MIS 2 section of figure 3.16 in Chapter 3.



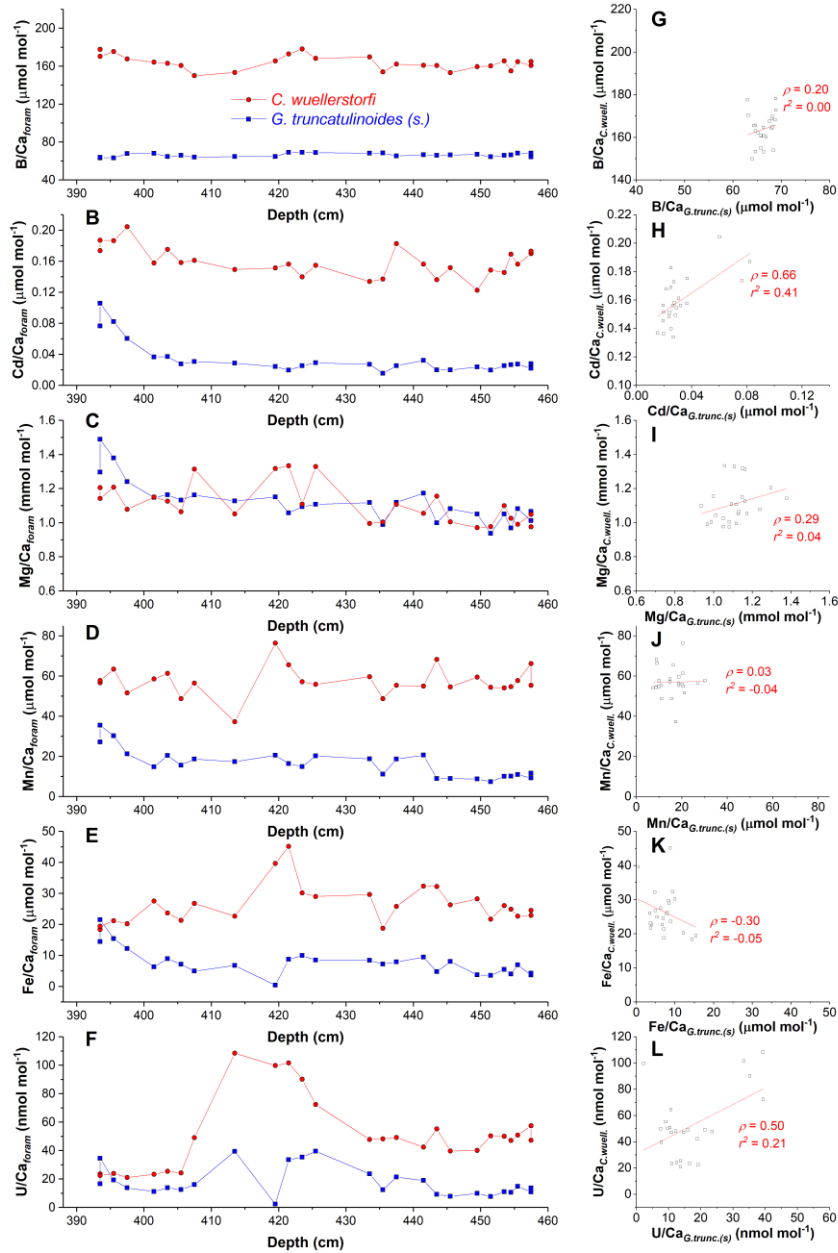
Appendix Figure 3.32. Detailed view of the MIS 3 section of figure 3.16 in Chapter 3.



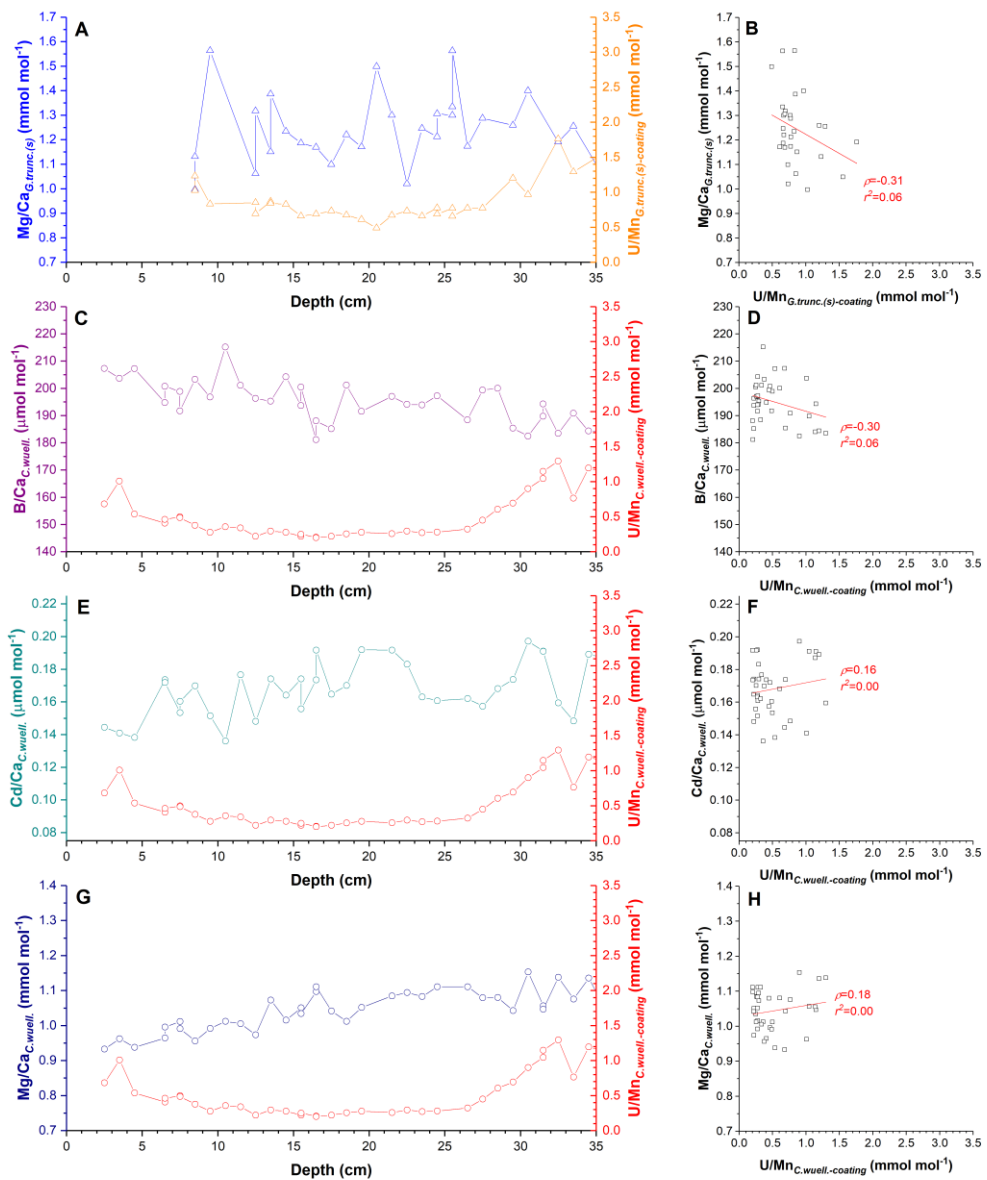
Appendix Figure 3.33. Detailed view of the MIS 4 section of figure 3.16 in Chapter 3.



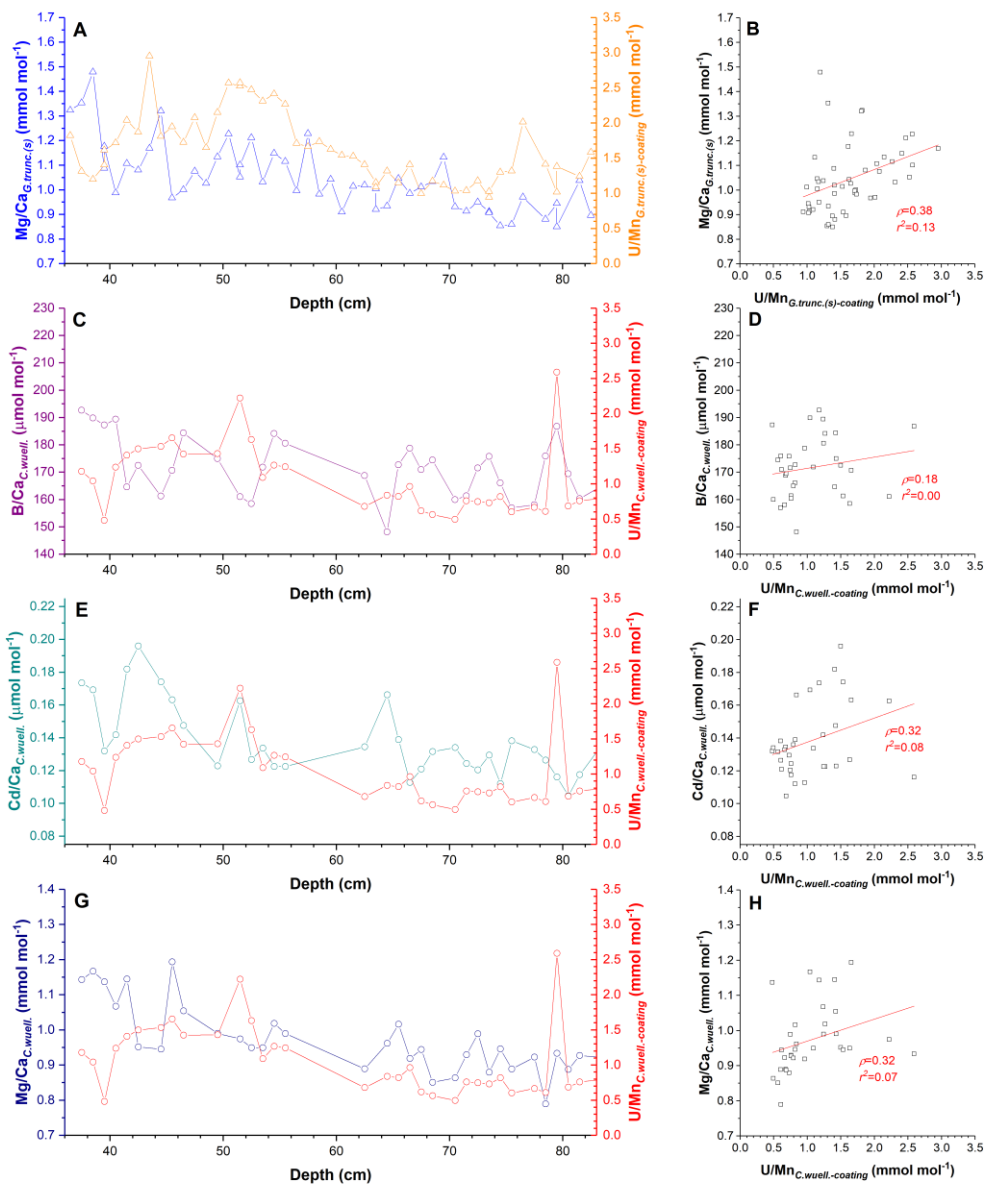
Appendix Figure 3.34. Detailed view of the MIS 5 section of figure 3.16 in Chapter 3.



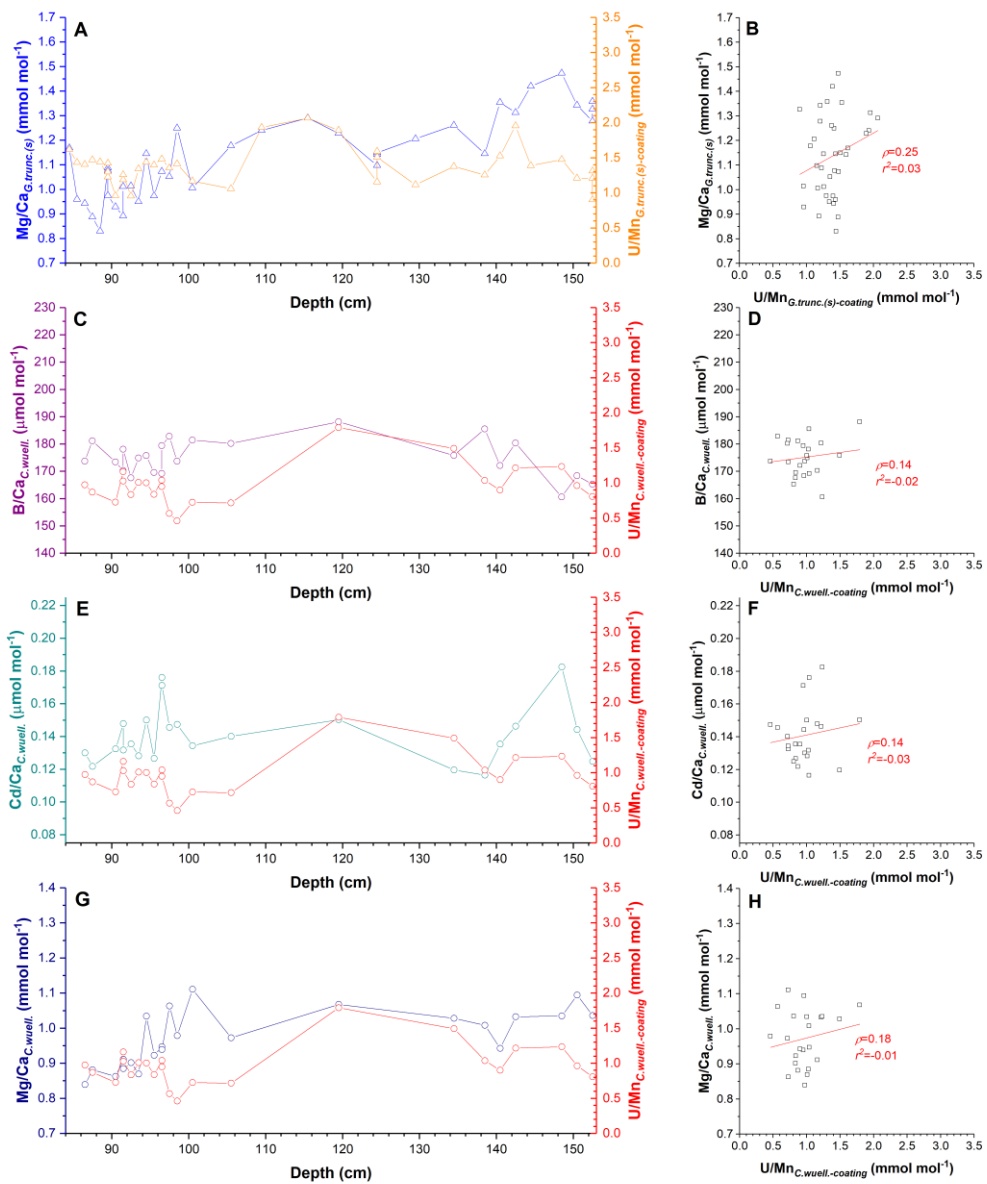
Appendix Figure 3.35. Detailed view of the MIS 6 section of figure 3.16 in Chapter 3.



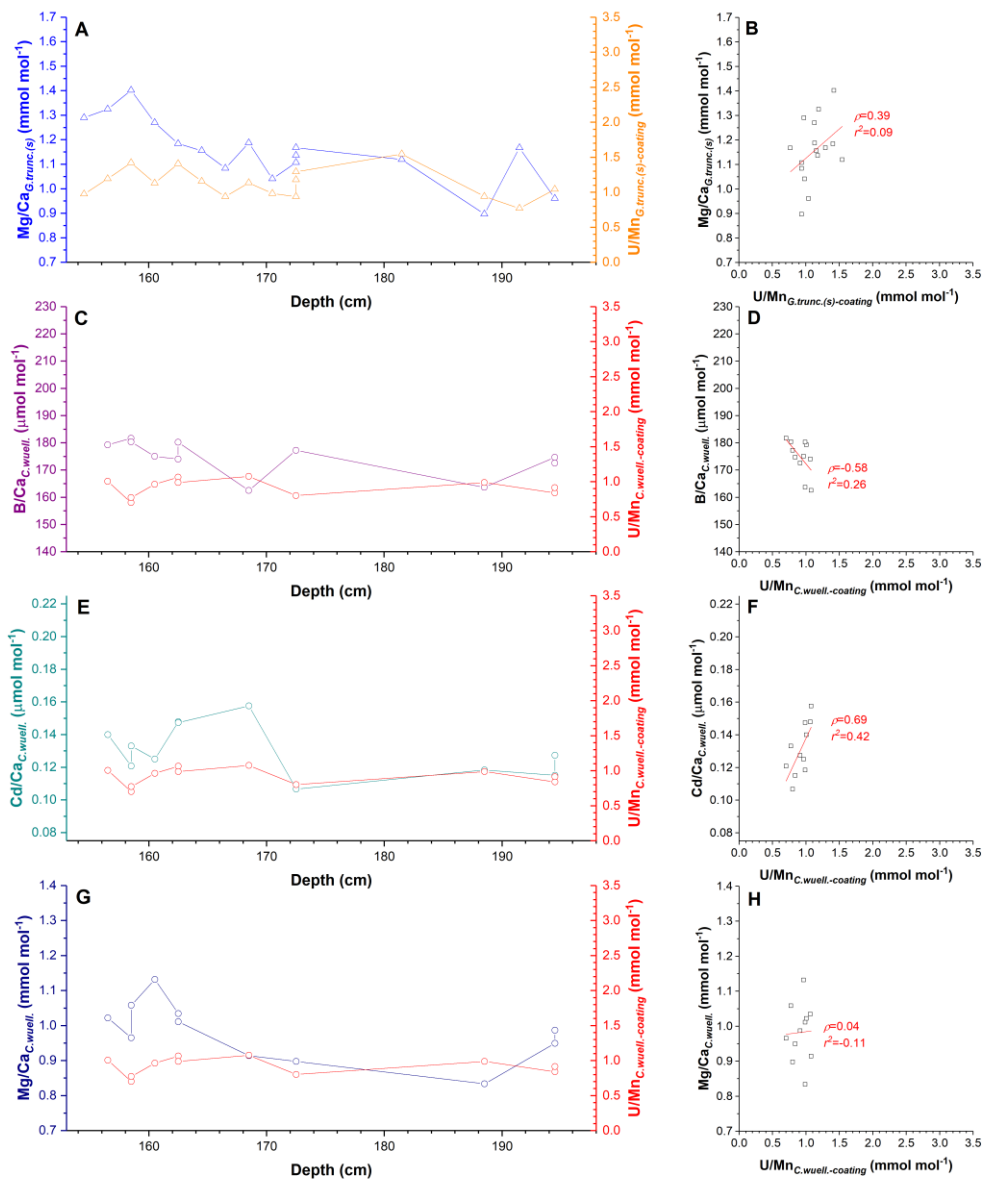
Appendix Figure 3.36. Detailed view of the MIS 1 section of figure 3.18 in Chapter 3.



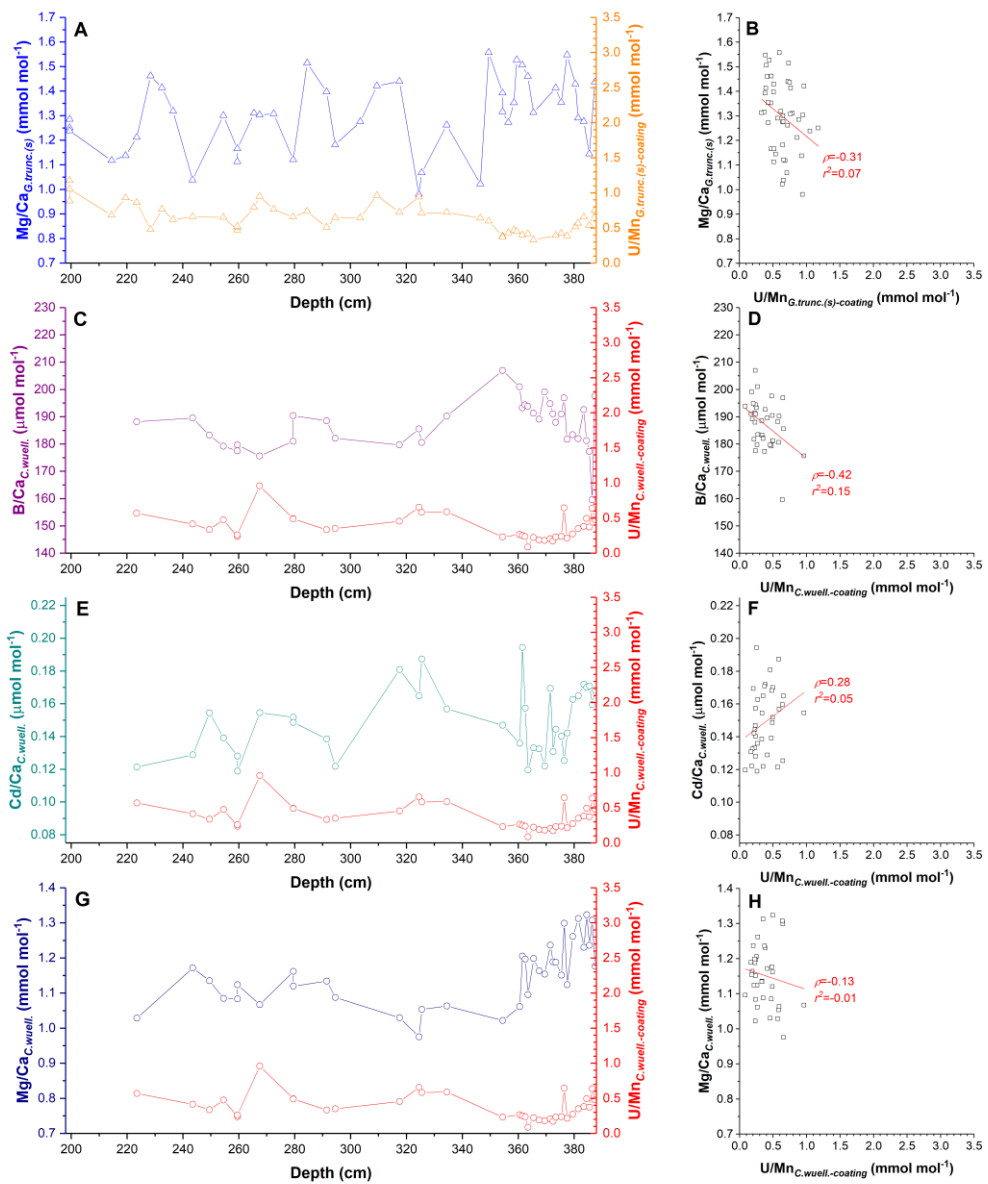
Appendix Figure 3.37. Detailed view of the MIS 2 section of figure 3.18 in Chapter 3.



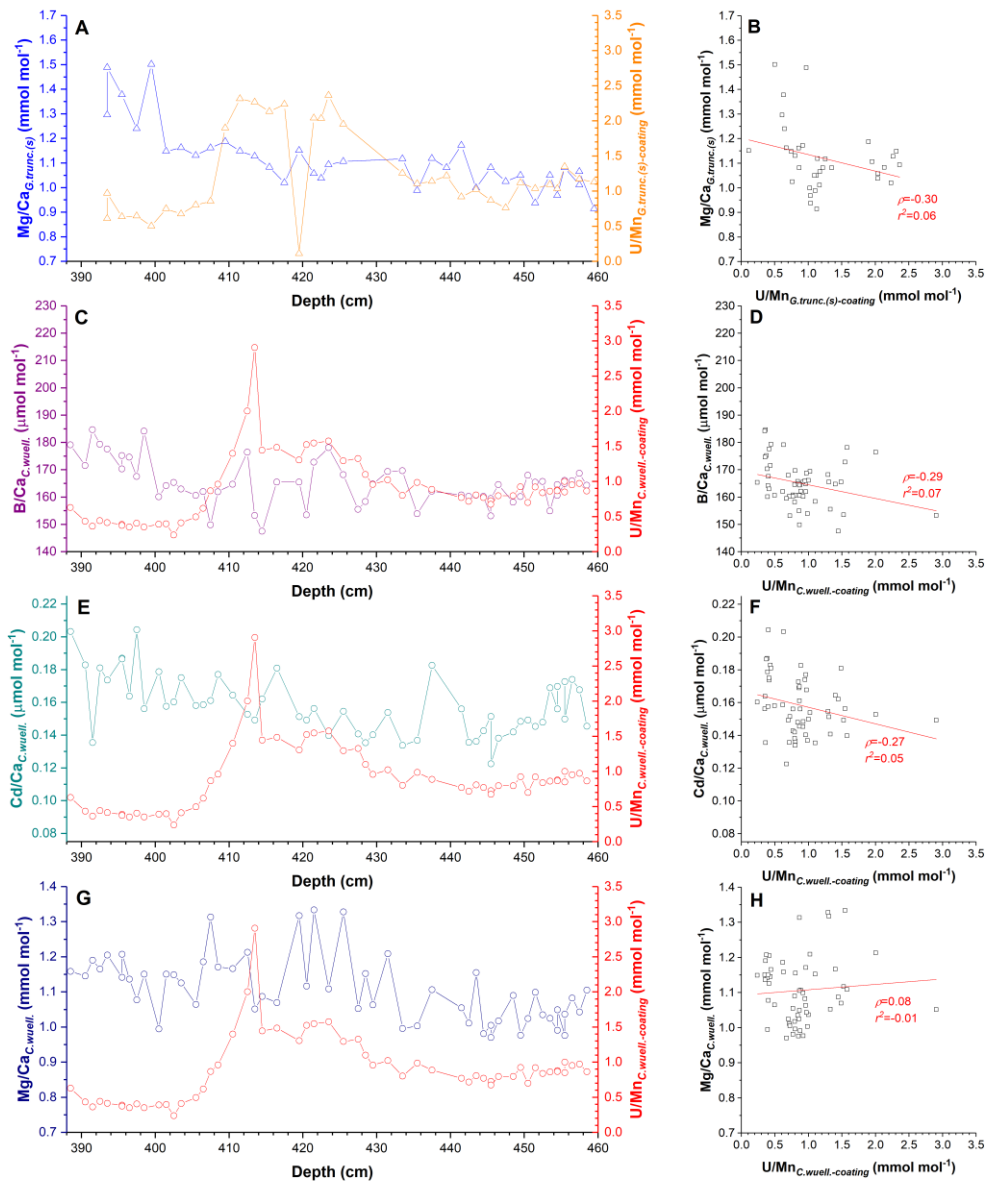
Appendix Figure 3.38. Detailed view of the MIS 3 section of figure 3.18 in Chapter 3.



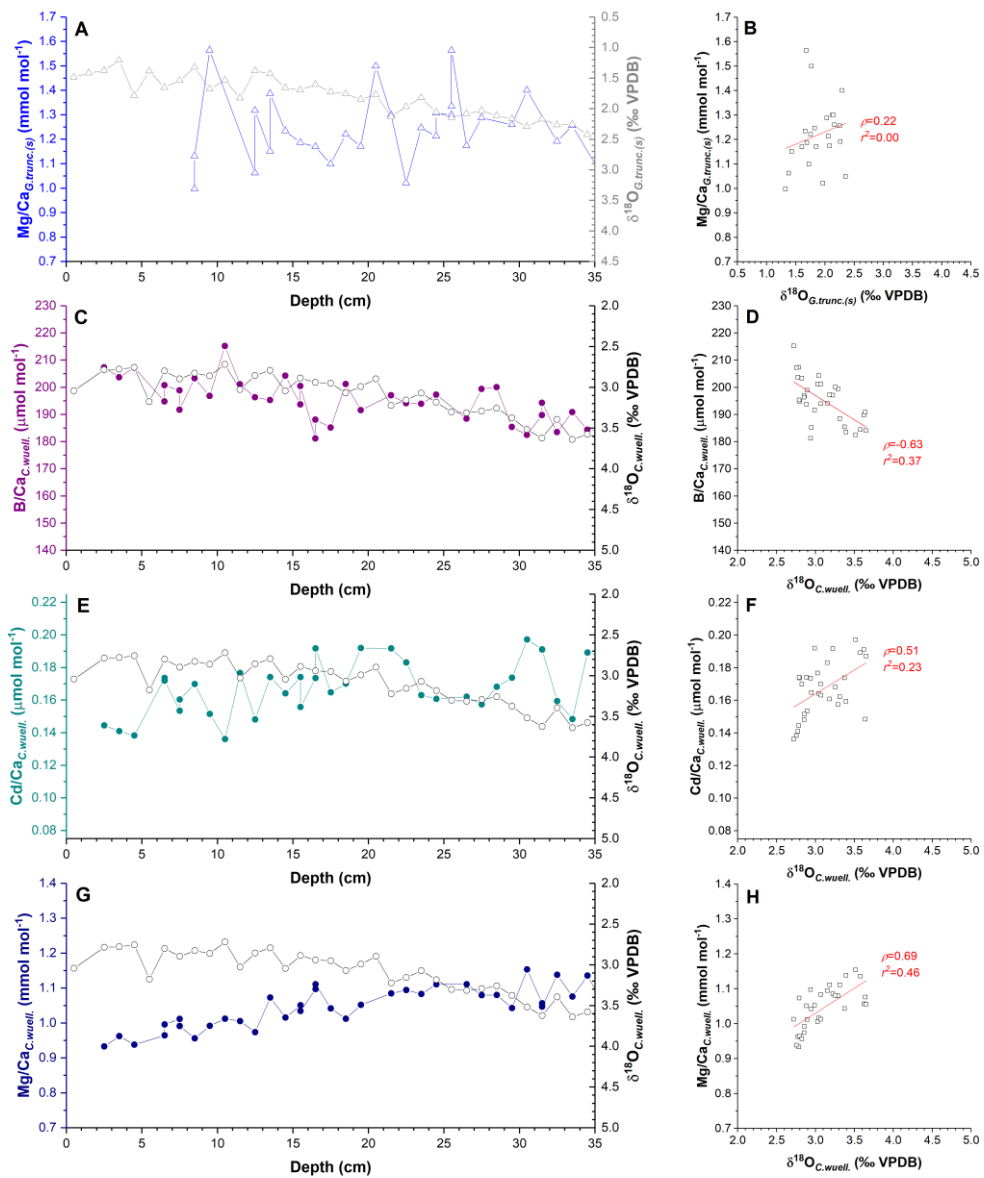
Appendix Figure 3.39. Detailed view of the MIS 4 section of figure 3.18 in Chapter 3.



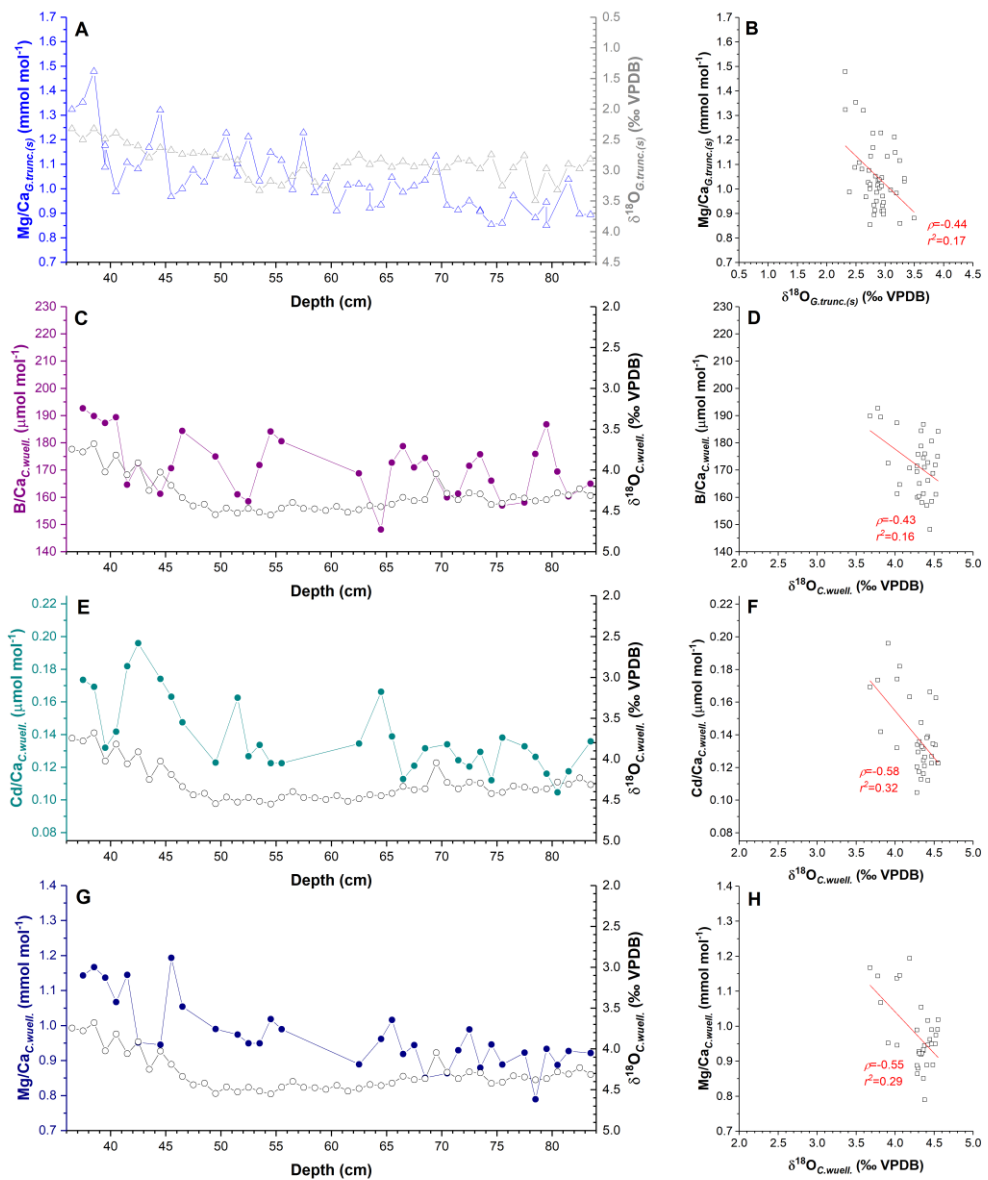
Appendix Figure 3.40. Detailed view of the MIS 5 section of figure 3.18 in Chapter 3.



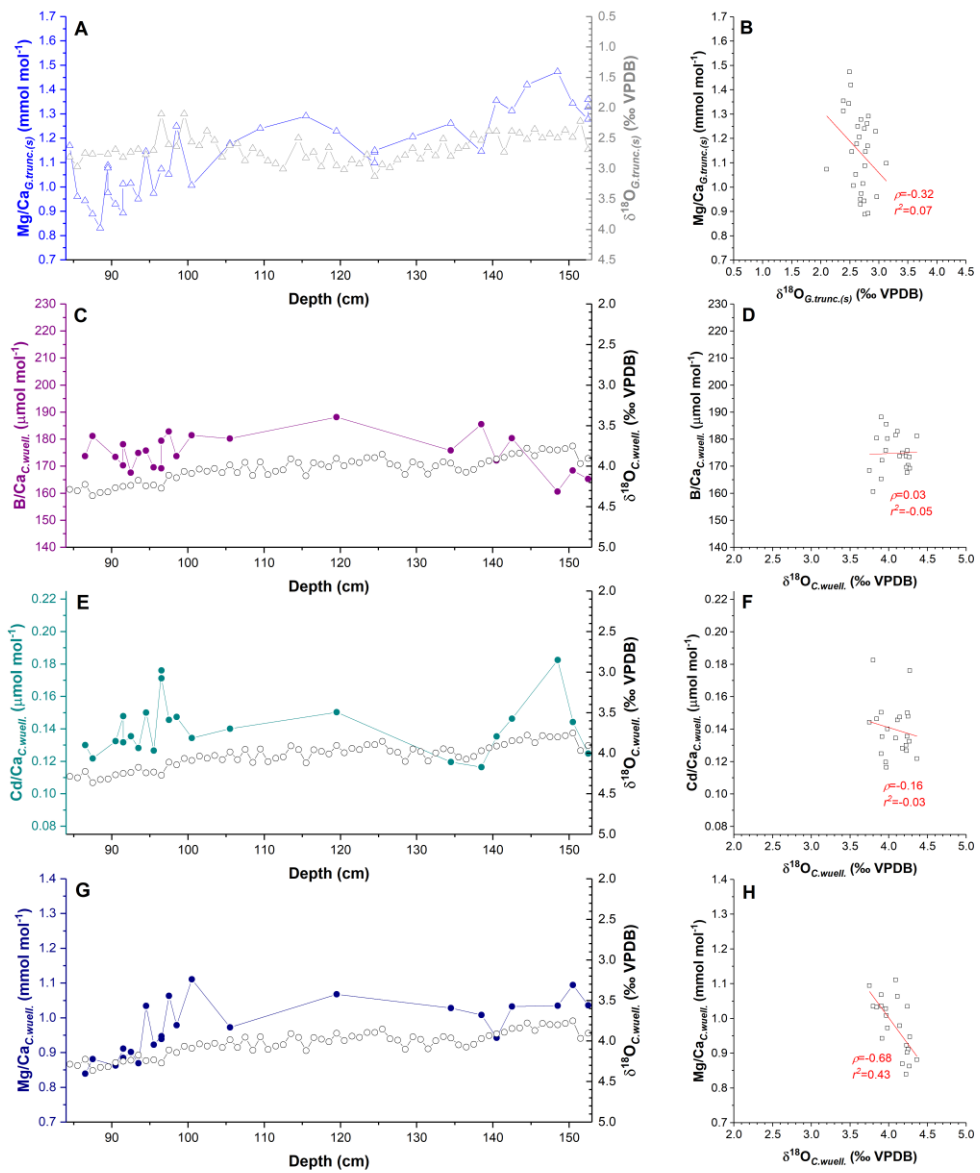
Appendix Figure 3.41. Detailed view of the MIS 6 section of figure 3.18 in Chapter 3.



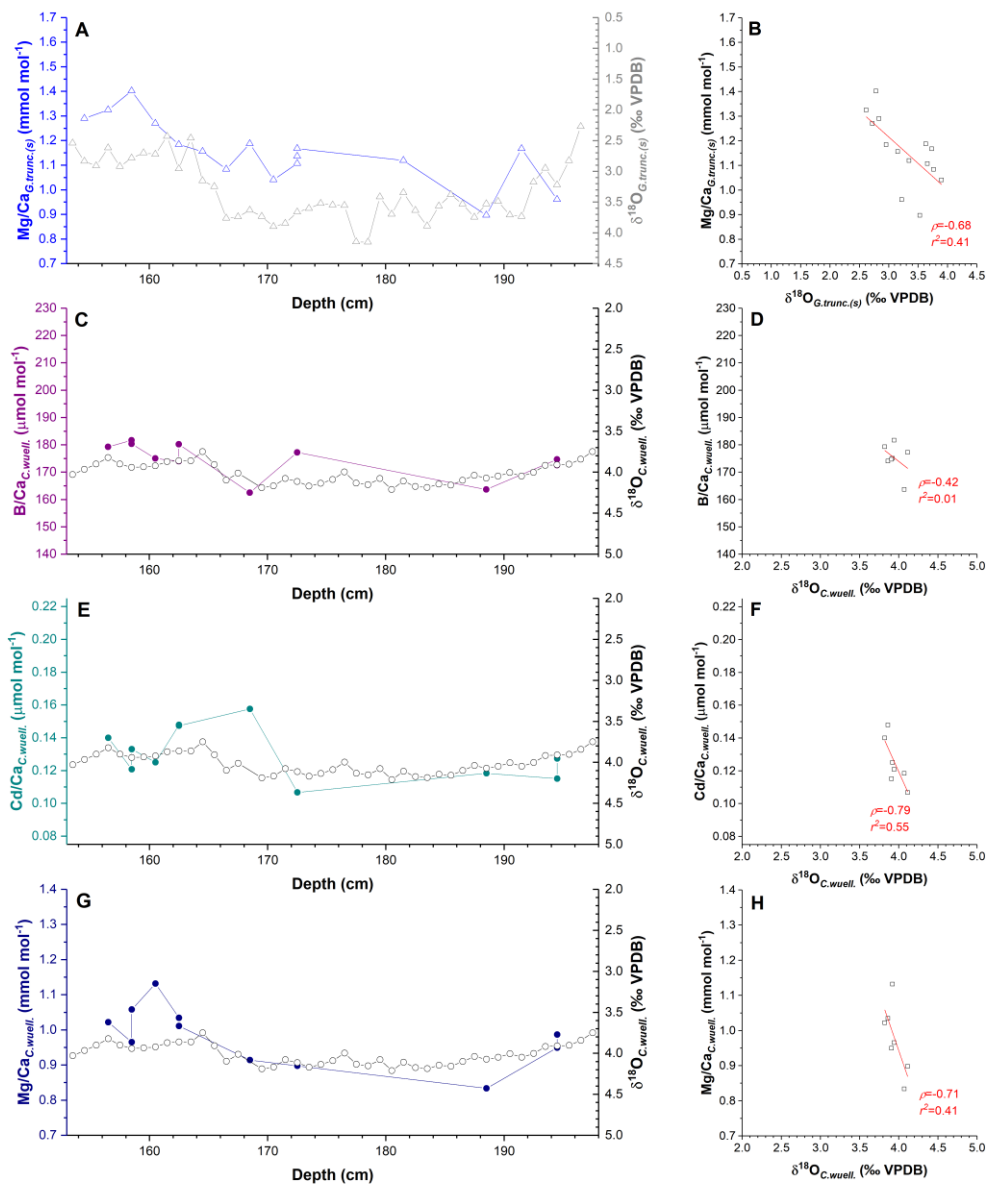
Appendix Figure 3.42. Detailed view of the MIS 1 section of figure 3.20 in Chapter 3.



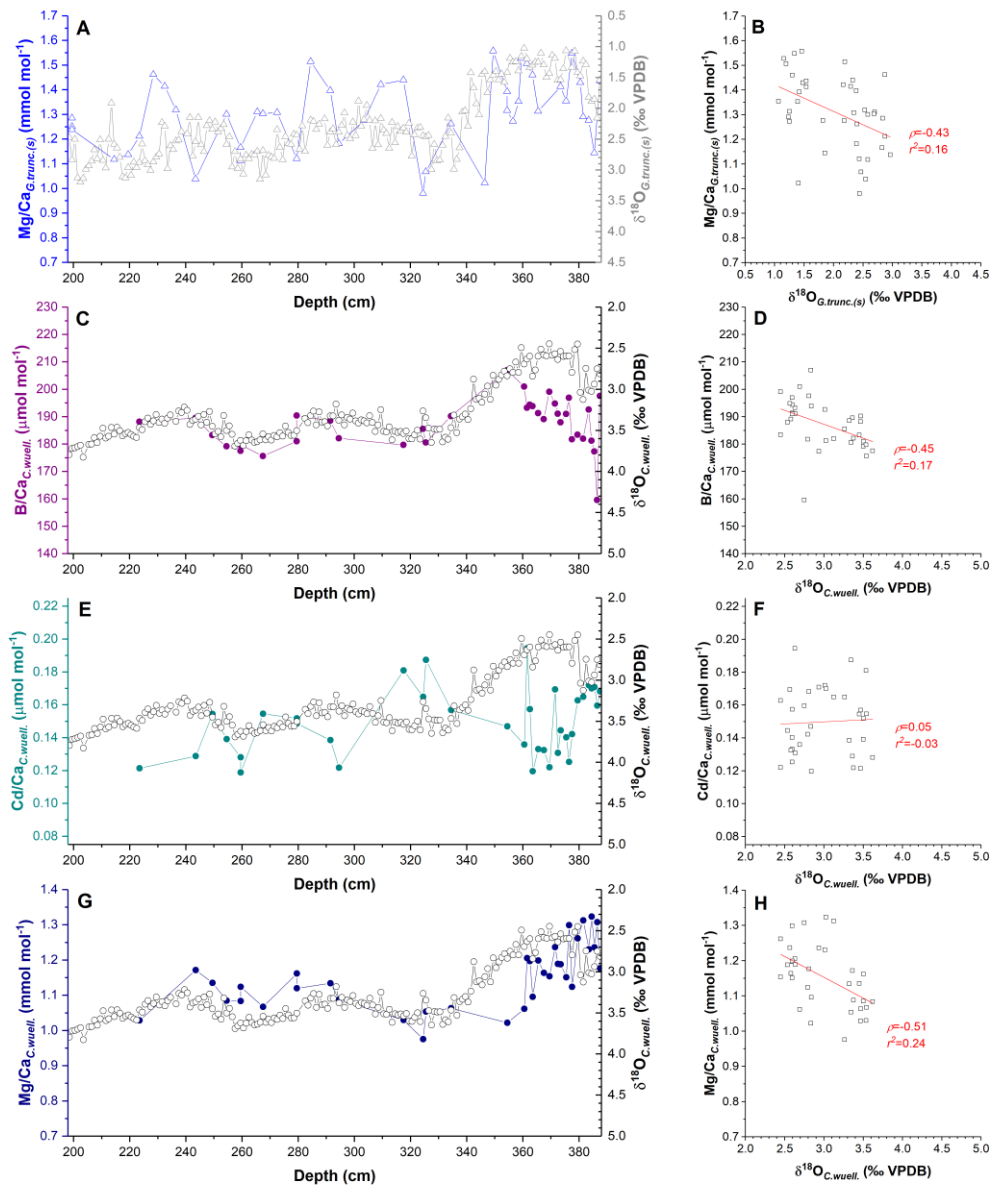
Appendix Figure 3.43. Detailed view of the MIS 2 section of figure 3.20 in Chapter 3.



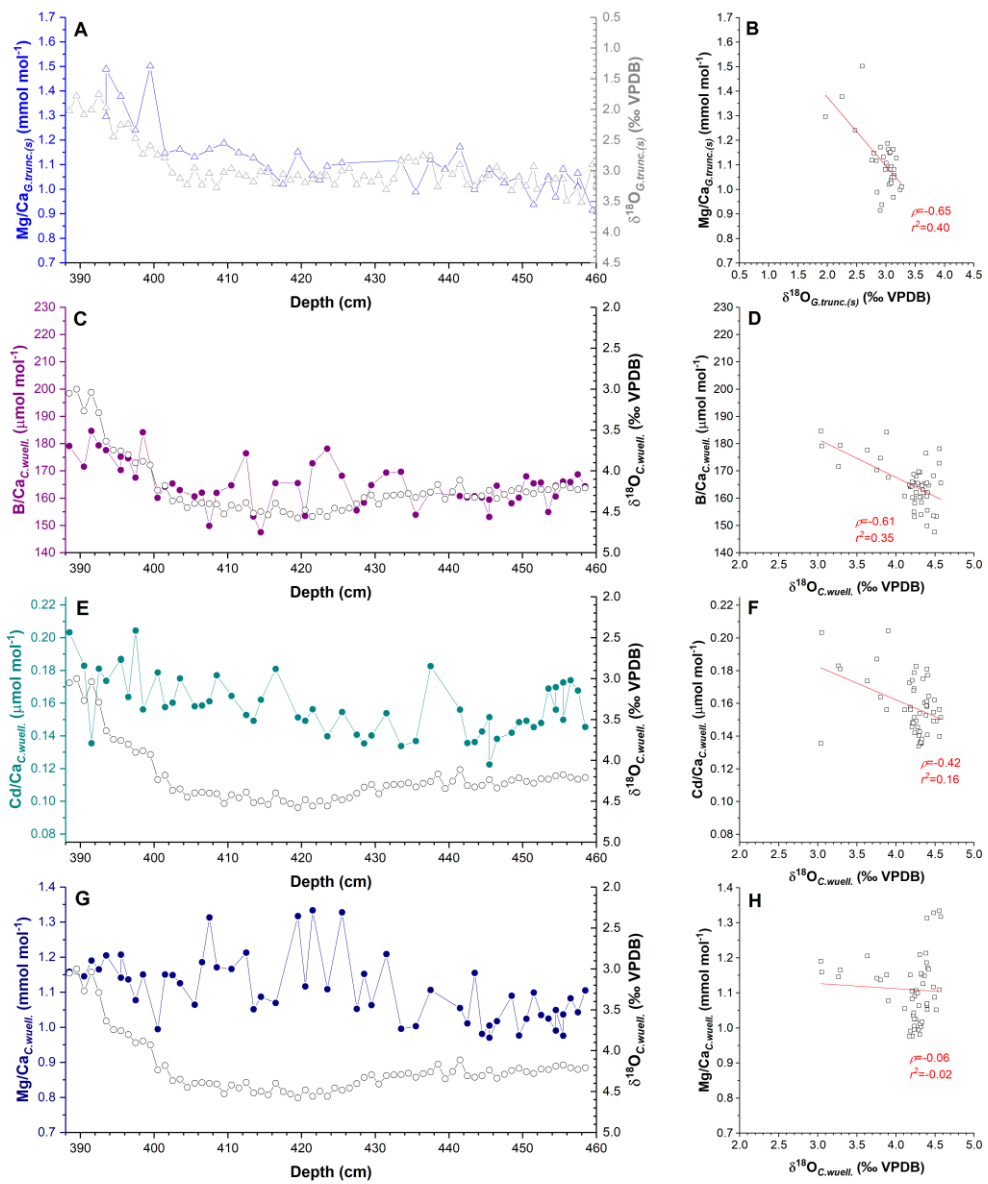
Appendix Figure 3.44. Detailed view of the MIS 3 section of figure 3.20 in Chapter 3.



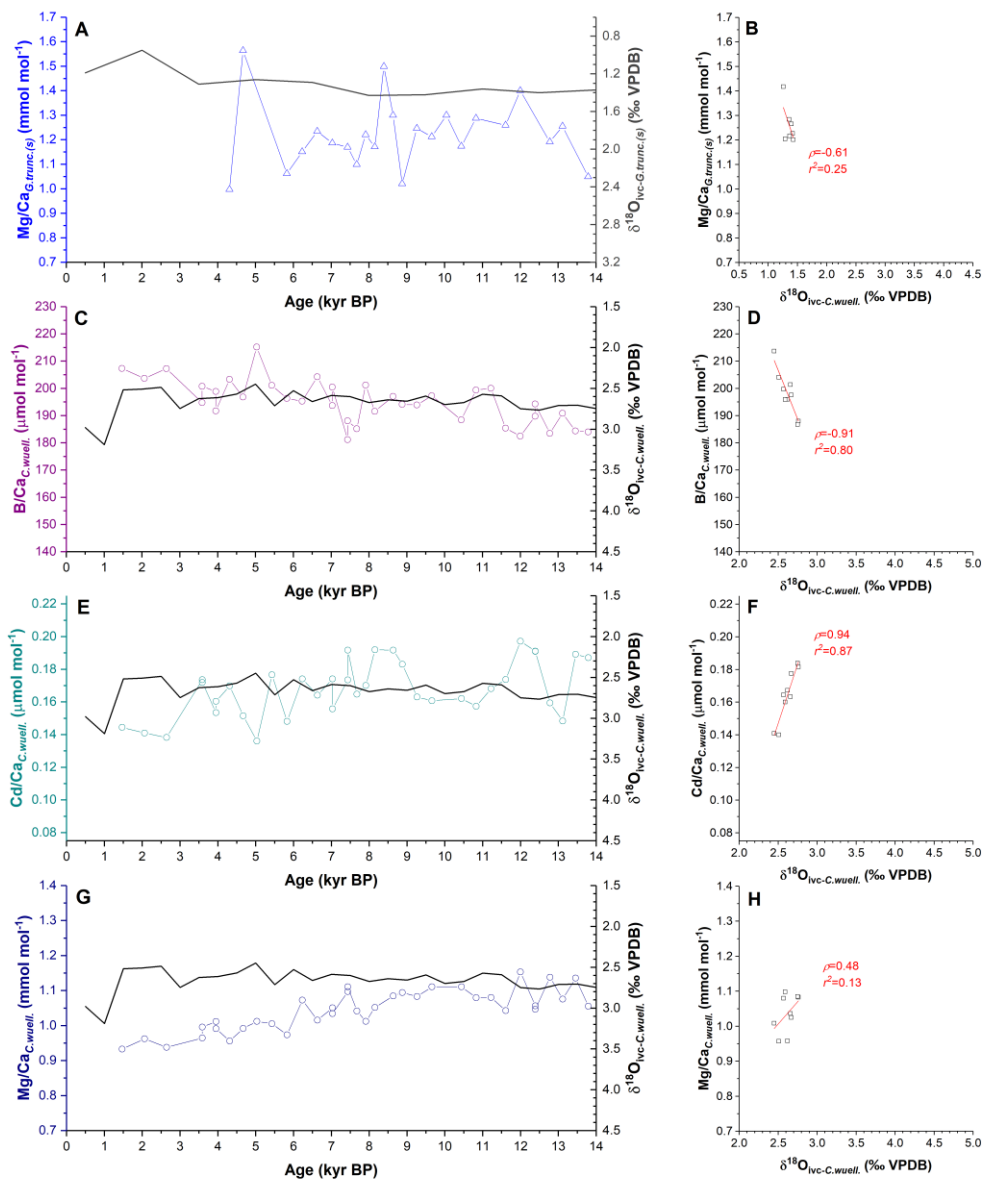
Appendix Figure 3.45. Detailed view of the MIS 4 section of figure 3.20 in Chapter 3.



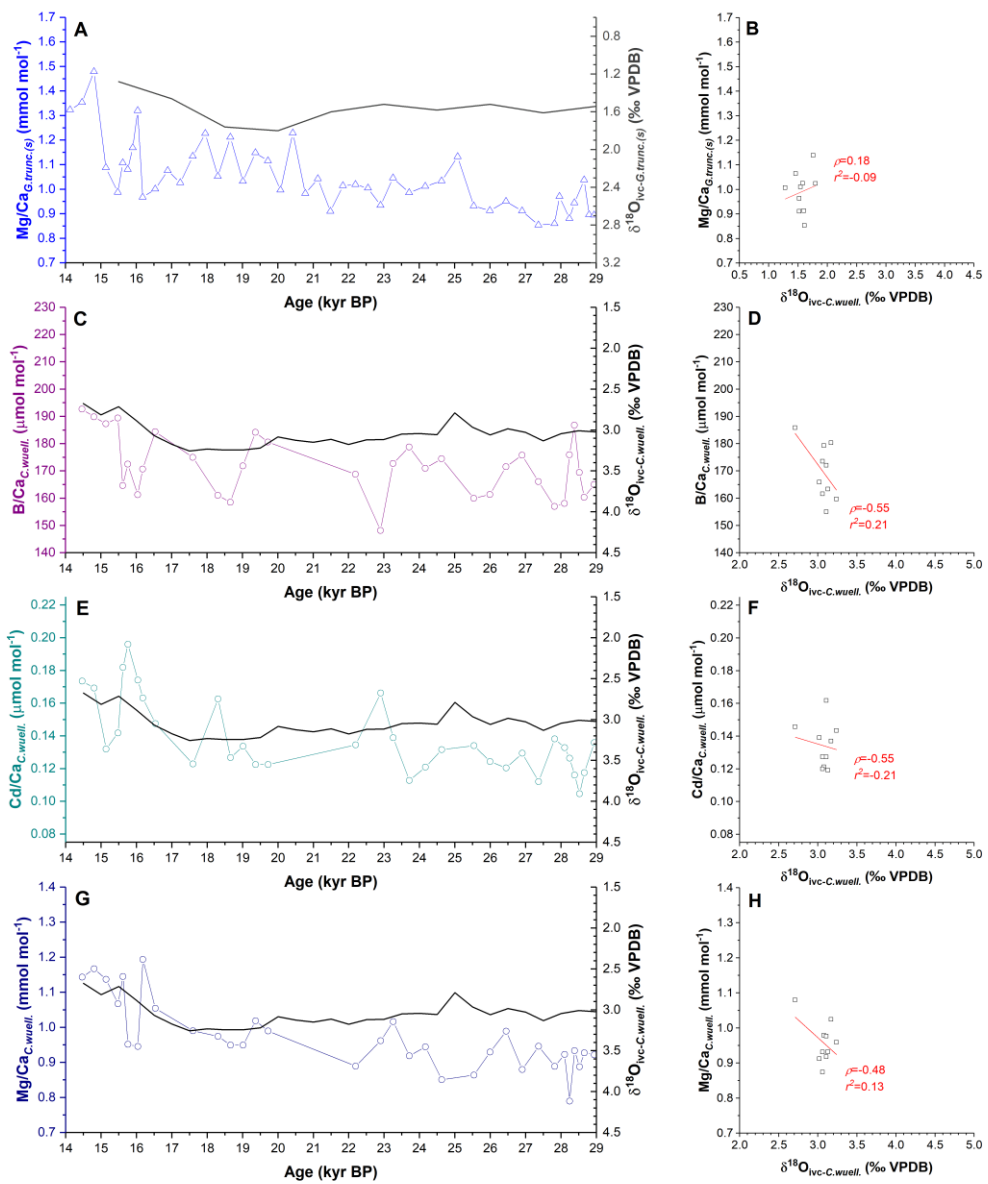
Appendix Figure 3.46. Detailed view of the MIS 5 section of figure 3.20 in Chapter 3.



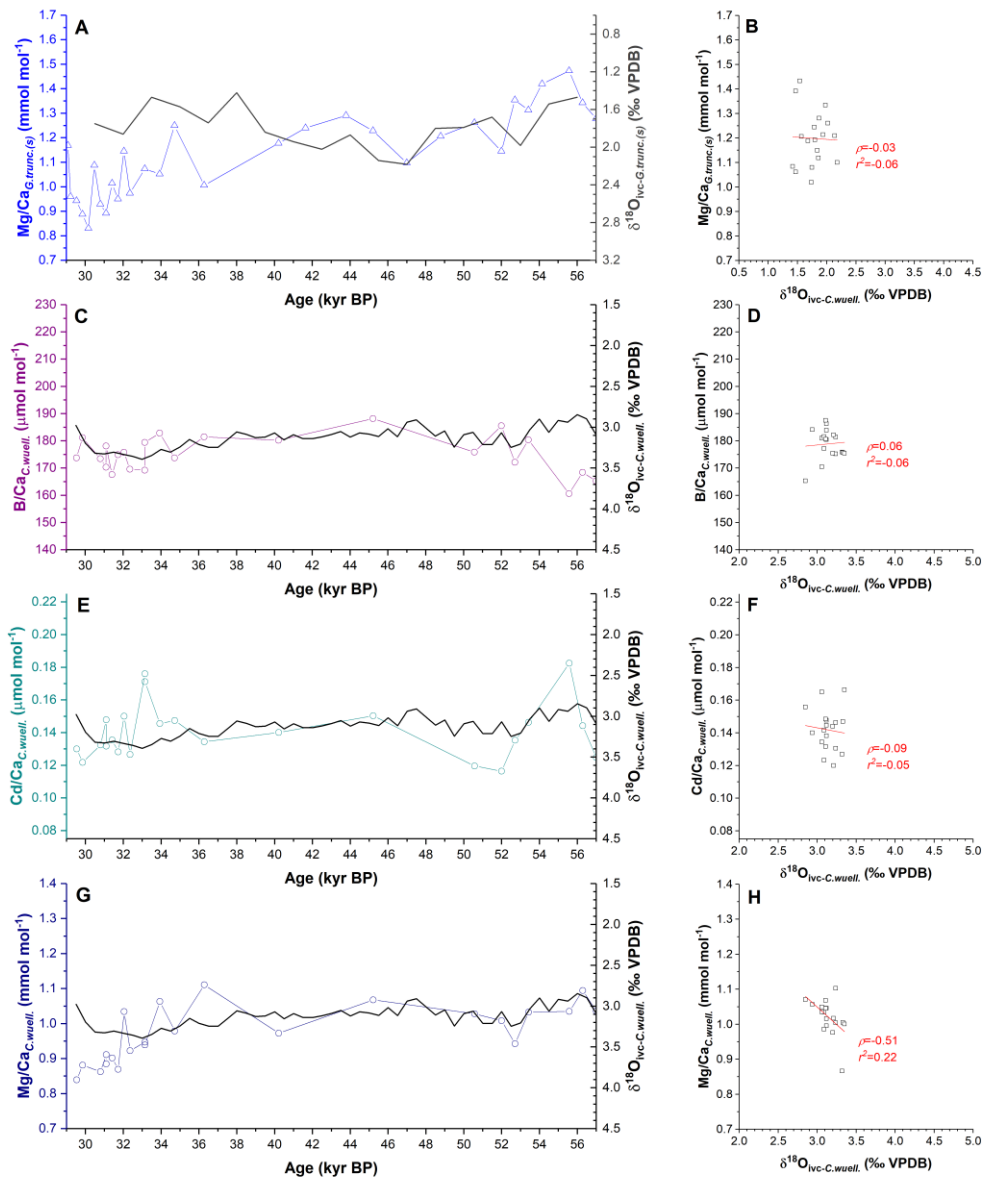
Appendix Figure 3.47. Detailed view of the MIS 6 section of figure 3.20 in Chapter 3.



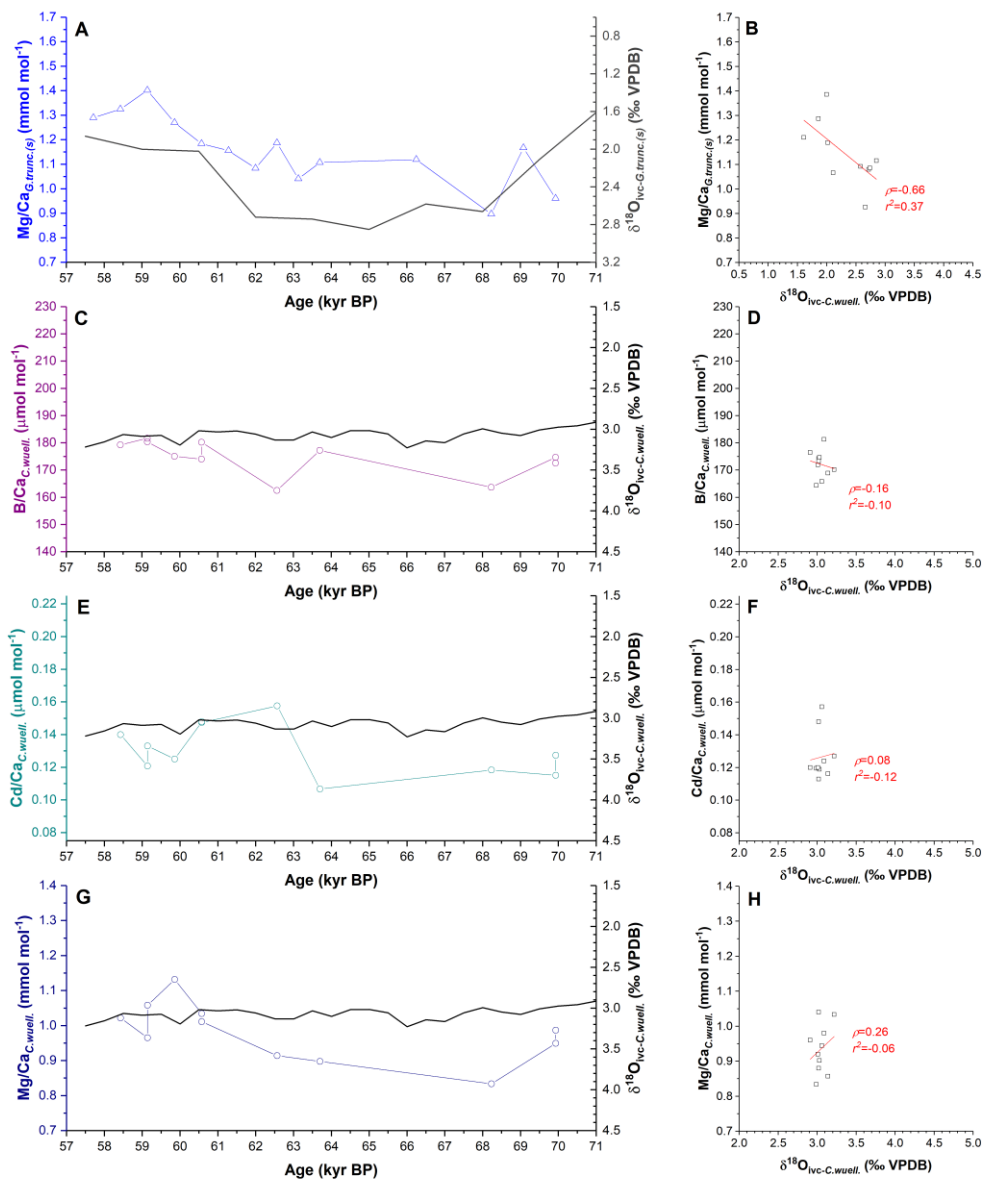
Appendix Figure 3.48. Detailed view of the MIS 1 section of figure 3.21 in Chapter 3.



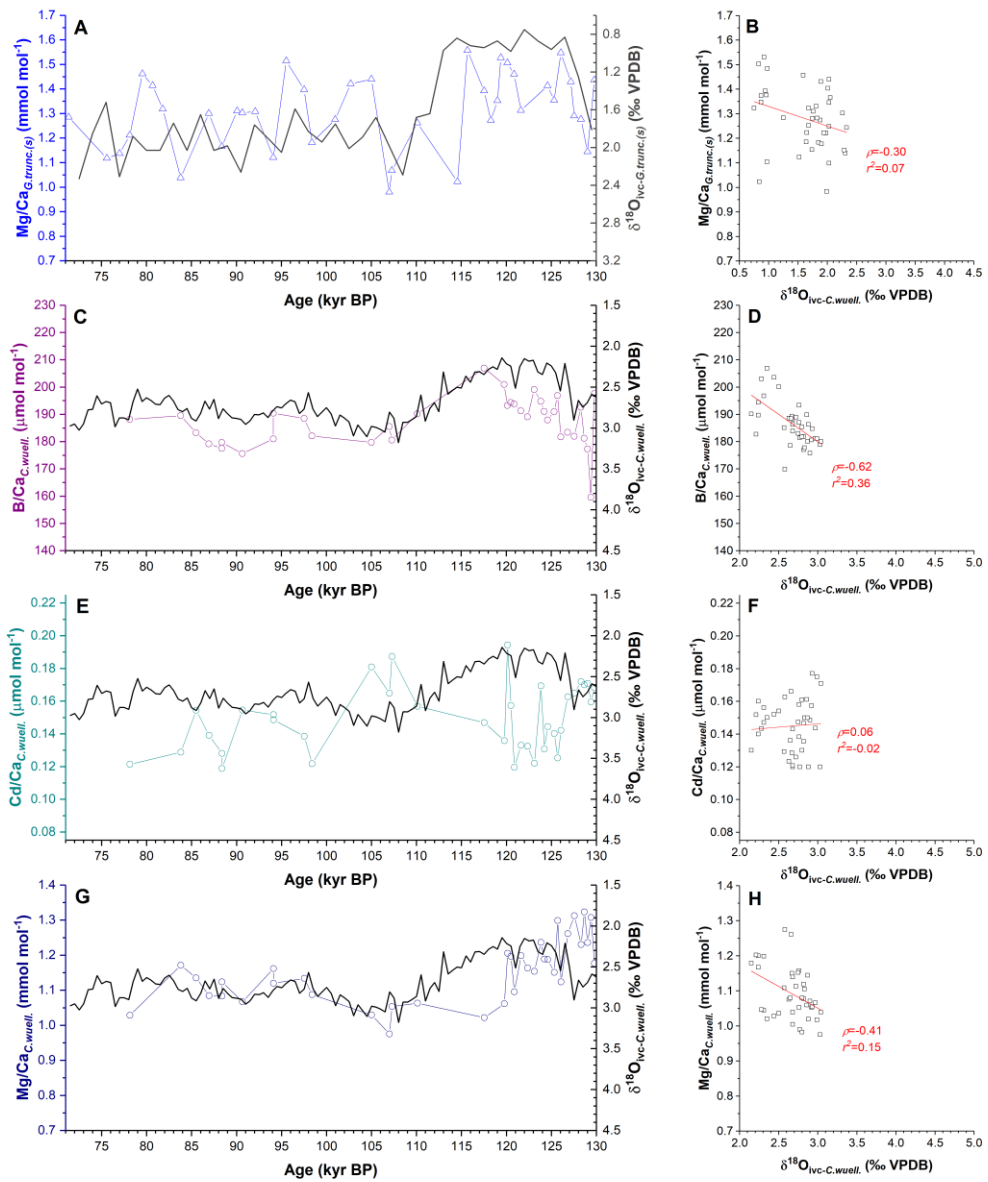
Appendix Figure 3.49. Detailed view of the MIS 2 section of figure 3.21 in Chapter 3.



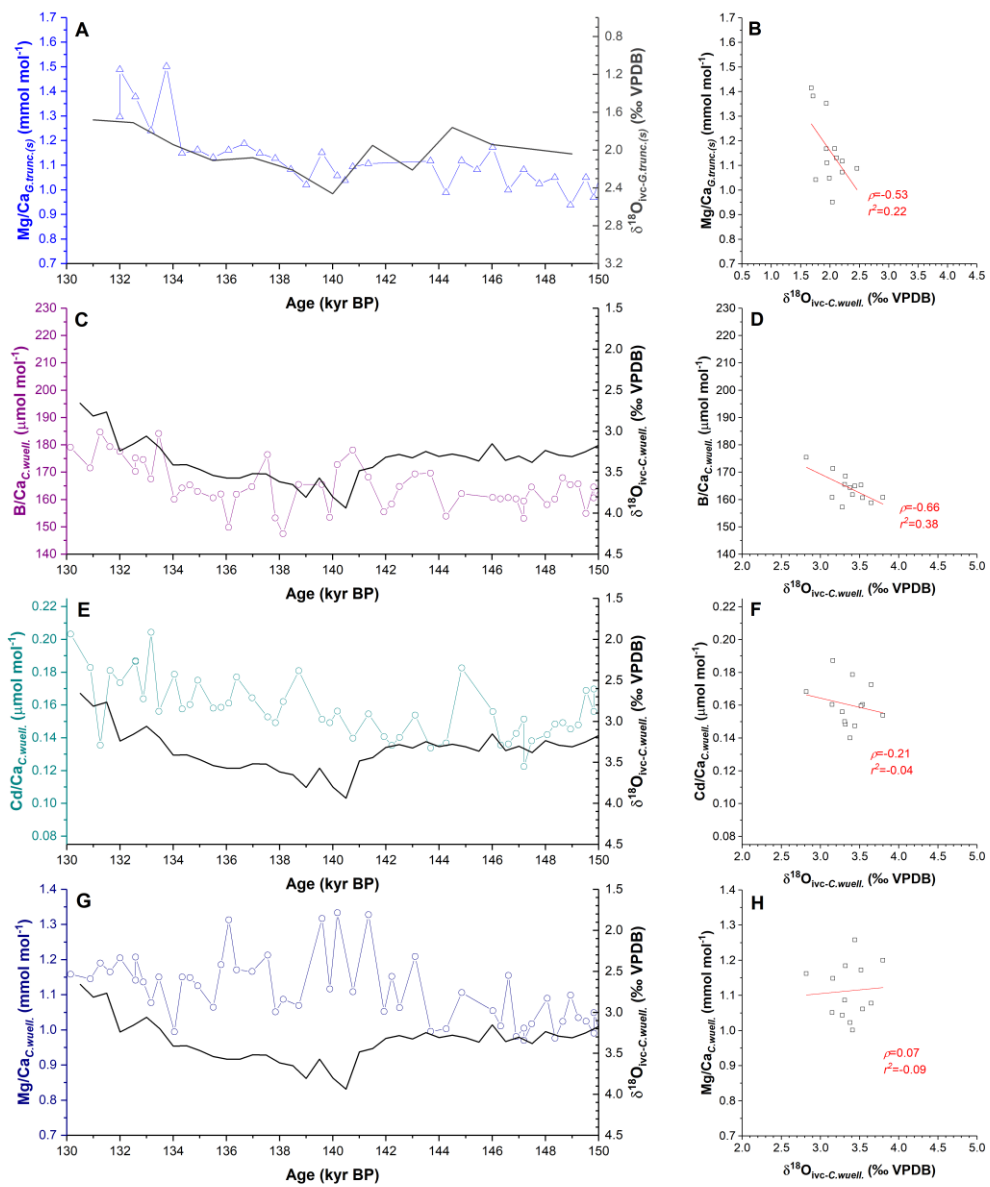
Appendix Figure 3.50. Detailed view of the MIS 3 section of figure 3.21 in Chapter 3.



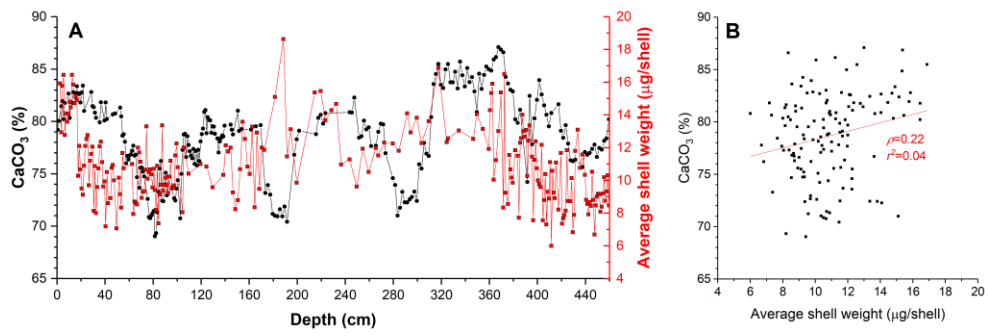
Appendix Figure 3.51. Detailed view of the MIS 4 section of figure 3.21 in Chapter 3.



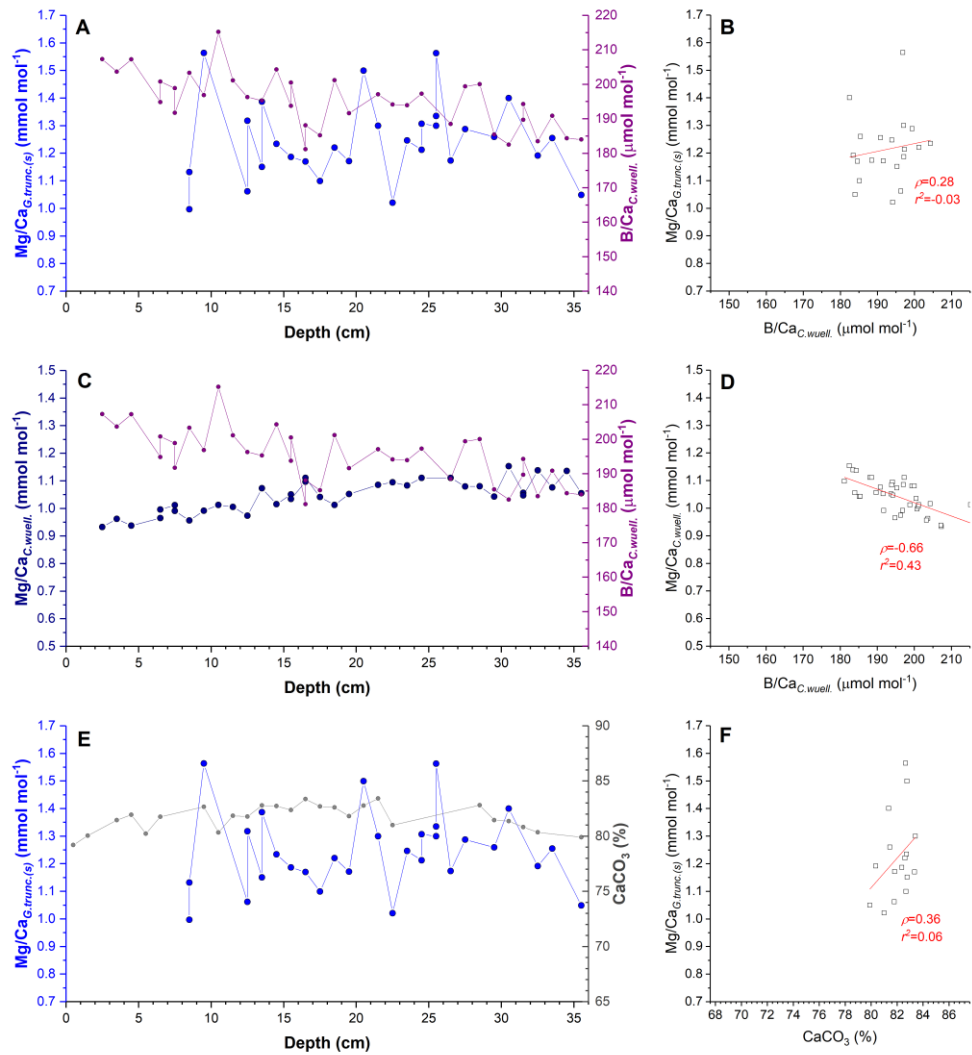
Appendix Figure 3.52. Detailed view of the MIS 5 section of figure 3.21 in Chapter 3.



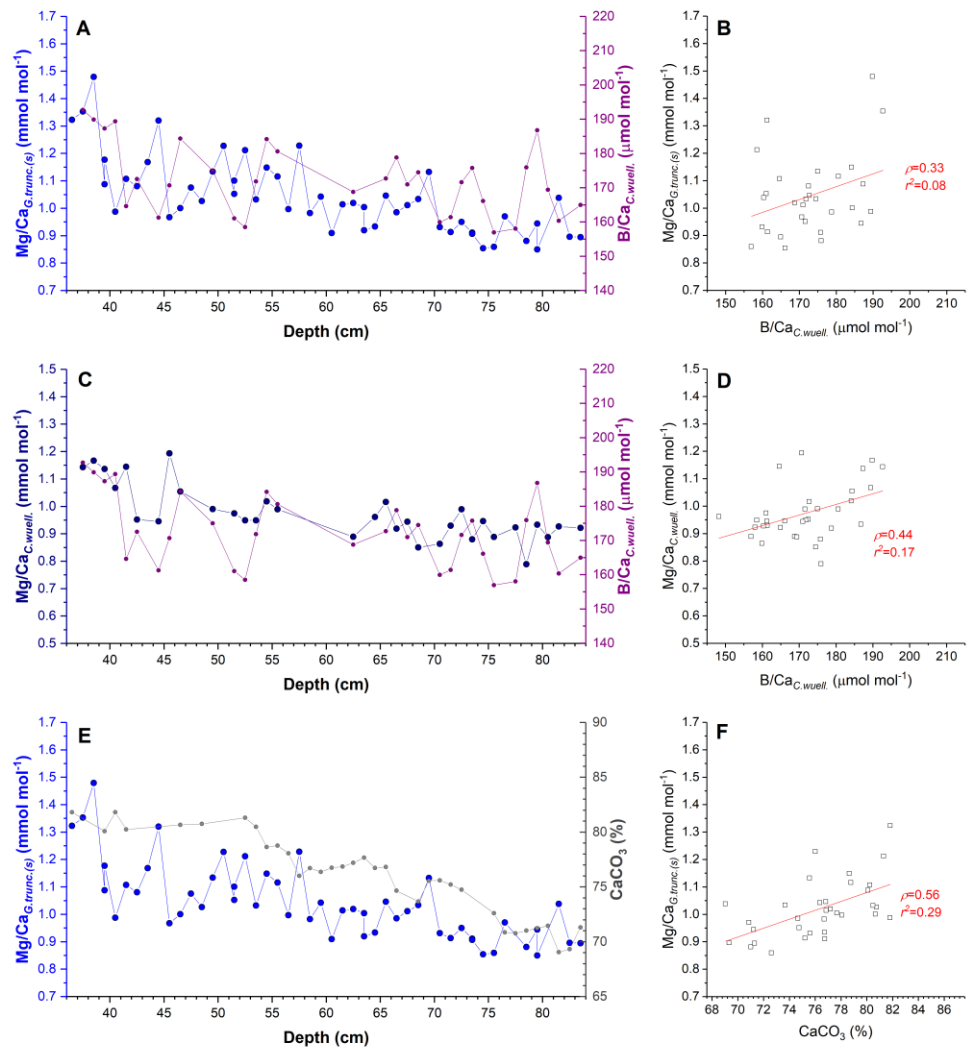
Appendix Figure 3.53. Detailed view of the MIS 6 section of figure 3.21 in Chapter 3.



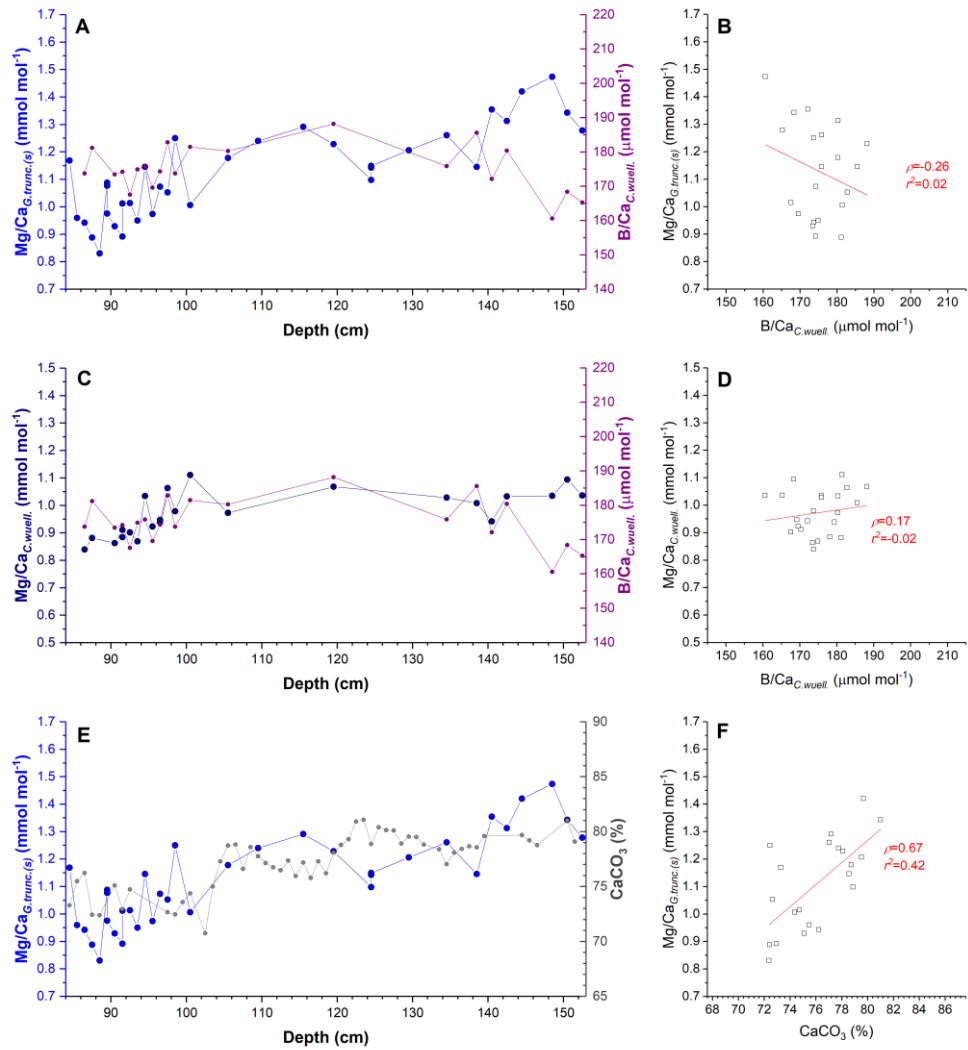
**Appendix Figure 3.54.** A) Comparison of the downcore record of bulk carbonate (CaCO<sub>3</sub>) content from sediment core MD02-2588 with the corresponding record of average *C. wuellerstorfi* shell weights. B) Cross plot of CaCO<sub>3</sub> versus average *C. wuellerstorfi* shell weight. Also shown in panel B is the lines of best fit through the dataset and the corresponding Pearson's r value ( $\rho$ ) and coefficient of determination ( $R^2$ ).



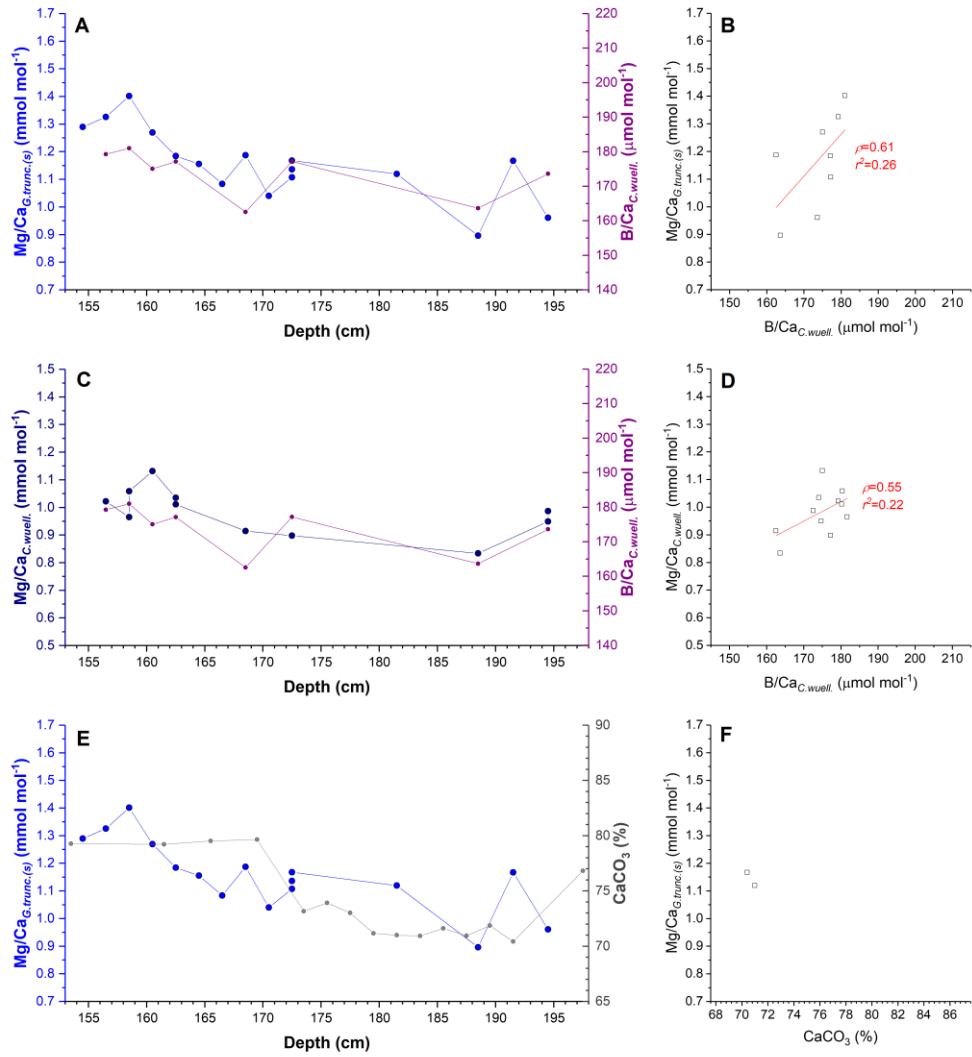
Appendix Figure 3.55. Detailed view of the MIS 1 section of figure 3.27 in Chapter 3.



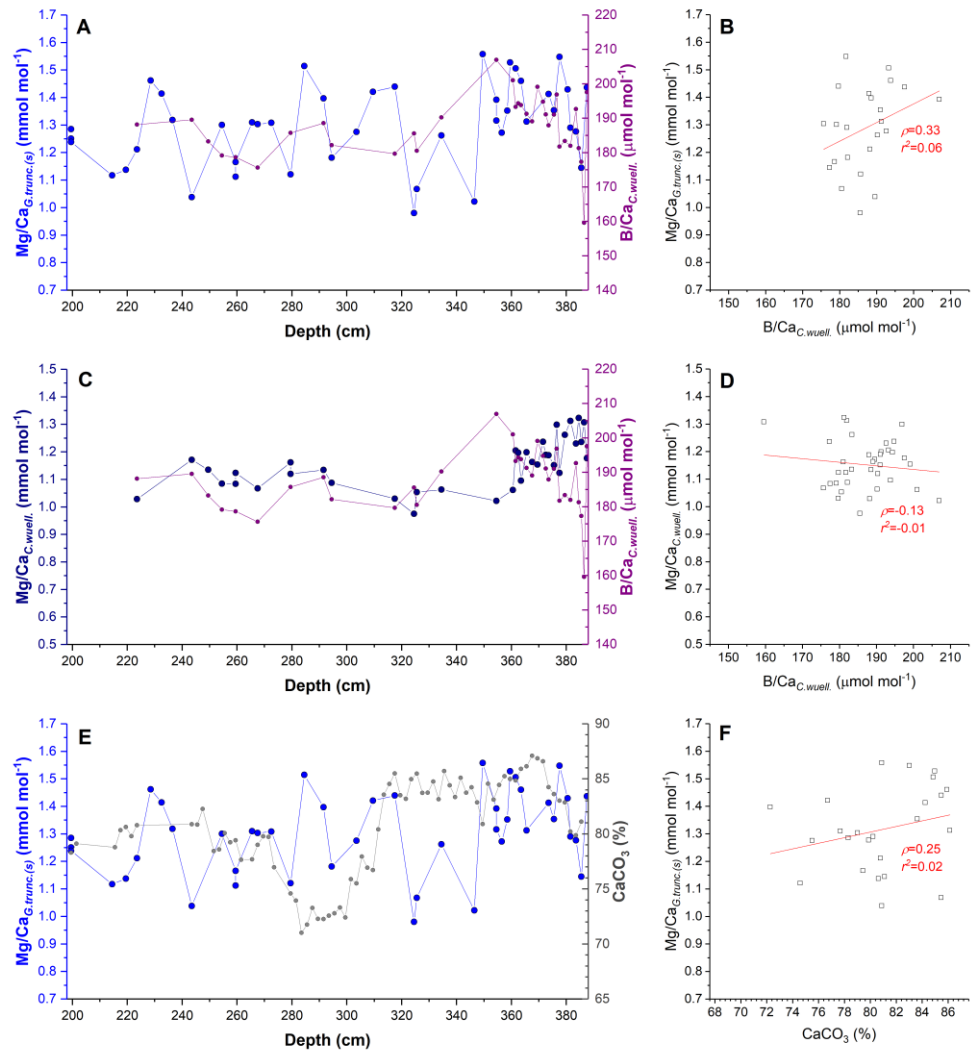
Appendix Figure 3.56. Detailed view of the MIS 2 section of figure 3.27 in Chapter 3.



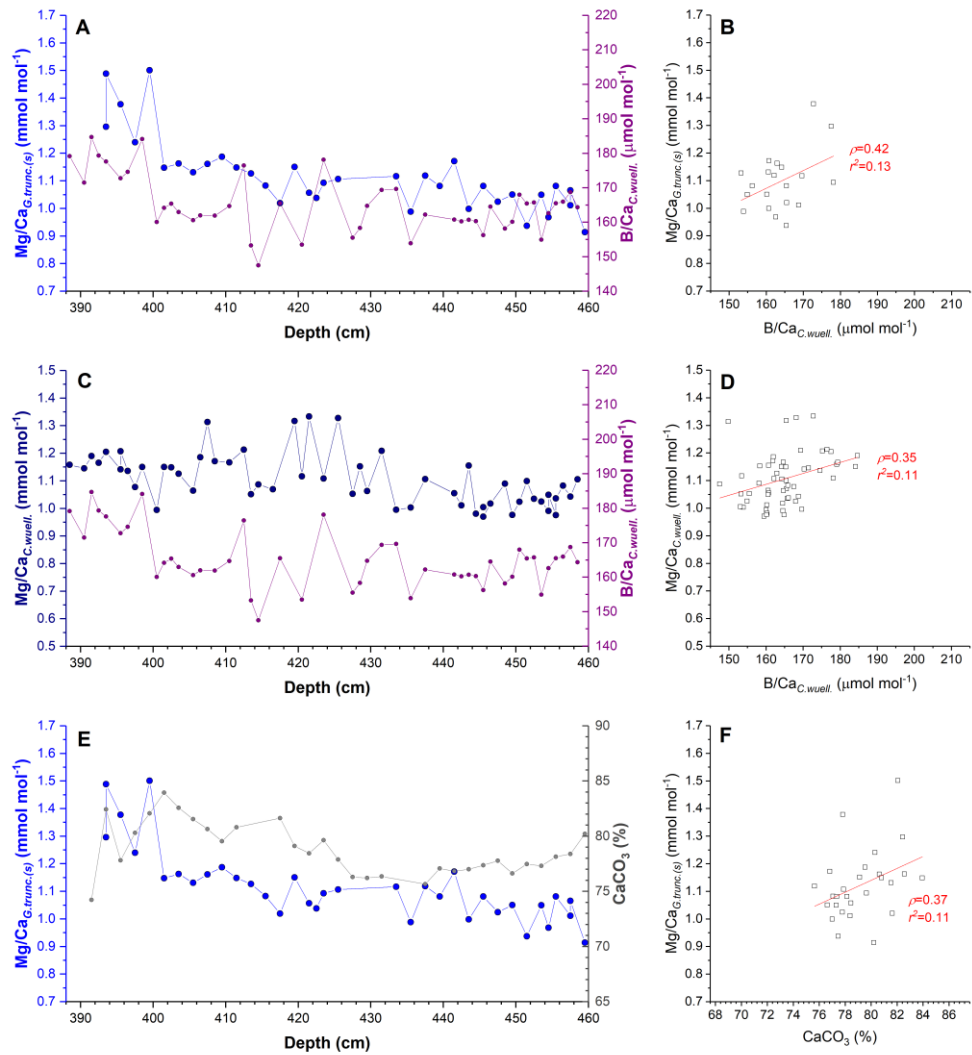
Appendix Figure 3.57. Detailed view of the MIS 3 section of figure 3.27 in Chapter 3.



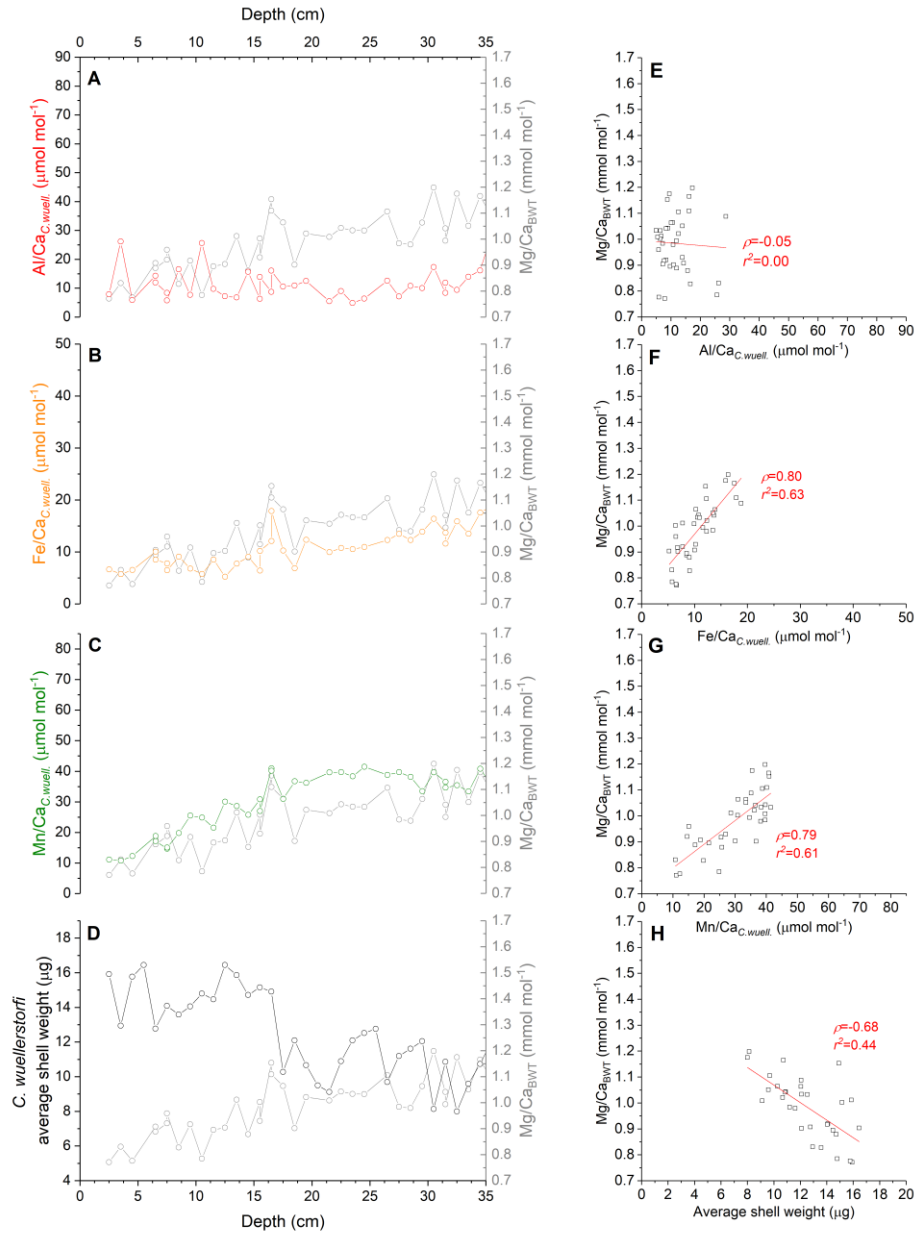
**Appendix Figure 3.58.** Detailed view of the MIS 4 section of figure 3.27 in Chapter 3.



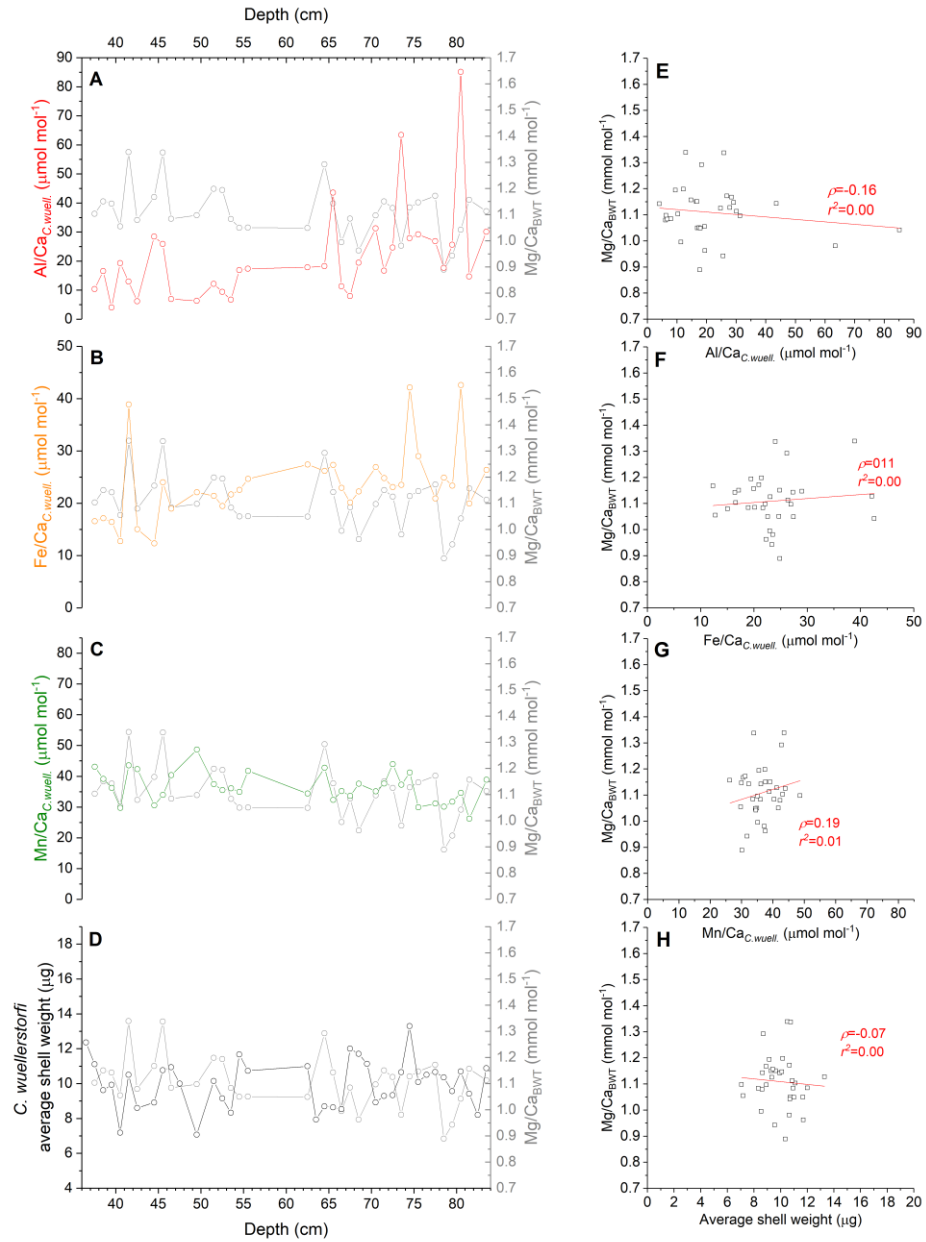
Appendix Figure 3.59. Detailed view of the MIS 5 section of figure 3.27 in Chapter 3.



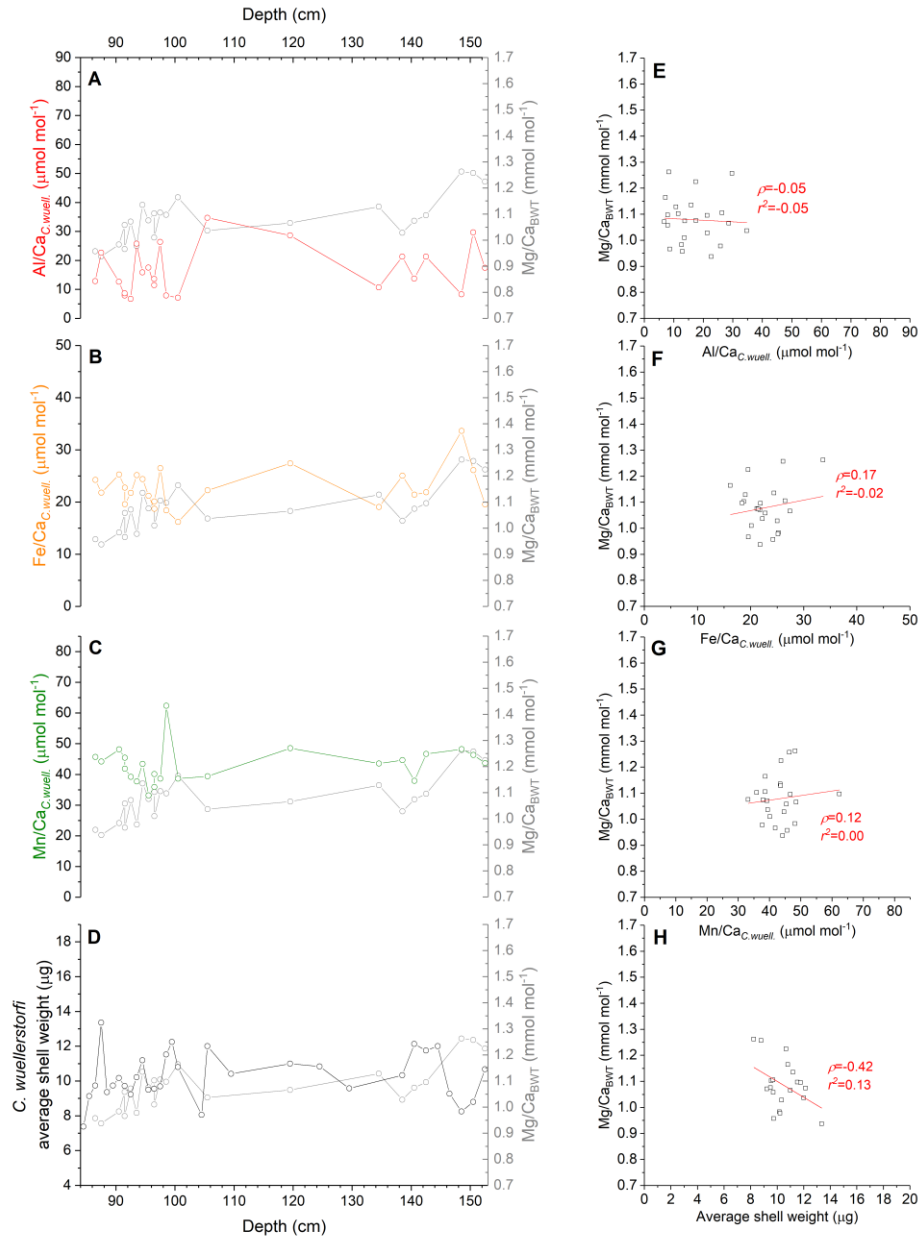
Appendix Figure 3.60. Detailed view of the MIS 6 section of figure 3.27 in Chapter 3.



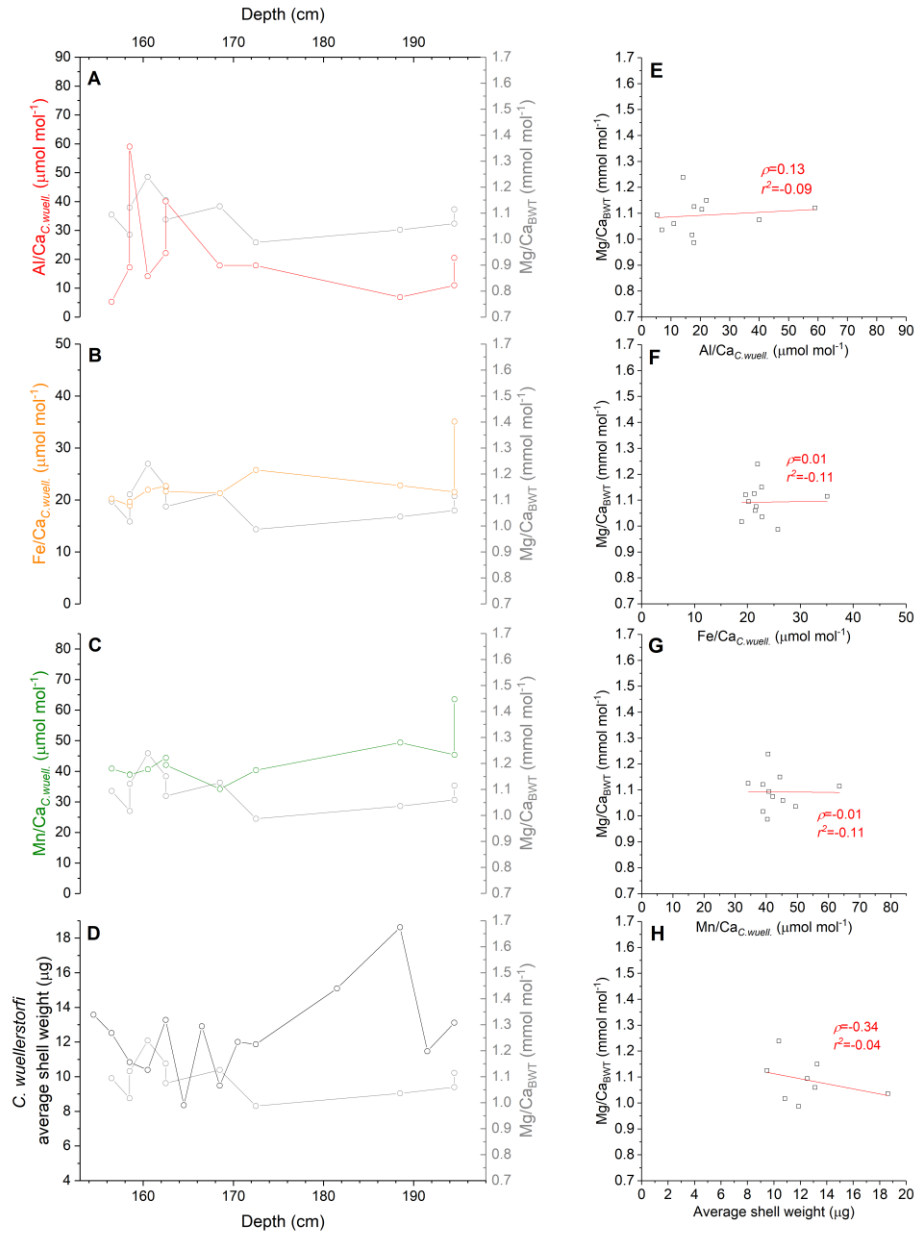
Appendix Figure 3.61. Detailed view of the MIS 1 section of figure 3.30 in Chapter 3.



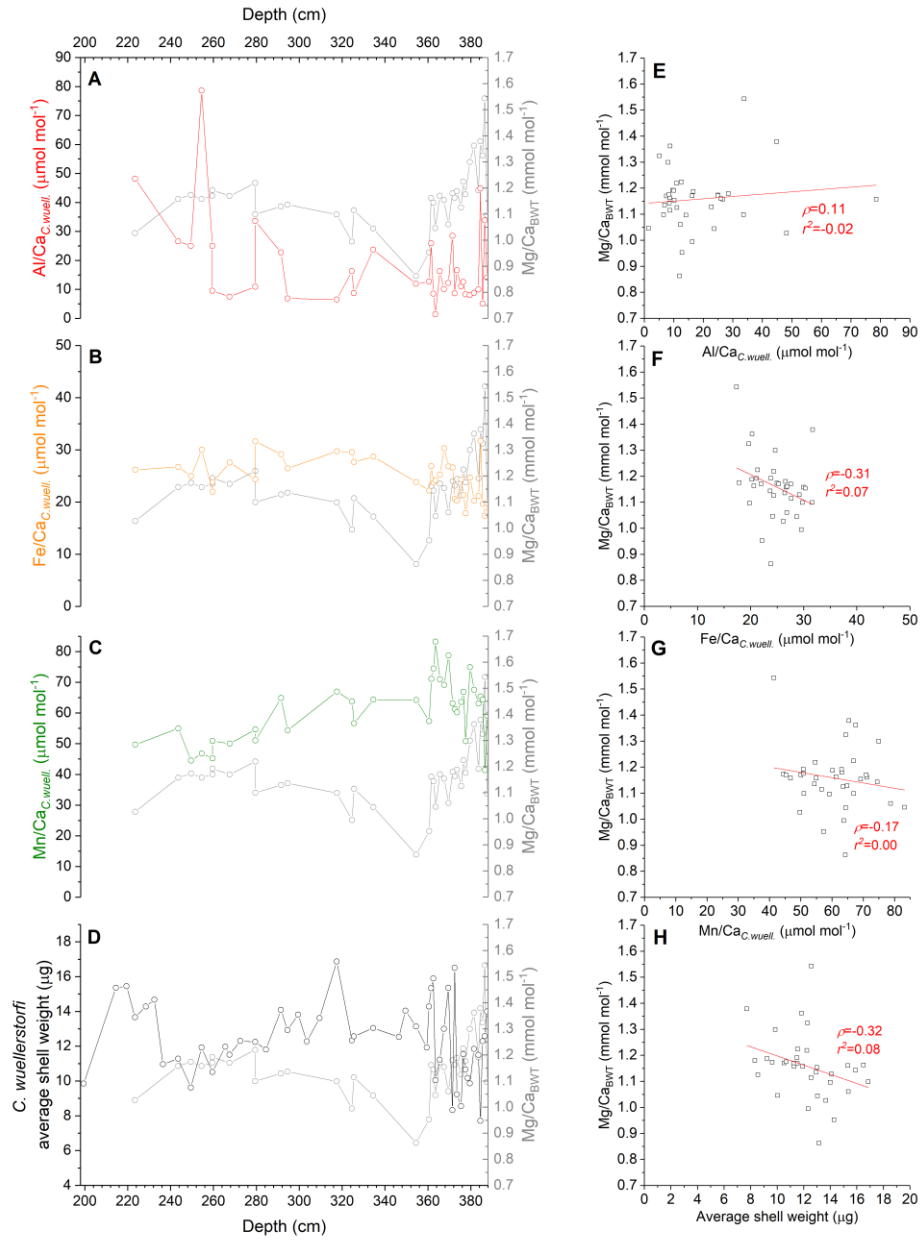
Appendix Figure 3.62. Detailed view of the MIS 2 section of figure 3.30 in Chapter 3.



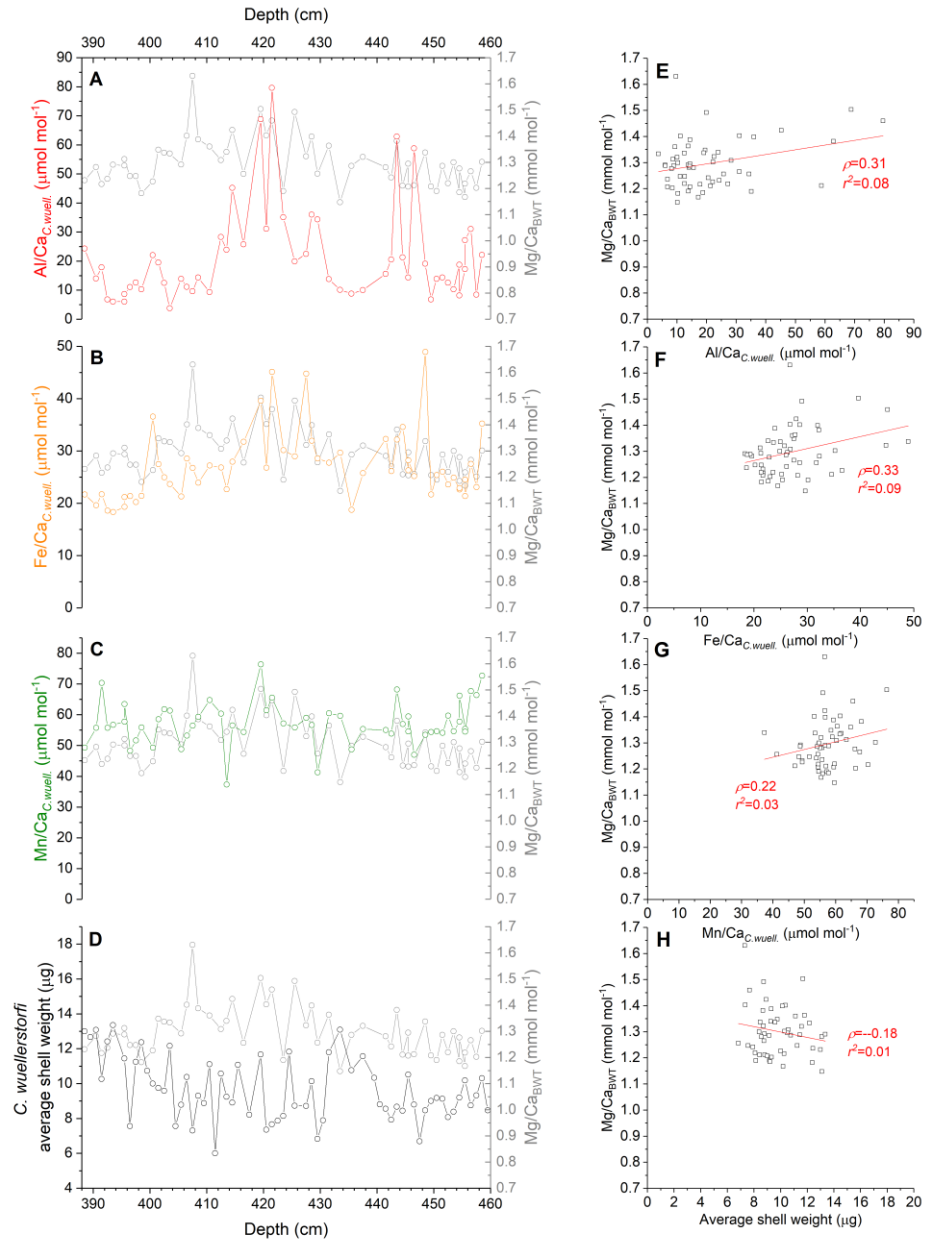
Appendix Figure 3.63. Detailed view of the MIS 3 section of figure 3.30 in Chapter 3.



Appendix Figure 3.64. Detailed view of the MIS 4 section of figure 3.30 in Chapter 3.



Appendix Figure 3.65. Detailed view of the MIS 5 section of figure 3.30 in Chapter 3.



Appendix Figure 3.66. Detailed view of the MIS 6 section of figure 3.30 in Chapter 3.

---

## References

---

Abelmann, A., R. Gersonde, G. Cortese, G. Kuhn, and V. Smetacek (2006), Extensive Phytoplankton Blooms in the Atlantic Sector of the Glacial Southern Ocean, *Paleoceanography*, 21(1), doi: 10.1029/2005pa001199.

Adkins, J. F. (2013), The Role of Deep Ocean Circulation in Setting Glacial Climates, *Paleoceanography*, 28(3), 539-561, doi: 10.1002/palo.20046.

Adkins, J. F., K. McIntyre, and D. P. Schrag (2002), The Salinity, Temperature, and Delta O-18 of the Glacial Deep Ocean, *Science*, 298(5599), doi: 10.1126/science.1076252.

Ahn, J., and E. Brook (2008), Atmospheric Co(2) and Climate on Millennial Time Scales During the Last Glacial Period, *Science*, 322(5898), 83-85, doi: 10.1126/science.1160832.

Allen, C. S., J. Pike, C. J. Pudsey, and A. Leventer (2005), Submillennial Variations in Ocean Conditions During Deglaciation Based on Diatom Assemblages from the Southwest Atlantic, *Paleoceanography*, 20(2), doi: 10.1029/2004pa001055.

Altabet, M. A. (1988), Variations in Nitrogen Isotopic Composition between Sinking and Suspended Particles - Implications for Nitrogen Cycling and Particle Transformation in the Open Ocean, *Deep-Sea Research Part a-Oceanographic Research Papers*, 35(4), 535-554, doi: 10.1016/0198-0149(88)90130-6.

Altabet, M., and R. Francois (1994), Sedimentary Nitrogen Isotopic Ratio as a Recorder for Surface Ocean Nitrate Utilization, *Global Biogeochemical Cycles*, 8(1), 103-116, doi: 10.1029/93GB03396.

Altabet, M. A., and R. Francois (2001), Nitrogen Isotope Biogeochemistry of the Antarctic Polar Frontal Zone at 170 Degrees W, *Deep-Sea Research Part II-Topical Studies in Oceanography*, 48(19-20), 4247-4273, doi: 10.1016/s0967-0645(01)00088-1.

Altabet, M. A., M. J. Higginson, and D. W. Murray (2002), The Effect of Millennial-Scale Changes in Arabian Sea Denitrification on Atmospheric CO<sub>2</sub>, *Nature*, 415(6868), doi: 10.1038/415159a.

Altabet, M., W. Deuser, S. Honjo, and C. Stienen (1991), Seasonal and Depth-Related Changes in the Source of Sinking Particles in the North-Atlantic, *Nature*, 354(6349), 136-139, doi: 10.1038/354136a0.

Altabet, M. A., C. Pilskaln, R. Thunell, C. Pride, D. Sigman, F. Chavez, and R. Francois (1999), The Nitrogen Isotope Biogeochemistry of Sinking Particles from the Margin of the Eastern North Pacific, *Deep-Sea Research Part I-Oceanographic Research Papers*, 46(4), 655-679, doi: 10.1016/s0967-0637(98)00084-3.

Anand, P., H. Elderfield, and M. H. Conte (2003), Calibration of Mg/Ca Thermometry in Planktonic Foraminifera from a Sediment Trap Time Series, *Paleoceanography*, 18(2), doi: 10.1029/2002kpa000846.

Andersen, K. K., et al. (2004), High-Resolution Record of Northern Hemisphere Climate Extending into the Last Interglacial Period, *Nature*, 431(7005), doi: 10.1038/nature02805.

Anderson, D. M., and D. Archer (2002), Glacial-Interglacial Stability of Ocean Ph Inferred from Foraminifer Dissolution Rates, *Nature*, 416(6876), doi: 10.1038/416070a.

Anderson, R. F., Z. Chase, M. Q. Fleisher, and J. Sachs (2002), The Southern Ocean's Biological Pump During the Last Glacial Maximum, *Deep-Sea Research Part II-Topical Studies in Oceanography*, 49(9-10), doi: 10.1016/s0967-0645(02)00018-8.

Anderson, R., S. Ali, L. Bradtmiller, S. Nielsen, M. Fleisher, B. Anderson, and L. Burckle (2009), Wind-Driven Upwelling in the Southern Ocean and the Deglacial Rise in Atmospheric CO<sub>2</sub>, *Science*, 323(5920), 1443-1448, doi: 10.1126/science.1167441.

Archer, D. (2005), Fate of Fossil Fuel CO<sub>2</sub> in Geologic Time, *Journal of Geophysical Research-Oceans*, 110(C9), doi: 10.1029/2004jc002625.

Archer, D., and E. Maierreimer (1994), Effect of Deep-Sea Sedimentary Calcite Preservation on Atmospheric CO<sub>2</sub> Concentration, *Nature*, 367(6460), 260-263, doi: 10.1038/367260a0.

Archer, D., and V. Brovkin (2008), The Millennial Atmospheric Lifetime of Anthropogenic CO<sub>2</sub>, *Climatic Change*, 90(3), doi: 10.1007/s10584-008-9413-1.

Archer, D., A. Winguth, D. Lea, and N. Mahowald (2000), What Caused the Glacial/Interglacial Atmospheric Pco(2) Cycles?, *Reviews of Geophysics*, 38(2), 159-189, doi: 10.1029/1999RG000066.

Archer, D. E., P. A. Martin, J. Milovich, V. Brovkin, G. K. Plattner, and C. Ashendel (2003), Model Sensitivity in the Effect of Antarctic Sea Ice and Stratification on Atmospheric Pco(2), *Paleoceanography*, 18(1), doi: 10.1029/2002pa000760.

Arhan, M., H. Mercier, and Y. H. Park (2003), On the Deep Water Circulation of the Eastern South Atlantic Ocean, *Deep-Sea Research Part I-Oceanographic Research Papers*, 50(7), 889-916, doi: 10.1016/s0967-0637(03)00072-4.

Augustin, L., et al. (2004), Eight Glacial Cycles from an Antarctic Ice Core, *Nature*, 429(6992), doi: 10.1038/nature02599.

Bailey, G. W., and J. Rogers (1997), Chemical Oceanography and Marine Geoscience Off Southern Africa: Past Discoveries in the Post-Gilchrist Era, and Future Prospects, *Transactions of the Royal Society of South Africa*, 52, 51-79.

Baker, A. R., and T. D. Jickells (2017), Atmospheric Deposition of Soluble Trace Elements Along the Atlantic Meridional Transect (Amt), *Progress in Oceanography*, 158, 41-51, doi: 10.1016/j.pocean.2016.10.002.

Barbante, C., et al. (2006), One-to-One Coupling of Glacial Climate Variability in Greenland and Antarctica, *Nature*, 444(7116), 195-198, doi: 10.1038/nature05301.

Bard, E., and R. Rickaby (2009), Migration of the Subtropical Front as a Modulator of Glacial Climate, *Nature*, 460(7253), 380-U393, doi: 10.1038/nature08189.

Barker, S., and H. Elderfield (2002), Foraminiferal Calcification Response to Glacial-Interglacial Changes in Atmospheric CO<sub>2</sub>, *Science*, 297(5582), doi: 10.1126/science.1072815.

Barker, P., and E. Thomas (2004), Origin, Signature and Palaeoclimatic Influence of the Antarctic Circumpolar Current, *Earth-Science Reviews*, 66(1-2), 143-162, doi: 10.1016/j.earscirev.2003.10.003.

Barker, S., and P. Diz (2014), Timing of the Descent into the Last Ice Age Determined by the Bipolar Seesaw, *Paleoceanography*, 29(6), 489-507, doi:

10.1002/2014pa002623.

Barker, S., M. Greaves, and H. Elderfield (2003), A Study of Cleaning Procedures Used for Foraminiferal Mg/Ca Paleothermometry, *Geochemistry Geophysics Geosystems*, 4, doi: 10.1029/2003gc000559.

Barker, S., G. Knorr, M. J. Vautravers, P. Diz, and L. C. Skinner (2010), Extreme Deepening of the Atlantic Overturning Circulation During Deglaciation, *Nature Geoscience*, 3(8), doi: 10.1038/ngeo921.

Barker, S., P. Diz, M. Vautravers, J. Pike, G. Knorr, I. Hall, and W. Broecker (2009), Interhemispheric Atlantic Seesaw Response During the Last Deglaciation, *Nature*, 457(7233), 1097-U1050, doi: 10.1038/nature07770.

Barker, S., G. Knorr, R. L. Edwards, F. Parrenin, A. E. Putnam, L. C. Skinner, E. Wolff, and M. Ziegler (2011), 800,000 Years of Abrupt Climate Variability, *Science*, 334(6054), 347-351, doi: 10.1126/science.1203580.

Barnola, J., D. Raynaud, Y. Korotkevich, and C. Lorius (1987), Vostok Ice Core Provides 160,000-Year Record of Atmospheric CO<sub>2</sub>, *Nature*, 329(6138), 408-414, doi: 10.1038/329408a0.

Bar-Or, R., C. Erlick, and H. Gildor (2008), The Role of Dust in Glacial-Interglacial Cycles, *Quaternary Science Reviews*, 27(3-4), doi: 10.1016/j.quascirev.2007.10.015.

Basile, I., F. Grousset, M. Revel, J. Petit, P. Biscaye, and N. Barkov (1997), Patagonian Origin of Glacial Dust Deposited in East Antarctica (Vostok and Dome C) During Glacial Stages 2, 4 and 6, *Earth and Planetary Science Letters*, 146(3-4), 573-589, doi: 10.1016/S0012-821X(96)00255-5.

Baturin, G.N. (1988), *The Geochemistry of Manganese and Manganese Nodules in the Ocean*, *Sedimentology and Petroleum Geology*, vol 2. Springer, Dordrecht

Bé, A. W. (1968), Shell Porosity of Recent Planktonic Foraminifera as a Climatic Index, *Science*, 161(3844), 881-884, doi: 10.1126/science.161.3844.881.

Bé, A. W. (1977), An ecological, zoogeographic, and taxonomic review of recent planktonic foraminifera, in Ramsay, A. T. S. (ed.), *Oceanic Micropalaeontology*, Academic Press, London, 1-100.

Bé, A.W., and Tolderlund, D.S. (1971), Distribution and ecology of living planktonic foraminifera in surface waters of the Atlantic and Indian Oceans, in Funnel, B.M. and Riedel, W.R. (eds.), *The Micropaleontology of Oceans*, 105-149.

Bé, A. W., Hemleben C., Anderson O. R., and Spindler M. (1979), Chamber formation in planktonic foraminifera, *Micropaleontology*, 25, 294–307.

Beal, L. M., W. P. M. De Ruijter, A. Biastoch, R. Zahn, and S. W. I. W. Grp (2011), On the Role of the Agulhas System in Ocean Circulation and Climate, *Nature*, 472(7344), 429-436, doi: 10.1038/nature09983.

Becquey, S., and R. Gersonde (2002), Past Hydrographic and Climatic Changes in the Subantarctic Zone of the South Atlantic - the Pleistocene Record from Odp Site 1090, *Palaeogeography Palaeoclimatology Palaeoecology*, 182(3-4), doi: 10.1016/s0031-0182(01)00497-7.

Belkin, I. M., and A. L. Gordon (1996), Southern Ocean Fronts from the Greenwich Meridian to Tasmania, *Journal of Geophysical Research-Oceans*, 101(C2), 3675-3696, doi: 10.1029/95jc02750.

Bemis, B. E., H. J. Spero, J. Bijma, and D. W. Lea (1998), Reevaluation of the Oxygen Isotopic Composition of Planktonic Foraminifera: Experimental Results and Revised Paleotemperature Equations, *Paleoceanography*, 13(2), 150-160, doi: 10.1029/98pa00070.

Bender, M. M. (1971), Variations in C-13/C-12 Ratios of Plants in Relation to Pathway of Photosynthetic Carbon Dioxide Fixation, *Phytochemistry*, 10(6), 1239-&, doi: 10.1016/s0031-9422(00)84324-1.

Bender, M. L., K. A. Fanning, P. N. Froelich, G. R. Heath, and V. Maynard (1977), Interstitial Nitrate Profiles and Oxidation of Sedimentary Organic-Matter in Eastern Equatorial Atlantic, *Science*, 198(4317), 605-609, doi: 10.1126/science.198.4317.605.

Berger, A. L. (1978), Long-Term Variations of Daily Insolation and Quaternary Climatic Changes, *Journal of the Atmospheric Sciences*, 35(12), 2362-2367, doi: 10.1175/1520-0469(1978)035<2362:ltvodi>2.0.co;2.

Berger, A. (1988), Milankovitch Theory and Climate, *Reviews of Geophysics*, 26(4),

624-657, doi: 10.1029/RG026i004p00624.

Bian, N. X., and P. A. Martin (2010), Investigating the Fidelity of Mg/Ca and Other Elemental Data from Reductively Cleaned Planktonic Foraminifera, *Paleoceanography*, 25, doi: 10.1029/2009pa001796.

Biastoch, A., C. W. Boening, and J. R. E. Lutjeharms (2008), Agulhas Leakage Dynamics Affects Decadal Variability in Atlantic Overturning Circulation, *Nature*, 456(7221), 489-492, doi: 10.1038/nature07426.

Biastoch, A., L. M. Beal, J. R. E. Lutjeharms, and T. G. D. Casal (2009), Variability and Coherence of the Agulhas Undercurrent in a High-Resolution Ocean General Circulation Model, *Journal of Physical Oceanography*, 39(10), 2417-2435, doi: 10.1175/2009jpo4184.1.

Bigg, G. R., and E. J. Rohling (2000), An Oxygen Isotope Data Set for Marine Waters, *Journal of Geophysical Research-Oceans*, 105(C4), 8527-8535, doi: 10.1029/2000jc900005.

Blain, S., et al. (2007), Effect of Natural Iron Fertilization on Carbon Sequestration in the Southern Ocean, *Nature*, 446(7139), 1070-U1071, doi: 10.1038/nature05700.

Boiteau, R., M. Greaves, and H. Elderfield (2012), Authigenic Uranium in Foraminiferal Coatings: A Proxy for Ocean Redox Chemistry, *Paleoceanography*, 27, doi: 10.1029/2012pa002335.

Bonn, W. J., F. X. Gingele, H. Grobe, A. Mackensen, and D. K. Futterer (1998), Palaeoproductivity at the Antarctic Continental Margin: Opal and Barium Records for the Last 400 Ka, *Palaeogeography Palaeoclimatology Palaeoecology*, 139(3-4), doi: 10.1016/s0031-0182(97)00144-2.

Bopp, L., K. E. Kohfeld, C. Le Quere, and O. Aumont (2003), Dust Impact on Marine Biota and Atmospheric CO<sub>2</sub> During Glacial Periods, *Paleoceanography*, 18(2), doi: 10.1029/2002pa000810.

Bostock, H. C., B. N. Opdyke, and M. J. M. Williams (2010), Characterising the Intermediate Depth Waters of the Pacific Ocean Using Delta C-13 and Other Geochemical Tracers, *Deep-Sea Research Part I-Oceanographic Research Papers*, 57(7), 847-

859, doi: 10.1016/j.dsr.2010.04.005.

Boyd, P., et al. (2007), Mesoscale Iron Enrichment Experiments 1993-2005: Synthesis and Future Directions, *Science*, 315(5812), 612-617, doi: 10.1126/science.1131669.

Boyle, E. A. (1983), Manganese Carbonate Overgrowths on Foraminifera Tests, *Geochimica Et Cosmochimica Acta*, 47(10), 1815-1819, doi: 10.1016/0016-7037(83)90029-7.

Boyle, E. A. (1988), Cadmium: Chemical Tracer of Deepwater Paleoceanography, *Paleoceanography*, 3(4), doi: 10.1029/PA003i004p00471.

Boyle, E. (1988), Vertical Oceanic Nutrient Fractionation and Glacial Interglacial CO<sub>2</sub> Cycles, *Nature*, 331(6151), 55-56, doi: 10.1038/331055a0.

Boyle, E. A. (1992), Cadmium and Delta-C-13 Paleochemical Ocean Distributions During the Stage-2 Glacial Maximum, *Annual Review of Earth and Planetary Sciences*, 20, 245-287.

Boyle, E. A., and L. D. Keigwin (1985), Comparison of Atlantic and Pacific Paleochemical Records for the Last 215,000 Years - Changes in Deep Ocean Circulation and Chemical Inventories, *Earth and Planetary Science Letters*, 76(1-2), 135-150, doi: 10.1016/0012-821x(85)90154-2.

Boyle, E., and Y. Rosenthal (1996), Chemical Hydrography of the South Atlantic During the Last Glacial Maximum: Cd Vs. Delta C-13, *South Atlantic: Present and Past Circulation*, 423-443.

Boyle, E. A., F. Sclater, and J. M. Edmond (1976), Marine Geochemistry of Cadmium, *Nature*, 263(5572), 42-44, doi: 10.1038/263042a0.

Bradt Miller, L., R. Anderson, M. Fleisher, and L. Burckle (2006), Diatom Productivity in the Equatorial Pacific Ocean from the Last Glacial Period to the Present: A Test of the Silicic Acid Leakage Hypothesis, *Paleoceanography*, 21(4), doi: 10.1029/2006PA001282.

Brandes, J. A., and A. H. Devol (2002), A Global Marine-Fixed Nitrogen Isotopic Budget: Implications for Holocene Nitrogen Cycling, *Global Biogeochemical Cycles*, 16(4), doi: 10.1029/2001gb001856.

- Brassell, S. C., G. Eglinton, I. T. Marlowe, U. Pflaumann, and M. Sarnthein (1986), Molecular Stratigraphy - a New Tool for Climatic Assessment, *Nature*, 320(6058), 129-133, doi: 10.1038/320129a0.
- Broecker, W. (1982), Glacial to Interglacial Changes in Ocean Chemistry, *Progress in Oceanography*, 11(2), 151-197, doi: 10.1016/0079-6611(82)90007-6.
- Broecker, W. S. (1982), Ocean Chemistry During Glacial Time, *Geochimica Et Cosmochimica Acta*, 46(10), 1689-1705, doi: 10.1016/0016-7037(82)90110-7.
- Broecker, W. S. (1987), The biggest chill, *Natural History*, Vol. 96 Issue 10, p74.
- Broecker, W. S. (1991), The great ocean conveyor, *Oceanography* 4(2):79–89.
- Broecker, W. S. (1998), Paleocean Circulation During the Last Deglaciation: A Bipolar Seesaw?, *Paleoceanography*, 13(2), doi: 10.1029/97pa03707.
- Broecker, W. S., and T. H. Peng (1987), The Role of  $\text{CaCO}_3$  Compensation in the Glacial to Interglacial Atmospheric  $\text{CO}_2$  Change, *Global Biogeochemical Cycles*, 1(1), 15-29, doi: 10.1029/GB001i001p00015.
- Broecker, W. S., and Maier-Reimer, E. (1992), The influence of air and sea exchange on the carbon isotope distribution in the sea, *Global Biogeochemical Cycles*, 6, 315-320.
- Broecker, W. S., and Peng, T.-H. (1982), *Tracers in the Sea*, Eldigio Press, Palisades, New York.
- Broecker, W., and G. Henderson (1998), The Sequence of Events Surrounding Termination Ii and Their Implications for the Cause of Glacial-Interglacial  $\text{CO}_2$  Changes, *Paleoceanography*, 13(4), 352-364, doi: 10.1029/98PA00920.
- Brovkin, V., A. Ganopolski, D. Archer, and S. Rahmstorf (2007), Lowering of Glacial Atmospheric  $\text{CO}_2$  in Response to Changes in Oceanic Circulation and Marine Biogeochemistry, *Paleoceanography*, 22(4), doi: 10.1029/2006pa001380.
- Brzezinski, M., D. Nelson, V. Franck, and D. Sigmon (2001), Silicon Dynamics within an Intense Open-Ocean Diatom Bloom in the Pacific Sector of the Southern Ocean, *Deep-Sea Research Part II-Topical Studies in Oceanography*, 48(19-20), 3997-4018,

doi: 10.1016/S0967-0645(01)00078-9.

Brzezinski, M., C. Pride, V. Franck, D. Sigman, J. Sarmiento, K. Matsumoto, N. Gruber, G. Rau, and K. Coale (2002), A Switch from Si(OH)<sub>4</sub> to NO<sub>3</sub><sup>-</sup> Depletion in the Glacial Southern Ocean, *Geophysical Research Letters*, 29(12), doi: 10.1029/2001GL014349.

Buckley, M. W., and J. Marshall (2016), Observations, Inferences, and Mechanisms of the Atlantic Meridional Overturning Circulation: A Review, *Reviews of Geophysics*, 54(1), 5-63, doi: 10.1002/2015rg000493.

Burdige, D. J. (1993), The Biogeochemistry of Manganese and Iron Reduction in Marine-Sediments, *Earth-Science Reviews*, 35(3), 249-284, doi: 10.1016/0012-8252(93)90040-e.

Burke, A., and L. F. Robinson (2012), The Southern Ocean's Role in Carbon Exchange During the Last Deglaciation, *Science*, 335(6068), doi: 10.1126/science.1208163.

Burke, A., A. L. Stewart, J. F. Adkins, R. Ferrari, M. F. Jansen, and A. F. Thompson (2015), The Glacial Mid-Depth Radiocarbon Bulge and Its Implications for the Overturning Circulation, *Paleoceanography*, 30(7), 1021-1039, doi: 10.1002/2015pa002778.

Caley, T., J. Giraudeau, B. Malaize, L. Rossignol, and C. Pierre (2012), Agulhas Leakage as a Key Process in the Modes of Quaternary Climate Changes, *Proceedings of the National Academy of Sciences of the United States of America*, 109(18), 6835-6839, doi: 10.1073/pnas.1115545109.

Caley, T., F. J. C. Peeters, A. Biastoch, L. Rossignol, E. Van Sebille, J. Durgadoo, B. Malaize, J. Giraudeau, K. Arthur, and R. Zahn (2014), Quantitative Estimate of the Paleo-Agulhas Leakage, *Geophysical Research Letters*, 41(4), 1238-1246, doi: 10.1002/2014gl059278.

Caley, T., et al. (2011), High-Latitude Obliquity as a Dominant Forcing in the Agulhas Current System, *Climate of the Past*, 7(4), 1285-1296, doi: 10.5194/cp-7-1285-2011.

Calvert, S. E., and T. F. Pedersen (1996), *Sedimentary Geochemistry of Manganese:*

Implications for the Environment of Formation of Manganiferous Black Shales, *Economic Geology and the Bulletin of the Society of Economic Geologists*, 91(1), 36-47.

Calvo, E., C. Pelejero, P. De Deckker, and G. A. Logan (2007), Antarctic Deglacial Pattern in a 30 Kyr Record of Sea Surface Temperature Offshore South Australia, *Geophysical Research Letters*, 34(13), doi: 10.1029/2007gl029937.

Cappelli, E. L., M. Regenberg, A. Holbourn, W. Kuhnt, D. Garbe-Schonberg, and N. Andersen (2015), Refining C. Wuellerstorfi and H. Elegans Mg/Ca Temperature Calibrations, *Marine Micropaleontology*, 121, 70-84, doi: 10.1016/j.marmicro.2015.10.001.

Carpenter, E. J., H. R. Harvey, B. Fry, and D. G. Capone (1997), Biogeochemical Tracers of the Marine Cyanobacterium *Trichodesmium*, *Deep-Sea Research Part I-Oceanographic Research Papers*, 44(1), 27-38, doi: 10.1016/s0967-0637(96)00091-x.

Cassar, N., M. Bender, B. Barnett, S. Fan, W. Moxim, H. Levy, and B. Tilbrook (2007), The Southern Ocean Biological Response to Aeolian Iron Deposition, *Science*, 317(5841), 1067-1070, doi: 10.1126/science.1144602.

Charles, C. D., J. D. Wright, and R. G. Fairbanks (1993), Thermodynamic Influences on the Marine Carbon-Isotope Record, *Paleoceanography*, 8(6), 691-697, doi: 10.1029/93pa01803.

Charles, C. D., J. Lynch-Stieglitz, U. S. Ninnemann, and R. G. Fairbanks (1996), Climate Connections between the Hemisphere Revealed by Deep Sea Sediment Core Ice Core Correlations, *Earth and Planetary Science Letters*, 142(1-2), 19-27, doi: 10.1016/0012-821x(96)00083-0.

Charles, C. D., P. N. Froelich, M. A. Zibello, R. A. Mortlock, and J. J. Morley (1991), Biogenic Opal in Southern Ocean Sediments over the Last 450,000 Years: Implications for Surface Water Chemistry and Circulation, *Paleoceanography*, 6(6), doi: 10.1029/91pa02477.

Charles, C., K. Pahnke, R. Zahn, P. Mortyn, U. Ninnemann, and D. Hodell (2010), Millennial Scale Evolution of the Southern Ocean Chemical Divide, *Quaternary Science Reviews*, 29(3-4), 399-409, doi: 10.1016/j.quascirev.2009.09.021.

Chase, Z., R. F. Anderson, and M. Q. Fleisher (2001), Evidence from Authigenic Uranium for Increased Productivity of the Glacial Subantarctic Ocean, *Paleoceanography*, 16(5), doi: 10.1029/2000pa000542.

Chase, Z., R. F. Anderson, M. Q. Fleisher, and P. W. Kubik (2003), Accumulation of Biogenic and Lithogenic Material in the Pacific Sector of the Southern Ocean During the Past 40,000 Years, *Deep-Sea Research Part II-Topical Studies in Oceanography*, 50(3-4), doi: 10.1016/s0967-0645(02)00595-7.

Chen, P. J., J. M. Yu, and Z. D. Jin (2017), An Evaluation of Benthic Foraminiferal U/Ca and U/Mn Proxies for Deep Ocean Carbonate Chemistry and Redox Conditions, *Geochemistry Geophysics Geosystems*, 18(2), 617-630, doi: 10.1002/2016gc006730.

Cheng, H., R. L. Edwards, Y. J. Wan, X. G. Ko, Y. F. Ming, M. J. Kelly, X. F. Wang, C. D. Gallup, and W. G. Liu (2006), A Penultimate Glacial Monsoon Record from Hulu Cave and Two-Phase Glacial Terminations, *Geology*, 34(3), 217-220, doi: 10.1130/g22289.1.

Chevalier, M., and B. M. Chase (2015), Southeast African Records Reveal a Coherent Shift from High- to Low-Latitude Forcing Mechanisms Along the East African Margin across Last Glacial-Interglacial Transition, *Quaternary Science Reviews*, 125, 117-130, doi: 10.1016/j.quascirev.2015.07.009.

Clark, P. U., D. Archer, D. Pollard, J. D. Blum, J. A. Rial, V. Brovkin, A. C. Mix, N. G. Pisias, and M. Roy (2006), The Middle Pleistocene Transition: Characteristics, Mechanisms, and Implications for Long-Term Changes in Atmospheric PCO<sub>2</sub>, *Quaternary Science Reviews*, 25(23-24), 3150-3184, doi: 10.1016/j.quascirev.2006.07.008.

Cleroux, C., E. Cortijo, J. C. Duplessy, and R. Zahn (2007), Deep-Dwelling Foraminifera as Thermocline Temperature Recorders, *Geochemistry Geophysics Geosystems*, 8, doi: 10.1029/2006gc001474.

Cleroux, C., P. Demenocal, J. Arbuszewski, and B. Linsley (2013), Reconstructing the Upper Water Column Thermal Structure in the Atlantic Ocean, *Paleoceanography*, 28(3), 503-516, doi: 10.1002/palo.20050.

Cleroux, C., J. Lynch-Stieglitz, M. W. Schmidt, E. Cortijo, and J. C. Duplessy (2009),

Evidence for Calcification Depth Change of *Globorotalia Truncatulinoides* between Deglaciation and Holocene in the Western Atlantic Ocean, *Marine Micropaleontology*, 73(1-2), 57-61, doi: 10.1016/j.marmicro.2009.07.001.

Cleroux, C., E. Cortijo, P. Anand, L. Labeyrie, F. Bassinot, N. Caillon, and J. C. Duplessy (2008), Mg/Ca and Sr/Ca Ratios in Planktonic Foraminifera: Proxies for Upper Water Column Temperature Reconstruction, *Paleoceanography*, 23(3), doi: 10.1029/2007pa001505.

CLIMAP Project Members (1981), Seasonal reconstructions of the earth's surface at the last glacial maximum, Geological Society of America, Map and Chart Series, MC-36, 18.

Cline, J. D., and Kaplan, I. R. (1975), Isotopic fractionation of dissolved nitrate during denitrification in the eastern tropical north Pacific Ocean, *Marine Chemistry*, 3, 271-299.

Cochran, J. K., A. E. Carey, E. R. Sholkovitz, and L. D. Surprenant (1986), The Geochemistry of Uranium and Thorium in Coastal Marine-Sediments and Sediment Pore Waters, *Geochimica Et Cosmochimica Acta*, 50(5), 663-680, doi: 10.1016/0016-7037(86)90344-3.

Codispoti, L. A., J. A. Brandes, J. P. Christensen, A. H. Devol, S. W. A. Naqvi, H. W. Paerl, and T. Yoshinari (2001), The Oceanic Fixed Nitrogen and Nitrous Oxide Budgets: Moving Targets as We Enter the Anthropocene?, *Scientia Marina*, 65, 85-105.

Cooper, D. J., A. J. Watson, and P. D. Nightingale (1996), Large Decrease in Ocean-Surface CO<sub>2</sub> Fugacity in Response to in Situ Iron Fertilization, *Nature*, 383(6600), doi: 10.1038/383511a0.

Craig, H., and Gordon, L. I. (1965), Deuterium and oxygen 18 variations in the ocean and the marine atmosphere, in *Stable Isotopes in Oceanographic Studies and Paleotemperatures*, pages 9–130, Pisa, Italy, 1965. Laboratorio di Geologia Nucleate.

Cronan, D. S. (1975), Manganese Nodules and Other Ferromanganese Oxide Deposits from Atlantic Ocean, *Journal of Geophysical Research-Oceans and Atmospheres*, 80(27), 3831-3837, doi: 10.1029/JC080i027p03831.

Crosta, X., and A. Shemesh (2002), Reconciling Down Core Anticorrelation of Diatom Carbon and Nitrogen Isotopic Ratios from the Southern Ocean, *Paleoceanography*, 17(1), doi: 10.1029/2000pa000565.

Crosta, X., J. Pichon, and L. Burckle (1998), Reappraisal of Antarctic Seasonal Sea-Ice at the Last Glacial Maximum, *Geophysical Research Letters*, 25(14), 2703-2706, doi: 10.1029/98GL02012.

Crosta, X., J. Pichon, and L. Burckle (1998), Application of Modern Analog Technique to Marine Antarctic Diatoms: Reconstruction of Maximum Sea-Ice Extent at the Last Glacial Maximum, *Paleoceanography*, 13(3), 284-297, doi: 10.1029/98PA00339.

Crosta, X., A. Sturm, L. Armand, and J. J. Pichon (2004), Late Quaternary Sea Ice History in the Indian Sector of the Southern Ocean as Recorded by Diatom Assemblages, *Marine Micropaleontology*, 50(3-4), doi: 10.1016/s0377-8398(03)00072-0.

Crosta, X., A. Shemesh, J. Etourneau, R. Yam, I. Billy, and J. J. Pichon (2005), Nutrient Cycling in the Indian Sector of the Southern Ocean over the Last 50,000 Years, *Global Biogeochemical Cycles*, 19(3), doi: 10.1029/2004gb002344.

Cunningham, S. A., S. G. Alderson, B. A. King, and M. A. Brandon (2003), Transport and Variability of the Antarctic Circumpolar Current in Drake Passage, *Journal of Geophysical Research-Oceans*, 108(C5), doi: 10.1029/2001jc001147.

Curry, W. B., and T. J. Crowley (1987), The Delta C-13 of Equatorial Atlantic Surface Waters: Implications for Ice Age Pco(2) Levels, *Paleoceanography*, 2(5), 489-517, doi: 10.1029/PA002i005p00489.

Curry, W. B., and D. W. Oppo (2005), Glacial Water Mass Geometry and the Distribution of Delta C-13 of Sigma CO2 in the Western Atlantic Ocean, *Paleoceanography*, 20(1), doi: 10.1029/2004pa001021.

Curry, W., J. Duplessy, L. Labeyrie, and N. Shackleton (1988), Changes in the Distribution of Partial Derivative C-13 of Deep Water Sigma CO2 between the Last Glaciation and the Holocene, *Paleoceanography*, 3(3), 317-341, doi: 10.1029/PA003i003p00317.

d'Orbigny, A. D. (1839), Foraminifères, in Barker-Webb, P. and Berthelot, S. (eds.),

Histoire Naturelle des Iles Canaries, Zoologie, vol. 2, 119–146, Arthus Bertrand, Paris.

De Baar, H., et al. (2005), Synthesis of Iron Fertilization Experiments: From the Iron Age in the Age of Enlightenment, *Journal of Geophysical Research-Oceans*, 110(C9), doi: 10.1029/2004JC002601.

De Boer, A. M., D. M. Sigman, J. R. Toggweiler, and J. L. Russell (2007), Effect of Global Ocean Temperature Change on Deep Ocean Ventilation, *Paleoceanography*, 22(2), doi: 10.1029/2005pa001242.

De Boer, A. M., R. M. Graham, M. D. Thomas, and K. E. Kohfeld (2013), The Control of the Southern Hemisphere Westerlies on the Position of the Subtropical Front, *Journal of Geophysical Research-Oceans*, 118(10), 5669-5675, doi: 10.1002/jgrc.20407.

De Boyer Montegut, C., G. Madec, A. S. Fischer, A. Lazar, and D. Iudicone (2004), Mixed Layer Depth over the Global Ocean: An Examination of Profile Data and a Profile-Based Climatology, *Journal of Geophysical Research-Oceans*, 109(C12), doi: 10.1029/2004jc002378.

De La Rocha, C. L., M. A. Brzezinski, M. J. Deniro, and A. Shemesh (1998), Silicon-Isotope Composition of Diatoms as an Indicator of Past Oceanic Change, *Nature*, 395(6703), 680-683, doi: 10.1038/27174.

De Ruijter, W. P. M., A. Biastoch, S. S. Drijfhout, J. R. E. Lutjeharms, R. P. Matano, T. Pichevin, P. J. Van Leeuwen, and W. Weijer (1999), Indian-Atlantic Interocean Exchange: Dynamics, Estimation and Impact, *Journal of Geophysical Research-Oceans*, 104(C9), 20885-20910, doi: 10.1029/1998jc900099.

De Vargas, C., S. Renaud, H. Hilbrecht, and J. Pawlowski (2001), Pleistocene Adaptive Radiation in Globorotalia Truncatulinoides: Genetic, Morphologic, and Environmental Evidence, *Paleobiology*, 27(1), 104-125, doi: 10.1666/0094-8373(2001)027<0104:parigt>2.0.co;2.

Delange, G. J., B. Vanos, and R. Poorter (1992), Geochemical Composition and Inferred Accretion Rates of Sediments and Manganese Nodules from a Submarine Hill in the Madeira Abyssal-Plain, Eastern North-Atlantic, *Marine Geology*, 109(1-2), 171-194, doi: 10.1016/0025-3227(92)90227-9.

Delmas, R., J. Ascencio, and M. Legrand (1980), Polar Ice Evidence That Atmospheric CO<sub>2</sub> 20,000-Yr Bp Was 50-Percent of Present, *Nature*, 284(5752), 155-157, doi: 10.1038/284155a0.

Delmonte, B., I. Basile-Doelsch, J. Petit, V. Maggi, M. Revel-Rolland, A. Michard, E. Jagoutz, and F. Grousset (2004), Comparing the Epica and Vostok Dust Records During the Last 220,000 Years: Stratigraphical Correlation and Provenance in Glacial Periods, *Earth-Science Reviews*, 66(1-2), 63-87, doi: 10.1016/j.earscirev.2003.10.004.

Deuser, W. G., and E. H. Ross (1989), Seasonally Abundant Planktonic-Foraminifera of the Sargasso Sea - Succession, Deep-Water Fluxes, Isotopic Compositions, and Paleoceanographic Implications, *Journal of Foraminiferal Research*, 19(4), 268-293.

Deutsch, C., D. M. Sigman, R. C. Thunell, A. N. Meckler, and G. H. Haug (2004), Isotopic Constraints on Glacial/Interglacial Changes in the Oceanic Nitrogen Budget, *Global Biogeochemical Cycles*, 18(4), doi: 10.1029/2003gb002189.

Dickson, A. G. (1990), Thermodynamics of the Dissociation of Boric-Acid in Synthetic Seawater from 273.15-K to 318.15-K, *Deep-Sea Research Part a-Oceanographic Research Papers*, 37(5), 755-766, doi: 10.1016/0198-0149(90)90004-f.

Dickson, A. G., and F. J. Millero (1987), A Comparison of the Equilibrium-Constants for the Dissociation of Carbonic-Acid in Seawater Media, *Deep-Sea Research Part a-Oceanographic Research Papers*, 34(10), 1733-1743, doi: 10.1016/0198-0149(87)90021-5.

Diekmann, B. (2007), Sedimentary Patterns in the Late Quaternary Southern Ocean, *Deep-Sea Research Part II-Topical Studies in Oceanography*, 54(21-22), doi: 10.1016/j.dsr2.2007.07.025.

Difiore, P. J., D. M. Sigman, T. W. Trull, M. J. Lourey, K. Karsh, G. Cane, and R. Ho (2006), Nitrogen Isotope Constraints on Subantarctic Biogeochemistry, *Journal of Geophysical Research-Oceans*, 111(C8), doi: 10.1029/2005jc003216.

Diz, P., I. R. Hall, R. Zahn, and E. G. Molyneux (2007), Paleoceanography of the Southern Agulhas Plateau During the Last 150 Ka: Inferences from Benthic Foraminiferal Assemblages and Multispecies Epifaunal Carbon Isotopes, *Paleoceanography*, 22(4), doi: 10.1029/2007pa001511.

Dubois, N., and M. Kienast (2011), Spatial Reorganization in the Equatorial Divergence in the Eastern Tropical Pacific During the Last 150 Kyr, *Geophysical Research Letters*, 38, doi: 10.1029/2011gl048325.

Dubois, N., M. Kienast, S. Kienast, C. Normandeau, S. E. Calvert, T. D. Herbert, and A. Mix (2011), Millennial-Scale Variations in Hydrography and Biogeochemistry in the Eastern Equatorial Pacific over the Last 100 Kyr, *Quaternary Science Reviews*, 30(1-2), 210-223, doi: 10.1016/j.quascirev.2010.10.012.

Duplessy, J. C., N. J. Shackleton, R. G. Fairbanks, L. Labeyrie, D. Oppo, and N. Kallel (1988), Deepwater Source Variations During the Last Climatic Cycle and Their Impact on the Global Deepwater Circulation, *Paleoceanography*, 3(3), 343-360, doi: 10.1029/PA003i003p00343.

Durazzi, J. T. (1981), Stable-Isotope Studies of Planktonic-Foraminifera in North-Atlantic Core Tops, *Palaeogeography Palaeoclimatology Palaeoecology*, 33(1-3), 157-172, doi: 10.1016/0031-0182(81)90036-5.

Durgadoo, J. V., B. R. Loveday, C. J. C. Reason, P. Penven, and A. Biastoch (2013), Agulhas Leakage Predominantly Responds to the Southern Hemisphere Westerlies, *Journal of Physical Oceanography*, 43(10), 2113-2131, doi: 10.1175/jpo-d-13-047.1.

Dyez, K. A., R. Zahn, and I. R. Hall (2014), Multicentennial Agulhas Leakage Variability and Links to North Atlantic Climate During the Past 80,000 Years, *Paleoceanography*, 29(12), 1238-1248, doi: 10.1002/2014pa002698.

Eggleston, S., J. Schmitt, B. Bereiter, R. Schneider, and H. Fischer (2016), Evolution of the Stable Carbon Isotope Composition of Atmospheric CO<sub>2</sub> over the Last Glacial Cycle, *Paleoceanography*, 31(3), 434-452, doi: 10.1002/2015pa002874.

Elderfield, H., and R. Rickaby (2000), Oceanic Cd/P Ratio and Nutrient Utilization in the Glacial Southern Ocean, *Nature*, 405(6784), 305-310, doi: 10.1038/35012507.

Elderfield, H., and G. Ganssen (2000), Past Temperature and Delta O-18 of Surface Ocean Waters Inferred from Foraminiferal Mg/Ca Ratios, *Nature*, 405(6785), 442-445, doi: 10.1038/35013033.

Elderfield, H., C. J. Bertram, and J. Erez (1996), Biomineralization Model for the Incorporation of Trace Elements into Foraminiferal Calcium Carbonate, *Earth and Planetary Science Letters*, 142(3-4), 409-423, doi: 10.1016/0012-821x(96)00105-7.

Elderfield, H., J. Yu, P. Anand, T. Kiefer, and B. Nyland (2006), Calibrations for Benthic Foraminiferal Mg/Ca Paleothermometry and the Carbonate Ion Hypothesis, *Earth and Planetary Science Letters*, 250(3-4), 633-649, doi: 10.1016/j.epsl.2006.07.041.

Elderfield, H., P. Ferretti, M. Greaves, S. Crowhurst, I. N. McCave, D. Hodell, and A. M. Piotrowski (2012), Evolution of Ocean Temperature and Ice Volume through the Mid-Pleistocene Climate Transition, *Science*, 337(6095), 704-709, doi: 10.1126/science.1221294.

Elderfield, H., M. Greaves, S. Barker, I. R. Hall, A. Tripathi, P. Ferretti, S. Crowhurst, L. Booth, and C. Daunt (2010), A Record of Bottom Water Temperature and Seawater Delta O-18 for the Southern Ocean over the Past 440 Kyr Based on Mg/Ca of Benthic Foraminiferal *Uvigerina* Spp, *Quaternary Science Reviews*, 29(1-2), 160-169, doi: 10.1016/j.quascirev.2009.07.013.

Elsig, J., J. Schmitt, D. Leuenberger, R. Schneider, M. Eyer, M. Leuenberger, F. Joos, H. Fischer, and T. F. Stocker (2009), Stable Isotope Constraints on Holocene Carbon Cycle Changes from an Antarctic Ice Core, *Nature*, 461(7263), 507-510, doi: 10.1038/nature08393.

Emiliani, C. (1955), Pleistocene Temperatures, *Journal of Geology*, 63(6), 538-578.

Epstein, S., R. Buchsbaum, H. A. Lowenstam, and H. C. Urey (1953), Revised Carbonate-Water Isotopic Temperature Scale, *Geological Society of America Bulletin*, 64(11), 1315-1325, doi: 10.1130/0016-7606(1953)64[1315:rcits]2.0.co;2.

Erez, J., and S. Honjo (1981), Comparison of Isotopic Composition of Planktonic-Foraminifera in Plankton Tows, Sediment Traps and Sediments, *Palaeogeography Palaeoclimatology Palaeoecology*, 33(1-3), 129-156, doi: 10.1016/0031-0182(81)90035-3.

Ericson, D. B., G. Wollin, and J. Wollin (1954), Coiling Direction of *Globorotalia-Truncatulinoidea* in Deep-Sea Cores, *Deep-Sea Research*, 2(2), 152-158.

Fairbanks, R. G., P. H. Wiebe, and A. W. H. Be (1980), Vertical-Distribution and Isotopic Composition of Living Planktonic-Foraminifera in the Western North-Atlantic, *Science*, 207(4426), 61-63, doi: 10.1126/science.207.4426.61.

Fairbanks, R. G., R. A. Mortlock, T. C. Chiu, L. Cao, A. Kaplan, T. P. Guilderson, T. W. Fairbanks, A. L. Bloom, P. M. Grootes, and M. J. Nadeau (2005), Radiocarbon Calibration Curve Spanning 0 to 50,000 Years Bp Based on Paired Th-230/U-234/U-238 and C-14 Dates on Pristine Corals, *Quaternary Science Reviews*, 24(16-17), 1781-1796, doi: 10.1016/j.quascirev.2005.04.007.

Falkowski, P. G. (1997), Evolution of the Nitrogen Cycle and Its Influence on the Biological Sequestration of CO<sub>2</sub> in the Ocean, *Nature*, 387(6630), doi: 10.1038/387272a0.

Farrell, J., T. Pedersen, S. Calvert, and B. Nielsen (1995), Glacial-Interglacial Changes in Nutrient Utilization in the Equatorial Pacific-Ocean, *Nature*, 377(6549), 514-517, doi: 10.1038/377514a0.

Feldmeijer, W., B. Metcalfe, G. J. A. Brummer, and G. M. Ganssen (2015), Reconstructing the Depth of the Permanent Thermocline through the Morphology and Geochemistry of the Deep Dwelling Planktonic Foraminifer *Globorotalia truncatulinoides*, *Paleoceanography*, 30(1), 1-22, doi: 10.1002/2014pa002687.

Ferrari, R., M. F. Jansen, J. F. Adkins, A. Burke, A. L. Stewart, and A. F. Thompson (2014), Antarctic Sea Ice Control on Ocean Circulation in Present and Glacial Climates, *Proceedings of the National Academy of Sciences of the United States of America*, 111(24), 8753-8758, doi: 10.1073/pnas.1323922111.

Fischer, H., et al. (2010), The Role of Southern Ocean Processes in Orbital and Millennial CO<sub>2</sub> Variations - a Synthesis, *Quaternary Science Reviews*, 29(1-2), doi: 10.1016/j.quascirev.2009.06.007.

Fischer, H., et al. (2007), Reconstruction of Millennial Changes in Dust Emission, Transport and Regional Sea Ice Coverage Using the Deep Epica Ice Cores from the Atlantic and Indian Ocean Sector of Antarctica, *Earth and Planetary Science Letters*, 260(1-2), doi: 10.1016/j.epsl.2007.06.014.

Flores, J. A., R. Gersonde, and F. J. Sierro (1999), Pleistocene Fluctuations in the

Agulhas Current Retroflexion Based on the Calcareous Plankton Record, *Marine Micropaleontology*, 37(1), 1-22, doi: 10.1016/s0377-8398(99)00012-2.

Ford, H. L., Sosdian, S. M., Rosenthal, Y., and Raymo, M. E. (2016), Gradual and abrupt changes during the Mid-Pleistocene Transition', *Quaternary Science Reviews*, Volume 148, 222-233.

Foster, G. L. (2008), Seawater Ph, PCO<sub>2</sub> and Co<sub>32</sub>- Variations in the Caribbean Sea over the Last 130 Kyr: A Boron Isotope and B/Ca Study of Planktic Foraminifera, *Earth and Planetary Science Letters*, 271(1-4), doi: 10.1016/j.epsl.2008.04.015.

Francey, R. J., C. E. Allison, D. M. Etheridge, C. M. Trudinger, I. G. Enting, M. Leuenberger, R. L. Langenfelds, E. Michel, and L. P. Steele (1999), A 1000-Year High Precision Record of Delta C-13 in Atmospheric CO<sub>2</sub>, *Tellus Series B-Chemical and Physical Meteorology*, 51(2), 170-193, doi: 10.1034/j.1600-0889.1999.t01-1-00005.x.

Francois, R., M. Altabet, E. Yu, D. Sigman, M. Bacon, M. Frank, G. Bohrmann, G. Bareille, and L. Labeyrie (1997), Contribution of Southern Ocean Surface-Water Stratification to Low Atmospheric CO<sub>2</sub> Concentrations During the Last Glacial Period, *Nature*, 389(6654), 929-935, doi: 10.1038/40073.

Frank, M., R. Gersonde, M. R. Van Der Loeff, G. Bohrmann, C. C. Nurnberg, P. W. Kubik, M. Suter, and A. Mangini (2000), Similar Glacial and Interglacial Export Bioproductivity in the Atlantic Sector of the Southern Ocean: Multiproxy Evidence and Implications for Glacial Atmospheric CO<sub>2</sub>, *Paleoceanography*, 15(6), doi: 10.1029/2000pa000497.

Freeman, E., L. C. Skinner, C. Waelbroeck, and D. Hodell (2016), Radiocarbon Evidence for Enhanced Respired Carbon Storage in the Atlantic at the Last Glacial Maximum, *Nature Communications*, 7, doi: 10.1038/ncomms11998.

Froelich, P. N., G. P. Klinkhammer, M. L. Bender, N. A. Luedtke, G. R. Heath, D. Cullen, P. Dauphin, D. Hammond, B. Hartman, and V. Maynard (1979), Early Oxidation of Organic-Matter in Pelagic Sediments of the Eastern Equatorial Atlantic - Suboxic Diagenesis, *Geochimica Et Cosmochimica Acta*, 43(7), 1075-1090, doi: 10.1016/0016-7037(79)90095-4.

Gaiero, D. (2007), Dust Provenance in Antarctic Ice During Glacial Periods: From

Where in Southern South America?, *Geophysical Research Letters*, 34(17), doi: 10.1029/2007GL030520.

Galbraith, E. D., M. Kienast, T. F. Pedersen, and S. E. Calvert (2004), Glacial-Interglacial Modulation of the Marine Nitrogen Cycle by High-Latitude O<sub>2</sub> Supply to the Global Thermocline, *Paleoceanography*, 19(4), doi: 10.1029/2003pa001000.

Galbraith, E. D., S. L. Jaccard, T. F. Pedersen, D. M. Sigman, G. H. Haug, M. Cook, J. R. Southon, and R. Francois (2007), Carbon Dioxide Release from the North Pacific Abyss During the Last Deglaciation, *Nature*, 449(7164), doi: 10.1038/nature06227.

Galbraith, E. D., D. M. Sigman, L. F. Robinson, and T. F. Pedersen (2008), Nitrogen in past marine environments, in Capone, D. G., Bronk, D. A., Mulholland M. R., and Carpenter, E. J., (eds.), *Nitrogen in the Marine Environment*, Academic, San Diego, California, 2nd ed., pp. 1497–1535.

Ganeshram, R. S., T. F. Pedersen, S. E. Calvert, and J. W. Murray (1995), Large Changes in Oceanic Nutrient Inventories from Glacial to Interglacial Periods, *Nature*, 376(6543), doi: 10.1038/376755a0.

Ganssen, G. M., and D. Kroon (2000), The Isotopic Signature of Planktonic Foraminifera from Ne Atlantic Surface Sediments: Implications for the Reconstruction of Past Oceanic Conditions, *Journal of the Geological Society*, 157, 693-699.

Garzoli, S. L., and A. L. Gordon (1996), Origins and Variability of the Benguela Current, *Journal of Geophysical Research-Oceans*, 101(C1), 897-906, doi: 10.1029/95jc03221.

Gaspari, V., C. Barbante, G. Cozzi, P. Cescon, C. F. Boutron, P. Gabrielli, G. Capodaglio, C. Ferrari, J. R. Petit, and B. Delmonte (2006), Atmospheric Iron Fluxes over the Last Deglaciation: Climatic Implications, *Geophysical Research Letters*, 33(3), doi: 10.1029/2005gl024352.

Gersonde, R., X. Crosta, A. Abelmann, and L. Armand (2005), Sea-Surface Temperature and Sea Ice Distribution of the Southern Ocean at the Epilog Last Glacial Maximum - a Circum-Antarctic View Based on Siliceous Microfossil Records, *Quaternary Science Reviews*, 24(7-9), 869-896, doi: 10.1016/j.quascirev.2004.07.015.

Gherardi, J. M., L. Labeyrie, S. Nave, R. Francois, J. F. McManus, and E. Cortijo (2009), Glacial-Interglacial Circulation Changes Inferred from Pa-231/Th-230 Sedimentary Record in the North Atlantic Region, *Paleoceanography*, 24, doi: 10.1029/2008pa001696.

Gildor, H., and E. Tziperman (2001), Physical Mechanisms Behind Biogeochemical Glacial-Interglacial CO<sub>2</sub> Variations, *Geophysical Research Letters*, 28(12), doi: 10.1029/2000gl012571.

Gildor, H., E. Tziperman, and J. R. Toggweiler (2002), Sea Ice Switch Mechanism and Glacial-Interglacial CO<sub>2</sub> Variations, *Global Biogeochemical Cycles*, 16(3), doi: 10.1029/2001gb001446.

Gille, S. T. (1994), Mean Sea-Surface Height of the Antarctic Circumpolar Current from Geosat Data - Method and Application, *Journal of Geophysical Research-Oceans*, 99(C9), 18255-18273, doi: 10.1029/94jc01172.

Giraudeau, J. (2002), MD 128 / SWAF cruise, RV Marion Dufresne

Gordon, A. L. (1986), Inter-Ocean Exchange of Thermocline Water, *Journal of Geophysical Research-Oceans*, 91(C4), 5037-5046, doi: 10.1029/JC091iC04p05037.

Gordon, A. L. (1996), Comment on the South Atlantic's Role in the Global Circulation, *South Atlantic: Present and Past Circulation*, 121-124.

Gordon, A. L., and P. Lamont-Doherty Geological Observatory, N.Y. (1986), Is There a Global Scale Ocean Circulation?, *Eos, Transactions American Geophysical Union*, 67(9), 109-110, doi: 10.1029/EO067i009p00109.

Gordon, A. L., R. F. Weiss, W. M. Smethie, and M. J. Warner (1992), Thermocline and Intermediate Water Communication between the South-Atlantic and Indian Oceans, *Journal of Geophysical Research-Oceans*, 97(C5), 7223-7240, doi: 10.1029/92jc00485.

Gottschalk, J., L. C. Skinner, J. Lippold, H. Vogel, N. Frank, S. L. Jaccard, and C. Waelbroeck (2016), Biological and Physical Controls in the Southern Ocean on Past Millennial-Scale Atmospheric CO<sub>2</sub> Changes, *Nature Communications*, 7, doi: 10.1038/ncomms11539.

- Govin, A., U. Holzwarth, D. Heslop, L. F. Keeling, M. Zabel, S. Mulitza, J. A. Collins, and C. M. Chiessi (2012), Distribution of Major Elements in Atlantic Surface Sediments (36 Degrees N-49 Degrees S): Imprint of Terrigenous Input and Continental Weathering, *Geochemistry Geophysics Geosystems*, 13, doi: 10.1029/2011gc003785.
- Graham, R. M., and A. M. De Boer (2013), The Dynamical Subtropical Front, *Journal of Geophysical Research-Oceans*, 118(10), 5676-5685, doi: 10.1002/jgrc.20408.
- Grant, K. M., E. J. Rohling, M. Bar-Matthews, A. Ayalon, M. Medina-Elizalde, C. B. Ramsey, C. Satow, and A. P. Roberts (2012), Rapid Coupling between Ice Volume and Polar Temperature over the Past 150,000 Years, *Nature*, 491(7426), 744-747, doi: 10.1038/nature11593.
- Gruber, N. (2004), The Dynamics of the Marine Nitrogen Cycle and its Influence on Atmospheric CO<sub>2</sub> Variations, in Volume 40 of the series NATO Science Series, The Ocean Carbon Cycle and Climate, pp. 97-148.
- Gründlingh, M. L. (1983), On the course of the Agulhas Current, *South African Geographical Journal*, 65, 49-57.
- Guilderson, T. P., R. G. Fairbanks, and J. L. Rubenstone (1994), Tropical Temperature-Variations since 20,000 Years Ago - Modulating Interhemispheric Climate-Change, *Science*, 263(5147), doi: 10.1126/science.263.5147.663.
- Hain, M.P., Sigman, D.M. and Haug, G.H. (2014), 8.18 - The biological pump in the past, in Holland H. D., and Turekian, K. K. (eds.), *Treatise on Geochemistry (Second Edition), Volume 8: The Oceans and Marine Geochemistry*. Amsterdam, NL, Elsevier, 485-517.
- Hall, I. R., and I. N. McCave (2000), Palaeocurrent Reconstruction, Sediment and Thorium Focussing on the Iberian Margin over the Last 140 Ka, *Earth and Planetary Science Letters*, 178(1-2), 151-164, doi: 10.1016/s0012-821x(00)00068-6.
- Hall, I.R., and Zahn, R., (2004), Cruise Report RRS Charles Darwin Cruise 154: 13/12/2003 -10/01/2004, Durban to Cape Town, South Africa, Agulhas 'Leakage' and Abrupt Climate Change.
- Hall, I. R., I. N. McCave, N. J. Shackleton, G. P. Weedon, and S. E. Harris (2001),

Intensified Deep Pacific Inflow and Ventilation in Pleistocene Glacial Times, *Nature*, 412(6849), 809-812, doi: 10.1038/35090552.

Hall, I.R., Hemming, S.R., LeVay, L.J., and the Expedition 361 Scientists (2016), Expedition 361 Preliminary Report: South African Climates (Agulhas LGM Density Profile), International Ocean Discovery Program.

Harrison, K. G. (2000), Role of Increased Marine Silica Input on Paleo-Pco(2) Levels, *Paleoceanography*, 15(3), doi: 10.1029/1999pa000427.

Hasenfratz, A. P., A. Martinez-Garcia, S. L. Jaccard, D. Vance, M. Walle, M. Greaves, and G. H. Haug (2017), Determination of the Mg/Mn Ratio in Foraminiferal Coatings: An Approach to Correct Mg/Ca Temperatures for Mn-Rich Contaminant Phases, *Earth and Planetary Science Letters*, 457, 335-347, doi: 10.1016/j.epsl.2016.10.004.

Haug, G., D. Sigman, R. Tiedemann, T. Pedersen, and M. Sarnthein (1999), Onset of Permanent Stratification in the Subarctic Pacific Ocean, *Nature*, 401(6755), 779-782, doi: 10.1038/44550.

Hays, J. D., J. Imbrie, and N. J. Shackleton (1976), Variations in Earths Orbit - Pacesetter of Ice Ages, *Science*, 194(4270), 1121-1132, doi: 10.1126/science.194.4270.1121.

Hayward, B. W., et al. (2008), The Effect of Submerged Plateaux on Pleistocene Gyral Circulation and Sea-Surface Temperatures in the Southwest Pacific, *Global and Planetary Change*, 63(4), 309-316, doi: 10.1016/j.gloplacha.2008.07.003.

Headly, M. A., and J. P. Severinghaus (2007), A Method to Measure Kr/N-2 Ratios in Air Bubbles Trapped in Ice Cores and Its Application in Reconstructing Past Mean Ocean Temperature, *Journal of Geophysical Research-Atmospheres*, 112(D19), doi: 10.1029/2006jd008317.

Healey, S. L., R. C. Thunell, and B. H. Corliss (2008), The Mg/Ca-Temperature Relationship of Benthic Foraminiferal Calcite: New Core-Top Calibrations in the < 4 Degrees C Temperature Range, *Earth and Planetary Science Letters*, 272(3-4), 523-530, doi: 10.1016/j.epsl.2008.05.023.

Heinrich, H. (1988), Origin and Consequences of Cyclic Ice Rafting in the Northeast

Atlantic-Ocean During the Past 130,000 Years, *Quaternary Research*, 29(2), doi: 10.1016/0033-5894(88)90057-9.

Hemleben, C., M. Spindler, I. Breiting, and W. G. Deuser (1985), Field and Laboratory Studies on the Ontogeny and Ecology of Some Globorotaliid Species from the Sargasso Sea Off Bermuda, *Journal of Foraminiferal Research*, 15(4), 254-272.

Hemming, S. R. (2004), Heinrich Events: Massive Late Pleistocene Detritus Layers of the North Atlantic and Their Global Climate Imprint, *Reviews of Geophysics*, 42(1), doi: 10.1029/2003rg000128.

Higginson, M., and M. Altabet (2004), Initial Test of the Silicic Acid Leakage Hypothesis Using Sedimentary Biomarkers, *Geophysical Research Letters*, 31(18), doi: 10.1029/2004GL020511.

Ho, S. L., G. Mollenhauer, F. Lamy, A. Martinez-Garcia, M. Mohtadi, R. Gersonde, D. Hebbeln, S. Nunez-Ricardo, A. Rosell-Mele, and R. Tiedemann (2012), Sea Surface Temperature Variability in the Pacific Sector of the Southern Ocean over the Past 700 Kyr, *Paleoceanography*, 27, doi: 10.1029/2012pa002317.

Hodell, D. A., C. D. Charles, and F. J. Sierro (2001), Late Pleistocene Evolution of the Ocean's Carbonate System, *Earth and Planetary Science Letters*, 192(2), doi: 10.1016/s0012-821x(01)00430-7.

Hodell, D., K. Venz, C. Charles, and U. Ninnemann (2003), Pleistocene Vertical Carbon Isotope and Carbonate Gradients in the South Atlantic Sector of the Southern Ocean, *Geochemistry Geophysics Geosystems*, 4, doi: 10.1029/2002GC000367.

Honisch, B., N. G. Hemming, D. Archer, M. Siddall, and J. F. McManus (2009), Atmospheric Carbon Dioxide Concentration across the Mid-Pleistocene Transition, *Science*, 324(5934), 1551-1554, doi: 10.1126/science.1171477.

Horikawa, K., M. Minagawa, Y. Kato, M. Murayama, and S. Nagao (2006), N<sub>2</sub> Fixation Variability in the Oligotrophic Sulu Sea, Western Equatorial Pacific Region over the Past 83 Kyr, *Journal of Oceanography*, 62(4), 427-439, doi: 10.1007/s10872-006-0066-2.

Howard, W. R., and W. L. Prell (1992), Late Quaternary Surface Circulation of the

Southern Indian Ocean and Its Relationship to Orbital Variations, *Paleoceanography*, 7(1), 79-117, doi: 10.1029/91pa02994.

Hughen, K., S. Lehman, J. Southon, J. Overpeck, O. Marchal, C. Herring, and J. Turnbull (2004), C-14 Activity and Global Carbon Cycle Changes over the Past 50,000 Years, *Science*, 303(5655), doi: 10.1126/science.1090300.

Huon, S., F. E. Grousset, D. Burdloff, G. Bardoux, and A. Mariotti (2002), Sources of Fine-Sized Organic Matter in North Atlantic Heinrich Layers: Delta C-13 and Delta N-15 Tracers, *Geochimica Et Cosmochimica Acta*, 66(2), 223-239, doi: 10.1016/s0016-7037(01)00776-1.

Hut, G. (1987), Consultants' group meeting on stable isotope reference samples for geochemical and hydrological investigations, International Atomic Energy Agency (IAEA).

Ikehara, M., K. Kawamura, N. Ohkouchi, M. Murayama, T. Nakamura, and A. Taira (2000), Variations of Terrestrial Input and Marine Productivity in the Southern Ocean (48 Degrees S) During the Last Two Deglaciations, *Paleoceanography*, 15(2), 170-180, doi: 10.1029/1999PA000425.

Indermuhle, A., E. Monnin, B. Stauffer, T. Stocker, and M. Wahlen (2000), Atmospheric CO<sub>2</sub> Concentration from 60 to 20 Kyr Bp from the Taylor Dome Ice Core, Antarctica, *Geophysical Research Letters*, 27(5), 735-738, doi: 10.1029/1999GL010960.

Indermuhle, A., et al. (1999), Holocene Carbon-Cycle Dynamics Based on CO<sub>2</sub> Trapped in Ice at Taylor Dome, Antarctica, *Nature*, 398(6723), 121-126.

Ito, T., and M. Follows (2005), Preformed Phosphate, Soft Tissue Pump and Atmospheric CO<sub>2</sub>, *Journal of Marine Research*, 63(4), 813-839, doi: 10.1357/0022240054663231.

Jaccard, S. L., G. H. Haug, D. M. Sigman, T. F. Pedersen, H. R. Thierstein, and U. Rohl (2005), Glacial/Interglacial Changes in Subarctic North Pacific Stratification, *Science*, 308(5724), doi: 10.1126/science.1108696.

Jenkins, R., (1999), *X-Ray Fluorescence Spectroscopy*, Second Edition. Wiley &

Sons, New York.

Johnson, T. C., E. T. Brown, J. McManus, S. Barry, P. Barker, and F. Gasse (2002), A High-Resolution Paleoclimate Record Spanning the Past 25,000 Years in Southern East Africa, *Science*, 296(5565), 113-+, doi: 10.1126/science.1070057.

Jouzel, J., et al. (1993), Extending the Vostok Ice-Core Record of Paleoclimate to the Penultimate Glacial Period, *Nature*, 364(6436), 407-412, doi: 10.1038/364407a0.

Jouzel, J., et al. (2007), Orbital and Millennial Antarctic Climate Variability over the Past 800,000 Years, *Science*, 317(5839), 793-796, doi: 10.1126/science.1141038.

Jury, M. R., H. R. Valentine, and J. R. E. Lutjeharms (1993), Influence of the Agulhas Current on Summer Rainfall Along the Southeast Coast of South-Africa, *Journal of Applied Meteorology*, 32(7), 1282-1287, doi: 10.1175/1520-0450(1993)032<1282:iotaco>2.0.co;2.

Karsten, R. H., and J. Marshall (2002), Constructing the Residual Circulation of the Acc from Observations, *Journal of Physical Oceanography*, 32(12), doi: 10.1175/1520-0485(2002)032<3315:ctrcot>2.0.co;2.

Katz, A. (1973), Interaction of Magnesium with Calcite During Crystal-Growth at 25-90 Degrees C and One Atmosphere, *Geochimica Et Cosmochimica Acta*, 37(6), 1563-&, doi: 10.1016/0016-7037(73)90091-4.

Keeling, R., and B. Stephens (2001), Antarctic Sea Ice and the Control of Pleistocene Climate Instability, *Paleoceanography*, 16(1), 112-131, doi: 10.1029/2000PA000529.

Keigwin, L. D. (2004), Radiocarbon and Stable Isotope Constraints on Last Glacial Maximum and Younger Dryas Ventilation in the Western North Atlantic, *Paleoceanography*, 19(4), doi: 10.1029/2004pa001029.

Keigwin, L. D., and E. A. Boyle (1989), Late Quaternary Paleochemistry of High-Latitude Surface Waters, *Palaeogeography Palaeoclimatology Palaeoecology*, 73(1-2), 85-106, doi: 10.1016/0031-0182(89)90047-3.

Kemp, A. E. S., I. Grigorov, R. B. Pearce, and A. C. N. Garabato (2010), Migration of the Antarctic Polar Front through the Mid-Pleistocene Transition: Evidence and Cli-

matic Implications, *Quaternary Science Reviews*, 29(17-18), doi: 10.1016/j.quasci-rev.2010.04.027.

Kennett, J. P. (1968), *Globorotalia Truncatulinoides* as a Paleo-Oceanographic Index, *Science*, 159(3822), 1461-&, doi: 10.1126/science.159.3822.1461.

Kerr, J., R. Rickaby, J. M. Yu, H. Elderfield, and A. Y. Sadekov (2017), The Effect of Ocean Alkalinity and Carbon Transfer on Deep-Sea Carbonate Ion Concentration During the Past Five Glacial Cycles, *Earth and Planetary Science Letters*, 471, 42-53, doi: 10.1016/j.epsl.2017.04.042.

Key, R. M., A. Kozyr, C. L. Sabine, K. Lee, R. Wanninkhof, J. L. Bullister, R. A. Feely, F. J. Millero, C. Mordy, and T. H. Peng (2004), A Global Ocean Carbon Climatology: Results from Global Data Analysis Project (Glodap), *Global Biogeochemical Cycles*, 18(4), doi: 10.1029/2004gb002247.

Key, R.M., A. Olsen, S. van Heuven, S. K. Lauvset, A. Velo, X. Lin, C. Schirnick, A. Kozyr, T. Tanhua, M. Hoppema, S. Jutterström, R. Steinfeldt, E. Jeansson, M. Ishii, F. F. Perez, T. Suzuki. (2015), Global Ocean Data Analysis Project, Version 2 (GLODAPv2)', ORNL/CDIAC- 162, NDP-093. Carbon Dioxide Information Analysis Center, Oak Ridge National Laboratory, US Dept. of Energy, Oak Ridge, Tennessee. doi: 10.3334/CDIAC/OTG.NDP093\_GLODAPv2

Kienast, S., I. Hendy, J. Crusius, T. Pedersen, and S. Calvert (2004), Export Production in the Subarctic North Pacific over the Last 800 Kyr: No Evidence for Iron Fertilization?, *Journal of Oceanography*, 60(1), 189-203, doi: 10.1023/B:JOCE.0000038326.73943.aa.

Kienast, S., M. Kienast, S. Jaccard, S. Calvert, and R. Francois (2006), Testing the Silica Leakage Hypothesis with Sedimentary Opal Records from the Eastern Equatorial Pacific over the Last 150 Kyr, *Geophysical Research Letters*, 33(15), doi: 10.1029/2006GL026651.

Kim, S. T., and J. R. Oneil (1997), Equilibrium and Nonequilibrium Oxygen Isotope Effects in Synthetic Carbonates, *Geochimica Et Cosmochimica Acta*, 61(16), 3461-3475, doi: 10.1016/s0016-7037(97)00169-5.

Knorr, G., and G. Lohmann (2003), Southern Ocean Origin for the Resumption of

Atlantic Thermohaline Circulation During Deglaciation, *Nature*, 424(6948), 532-536, doi: 10.1038/nature01855.

Knorr, G., and G. Lohmann (2007), Rapid Transitions in the Atlantic Thermohaline Circulation Triggered by Global Warming and Meltwater During the Last Deglaciation, *Geochemistry Geophysics Geosystems*, 8, doi: 10.1029/2007gc001604.

Knox, F., and M. Mcelroy (1984), Changes in Atmospheric CO<sub>2</sub> - Influence of the Marine Biota at High-Latitude, *Journal of Geophysical Research-Atmospheres*, 89(ND3), 4629-4637, doi: 10.1029/JD089iD03p04629.

Kohfeld, K., and S. Harrison (2001), Dirtmap: The Geological Record of Dust, *Earth-Science Reviews*, 54(1-3), 81-114, doi: 10.1016/S0012-8252(01)00042-3.

Kohfeld, K. E., R. F. Anderson, and J. Lynch-Stieglitz (2000), Carbon Isotopic Disequilibrium in Polar Planktonic Foraminifera and Its Impact on Modern and Last Glacial Maximum Reconstructions, *Paleoceanography*, 15(1), 53-64, doi: 10.1029/1999pa900049.

Kohfeld, K. E., C. Le Quere, S. P. Harrison, and R. F. Anderson (2005), Role of Marine Biology in Glacial-Interglacial CO<sub>2</sub> Cycles, *Science*, 308(5718), doi: 10.1126/science.1105375.

Kohfeld, K. E., R. M. Graham, A. M. De Boer, L. C. Sime, E. W. Wolff, C. Le Quere, and L. Bopp (2013), Southern Hemisphere Westerly Wind Changes During the Last Glacial Maximum: Paleo-Data Synthesis, *Quaternary Science Reviews*, 68, 76-95, doi: 10.1016/j.quascirev.2013.01.017.

Kohler, P., and H. Fischer (2006), Simulating Low Frequency Changes in Atmospheric CO<sub>2</sub> During the Last 740 000 Years, *Climate of the Past*, 2(2), 57-78.

Kohler, P., H. Fischer, and J. Schmitt (2010), Atmospheric Delta(CO<sub>2</sub>)-C-13 and Its Relation to Pco(2) and Deep Ocean Delta C-13 During the Late Pleistocene, *Paleoceanography*, 25, doi: 10.1029/2008pa001703.

Koziol, A. M., and R. C. Newton (1995), Experimental Determination of the Reactions Magnesite Plus Quartz Equals Enstatite Plus CO<sub>2</sub> and Magnesite Equals Periclase Plus CO<sub>2</sub>, and Enthalpies of Formation of Enstatite and Magnesite, *American Mineralogist*,

80(11-12), 1252-1260.

Kubota, Y., K. Kimoto, T. Itaki, Y. Yokoyama, Y. Miyairi, and H. Matsuzaki (2015), Bottom Water Variability in the Subtropical Northwestern Pacific from 26 Kyr Bp to Present Based on Mg/Ca and Stable Carbon and Oxygen Isotopes of Benthic Foraminifera, *Climate of the Past*, 11(6), 803-824, doi: 10.5194/cp-11-803-2015.

Kuhlbrodt, T., A. Griesel, M. Montoya, A. Levermann, M. Hofmann, and S. Rahmstorf (2007), On the Driving Processes of the Atlantic Meridional Overturning Circulation, *Reviews of Geophysics*, 45(1), doi: 10.1029/2004rg000166.

Kumar, N., R. Gwiazda, R. Anderson, and P. Froelich (1993), Pa-231/Th-230 Ratios in Sediments as a Proxy for Past Changes in Southern-Ocean Productivity, *Nature*, 362(6415), 45-48, doi: 10.1038/362045a0.

Kumar, N., R. Anderson, R. Mortlock, P. Froelich, P. Kubik, B. Dittrichhannen, and M. Suter (1995), Increased Biological Productivity and Export Production in the Glacial Southern-Ocean, *Nature*, 378(6558), 675-680, doi: 10.1038/378675a0.

Lambeck, K., H. Rouby, A. Purcell, Y. Y. Sun, and M. Sambridge (2014), Sea Level and Global Ice Volumes from the Last Glacial Maximum to the Holocene, *Proceedings of the National Academy of Sciences of the United States of America*, 111(43), 15296-15303, doi: 10.1073/pnas.1411762111.

Lambert, F., B. Delmonte, J. Petit, M. Bigler, P. Kaufmann, M. Hutterli, T. Stocker, U. Ruth, J. Steffensen, and V. Maggi (2008), Dust-Climate Couplings over the Past 800,000 Years from the Epica Dome C Ice Core, *Nature*, 452(7187), 616-619, doi: 10.1038/nature06763.

Lamy, F., R. Gersonde, G. Winckler, O. Esper, A. Jaeschke, G. Kuhn, J. Ullermann, A. Martinez-Garcia, F. Lambert, and R. Kilian (2014), Increased Dust Deposition in the Pacific Southern Ocean During Glacial Periods, *Science*, 343(6169), 403-407, doi: 10.1126/science.1245424.

Lazarus, D., H. Hilbrecht, C. Spencercervato, and H. Thierstein (1995), Sympatric Speciation and Phyletic Change in *Globorotalia truncatulinoides*, *Paleobiology*, 21(1), 28-51.

- Lea, D. W., T. A. Mashiotta, and H. J. Spero (1999), Controls on Magnesium and Strontium Uptake in Planktonic Foraminifera Determined by Live Culturing, *Geochimica Et Cosmochimica Acta*, 63(16), 2369-2379, doi: 10.1016/s0016-7037(99)00197-0.
- Lear, C. H., H. Elderfield, and P. A. Wilson (2000), Cenozoic Deep-Sea Temperatures and Global Ice Volumes from Mg/Ca in Benthic Foraminiferal Calcite, *Science*, 287(5451), 269-272, doi: 10.1126/science.287.5451.269.
- Lear, C. H., Y. Rosenthal, and N. Slowey (2002), Benthic Foraminiferal Mg/Ca-Paleothermometry: A Revised Core-Top Calibration, *Geochimica Et Cosmochimica Acta*, 66(19), 3375-3387, doi: 10.1016/s0016-7037(02)00941-9.
- Lear, C. H., K. Billups, R. E. M. Rickaby, L. Diester-Haass, E. M. Mawbey, and S. M. Sosdian (2016), Breathing More Deeply: Deep Ocean Carbon Storage During the Mid-Pleistocene Climate Transition, *Geology*, 44(12), 1035-1038, doi: 10.1130/g38636.1.
- Lee, K., T. W. Kim, R. H. Byrne, F. J. Millero, R. A. Feely, and Y. M. Liu (2010), The Universal Ratio of Boron to Chlorinity for the North Pacific and North Atlantic Oceans, *Geochimica Et Cosmochimica Acta*, 74(6), 1801-1811, doi: 10.1016/j.gca.2009.12.027.
- Lefevre, N., and A. J. Watson (1999), Modeling the Geochemical Cycle of Iron in the Oceans and Its Impact on Atmospheric CO<sub>2</sub> Concentrations, *Global Biogeochemical Cycles*, 13(3), doi: 10.1029/1999gb900034.
- Legrande, A. N., J. Lynch-Stieglitz, and E. C. Farmer (2004), Oxygen Isotopic Composition of *Globorotalia Truncatulinoidea* as a Proxy for Intermediate Depth Density, *Paleoceanography*, 19(4), doi: 10.1029/2004pa001045.
- Leuenberger, M., U. Siegenthaler, and C. C. Langway (1992), Carbon Isotope Composition of Atmospheric CO<sub>2</sub> During the Last Ice-Age from an Antarctic Ice Core, *Nature*, 357(6378), 488-490, doi: 10.1038/357488a0.
- Li, Y. H., J. Bischoff, and G. Mathieu (1969), Migration of Manganese in Arctic Basin Sediment, *Earth and Planetary Science Letters*, 7(3), 265-&.
- Li, F., P. Ginoux, and V. Ramaswamy (2008), Distribution, Transport, and Deposition

of Mineral Dust in the Southern Ocean and Antarctica: Contribution of Major Sources, *Journal of Geophysical Research-Atmospheres*, 113(D10), doi: 10.1029/2007jd009190.

Lisiecki, L., and M. Raymo (2005), A Pliocene-Pleistocene Stack of 57 Globally Distributed Benthic Delta O-18 Records, *Paleoceanography*, 20(1), doi: 10.1029/2004PA001071.

Lisiecki, L. E., M. E. Raymo, and W. B. Curry (2008), Atlantic Overturning Responses to Late Pleistocene Climate Forcings, *Nature*, 456(7218), doi: 10.1038/nature07425.

Liu, K. K., and I. R. Kaplan (1989), The Eastern Tropical Pacific as a Source of N-15-Enriched Nitrate in Seawater Off Southern-California, *Limnology and Oceanography*, 34(5), 820-830.

Liu, Z. Y., and H. J. Yang (2003), Extratropical Control of Tropical Climate, the Atmospheric Bridge and Oceanic Tunnel, *Geophysical Research Letters*, 30(5), doi: 10.1029/2002gl016492.

Lohmann, G. P. (1992), Increasing Seasonal Upwelling in the Subtropical South-Atlantic over the Past 700,000 Yrs - Evidence from Deep-Living Planktonic-Foraminifera, *Marine Micropaleontology*, 19(1-2), 1-12, doi: 10.1016/0377-8398(92)90018-f.

Lohmann, G. P., and B. A. Malmgren (1983), Equatorward Migration of *Globorotalia Truncatulinoides* Ecophenotypes through the Late Pleistocene - Gradual Evolution or Ocean Change, *Paleobiology*, 9(4), 414-421.

Lohmann, G. P., and P. N. Schweitzer (1990), *Globorotalia Truncatulinoides*' Growth and Chemistry as Probes of the Past Thermocline: 1. Shell Size, *Paleoceanography*, 5(1), 55-75, doi: 10.1029/PA005i001p00055.

Lourantou, A., J. Chappellaz, J. M. Barnola, V. Masson-Delmotte, and D. Raynaud (2010), Changes in Atmospheric CO<sub>2</sub> and Its Carbon Isotopic Ratio During the Penultimate Deglaciation, *Quaternary Science Reviews*, 29(17-18), 1983-1992, doi: 10.1016/j.quascirev.2010.05.002.

Lourantou, A., J. V. Lavric, P. Kohler, J. M. Barnola, D. Paillard, E. Michel, D. Ray-

naud, and J. Chappellaz (2010), Constraint of the CO<sub>2</sub> Rise by New Atmospheric Carbon Isotopic Measurements During the Last Deglaciation, *Global Biogeochemical Cycles*, 24, doi: 10.1029/2009gb003545.

Lumpkin, R., and K. Speer (2007), Global Ocean Meridional Overturning, *Journal of Physical Oceanography*, 37(10), 2550-2562, doi: 10.1175/jpo3130.1.

Lund, D. C., J. F. Adkins, and R. Ferrari (2011), Abyssal Atlantic Circulation During the Last Glacial Maximum: Constraining the Ratio between Transport and Vertical Mixing, *Paleoceanography*, 26, doi: 10.1029/2010pa001938.

Luthi, D., et al. (2008), High-Resolution Carbon Dioxide Concentration Record 650,000-800,000 Years before Present, *Nature*, 453(7193), 379-382, doi: 10.1038/nature06949.

Lutjeharms, J. R. E. (1996), The Exchange of Water between the South Indian and South Atlantic Oceans, 125-162 pp.

Lutjeharms, J. R. E., (2006) 'The Agulhas Current', Berlin (Springer-Verlag).

Lutjeharms, J. R. E. (2007), Three Decades of Research on the Greater Agulhas Current, *Ocean Science*, 3(1), 129-147.

Lutjeharms, J. R. E., and R. C. Vanballegooyen (1988), The Retroflexion of the Agulhas Current, *Journal of Physical Oceanography*, 18(11), 1570-1583, doi: 10.1175/1520-0485(1988)018<1570:trotac>2.0.co;2.

Luyten, J. R., J. Pedlosky, and H. Stommel (1983), The Ventilated Thermocline, *Journal of Physical Oceanography*, 13(2), 292-309, doi: 10.1175/1520-0485(1983)013<0292:tvt>2.0.co;2.

Lynch-Stieglitz, J., and R. G. Fairbanks (1994), A Conservative Tracer for Glacial Ocean Circulation from Carbon-Isotope and Palaeo-Nutrient Measurements in Benthic Foraminifera, *Nature*, 369(6478), 308-310, doi: 10.1038/369308a0.

Lynch-Stieglitz, J., A. Vangeen, and R. G. Fairbanks (1996), Interocean Exchange of Glacial North Atlantic Intermediate Water: Evidence from Subantarctic Cd/Ca and Carbon Isotope Measurements, *Paleoceanography*, 11(2), 191-201, doi: 10.1029/95pa03772.

Lynch-Stieglitz, J., T. F. Stocker, W. S. Broecker, and R. G. Fairbanks (1995), The Influence of Air-Sea Exchange on the Isotopic Composition of Oceanic Carbon - Observations and Modeling, *Global Biogeochemical Cycles*, 9(4), 653-665, doi: 10.1029/95gb02574.

Lynch-Stieglitz, J., W. B. Curry, and N. Slowey (1999), A Geostrophic Transport Estimate for the Florida Current from the Oxygen Isotope Composition of Benthic Foraminifera, *Paleoceanography*, 14(3), 360-373, doi: 10.1029/1999pa900001.

Lynch-Stieglitz, J., et al. (2007), Atlantic Meridional Overturning Circulation During the Last Glacial Maximum, *Science*, 316(5821), doi: 10.1126/science.1137127.

Mackensen, A. (2001), Oxygen and Carbon Stable Isotope Tracers of Weddell Sea Water Masses: New Data and Some Paleooceanographic Implications, *Deep-Sea Research Part I-Oceanographic Research Papers*, 48(6), 1401-1422, doi: 10.1016/s0967-0637(00)00093-5.

Mackensen, A. (2012), Strong Thermodynamic Imprint on Recent Bottom-Water and Epibenthic Delta C-13 in the Weddell Sea Revealed: Implications for Glacial Southern Ocean Ventilation, *Earth and Planetary Science Letters*, 317, 20-26, doi: 10.1016/j.epsl.2011.11.030.

Mackensen, A., Grobe, H., Hubberten, H.-W., and Kuhn, G., (1994), Benthic foraminiferal assemblages and the  $\delta^{13}\text{C}$ -signal in the Atlantic sector of the Southern Ocean: glacial-to-interglacial contrasts, in Zahn, R., Pederson, T. F., Kaminiski, M. A., and Labeyrie, L., (eds.), *Carbon cycling in the glacial ocean: constraints on the ocean's role in global change*, Springer-Verlag, Berlin, Heidelberg, NATO ASI Series I17, 105-144.

Mackensen, A., M. Rudolph, and G. Kuhn (2001), Late Pleistocene Deep-Water Circulation in the Subantarctic Eastern Atlantic, *Global and Planetary Change*, 30(3-4), 197-229, doi: 10.1016/s0921-8181(01)00102-3.

Mackensen, A., H. W. Hubberten, N. Scheele, and R. Schlitzer (1996), Decoupling of Delta C-13(Sigma CO<sub>2</sub>) and Phosphate in Recent Weddell Sea Deep and Bottom Water: Implications for Glacial Southern Ocean Paleooceanography, *Paleoceanography*, 11(2), 203-215, doi: 10.1029/95pa03840.

Maher, B. A., and P. F. Dennis (2001), Evidence against Dust-Mediated Control of Glacial-Interglacial Changes in Atmospheric CO<sub>2</sub>, *Nature*, 411(6834), doi: 10.1038/35075543.

Mahowald, N., K. Kohfeld, M. Hansson, Y. Balkanski, S. P. Harrison, I. C. Prentice, M. Schulz, and H. Rodhe (1999), Dust Sources and Deposition During the Last Glacial Maximum and Current Climate: A Comparison of Model Results with Paleodata from Ice Cores and Marine Sediments, *Journal of Geophysical Research-Atmospheres*, 104(D13), doi: 10.1029/1999jd900084.

Makou, M. C., D. W. Oppo, and W. B. Curry (2010), South Atlantic Intermediate Water Mass Geometry for the Last Glacial Maximum from Foraminiferal Cd/Ca, *Paleoceanography*, 25, doi: 10.1029/2010pa001962.

Mangini, A., M. Jung, and S. Laukenmann (2001), What Do We Learn from Peaks of Uranium and of Manganese in Deep Sea Sediments?, *Marine Geology*, 177(1-2), 63-78, doi: 10.1016/s0025-3227(01)00124-4.

Marchitto, T. M. (2004), Lack of a Significant Temperature Influence on the Incorporation of Cd into Benthic Foraminiferal Tests, *Geochemistry Geophysics Geosystems*, 5, doi: 10.1029/2004gc000753.

Marchitto, T. M., and W. S. Broecker (2006), Deep Water Mass Geometry in the Glacial Atlantic Ocean: A Review of Constraints from the Paleonutrient Proxy Cd/Ca, *Geochemistry Geophysics Geosystems*, 7, doi: 10.1029/2006gc001323.

Marchitto, T. M., W. B. Curry, and D. W. Oppo (1998), Millennial-Scale Changes in North Atlantic Circulation since the Last Glaciation, *Nature*, 393(6685), doi: 10.1038/31197.

Marchitto, T. M., W. B. Curry, and D. W. Oppo (2000), Zinc Concentrations in Benthic Foraminifera Reflect Seawater Chemistry, *Paleoceanography*, 15(3), 299-306, doi: 10.1029/1999pa000420.

Marchitto, T. M., D. W. Oppo, and W. B. Curry (2002), Paired Benthic Foraminiferal Cd/Ca and Zn/Ca Evidence for a Greatly Increased Presence of Southern Ocean Water in the Glacial North Atlantic, *Paleoceanography*, 17(3), doi: 10.1029/2000pa000598.

Marchitto, T. M., J. Lynch-Stieglitz, and S. R. Hemming (2005), Deep Pacific  $\text{CaCO}_3$  Compensation and Glacial-Interglacial Atmospheric  $\text{CO}_2$ , *Earth and Planetary Science Letters*, 231(3-4), doi: 10.1016/j.epsl.2004.12.024.

Marchitto, T., S. Lehman, J. Ortiz, J. Fluckiger, and A. Van Geen (2007), Marine Radiocarbon Evidence for the Mechanism of Deglacial Atmospheric  $\text{CO}_2$  Rise, *Science*, 316(5830), 1456-1459, doi: 10.1126/science.1138679.

Marchitto, T. M., W. B. Curry, J. Lynch-Stieglitz, S. P. Bryan, K. M. Cobb, and D. C. Lund (2014), Improved Oxygen Isotope Temperature Calibrations for Cosmopolitan Benthic Foraminifera, *Geochimica Et Cosmochimica Acta*, 130, 1-11, doi: 10.1016/j.gca.2013.12.034.

Marino, G., R. Zahn, M. Ziegler, C. Purcell, G. Knorr, I. R. Hall, P. Ziveri, and H. Elderfield (2013), Agulhas Salt-Leakage Oscillations During Abrupt Climate Changes of the Late Pleistocene, *Paleoceanography*, 28(3), 599-606, doi: 10.1002/palo.20038.

Marinov, I., A. Gnanadesikan, J. R. Toggweiler, and J. L. Sarmiento (2006), The Southern Ocean Biogeochemical Divide, *Nature*, 441(7096), doi: 10.1038/nature04883.

Marshall, J., and K. Speer (2012), Closure of the Meridional Overturning Circulation through Southern Ocean Upwelling, *Nature Geoscience*, 5(3), 171-180, doi: 10.1038/ngeo1391.

Martin, J. (1990), Glacial-Interglacial  $\text{CO}_2$  Change: The Iron Hypothesis, *Paleoceanography*, 5(1), 1-13, doi: 10.1029/PA005i001p00001.

Martin, J. M., and M. Meybeck (1979), Elemental Mass-Balance of Material Carried by Major World Rivers, *Marine Chemistry*, 7(3), 173-206, doi: 10.1016/0304-4203(79)90039-2.

Martin, P. A., D. W. Lea, Y. Rosenthal, N. J. Shackleton, M. Sarnthein, and T. Papenfuss (2002), Quaternary Deep Sea Temperature Histories Derived from Benthic Foraminiferal Mg/Ca, *Earth and Planetary Science Letters*, 198(1-2), 193-209, doi: 10.1016/s0012-821x(02)00472-7.

Martinez, J. I. (1994), Late Pleistocene Paleoceanography of the Tasman Sea - Implications for the Dynamics of the Warm Pool in the Western Pacific, *Palaeogeography Palaeoclimatology Palaeoecology*, 112(1-2), 19-62, doi: 10.1016/0031-0182(94)90133-3.

Martinez, J. I. (1997), Decreasing Influence of Subantarctic Mode Water North of the Tasman Front over the Past 150 Kyr, *Palaeogeography Palaeoclimatology Palaeoecology*, 131(3-4), 355-364, doi: 10.1016/s0031-0182(97)00011-4.

Martinez, J. I., G. Mora, and T. T. Barrows (2007), Paleoceanographic Conditions in the Western Caribbean Sea for the Last 560 Kyr as Inferred from Planktonic Foraminifera, *Marine Micropaleontology*, 64(3-4), 177-188, doi: 10.1016/j.marmicro.2007.04.004.

Martinez-Boti, M. A., G. Marino, G. L. Foster, P. Ziveri, M. J. Henahan, J. W. B. Rae, P. G. Mortyn, and D. Vance (2015), Boron Isotope Evidence for Oceanic Carbon Dioxide Leakage During the Last Deglaciation, *Nature*, 518(7538), 219-U154, doi: 10.1038/nature14155.

Martinez-Garcia, A., A. Rosell-Mele, S. L. Jaccard, W. Geibert, D. M. Sigman, and G. H. Haug (2011), Southern Ocean Dust-Climate Coupling over the Past Four Million Years, *Nature*, 476(7360), doi: 10.1038/nature10310.

Martinez-Garcia, A., A. Rosell-Mele, W. Geibert, R. Gersonde, P. Masque, V. Gaspari, and C. Barbante (2009), Links between Iron Supply, Marine Productivity, Sea Surface Temperature, and CO<sub>2</sub> over the Last 1.1 Ma, *Paleoceanography*, 24, doi: 10.1029/2008pa001657.

Martinez-Garcia, A., D. M. Sigman, H. J. Ren, R. F. Anderson, M. Straub, D. A. Hodell, S. L. Jaccard, T. I. Eglinton, and G. H. Haug (2014), Iron Fertilization of the Subantarctic Ocean During the Last Ice Age, *Science*, 343(6177), 1347-1350, doi: 10.1126/science.1246848.

Martinez-Mendez, G., E. G. Molyneux, I. R. Hall, and R. Zahn (2009), Variable Water Column Structure of the South Atlantic on Glacial-Interglacial Time Scales, *Quaternary Science Reviews*, 28(27-28), 3379-3387, doi: 10.1016/j.quascirev.2009.09.022.

Martinez-Mendez, G., R. Zahn, I. R. Hall, L. D. Pena, and I. Cacho (2008), 345,000-

Year-Long Multi-Proxy Records Off South Africa Document Variable Contributions of Northern Versus Southern Component Water to the Deep South Atlantic, *Earth and Planetary Science Letters*, 267(1-2), 309-321, doi: 10.1016/j.epsl.2007.11.050.

Martinez-Mendez, G., R. Zahn, I. R. Hall, F. J. C. Peeters, L. D. Pena, I. Cacho, and C. Negre (2010), Contrasting Multiproxy Reconstructions of Surface Ocean Hydrography in the Agulhas Corridor and Implications for the Agulhas Leakage During the Last 345,000 Years, *Paleoceanography*, 25, doi: 10.1029/2009pa001879.

Mashiotta, T. A., D. W. Lea, and H. J. Spero (1997), Experimental Determination of Cadmium Uptake in Shells of the Planktonic Foraminifera *Orbulina Universa* and *Globigerina Bulloides*: Implications for Surface Water Paleoreconstructions, *Geochimica Et Cosmochimica Acta*, 61(19), 4053-4065, doi: 10.1016/s0016-7037(97)00206-8.

Matsumoto, K., J. L. Sarmiento, and M. A. Brzezinski (2002), Silicic Acid Leakage from the Southern Ocean: A Possible Explanation for Glacial Atmospheric Pco(2), *Global Biogeochemical Cycles*, 16(3), doi: 10.1029/2001gb001442.

Mawji, E., et al. (2015), The Geotraces Intermediate Data Product 2014, *Marine Chemistry*, 177, 1-8, doi: 10.1016/j.marchem.2015.04.005.

McCartney, M. S. (1975), Subantarctic Mode Water, *Transactions-American Geophysical Union*, 56(12), 1011-1011.

McCave, I. N., and I. R. Hall (2006), Size Sorting in Marine Muds: Processes, Pitfalls, and Prospects for Paleoflow-Speed Proxies, *Geochemistry Geophysics Geosystems*, 7, doi: 10.1029/2006gc001284.

McCave, I. N., B. Manighetti, and S. G. Robinson (1995), Sortable Silt and Fine Sediment Size Composition Slicing - Parameters for Paleocurrent Speed and Paleoceanography, *Paleoceanography*, 10(3), 593-610, doi: 10.1029/94pa03039.

McCave, I. N., D. J. R. Thornalley, and I. R. Hall (2017), Relation of Sortable Silt Grain-Size to Deep-Sea Current Speeds: Calibration of the 'Mud Current Meter', *Deep-Sea Research Part I-Oceanographic Research Papers*, 127, 1-12, doi: 10.1016/j.dsr.2017.07.003.

McCorkle, D. C., P. A. Martin, D. W. Lea, and G. P. Klinkhammer (1995), Evidence

of a Dissolution Effect on Benthic Foraminiferal Shell Chemistry - Delta-C-13, Cd/Ca, Ba/Ca, and Sr/Ca Results from the Ontong Java Plateau, *Paleoceanography*, 10(4), 699-714, doi: 10.1029/95pa01427.

McGee, D., W. S. Broecker, and G. Winckler (2010), Gustiness: The Driver of Glacial Dustiness?, *Quaternary Science Reviews*, 29(17-18), doi: 10.1016/j.quasci-rev.2010.06.009.

McKenna, V. S., and W. L. Prell (2004), Calibration of the Mg/Ca of *Globorotalia truncatulinoides* (R) for the Reconstruction of Marine Temperature Gradients, *Paleoceanography*, 19(2), doi: 10.1029/2000pa000604.

McManus, J. F., R. Francois, J. M. Gherardi, L. D. Keigwin, and S. Brown-Leger (2004), Collapse and Rapid Resumption of Atlantic Meridional Circulation Linked to Deglacial Climate Changes, *Nature*, 428(6985), doi: 10.1038/nature02494.

McManus, J., W. M. Berelson, G. P. Klinkhammer, D. E. Hammond, and C. Holm (2005), Authigenic Uranium: Relationship to Oxygen Penetration Depth and Organic Carbon Rain, *Geochimica Et Cosmochimica Acta*, 69(1), 95-108, doi: 10.1016/j.gca.2004.06.023.

Mehrbach, C., C. H. Culberson, J. E. Hawley, and R. M. Pytkowicz (1973), Measurement of Apparent Dissociation-Constants of Carbonic-Acid in Seawater at Atmospheric-Pressure, *Limnology and Oceanography*, 18(6), 897-907.

Meyers, S.R. (2014) 'Astrochron: An R Package for Astrochronology. <http://cran.r-project.org/package=astrochron>

Middelburg, J. J., C. H. Vanderweijden, and J. R. W. Woittiez (1988), Chemical Processes Affecting the Mobility of Major, Minor and Trace-Elements During Weathering of Granitic-Rocks, *Chemical Geology*, 68(3-4), 253-273, doi: 10.1016/0009-2541(88)90025-3.

Molyneux, E. G., I. R. Hall, R. Zahn, and P. Diz (2007), Deep Water Variability on the Southern Agulhas Plateau: Interhemispheric Links over the Past 170 Ka, *Paleoceanography*, 22(4), doi: 10.1029/2006pa001407.

Monnin, E., A. Indermuhle, A. Dallenbach, J. Fluckiger, B. Stauffer, T. Stocker, D.

- Raynaud, and J. Barnola (2001), Atmospheric CO<sub>2</sub> Concentrations over the Last Glacial Termination, *Science*, 291(5501), 112-114, doi: 10.1126/science.291.5501.112.
- Mook, W. G., J. C. Bommerson, and W. H. Staverman (1974), Carbon Isotope Fractionation between Dissolved Bicarbonate and Gaseous Carbon-Dioxide, *Earth and Planetary Science Letters*, 22(2), 169-176, doi: 10.1016/0012-821x(74)90078-8.
- Moreno, P. I., J. P. Francois, C. M. Moy, and R. Villa-Martinez (2010), Covariability of the Southern Westerlies and Atmospheric CO<sub>2</sub> During the Holocene, *Geology*, 38(8), doi: 10.1130/g30962.1.
- Mortlock, R., C. Charles, P. Froelich, M. Zibello, J. Saltzman, J. Hays, and L. Burckle (1991), Evidence for Lower Productivity in the Antarctic Ocean During the Last Glaciation, *Nature*, 351(6323), 220-223, doi: 10.1038/351220a0.
- Mucci, A. (1987), Influence of Temperature on the Composition of Magnesian Calcite Overgrowths Precipitated from Seawater, *Geochimica Et Cosmochimica Acta*, 51(7), 1977-1984, doi: 10.1016/0016-7037(87)90186-4.
- Mulitza, S., A. Durkoop, W. Hale, G. Wefer, and H. S. Niebler (1997), Planktonic Foraminifera as Recorders of Past Surface-Water Stratification, *Geology*, 25(4), 335-338, doi: 10.1130/0091-7613(1997)025<0335:pfarop>2.3.co;2.
- Munk, W., and C. Wunsch (1998), Abyssal Recipes Ii: Energetics of Tidal and Wind Mixing, *Deep-Sea Research Part I-Oceanographic Research Papers*, 45(12), 1977-2010, doi: 10.1016/s0967-0637(98)00070-3.
- Neftel, A., H. Oeschger, T. Staffelbach, and B. Stauffer (1988), CO<sub>2</sub> Record in the Byrd Ice Core 50,000-5,000 Years Bp, *Nature*, 331(6157), 609-611, doi: 10.1038/331609a0.
- Neftel, A., H. Oeschger, J. Schwander, B. Stauffer, and R. Zimbrunn (1982), Ice Core Sample Measurements Give Atmospheric CO<sub>2</sub> Content During the Past 40,000 Yr, *Nature*, 295(5846), 220-223, doi: 10.1038/295220a0.
- Neil, H. L., L. Carter, and M. Y. Morris (2004), Thermal Isolation of Campbell Plateau, New Zealand, by the Antarctic Circumpolar Current over the Past 130 Kyr, *Paleoceanography*, 19(4), doi: 10.1029/2003pa000975.

Ninnemann, U. S., and C. D. Charles (1997), Regional Differences in Quaternary Subantarctic Nutrient Cycling: Link to Intermediate and Deep Water Ventilation, *Paleoceanography*, 12(4), doi: 10.1029/97pa01032.

Ninnemann, U. S., and C. D. Charles (2002), Changes in the Mode of Southern Ocean Circulation over the Last Glacial Cycle Revealed by Foraminiferal Stable Isotopic Variability, *Earth and Planetary Science Letters*, 201(2), doi: 10.1016/s0012-821x(02)00708-2.

Nowlin, W. D., and J. M. Klinck (1986), The Physics of the Antarctic Circumpolar Current, *Reviews of Geophysics*, 24(3), 469-491, doi: 10.1029/RG024i003p00469.

Nurnberg, D., J. Bijma, and C. Hemleben (1996), Assessing the Reliability of Magnesium in Foraminiferal Calcite as a Proxy for Water Mass Temperatures, *Geochimica Et Cosmochimica Acta*, 60(5), 803-814, doi: 10.1016/0016-7037(95)00446-7.

Olbers, D., Gouretski, V. V., Seiß, G., Schröter, J., (1992), *Hydrographic Atlas of the Southern Ocean*, Alfred Wegener Institute for Polar and Marine Research, Bremerhaven, Germany & Arctic and Antarctic Research Institute, St. Petersburg, Russia: 17 pages, 82 plates.

Oliver, K. I. C., B. a. A. Hoogakker, S. Crowhurst, G. M. Henderson, R. E. M. Rickaby, N. R. Edwards, and H. Elderfield (2010), A Synthesis of Marine Sediment Core Delta C-13 Data over the Last 150 000 Years, *Climate of the Past*, 6(5), 645-673, doi: 10.5194/cp-6-645-2010.

Olsen, A., R. M. Key, S. van Heuven, S. K. Lauvset, A. Velo, X. Lin, C. Schirnick, A. Kozyr, T. Tanhua, M. Hoppema, S. Jutterström, R. Steinfeldt, E. Jeansson, M. Ishii, F. F. Pérez & T. Suzuki, (2016) The Global Ocean Data Analysis Project version 2 (GLODAPv2) - an internally consistent data product for the world ocean, *Earth System Science Data*, 8, 297-323. doi:10.5194/essd-8-297-2016.

Oomori, T., H. Kaneshima, Y. Maezato, and Y. Kitano (1987), Distribution Coefficient of Mg-2+ Ions between Calcite and Solution at 10-50-Degrees-C, *Marine Chemistry*, 20(4), 327-336, doi: 10.1016/0304-4203(87)90066-1.

Oppo, D. W., and R. G. Fairbanks (1987), Variability in the Deep and Intermediate Water Circulation of the Atlantic-Ocean During the Past 25,000 Years - Northern-

Hemisphere Modulation of the Southern-Ocean, *Earth and Planetary Science Letters*, 86(1), 1-15, doi: 10.1016/0012-821x(87)90183-x.

Oppo, D. W., and Y. Rosenthal (1994), Cd/Ca Changes in a Deep Cape Basin Core over the Past 730,000 Years - Response of Circumpolar Deep-Water Variability to Northern-Hemisphere Ice-Sheet Melting, *Paleoceanography*, 9(5), 661-675, doi: 10.1029/93pa02199.

Oppo, D. W., and M. Horowitz (2000), Glacial Deep Water Geometry: South Atlantic Benthic Foraminiferal Cd/Ca and Delta C-13 Evidence, *Paleoceanography*, 15(2), 147-160, doi: 10.1029/1999pa000436.

Oppo, D. W., R. G. Fairbanks, A. L. Gordon, and N. J. Shackleton (1990), Late Pleistocene Southern Ocean Delta C-13 Variability, *Paleoceanography*, 5(1), 43-54, doi: 10.1029/PA005i001p00043.

Orsi, A. H., T. Whitworth, and W. D. Nowlin (1995), On the Meridional Extent and Fronts of the Antarctic Circumpolar Current, *Deep-Sea Research Part I-Oceanographic Research Papers*, 42(5), 641-673, doi: 10.1016/0967-0637(95)00021-w.

Ostlund, H.G., Craig, H., Broecker, W.S., Spencer, D., (1987), *Geosecs Atlantic, Pacific, and Indian Ocean expeditions, Shorebased Data and Graphics*, National Science Foundation, 7.

Pahnke, K., R. Zahn, H. Elderfield, and M. Schulz (2003), 340,000-Year Centennial-Scale Marine Record of Southern Hemisphere Climatic Oscillation, *Science*, 301(5635), 948-952, doi: 10.1126/science.1084451.

Paillard, D. (2001), Glacial Cycles: Toward a New Paradigm, *Reviews of Geophysics*, 39(3), doi: 10.1029/2000rg000091.

Park, R., and S. Epstein (1960), Carbon Isotope Fractionation During Photosynthesis, *Geochimica Et Cosmochimica Acta*, 21(1-2), 110-126, doi: 10.1016/s0016-7037(60)80006-3.

Parnell, A. C., C. E. Buck, and T. K. Doan (2011), A Review of Statistical Chronology Models for High-Resolution, Proxy-Based Holocene Palaeoenvironmental Recon-

struction, *Quaternary Science Reviews*, 30(21-22), 2948-2960, doi: 10.1016/j.quasci-rev.2011.07.024.

Parrenin, F., et al. (2007), The Edc3 Chronology for the Epica Dome C Ice Core, *Climate of the Past*, 3(3), 485-497.

Pattan, J. N. (1993), Manganese Micronodules - a Possible Indicator of Sedimentary Environments, *Marine Geology*, 113(3-4), 331-344, doi: 10.1016/0025-3227(93)90026-r.

Peeters, F., R. Acheson, G. Brummer, W. De Ruijter, R. Schneider, G. Ganssen, E. Ufkes, and D. Kroon (2004), Vigorous Exchange between the Indian and Atlantic Oceans at the End of the Past Five Glacial Periods, *Nature*, 430(7000), 661-665, doi: 10.1038/nature02785.

Pena, L. D., I. Cacho, P. Ferretti, and M. A. Hall (2008), El Nino-Southern Oscillation-Like Variability During Glacial Terminations and Interlatitudinal Teleconnections, *Paleoceanography*, 23(3), doi: 10.1029/2008pa001620.

Pena, L. D., E. Calvo, I. Cacho, S. Eggins, and C. Pelejero (2005), Identification and Removal of Mn-Mg-Rich Contaminant Phases on Foraminiferal Tests: Implications for Mg/Ca Past Temperature Reconstructions, *Geochemistry Geophysics Geosystems*, 6, doi: 10.1029/2005gc000930.

Pepin, L., D. Raynaud, J. M. Barnola, and M. F. Loutre (2001), Hemispheric Roles of Climate Forcings During Glacial-Interglacial Transitions as Deduced from the Vostok Record and LIn-2d Model Experiments, *Journal of Geophysical Research-Atmospheres*, 106(D23), 31885-31892, doi: 10.1029/2001jd900117.

Peterson, R. G., and L. Stramma (1991), Upper-Level Circulation in the South-Atlantic Ocean, *Progress in Oceanography*, 26(1), 1-73, doi: 10.1016/0079-6611(91)90006-8.

Petit, J. R., et al. (1999), Climate and Atmospheric History of the Past 420,000 Years from the Vostok Ice Core, Antarctica, *Nature*, 399(6735), doi: 10.1038/20859.

Petrick, B. F., E. L. McClymont, F. Marret, and M. T. J. Van Der Meer (2015), Changing Surface Water Conditions for the Last 500 Ka in the Southeast Atlantic: Implica-

tions for Variable Influences of Agulhas Leakage and Benguela Upwelling, *Paleoceanography*, 30(9), 1153-1167, doi: 10.1002/2015pa002787.

Pharr, R. B., and D. F. Williams (1987), Shape Changes in Globorotalia-Truncatulinoidea as a Function of Ontogeny and Paleobiogeography in the Southern-Ocean, *Marine Micropaleontology*, 12(4), 343-355, doi: 10.1016/0377-8398(87)90027-2.

Piotrowski, A. M., S. L. Goldstein, S. R. Hemming, and R. G. Fairbanks (2004), Intensification and Variability of Ocean Thermohaline Circulation through the Last Deglaciation, *Earth and Planetary Science Letters*, 225(1-2), 205-220, doi: 10.1016/j.epsl.2004.06.002.

Piotrowski, A. M., S. L. Goldstein, S. R. Hemming, and R. G. Fairbanks (2005), Temporal Relationships of Carbon Cycling and Ocean Circulation at Glacial Boundaries, *Science*, 307(5717), 1933-1938, doi: 10.1126/science.1104883.

Polzin, K. L., J. M. Toole, J. R. Ledwell, and R. W. Schmitt (1997), Spatial Variability of Turbulent Mixing in the Abyssal Ocean, *Science*, 276(5309), 93-96, doi: 10.1126/science.276.5309.93.

Prell, W. L., W. H. Hutson, D. F. Williams, A. W. H. Be, K. Geitzenauer, and B. Molino (1980), Surface Circulation of the Indian-Ocean During the Last Glacial Maximum, Approximately 18,000 Yr Bp, *Quaternary Research*, 14(3), 309-336, doi: 10.1016/0033-5894(80)90014-9.

Quillevere, F., R. Morard, G. Escarguel, C. J. Douady, Y. Ujiie, T. De Garidel-Thoron, and C. De Vargas (2013), Global Scale Same-Specimen Morpho-Genetic Analysis of Truncorotalia Truncatulinoidea: A Perspective on the Morphological Species Concept in Planktonic Foraminifera, *Palaeogeography Palaeoclimatology Palaeoecology*, 391, 2-12, doi: 10.1016/j.palaeo.2011.03.013.

Rae, J. W. B., G. L. Foster, D. N. Schmidt, and T. Elliott (2011), Boron Isotopes and B/Ca in Benthic Foraminifera: Proxies for the Deep Ocean Carbonate System, *Earth and Planetary Science Letters*, 302(3-4), 403-413, doi: 10.1016/j.epsl.2010.12.034.

Rahmstorf, S. (1994), Rapid Climate Transitions in a Coupled Ocean-Atmosphere Model, *Nature*, 372(6501), 82-85, doi: 10.1038/372082a0.

Rahmstorf, S. (2002), Ocean Circulation and Climate During the Past 120,000 Years, *Nature*, 419(6903), 207-214, doi: 10.1038/nature01090.

Raitzsch, M., H. Kuhnert, J. Groeneveld, and T. Bickert (2008), Benthic Foraminifer Mg/Ca Anomalies in South Atlantic Core Top Sediments and Their Implications for Paleothermometry, *Geochemistry Geophysics Geosystems*, 9, doi: 10.1029/2007gc001788.

Raitzsch, M., H. Kuhnert, E. C. Hathorne, J. Groeneveld, and T. Bickert (2011), U/Ca in Benthic Foraminifers: A Proxy for the Deep-Sea Carbonate Saturation, *Geochemistry Geophysics Geosystems*, 12, doi: 10.1029/2010gc003344.

Ramsey, M. H., P. J. Potts, P. C. Webb, P. Watkins, J. S. Watson, and B. J. Coles (1995), An Objective Assessment of Analytical Method Precision - Comparison of Icp-Aes and Xrf for the Analysis of Silicate Rocks, *Chemical Geology*, 124(1-2), 1-19, doi: 10.1016/0009-2541(95)00020-m.

Rau, A., J. Rogers, and M. T. Chen (2006), Late Quaternary Palaeoceanographic Record in Giant Piston Cores Off South Africa, Possibly Including Evidence of Neotectonism, *Quaternary International*, 148, 65-77, doi: 10.1016/j.quaint.2005.11.007.

Rau, G. H., P. N. Froelich, T. Takahashi, and D. J. Des Marais (1991), Does Sedimentary Organic  $\delta^{13}\text{C}$  Record Variations in Quaternary Ocean  $[\text{CO}_2(\text{aq})]$ ?, *Paleoceanography*, 6(3), 335-347, doi: 10.1029/91pa00321.

Rau, A. J., J. Rogers, J. R. E. Lutjeharms, J. Giraudeau, J. A. Lee-Thorp, M. T. Chen, and C. Waelbroeck (2002), A 450-Kyr Record of Hydrological Conditions on the Western Agulhas Bank Slope, South of Africa, *Marine Geology*, 180(1-4), 183-201, doi: 10.1016/s0025-3227(01)00213-4.

Ravelo, A. C., and R. G. Fairbanks (1992), Oxygen Isotopic Composition of Multiple Species of Planktonic Foraminifera: Recorders of the Modern Photic Zone Temperature Gradient, *Paleoceanography*, 7(6), 815-831, doi: 10.1029/92pa02092.

Ravelo, A. C. and Hillaire-Marcel, C., (2007) 'Chapter Eighteen - The Use of Oxygen and Carbon Isotopes of Foraminifera in Paleoceanography', in Hillaire-Marcel, C., and De Vernal, A., (eds.), 'Developments in Marine Geology', Elsevier, Volume 1, Pages 735-764, ISSN1572-5480, ISBN9780444527554,

[http://dx.doi.org/10.1016/S1572-5480\(07\)01023-8](http://dx.doi.org/10.1016/S1572-5480(07)01023-8).

Raven, J. A., and P. G. Falkowski (1999), Oceanic Sinks for Atmospheric Co(2), *Plant Cell and Environment*, 22(6), doi: 10.1046/j.1365-3040.1999.00419.x.

Rea, D. (1994), The Paleoclimatic Record Provided by Eolian Deposition in the Deep-Sea - the Geologic History of Wind, *Reviews of Geophysics*, 32(2), 159-195, doi: 10.1029/93RG03257.

Read, J. F., M. I. Lucas, S. E. Holley, and R. T. Pollard (2000), Phytoplankton, Nutrients and Hydrography in the Frontal Zone between the Southwest Indian Subtropical Gyre and the Southern Ocean, *Deep-Sea Research Part I-Oceanographic Research Papers*, 47(12), 2341-2368, doi: 10.1016/s0967-0637(00)00021-2.

Regenberg, M., S. Steph, D. Nurnberg, R. Tiedemann, and D. Garbe-Schonberg (2009), Calibrating Mg/Ca Ratios of Multiple Planktonic Foraminiferal Species with Delta O-18-Calcification Temperatures: Paleothermometry for the Upper Water Column, *Earth and Planetary Science Letters*, 278(3-4), 324-336, doi: 10.1016/j.epsl.2008.12.019.

Reimer, P. J., et al. (2013), Intcal13 and Marine13 Radiocarbon Age Calibration Curves 0-50,000 Years Cal Bp, *Radiocarbon*, 55(4), 1869-1887.

Ren, H. J., D. M. Sigman, R. C. Thunell, and M. G. Prokopenko (2012), Nitrogen Isotopic Composition of Planktonic Foraminifera from the Modern Ocean and Recent Sediments, *Limnology and Oceanography*, 57(4), 1011-1024, doi: 10.4319/lo.2012.57.4.1011.

Ren, H., D. Sigman, A. Meckler, B. Plessen, R. Robinson, Y. Rosenthal, and G. Haug (2009), Foraminiferal Isotope Evidence of Reduced Nitrogen Fixation in the Ice Age Atlantic Ocean, *Science*, 323(5911), 244-248, doi: 10.1126/science.1165787.

Renaud, S., and D. N. Schmidt (2003), Habitat Tracking as a Response of the Planktic Foraminifer *Globorotalia Truncatulinoides* to Environmental Fluctuations During the Last 140 Kyr, *Marine Micropaleontology*, 49(1-2), 97-122, doi: 10.1016/s0377-8398(03)00031-8.

Revel-Rolland, M., P. De Deckker, B. Delmonte, P. P. Hesse, J. W. Magee, I. Basile-

- Doelsch, F. Grousset, and D. Bosch (2006), Eastern Australia: A Possible Source of Dust in East Antarctica Interglacial Ice, *Earth and Planetary Science Letters*, 249(1-2), doi: 10.1016/j.epsl.2006.06.028.
- Rickaby, R. E. M., and H. Elderfield (1999), Planktonic Foraminiferal Cd/Ca: Paleonutrients or Paleotemperature?, *Paleoceanography*, 14(3), 293-303, doi: 10.1029/1999pa900007.
- Rickaby, R. E. M., and H. Elderfield (2005), Evidence from the High-Latitude North Atlantic for Variations in Antarctic Intermediate Water Flow During the Last Deglaciation, *Geochemistry Geophysics Geosystems*, 6, doi: 10.1029/2004gc000858.
- Ridgwell, A. J. (2003), An End to the "Rain Ratio" Reign?, *Geochemistry Geophysics Geosystems*, 4, doi: 10.1029/2003gc000512.
- Ridgwell, A. J. (2003), Implications of the Glacial CO<sub>2</sub> "Iron Hypothesis" for Quaternary Climate Change, *Geochemistry Geophysics Geosystems*, 4, doi: 10.1029/2003gc000563.
- Ridgwell, A. J., and A. J. Watson (2002), Feedback between Aeolian Dust, Climate, and Atmospheric CO<sub>2</sub> in Glacial Time, *Paleoceanography*, 17(4), doi: 10.1029/2001pa000729.
- Ridgwell, A. J., A. J. Watson, and D. E. Archer (2002), Modeling the Response of the Oceanic Si Inventory to Perturbation, and Consequences for Atmospheric Co(2), *Global Biogeochemical Cycles*, 16(4), doi: 10.1029/2002gb001877.
- Rintoul, S. R., and T. W. Trull (2001), Seasonal Evolution of the Mixed Layer in the Subantarctic Zone South of Australia, *Journal of Geophysical Research-Oceans*, 106(C12), 31447-31462, doi: 10.1029/2000jc000329.
- Rintoul, S. R., Hughes, C., and Olbers, D., (2001), 'The Antarctic Circumpolar System', in Sielder, G., Church, J., and Gould, J., (eds.) 'Ocean Circulation and Climate', pp. 271–302, Academic Press, London.
- Robbins, L. L., Hansen, M. E., Kleypas, J. A., and Meylan, S. C., (2010), CO<sub>2</sub>calc—a user-friendly seawater carbon calculator for Windows, Max OS X, and iOS (iPhone), p. 17. U.S. Geological Survey Open-File Report 2010–1280.

- Roberts, J., J. Gottschalk, L. C. Skinner, V. L. Peck, S. Kender, H. Elderfield, C. Waelbroeck, N. V. Riveiros, and D. A. Hodell (2016), Evolution of South Atlantic Density and Chemical Stratification across the Last Deglaciation, *Proceedings of the National Academy of Sciences of the United States of America*, 113(3), 514-519, doi: 10.1073/pnas.1511252113.
- Robinson, R. S., and D. M. Sigman (2008), Nitrogen Isotopic Evidence for a Poleward Decrease in Surface Nitrate within the Ice Age Antarctic, *Quaternary Science Reviews*, 27(9-10), doi: 10.1016/j.quascirev.2008.02.005.
- Robinson, R. S., B. G. Brunelle, and D. M. Sigman (2004), Revisiting Nutrient Utilization in the Glacial Antarctic: Evidence from a New Method for Diatom-Bound N Isotopic Analysis, *Paleoceanography*, 19(3), doi: 10.1029/2003pa000996.
- Robinson, R. S., D. M. Sigman, P. J. Difiore, M. M. Rohde, T. A. Mashiotta, and D. W. Lea (2005), Diatom-Bound N-15/N-14: New Support for Enhanced Nutrient Consumption in the Ice Age Subantarctic, *Paleoceanography*, 20(3), doi: 10.1029/2004pa001114.
- Robinson, R. S., et al. (2012), A Review of Nitrogen Isotopic Alteration in Marine Sediments, *Paleoceanography*, 27, doi: 10.1029/2012pa002321.
- Rohling, E. J. (2000), Paleosalinity: Confidence Limits and Future Applications, *Marine Geology*, 163(1-4), 1-11, doi: 10.1016/s0025-3227(99)00097-3.
- Rohling, E. J. (2007), Progress in Paleosalinity: Overview and Presentation of a New Approach, *Paleoceanography*, 22(3), doi: 10.1029/2007pa001437.
- Rohling, E. J., and G. R. Bigg (1998), Paleosalinity and Delta O-18: A Critical Assessment, *Journal of Geophysical Research-Oceans*, 103(C1), 1307-1318, doi: 10.1029/97jc01047.
- Romero, O. E., J. H. Kim, M. A. Barcena, I. R. Hall, R. Zahn, and R. Schneider (2015), High-Latitude Forcing of Diatom Productivity in the Southern Agulhas Plateau During the Past 350kyr, *Paleoceanography*, 30(2), 118-132, doi: 10.1002/2014pa002636.
- Rosenthal, Y., E. A. Boyle, and L. Labeyrie (1997), Last Glacial Maximum Paleo-

chemistry and Deepwater Circulation in the Southern Ocean: Evidence from Foraminiferal Cadmium, *Paleoceanography*, 12(6), doi: 10.1029/97pa02508.

Rosenthal, Y., M. Dahan, and A. Shemesh (2000), Southern Ocean Contributions to Glacial-Interglacial Changes of Atmospheric  $P_{CO_2}$ : An Assessment of Carbon Isotope Records in Diatoms, *Paleoceanography*, 15(1), doi: 10.1029/1999pa000369.

Rosenthal, Y., P. Lam, E. A. Boyle, and J. Thomson (1995), Authigenic Cadmium Enrichments in Suboxic Sediments - Precipitation and Postdepositional Mobility, *Earth and Planetary Science Letters*, 132(1-4), 99-111, doi: 10.1016/0012-821x(95)00056-i.

Rothlisberger, R., M. Bigler, E. W. Wolff, F. Joos, E. Monnin, and M. A. Hutterli (2004), Ice Core Evidence for the Extent of Past Atmospheric  $CO_2$  Change Due to Iron Fertilisation, *Geophysical Research Letters*, 31(16), doi: 10.1029/2004gl020338.

Rothwell, R.G., and Rack, F. R., (2006), New techniques in sediment core analysis: an introduction, in Rothwell, R.G. (Ed.), *New Techniques in Sediment Core Analysis*. Special Publication, Geological Society, London. 267, 1-29.

Russell, A. D., S. Emerson, A. C. Mix, and L. C. Peterson (1996), The Use of Foraminiferal Uranium/Calcium Ratios as an Indicator of Changes in Seawater Uranium Content, *Paleoceanography*, 11(6), 649-663, doi: 10.1029/96pa02058.

Russell, A. D., B. Honisch, H. J. Spero, and D. W. Lea (2004), Effects of Seawater Carbonate Ion Concentration and Temperature on Shell U, Mg, and Sr in Cultured Planktonic Foraminifera, *Geochimica Et Cosmochimica Acta*, 68(21), 4347-4361, doi: 10.1016/j.gca.2004.03.013.

Russell, A. D., S. Emerson, B. K. Nelson, J. Erez, and D. W. Lea (1994), Uranium in Foraminiferal Calcite as a Recorder of Seawater Uranium Concentrations, *Geochimica Et Cosmochimica Acta*, 58(2), 671-681, doi: 10.1016/0016-7037(94)90497-9.

Rutberg, R. L., S. R. Hemming, and S. L. Goldstein (2000), Reduced North Atlantic Deep Water Flux to the Glacial Southern Ocean Inferred from Neodymium Isotope Ratios, *Nature*, 405(6789), 935-938.

Sachs, J. P., and R. F. Anderson (2003), Fidelity of Alkenone Paleotemperatures in

Southern Cape Basin Sediment Drifts, *Paleoceanography*, 18(4), doi: 10.1029/2002pa000862.

Sachs, J. P., and R. F. Anderson (2005), Increased Productivity in the Subantarctic Ocean During Heinrich Events, *Nature*, 434(7037), doi: 10.1038/nature03544.

Sanyal, A., N. G. Hemming, G. N. Hanson, and W. S. Broecker (1995), Evidence for a Higher Ph in the Glacial Ocean from Boron Isotopes in Foraminifera, *Nature*, 373(6511), doi: 10.1038/373234a0.

Sarmiento, J., and J. Toggweiler (1984), A New Model for the Role of the Oceans in Determining Atmospheric PCO<sub>2</sub>, *Nature*, 308(5960), 621-624, doi: 10.1038/308621a0.

Sarmiento, J. L., and Gruber, N. (2006), *Ocean Biogeochemical Dynamics*, Princeton University Press.

Sarmiento, J., N. Gruber, M. Brzezinski, and J. Dunne (2004), High-Latitude Controls of Thermocline Nutrients and Low Latitude Biological Productivity, *Nature*, 427(6969), 56-60, doi: 10.1038/nature02127.

Schefuss, E., H. Kuhlmann, G. Mollenhauer, M. Prange, and J. Patzold (2011), Forcing of Wet Phases in Southeast Africa over the Past 17,000 Years, *Nature*, 480(7378), 509-512, doi: 10.1038/nature10685.

Schlitzer, R., (2016), Ocean Data View, <http://odv.awi.de>.

Schmidt, G. A. (1999), Forward Modeling of Carbonate Proxy Data from Planktonic Foraminifera Using Oxygen Isotope Tracers in a Global Ocean Model, *Paleoceanography*, 14(4), 482-497, doi: 10.1029/1999pa900025.

Schmidt, G. A. (1999), Error Analysis of Paleosalinity Calculations, *Paleoceanography*, 14(3), 422-429, doi: 10.1029/1999pa900008.

Schmidt, G. A., and S. Mulitza (2002), Global Calibration of Ecological Models for Planktic Foraminifera from Coretop Carbonate Oxygen-18, *Marine Micropaleontology*, 44(3-4), 125-140, doi: 10.1016/s0377-8398(01)00041-x.

Schmitt, J., et al. (2012), Carbon Isotope Constraints on the Deglacial CO<sub>2</sub> Rise from

Ice Cores, *Science*, 336(6082), 711-714, doi: 10.1126/science.1217161.

Schneider, R., J. Schmitt, P. Kohler, F. Joos, and H. Fischer (2013), A Reconstruction of Atmospheric Carbon Dioxide and Its Stable Carbon Isotopic Composition from the Penultimate Glacial Maximum to the Last Glacial Inception, *Climate of the Past*, 9(6), 2507-2523, doi: 10.5194/cp-9-2507-2013.

Schouten, S., E. C. Hopmans, E. Schefuss, and J. S. S. Damste (2002), Distributional Variations in Marine Crenarchaeotal Membrane Lipids: A New Tool for Reconstructing Ancient Sea Water Temperatures?, *Earth and Planetary Science Letters*, 204(1-2), 265-274, doi: 10.1016/s0012-821x(02)00979-2.

Schrag, D. P., J. F. Adkins, K. McIntyre, J. L. Alexander, D. A. Hodell, C. D. Charles, and J. F. McManus (2002), The Oxygen Isotopic Composition of Seawater During the Last Glacial Maximum, *Quaternary Science Reviews*, 21(1-3), 331-342, doi: 10.1016/s0277-3791(01)00110-x.

Scussolini, P., and F. J. C. Peeters (2013), A Record of the Last 460 Thousand Years of Upper Ocean Stratification from the Central Walvis Ridge, South Atlantic, *Paleoceanography*, 28(3), 426-439, doi: 10.1002/palo.20041.

Shackleton, N. (1967), Oxygen Isotope Analyses and Pleistocene Temperatures Re-Assessed, *Nature*, 215(5096), 15-+, doi: 10.1038/215015a0.

Shackleton, N. J., (1974), Attainment of isotopic equilibrium between ocean water and the benthonic foraminifera genus *Uvigerina*: isotopic changes in the ocean during the last glacial, *Colloques Internationaux du C.N.R.S* 219, 203–209.

Shackleton, N.J., (1977), Carbon 13 in *Uvigerina*: Tropical rain forest history and the equatorial Pacific carbonate dissolution cycles, in Anderson, N.R., and Malahoff, A., (eds.), *The Fate of Fossil Fuel CO<sub>2</sub> in the Ocean*, pp. 401-428. New York: Plenum.

Shackleton, N. J. (2000), The 100,000-Year Ice-Age Cycle Identified and Found to Lag Temperature, Carbon Dioxide, and Orbital Eccentricity, *Science*, 289(5486), 1897-1902, doi: 10.1126/science.289.5486.1897.

Shackleton, N. J., M. A. Hall, J. Line, and C. Shuxi (1983), Carbon Isotope Data in

Core V19-30 Confirm Reduced Carbon-Dioxide Concentration in the Ice-Age Atmosphere, *Nature*, 306(5941), 319-322, doi: 10.1038/306319a0.

Shemesh, A., D. Hodell, X. Crosta, S. Kanfoush, C. Charles, and T. Guilderson (2002), Sequence of Events During the Last Deglaciation in Southern Ocean Sediments and Antarctic Ice Cores, *Paleoceanography*, 17(4), doi: 10.1029/2000pa000599.

Siddall, M., E. J. Rohling, A. Almogi-Labin, C. Hemleben, D. Meischner, I. Schmelzer, and D. A. Smeed (2003), Sea-Level Fluctuations During the Last Glacial Cycle, *Nature*, 423(6942), doi: 10.1038/nature01690.

Siegenthaler, U., and T. Wenk (1984), Rapid Atmospheric CO<sub>2</sub> Variations and Ocean Circulation, *Nature*, 308(5960), 624-626, doi: 10.1038/308624a0.

Siegenthaler, U., and J. L. Sarmiento (1993), Atmospheric Carbon-Dioxide and the Ocean, *Nature*, 365(6442), 119-125, doi: 10.1038/365119a0.

Siegenthaler, U., et al. (2005), Stable Carbon Cycle-Climate Relationship During the Late Pleistocene, *Science*, 310(5752), 1313-1317, doi: 10.1126/science.1120130.

Sigman, D., and E. Boyle (2000), Glacial/Interglacial Variations in Atmospheric Carbon Dioxide, *Nature*, 407(6806), 859-869, doi: 10.1038/35038000.

Sigman, D.M., and Haug, G.H., (2003), The biological pump in the past, in Elderfield, H., (ed.) *Treatise on Geochemistry, The Oceans and Marine Geochemistry*, vol. 6, pp. 491-528. Oxford: Elsevier Pergamon.

Sigman, D. M., D. C. McCorkle, and W. R. Martin (1998), The Calcite Lysocline as a Constraint on Glacial/Interglacial Low-Latitude Production Changes, *Global Biogeochemical Cycles*, 12(3), doi: 10.1029/98gb01184.

Sigman, D., S. Jaccard, and G. Haug (2004), Polar Ocean Stratification in a Cold Climate, *Nature*, 428(6978), 59-63, doi: 10.1038/nature02357.

Sigman, D., M. Hain, and G. Haug (2010), The Polar Ocean and Glacial Cycles in Atmospheric CO<sub>2</sub> Concentration, *Nature*, 466(7302), 47-55, doi: 10.1038/nature09149.

Sigman, D. M., M. A. Altabet, R. Francois, D. C. McCorkle, and J. F. Gaillard (1999),

The Isotopic Composition of Diatom-Bound Nitrogen in Southern Ocean Sediments, *Paleoceanography*, 14(2), doi: 10.1029/1998pa900018.

Sigman, D. M., M. A. Altabet, D. C. McCorkle, R. Francois, and G. Fischer (1999), The Delta N-15 of Nitrate in the Southern Ocean: Consumption of Nitrate in Surface Waters, *Global Biogeochemical Cycles*, 13(4), 1149-1166, doi: 10.1029/1999gb900038.

Sigman, D. M., M. A. Altabet, D. C. McCorkle, R. Francois, and G. Fischer (2000), The Delta N-15 of Nitrate in the Southern Ocean: Nitrogen Cycling and Circulation in the Ocean Interior, *Journal of Geophysical Research-Oceans*, 105(C8), 19599-19614, doi: 10.1029/2000jc000265.

Sikes, E. L., C. R. Samson, T. P. Guilderson, and W. R. Howard (2000), Old Radiocarbon Ages in the Southwest Pacific Ocean During the Last Glacial Period and Deglaciation, *Nature*, 405(6786), doi: 10.1038/35014581.

Simon, M. H., M. Ziegler, J. Bosmans, S. Barker, C. J. C. Reason, and I. R. Hall (2015), Eastern South African Hydroclimate over the Past 270,000 Years, *Scientific Reports*, 5, doi: 10.1038/srep18153.

Simon, M. H., K. L. Arthur, I. R. Hall, F. J. C. Peeters, B. R. Loveday, S. Barker, M. Ziegler, and R. Zahn (2013), Millennial-Scale Agulhas Current Variability and Its Implications for Salt-Leakage through the Indian-Atlantic Ocean Gateway, *Earth and Planetary Science Letters*, 383, 101-112, doi: 10.1016/j.epsl.2013.09.035.

Skinner, L. C., S. Fallon, C. Waelbroeck, E. Michel, and S. Barker (2010), Ventilation of the Deep Southern Ocean and Deglacial CO<sub>2</sub> Rise, *Science*, 328(5982), doi: 10.1126/science.1183627.

Smith, H. J., H. Fischer, M. Wahlen, D. Mastroianni, and B. Deck (1999), Dual Modes of the Carbon Cycle since the Last Glacial Maximum, *Nature*, 400(6741), 248-250, doi: 10.1038/22291.

Sokolov, S., and S. R. Rintoul (2002), Structure of Southern Ocean Fronts at 140 Degrees E, *Journal of Marine Systems*, 37(1-3), 151-184, doi: 10.1016/s0924-7963(02)00200-2.

- Sokolov, S., and S. R. Rintoul (2009), Circumpolar Structure and Distribution of the Antarctic Circumpolar Current Fronts: 1. Mean Circumpolar Paths, *Journal of Geophysical Research-Oceans*, 114, doi: 10.1029/2008jc005108.
- Sosdian, S., and Y. Rosenthal (2009), Deep-Sea Temperature and Ice Volume Changes across the Pliocene-Pleistocene Climate Transitions, *Science*, 325(5938), 306-310, doi: 10.1126/science.1169938.
- Southon, J., M. Kashgarian, M. Fontugne, B. Metivier, and W. W. S. Yim (2002), Marine Reservoir Corrections for the Indian Ocean and Southeast Asia, *Radiocarbon*, 44(1), 167-180.
- Spencer, C., and H. R. Thierstein (1997), First Appearance of *Globorotalia truncatulinoides*: Cladogenesis and Immigration, *Marine Micropaleontology*, 30(4), 267-291, doi: 10.1016/s0377-8398(97)00004-2.
- Spero, H., and D. Lea (2002), The Cause of Carbon Isotope Minimum Events on Glacial Terminations, *Science*, 296(5567), 522-525, doi: 10.1126/science.1069401.
- Stager, J. C., D. B. Ryves, B. M. Chase, and F. S. R. Pausata (2011), Catastrophic Drought in the Afro-Asian Monsoon Region During Heinrich Event 1, *Science*, 331(6022), 1299-1302, doi: 10.1126/science.1198322.
- Steph, S., M. Regenberg, R. Tiedemann, S. Mulitza, and D. Nurnberg (2009), Stable Isotopes of Planktonic Foraminifera from Tropical Atlantic/Caribbean Core-Tops: Implications for Reconstructing Upper Ocean Stratification, *Marine Micropaleontology*, 71(1-2), 1-19, doi: 10.1016/j.marmicro.2008.12.004.
- Stephens, B., and R. Keeling (2000), The Influence of Antarctic Sea Ice on Glacial-Interglacial CO<sub>2</sub> Variations, *Nature*, 404(6774), 171-174, doi: 10.1038/35004556.
- Straub, M., D. M. Sigman, H. J. Ren, A. Martinez-Garcia, A. N. Meckler, M. P. Hain, and G. H. Haug (2013), Changes in North Atlantic Nitrogen Fixation Controlled by Ocean Circulation, *Nature*, 501(7466), 200-+, doi: 10.1038/nature12397.
- Stüber, A., (1999), Spätpleistocene Variabilität der Zwischenwasserzirkulation im subtropischen Westatlantik auf glazial-interglazialen und suborbitalen Zeitskalen: Rekonstruktion anhand stabiler Kohlenstoffisotope und Spurenmetallverhältnissen in

- kalkschaligen Benthosforaminiferen, Christian-Albrechts Universität, Kiel.
- Stuiver, M., and T. F. Braziunas (1993a), Modeling Atmospheric C-14 Influences and C-14 Ages of Marine Samples to 10,000 BC, *Radiocarbon*, 35(1), 137-189.
- Stuiver, M., and Braziunas, T.F., (1993b), Sun, ocean, climate and atmospheric  $^{14}\text{CO}_2$ : an evaluation of causal and spectral relationships, *The Holocene* 3, 289-305.
- Stuiver, M., P. J. Reimer, E. Bard, J. W. Beck, G. S. Burr, K. A. Hughen, B. Kromer, G. McCormac, J. Van Der Plicht, and M. Spurk (1998), Intcal98 Radiocarbon Age Calibration, 24,000-0 Cal Bp, *Radiocarbon*, 40(3), 1041-1083.
- Takayanagi, Y., N. Niitsuma, and T. Sakai (1968), Wall microstructure of *Globorotalia truncatulinoides* (d'Orbigny), *Sci. Rep. Tohoku Univ.*, 40(2), 141-170.
- Takeda, S. (1998), Influence of Iron Availability on Nutrient Consumption Ratio of Diatoms in Oceanic Waters, *Nature*, 393(6687), 774-777, doi: 10.1038/31674.
- Talley, L. D. (2013), Closure of the Global Overturning Circulation through the Indian, Pacific, and Southern Oceans: Schematics and Transports, *Oceanography*, 26(1), 80-97.
- Talley, L. D., Pickard, G. E., Emery, W. J., and Swift, J. H., (2011), *Descriptive Physical Oceanography: An introduction*, 6th ed. Elsevier, Burlington, MA, 560 pp.
- Tisserand, A. A., T. M. Dokken, C. Waelbroeck, J. M. Gherardi, V. Scao, C. Fontanier, and F. Jorissen (2013), Refining Benthic Foraminiferal Mg/Ca-Temperature Calibrations Using Core-Tops from the Western Tropical Atlantic: Implication for Paleotemperature Estimation, *Geochemistry Geophysics Geosystems*, 14(4), 929-946, doi: 10.1002/ggge.20043.
- Toggweiler, J. (1999), Variation of Atmospheric CO<sub>2</sub> by Ventilation of the Ocean's Deepest Water, *Paleoceanography*, 14(5), 571-588, doi: 10.1029/1999PA900033.
- Toggweiler, J. (2009), Shifting Westerlies, *Science*, 323(5920), 1434-1435, doi: 10.1126/science.1169823.
- Toggweiler, J. R., K. Dixon, and W. S. Broecker (1991), The Peru Upwelling and the Ventilation of the South-Pacific Thermocline, *Journal of Geophysical Research-*

Oceans, 96(C11), 20467-20497, doi: 10.1029/91jc02063.

Toggweiler, J., J. Russell, and S. Carson (2006), Midlatitude Westerlies, Atmospheric CO<sub>2</sub>, and Climate Change During the Ice Ages, *Paleoceanography*, 21(2), doi: 10.1029/2005PA001154.

Toggweiler, J. R., A. Gnanadesikan, S. Carson, R. Murnane, and J. L. Sarmiento (2003), Representation of the Carbon Cycle in Box Models and Gcms: 1. Solubility Pump, *Global Biogeochemical Cycles*, 17(1), doi: 10.1029/2001gb001401.

Toggweiler, J., R. Murnane, S. Carson, A. Gnanadesikan, and J. Sarmiento (2003), Representation of the Carbon Cycle in Box Models and Gcms - 2. Organic Pump, *Global Biogeochemical Cycles*, 17(1), doi: 10.1029/2001GB001841.

Treguer, P. (2002), Silica and the Cycle of Carbon in the Ocean, *Comptes Rendus Geoscience*, 334(1), doi: 10.1016/s1631-0713(02)01680-2.

Treguer, P., and P. Pondaven (2000), Global Change - Silica Control of Carbon Dioxide, *Nature*, 406(6794), 358-359, doi: 10.1038/35019236.

Tucholke, B. E., and G. B. Carpenter (1977), Sediment Distribution and Cenozoic Sedimentation Patterns on Agulhas Plateau, *Geological Society of America Bulletin*, 88(9), 1337-1346, doi: 10.1130/0016-7606(1977)88<1337:sdacsp>2.0.co;2.

Tyrrell, T. (1999), The Relative Influences of Nitrogen and Phosphorus on Oceanic Primary Production, *Nature*, 400(6744), doi: 10.1038/22941.

Uenzelmann-Neben, G. (2001), Seismic Characteristics of Sediment Drifts: An Example from the Agulhas Plateau, Southwest Indian Ocean, *Marine Geophysical Researches*, 22(5-6), 323-+, doi: 10.1023/a:1016391314547.

Ujii, Y., and J. H. Lipps (2009), Cryptic Diversity in Planktic Foraminifera in the Northwest Pacific Ocean, *Journal of Foraminiferal Research*, 39(3), 145-154.

Urey, H. C. (1947), The Thermodynamic Properties of Isotopic Substances, *Journal of the Chemical Society(MAY)*, 562-581, doi: 10.1039/jr9470000562.

Urey, H. C. (1948), Oxygen Isotopes in Nature and in the Laboratory, *Science*, 108(2810), 489-496, doi: 10.1126/science.108.2810.489.

Van Sebille, E., A. Biastoch, P. J. Van Leeuwen, and W. P. M. De Ruijter (2009), A Weaker Agulhas Current Leads to More Agulhas Leakage, *Geophysical Research Letters*, 36, doi: 10.1029/2008gl036614.

Vellinga, M., and R. A. Wood (2002), Global Climatic Impacts of a Collapse of the Atlantic Thermohaline Circulation, *Climatic Change*, 54(3), 251-267, doi: 10.1023/a:1016168827653.

Venz, K. A., and D. A. Hodell (2002), New Evidence for Changes in Plio-Pleistocene Deep Water Circulation from Southern Ocean ODP Leg 177 Site 1090, *Palaeogeography Palaeoclimatology Palaeoecology*, 182(3-4), doi: 10.1016/s0031-0182(01)00496-5.

Vergnaud-Grazzini, C., (1976), Non-equilibrium isotopic compositions of shells of planktonic foraminifera in the Mediterranean Sea, *Palaeogeography, Palaeoclimatology, Palaeoecology*, 20(4), 263–276.

Volk, T., and Hoffert, M. I., (1985), Ocean carbon pumps: Analysis of relative strengths and efficiencies in ocean driven atmospheric CO<sub>2</sub> changes, in Sundquist, E. T., and Broecker, W. S., (eds.), *The Carbon Cycle and Atmospheric CO<sub>2</sub>: Natural Variations Archean to Present*, Geophysical Monograph Series, vol. 32, pp. 99–110. Washington, DC: American Geophysical Union.

Voss, M., J. W. Dippner, and J. P. Montoya (2001), Nitrogen Isotope Patterns in the Oxygen-Deficient Waters of the Eastern Tropical North Pacific Ocean, *Deep-Sea Research Part I-Oceanographic Research Papers*, 48(8), 1905-1921, doi: 10.1016/s0967-0637(00)00110-2.

Waelbroeck, C., L. Labeyrie, E. Michel, J. C. Duplessy, J. F. McManus, K. Lambeck, E. Balbon, and M. Labracherie (2002), Sea-Level and Deep Water Temperature Changes Derived from Benthic Foraminifera Isotopic Records, *Quaternary Science Reviews*, 21(1-3), 295-305, doi: 10.1016/s0277-3791(01)00101-9.

Waelbroeck, C., et al. (2009), Constraints on the Magnitude and Patterns of Ocean Cooling at the Last Glacial Maximum, *Nature Geoscience*, 2(2), 127-132, doi: 10.1038/ngeo411.

Wang, Y. J., H. Cheng, R. L. Edwards, Z. S. An, J. Y. Wu, C. C. Shen, and J. A. Dorale

(2001), A High-Resolution Absolute-Dated Late Pleistocene Monsoon Record from Hulu Cave, China, *Science*, 294(5550), 2345-2348, doi: 10.1126/science.1064618.

Wang, Y. J., H. Cheng, R. L. Edwards, X. G. Kong, X. H. Shao, S. T. Chen, J. Y. Wu, X. Y. Jiang, X. F. Wang, and Z. S. An (2008), Millennial- and Orbital-Scale Changes in the East Asian Monsoon over the Past 224,000 Years, *Nature*, 451(7182), 1090-1093, doi: 10.1038/nature06692.

Watson, A. J., and N. Lefevre (1999), The Sensitivity of Atmospheric CO<sub>2</sub> Concentrations to Input of Iron to the Oceans, *Tellus Series B-Chemical and Physical Meteorology*, 51(2), doi: 10.1034/j.1600-0889.1999.00022.x.

Watson, A. J., and A. C. N. Garabato (2006), The Role of Southern Ocean Mixing and Upwelling in Glacial-Interglacial Atmospheric CO<sub>2</sub> Change, *Tellus Series B-Chemical and Physical Meteorology*, 58(1), doi: 10.1111/j.1600-0889.2005.00167.x.

Watson, A. J., D. C. E. Bakker, A. J. Ridgwell, P. W. Boyd, and C. S. Law (2000), Effect of Iron Supply on Southern Ocean CO<sub>2</sub> Uptake and Implications for Glacial Atmospheric CO<sub>2</sub>, *Nature*, 407(6805), 730-733, doi: 10.1038/35037561.

Watson, A. J., C. S. Law, K. A. Vanscoy, F. J. Millero, W. Yao, G. E. Friederich, M. I. Liddicoat, R. H. Wanninkhof, R. T. Barber, and K. H. Coale (1994), Minimal Effect of Iron Fertilization on Sea-Surface Carbon-Dioxide Concentrations, *Nature*, 371(6493), doi: 10.1038/371143a0.

Weaver, P. P. E., L. Carter, and H. L. Neil (1998), Response of Surface Water Masses and Circulation to Late Quaternary Climate Change East of New Zealand, *Paleoceanography*, 13(1), 70-83, doi: 10.1029/97pa02982.

Weijer, W., W. P. M. De Ruijter, H. A. Dijkstra, and P. J. Van Leeuwen (1999), Impact of Interbasin Exchange on the Atlantic Overturning Circulation, *Journal of Physical Oceanography*, 29(9), 2266-2284, doi: 10.1175/1520-0485(1999)029<2266:ioieot>2.0.co;2.

Weijer, W., W. P. M. De Ruijter, A. Sterl, and S. S. Drujfhout (2002), Response of the Atlantic Overturning Circulation to South Atlantic Sources of Buoyancy, *Global and Planetary Change*, 34(3-4), 293-311, doi: 10.1016/s0921-8181(02)00121-2.

Weltje, G. J., and R. Tjallingii (2008), Calibration of Xrf Core Scanners for Quantitative Geochemical Logging of Sediment Cores: Theory and Application, *Earth and Planetary Science Letters*, 274(3-4), 423-438, doi: 10.1016/j.epsl.2008.07.054.

Whitworth, T., and R. G. Peterson (1985), Volume Transport of the Antarctic Circumpolar Current from Bottom Pressure Measurements, *Journal of Physical Oceanography*, 15(6), 810-816, doi: 10.1175/1520-0485(1985)015<0810:vtotac>2.0.co;2.

Willamowski, C., and R. Zahn (2000), Upper Ocean Circulation in the Glacial North Atlantic from Benthic Foraminiferal Isotope and Trace Element Fingerprinting, *Paleoceanography*, 15(5), 515-527, doi: 10.1029/1999pa000467.

Wolff, E., H. Fischer, and R. Rothlisberger (2009), Glacial Terminations as Southern Warmings without Northern Control, *Nature Geoscience*, 2(3), 206-209, doi: 10.1038/NGEO442.

Wolff, E., et al. (2006), Southern Ocean Sea-Ice Extent, Productivity and Iron Flux over the Past Eight Glacial Cycles, *Nature*, 440(7083), 491-496, doi: 10.1038/nature04614.

Woodard, S. C., Y. Rosenthal, K. G. Miller, J. D. Wright, B. K. Chiu, and K. T. Lawrence (2014), Antarctic Role in Northern Hemisphere Glaciation, *Science*, 346(6211), 847-851, doi: 10.1126/science.1255586.

Wyrwoll, K. H., B. W. Dong, and P. Valdes (2000), On the Position of Southern Hemisphere Westerlies at the Last Glacial Maximum: An Outline of Agcm Simulation Results and Evaluation of Their Implications, *Quaternary Science Reviews*, 19(9), doi: 10.1016/s0277-3791(99)00047-5.

Yu, J. M., and H. Elderfield (2007), Benthic Foraminiferal B/Ca Ratios Reflect Deep Water Carbonate Saturation State, *Earth and Planetary Science Letters*, 258(1-2), 73-86, doi: 10.1016/j.epsl.2007.03.025.

Yu, J. M., and W. S. Broecker (2010), Comment on "Deep-Sea Temperature and Ice Volume Changes across the Pliocene-Pleistocene Climate Transitions", *Science*, 328(5985), doi: 10.1126/science.1186544.

Yu, J. M., H. Elderfield, and B. Honisch (2007), B/Ca in Planktonic Foraminifera as a

Proxy for Surface Seawater Ph, *Paleoceanography*, 22(2), doi: 10.1029/2006pa001347.

Yu, J. M., H. Elderfield, Z. D. Jin, and L. Booth (2008), A Strong Temperature Effect on U/Ca in Planktonic Foraminiferal Carbonates, *Geochimica Et Cosmochimica Acta*, 72(20), 4988-5000, doi: 10.1016/j.gca.2008.07.011.

Yu, J. M., D. J. R. Thornalley, J. W. B. Rae, and N. I. McCave (2013), Calibration and Application of B/Ca, Cd/Ca, and Delta B-11 in *Neogloboquadrina Pachyderma* (Sinistral) to Constrain CO<sub>2</sub> Uptake in the Subpolar North Atlantic During the Last Deglaciation, *Paleoceanography*, 28(2), 237-252, doi: 10.1002/palo.20024.

Yu, J. M., R. F. Anderson, Z. D. Jin, L. Menviel, F. Zhang, F. J. Ryerson, and E. J. Rohling (2014), Deep South Atlantic Carbonate Chemistry and Increased Interocean Deep Water Exchange During Last Deglaciation, *Quaternary Science Reviews*, 90, 80-89, doi: 10.1016/j.quascirev.2014.02.018.

Yu, J., et al. (2016), Sequestration of Carbon in the Deep Atlantic During the Last Glaciation, *Nature Geoscience*, 9(4), 319+, doi: 10.1038/ngeo2657.

Yuan, D. X., et al. (2004), Timing, Duration, and Transitions of the Last Interglacial Asian Monsoon, *Science*, 304(5670), 575-578, doi: 10.1126/science.1091220.

Zabel, M., R. R. Schneider, T. Wagner, A. T. Adegbe, U. De Vries, and S. Kolonic (2001), Late Quaternary Climate Changes in Central Africa as Inferred from Terrestrial Input to the Niger Fan, *Quaternary Research*, 56(2), 207-217, doi: 10.1006/qres.2001.2261.

Zahn, R., and A. Stuber (2002), Suborbital Intermediate Water Variability Inferred from Paired Benthic Foraminiferal Cd/Ca and Delta C-13 in the Tropical West Atlantic and Linking with North Atlantic Climates, *Earth and Planetary Science Letters*, 200(1-2), 191-205, doi: 10.1016/s0012-821x(02)00613-1.

Zeebe, R. E., and Wolf-Gladrow, D. A., (2001), CO<sub>2</sub> in Seawater: Equilibrium, Kinetics, *Isotopes*, Elsevier Oceanography Series, 65, pp. 346, Amsterdam, 2001.

Ziegler, M., P. Diz, I. R. Hall, and R. Zahn (2013), Millennial-Scale Changes in Atmospheric CO<sub>2</sub> Levels Linked to the Southern Ocean Carbon Isotope Gradient and

Dust Flux, Nature Geoscience, 6(6), 457-461, doi: 10.1038/ngeo1782.